

**Structure-guided Approaches to the Design of Novel Autotaxin
Inhibitors**

Frances Potjewyd

Thesis

October 2016

**Structure-guided Approaches to the Design of Novel Autotaxin
Inhibitors**

by

Frances Potjewyd

Declaration of Copyright

This thesis is a result of the author's original research. It has been composed by the author and has not been previously submitted for examination which has led to the award of a degree.

The copyright of this thesis belongs to the author under the terms of the United Kingdom Copyright Acts as qualified by University of Strathclyde Regulation 3.50. Due acknowledgement must always be made of the use of any material contained in, or derived from, this thesis.

Signed:

Date:

Abstract

Autotaxin (ATX) is a secreted enzyme responsible for the production and subsequent delivery of lysophosphatidic acid (LPA) to G-protein coupled receptors (GPCR) LPA₁₋₆. LPA binds at LPA₁ to induce downstream signaling effects such as migration, proliferation and survival of cells.¹ The ATX-LPA signaling pathway is implicated in a vast number of conditions such as; idiopathic pulmonary fibrosis, cancer, angiogenesis, osteoarthritis, and cardiovascular diseases.² ATX consists of an active site containing two zinc atoms adjacent to a large hydrophobic pocket. The active site is solvent accessible *via* a hydrophobic tunnel unique to this family of enzymes. Reported ATX inhibitors contain common pharmacophores consisting of a zinc binding ‘warhead’ and a lipophilic region, which reside in the active site and hydrophobic pocket respectively. This is best exemplified by PF-8380, a known ATX inhibitor (IC₅₀ = 2.8 nM, **Figure 1**).²

This thesis will explore the development of a structure-activity relationship (SAR) of tool compound PF-8380, resulting in a highly potent hit compound containing a novel diamine core. Within this emerging series, we sought to tune key physicochemical parameters whilst maintaining potency at ATX. The lead series focused on compounds containing this diamine core in combination with novel zinc binders. Resulting compounds were tested in BJEH fibroblast cell lines, showing a significant inhibitory effect on downstream signaling.

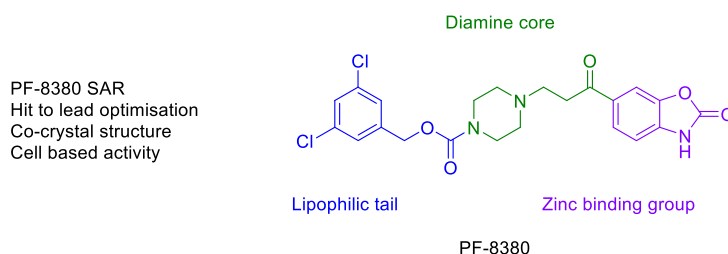


Figure 1 Development of PF-8380 SAR.

In a related study, analysis of the apo form of ATX showed the presence of ‘ghost’ electron density in the tunnel region. This density was resolved as a bile salt, which was residing in the hydrophobic tunnel of ATX (UDCA IC₅₀ = 8.8 μM).³ Merging this information with the SAR landscape described above, we developed a structure based design approach of hybrid UDCA-PF compounds, utilizing this endogenous modulator of ATX. Hybrid compounds span both the tunnel and hydrophobic pocket of ATX, resulting in highly potent steroid-PF analogues.

The binding mode hypothesis was confirmed by co-crystallographic data bound to ATX, and a kinetic study. Additionally, compounds also exhibited significant cell based activity and promising *in vivo* results (**Figure 2**).

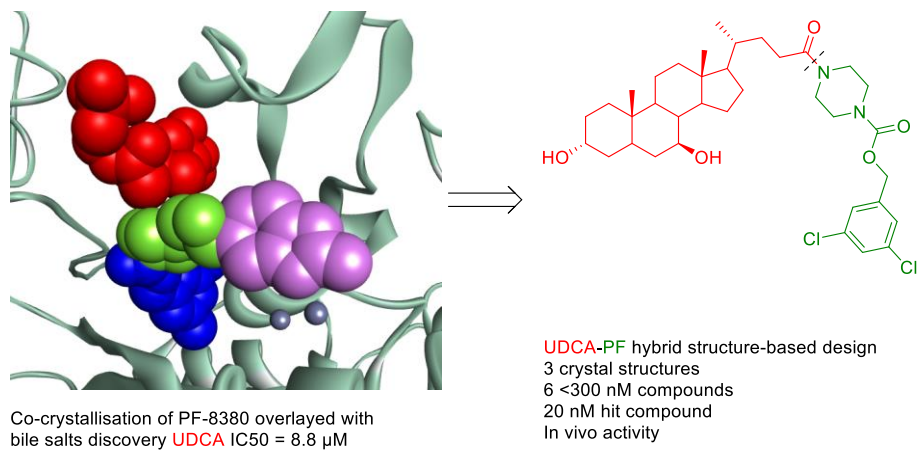


Figure 2 Co-crystallographic data leading to structure-based design of UDCA-PF hybrid inhibitors.

Acknowledgements

Firstly, I would like to thank my supervisor Dr Craig Jamieson for providing me with a great project, and his support along the way. Thanks also go to my second supervisor Dr Allan Watson for his advice and enthusiasm, and I hope to one day beat him at the toastie and gin challenge.

I would like to thank my collaborators at NKI, Dr Willem-Jan Keune, Fernando Salgado-Pollo, Tatjana Heidebrecht, and Prof Anastassis Perrakis for their biology expertise, as the project would be insurmountable without their help and dedication. The team ran the kinetics, the biochemical assay data, and BJEH cell based assay in Chapter 3, as well as co-crystallising compounds **2.1**, **3.25**, **3.31**, and **3.40** within ATX. I also show gratitude to the team at NKI for teaching me how to run biochemical assays, and looking after me during my secondment in Amsterdam.

I thank GSK and the EPSRC for funding my project, and my PhD supervisor Simon Macdonald for his advice during my secondment and throughout the PhD.

I would like to thank collaborators Prof Andrew Morris, Lakshman Chelvarajan, Dr Ahmed Abdel Latif, and Sony Soman from the Division of Cardiovascular Medicine and the Gill Heart Institute in Kentucky for their *in vivo* data in Chapter 3.

Special thanks go to Craig Irving in NMR for running the NMR facilities to such a high standard and for his entertaining conversations during my PhD.

I value the support from team fibrosis Emma Duffy, Diana Castagna, Lisa Miller, and Jenny Clark who represent the past, present and future of the team, and for their support during my PhD. Alongside all members of the Watson-Jamieson research groups who have brought hilarity to every day. Especially Jamie Fyfe, and Lisa Miller who have been with me from day one, and put up with my bold claims in the pub.

I am grateful for my families love, understanding, and providing me with many roast dinners and cake. In particular I would like to thank Ciaran Seath for his constant support, encouragement, care, and occasional humour throughout my time in Glasgow – he's a funny guy.

Abbreviations

EC ₅₀	Concentration of substrate required to cause a half maximal response for the activation of ATX
AIBN	2,2'-Azobis(2-methylpropionitrile)
Ala	Alanine
AMP	Adenosine monophosphate
App.	Apparent
ATP	Adenosine triphosphate
ATX	Autotaxin
BALF	Broncoalveolar fluid
Bis- <i>p</i> NPP	Bis-(<i>p</i> -nitrophenol) phosphate
BLM	Bleomycin
BMS	Bristol-Meyers Squibb
Brp-	Bromo-LPA
LPA	Lysophosphatidic acid
C	Competitive
CDI	1,1'-carbonyldiimidzole
Cl	Clearance
C _{LPA}	Concentration of lysophosphatidyl choline
C _{LPC}	Concentration of lysophosphatidic acid
COMU	(1-Cyano-2-ethoxy-2-oxoethylidenaminoxy)dimethylamino-morpholino-carbenium hexafluorophosphate
COPD	Chronic obstructive pulmonary disorder
CYP	Cytochrome P450
CHEMPLP	Chem piecewise linear potential
DMSO	Dimethylsulfoxide
DIPEA	<i>N,N</i> -Diisopropylethylamine
DM	Drug metabolism
DMF	Dimethylformamide
DS	Discovery Studio
E	Enzyme
EI	Enzyme-inhibitor complex

ENPP2	Ectonucleotide pyrophosphate phosphodiesterase 2
EPSRC	Engineering and Physical Sciences Research Council
equiv.	Equivalents
ES	Enzyme-substrate complex
ESI	Enzyme-substrate-inhibitor complex
ET-1	Endothelin-1
FGF	Fibroblast growth factor
FRET	Förster resonance energy transfer
FTIR	Fourier transformed infrared spectroscopy
FVC	Forced vital capacity
F	Oral Bioavailability
GCDCA	Glycochenodeoxycholic acid
GPC	Glycerolphosphocholine
GPCR	G-protein coupled receptors
GSK	GlaxoSmithKline
HAC	Heavy atom account
HATU	1-[Bis(dimethylamino)methylene]-1 <i>H</i> -1,2,3-triazolo[4,5- <i>b</i>]pyridinium 3-oxid hexafluorophosphate
HBD	Hydrogen bond donor
His	Histidine
HPLC	High performance liquid chromatography
hr	Hours
HRMS	High resolution mass spectrometry
HRP	Horseradish peroxidase
HSP47	Heat shock protein 47
HVA	Homovanillic acid
Hz	Hertz
I	Inhibitor
IIP	Idiopathic interstitial pneumonias
IL-13	Interleukin-13
ILD	Interstitial lung diseases
Ile	Isoleucine
INF- γ	Interferon- γ
IPF	Idiopathic pulmonary fibrosis

k_A	Activation constant
k_{cat}	Rate of formation of product
k_{cat}/k_m	Measure of catalytic efficiency
k_D	Dissociation constant
k_i	Inhibition constant
k_M	Michaelis-Menten constant – the substrate concentration at which the reaction rate is half maximal
k_{off}	Rate of dissociation of enzyme-substrate complex
k_{on}	Rate of formation of enzyme-substrate complex
LE	Ligand efficiency
Leu	Leucine
LLE	Ligand Lipophilicity Efficiency
LOXL-2	Lysyl oxidase-like 2
LPA	Lysophosphatidic acid
LPAR	LPA receptors
LPC	Lysophosphatidyl choline
lysoPLD	Lysophospholipase D
MDAP	Mass directed automated purification
Met	Methionine
min	Minutes
MMP	Matrix metalloproteinase
MWT	Molecular weight
NEt ₃	Triethylamine
NAC	<i>N</i> -acetylcysteine
NBS	<i>N</i> -bromosuccinamide
NKI	Netherlands Cancer Institute
nm	Nanomolar
NMR	Nuclear magnetic resonance
NC	Non-competitive
P	Product
PBS	Phosphate-buffered saline
PDB	Protein data bank
PDGF	Platelet derived growth factor
PF	Pfizer
PFI	Property forecast index

Phe	Phenylalanine
PK	Pharmacokinetics
PLA1/2	Phospholipase A1/2
PLD	Phospholipase D
<i>p</i> NP-TMP	<i>p</i> -nitrophenol-thymidinemonophosphate
ppm	Parts per million
RGD	Arginine Glycine Aspartic acid
SAR	Structure-Activity relationship
SCX	Strong cation exchange
SEM	Standard error of the mean
SMB	Somatomedin B
Sol	Solubility
TDI	Time-dependent inhibition
TGFβ	Transforming growth factor β
THF	Tetrahydrofuran
Thr	Threonine
TNF-α	Tumour necrosis factor-α
Tris	Tris(hydroxymethyl)ammonomethane
Trp	Tryptophan
TUDCA	Tauroursodeoxycholic acid
Tyr	Tyrosine
UC	Un-competitive
UDCA	Ursodeoxycholic acid
UV	Ultraviolet
V _d	Volume of distribution
VEGF	Vascular endothelial growth factor
V _{max}	Rate of formation of product at the catalytic site of enzymes saturated with substrate
ZBG	Zinc binding group

Contents

Structure-guided Approaches to the Design of Novel Autotaxin Inhibitors	i
Abstract	ii
Acknowledgements	iv
Abbreviations	v
Contents	ix
Figures	xiii
Tables	xviii
Schemes	xix
1. Introduction	1
1.1. Overview of Respiratory Diseases	1
1.2. The Structure and Homology of Autotaxin	6
1.3. Structural Differentiation of ATX from the ENPP Family Members	9
1.4. The lysoPLD Activity of ATX	10
1.5. The Relationship between Idiopathic Pulmonary Fibrosis, Cancer and the ATX-LPA Signalling Pathway	15
1.5.1. Idiopathic Pulmonary Fibrosis - Disease Background	15
1.5.2. Postulated Causes of IPF	16
1.5.3. ATX-LPA Produced after Bleomycin Induced Injury	17
1.5.4. Drugs and Treatments for IPF	18
1.5.5. Cancer and ATX	21
1.5.6. Autotaxin Inhibitors as Drugs for the Treatment of Cancer	23
1.6. ATX as a Therapeutic Target	24
1.7. Physicochemical Properties of Compounds	25
1.8. The Development of ATX Inhibitors	28
1.8.1. Lipid-like ATX Inhibitors	28
1.8.2. The Development of Non-lipid Small Molecule ATX Inhibitors Binding in the Active Site and Hydrophobic Pocket of ATX	30
1.8.3. Small Molecule ATX Inhibitors with a Distinct Binding Mode in the Tunnel or Hydrophobic Pocket of ATX	33
1.9. Biological Evaluation of ATX Inhibitors <i>in vitro</i>	35
Chapter 2 – The Structure Activity Relationship of PF-8380 and the Development of Novel Autotaxin Inhibitors	39
2.1. Introduction	40
2.1.1. Project Aims	41

2.2. Binding Mode Analysis Through Co-crystallography with ATX.....	42
2.3. PF-8380 SAR.....	44
2.3.1. Retrosynthetic Analysis of PF-8380	44
2.3.2. Synthesis of Key Building Blocks	45
2.3.3. Synthesis of Final Compounds	50
2.4. Results and Discussion	57
2.4.1. Lipophilic Tail Modifications	57
2.4.2. Structure-activity Relationship of Aromaticity on the Lipophilic Region.....	57
2.4.3. Zinc Binding Group Modifications.....	60
2.4.4. Modifications to the Benzo[<i>d</i>]oxazol-2(3 <i>H</i>)-one Zinc Binding Group	61
2.4.5. Removal of the Zinc Binding Warhead	62
2.4.6. A Suzuki-Miyaura Array to Develop Novel Zinc Binding Groups	64
2.4.7. Core and Linker Modifications	66
2.4.8. Truncation of the Carbon Linker	66
2.4.9. Elaboration of the Carbonyl.....	68
2.4.10. Core and Linker Modifications with the Development of a Novel Sulfonamide Series.....	69
2.4.11. The Development of an Amide Series	70
2.4.12. Substituted Piperazine Cores	73
2.5. The Development of Novel Series of ATX Inhibitors with a Spirocyclic Core	75
2.5.1. Hit Identification of a 2,6-diazaspiro[3.3]heptane Core as a Bioisostere of Piperazine.....	76
2.5.2. Identification of Alternative Zinc Binding Groups in the Spirocyclic Series	78
2.5.3. Identification of a Homologated (2-azaspiro[3.3]heptan-6-yl)methanamine Core	81
2.6. BJEH Cell Based aAssay	83
2.7. Development of the physicochemical profile	86
2.8. Conclusion	92
2.9. Future work.....	97
2.10. Experimental	100
2.10.1. GOLD Docking Procedure.....	100
2.10.2. Biology.....	100
2.10.3. Bis- <i>p</i> NPP Assay Procedure.....	100
2.10.4. Chemistry	101
2.10.5. General	101

2.10.6. Experimental Details.....	101
2.10.7. Purification of Products	101
2.10.8. Analysis of Products	101
2.10.9. HPLC Procedures.....	102
2.10.10. General Procedures	103
General Procedure A: Friedel Crafts Acylation Reaction for the Formation of Alkyl Chlorides	103
General Procedure B: Reaction for the Formation of Sulfonyl Chlorides	104
General Procedure C: Carbamate Formation	105
General Procedure D: Methyl Carbamate Formation	106
General Procedure E: <i>N</i> -Benzyl Carbamate Formation	107
General Procedure F: <i>N</i> -Boc Deprotection	108
General Procedure G: <i>N</i> -carbamoyl Chloride Synthesis.....	109
General Procedure H: <i>N</i> -benzyl Carbamate Synthesis from the Carbamoyl Chloride Intermediate	110
General Procedure I: NaBH ₄ Reduction.	111
General Procedure J: Alkylation Reaction.....	112
General Procedure K: Suzuki-Miyaura Cross Coupling.....	113
General Procedure L: <i>Tert</i> -butyl Ester Hydrolysis	114
General Procedure M: Sulfonylation	115
General Procedure N: Ester Hydrolysis with LiOH.....	116
General Procedure O: Amidation Reaction with HATU	117
General Procedure P: Alkyl Bromination.	118
General Procedure Q: Hydrolysis and Borocycle Cyclisation.	119
General Procedure R: Miyaura Borylation	120
2.10.11. Experimental Procedures	121
Chapter 3 – Structure Based Design of Selective Autotaxin Inhibitors with a Novel Binding Mode	197
3.1. Introduction to Bile Salts as ATX Inhibitors and Allosteric Inhibitors	198
3.2. Aims.....	204
3.2.1. Retrosynthesis	205
3.2.2. Synthetic Strategy	206
3.3. Biochemical Assays to Aid Confirmation of the Binding Mode Hypothesis	208
3.4. Results and Discussion - Tunnel-hydrophobic Pocket Hybrids.....	209
3.4.1. Initial Compound Screen of Tunnel-hydrophobic Pocket Hybrids.....	209

3.4.2. Crystallography of Compounds Bound in ATX	213
3.4.3. Structure-based Design of ATX Inhibitors	217
3.4.4. Enzyme Kinetics	221
3.4.5. Mode of Inhibition of ATX Inhibitors	228
3.4.6. BJEH Cell Based Assay and <i>in vivo</i> Activity	232
3.5. Conclusions.....	237
3.6. Future Work.....	239
3.7. Experimental.....	243
3.7.1. General.....	243
3.7.2. Experimental Details.....	243
3.7.3. Purification of Products	243
3.7.4. Analysis of Products	243
3.7.5. General Procedures	244
General Procedure A: Carbamate Formation.....	244
General Procedure B: <i>N</i> -Benzyl Carbamate Formation.....	245
General Procedure C: <i>N</i> -Boc Deprotection.....	246
General Procedure D: HATU Amidation.....	247
General Procedure E: Amine Alkylation	248
General Procedure F: Amide Reduction	249
3.7.6. Experimental Details.....	250
References.....	284

Figures

Figure 1 Development of PF-8380 SAR.....	ii
Figure 2 Co-crystallographic data leading to structure-based design of UDCA-PF hybrid inhibitors.....	iii
Figure 3 Progression of IPF from an initial epithelial cell injury.....	2
Figure 4 Regulatory signalling pathways involved in the pathogenesis of IPF and the compounds or drugs which inhibit them.....	5
Figure 5 Crystal structure of rat ATX highlighting the key domains and residues of the enzyme (PDB ID: 2XR9).....	6
Figure 6 a) Catalytic region in the active site of ATX with the key residues stabilising the two zinc atoms. b) 2D view of the residues stabilising the proximal and distal zinc atoms, with the catalytic triad (green) and the catalytic Thr209 (blue).....	7
Figure 7 Important residues for activity in a) the tunnel of ATX b) in the hydrophobic pocket of ATX.....	8
Figure 8 Structure of LPA in the active site of ATX.....	8
Figure 9 a) The pharmacophoric features of LPA 18:1. b) The co-crystal structure of LPA 18:1 in the active site of ATX and nearby residues (PDB ID: 3NKP) viewed in DS visualizer.....	9
Figure 10 2D representations of the crystal structures of ENPP1, ENPP2 (ATX), ENPP4 and ENP6 which have distinctly different active sites.....	10
Figure 11 LysoPLD activity on the hydrolysis of LPC to LPA and subsequent delivery to LPA receptors.....	11
Figure 12 LPA 18:1, LPA 18:3 and LPA 14:0 which are different known substrates of ATX (PDB ID: 3NKP, 3NKQ, and 3NKN respectively) viewed in DS visualizer.....	12
Figure 13 The two pathways for LPA production by ATX hydrolysis of LPC and phosphatidic acid hydrolysis by PLA1/2.....	13
Figure 14 Proposed catalytic mechanism by Hausmann et al of the phosphodiesterase activity of ATX.....	13
Figure 15 Residues in the SMB2 domains proposed to be responsible for the binding of ATX to integrin.....	14
Figure 16 The lysoPLD activity of ATX with the hydrolysis of LPC to LPA and subsequent delivery of LPA to LPA ₁ , activation of downstream pathways leading to proliferation, migration, and survival of cells.....	15
Figure 17 5-year survival rate % of IPF compared to common forms of cancer.....	16
Figure 18 The lysoPLD activity of ATX and downstream signalling that leads to the development of IPF.....	17
Figure 19 The mean change in forced vital capacity (FVC) of the lungs of 55 patients either treated with Pirfenidone or a placebo.....	20
Figure 20 Collagen level comparison after dosing with Pirfenidone and GLPG1690.....	21

Figure 21 The ATX – LPA axis in the development and progression of cancer.	22
Figure 22 BrP-LPA compound developed as a dual ATX inhibitor-LPA antagonist for the treatment of non–small cell lung cancer and breast cancer in vivo.	23
Figure 23 PF-8380 ATX inhibitor.....	24
Figure 24 LPAR antagonists Ki16425 and AM095 and integrin antagonist GSK compound 1.1.....	25
Figure 25 (1) Ligand efficiency. (2) Ligand lipophilicity efficiency LLE _{LS} (3) Calculation of Gibbs Free Energy. (4) Ligand lipophilicity efficiency LLE _{AT}	27
Figure 26 Structure of LPA and S1P.....	29
Figure 27 Aromatic phosphonate ATX inhibitor 2.....	29
Figure 28 Non-lipid ATX inhibitors HA155 and PF-8380.....	30
Figure 29 Pharmacophoric features of HA155 ATX inhibitor and the crystal structure of HA155 (Hydrophobic regions = blue, neutral = green, polar = red.) viewed in DSVisualaser (Resolution 3.2 Å, PDB ID: 2XRG).....	31
Figure 30 Pharmacophoric features of PF-8380 ATX inhibitor and the crystal structure (Hydrophobic regions = blue, neutral = green, polar = red.) viewed in DSVisualizer (PDB ID: 5L0K).....	31
Figure 31 a) Galapagos Inhibitor GLPG1690 for the treatment of IPF and Important moieties for activity and DMPK profile of GLP1690. b) In silico GOLD docking of GLPG1690 in ATX with interactions from key residues visualised in DSVisualizer. c) In silico GOLD docking of GLPG1690 in ATX visualised in DSVisualizer with hydrophobicity by colour (polar = red, neutral = green and lipophilic = blue).	35
Figure 32 a) PF-8380 in the active site of ATX. b) LPA in the active site of ATX. 40	
Figure 33 Images viewed or generated in DS visualizer. a) Co-crystal structure of PF-8380 (PDB ID:5L0K) in the active site of ATX and the proximity of the ZBG to the zinc atoms and Thr209. b) Co-crystal structure of 2.1 in the active site of ATX and the proximity of the ZBG to the zinc atoms and Thr209. c) Visualization of nearby amino acid residues for ATX inhibition with PF-8380 in the active site and hydrophobic pocket (Colour coded based on Interactions). d) Visualization of nearby amino acid residues for ATX inhibition with 2.1 in the active site and hydrophobic pocket (Colour coded based on Interactions). e) 2D visualisation of interactions with PF-8380. f) 2D visualisation of interactions with 2.1.	43
Figure 34 Overlay of the two crystal structures of LPA 18:1 (PDB ID: 3NKP), and 2.1 in the active site of ATX showing the similarity in binding modes in DS visualizer	44
Figure 35 Retrosynthetic analysis of PF-8380.....	44
Figure 36 Proposed PF-8380 SAR exploration.....	45
Figure 37 In silico modelling of PF-8380 (yellow), 2.56 (green) and 2.58 (pink) in the active site of ATX using GOLD and viewed in DS visualizer.....	62
Figure 38 In silico modelling of compound in GOLD and viewed in DS visualizer. a) 2.89 in the active site of ATX. b) In silico modelling and overlay of compounds 2.89	

(purple) and PF-8380 (green) interacting with the distal zinc atom in the active site of ATX.	68
Figure 39 In silico modelling of compound 2.99 in the active site of ATX using GOLD and viewed in DS visualizer.....	70
Figure 40 In silico modelling of compounds in GOLD and viewed in DSvisualizer. a) 2.100 in the active site, with intramolecular hydrogen bonding between the alcohol and carbonyl adjacent the benzo[d]oxazol-2(3H)-one showing the distance of hydrogen bonding between NH and Tyr306 R-OH. b) 2.101 in the active site without hydrogen bonding to Tyr306, and the piperidin-4-ol alcohol projecting towards the tunnel. c) 2.103 in the active site, the N-H hydrogen bonds with Tyr306 at a distance of 2.208 Å. d) 2.105 in the active site, the C=O hydrogen bonds with Tyr306 at a greater distance of 3.028 Å.	73
Figure 41 In silico modelling of compound 2.111 with a benzyl substituted piperazine in the active site of ATX in GOLD and DS visualizer.	75
Figure 42 Comparison of the length of the piperazine and 2,6-diazaspiro[3.3]heptane core.....	76
Figure 43 In silico modelling in GOLD and DS visualizer of a) benzo[d]oxazol-2(3H)-one ZBG compound 2.127. b) Sulfonamide ZBG 2.122. c) Borocycle ZBG 2.125. d) Benzimidazole ZBG 2.124.....	80
Figure 44 Compounds docked in GOLD and viewed in DS visualizer. Overlay of compound 2.115 (orange, $K_i = 0.001 \mu\text{M}$), 2.127 (blue, $K_i = 0.094 \mu\text{M}$), and proposed PF analogue with the (2-azaspiro[3.3]heptan-6-yl)methanamine core (green) showing the vector change in the zinc binding region.....	81
Figure 45 a) Overlay of in silico modelling in GOLD and DS visualizer of 2.123 and 2.131. b) Key residues for potency with 2.131.	83
Figure 46 Dose response curve of 2.1 in the cell. The control blot contains the inhibitor 2.1 in the cell media, then the next blot contains ATX and LPA showing phosphorylation of AKT as a negative control, and thirdly the cell media alone.....	84
Figure 47 Structure of compound 2.1.	84
Figure 48 Compounds tested in BJEH fibroblast cell based assay for the phosphorylation of AKT. The controls are the cell based media alone, ATX alone, and then LPA alone which is expected to have significant downstream signalling effects by phosphorylating AKT.	85
Figure 49 Compounds tested in the BJEH cell-based assay.	86
Figure 50 The development of cLogD from PF-8380 to compound 2.100, 2.116, and 2.122. Size of circle indicates the K_i (large $K_i =$ large circle) and the solubility in μM indicated.	87
Figure 51 cLogD vs MWT 2.100 green, 2.116 orange, and 2.122 blue. Trends analysed using Spotfire. Size of circle indicates the K_i (large $K_i =$ large circle) and the colours represent a compound from each sub-series. The key for these compounds are present in Figure 52.....	88
Figure 52 Compounds from each sub-series of compounds present in Figure 51...	89

Figure 53 a) Compound library of LLE _{AT} vs PFI. b) cLogD vs MWT. (Larger K _i with a bigger circle) using Spotfire.	90
Figure 54 LLE vs chromLogD of the compound library with the size of the circle corresponding to the K _i of the compounds.....	91
Figure 55 pKa analysis of ZBGs with the optimum range as 8-11. ¹²²	93
Figure 56 PF-8380 SAR summary highlighting the key pharmacophoric features required for activity.....	94
Figure 57 Development of compound with spirocyclic cores.....	95
Figure 58 Project development and future work.....	96
Figure 59 Lead-like compounds developed in this project.	97
Figure 60 Series 2 ZBG screen containing the 4-(aminomethyl)piperidin-4-ol core.	98
Figure 61 Development of a 6-(aminomethyl)-2-azaspiro[3.3]heptan-6-ol core.....	98
Figure 62 Alternative zinc binding groups.....	99
Figure 63 2D diagram showing the allosteric site in the tunnel of ATX (pink), and the orthosteric site in the active site and hydrophobic pocket of ATX (purple).....	198
Figure 64 The structure of Amira compound 3.1. ¹⁷¹	198
Figure 65 a) Co-crystallography of 3.1 bound to ATX, viewed in DSVisualizer. b) 2D diagram of 3.1 in the tunnel of ATX.....	199
Figure 66 Compound developed by PharmAkea with novel binding modes.....	200
Figure 67 Crystal structures of PAT-347 and PAT-078 a) Non-competitive inhibitor PAT-347 bound to ATX in the tunnel region, co-crystallised with LPA at the orthosteric site. b) Competitive inhibitor PAT-078 bound to ATX in the hydrophobic pocket and partially in the tunnel region. c) 2D diagram of PAT-347 in the orthosteric site of ATX. d) 2D diagram of PAT-078 in the orthosteric site of ATX.....	201
Figure 68 a) Stereochemistry of the UDCA fragment, which shall be simplified to the structure in b) throughout. For UDCA X = OH b) Functionality important for activity on bile salts.....	202
Figure 69 Co-crystal structure of TUDCA bound to ATX (PDB ID: 5DLW), viewed in DS visualizer.....	203
Figure 70 Design of steroid-PF hybrids that reside in the tunnel-active site. Co-crystallisation of 2.1 and TUDCA in the orthosteric and allosteric sites of ATX, respectively.	204
Figure 71 Design of the steroid-PF hybrids that reside in the tunnel-hydrophobic pocket.	205
Figure 72 The LPC, pNP-TMP, and bisp-NPP biochemical assays with the proposed inhibitor binding mode (pink).	209
Figure 73 Hybrid compound 3.30 containing UDCA in the tunnel region and a 3,5-dichlorobenzyl carbamate moiety in the core region blocking entrance to the active site.	213
Figure 74 The crystal structure of compound 3.31 viewed in DS visualiser a) 3.31 and the nearby residues for interactions on ATX. b) 3.31 bound to ATX with HBD (pink)	

/HBA(green) surface. c) The 2D interaction map of nearby residues. d) Hydrophobicity surface of the enzyme with 3.31 bound (lipophilic–blue, neutral–green, polar–red.).	214
Figure 75 The crystal structure overlay of 3.31 and TMP (PDB ID: 4GTX) viewed in DS visualizer	215
Figure 76 The crystal structure of compound 3.25 by NKI, viewed in DS visualiser a) 3.25 and the nearby residues for interactions on ATX. b) 3.25 bound to ATX with HBD (pink)/HBA (green) surface. c) The 2D interaction map of nearby residues. d) Hydrophobicity surface of the enzyme with 3.25 bound (lipophilic–blue, neutral–green, polar–red.).	215
Figure 77 Overlay of the crystal structures of compound 3.25 and 3.31 in the active site of ATX views in DS visualizer.	216
Figure 78 Diamine cores for the synthesis of hybrid compounds.	218
Figure 79 In silico docking of 3.38 in ATX in GOLD and viewed in DS visualizer.	220
Figure 80 Co-crystal structure of 3.40 bound to ATX by NKI, viewed in DS visualizer. a) Co-crystal structure and nearby residues. b) Co-crystal structure and two important residues for potency which interact with both the tunnel and hydrophobic pocket region. c) 2D interaction map generated from DS visualizer of nearby residue interactions.	221
Figure 81 Binding sites of non-competitive and competitive inhibitors with the enzyme.	221
Figure 82 a) Rate of formation of the enzyme-substrate complex (ES), and the release of product P. b) Michaelis-Menten equation.	222
Figure 83 a) The initial rate of reaction b) The rate of formation of ES c) The rate of breakdown of ES d) The steady state assumption of ES e) Rearrangement of equation f) Definition of the Michaelis-Menten constant.	223
Figure 84 g) The concentration of the ES complex. h) The total concentration of E present. i) The concentration of the ES complex taking into account the concentration of E available. j) The concentration of the ES complex present with defined constants.	223
Figure 85 a) The initial rate of the reaction b) The Michaelis-Menten equation.	224
Figure 86 Lineweaver-Burk equation.	224
Figure 87 Comparison of a competitive and non-competitive ATX inhibitor through a linear regression (A, C) and a Lineweaver-Burk plot (B, D).	225
Figure 88 a) Regions of non-competitive ATX inhibitors and competitive inhibitors b) TUDCA in the non-competitive site and LPA in the competitive site (bioactive product of ATX after hydrolysis of LPC) c) PF-8380 residing in the competitive site of ATX d) 3.40 in both the tunnel and hydrophobic pocket acting as a competitive inhibitor.	226
Figure 89 Mechanism for competitive inhibition of ATX.	227
Figure 90 Mechanism for non-competitive inhibition of ATX.	228

Figure 91 Compounds 3.25, 3.2, 3.30, 3.31, and 3.40.	228
Figure 92 Equations for competitive and non-competitive inhibitors.....	229
Figure 93 a) The enzyme-inhibitor binding equilibria b) The Michaelis-Menten equation taking into account for αK_M	231
Figure 94 The structure of 3.40.....	232
Figure 95 BJEH cell based assay for a dose response curve of 3.40 by NKI.	233
Figure 96 The structure of GLPG1690.	234
Figure 97 In vivo LPA reduction of 18:2 of GLPG1690 at 3, 10, and 30 mg/kg in mice.....	234
Figure 98 The structure of orthosteric ATX inhibitor 3.43 developed by Jones et al.	235
Figure 99 In vivo results of dosing compound 3.43 in mice by Jones et al. Red = concentration of LPA, black = concentration of 3.43.	235
Figure 100 The effect of PF-8380 and 3.40 on extracellular LPA levels in mice (circles), with a median value indicated by a line. Students unpaired two tailed T-test suggests the difference of PF-8380 and 3.39 to the control is significant ($p < 0.05$). Results by Morris et al.	236
Figure 101 Optimisation trajectory using biostructural data.....	238
Figure 102 Novel cores to probe the SAR of the tunnel-hydrophobic pocket inhibitors.	239
Figure 103 Tunnel and active site hybrids based around compound 2.1 and HA155.	240
Figure 104 Proposed tunnel-active site compounds.....	241
Figure 105 In silico modelling of compounds 3.48–3.51 Figure 104 using GOLD and DS Visualizer.	241
Figure 106 Proposed synthesis of a tunnel-active site inhibitor.....	242
Figure 107 2D diagrams showing the proposed compound in the tunnel-active site and 3.40 in the tunnel-hydrophobic pocket.	242

Tables

Table 1 Compounds or drugs, their therapeutic target and results in clinical trials for IPF. ^a No significant efficacy ^b Increased mortality rates and side effects. ^c No information available. ...	4
Table 2 Approved drugs Pirfenidone and Nintedanib and clinic compound GLPG1690.	18
Table 3 Parameters for a drug-like compound	27
Table 4 <i>In vivo</i> pharmacokinetic profile.....	28
Table 5 Physicochemical properties and potency of LPA and S1P. ¹¹⁶ ^a cLogD was calculated using JChem for Excel	29
Table 6 Physicochemical properties and potency of 2. ^a cLogD was calculated using JChem for Excel. ^b Reported value.	29
Table 7 Physicochemical properties of HA155 and PF-8380. ^a cLogD was calculated using JChem for Excel.....	30

Table 8 Patented ATX inhibitor compounds.....	32
Table 9 ATX inhibitors that reside in the tunnel. ^a PAT-347 ^b TUDCA ^c GLPG1690.....	34
Table 10 Physicochemical and pharmacokinetic properties of PF-8380 ^a Calculated with JChem. ^c Solubility mg/ml	41
Table 11 Pharmokinetic properties of PF-8380. Cl = Clearance, V _d = Volume of distribution.	41
Table 12 Evaluating the importance of the aromatic tail of PF-8380, and the corresponding physicochemical profile. ^a Synthesised by another member of our laboratories. ^b PF-8380....	57
Table 13 Lipophilic tail analogues 2.46–2.55. ^a Synthesised by another member of our laboratories.....	59
Table 14 ZBG modifications with 1,3-dihydro-2 <i>H</i> -benzo[<i>d</i>]imidazol-2-one and indolin-2-one groups.....	61
Table 15 Carboxylic acid, and hydroxamic acid compounds without the benzo[<i>d</i>]oxazol-2(3 <i>H</i>)-one ZBG. ^a Synthesised by another member of the laboratory. ¹⁴⁶	63
Table 16 Suzuki-Miyaura compound screen for a novel ZBG.	64
Table 17 Truncated compounds containing the 3,5-dichlorobenzyl carbamate tail and benzylcarbamate tail with either benzo[<i>d</i>]oxazol-2(3 <i>H</i>)-one, 1,3-dihydro-2 <i>H</i> -benzo[<i>d</i>]imidazol-2-one or indolin-2-one ZBG.	66
Table 18 Alcohol analogues of PF-8380 and 2.42	68
Table 19 Sulfonamide series with a piperidin-4-ylmethanamine core.....	69
Table 20 Amide series containing a methylaminopiperidine, (aminomethyl)piperidin-4-ol and ethylenediamine core. ^a Synthesised by another member of the laboratory.....	71
Table 21 Substituted and bicyclic diamine cores.	74
Table 22 Investigation of a novel 2,6-diazaspiro[3.3]heptane core.	77
Table 23 Zinc binding groups with the 2,6-diazaspiro[3.3]heptane core. ^a Synthesised by another member of our laboratory	79
Table 24 Homologated (2-azaspiro[3.3]heptan-6-yl)methanamine core.	82
Table 25 Initial ATX inhibition of compounds. ^a TUDCA ^b UDCA.	210
Table 26 Inhibitors containing a hexahydroimidazo[1,5- <i>a</i>]pyrazin-3(2 <i>H</i>)-one core.	217
Table 27 ATX inhibitors containing novel diamine cores. Inh = Inhibition (C) Competitive Inhibition (NC) Non-competitive inhibition (UC) Uncompetitive Inhibition.	218
Table 28 Lineweaver-Burk and Michaelis-Menten plots of compounds 3.25, 3.2, 3.29, 3.30, and 3.25 reported by Keune <i>et al.</i>	229
Table 29 ^a TUDCA ^b UDCA. The mode of inhibition of compounds (C) Competitive Inhibition (NC) Non-competitive inhibition (UC) Uncompetitive Inhibition.	231

Schemes

Scheme 1 Biological assay with the unnatural substrate bis- <i>p</i> NPP with <i>para</i> -nitrophenol as the detectable product.	36
Scheme 2 Substrate pNP-TMP used in the unnatural substrate assay with <i>para</i> -nitrophenol as the detectable product.	36
Scheme 3 ATX inhibition assay with the natural substrate LPC and detectable product a homovanillic acid dimer.	37

Scheme 4 FS-3 assay with the detectable product.....	38
Scheme 5 Outline of core reagents for the synthesis of common intermediates.	46
Scheme 6 Friedel-Crafts acylation for the preparation of alkyl halide starting materials 2.5–2.10.	46
Scheme 7 Sulfonylation reaction to afford 2.11–2.12.	47
Scheme 8 Carbamate synthesis for carboxylic acid starting materials.	47
Scheme 9 Synthesis of the 1-hydroxy-1,3-dihydrobenzoxaborole intermediate.	47
Scheme 10 General route for the synthesis of piperazine intermediates.	48
Scheme 11 Synthesis of 2-methylpiperazine and (1 <i>S</i> ,4 <i>S</i>)-2,5-diazabicyclo[2.2.1]heptane building blocks 2.32 and 2.33.	49
Scheme 12 Synthesis of methylsubstituted piperazines with a benzyl carbamate tail.	49
Scheme 13 Synthesis of isopropyl substituted piperazine core.	50
Scheme 14 Retrosynthesis of amine, alkylation and sulfonamide linked final compounds. .	50
Scheme 15 The alkylation reaction for the synthesis of lipophilic tail analogues of PF-8380, and the subsequent <i>N</i> -Boc deprotection or reduction of the carbonyl moiety.	51
Scheme 16 Synthesis of ATX inhibitors with a carboxylic acid motif.	51
Scheme 17 Suzuki-Miyaura array from intermediate 2.72.....	52
Scheme 18 The alkylation reaction of truncated PF-8380 analogues with alternative ZBG 2.89–2.94.	52
Scheme 19 The synthesis of the sulfonamide sub-series with the piperidin-4-ylmethanamine core. a) Methyl chloroformate (1.1 equiv), NEt ₃ (2.1 equiv), THF (2 mL). b) Cbz-succinamide (1.1 equiv), NaHCO ₃ (1.5 equiv), THF:H ₂ O (1 mL:1 mL). c) (3,5-dichlorophenyl)methanol (1.1 equiv), 1,1'-carbonyldiimidazole (1.1 equiv), DMF (2 mL).	53
Scheme 20 Synthesis of compounds from the amide sub-series. a) (3,5-dichlorophenyl)methanol (1.1 equiv), 1,1'-carbonyldiimidazole (1.1 equiv), DMF (2 mL).	54
Scheme 21 The alkylation for the synthesis of analogues 2.107-2.114 with substituted and bicyclic piperazines.....	54
Scheme 22 The alkylation reaction with a 2,6-diazaspiro[3.3]heptane core, and further elaboration of the carbonyl.	55
Scheme 23 The synthesis of sulfonamide analogues with the novel 2,6-diazaspiro[3.3]heptane core.....	55
Scheme 24 The synthesis of amide analogues with the novel 2,6-diazaspiro[3.3]heptane core.	56
Scheme 25 The synthesis of amide analogues with the novel homologated (2-azaspiro[3.3]heptan-6-yl)methanamine core. a) (3,5-dichlorophenyl)methanol (1.1 equiv), 1,1'-carbonyldiimidazole (1.1 equiv), DMF (2 mL).....	56
Scheme 26 Retrosynthesis of the hybrid compounds from TUDCA and 2.1.....	205
Scheme 27 Forward synthesis of tunnel-hydrophobic pocket hybrids and tunnel-active site hybrids.	206
Scheme 28 The synthesis of diamine core building blocks 3.9–3.14.....	207
Scheme 29 The synthesis of intermediate 3.16.	207
Scheme 30 Synthesis of intermediates with the hexahydroimidazo[1,5- <i>a</i>]pyrazin-3(2 <i>H</i>)-one core.....	207
Scheme 31 Synthesis of final compounds <i>via</i> a) amidation reaction with HATU (1.1 equiv), DIPEA (5.0 equiv) and DMF b) Borane reduction with BH ₃ -THF.	208

1. Introduction

1.1. Overview of Respiratory Diseases

Many respiratory diseases affect the general population, the most common being asthma, pulmonary fibrosis, and chronic obstructive pulmonary disorder (COPD). Of these, fibrosis accounts for approximately 45% of deaths in the developed world.⁴ Pulmonary fibrosis is a broad term for a large number of individual interstitial lung diseases (ILD). ILD can be divided further into subdomains, one of which includes idiopathic interstitial pneumonias (IIP). There are nine forms of IIP all of which have a similar pathophysiology, and commonly with these conditions, the aetiology of the disease is unknown and hence termed idiopathic. One of the most devastating forms of IIP is idiopathic pulmonary fibrosis, where there is a less than 5-year survival rate after prognosis and currently there is no known cure for this disease.⁵

Most IIPs are believed to begin with an initial epithelial cell injury which could be caused by mechanical or oxidative stress (**Figure 3 A**) to epithelial cells, which can lead to apoptosis or the reprogramming of these cells.⁶⁻¹² After this epithelial cell injury, the profibrotic cytokine interleukin-13 (IL-13) is activated and an immune response to the injury begins by recruiting macrophages to the site of injury (**Figure 3 B**).^{13,14} This leads to vascular leaking and the formation of a fibrin clot (**Figure 3 C**). Fibroblasts are then recruited to the site of injury and transformed into myofibroblasts (**Figure 3 D**). This process is attenuated by a multitude of tyrosine kinases, and growth factors such as transforming growth factor β (TGF β), connective tissue growth factors (CTGF), endothelin-1 (ET-1), and enzymes, which convert epithelial cells into myofibroblasts (**Figure 3 E**). The myofibroblasts then produce additional cytokines, chemokines and enzymes which further promote fibrogenesis. Additionally, myofibroblasts secrete collagen and produce matrix metalloproteinases (MMPs), which regulate collagen synthesis. The accumulation of collagen in the extracellular matrix leads to scarring of the lungs (**Figure 3 F**). With the accumulative deposition of collagen, fibroblasts, myofibroblasts, and fibrin in the extracellular matrix the alveolar cell eventually collapses and forms a new layer of impaired epithelial cells which cannot undergo gas exchange (**Figure 3 G**). Due to the uncertainty in the aetiology of the condition, most of these regulatory pathways implicated in the development of the disease have been explored as potential therapeutic targets for IPF.¹⁵

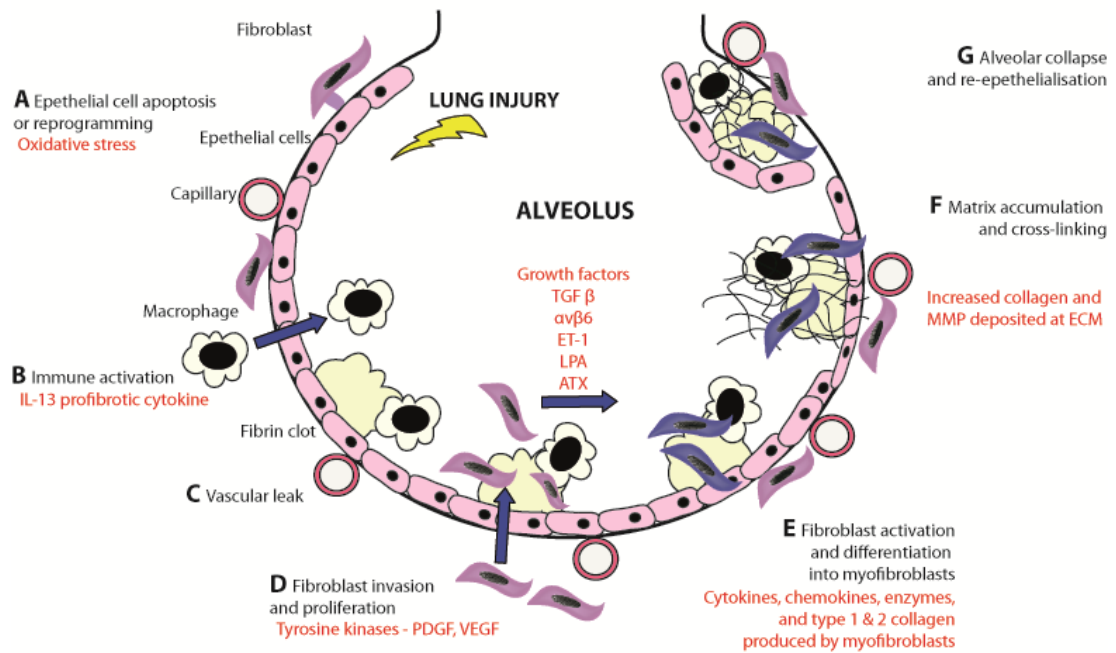


Figure 3 Progression of IPF from an initial epithelial cell injury.¹⁵

Although there are many different regulatory pathways that have been implicated in the onset of IPF, there are still no drugs which cure the condition. However, as previously discussed, regulatory pathways **A-G (Figure 3)** are potential therapeutic targets for IPF, and a number of compounds have reached clinical trials for each of these (**Table 1**).

The mechanical, or oxidative stress is the first point of call with regards to the believed aetiology of the disease (**Figure 3 A**). It is also reported that patients with IPF have reduced levels of an antioxidant called glutathione, which could lead to the increased epithelial cell injury. *N*-acetylcysteine is a glutathione precursor which was postulated to minimise epithelial cell injury and limit disease progression, however there was no significant efficacy observed in phase III clinical trials (**Table 1**).^{16,17}















IL-13 is the profibrotic cytokine that activates an immune response to alveolar cell injury within the lungs (**Figure 3 B**). This immune response recruits macrophages and the production of TGF- β which is also implicated in IPF.^{13,15} It was believed that targeting IL-13 using an anti-IL-13 antibody QAX576 could inhibit recruitment of macrophages and activation of TGF- β . QAX576 was developed by Novartis, however the compound was terminated during safety and efficacy phase II trials with no results published (**Table 1**). A

recent report by Wynn *et al* reported that the blockade of IL-13 can also cause undesired side effects such as increased Interferon- γ (IFN- γ), and it was only with double knockout mice lacking both IL-13 and IFN- γ that a reduction in fibrosis was observed.¹⁸ IFN- γ , which is also elevated in the BALF of IPF patients was also investigated as a potential therapy, however this failed due to lack of significant efficacy (**Figure 3 E, Table 1**).^{18–21}

Another therapeutic target is lysyl oxidase-like 2 (LOXL2), which is an enzyme produced by fibroblasts that increases production of collagen mediating enzymes and promotes the cross-linking of collagen (**Figure 3 F, Table 1**). This ultimately leads to irreparable damage to alveolar cells by hardening and honeycombing of the extracellular matrix.^{22,23} Simtuzumab was developed by Gilead with the aim of inhibiting this enzyme, although Gilead terminated the study during Phase II trials due to a lack of efficacy.^{4,16,24}

Currently the most promising targets for the treatment of IPF are kinases, enzymes and receptors implicated in the recruitment and differentiation of myofibroblasts to fibroblasts (**Figure 3 D, Table 1**). Nintedanib and Pirfenidone are marketed tyrosine kinase inhibitors which shall be discussed in greater detail in Section **1.5.4**. Despite the small improvement in quality of life these drugs are by no means a cure for the condition.^{16,25–29} As a result of this, new targets have emerged, including lysophosphatidic acid (LPA) antagonists BMS-986020 developed by Bristol-Meyers Squibb,^{15,30,31} Autotaxin (ATX) inhibitors GLPG1690 developed by Galapagos,^{32–34} and $\alpha_v\beta_6$ integrin antagonists STX-100 first developed by Stromedix and Biogen,^{10,15,16} and GSK3008348 developed by GSK.^{15,35} Autotaxin is an enzyme which delivers LPA to lysophosphatidic acid receptors (LPA), which is potentially aided at the cell surface by integrin $\alpha_v\beta_6$. As a result, these three closely related potential therapeutic targets of ATX represent an exciting prospect in the treatment of IPF.^{36–41}

Table 1 Compounds or drugs, their therapeutic target and results in clinical trials for IPF. ^aNo significant efficacy ^bIncreased mortality rates and side effects. ^cNo information available.

Progression of IPF	Mode of action	Compound	Clinical trials
A	Antioxidant	NAC ¹⁷	^a 
	Immunosuppression	NAC Prednisone Azathioprine ¹⁷	^b 
B	Anti-IL-13 antibody	QAX576 ¹⁵	^c 
D	Tyrosine kinase inhibitor for VEGFR, FGFR, and PDGFR	Nintedanib ^{16,25,26}	
	Multiple receptor inhibitor	Pirfenidone ²⁷⁻²⁹	
	Tyrosine kinase inhibitor	Imatinib ⁴²	^a 
	LPA antagonist	BMS-986020 ^{15,30,31}	
E	$\alpha_v\beta_6$ antagonist	STX-100 ^{10,15,16} GSK3008348 ³⁵	
	ATX inhibitor	GLPG1690 ³²⁻³⁴	
	Immunoregulatory cytokine	Interferon ^{18,20,21}	^a 
F	LOXL2	Simtuzumab ^{4,16,24}	^a 
Clinical Trial Stage  On-going  Negative results  Positive results			

The compounds discussed and their proposed mode of action for the treatment of IPF are highlighted in **Figure 4**. It is evident that there are many potential therapeutic targets for the

treatment of IPF, however the lack of efficacious drugs in phase II clinical trials is likely a result of the lack of knowledge on the exact aetiology and the pathophysiology of the condition. Moeller *et al* reported that although there are many compounds which are deemed effective in the bleomycin mouse model for IPF, the reduction of IPF can be misconstrued for anti-inflammatory effects.⁴³ This is evident with the only FDA approved drugs Nintedanib and Pirfenidone, which only slow down the decline of the patient and improve quality of life rather than treating the condition.

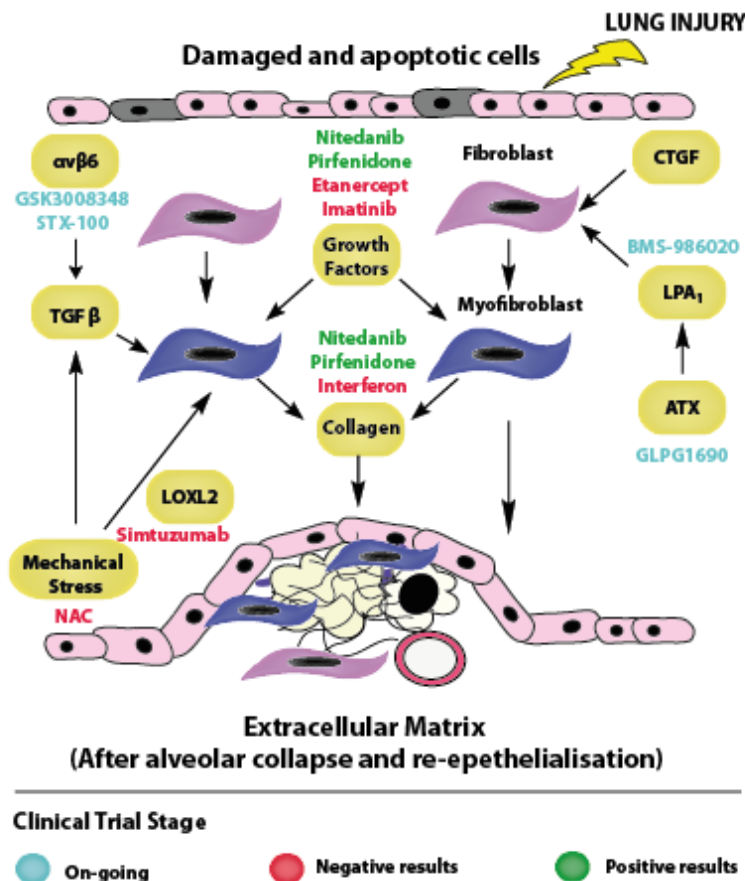


Figure 4 Regulatory signalling pathways involved in the pathogenesis of IPF and the compounds or drugs which inhibit them.

There is clearly an unmet need for a compound which can halt the progression of the disease, and hence for new areas of therapy such as that of integrin antagonists, LPA antagonists, and ATX inhibitors. As a result of this, the focus of this work is based around the inhibition of ATX.

1.2. The Structure and Homology of Autotaxin

Autotaxin (ATX) is a 125 kDa enzyme which is also known as ectonucleotide pyrophosphate phosphodiesterase 2 (ENPP2). ATX is a member of the ENPP family of enzymes, which consists of ENPP1–7. ATX can be spliced into four main isoforms called the α , β , γ and δ subunits. The β isoform is the most common, and is responsible for the lysophospholipase D (lysoPLD) activity, which is the hydrolysis of lysophosphatidyl choline (LPC) to lysophosphatidic acid (LPA), by ATX in the extracellular matrix of cells.² ATX is expressed in mouse, rat, and humans, and ATX from these species has been co-crystallised with inhibitors and LPA species of varying lengths. Rat, bovine, and human ATX show greater than 95% homology based upon their amino acid sequence. Pharmakea reported a structural homology of > 90% between murine and human ATX.^{44–45} ATX is constructed of two somatomedin B (SMB)-like domains; SMB1, SMB2, a catalytic (phosphodiesterase), and a nuclease domain (**Figure 5**). The SMB2 domain is connected to the catalytic domain *via* a linker region of amino acids. The catalytic and nuclease domains are connected by a ‘lasso’ of amino acids which wraps around the catalytic domain (orange, **Figure 5**). Arguably the most important region of the enzyme is the catalytic domain, which represents the active site of the enzyme, and is responsible for the phosphodiesterase activity.

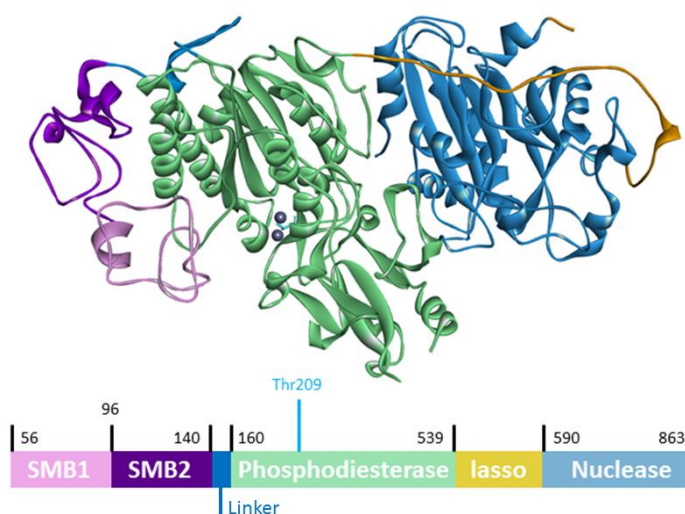


Figure 5 Crystal structure of rat ATX highlighting the key domains and residues of the enzyme (PDB ID: 2XR9).⁴¹

ATX consists of three distinct regions, which include the active site, hydrophobic pocket, and the tunnel. The distinguishing features within the active site are two zinc atoms, a Thr209, and an Asn230 residue. Both Thr209 and Asn230 residues are critical to the phosphodiesterase catalytic cycle of ATX, as reported by both Hausmann and Stracke *et al.*^{46–47} This has been

established through the expression of mutated enzymes without an Asn230 residue, that were unable to hydrolyse LPC.¹ Of the two zinc atoms the closest to the Thr209 residue is referred to as the proximal zinc atom, and the farthest the distal zinc atom. The distal zinc atom is stabilised by residues Asp473, Asp311, His474, and His315, and the proximal zinc atom by residues His359, Asp311, Asp171, Asp 358, and Asn230 (**Figure 6 a**). Residues His359, Asp358, and Asn230 are often referred to as a catalytic triad and play a role in the phosphodiesterase activity of ATX (**Figure 6 b**).⁴¹

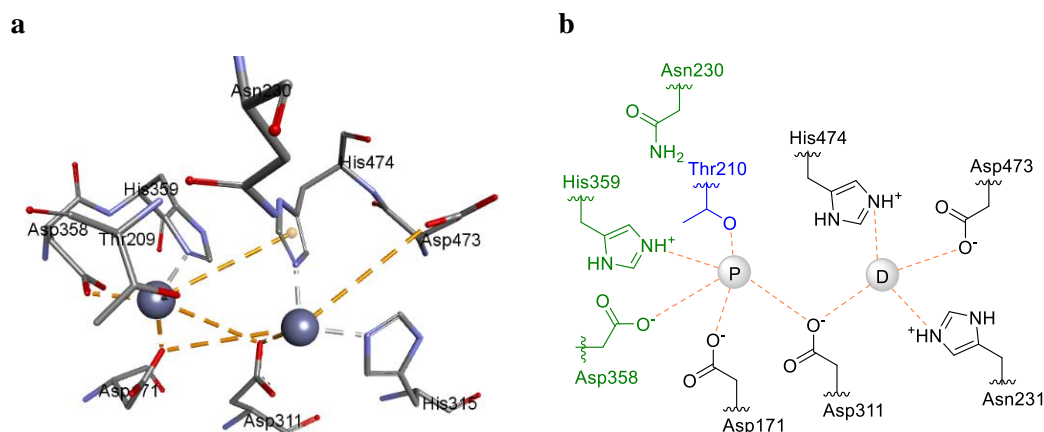


Figure 6 a) Catalytic region in the active site of ATX with the key residues stabilising the two zinc atoms. **b)** 2D view of the residues stabilising the proximal and distal zinc atoms, with the catalytic triad (green) and the catalytic Thr209 (blue).

The hydrophobic pocket is a cavity only present in ATX, in contrast to other phosphodiesterase enzymes and is situated adjacent to the active site. Within the hydrophobic pocket, the key residues involved in interactions with the substrate core are Leu213, Trp260, Phe273, Leu259, Ile167, Ala 217, and Met512 (**Figure 7 b**). Access to these sites from the solvent is possible through the tunnel of the enzyme, which is primarily constructed from a mixture of hydrophobic and polar residues Trp254, His251, Phe249, Tyr82, Leu78, Phe274, and Trp260, and collectively are able to accommodate lipophilic moieties (**Figure 7 a**). The presence of residues such as His251 allow polar or charged ligands to enter and leave the active site.

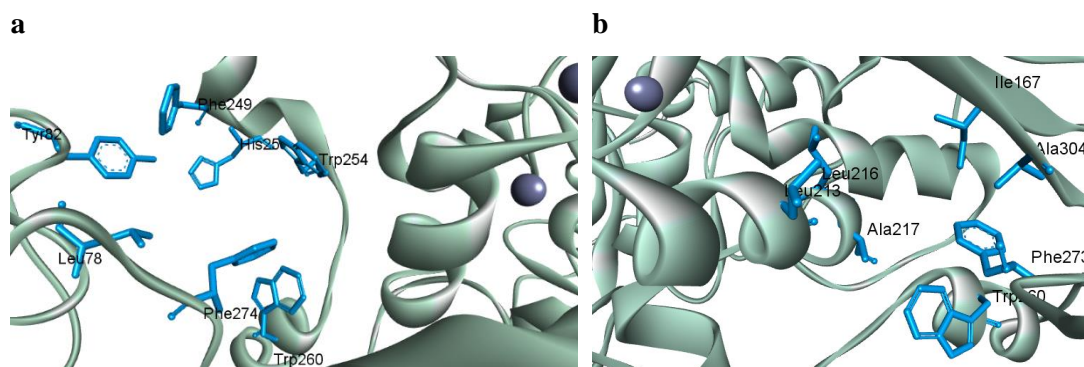


Figure 7 Important residues for activity in **a)** the tunnel of ATX **b)** in the hydrophobic pocket of ATX.

The natural substrate of ATX, LPC, is hydrolysed to LPA in the active site of ATX. Co-crystallography of LPA bound to ATX by Nishimasu *et al* confirms that the phosphate zinc binding group (ZBG) of LPA resides in the active site, with the large lipophilic alkyl chain accommodated inside the hydrophobic pocket (**Figure 8**).¹ Interactions in the active site include hydrogen bonding between the phosphate ZBG to residues Thr209, and Asn230, and electrostatic interactions with both zinc atoms. The ester and alcohol of LPA reside in the active site and core region. These moieties hydrogen bond to surrounding residues Asp171, Asp311, and Tyr306 to further increase affinity in the active site.

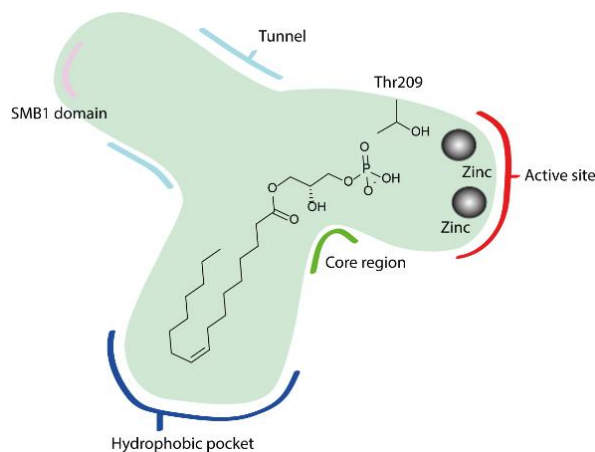


Figure 8 Structure of LPA in the active site of ATX.

Nishimasu *et al* report that the hydrophobic residues discussed and Leu243, Phe249, Trp254, and Tyr306 are essential for lysoPLD activity.¹ The co-crystal structure of one of the forms of LPA, 18:1, bound to ATX shows the depth of the hydrophobic pocket. The long lipophilic tail is able to interact with hydrophobic residues Ile167 and Met512, which are at the farthest

region of the pocket (**Figure 9 b**). The structural data presented above indicates that a lipophilic tail, a ZBG, and a core region to link these two moieties are necessary to complement the hydrophobicity of the enzyme in order to achieve competitive ATX inhibition (**Figure 9 a, c**).

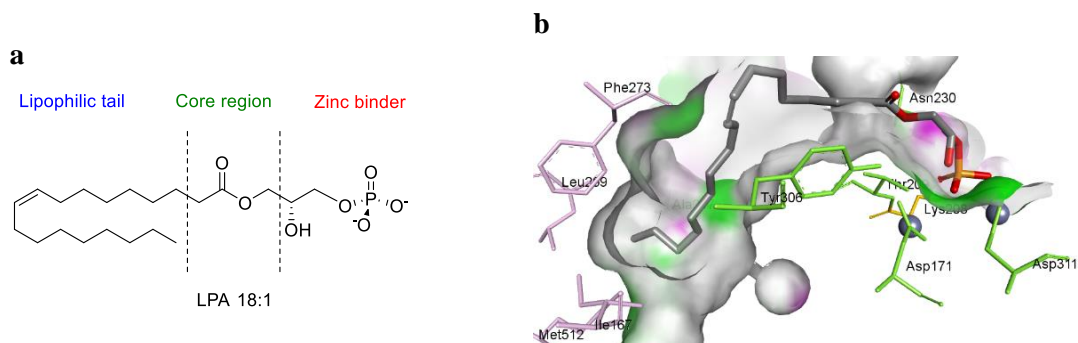


Figure 9 a) The pharmacophoric features of LPA 18:1. **b)** The co-crystal structure of LPA 18:1 in the active site of ATX and nearby residues (PDB ID: 3NKP) viewed in DS visualizer.^{1,48}

1.3. Structural Differentiation of ATX from the ENPP Family Members

Of the 7 members of the ENPP family, four have been solved by crystallography (ENPP1, ENPP2, ENPP4, and ENPP6, (**Figure 10**). The structural insight into the different features of each of the active sites allows inhibitors to be designed with ENPP enzyme selectivity in mind. Assessment of the topology of each of the enzymes enables structural comparison with ENPP1, ENPP4, and ENPP6 (**Figure 10**). These enzymes do not contain a deep hydrophobic pocket like ATX, instead they possess an insertion loop (**Figure 10**, Yellow). This insertion loop is comprised of 18 amino acids, which creates a small hydrophobic pocket cavity. The presence of a smaller cavity within ENPP1 and ENPP4 accommodates the natural substrate adenosine triphosphate (ATP). ATP is hydrolysed to adenosine monophosphate (AMP), which then resides in the nucleotide binding pocket (**Figure 10**). ENPP6 has a choline binding pocket to accommodate the choline moiety of cholinephosphate, the product from hydrolysis of the natural substrate glycerolphosphocholine (GPC). Both the nucleotide binding pocket and the choline binding pocket are much shorter than ATX, which has a larger natural substrate, LPC.

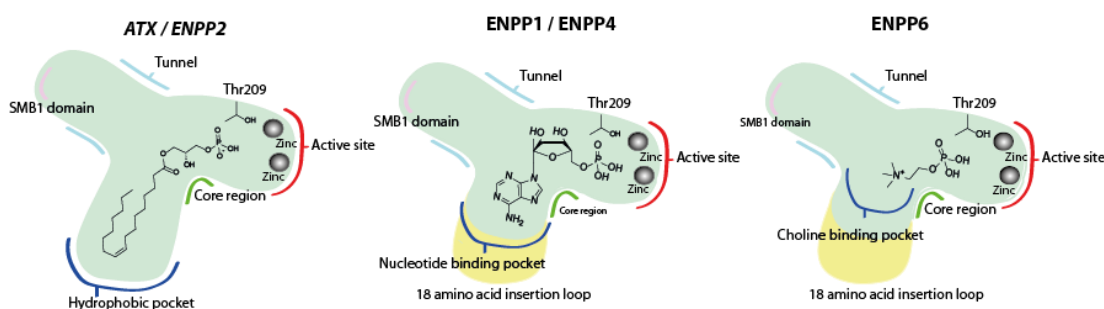


Figure 10 2D representations of the crystal structures of of ENPP1, ENPP2 (ATX), ENPP4 and ENP6 which have distinctly different active sites.⁴⁹

Uniquely, in comparison to the other members of the ENPP family, ATX does not have this 18 amino acid insertion loop, which creates a void which is known as the hydrophobic pocket. The presence of this spacious hydrophobic pocket adjacent to the catalytic site allows for the design of small molecule inhibitors that target the hydrophobic pocket of ATX. Based on differences in the binding sites found in the ENPP family, inhibitors which target the hydrophobic pocket therefore have the potential to be selective for ATX.

1.4. The lysoPLD Activity of ATX

ATX was first identified as a cell-motility stimulating factor, causing the random and directed migration of human A2058 melanoma cells.⁵⁰ Cell migration is the movement of cells from one location to another and is one of the many biological pathways initiated by the action of ATX. Other signalling pathways can lead to cell proliferation, survival, and apoptosis (**Figure 11**). The process begins with extracellular LPC, which is cleaved by Thr209 in the active site of ATX to release LPA and choline. LPA is also delivered by ATX to LPA receptors 1–6 (LPAR)_{1–6}, which activates G-protein coupled receptors, and causes downstream signalling effects which regulate the cell life cycle.

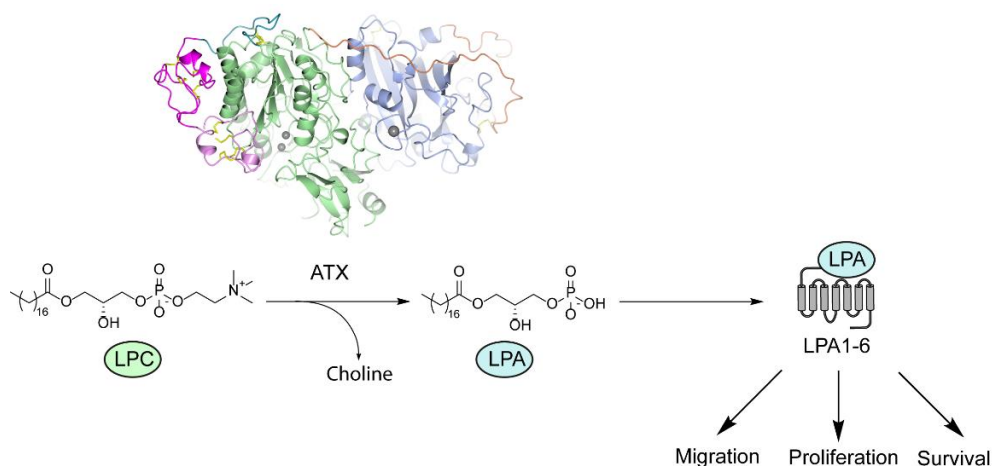


Figure 11 LysoPLD activity on the hydrolysis of LPC to LPA and subsequent delivery to LPA receptors.

LPA can exist in numerous forms with different hydrocarbon chain lengths and degrees of saturation of the lipophilic alkyl tail. Common LPA substrates of ATX are 14:0, 16:0, 18:0, 18:1, 18:3, and 22:6. The ratio denotes the total number of carbons in the lipophilic tail to unsaturated double bonds. LPA 18:0 clashes with residues in the hydrophobic pocket due to its length, and as a result is hydrolysed to a lesser extent by ATX. The rest of these LPA species are of the correct length to fit inside the hydrophobic pocket, with *Z*- isomers of the unsaturated bond to allow the longer tails to coil back out of the pocket (**Figure 12**). The degree to which these lipophilic tails fit in the hydrophobic pocket correlates with selectivity of LPC hydrolysis.¹ Kinetic studies by Caunt *et al* determined the enzyme kinetics of LPC hydrolysis of the varying chain lengths using a choline release assay. In these studies, k_{cat}/K_m ratio is a constant that is used to determine the relative rates of hydrolysis of different substrates in the enzyme. Comparison of this ratio with the different alkyl chain lengths revealed that LPA 18:1 had the fastest turnover rate at $0.8 \text{ min}^{-1}\mu\text{M}^{-1}$ compared to unsaturated LPA 20:0 with a slow turnover rate of $0.27 \text{ min}^{-1}\mu\text{M}^{-1}$.⁵¹

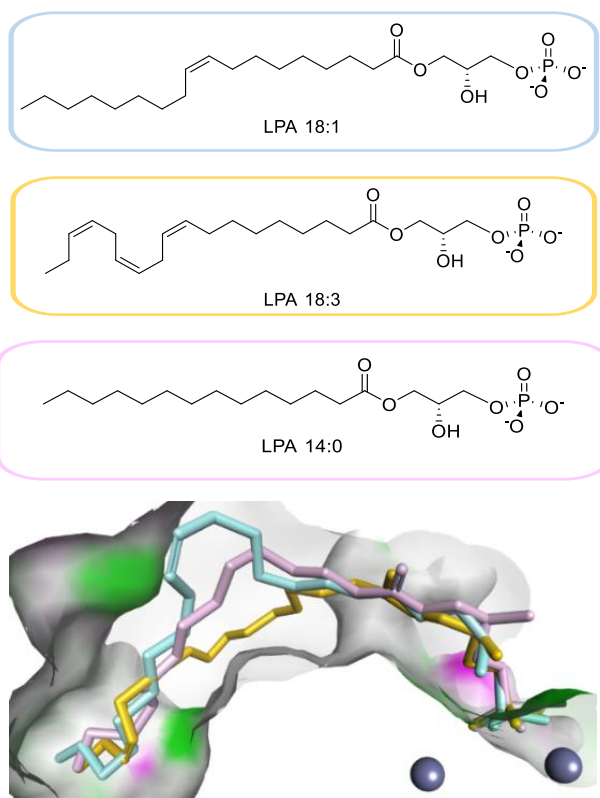


Figure 12 LPA 18:1, LPA 18:3 and LPA 14:0 which are different known substrates of ATX (PDB ID: 3NKP, 3NKQ, and 3NKN respectively) viewed in DS visualizer.^{1,48}

The majority of extracellular LPA accumulates as a result of the lysoPLD activity of ATX. However, a proportion is also produced by a competing pathway, *via* the action of the enzymes phospholipase D (PLD), and then phospholipase A1/2 (PLA1/2). PLA1/2 hydrolyses the *syn*-ester of phosphatidic acid to release LPA (**Figure 13**).

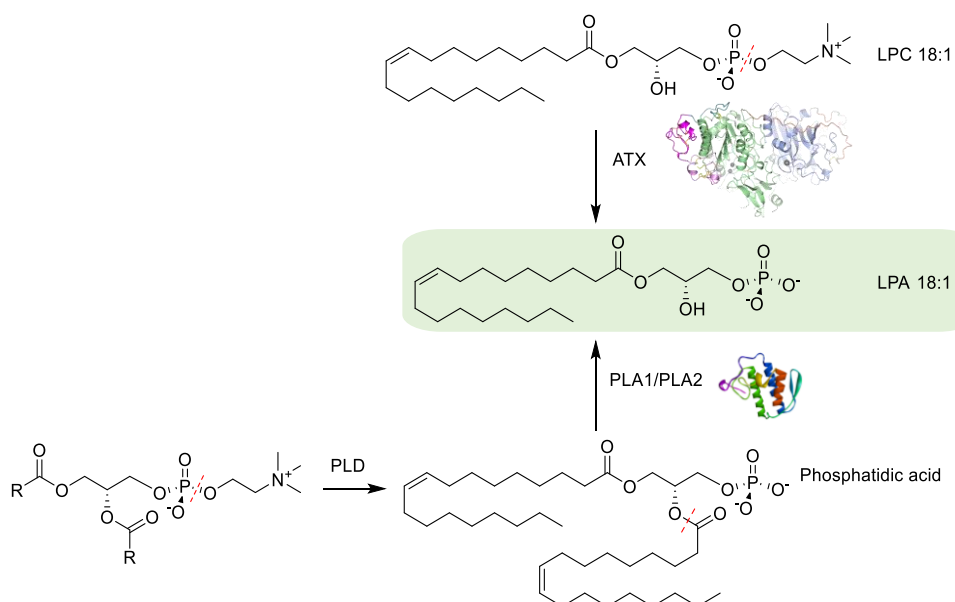


Figure 13 The two pathways for LPA production by ATX hydrolysis of LPC and phosphatidic acid hydrolysis by PLA1/2.

The mechanism of lysoPLD hydrolysis has been reported by Hausmann *et al* by co-crystallisation of LPA, LPC, VO_5 , and phosphorylated Thr species, bound to ATX as mechanistic probes for the process. The proposed mechanism begins with the nucleophilic attack of Thr209 into the phosphate ZBG, releasing choline (**Figure 14**), and the resulting intermediate is stabilised by the zinc atoms and Asn230 through hydrogen bonding. A hydroxide anion co-ordinates adjacent to the phosphate, primed for an $\text{S}_{\text{N}}2$ reaction on the LPA-ATX complex, releasing LPA, and regenerating the nucleophilic Thr209.⁴⁶

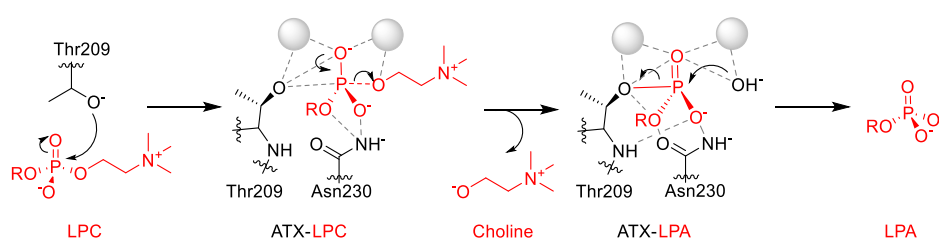


Figure 14 Proposed catalytic mechanism by Hausmann *et al* of the phosphodiesterase activity of ATX.

After the hydrolysis of LPC, LPA is released through the tunnel adjacent to the active site to LPAR_{1-6} . ATX is believed to achieve proximity to LPAR_{1-6} with the aid of interactions with an integrin receptor on the cell surface through the SMB1 and SMB2 domain of the enzyme.

The SMB2 domain is linked to the catalytic domain through a small sequence of amino acids, creating a large fold which comprises the tunnel, active site and hydrophobic pocket of the enzyme. Once ATX has bound to the integrin it is then in close enough proximity to the LPAR₁₋₆ to deliver LPA.^{39,41} It is believed that the interaction with the integrin receptor occurs primarily through SMB2, which contains an RGD amino acid binding sequence that is commonly associated with integrin recognition (**Figure 15**).⁵² Through mutations of the RGD amino acid sequence on the SMB domains, Hausmann *et al* showed that there are additional amino acids nearby the RGD sequence that are equally capable of binding to the integrin.^{41,16-17} The wall of the tunnel that delivers LPA contains part of the SMB2 domain and the catalytic domain. As a result of the SMB domain binding to the integrin on the cell surface, a conformational change in the tunnel occurs,⁹⁻¹⁰ which is proposed to prime ATX for the release of LPA to the nearby cognate receptors.^{41,55}

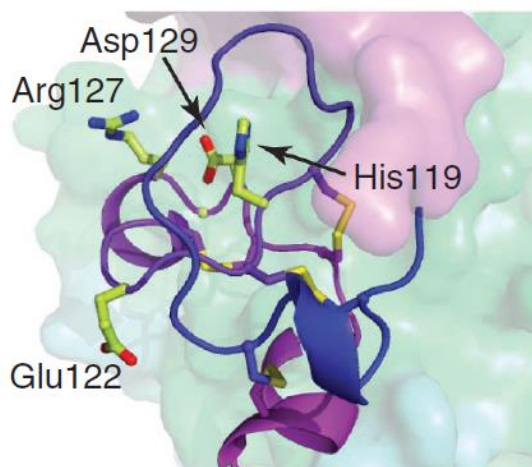


Figure 15 Residues in the SMB2 domains proposed to be responsible for the binding of ATX to integrin.⁴¹

Activation of each of the six different LPAR elicits a number of signalling cascades, such as the RHO, PLC, RAS, PI3K, and AC kinase pathways.² In particular, activation of GPCR LPA₁ leads to signal transduction through the RHO, PLC, RAS, and PI3K pathways, which are responsible for migration, proliferation, and survival of cells (**Figure 16**).⁵⁶ This increased level of cell proliferation causes the formation of fibroblasts, which are spindle shaped cells and constitute part of the extracellular matrix. Fibroblasts are also responsible for the production of myofibroblasts as a response to tissue injury which produce cytokines that can also activate the discussed signalling cascades. When this process is disrupted it can cause the pathogenesis of idiopathic pulmonary fibrosis (IPF), tumour progression, and cancer.⁵⁷⁻⁵⁸

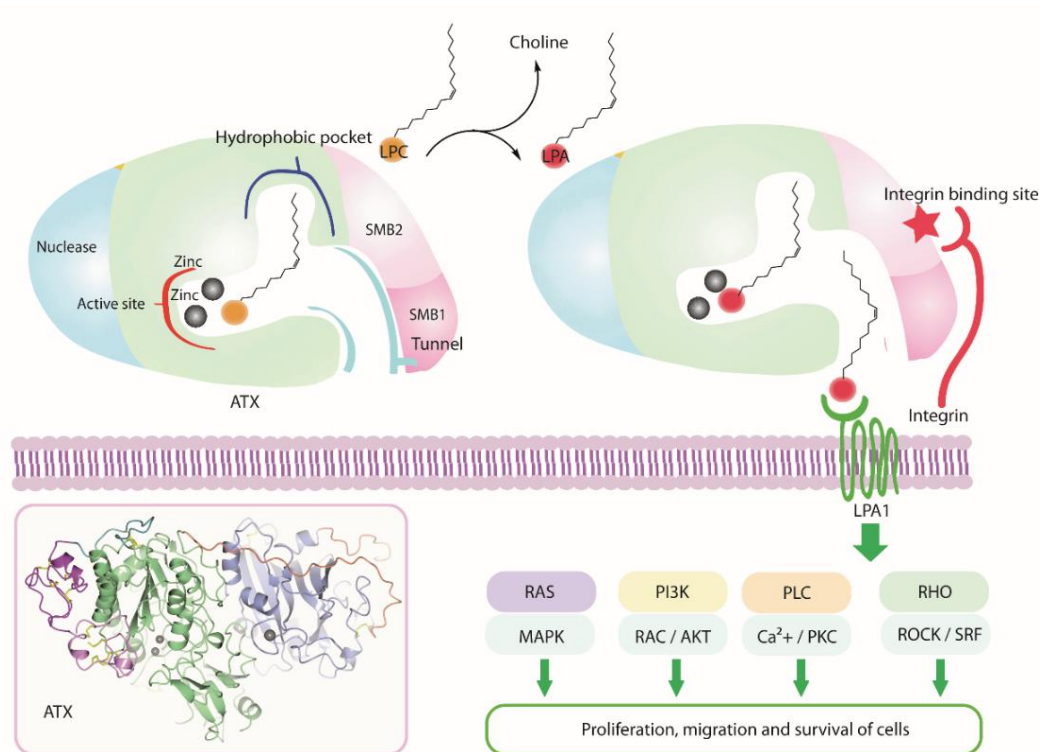


Figure 16 The lysoPLD activity of ATX with the hydrolysis of LPC to LPA and subsequent delivery of LPA to LPA₁, activation of downstream pathways leading to proliferation, migration, and survival of cells.

1.5. The Relationship between Idiopathic Pulmonary Fibrosis, Cancer and the ATX-LPA Signalling Pathway

As stated above, the ATX-LPA signalling pathway leads to cell motility, migration, and proliferation of cells, these phenotypic effects are ubiquitous in diseases such as cancer, IPF, osteoarthritis, biliary cholangitis, and multiple sclerosis.^{2,59-60} Elevated levels of ATX and LPA are often expressed in tumours of patients with cancer, BALF and extracellular fluid of IPF patients, indicating a strong connection between ATX activity and important disease states.^{2,60-61}

1.5.1. Idiopathic Pulmonary Fibrosis - Disease Background

IPF is a form of ILD, with no current cure or effective therapy. The term idiopathic means that there is no established cause for the development of the condition. IPF most commonly affects males ages 40 to 70, and has an average survival period of 2–5 years after prognosis of the disease.⁶²⁻⁶³ Additionally, IPF has a 5-year survival period, which is lower than the majority of cancers, with the exception of pancreatic and lung cancer, making it a particularly devastating disease (**Figure 17**).

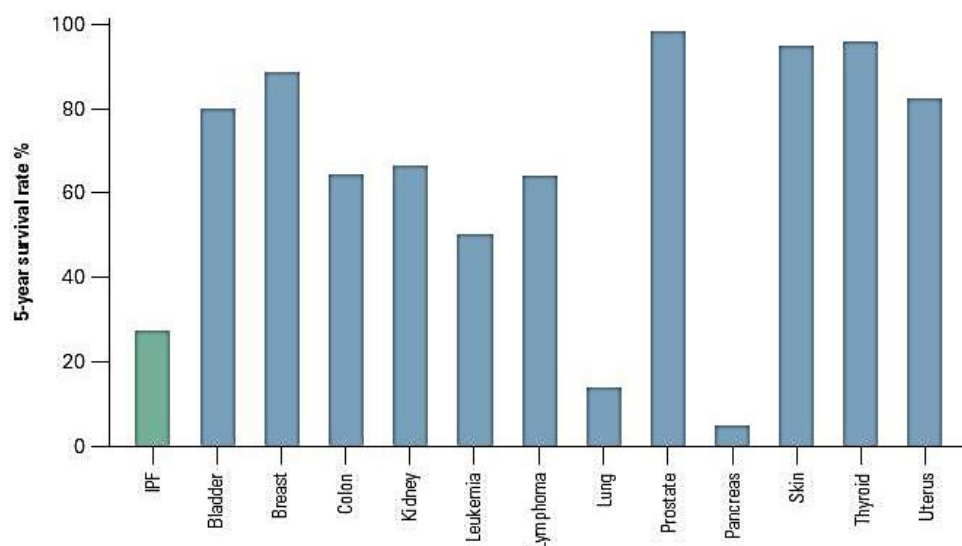


Figure 17 5-year survival rate % of IPF compared to common forms of cancer.⁶⁴

Diagnosis is often difficult and the treatment is limited, with only two approved drugs Pirfenidone and Nintedanib, and an experimental compound GLPG1690 currently in Phase II clinical trials.^{65–66} IPF leads to remodelling of the lung architecture, which decreases the number of alveoli in the lungs, shrinking the lung surface available for gas exchange. As a result of this, and the lack of effective therapies for the disease, often oxygen therapy is used to temporarily alleviate the symptoms. However, in order to completely mitigate the effects of the disease, in many cases the only viable option is a lung transplant, which is highly invasive and deemed a last resort for patients.¹⁹

1.5.2. Postulated Causes of IPF

Although the precise aetiology of IPF is illusive, there have been a number of proposals suggested to indicate potential causes for disease onset. The most widely accepted cause of IPF is an initial epithelial cell injury to the lungs. This epithelial injury is subject to the process of wound healing, which can be initiated by the hydrolysis of LPC to LPA by ATX, and delivery of LPA to LPA_{1–6}, which initiates the downstream signalling pathways RAS, PI3K, RHO, and PLC. Abnormalities in this process lead to increased cell proliferation and apoptosis of cells, resulting in the development of fibroblasts and myofibroblasts. Fibroblasts disrupt the extracellular matrix and cause extreme remodelling of the lung architecture (**Figure 18**). The process is often accompanied by honeycombing which is hardening of the lungs with the presence of large cavities. As discussed above such drastic destruction of the lung architecture

leads to the reduction in alveolar sacs available for gaseous exchange, resulting in the inability to breathe and ultimately death.

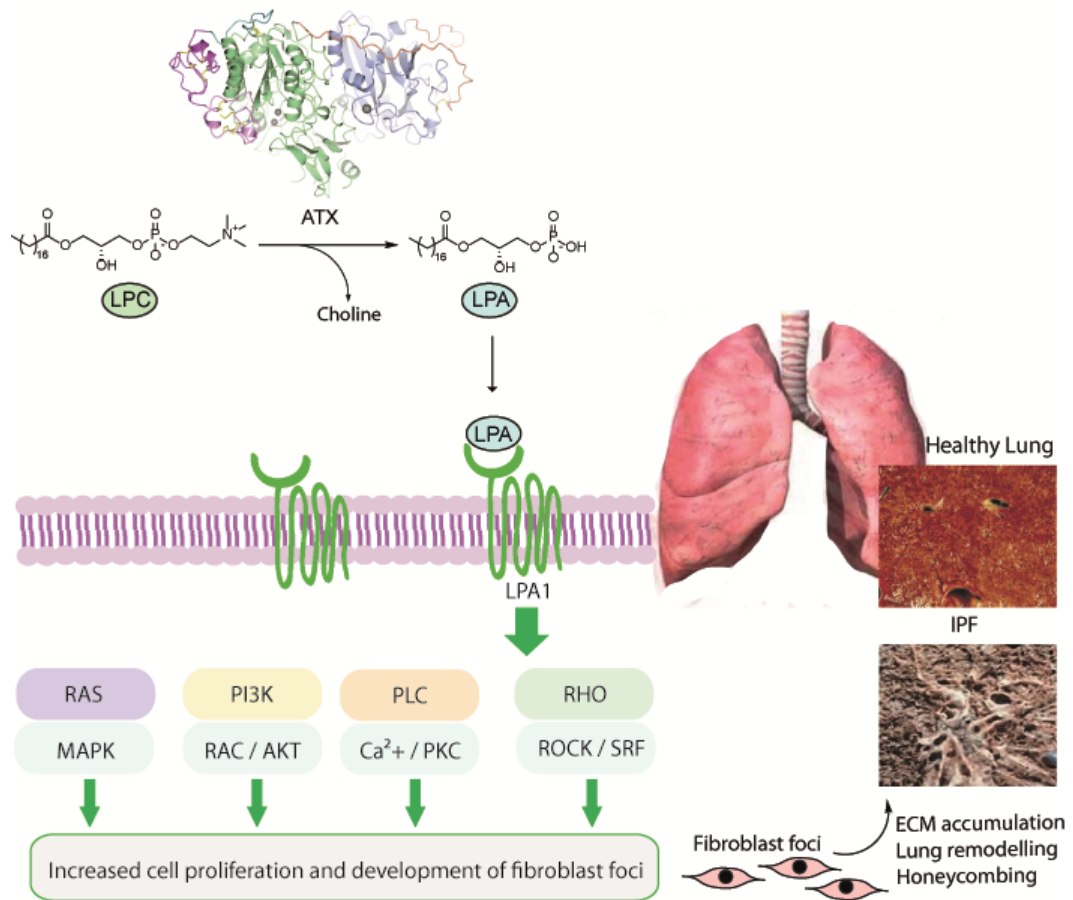


Figure 18 The lysophospholipid activity of ATX and downstream signalling that leads to the development of IPF.

1.5.3. ATX-LPA Produced after Bleomycin Induced Injury

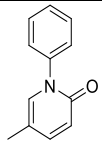
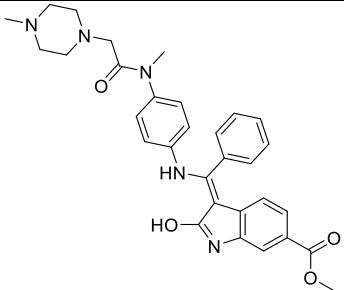
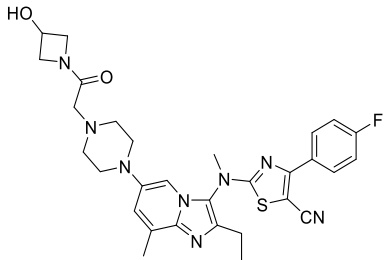
Based on the bleomycin induced model of lung injury in mice it was demonstrated that after such an injury there is an increase in ATX and LPA in BALF, thus confirming the role of the ATX-LPA signalling pathway within IPF.^{2,67} Additionally, the knockout of LPA₁ and LPA₂ in mice protects them from the development of fibrosis when using this model.⁶⁸⁻⁶⁹ Although ATX knockout mice have lower concentrations of extracellular LPA than wild-type mice, it has recently been reported by Black *et al* that some LPA detected in BALF of patients is not locally produced by ATX. Instead, the extracellular LPA is believed to be present at the site of injury due to disruption of membranes during the initial tissue injury resulting in vascular leaking from plasma ATX and LPA into extracellular regions. Another source of LPA can be ascribed to a competing pathway, with hydrolysis of phosphatidyl choline to phosphatidic acid

by PLD, followed by PLA1/2 hydrolysis of the *syn*-2 ester to produce LPA (**Figure 13**).⁷⁰ Although this pathway is an alternative source of LPA, the LPA-ATX signalling pathway has been validated *in vivo* for IPF, supporting that these targets could be efficacious in treating the condition.^{4,68,71,72}

1.5.4. Drugs and Treatments for IPF

As stated above, to date there currently are no disease modifying therapies available for IPF. The two approved drugs for the treatment of IPF, Pifenidone and Nintedanib (**Table 2**), are both unable to improve lung function of patients, merely delaying the effects of the condition. Following on from these compounds, the ATX inhibitor GLPG1690 (**Table 2**) is in Phase II trials for the treatment of IPF, and despite promising preclinical and phase I data, details of its efficacy have yet to be disclosed.

Table 2 Approved drugs Pirfenidone and Nintedanib and clinic compound GLPG1690.

Structure	Identifier	Mode of Action
	Pirfenidone	Exact mode of action unknown. TGFβ, PDGF, TNF-α, growth factor and cytokine inhibitor. ²⁷⁻²⁸
	Nintedanib	Tyrosine kinase inhibitor PDGF, VEGF and FGF. ⁷³
	GLPG1690	Competitive ATX inhibitor. ³³⁻⁷⁴

Pirfenidone (**Table 2**) was approved for the Japanese market in 2008, followed by Europe in 2011. The drug is prescribed to patients that have a severely decreased lung function with a forced vital capacity (FVC) between 50-80% of a healthy patient.²⁹ Although the exact pharmacological effects of Pirfenidone on IPF remain elusive, inhibition of cytokines and growth factors are the most likely mode of action. Pirfenidone is believed to act as an immunosuppressant that has anti-inflammatory, anti-fibrotic, and antioxidant effects.^{27,75-76} Some of the cytokine and growth factors affected by Pirfenidone include transforming growth factor β (TGF β), platelet derived growth factor (PDGF), and tumour necrosis factor- α (TNF- α). These are all cytokines implicated in the pathogenesis of IPF that promote the development of fibroblasts into myofibroblasts, and destruction of the extracellular matrix of the lungs.^{77-78,6,65} Despite the success of the drug, studies by Minnicozzi *et al* prove Pirfenidone is only able to inhibit TNF- α at large doses, and that the observed anti-inflammatory activity is not linked to this inhibition at a cellular level. Instead, Pirfenidone inhibits the production and release of another closely related cytokine IL-6, which is equally implicated in disease development.^{66,79} Further to this, Pirfenidone has also been shown to reduce mRNA expression levels of a collagen molecular chaperone, heat shock protein 47 (HSP47), believed to be responsible for collagen delivery and deposition in the extracellular matrix, which leads to honeycombing of the lungs.⁸⁰ It is likely that a combination of these inhibitory pathways are linked to the efficacy of Pirfenidone as a treatment for IPF. A phase III trial shows that treatment with Pirfenidone provides a 49% 5-year survival rate out of the 345 patients tested in a randomised trial.²⁹ This percentage is clearly significantly higher than the 5-year survival rate highlighted for IPF without any treatment (**Figure 17**). A further phase III study in 55 patients also showed no severe side effects from Pirfenidone, the decline in FVC of patients was decreased and the 6-minute walk distance increased slightly.²⁸ However, while this improves the quality of life and slows down progression of the disease, it does not cure it. Pirfenidone is speculated to inhibit multiple receptors, meaning that the exact mode of inhibition is unknown, which is largely undesirable when attempting to define the therapeutic target of the condition.⁴

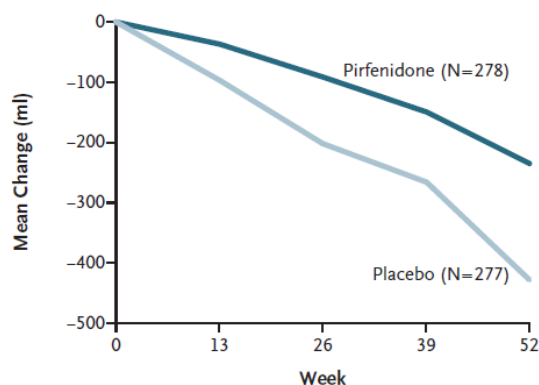


Figure 19 The mean change in forced vital capacity (FVC) of the lungs of 55 patients either treated with Pirfenidone or a placebo.²⁸

Nintedanib (**Table 2**) was approved for the treatment of IPF within the EU in 2014.⁷³ Nintedanib is an orally available tyrosine kinase receptor antagonist that acts on multiple profibrotic growth factors. Each of these growth factors are therapeutic targets that are linked to the pathogenesis of IPF in human and animal models.^{81,78} Profibrotic mediators include platelet derived growth factor (PDGF), vascular endothelial growth factor (VEGF), and fibroblast growth factor (FGF). Each of these profibrotic mediators are inhibited by Nintedanib ($IC_{50} = 20\text{--}100\text{ nM}$).⁸² The results of clinical trials showed that with twice daily doses (150 mg) there was a 68.4% reduction in the rate of decline in FVC, as well as a reduction in acute exacerbations of the disease, which normally leads to rapid progression of the disease and death.^{73,83} A phase III trial of Nintedanib highlighted several serious side effects, including diarrhoea, gastrointestinal perforations, and bleeding in a large proportion of patients.^{83,84} This is believed to be because Nintedanib is known to inhibit tyrosine kinases VEGF and VEGFR, and a large number of these receptors are present in the gastrointestinal and endocrine system, causing the adverse side effects.⁸⁴

Another promising compound currently in Phase II trials is GLPG1690 (**Table 2**), which is being developed by Galapagos. GLPG1690 is a dual tunnel-hydrophobic pocket ATX inhibitor, with clinical results likely to be released in 2017. The compound is relatively potent *in vitro* ($IC_{50} \sim 100\text{ nM}$) with different LPA species and isoforms of ATX including mATX ($IC_{50} = 224\text{ nM}$), and hATX ($IC_{50} = 131\text{ nM}$, $K_i = 14.7\text{ nM}$) with the results correlating well *in vivo* ($IC_{50} = 118\text{ nM}$).⁸⁵ Importantly for IPF, the collagen content of cells when the compound is dosed at 30 mg/kg is reduced comparably to Nintedanib (dosed 60 mg/kg) and reduced more than Pirfenidone (dosed 50 mg/kg). The comparison of the extent of collagen reduction (**Figure 20**) shows the phosphate-buffered saline (PBS) plus vehicle with no excess

collagen, and Bleomycin (BLM) plus vehicle with damaging collagen. BLM plus GLPG1690 gives a marked improvement in the lung function compared to Pirfenidone, with GLPG1690 administered at a smaller dose (30 mg/kg).³³ Results indicate that GLPG1690 is disease modifying for IPF *in vivo* bleomycin mouse models, reducing levels of cytokines and collagen regulating enzymes which are all upregulated in bleomycin and human IPF.^{22,34,86–88} Although these are promising initial results, phase II clinical trials are still on-going in order to demonstrate efficacy.

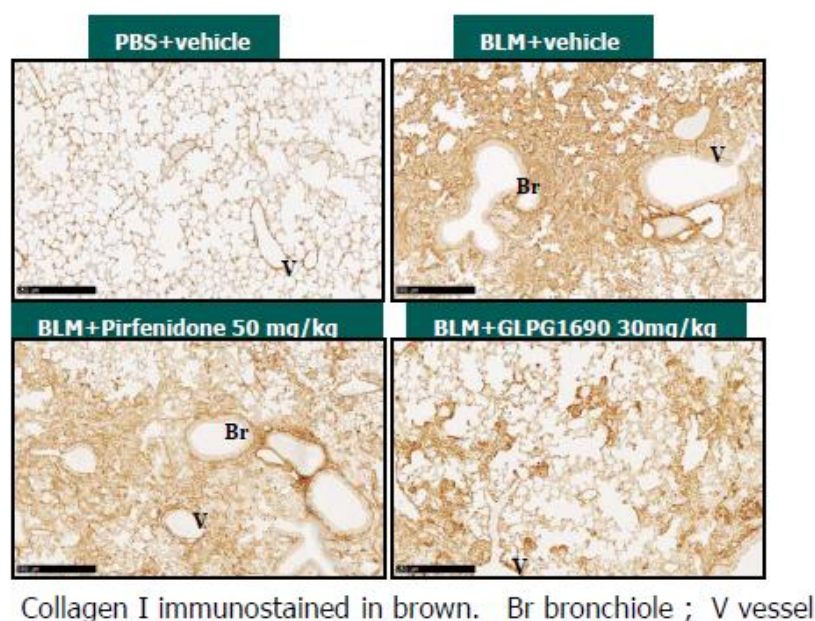


Figure 20 Collagen level comparison after dosing with Pirfenidone and GLPG1690.³³

1.5.5. Cancer and ATX

The initial discovery of the lysoPLD activity of ATX was first exhibited in A2058 melanoma cells, and as expected based on this observation the ATX-LPA signalling pathway is strongly implicated in many subsets of cancer.⁵⁰ Similarly to IPF, the interaction of LPA at LPAR₁₋₆ leads to the downstream signalling effects in the RA, RHO/RAC kinase pathways. Activation of LPAR₁₋₆ is also responsible for cell-cycle progression, tumour cell migration, invasion, and metastasis.⁸⁹ The increased migration and proliferation of cells is highly relevant to the formation, progression, chemotaxis, and metastasis of tumours in cancer (**Figure 21**). Additionally, tumours can secrete ATX, leading to a further increase in the extracellular LPA, and enhancing the development of tumour cells.⁹⁰ Overexpression of ATX and LPA in tumours such as non-small cell lung cancer, and neuroblastoma has been reported to be linked

to tumour progression and metastasis of cancer in mouse models.⁶⁰ Furthermore, the ATX-LPA pathway also promotes angiogenesis, which is the development of new blood vessels, leading to increased localised blood flow and disease progression. Increased plasma levels of ATX are often observed once chemotherapy treatment has begun, which can result in resistance to therapy.² The combination of increased LPA receptors on tumour cell surfaces, and ATX secretion leading to increased LPA-LPAR agonism, is likely additive, resulting in elevated levels of angiogenesis, metastasis, and resistance of tumours to chemotherapy treatment.⁹¹

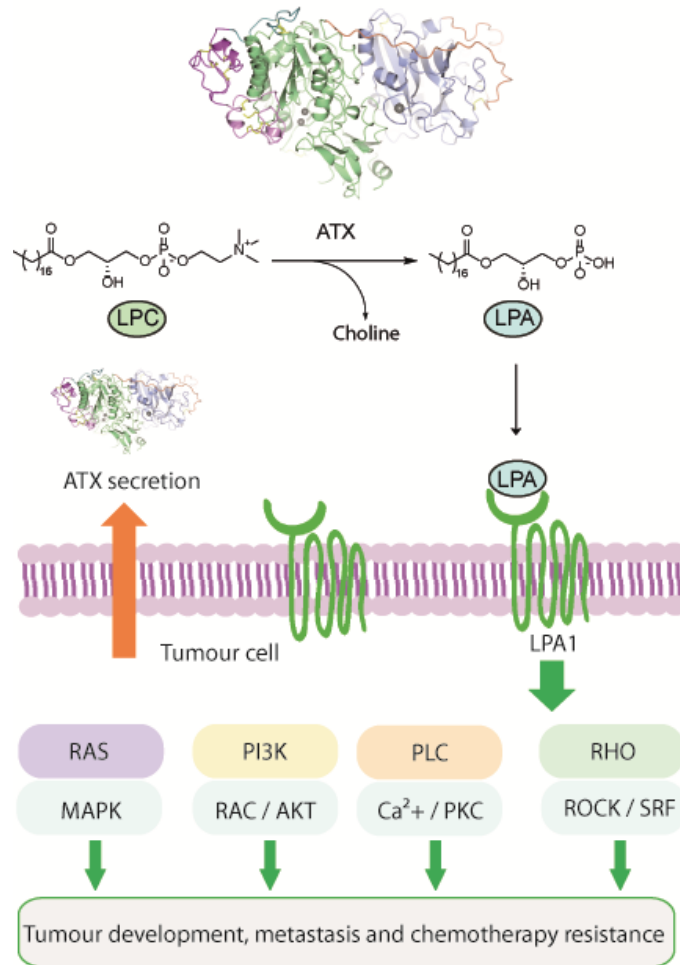


Figure 21 The ATX – LPA axis in the development and progression of cancer.

High levels of ATX mRNA have been observed in numerous types of cancer, suggesting that ATX inhibition could be a possible therapeutic target.⁸⁹ Comparison of the ATX mRNA levels in normal tissue and tumour cells can give an indication of the quantity of ATX produced locally by tumours, or if normal tissue cells merely contain high levels originally. High ATX

mRNA levels naturally occur in nervous and adipose tissues, and as a result ATX is overexpressed in brain tumours such as glioblastoma multiforme, an aggressive form of brain tumour.^{31,2}

1.5.6. Autotaxin Inhibitors as Drugs for the Treatment of Cancer

Currently there are no FDA approved drugs for the treatment of cancers utilising ATX inhibitors. However, ATX inhibitors have been reported to decrease the resistance of treatment by radiotherapy or chemotherapy, assisting current therapies during treatment. Xu *et al* reported the reduction in tumour growth and metastasis in breast cancer, and non-small lung cancer lines with a dual Bromo-LPA (BrP-LPA) ATX inhibitor-LPAR antagonist (**Figure 22**). The inhibitor is structurally similar to LPA which makes it an ideal dual inhibitor-antagonist probe, however, phosphate groups are often toxic in humans. Phosphates have an increased affinity for acetylcholine receptors, which can lead to irreversible binding of the agonist, and hinder neurotransmission in the peripheral nervous system.⁹² Additionally, alkyl bromide moieties are alkylating agents that can damage DNA and hence cause toxicity.⁹³ All of these features limit the use of BrP-LPA to being a tool compound rather than a viable therapy.

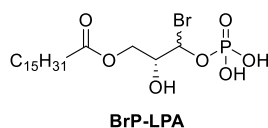
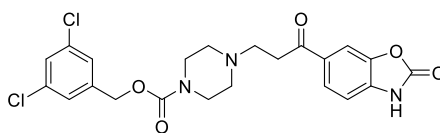


Figure 22 BrP-LPA compound developed as a dual ATX inhibitor-LPA antagonist for the treatment of non-small cell lung cancer and breast cancer *in vivo*.

PF-8380 is a potent ATX inhibitor ($K_i = 1.7$ nM, **Figure 23**), which is used to increase radio sensitivity *in vivo* with glioblastoma multiforme (GBM). Bhavé *et al* show that the combination of PF-8380 and irradiation leads to decreased cancer cell survival, tumour development, migration, and neovascularization of cells. Neovascularization is the formation of microvascular networks, it differs from angiogenesis which is the formation of new capillaries from existing blood vessels however, both are recognised in cancer development.^{2,94}



PF-8380

Figure 23 PF-8380 ATX inhibitor.⁹⁵

As highlighted by Xu and Bhave *et al*, the use of non-lipid like small molecule ATX inhibitors in combination with irradiation is a promising development in the treatment of aggressive forms of cancer where patients have developed resistance to radiation therapy.

1.6. ATX as a Therapeutic Target

Due to the implication of ATX in a number of diseases (Section 1.2.), in recent years it has emerged as an attractive therapeutic target within both academia and industry. The action of ATX and subsequent delivery of LPA to LPAR₁₋₆ can be inhibited in a multitude of ways which include the development of LPAR antagonists, integrin antagonists, as well as inhibitors of ATX itself.

LPAR antagonists include small molecule compounds Ki16425 and AM095 (**Figure 24**). These compounds are LPA₁₋₃ and LPA₁ selective antagonists, respectively. Another approach is the development of integrin antagonists, with the aim of antagonising ATX-integrin recognition and inhibiting the release of LPA to the nearby LPAR. There are a number of different integrin isoforms, with $\alpha_v\beta_6$ linked to the development of fibrosis.⁹⁶⁻⁴⁰ However, integrin antagonists are often quite large and do not necessarily always comply with drug-like molecule parameters, however more drug-like antagonists are emerging, and an example is GSK integrin antagonist **1.1** (**Figure 24**).⁹⁷ While LPAR and integrin antagonists effect downstream signalling *in vivo*, it is still uncertain whether compounds such as BMS-986020, STX-100, and GSK3008348 will have efficacy in phase III.^{16,30,35,97} Due to the unmet need for therapeutic targets which are disease modifying, and the closely related role of ATX with integrins and LPA, ATX could be a more viable therapeutic strategy.

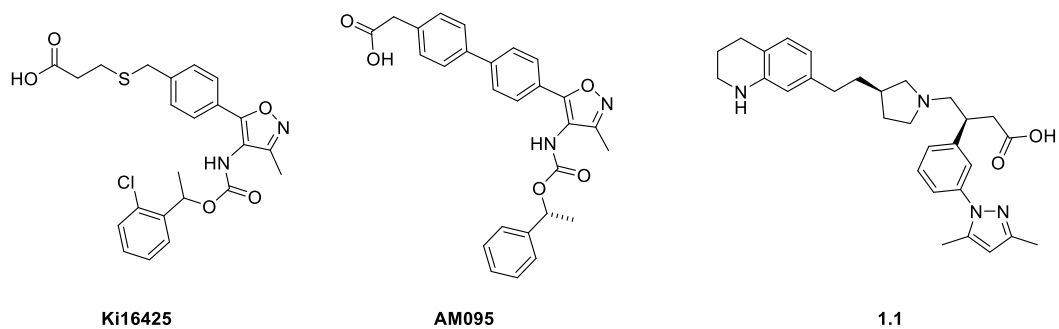


Figure 24 LPAR antagonists Ki16425 and AM095 and integrin antagonist GSK compound **1.1**.^{97–100}

The nature of the catalytic site of ATX potentially facilitates the development of a range of chemotypes that could act as inhibitors of the enzyme. Common pharmacophoric features include the presence of a zinc binding ‘war head’ which is able to interact electrostatically with the zinc atom in the active site, a space region to link the polar and hydrophobic portions of the molecules, and a lipophilic ‘tail’ which resides in the hydrophobic pocket of ATX.¹⁰¹

1.7. Physicochemical Properties of Compounds

Given that the endogenous substrate of ATX contains a large lipophilic alkyl chain, there are numerous ATX inhibitors with high lipophilicity and molecular weight, and hence they display poor physicochemical properties. In particular, compounds with high lipophilicity and molecular weight often have sub-optimal aqueous solubility, cLogD, and property forecast index (PFI).^{102–104}

The lipophilicity (LogD) of a compound is calculated based on the partition coefficient of the compound between octanol and water at a physiological pH (7.4), and can be calculated using *in silico* software JChem for Excel.^{105,106} Although moderate lipophilicity can result in better absorption through the lipid bilayers, high levels of lipophilicity results in poor aqueous solubility which negatively impacts both absorbance and clearance.¹⁰⁷ PFI is a measure of lipophilicity (LogD) plus the number of aromatic rings in the compound. This value is a forecast for predicting aqueous solubility, cytochrome p450 (CYP450) activity, clearance, human ether-a-go-go-related potassium channel protein (hERG) activity, and permeability. An optimum PFI value of 3–5 is predicted to result in good aqueous solubility (> 200 μM), decreased CYP activity ($\text{pIC}_{50} < 5$), low clearance (< 3 mL/min/kg), and hERG activity ($\text{pIC}_{50} < 5$).¹⁰⁸ CYP 450 enzymes are most abundant in the liver, and activity at these enzymes can lead to an increase in the production of metabolites which can be toxic or more reactive than

the parent compound.¹⁰⁹ Compounds which bind to the potassium channel protein which is encoded by the hERG gene result in inhibition of the cardiac current, which is believed to potentially lead to cardiovascular effects including elongation of the QT interval of the heart, and arrhythmia.^{105,109} Although a PFI of 3–5 is optimal, a value below 7 is considered to produce low risk parameters for the properties discussed above (**Table 3**). The aqueous solubility of a compound is often linked to the molecular weight and LogD as discussed above, with a high molecular weight and often corresponding to poor solubility.

In the past decade physicochemical properties have been shown to be important in reducing attrition of compounds, as deviation from optimal drug-like parameters can often cause an increase in toxicity, poor drug metabolism (DM), disadvantageous pharmacokinetics (PK), and off target toxicity such as hERG activity.¹⁰⁴ The physicochemical properties of drug-like compounds often follow Lipinski's rule of 5; with a cLogP < 5, molecular weight < 500, hydrogen bond donor (HBD) < 5, and hydrogen bond acceptor (HBA) < 10.¹¹⁰ Similarly, Gleeson's rules have stricter parameters for drug-like properties of a molecular weight < 400, and cLogP < 4.¹⁰⁴ Keeping compound parameters within these defined margins may help to improve drug metabolism and pharmacokinetics (DMPK). Most of these values can be predicted *in silico*, however chromatographic assays are useful for determining physiologically important parameters.

Ligand lipophilicity Efficiency (LLE) is another important metric that evaluates both the potency, heavy atom count (HAC) and the lipophilicity of the compound (**Figure 25 (4)**).¹⁰⁵ This equation is an adaption of the ligand efficiency (LE) equation which considers potency and molecular weight, and LLE_{LS} developed by Leeson and Springthorpe which considers both potency and lipophilicity (**Figure 25 (1, 2)**).¹⁰⁵ LLE_{AT} developed by Astex Therapeutics uses the Gibbs free energy change (ΔG^*) when a ligand in a hydrophobic environment becomes bound to a protein, which accounts for both potency and lipophilicity, and the HAC. An optimum compound based around a HAC of 36 and 10 nM potency giving an ideal value of 0.3 (**Figure 25, Table 3**).¹⁰⁵

$$(1) LE = \frac{pIC_{50} \text{ (or } pKi)}{HAC}$$

$$(2) LLE_{LS} = pIC_{50} - cLogP$$

$$(3) \Delta G^* = \Delta G - \Delta G_{lipo}$$

$$= RT \ln(IC_{50}) + RT \ln(P)$$

$$\approx -1.36 LLE_{LS}$$

$$(4) LLE_{AT} = 0.11 - \frac{\Delta G^*}{HAC}$$

Figure 25 (1) Ligand efficiency. (2) Ligand lipophilicity efficiency LLE_{LS} (3) Calculation of Gibbs Free Energy. (4) Ligand lipophilicity efficiency LLE_{AT} .

The ideal properties for a lead-like compound should have a potency of less than 50 nM, chromLogD (cLogD) of less than 3, solubility of greater than 100 μ M, LE and LLE_{AT} of greater than 0.3, and PFI of less than 6 (**Table 3**).¹⁰⁴

Table 3 Parameters for a drug-like compound.^{108,111,112}

Parameter	Lead Quality Physicochemical Properties		
	Good	Intermediate	Poor
K_i (nM)	<50	$50 < K_i < 300$	$300 \leq$
cLogD	≤ 3	$3 < cLogD < 5$	$5 \leq$
Solubility (μ M)	≥ 100	$30 < Sol < 100$	≤ 30
LE/ LLE_{AT}	≥ 0.3	$0.2 < LE/LLE_{AT} < 0.3$	≤ 0.2
PFI	< 5	$5 < PFI < 7$	$7 <$

Once the compound has shown good drug-like physicochemical properties the next step is assessing the pharmacokinetics. There are *in vitro* methods which are analysed by chromatography for calculating these parameters, but the best indication arises from *in vivo* determination.

The volume of distribution is a measure of how widely distributed the compound is within the body, with a high volume of distribution often resulting in a higher chance of interacting with the target. The combination of clearance (CL) and volume of distribution determines the half life, and ideally a low clearance combined with a high volume of distribution allows the compound enough time to reach the desired target in the body.¹¹³ Clearance is a measure of

the rate of metabolism of a compound in liver microsome preparation or *in vivo*, and is a hydrophobicity dependent value, with a PFI value of greater than 7 often correlating to an increase in clearance.¹¹⁴ Oral bioavailability (% F) is an important parameter for the fraction of an orally administered drug that is in systemic circulation and as a result, how readily available the compound is at the target.¹⁰⁵ Oral bioavailability can be affected by the solubility, permeability, and the clearance of a compound.^{104,115} A high oral bioavailability is ideal in order to give the highest chance of compound interaction with the target.

Table 4 *In vivo* pharmacokinetic profile.

Parameter	<i>In vivo</i> Pharmacokinetic Properties		
	Good	Intermediate	Poor
<i>In vivo</i> CL	< 30%	30 < CL < 70	≥ 70
Oral Bioavailability (% F)	≥ 70	30 < %F < 70	≤ 30

1.8. The Development of ATX Inhibitors

1.8.1. Lipid-like ATX Inhibitors

Perhaps unsurprisingly, early ATX inhibitors were structurally similar to LPA to mimic the binding mode of the endogenous ligand. Both LPA and a related phospholipid S1P (**Figure 26**) were identified as potent ‘mixed’ inhibitors of ATX.¹¹⁶ As expected these molecules are both potent inhibitors of ATX and LPA (LPA K_i = 110 nM, S1P K_i = 50 nM, **Table 5**).^{116–117} When LPA is used as an inhibitor of ATX, this is known as feedback inhibition.¹¹⁸ Feedback inhibition is more generally when the molecule produced by an enzyme is used as an inhibitor for the same enzyme. The use of both LPA and S1P as feedback inhibitors of ATX was believed to limit localised production of LPA at the site of action, reducing further extracellular LPA production. However, this approach was deemed ineffective in reducing LPA production *in vivo*.^{116,119}

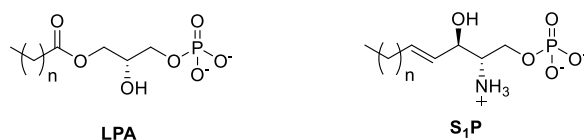


Figure 26 Structure of LPA and S1P.

Table 5 Physicochemical properties and potency of LPA and S1P.¹¹⁷ ^acLogD was calculated using JChem for Excel.¹⁰⁶

Substrate	K _i (nM)	cLogD ^a	LLE _{AT}
LPA	110	2.20	0.18
S1P	50	2.53	0.32

While using LPA as a feedback inhibitor of ATX was ineffective, other LPA analogues which are structurally distinct from LPA did demonstrate ATX inhibition. A LPA analogue containing an aromatic phosphonate synthesised by Oikonomou *et al* is an example of another lipid like ATX inhibitor (**Figure 27**). Compound **1.2** had good ATX phosphodiesterase inhibition (K_i = 24 nM, **Table 6**) and attenuated development of IPF, helping to further validate ATX as a therapeutic target.¹¹⁸ The initial development of **1.2** included reduction of the alkyl chain length to improve solubility, and resulted in good physicochemical properties (K_i < 50 nM), cLogD < 0.3, Sol > 10 μM, LLE_{AT} > 0.30).¹¹⁹ However, like BrP-LPA the phosphate moiety is still a known toxicophore.

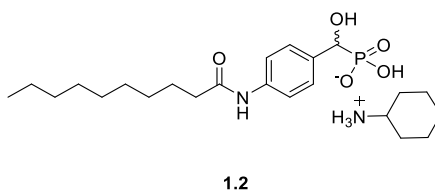


Figure 27 Aromatic phosphonate ATX inhibitor **2**.¹¹⁸

Table 6 Physicochemical properties and potency of **2**. ^acLogD was calculated using JChem for Excel.¹⁰⁶ ^bReported value.¹¹⁸

K _i (nM)	cLogD ^a	Solubility ^b (mg/mL)	LLE _{AT}
24	0.65	4	0.31

The majority of ATX inhibitors either contain a phosphate ZBG, large lipophilic tails or both. As a result of this the compounds possess high molecular weights, contained potential toxicophores, and do not fulfil Lipinski's rule of 5 for a drug like compound.¹⁰⁵ The development of non-lipid like small ATX inhibitors with lead-like properties is therefore essential for compound progression as treatments for diseases such as cancer and IPF.

1.8.2. The Development of Non-lipid Small Molecule ATX Inhibitors Binding in the Active Site and Hydrophobic Pocket of ATX

Following on from these initial studies targeting LPA mimetics non-lipid small molecule ATX inhibitors with more drug-like properties have emerged in the literature. Despite disparate structures to LPA the compounds retained excellent levels of ATX inhibition. Some examples of these compounds include HA155 (LPC substrate, $IC_{50} = 5.7$ nM)¹²⁰, and PF-8380 previously discussed in Section 1.4.7. (LPC substrate, $IC_{50} = 1.7$ nM, FS-3 assay 2.8 nM)^{95,101} (**Figure 28, Table 7**).

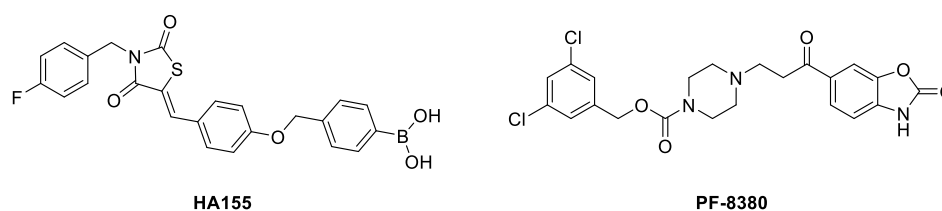


Figure 28 Non-lipid ATX inhibitors HA155 and PF-8380.

Table 7 Physicochemical properties of HA155 and PF-8380. ^acLogD was calculated using JChem for Excel.¹⁰⁶

Substrate	Ki (nM)	cLogD ^a	LLE _{AT}
PF-8380	1.7	3.62	0.34
HA 155	5.6	4.8	0.13

Although these inhibitors are structurally different to LPA, this class of potent ATX inhibitors contain common pharmacophoric features similar to the natural substrate LPA. These include a ZBG, core or spacer region, and a lipophilic tail. HA155 was co-crystallised in the active site of rat ATX by Albers *et al*, and the crystal structure bound to ATX illustrates the fluorobenzene moiety residing in the hydrophobic pocket, and the boronic acid moiety interacting with the active site (**Figure 29**).¹²¹ Key interactions of this boronic acid moiety

include a covalent bond (distance ~ 1.6 Å) with Thr209, and electrostatic interactions with both zinc atoms.

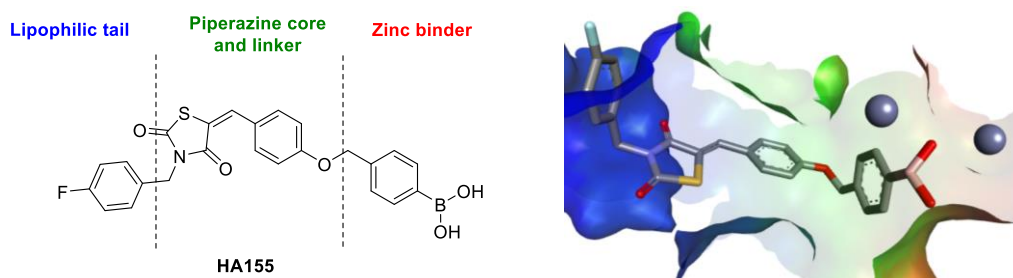


Figure 29 Pharmacophoric features of HA155 ATX inhibitor and the crystal structure of HA155 (Hydrophobic regions = blue, neutral = green, polar = red.) viewed in DSVisualizer⁴⁸ (Resolution 3.2 Å, PDB ID: 2XRG).

PF-8380 is a compound first reported by Pfizer, first developed by Merck KGA, which contains a benzo[*d*]oxazol-2(3*H*)-one ZBG, piperazine core, and a 3,5-dichlorobenzyl carbamate tail. These moieties reside in the active site, core region, and hydrophobic pocket, respectively, and result in a potent ATX inhibitor. A recent crystal structure of PF-8380 bound to ATX recently disclosed by Jones *et al* confirms this binding mode hypothesis, with the benzo[*d*]oxazol-2(3*H*)-one nitrogen interacting electrostatically with the distal zinc atom (**Figure 30**).¹²²

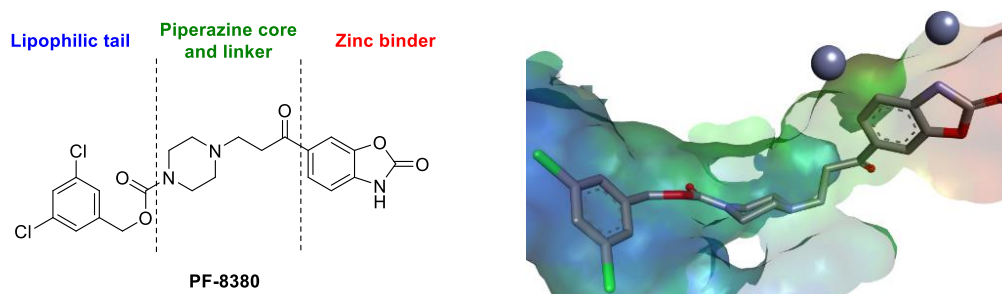
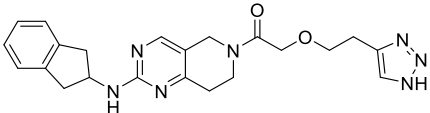
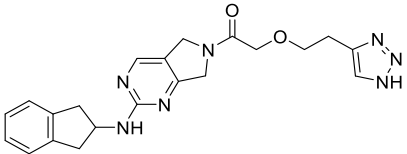
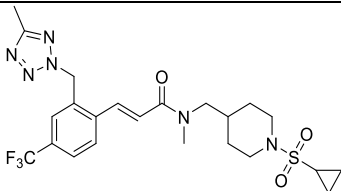
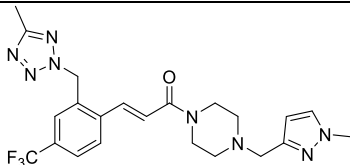
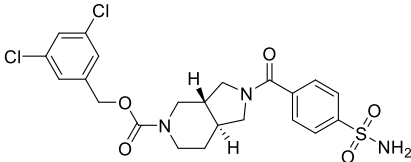


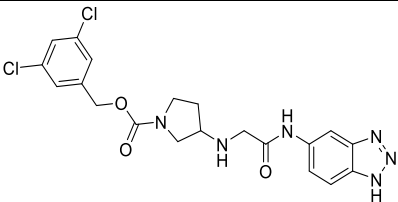
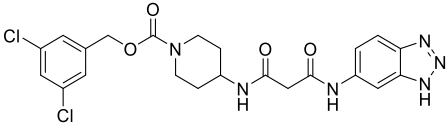
Figure 30 Pharmacophoric features of PF-8380 ATX inhibitor and the crystal structure (Hydrophobic regions = blue, neutral = green, polar = red.) viewed in DSVisualizer (PDB ID: 5L0K).^{48,122}

ATX inhibitors in the literature with structural similarities to HA155 and PF-8380 have been developed by Hoffman–La Roche,¹²³ Eli Lilly,¹²⁴ Merck,¹²⁵ and Novartis.^{126,127} This patent data represents extensive scanning of various ZBG, cores, and lipophilic tail regions. However, given that this information is largely only available in the patent literature the biological activity is often inaccessible or binned by zones of activity, making structure–activity relationship (SAR) trends difficult to quantify. Recurrent modifications in the ZBG consist of

triazoles **1.4–1.5**, benzimidazoles **1.9–1.10**, sulfonamides **1.6–1.7**, among many other known ZBG systems, and all resulting in potent compounds (Eli Lilly, Hoffman-La Roche, and Merck KGA, **Table 8**). The core region is the most variable in the patent literature and can tolerate piperazines **7**, methylaminopiperidines **6**, aminopiperidines **1.10**, aminopyrrolidines **1.9**, and bicyclic diamines **1.4–1.5** and **1.8** without any detrimental effect on ATX inhibition (Hoffman-La Roche, Novartis, Merck, and Eli Lilly, **Table 8**). The lipophilic region of these compounds usually contains aromatic groups, with lipophilic substitution from the aromatic rings also generally present. A library of analogues to PF-8380 have been developed by Merck KGA with lipophilic tail variations, however no ATX inhibition is reported in these patents.¹²⁸

Table 8 Patented ATX inhibitor compounds.

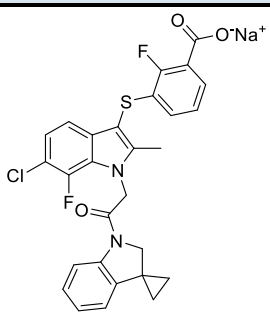
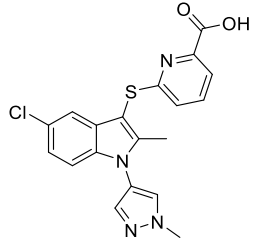
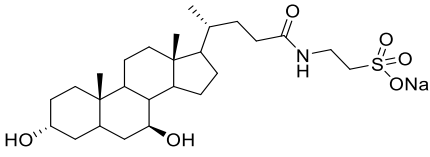
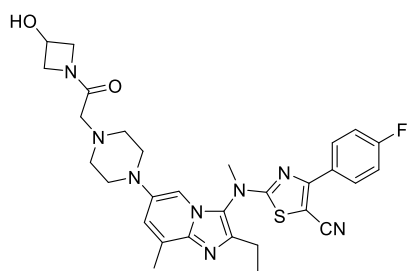
Structure	Organisation	Biological Activity
	1.3 Eli Lilly	Choline release assay Amplex red IC ₅₀ = 5.7 nM ¹²⁴
	1.4 Eli Lilly	Choline release assay Amplex red IC ₅₀ < 1.7 nM ¹²⁴
	1.5 Novartis	Choline release assay Amplex red IC ₅₀ = 4.9 nM ¹²⁶
	1.6 Novartis	Choline release assay Amplex red IC ₅₀ = 3.5 nM ¹²⁷
	1.7 Hoffman-La Roche	Choline release assay Amplex red IC ₅₀ = 4.0 nM ¹²³

	1.8	Merck KGA	Choline release assay Amplex red IC ₅₀ > 1 μM ¹²⁵
	1.9	Merck KGA	Choline release assay Amplex red IC ₅₀ = 100 nM–1 μM ¹²⁵

1.8.3. Small Molecule ATX Inhibitors with a Distinct Binding Mode in the Tunnel or Hydrophobic Pocket of ATX

Currently there are a wealth of ATX inhibitors which target the zinc binding active site and hydrophobic pocket of ATX (**Table 9**). Recently there has been a growing interest in non-competitive inhibitors and competitive allosteric inhibitors, either residing in the tunnel, or occupying both the tunnel and hydrophobic pocket of ATX. Non-competitive inhibitors include compounds such as Amira **1.10**, Pharmakea **PAT-347** and bile salt compounds such as TUDCA identified by The Netherlands Cancer Institute (NKI).^{3,45,129} Based on a wealth of crystallographic data by NKI and Pharmakea it has come to light that these non-competitive inhibitors reside in the tunnel region of the enzyme.^{74,3,45} Their activity is similarly due to inhibition of the lysoPLD activity of ATX, with the ability to either block the access of LPC through the tunnel to the active site, or stop the delivery of LPA to receptors. Compounds which bind in the hydrophobic tunnel are most often non-competitive or un-competitive inhibitors, however recently competitive dual tunnel-hydrophobic pocket binding inhibitors such as GLPG1690 have been developed (**Table 9**).

Table 9 ATX inhibitors that reside in the tunnel. ^aPAT-347 ^bTUDCA ^cGLPG1690.

Structure	Organisation	Biological Activity
	a Pharmakea	Choline release assay IC ₅₀ = 2.0 nM (Inhibitor = 100%) Bis- <i>p</i> NPP assay IC ₅₀ = 3.0 nM (Inhibitor = 57%) ⁴⁵
	1.10 Amira	Human serum ATX assay IC ₅₀ < 300 nM ¹²⁹
	b NKI	Choline release assay, homovanillic acid IC ₅₀ = 10.4 μM (Partial non-competitive inhibitor) ³
	c Galapagos	Choline release assay mATX IC ₅₀ = 224 nM hATX (IC ₅₀ = 131 nM, K _i = 14.7 nM) (Competitive inhibitor) <i>in vivo</i> (IC ₅₀ = 118 nM) ⁷⁴

The novel and selective ATX inhibitor GLPG1690 (LPC IC₅₀ = 131 nM, K_i = 15 nM) was co-crystallised at a resolution of 2.5 Å, with no reported PDB data to date.⁷⁴ Based on this image, GLPG1690 was docked using GOLD to mimic this suggested binding pose, with the compound residing in both the tunnel and the hydrophobic pocket of ATX. The important features of GLPG1690 are an azetidin-3-ol moiety which resides in the tunnel of ATX, the core region resides between the tunnel and hydrophobic pocket, and the fluorobenzene moiety that resides in the hydrophobic pocket (**Figure 31 b**). With the inhibitor in both the tunnel and the hydrophobic pocket of ATX, it is likely to block access of enzyme substrates to the active site, and also out-competes substrates in the active site of the enzyme. Lead development of

GLPG1690 led to a piperazine moiety that decreased hERG activity and a methyl substituted aminothiazole that reduced cytochrome P450 time-dependent inhibition (CYP TDI). The nitrile group was found to be important for potency, residing in a small cleft at the entrance to the hydrophobic pocket where nucleotides have been found to bind (**Figure 31 a**).⁷⁴

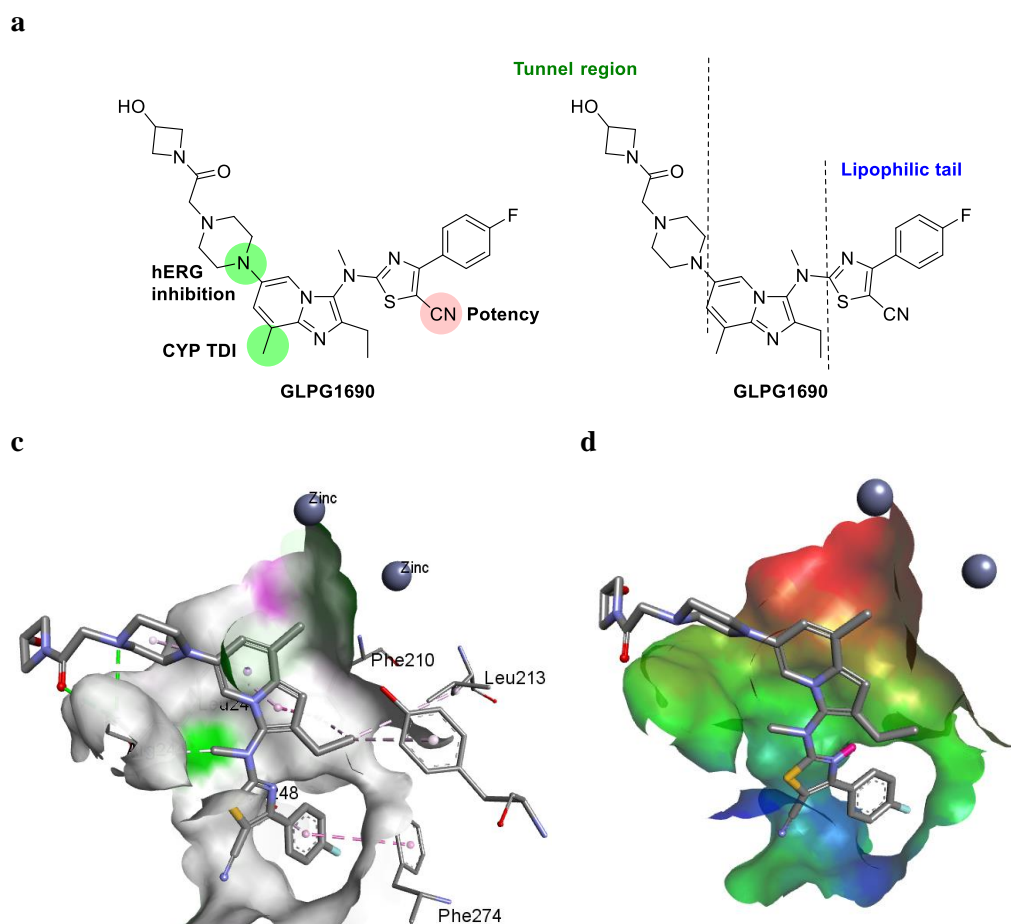
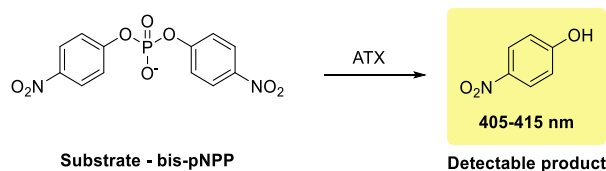


Figure 31 a) Galapagos Inhibitor GLPG1690 for the treatment of IPF and Important moieties for activity and DMPK profile of GLP1690. **b)** *In silico* GOLD¹³⁰ docking of GLPG1690 in ATX with interactions from key residues visualised in DSVisualizer. **c)** *In silico* GOLD docking of GLPG1690 in ATX visualised in DSVisualizer⁴⁸ with hydrophobicity by colour (polar = red, neutral = green and lipophilic = blue).

1.9. Biological Evaluation of ATX Inhibitors *in vitro*

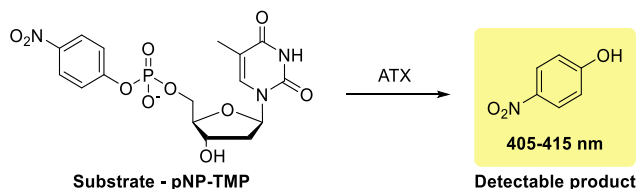
Currently the methods for determining ATX inhibition activity are primarily divided by the use of an unnatural substrate, or by analysis of the natural substrate of ATX, LPC.¹⁰¹ Biological assays most amenable to high-throughput screening are more desirable in both the pharmaceutical industry and academia, and as a result a common unnatural substrate is bis-(*p*-nitrophenol) phosphate (bis-*p*NPP) (**Scheme 1**).¹³¹ ATX catalyses the hydrolysis of bis-*p*NPP into *p*-nitrophenolphosphate, and *p*-nitrophenol, which is detected at an absorbance of 405-

415 nM. The bis-*p*NPP assay is predominantly useful for detecting ATX inhibition of zinc binding inhibitors, as *p*-nitrophenolphosphate interacts with the zinc atoms through the phosphate moiety.



Scheme 1 Biological assay with the unnatural substrate bis-*p*NPP with *para*-nitrophenol as the detectable product.

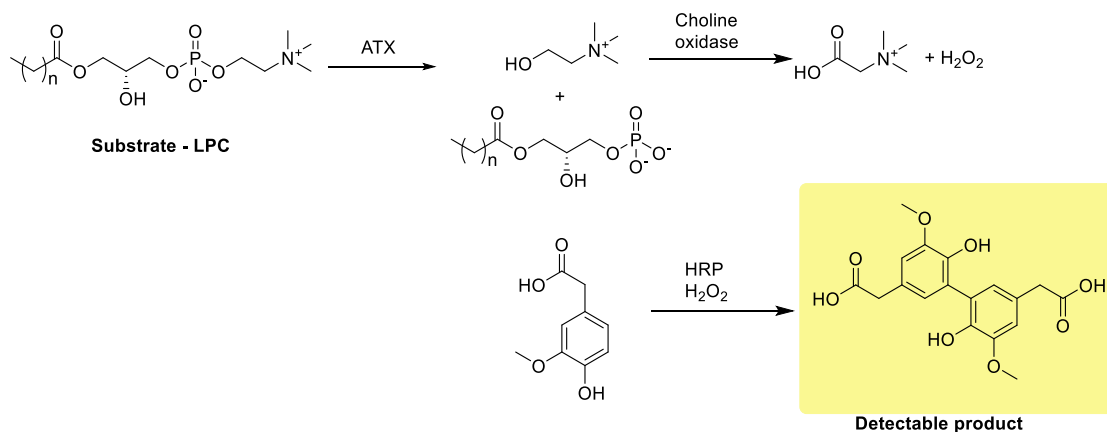
The *p*-nitrophenol-thymidinemonophosphate (*p*NP-TMP) assay similarly relies on the release and detection of *p*-nitrophenol, this time from the hydrolysis of *p*NP-TMP (**Scheme 2**). The *p*NP-TMP assay determines the phosphodiesterase activity on nucleotide substrate *p*NP-TMP, and is also primarily focused on ATX inhibition in the active site region. Once TMP is released it again interacts with the zinc atoms through electrostatic interactions with the phosphate moiety.



Scheme 2 Substrate pNP-TMP used in the unnatural substrate assay with *para*-nitrophenol as the detectable product.

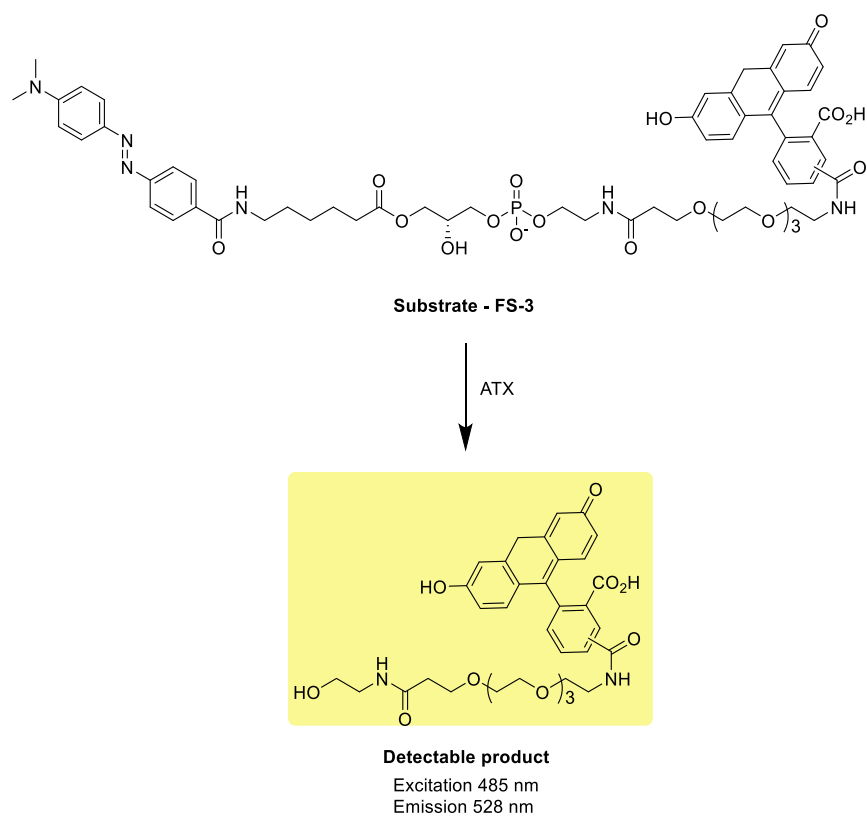
Assays containing the natural substrate LPC generally focus on the hydrolysis of LPC to LPA and the release of choline as a by-product. Once the choline has been cleaved by ATX the enzyme choline oxidase generates betaine and hydrogen peroxide, which once released can dimerise homovanillic acid (HVA) *via* oxidation of horseradish peroxidase (HRP). It is this substrate, which is measured by fluorescence, which allows quantification of ATX inhibition (**Scheme 3**). False positives may be observed with this assay if the compound inhibits choline oxidase or HRP. It has also been reported that ATX inhibition can suffer from a 10-fold potency loss in the choline release assay compared to the bis-*p*NPP when using zinc binding

inhibitors.¹³² This is because inhibitors which have high affinity at the zinc atom, and hence good bis-*p*NPP potency do not necessarily always reside in the hydrophobic pocket of ATX, therefore LPC can outcompete the inhibitor resulting in a drop in potency. The LPC assay is often related to potency within the tunnel and hydrophobic pocket of ATX, therefore false negatives can be observed with zinc binding inhibitors.¹³²



Scheme 3 ATX inhibition assay with the natural substrate LPC and detectable product a homovanillic acid dimer.

Another common assay found in the patent literature is the FS-3 assay. The phosphate bond of FS-3 is hydrolysed releasing the detectable product *via* Förster resonance energy transfer (FRET) with an excitation at 485 nm and emission at 528 nm (**Scheme 4**).¹³³



Scheme 4 FS-3 assay with the detectable product.

It is important when using these assays to determine whether the ATX inhibitor binds to the active site at the zinc atom, or if it resides primarily in the hydrophobic pocket or tunnel. This variable can have a drastic impact on the most valuable assay to use in order to determine ATX inhibition and avoid false positives or negatives. Whilst a tunnel inhibitor is potent in the LPC assay, it is often less active in the bis-*p*NPP assay. Similarly, potent zinc binding inhibitors in the bis-*p*NPP assay can appear less active in the LPC assay. Based on this, appropriate selection of assay format is an important consideration in the design of ATX inhibitors.

**Chapter 2 – The Structure Activity Relationship of PF-8380 and the
Development of Novel Autotaxin Inhibitors**

2.1. Introduction

The pharmacophoric features of the known ATX inhibitor PF-8380 as previously discussed, consist of a benzo[*d*]oxazol-2(3*H*)-one zinc binding moiety, a piperazine core, and a 3,5-dichlorobenzyl lipophilic tail. At the outset of the current study these key regions were hypothesised to reside in the active site, core region, and the hydrophobic pocket of ATX, respectively (**Figure 32 a**).¹²⁵ The binding mode observed with PF-8380 is identical to the bioactive product of the lysoPLD activity of ATX, LPA. The phosphate ZBG of LPA hydrogen bonds to Thr209, and additionally interacts electrostatically with the zinc atoms in the active site, and the long lipophilic alkyl chain resides in the hydrophobic pocket (**Figure 32 b**).

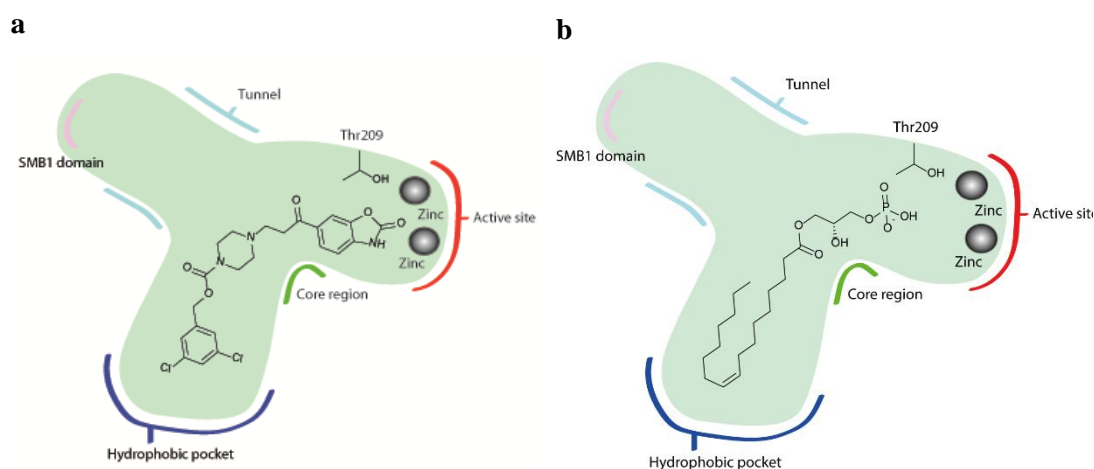


Figure 32 a) PF-8380 in the active site of ATX. **b)** LPA in the active site of ATX.

Although PF-8380 is reported as a potent tool compound ($K_i = 8$ nM, **Table 10**), it lacks the physicochemical properties of a lead-like compound (**Table 10**). Markedly, PF-8380 has incredibly poor aqueous solubility (Solubility = 3-5 mg/mL (3–5 μ M), **Table 10**), combined with moderate lipophilicity (cLogD = 3.62, **Table 10**), and a high PFI value (PFI = 6.62, **Table 10**).¹³⁴ As a direct result of these properties PF-8380 is projected to have a reduced efficacy and a greater potential for off-target effects *in vivo*.¹⁰⁵ A pharmacokinetic study of PF-8380 *in vivo* suggested that the compound had a high clearance, short half-life, high volume of distribution, and a variable degree of oral bioavailability. Despite the modest pharmacokinetic parameters, the concentration of LPA in plasma and the site of inflammation was lowered suggesting good pharmacodynamics *in vivo*, further validating the use of PF-8380 as a potent tool compound.¹³⁵

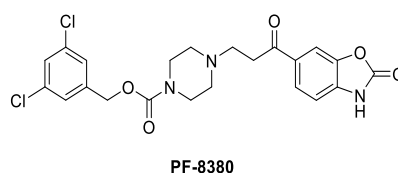


Table 10 Physicochemical and pharmacokinetic properties of PF-8380 ^aCalculated with JChem. ^cSolubility mg/ml¹³⁴

Physicochemical Properties				
K_i	cLogD ^a	Sol (mg/mL) ^c	LLE _{AT} ^a	PFI ^a
8 nM	3.62	3-5	0.30	6.62

Table 11 Pharmacokinetic properties of PF-8380. CL = Clearance, V_d = Volume of distribution.¹³⁵

Pharmacokinetic Properties			
CL (ml/min/kg)	V _d (L/kg)	t _{1/2} (h)	F %
31	3.2	1.2	43-83

2.1.1. Project Aims

In the current study, we aim to design and synthesise a focussed compound library of compounds in order to probe the SAR around the known tool compound PF-8380. At present there is limited detailed biological activity relating to PF-8380 analogues, with the patent literature revealing biological activity ranges on a few selected compounds.¹²⁵ Within this SAR study of PF-8380 analogues, we aimed to confirm our proposed binding mode hypothesis, with the ZBG electrostatically interacting with the zinc atoms in the active site, and the lipophilic tail residing in the hydrophobic pocket. In addition, we aimed to confirm the binding mode with the aid of co-crystallography combined with *in silico* modelling, and the biochemical assay data. Based on the poor solubility of PF-8380, improvements to the physicochemical properties of the compounds was investigated throughout the course of the SAR study, with the intention of improving the aqueous solubility, and decreasing the cLogD. With the knowledge generated from the initial SAR scope we aspired to generate a novel series of orthosteric ATX inhibitors, which are structurally distinct from PF-8380, exploiting the wealth of data established from the SAR study to maintain potent ATX inhibitors. Through the design of these novel ATX inhibitors, with improved physicochemical properties, we aimed to generate lead-like compounds with potency correlation in both biochemical, and cell

based assays. After evaluation of the cell based potency of the compounds we aimed to have identified a promising candidate to evaluate the effect of ATX inhibition in an *in vivo* setting.

2.2. Binding Mode Analysis Through Co-crystallography with ATX

A crystal structure of PF-8380 bound to ATX was recently reported by Jones *et al.*¹²² The structure shows the nitrogen of the carbamate warhead interacting directly with the distal zinc atom (**Figure 33**). The distance between the zinc atom and the nitrogen is approximately 2.12 Å, with close proximity for beneficial monodentate electrostatic interactions with one of the zinc atoms as a distance of less than 2.5 Å is within the coordination sphere of zinc, which suggests an interaction is occurring.^{122,136,137} The ZBG does not necessarily interact with the zinc through the carbonyl group, which is one of the other potential binding modes of the inhibitor.¹³⁸ This suggests there are potentially a few active site binding modes which can result in potent ATX inhibitors; a monodentate binding mode through the nitrogen, or bidentate through the carbonyl moiety. The ligand can interact with one of or both of the zinc atoms electrostatically or additionally through the formation of covalent bonds or hydrogen bonds with Thr209 (**Figure 33 c**). ATX inhibitors evidently do not have to directly interact with Thr209 for potency in the same way that LPC does for hydrolysis to LPA, although HA155 does, through the boronic acid moiety (Section 1.3.2., **Figure 29**).¹²²

Further confirmation of this binding mode hypothesis was obtained from co-crystallisation of an alcohol analogue of PF-8380 (**2.1**) within the active site of ATX (**Figure 33 b**). Compound **2.1** is reported with an $IC_{50} = 100 \text{ nM} - 1 \text{ }\mu\text{M}$ in a Merck patent using the natural substrate LPC, and Amplex red rather than HVA as described in Section 1.9.¹²⁵ When tested in a different assay, compound **2.1** ($K_i = 2.3 \text{ nM}$, bis-*p*NPP assay) was found to have comparable activity to PF-8380 ($K_i = 8.0 \text{ nM}$, bis-*p*NPP assay). The co-crystal structure exhibits an almost identical binding mode to the reported PF-8380 structure (**Figure 33 b**), however the benzo[*d*]oxazol-2(3*H*)-one projects with a different vector due to the adjacent sp^3 alcohol centre. In both crystal structures the piperazine is stacked nearby a Tyr306 residue where π -alkyl interactions are observed, and additionally PF-8380 has π -alkyl interactions with Phe210 in this region. The lipophilic 3,5-dichlorobenzyl carbamate tail of both PF-8380 and **2.1** resides in the pocket, forming hydrophobic interactions with nearby residues, which as previously discussed are postulated to be important for ATX inhibition.

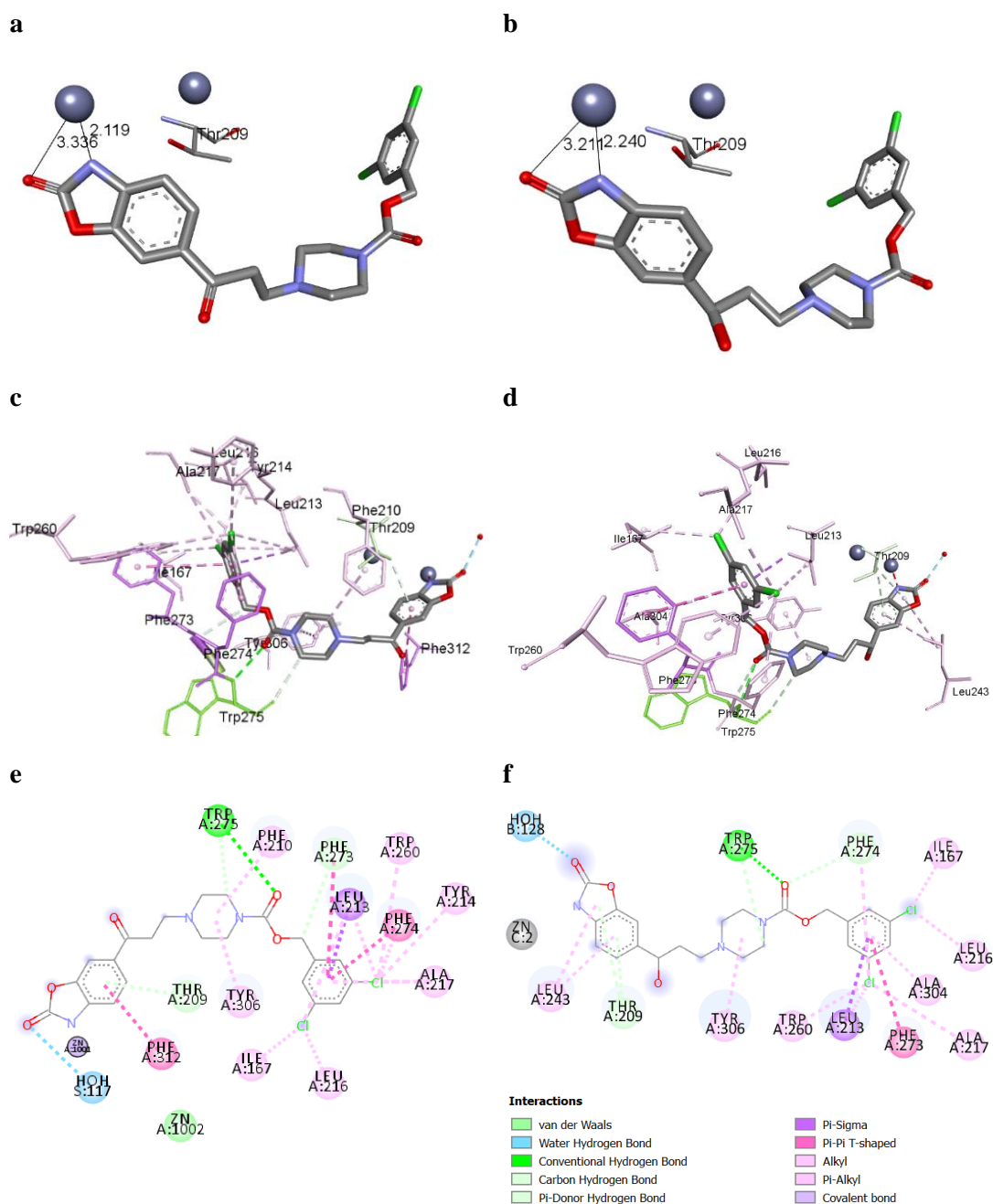


Figure 33 Images viewed or generated in DS visualizer.⁴⁸ **a)** Co-crystal structure of PF-8380 (PDB ID:5L0K) in the active site of ATX and the proximity of the ZBG to the zinc atoms and Thr209.⁸⁸ **b)** Co-crystal structure of **2.1** in the active site of ATX and the proximity of the ZBG to the zinc atoms and Thr209. **c)** Visualization of nearby amino acid residues for ATX inhibition with PF-8380 in the active site and hydrophobic pocket (Colour coded based on Interactions). **d)** Visualization of nearby amino acid residues for ATX inhibition with **2.1** in the active site and hydrophobic pocket (Colour coded based on Interactions). **e)** 2D visualisation of interactions with PF-8380. **f)** 2D visualisation of interactions with **2.1**.

The co-crystallographic results reveal that the original binding mode hypothesis, mimicking the binding mode of LPA, is correct. Additionally, our *in silico* model using GOLD¹³⁰ is in accordance with the binding mode in the co-crystal structures suggesting that this algorithm

could be used in a predictive sense going forward. An overlay of the co-crystallographic data of LPA 18:1 and **2.1** bound to ATX indicates the complementary poses adopted by the two compounds within the active site and the hydrophobic pocket (LPA blue, **2.1** yellow, **Figure 34**).

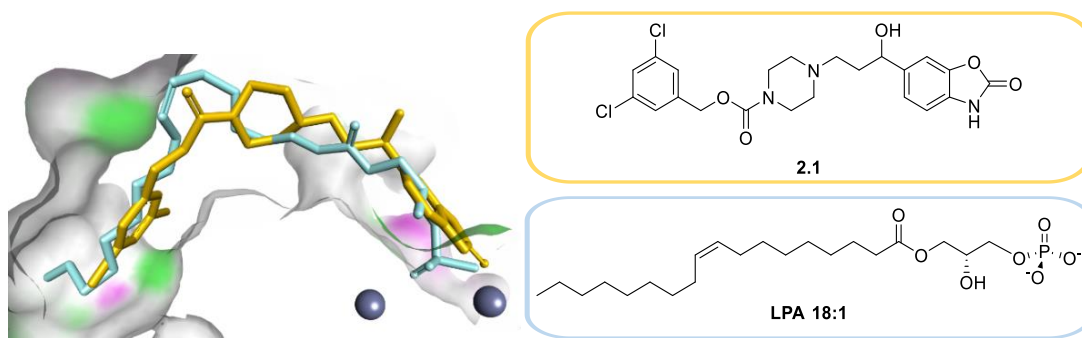


Figure 34 Overlay of the two crystal structures of LPA 18:1 (PDB ID: 3NKP), and **2.1** in the active site of ATX showing the similarity in binding modes in DS visualizer.^{1,48}

2.3. PF-8380 SAR

2.3.1. Retrosynthetic Analysis of PF-8380

The retrosynthetic analysis of PF-8380 leads to two core fragments A and B (**Figure 35**). Synthesis of the building blocks for fragments A and B is readily achieved from commercially available materials, or the components can be prepared in a minimal number of steps. Small modifications to each region quickly allows for the generation of a substantial compound library, which enables rapid investigation of the SAR.

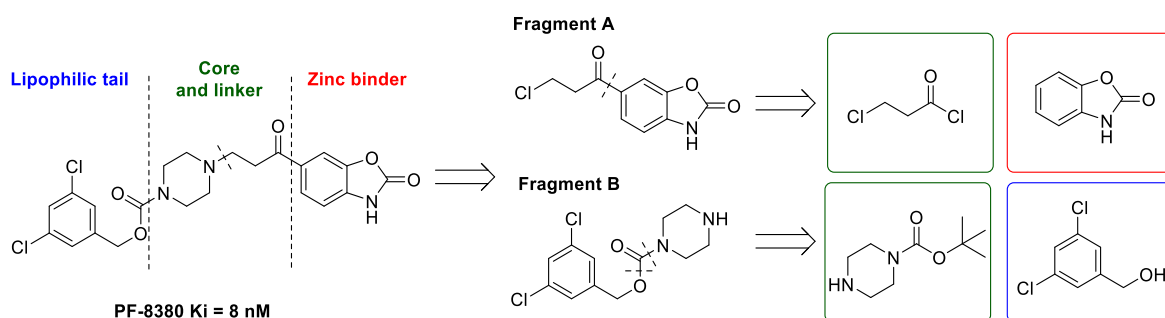


Figure 35 Retrosynthetic analysis of PF-8380.

The three key regions to explore include the lipophilic tail region which resides in the hydrophobic pocket, the ZBG located in the active site, and the core region linking both sites. Initial focus on the lipophilic region will determine the necessity for aromaticity in the hydrophobic pocket. Additionally, improvements to this region can be made by removing the di-chloro groups, using alternative halogens, and by increasing the polarity *via* the introduction of charged heteroatoms (Blue, **Figure 36**). The core region can be modified with small changes to the ketone moiety, investigating alternative diamine cores, and the length of the ethylene linker to modify the overall length of the compound (Green, **Figure 36**). In the zinc binding region, firstly the effect on potency with small modifications to the benzo[*d*]oxazol-2(3*H*)-one ZBG can be assessed by modifying the heteroatom X. The benzo[*d*]oxazol-2(3*H*)-one can also be replaced with known ZBGs in order to enter more structurally diverse space from current ATX inhibitors (Red, **Figure 36**).

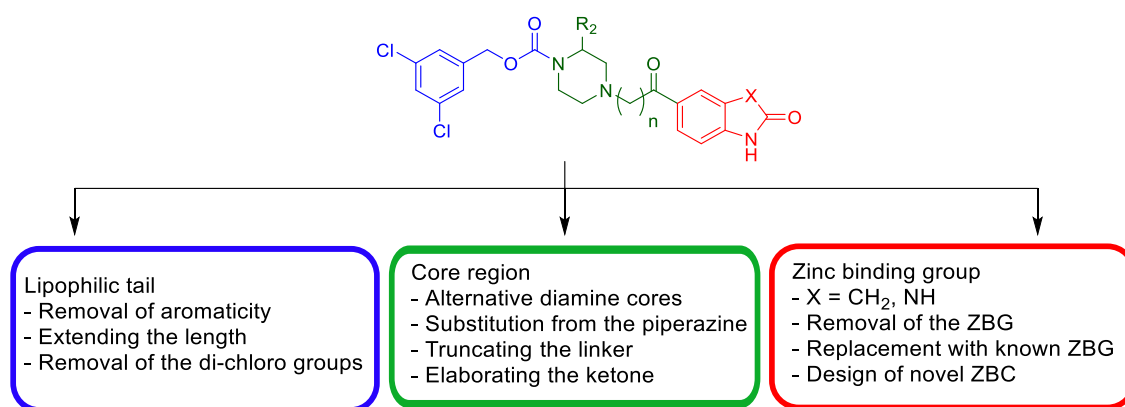
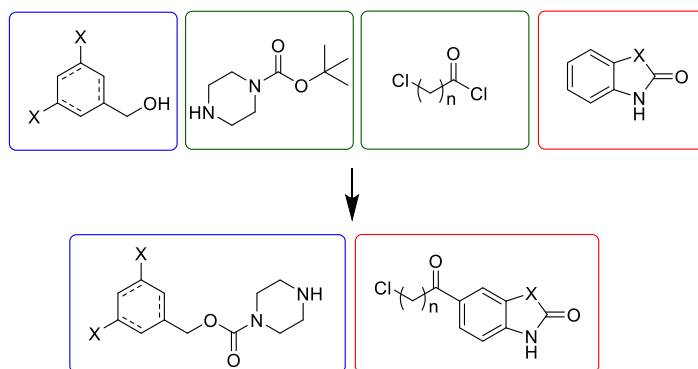


Figure 36 Proposed PF-8380 SAR exploration.

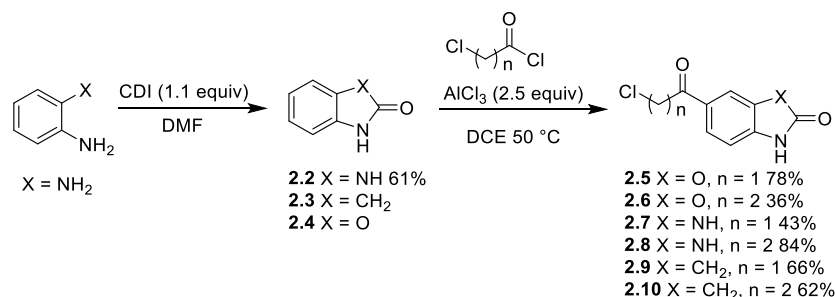
2.3.2 Synthesis of Key Building Blocks

Throughout this work, common intermediates were synthesised from readily available starting materials. A modular synthesis was employed for the building blocks necessary for a primary SAR screen (**Scheme 5**).⁹⁵



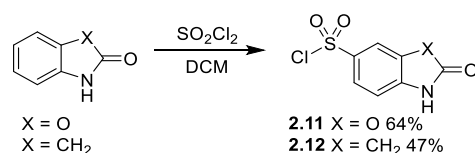
Scheme 5 Outline of core reagents for the synthesis of common intermediates.

The precursor for the Friedel-Crafts acylation reaction, 1,3-dihydro-2*H*-benzo[*d*]imidazol-2-one **2.2**, was synthesised with 1,1'-carbonyldiimidazole (CDI) from benzene-1,2-diamine.¹³⁹ A Friedel-Crafts acylation reaction with **2.2**, benzo[*d*]oxazol-2(3*H*)-one, and indolin-2-one with either chloroacetyl chloride or 3-chloropropanoyl chloride afforded alkyl halide intermediates **2.5–2.10** (**Scheme 6**), which are the starting reagents for subsequent alkylation reactions (Section **2.4.1**).^{95,140,141}



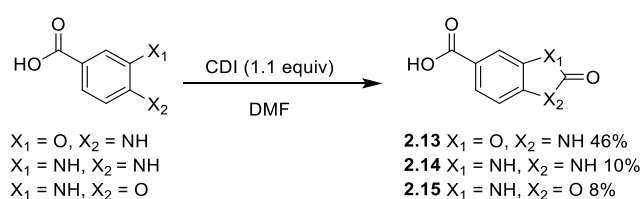
Scheme 6 Friedel-Crafts acylation for the preparation of alkyl halide starting materials **2.5–2.10**.

The sulfonyl chloride ZBG **2.11–2.12** for the sulfonamide series (Section **2.6.3**) was synthesised from benzo[*d*]oxazol-2(3*H*)-one or indolin-2-one starting materials *via* a sulfonylation reaction with sulfonyl chloride (**Scheme 7**).^{142,143}



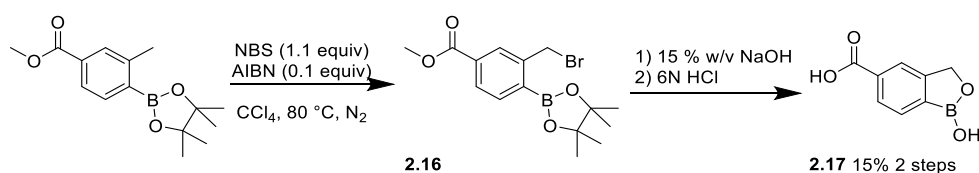
Scheme 7 Sulfonylation reaction to afford **2.11–2.12**.

Carboxylic acid intermediates **2.13–2.15** for the synthesis of the amide analogues (Section **2.6.4**) were synthesised from 4-amino-3-hydroxybenzoic acid, 3,4-diaminobenzoic acid or 3-amino-4-hydroxybenzoic acid starting materials, respectively, which were cyclised with CDI to form the carbamate in one step (**Scheme 8**).



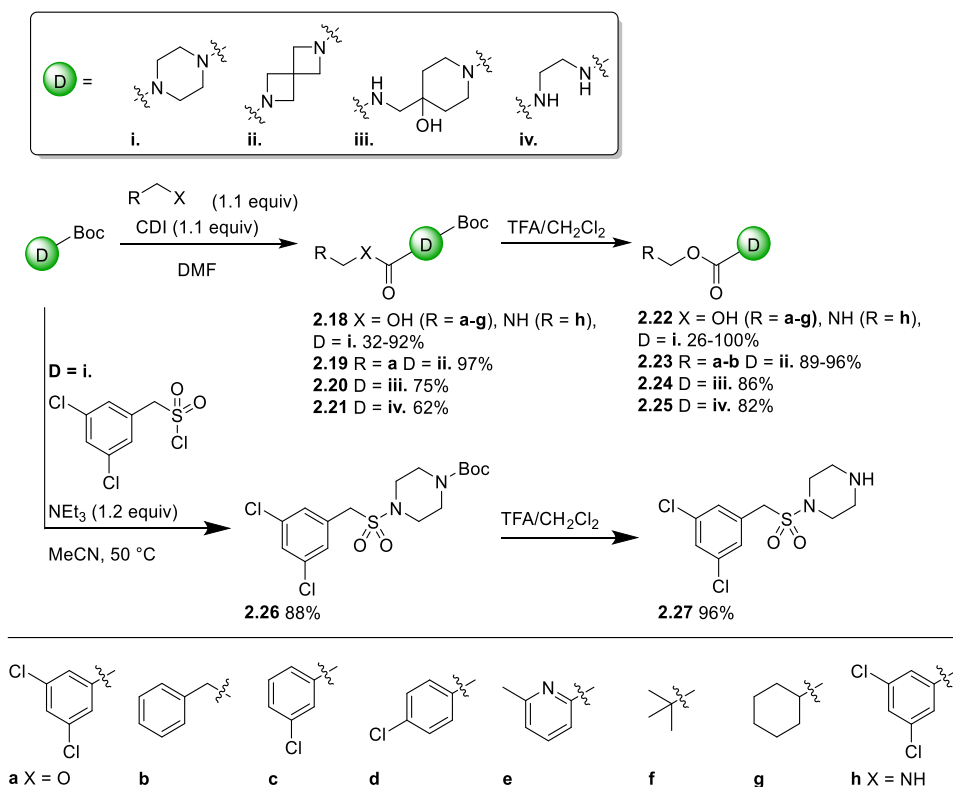
Scheme 8 Carbamate synthesis for carboxylic acid starting materials.

In addition to the intermediates used in the primary SAR screen, a novel borocycle ZBG was synthesised. Intermediate **2.16** was synthesised *via* bromination of methyl 3-methyl-4-(4,4,5,5-tetramethyl-1,3,2-dioxaborolan-2-yl)benzoate, followed by hydrolysis of the methyl ester, and displacement of the bromine atom with hydroxide using 15% w/v KOH. This intermediate then undergoes intramolecular cyclisation to form the 1-hydroxy-1,3-dihydrobenzo[*c*][1,2]oxaborole-5-carboxylic acid **2.17**, which precipitates under acidic conditions (**Scheme 9**).¹⁴⁴



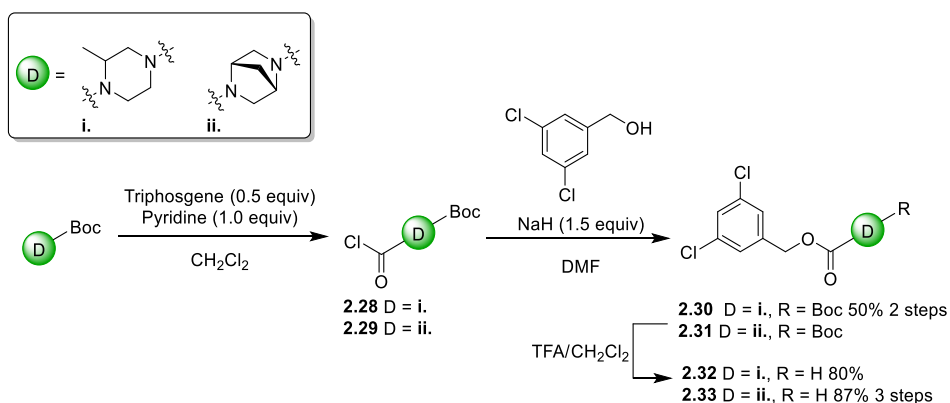
Scheme 9 Synthesis of the 1-hydroxy-1,3-dihydrobenzoxaborole intermediate.

The piperazine, 2,6-diazaspiro[3.3]heptane, or 4-(aminomethyl)piperidin-4-ol core and tail building blocks are synthesised from the corresponding alcohol, *N*-Boc diamine, and CDI to afford the *N*-Boc intermediates **2.18–2.21** (Scheme 10). Analogously, the sulfonamide intermediate **2.26** is synthesised with *N*-Boc piperazine, (3,5-dichlorophenyl)methanesulfonyl chloride, and triethylamine in acetonitrile at 50 °C. The *N*-Boc group is cleaved under acidic conditions, resulting in diamine building blocks **2.22–2.25**, and **2.27** (Scheme 10) for subsequent alkylation and amidation reactions (Section 2.4).¹²⁸



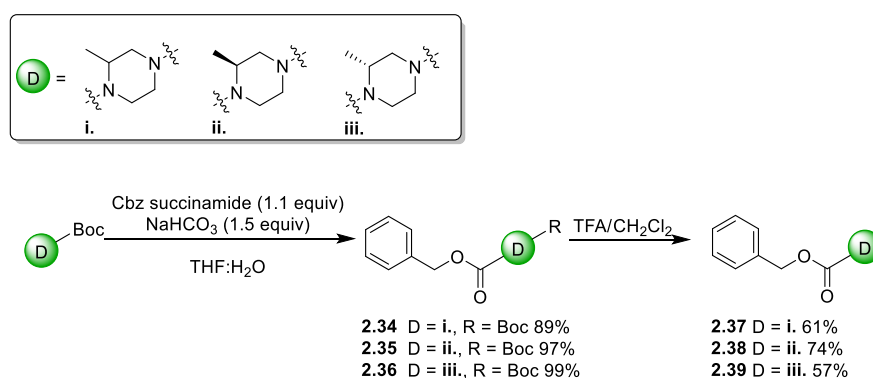
Scheme 10 General route for the synthesis of piperazine intermediates.

This synthesis did not yield product with bulky substituted piperazine intermediates 2-methylpiperazine and (1*S*,4*S*)-2,5-diazabicyclo[2.2.1]heptane (**D** = **i.** and **ii.** Scheme 11). A modified synthesis *via* a carbamoyl chloride intermediate generated using triphosgene gave intermediates **2.28** and **2.29**. Intermediates **2.30–2.31** were synthesised with the addition of (3,5-dichlorophenyl)methanol and sodium hydride, followed by *N*-Boc cleavage under acidic conditions to yield **2.32–2.33** (Scheme 11).¹⁴⁵



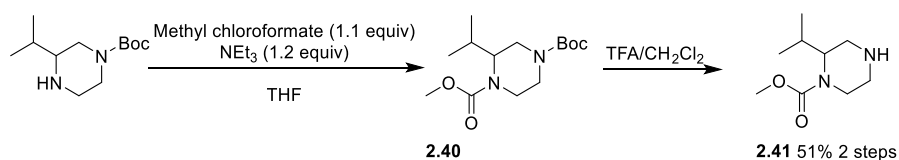
Scheme 11 Synthesis of 2-methylpiperazine and (1*S*,4*S*)-2,5-diazabicyclo[2.2.1]heptane building blocks **2.32** and **2.33**.

The *N*-Boc protected methyl substituted piperazines **2.34–2.36** bearing a benzyl carbamate could be synthesised with *N*-(Benzyloxycarbonyloxy)succinimide and base in THF and water (**Scheme 12**). The *N*-Boc intermediates were deprotected under acidic conditions to reveal the free amines **2.37–2.39** for use in subsequent alkylation reactions.



Scheme 12 Synthesis of methylsubstituted piperazines with a benzyl carbamate tail.

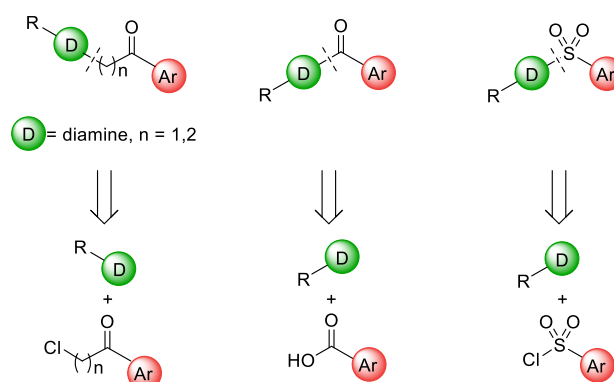
The isopropyl substituted piperazine was synthesised with the methylcarbamate tail using methyl chloroformate and triethylamine in THF to yield *N*-Boc intermediate **2.40**, which was cleaved under acidic conditions to yield **2.41** (**Scheme 13**). These less sterically hindered reagents allowed synthesis of the desired products despite the bulky piperazine substitution.



Scheme 13 Synthesis of isopropyl substituted piperazine core.

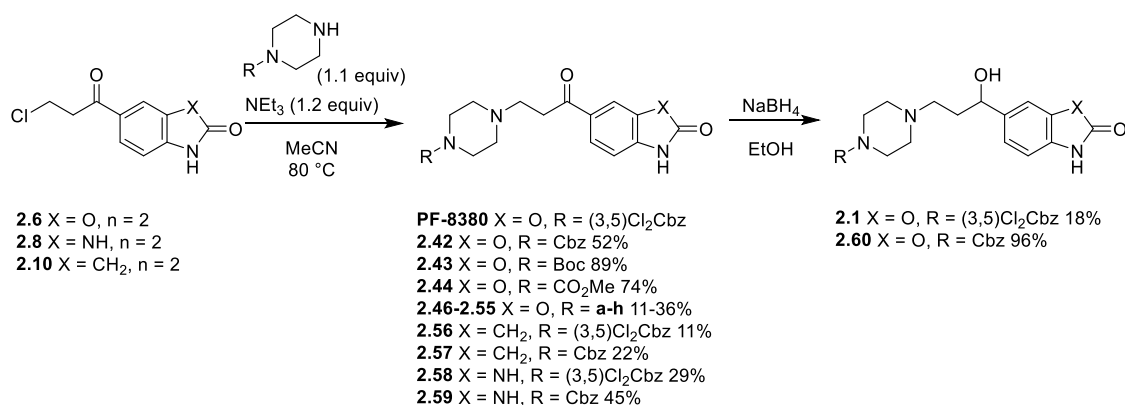
2.3.3. Synthesis of Final Compounds

Generally, final compounds were synthesised either *via* an alkylation, or amidation reaction (**Scheme 14**), with the key intermediates synthesised in Section 2.3.1.



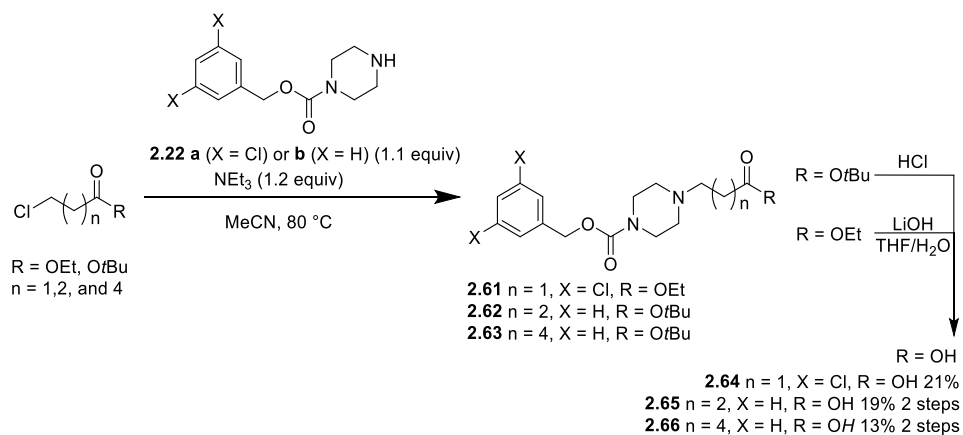
Scheme 14 Retrosynthesis of amine, alkylation and sulfonamide linked final compounds.

The compounds **2.42–2.59** were synthesised *via* an alkylation reaction (**Scheme 15**) using the the corresponding piperazine core **2.22 a-h** (**Scheme 10**), and the alkyl halide intermediate **2.6** (**Scheme 6**), discussed in Section 2.3.1. Further to this, using piperazine intermediates containing the 3,5-dichlorobenzyl carbamate intermediates **2.22 a**, **2.22 b** (**Scheme 10**), and alkyl halide intermediates **2.8** and **2.10** (**Scheme 6**) a series of compounds with varied ZBG **2.56–2.59** were synthesised. The *N*-Boc analogue **2.43** was deprotected under acidic conditions to reveal the free amine, and the ketone adjacent the benzo[*d*]oxazol-2(3*H*)-one was reduced with sodium borohydride to yield the sp³ alcohol in the relevant final compounds **2.1** and **2.60** (**Scheme 15**).



Scheme 15 The alkylation reaction for the synthesis of lipophilic tail analogues of PF-8380, and the subsequent *N*-Boc deprotection or reduction of the carbonyl moiety.

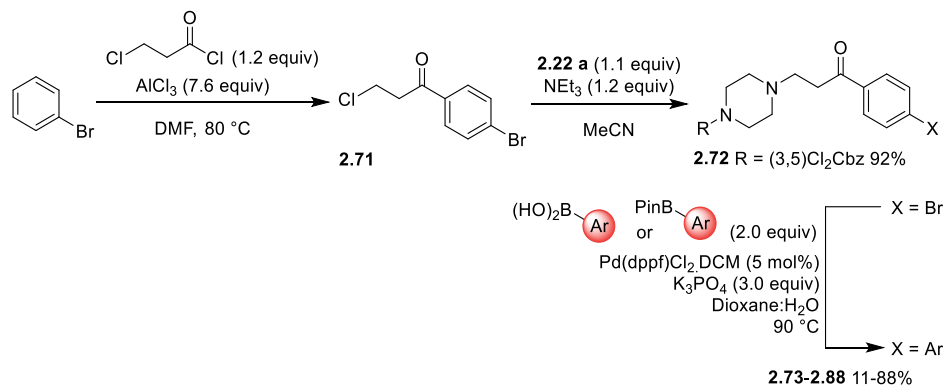
Compounds **2.64–2.66** with a carboxylic acid ZBG (Section 2.5.2.) were synthesised analogously *via* an alkylation reaction with the corresponding piperazine intermediates **2.22 a-b**, and ethyl 3-chloropropanoate, or the *tert*-butyl protected ester. The ethyl ester was hydrolysed under aqueous basic conditions (**Scheme 16**), and the *tert*-butyl ester intermediates were *N*-Boc deprotected through treatment with HCl (**Scheme 16**).



Scheme 16 Synthesis of ATX inhibitors with a carboxylic acid motif.

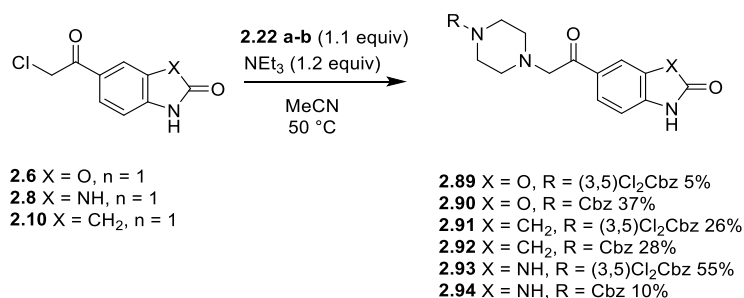
To access alternative heterocyclic warheads (Section 2.5.3.), an intermediate **2.71** was firstly synthesised by a Friedel-Crafts acylation of bromobenzene with 3-chloropropanoyl chloride, and then subjected to the standard alkylation procedure with piperazine intermediate **2.22 a**

(**Scheme 15**) to afford intermediate **2.72**. A Suzuki-Miyaura array with **2.72** and the corresponding boronate esters or boronic acids yielded the biaryl final compounds **2.73–2.87** (**Scheme 17**).¹⁴⁶



Scheme 17 Suzuki-Miyaura array from intermediate **2.72**.

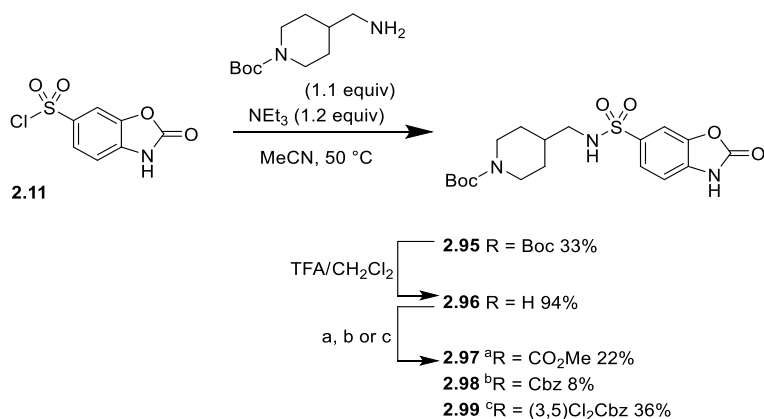
The standard alkylation reaction was repeated with a truncated linker ($n = 1$) synthesised in Section **2.3.2**. (**Scheme 6**), with intermediates **2.6–2.10** and the benzyl carbamate and 3,5-dichlorobenzyl carbamate piperazines **2.22 a-b** the reaction is performed at a reduced temperature due to the increased reactivity of the alkyl halide intermediate (**Scheme 15**).⁹⁵ These final compounds were synthesised with either the benzyl carbamate (**2.90**, **2.92**, and **2.94**) or the 3,5-dichlorobenzyl carbamate tail (**2.89**, **2.91**, and **2.93**) .



Scheme 18 The alkylation reaction of truncated PF-8380 analogues with alternative ZBG **2.89-2.94**.

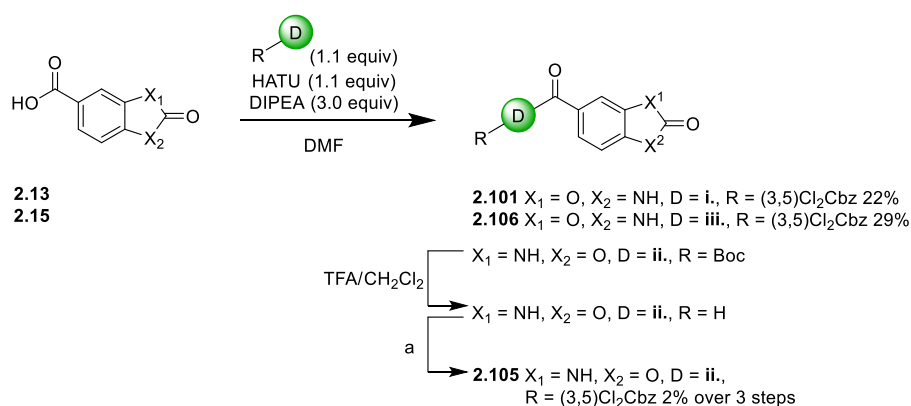
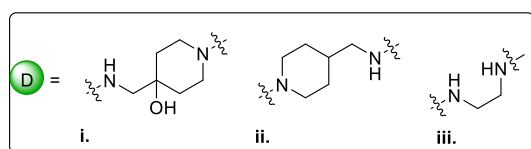
The sulfonamide series of compounds were synthesised with *tert*-butyl 4-(aminomethyl)piperidine-1-carboxylate and the corresponding sulfonyl chloride **2.11** (**Scheme 7**) to afford *N*-Boc protected intermediate **2.95**, which was deprotected under acidic

conditions to reveal the amine intermediate (**Scheme 19**). Either the methyl carbamate, benzyl carbamate, or 3,5-dichlorobenzyl carbamate could be synthesised from the free amine to yield the corresponding final compounds **2.97–2.99** (**Scheme 19**).



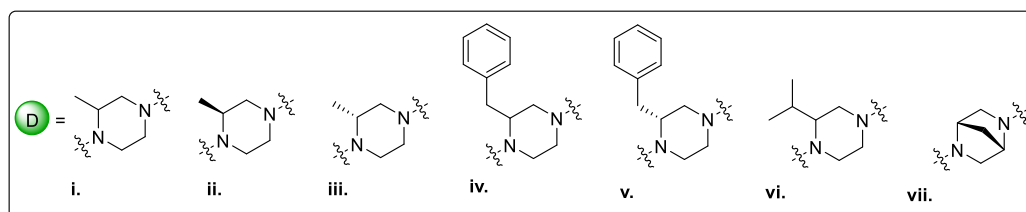
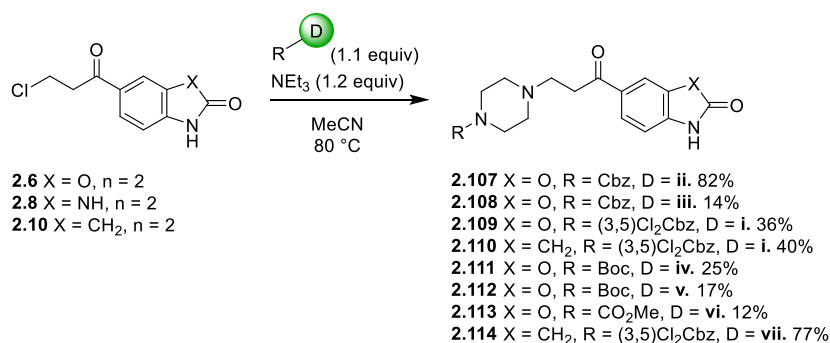
Scheme 19 The synthesis of the sulfonamide sub-series with the piperidin-4-ylmethanamine core. **a)** Methyl chloroformate (1.1 equiv), NEt₃ (2.1 equiv), THF (2 mL). **b)** Cbz-succinamide (1.1 equiv), NaHCO₃ (1.5 equiv), THF:H₂O (1 mL:1 mL). **c)** (3,5-dichlorophenyl)methanol (1.1 equiv), 1,1'-carbonyldiimidazole (1.1 equiv), DMF (2 mL).

The synthesis of the amide analogue **2.105** with *N*-Boc diamine starting material, *tert*-butyl 4-(aminomethyl)piperidine-1-carboxylate, is then deprotected under acidic conditions and a 3,5-dichlorobenzyl carbamate attached analogously to the sulfonamide series (**Scheme 20**). However, the final compounds containing the 3,5-dichlorobenzyl (2-aminoethyl)carbamate and 3,5-dichlorobenzyl ((4-hydroxypiperidin-4-yl)methyl)carbamate cores prepared in section **2.3.1**. (**Scheme 10**) are synthesised in one step with an amidation reaction to yield compounds **2.106** and **2.101** (**Scheme 20**).



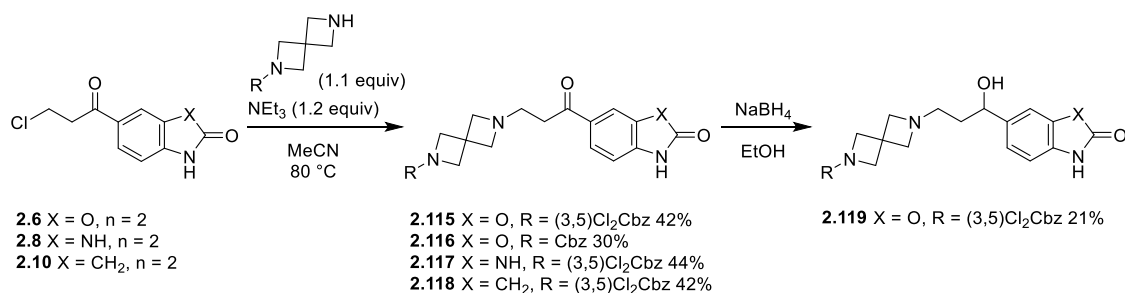
Scheme 20 Synthesis of compounds from the amide sub-series. **a**) (3,5-dichlorophenyl)methanol (1.1 equiv), 1,1'-carbonyldiimidazole (1.1 equiv), DMF (2 mL).

A sub-series of compounds **2.107–2.114** were synthesised containing substituted piperazines **i.–vii.** using the same alkylation methodology as the parent series (**Scheme 21**). The 2-methylpiperazine (**i.–iii.**), 2-benzylpiperazine (**iv.–v.**), 2-isopropylpiperazine (**vi.**), and (1*S*,4*S*)-2,5-diazabicyclo[2.2.1]heptane (**vii.**) cores were either commercially available or synthesised as discussed previously in Section 2.3.2. (**Scheme 11**, **Scheme 12**, **Scheme 13**).



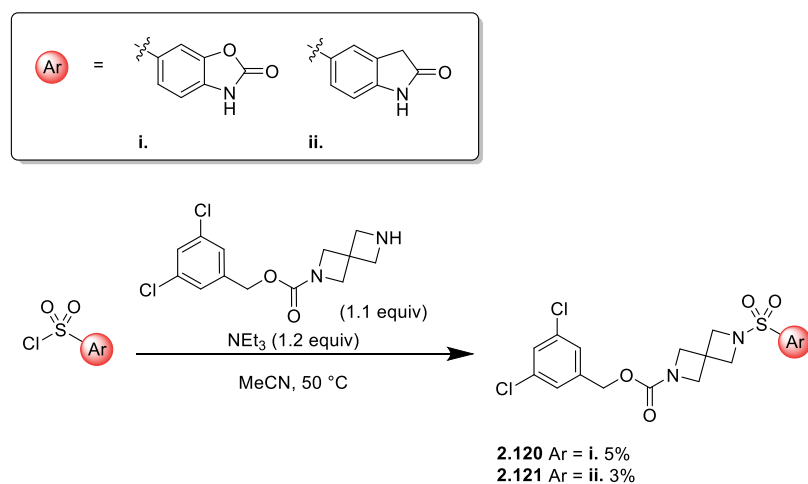
Scheme 21 The alkylation for the synthesis of analogues **2.107-2.114** with substituted and bicyclic piperazines.

With the same standard alkylation methodology to compounds **2.42–2.59** (Scheme 15) compounds were synthesised with a 2,6-diazaspiro[3.3]heptane core **2.19** (Scheme 10) and varied ZBG **2.6**, **2.8** and **2.10** which were discussed in Section 2.3.2. (Scheme 6, Scheme 22). In addition, compound **2.116** was further elaborated to the alcohol analogue **2.119** with sodium borohydride (Scheme 22).



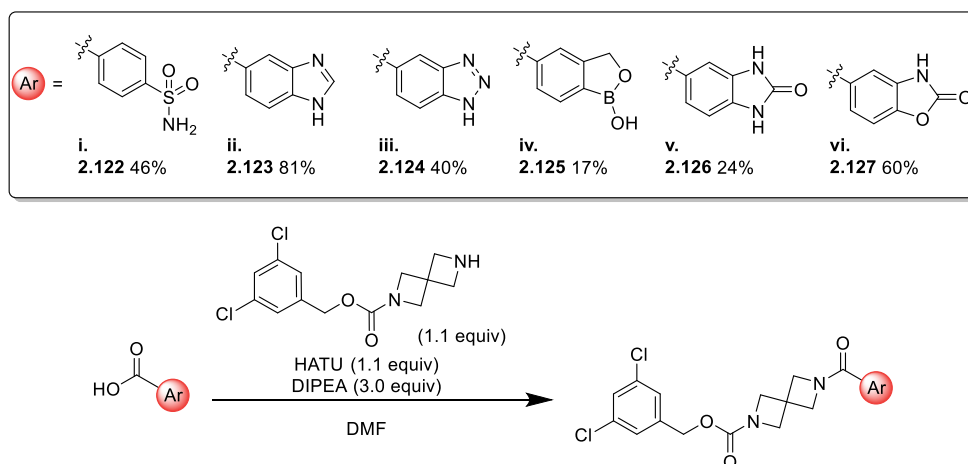
Scheme 22 The alkylation reaction with a 2,6-diazaspiro[3.3]heptane core, and further elaboration of the carbonyl.

Compounds **2.120–2.121** were synthesised using the same method as the sulfonamide sub-series (Scheme 19) with a 3,5-dichlorobenzyl 2,6-diazaspiro[3.3]heptane-2-carboxylate core **2.19** synthesised in Section 2.3.2. (Scheme 10), and sulfonyl chlorides **2.11** and **2.12** (Scheme 7, Scheme 23).



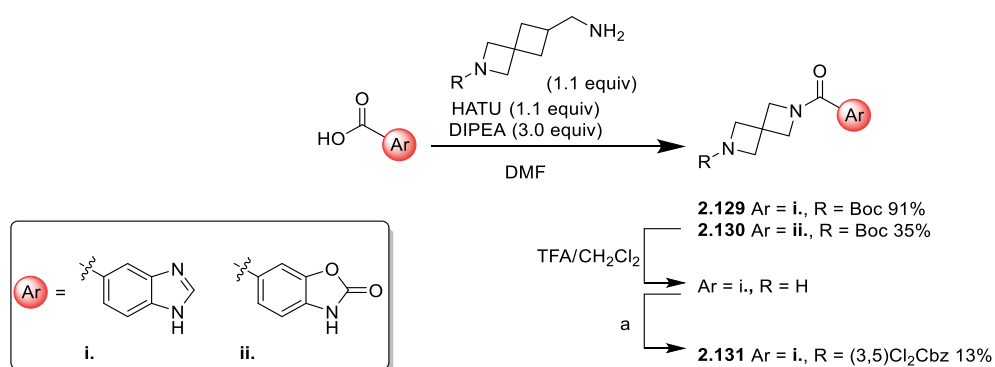
Scheme 23 The synthesis of sulfonamide analogues with the novel 2,6-diazaspiro[3.3]heptane core.

Akin to **Scheme 23**, a series of amides were synthesised using the 3,5-dichlorobenzyl 2,6-diazaspiro[3.3]heptane-2-carboxylate core **2.19** which was previously discussed in Section 2.3.2., and a selection of carboxylic acids **i.–vi.** (**Scheme 24**). Carboxylic acid starting materials were either commercially available or synthesised as discussed in Section 2.3.2. (**Scheme 8**, **Scheme 9**).



Scheme 24 The synthesis of amide analogues with the novel 2,6-diazaspiro[3.3]heptane core.

Compound **2.131** containing the (2-azaspiro[3.3]heptan-6-yl)methanamine core was synthesised from the *N*-Boc intermediate *tert*-butyl 6-(aminomethyl)-2-azaspiro[3.3]heptane-2-carboxylate to yield intermediates **2.129** and **2.130** (**Scheme 25**). Intermediates **2.129** and **2.130** were *N*-Boc deprotected under acidic conditions and the (3,5-dichlorophenyl)methanol attached to the free amine with CDI.



Scheme 25 The synthesis of amide analogues with the novel homologated (2-azaspiro[3.3]heptan-6-yl)methanamine core. **a**) (3,5-dichlorophenyl)methanol (1.1 equiv), 1,1'-carbonyldiimidazole (1.1 equiv), DMF (2 mL).

2.4. Results and Discussion

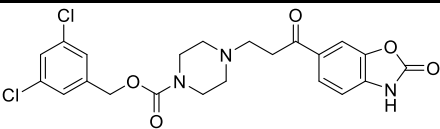
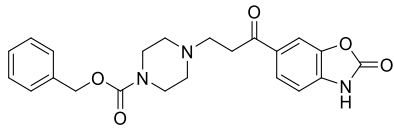
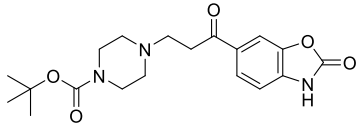
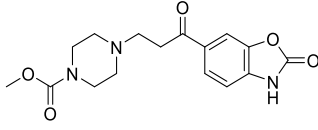
2.4.1. Lipophilic Tail Modifications

Firstly, it was paramount to evaluate the significance of the 3,5-dichlorobenzyl carbamate tail (PF-8380, **Table 12**), as both co-crystal structures of PF-8380 and **2.1** bound to ATX discussed in Section **2.2**. suggested this moiety helps to augment potency. The key pharmacophoric features investigated included the aromaticity, length, and substituents on the aromatic ring, which were to observe the effect within the hydrophobic pocket. Equally, an improvement in the physicochemical properties was a key aspect of compound development, as the highly lipophilic 3,5-dichlorobenzyl carbamate tail contributes to the high cLogD of PF-8380.

2.4.2. Structure-activity Relationship of Aromaticity on the Lipophilic Region

The direct analogues of PF-8380 without the chlorine atoms **2.42** (**Table 12**), and the aliphatic carbamate groups **2.43–2.44** were synthesised to assess the effect of removal of aromaticity on ATX inhibition. Further to this, the carbamate moiety was removed to reveal the free amine **2.45**, as this is shown to hydrogen bond to Trp275 in the co-crystallised structures (**Figure 33**).

Table 12 Evaluating the importance of the aromatic tail of PF-8380, and the corresponding physicochemical profile. ^aSynthesised by another member of our laboratories. ¹⁴⁷ ^bPF-8380.

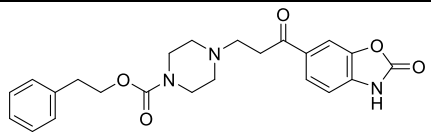
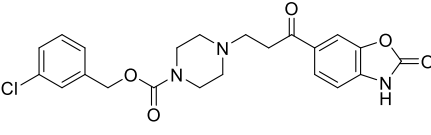
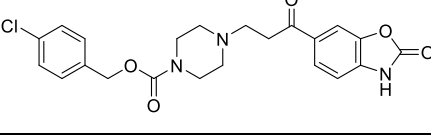
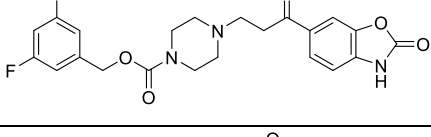
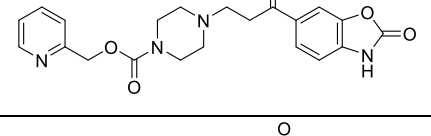
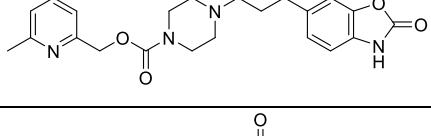
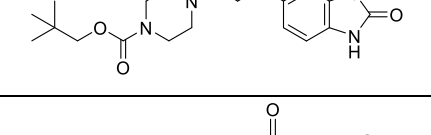
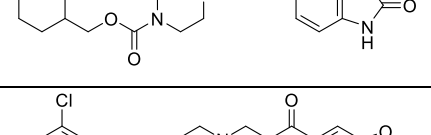
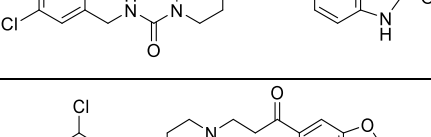
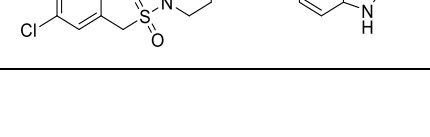
Structure	K _i (μM)	cLogD	LLE _{AT}	PFI
b 	0.008	3.62	0.30	6.62
2.42 	0.053	2.42	0.33	5.42
2.43 	> 30	1.75	0.24	3.75
2.44 	1.4	0.69	0.40	4.55

2.45^a		>30	-1.23	0.52	0.77
-------------------------	---	-----	-------	------	------

PF-8380 and the direct analogue **2.42** verify the need for an aromatic moiety in this region to obtain nanomolar ATX inhibitors. Compounds **2.43–2.45** without an aromatic moiety resulted in micromolar, or inactive compounds, proving that despite the fact that the carbamate can hydrogen bond with the back-bone of residue Trp275, this interaction alone is not enough to confer potency. As expected a significant decrease in cLogD and PFI, and an increase in LLE_{AT} is observed between PF-8380 and analogues **2.43–2.45**. Compound **2.42** has an improved physicochemical profile based on the removal of the two chlorine atoms, however, this is also accompanied by a 7-fold loss in potency. As a result of this SAR (**Table 12**), the next series of compounds contained either an aromatic moiety, or bulky lipophilic groups to probe this lipophilic region further.

Compound **2.46** was designed to extend the length of the aromatic lipophilic region to probe the depth of the hydrophobic pocket. Further to this, the aromatic substitution was varied to contain fluorine **2.49**. Additionally, instead of the benzyl group a pyridine ring was introduced **2.50–2.51** to reduce the cLogD of the compounds. The effect of mono-chloro substitution of the benzyl group in both the *para*- **2.48** and *meta*- **2.47** position was considered to find a balance between improved physicochemical properties and potency. The aromatic moiety was replaced with a neopentyl **2.52** and cyclohexyl group **2.53**, as although removal of aromaticity previously rendered compounds inactive, it was postulated that based on the binding mode of LPA bulky alkyl chains could maintain affinity in the pocket. Additionally, to improve the physicochemical profile of the series whilst maintaining the 3,5-dichloro substitution, both amide **2.54**, and sulfonamide **2.55** moieties were used as replacements for the carbamate group. Although compounds **2.46–2.50**, and **2.54** (**Table 13**) have been previously synthesised within the Merck patent, there is no biological data available to construct valid SAR.⁹⁵

Table 13 Lipophilic tail analogues **2.46–2.55**. ^aSynthesised by another member of our laboratories.¹⁴⁷

	Structure	K _i (μM)	cLogD	LLE _{AT}	PFI
2.46		0.22	2.70	0.28	5.70
2.47		0.006	3.02	0.32	6.02
2.48		0.058	3.02	0.37	6.02
2.49^a		0.67	2.70	0.25	5.70
2.50^a		1.5	0.49	0.32	4.20
2.51		0.46	1.41	0.33	4.41
2.52		1.4	2.31	0.29	4.31
2.53		0.044	2.81	0.39	4.81
2.54		0.034	2.89	0.29	5.89
2.55		0.17	2.66	0.30	5.66

Compounds **2.46** and **2.52** with extended lipophilic groups were less potent than the corresponding benzyl **2.42**, with the exception of the *N*-Boc analogue **2.43** (**Table 12**) in the initial series. However, compound **2.53** with a bulkier cyclohexyl moiety of a similar size to the benzyl group resulted in an equipotent compound to **2.42**, with an improved physicochemical profile apart from poor aqueous solubility. Due to the removal of an aromatic ring the cLogD and PFI are reduced, coupled with an increased in LLE_{AT}.

Replacement of the benzene ring with a pyridine **2.50** allowed the polarity of this region to be tuned to improve the physicochemical parameters, however unfortunately this led to a decrease in potency compared to **2.42** ($K_i = 0.053 \mu\text{M}$, **Table 12**). Incorporating a 3-methylpyridine group **2.51** increased the potency into the sub-micromolar range again, due to the lipophilic interactions gained from the additional methyl group. Given that drastic modifications to the lipophilic region led to a drop in potency, the carbamate linker was instead altered, whilst retaining the 3,5-dichlorobenzyl moiety. The carbamate was replaced with a urea **2.54**, which although was equipotent with **2.42** had an increased PFI and cLogD. The sulfonamide **2.55** decreased the cLogD, however was accompanied by a drop in potency. Direct analogues of PF-8380 with mono-chloro substitution were investigated, with the *meta*-chloro **2.47** and *para*-chloro **2.48** leading to potent compounds. These compounds have improved cLogD, LLE_{AT}, and PFI compared to PF-8380. However, there was no improvement to aqueous solubility with these modifications.

Due to the dramatic increase in potency observed with the 3,5-dichlorobenzyl carbamate, this group would be used to achieve optimum potency in the subsequent series, and the benzyl carbamate for improved physicochemical properties. Although compound **2.53** containing the cyclohexyl lipophilic tail had a good physicochemical profile, the compound lacked adequate aqueous solubility, and as a result the benzyl carbamate was favoured for further compound development.

2.4.3. Zinc Binding Group Modifications

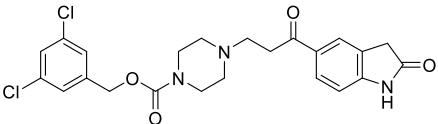
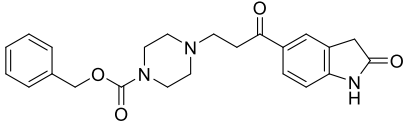
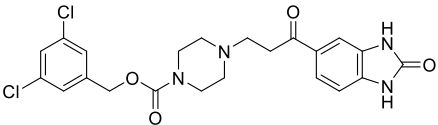
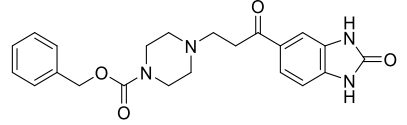
The 3,5-dichlorobenzyl carbamate and the benzyl carbamate tails were optimum for potency and the physicochemical profile, respectively, and therefore these lipophilic groups were utilised in conjunction with the ZBG modifications. Initially, small changes were made to assess the key interactions made by the benzo[*d*]oxazol-2(3*H*)-one warhead, followed by complete removal of this moiety. In addition, a number of established ZBG were assessed for both potency and physicochemical properties in comparison to the benzo[*d*]oxazol-2(3*H*)-one.

After primary analysis of this region, novel ZBG systems could then be designed in order to gain structural diversity.

2.4.4. Modifications to the Benzo[d]oxazol-2(3H)-one Zinc Binding Group

A series of compounds were synthesised changing the benzo[d]oxazol-2(3H)-one to a 1,3-dihydro-2H-benzo[d]imidazol-2-one and indolin-2-one **2.56–2.59** (Table 14). These subtle changes determine the significance of the carbonyl moiety on the binding mode of the compound, and the pKa of the nitrogen, which as discussed interacts with zinc through the nitrogen.

Table 14 ZBG modifications with 1,3-dihydro-2H-benzo[d]imidazol-2-one and indolin-2-one groups.

	Structure	K _i (μM)	cLogD	LLE _{AT}	PFI
2.56		0.022	3.36	0.30	5.36
2.57		> 30	2.16	0.27	4.16
2.58		0.005	3.44	0.32	6.44
2.59		1.5	2.23	0.27	5.23

As previously discussed, the benzo[d]oxazol-2(3H)-one could interact with zinc through the carbamate or the nitrogen of the warhead, and replacement of this ZBG with the indolin-2-one and 1,3-dihydro-2H-benzo[d]imidazol-2-one means that the ZBG can only interact with zinc through the nitrogen or the carbonyl moiety (Table 14). Biochemical analysis revealed that nanomolar levels of potency was only retained with compounds **2.56**, and **2.58**, which both

contained the 3,5-dichlorobenzyl carbamate tail. As expected, a decrease in cLogD and PFI, and a moderate increase in LLE_{AT} were observed with these modifications.

A recent report by Jones *et al* suggests there is an optimum pKa range for affinity of inhibitors with zinc atoms of between 8-11 with acidic heterocycles.¹²² The increased pKa (PF-8380 calculated using JChem for Excel pKa = 9.5, **2.56** pKa = 11.5, **2.58** pKa = 12.5)¹⁰⁶ could affect potency, especially at the pH of the assay (pH = 8.5), **2.56** and **2.58** are unlikely to be ionised, limiting how the compounds can interact with the zinc atom. This could explain the drop in potency with these ZBG modifications on compounds containing the benzylcarbamate tail (**2.57** and **2.59**, **Table 14**), as if the interactions with the zinc atom are limited it could make the presence of the 3,5-dichlorobenzyl carbamate tail (**2.57** and **2.59**) essential for potency. This trend is not exhibited with the parent series (PF-8380 and **2.42**, **Table 12**) containing the benzo[*d*]oxazol-2(3*H*)-one group, which is in the optimum calculated pKa range to interact fully with the zinc atoms.

In silico modelling of PF-8380, **2.56**, and **2.58** is consistent with the co-crystallography results, which explains why all three compounds are potent ATX inhibitors. The nitrogen atom on all three compounds is positioned to interact with the active site zinc, and it is evident that the 3,5-dichlorobenzyl carbamate tail is acting as a hydrophobic anchor, with limited movement from the adopted binding pose (**Figure 37**).

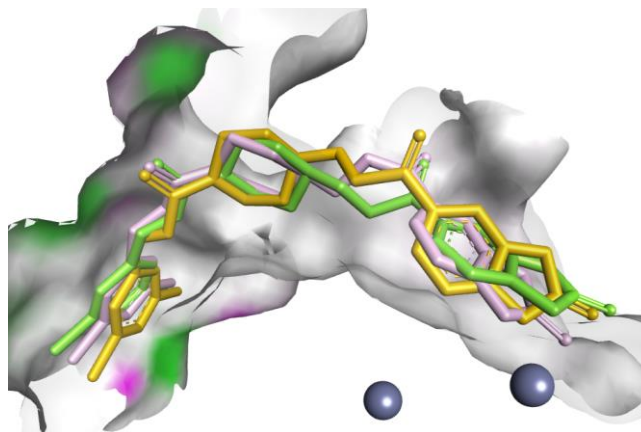


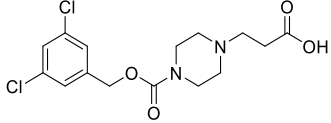
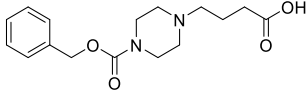
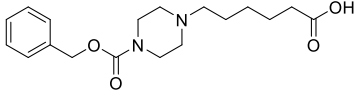
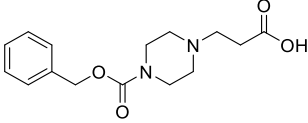
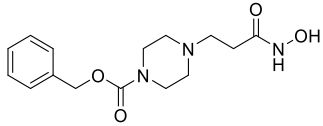
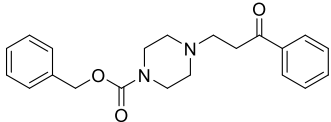
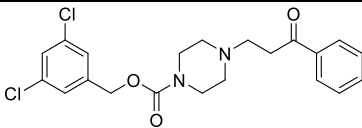
Figure 37 *In silico* modelling of PF-8380 (yellow), **2.56** (green) and **2.58** (pink) in the active site of ATX using GOLD¹³⁰ and viewed in DS visualizer.⁴⁸

2.4.5. Removal of the Zinc Binding Warhead

Given that initial ZBG modifications in combination with the 3,5-dichlorobenzyl carbamate tail were well tolerated, the benzo[*d*]oxazol-2(3*H*)-one was replaced with established ZBGs

such as a carboxylic acid, and hydroxamic acid. Not only are these moieties known to have strong affinity for zinc,¹⁴⁸ compounds containing such functionality will have drastically decreased cLogD, PFI, and improved aqueous solubility compared to the parent compounds, for example comparing PF-8380 (cLogD = 3.62, PFI = 6.62, **Table 12**) to compound **2.64**, which has a much improved physicochemical profile (cLogD = -0.40, PFI = 0.60, **Table 15**)

Table 15 Carboxylic acid, and hydroxamic acid compounds without the benzo[*d*]oxazol-2(3*H*)-one ZBG.
^aSynthesised by another member of the laboratory.¹⁴⁷

Structure	K _i (μM)	cLogD	LLE _{AT}	PFI
2.64 	>30	-0.40	-	0.60
2.65 	> 30	-1.26	-	-0.26
2.66 	> 30	-0.23	-	0.77
2.67^a 	> 30	1.93	-	-0.61
2.68^a 	> 30	0.42	-	1.42
2.69^a 	> 30	3.05	-	5.05
2.70^a 	> 30	4.26	-	6.26

Compounds **2.64–2.68** (**Table 15**) with a combination of the benzyl, and 3,5-dichlorobenzyl carbamate groups with a carboxylic acid or hydroxamic acid ZBG were inactive. Additionally, the length of alkyl chain of compounds **2.65–2.66** was extended in order to ensure the compound was able to reach both the active site and the hydrophobic pocket, however this

resulted in inactive compounds in every case. This confirms that a ZBG comparable to the benzo[*d*]oxazol-2(3*H*)-one is essential for potency, and potentially should contain an aromatic region to gain the benefits of hydrophobic interactions with Leu243 or Phe312, as the presence of a zinc binding group on an alkyl chain may not be sufficient to generate potent ATX inhibitors.

2.4.6. A Suzuki-Miyaura Array to Develop Novel Zinc Binding Groups

Due to the lack of activity observed in compounds without a heterocyclic derived ZBG with alkyl linked compounds **2.64–2.70** (Table 15), it was reasoned that a novel biaryl ZBG containing an aromatic, or heterocyclic group could be installed in a Suzuki-Miyaura array (Scheme 17). The first aromatic ring could be stabilised by hydrophobic interactions with Leu243 or Phe312 at the entrance to the active site, and the second aromatic ring or heterocycle interacting with the zinc atom. The aromatic and heterocyclic moieties selected contained hydrogen bond donor and acceptor groups, as well as potential zinc chelating groups (Table 16).

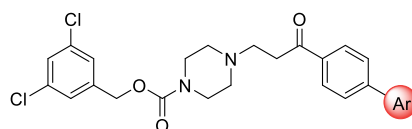
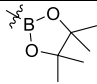
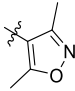
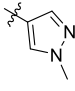
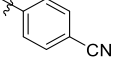
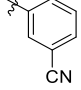
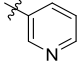
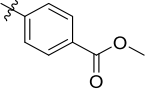
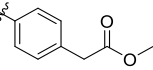
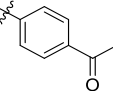


Table 16 Suzuki-Miyaura compound screen for a novel ZBG.

	Ar	K _i (μM)	cLogD	LLE _{AT}	PFI
2.72	Br	>30	5.03	-	7.03
2.73		> 30	5.13	-	8.13
2.74		0.51	5.13	0.15	8.13
2.75		> 30	5.60	-	8.60
2.76		> 30	5.75	-	8.75
2.77		> 30	5.15	-	8.15
2.78		> 30	4.57	-	6.57
2.79		> 30	5.17	-	8.17

2.80		0.027	5.74	0.18	7.74
2.81		> 30	4.60	-	7.61
2.82		2.1	4.34	0.16	7.34
2.83		> 30	5.77	-	8.77
2.84		> 30	5.77	-	8.77
2.85		> 30	4.69	-	7.69
2.86		> 30	5.91	-	8.92
2.87		> 30	5.69	-	8.69
2.88		> 30	5.47	-	8.47

The ZBG systems selected for this array contained potential metal chelating groups including a methoxypyridine **2.73–2.74**, pyridine **2.85**, nitrile **2.83–2.84**, and heterocycles such as 2-methyl furan **2.79**, isoxazoles **2.81**, dihydropyran **2.78**, and *N*-methylpyrazole **2.82**. Of this series, the only micromolar ATX inhibitors identified were the 3-methoxypyridine **2.74**, pinacol boronate ester **2.80**, and *N*-methylpyrazole **2.82**. The *N*-methyl-pyrazole is a common motif in current ATX inhibitors, including the zinc binding compound **1.7** designed by Novartis (Section **1.3.2.**, **Table 8**) and the tunnel binding non-competitive ATX inhibitor **1.10** reported by Amira (Section **1.3.2.**, **Table 9**). The pinacol boronate ester is similar to HA155 (Section **1.3.2.**, **Figure 29**), as boronic acids are known zinc binders, with the affinity for ATX maintained with the boronate ester. Compounds in this series had large cLogD and PFI values due to the increased number of aromatic rings and lipophilicity of the biaryl moiety, which combined with the lack of potency, made them poor candidates for further optimisation.

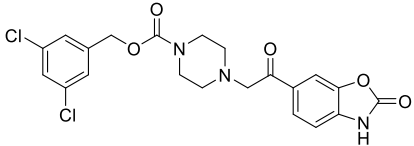
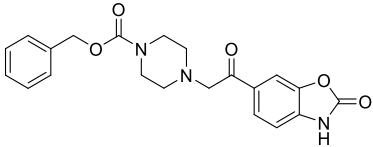
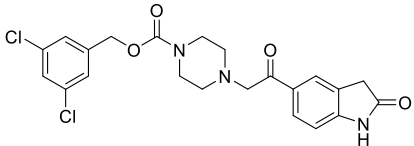
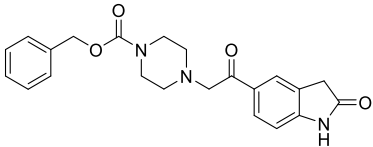
2.4.7. Core and Linker Modifications

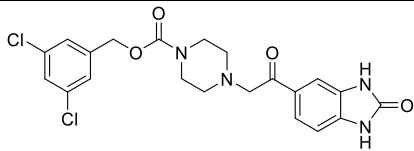
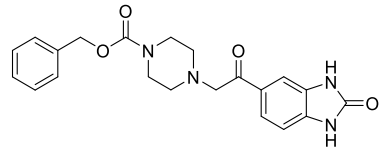
The next series of compounds were analogues which are modified in the core and linker region containing the ZBG previously shown to result in potent ATX inhibitors; the benzo[*d*]oxazol-2(3*H*)-one, 1,3-dihydro-2*H*-benzo[*d*]imidazol-2-one and indolin-2-one (Section 2.3.2.). Several series of compounds were synthesised, containing a truncated linker, novel diamine cores, and amide or sulfonamide linkers. Each of these compounds either possessed the 3,5-dichlorobenzyl or the benzyl carbamate tail which has been consistently shown to impart high levels of potency.

2.4.8. Truncation of the Carbon Linker

Shortening the length of the carbon linker was proposed to reduce the cLogD of the compounds, and as a result improved PFI and LLE_{AT}, and also probe the length of the molecule and effect on potency. Similar to section 2.5.1., the benzo[*d*]pxazol-2(3*H*)-one was replaced with 1,3-dihydro-2*H*-benzo[*d*]imidazole-2-one and indolin-2-one, with the 3,5-dichlorobenzyl carbamate and benzyl carbamate lipophilic region

Table 17 Truncated compounds containing the 3,5-dichlorobenzyl carbamate tail and benzylcarbamate tail with either benzo[*d*]oxazol-2(3*H*)-one, 1,3-dihydro-2*H*-benzo[*d*]imidazol-2-one or indolin-2-one ZBG.

	Structure	K _i (μM)	cLogD	LLE _{AT}	PFI
2.89		0.003	3.40	0.31	6.40
2.90		0.89	2.19	0.29	5.19
2.91		0.12	3.15	0.28	5.15
2.92		> 30	1.94	0.25	3.94

2.93		0.66	3.22	0.26	6.22
2.94		> 30	2.01	0.28	5.01

The only compound from this series that resulted in equipotent ATX inhibition with PF-8380 was **2.89** (Table 18). This is attributed to the benzo[*d*]oxazol-2(3*H*)-one ZBG, and the 3,5-dichlorobenzyl lipophilic tail, which are identical to the parent compound PF-8380. Interestingly, due to the decreased alkyl chain length the physicochemical properties were improved with a decreased cLogD, PFI, and increased LLE_{AT}. However, although the organic solubility improved, aqueous solubility remained poor. This is believed to be a direct result of the inherent insolubility of the combination of the benzo[*d*]oxazol-2(3*H*)-one ZBG, and the 3,5-dichlorobenzyl lipophilic tail in a molecule.

In silico modelling suggests that compound **2.89** resides in a similar pose to the crystal structure of PF-8380 (Figure 38), with the nitrogen of the benzo[*d*]oxazol-2(3*H*)-one interacting with the distal zinc atom at a distance of 3.12 Å, and nearby residue Asp311. The distance of interaction between the nitrogen atom and zinc atom is much greater than with PF-8380, which has a distance predicted at 2.24 Å. Despite the shorter length of the compound, and increased distance from the distal zinc atom, the lipophilic tail interacts with the same key hydrophobic residues in the pocket as PF-8380 (Section 2.2., Figure 38), confirming the 3,5-dichlorobenzyl carbamate tail as a hydrophobic anchor.

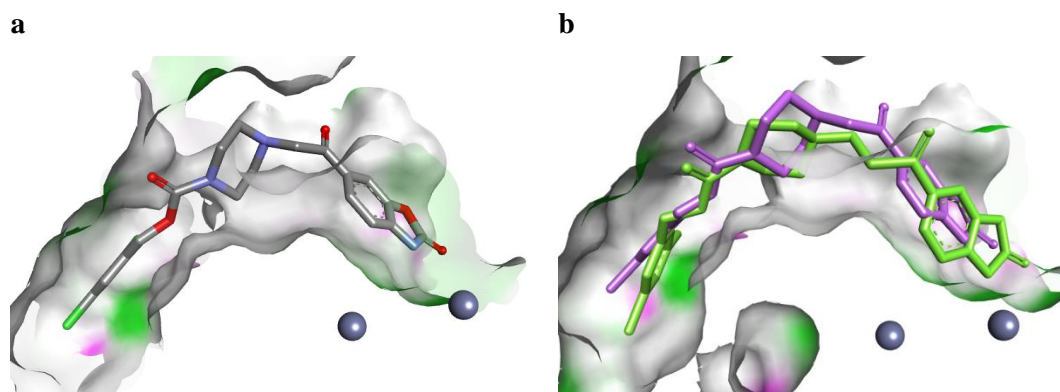


Figure 38 *In silico* modelling of compound in GOLD and viewed in DS visualizer.^{48,130} **a)** **2.89** in the active site of ATX. **b)** *In silico* modelling and overlay of compounds **2.89** (purple) and **PF-8380** (green) interacting with the distal zinc atom in the active site of ATX.

2.4.9. Elaboration of the Carbonyl

From consideration of the X-ray structure and *in silico* docking data, the carbonyl moiety adjacent to the benzo[*d*]oxazol-2(3*H*)-one on PF-8380 is important for hydrogen bonding with Arg244, which is nearby the active site of ATX. Based on this, reduction of the carbonyl to an alcohol would be expected to maintain that interaction.

Table 18 Alcohol analogues of PF-8380 and **2.42**.

	Structure	K_i (μM)	cLogD	LLE _{AT}	PFI
2.60		3.7	2.03	0.30	5.03
2.1		0.008	3.24	0.34	6.24

Compounds **2.60** and **2.1** had improved cLogD, LLE_{AT}, and PFI values (**Table 18**). From inspection of the co-crystal structure of **2.1** (Section 2.2., **Figure 33**), and as previously discussed, this compound interacts with the distal zinc atom in a monodentate binding mode through the nitrogen of the carbamate. This modification indicates that elaboration of the carbonyl adjacent the benzo[*d*]oxazol-2(3*H*)-one ZBG is tolerated in the active site and improves the physicochemical properties. The introduction of a hydrogen bond donor (HBD) will decrease the cLogD of the compounds improving the physicochemical profile.

Additionally, the sp^3 nature of this moiety should be able to disrupt the stacking of these compounds in solution which can contribute to insolubility.¹⁰⁵

2.4.10. Core and Linker Modifications with the Development of a Novel Sulfonamide Series

As established with compound **2.1** (Table 18) the carbonyl adjacent the benzo[*d*]oxazol-2(3*H*)-one can be modified with retention of ATX inhibition. The replacement of the carbonyl with a sulfonamide linker could have a positive impact on activity in conjunction with tuning the physicochemical profile. Based upon tolerance of the sp^3 alcohol of **2.1** (Table 18), a sulfonamide motif with tetrahedral character adjacent to the benzo[*d*]oxazol-2(3*H*)-one ZBG could improve the physicochemical properties (Table 19). In order to balance the length of compounds and ensure potency from occupancy of both the active site and hydrophobic pocket, this series was designed with a piperidin-4-ylmethanamine core.

Table 19 Sulfonamide series with a piperidin-4-ylmethanamine core.

	Structure	K_i (μ M)	cLogD	LLE _{AT}	PFI
2.95		> 30	1.54	0.28	3.54
2.96		> 30	-2.19	-	-0.19
2.97		> 30	0.48	-	2.49
2.98		0.18	2.12	0.31	5.21
2.99		0.003	3.42	0.33	6.42

Within the sulfonamide series, non-aromatic tail groups were generally inactive, which was consistent with the previous SAR on direct PF-8380 analogues (**Section 2.4.**). Compound **2.98** with the benzyl carbamate tail displayed moderate potency and excellent physicochemical properties. Addition of the 3,5-dichlorobenzyl carbamate with compound **2.99** resulted in the most potent ATX inhibitor in this sub-series, equipotent to PF-8380. The cLogD, and PFI were decreased, and LLE_{AT} increased, developing a compound with good potency and encouraging physicochemical profile.

In silico modelling of **2.99** (**Figure 39**)¹³⁰ indicates an identical binding mode to the co-crystal structure of PF-8380 and **2.1**, with the proximity of Tyr306 and the proton on the sulfonamide indicative of hydrogen bonding.¹²¹ This additional interaction, and the conserved positioning of the ZBG and 3,5-dichlorobenzyl lipophilic tail can account for the potency of the compounds.

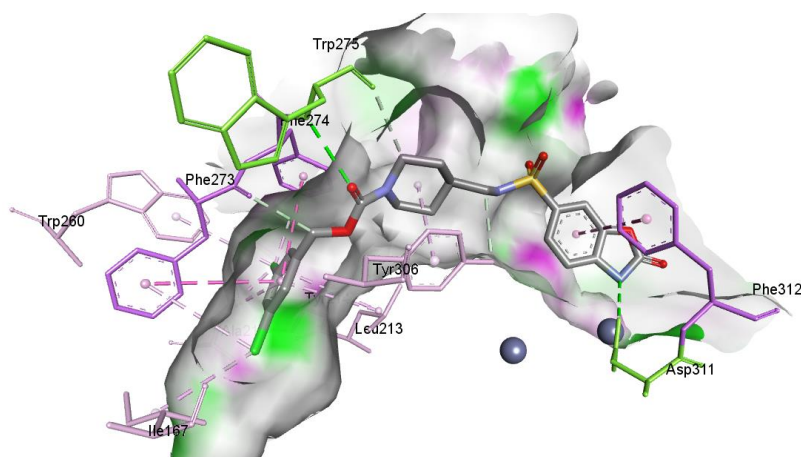


Figure 39 *In silico* modelling of compound **2.99** in the active site of ATX using GOLD and viewed in DS visualizer.^{48,130}

2.4.11. The Development of an Amide Series

Analogously to the sulfonamide series, the amide series contained an (aminomethyl)piperidin-4-ol **2.100–2.101**, piperidin-4-ylmethanamine **2.102–2.105**, and ethylenediamine core **2.106** (**Table 20**).

Table 20 Amide series containing a methylaminopiperidine, (aminomethyl)piperidin-4-ol and ethylenediamine core. ^aSynthesised by another member of the laboratory.¹⁴⁷

	Structure	K _i (μM)	cLogD	LLE _{AT}	PFI
2.100^a		0.17	1.23	0.36	4.23
2.101		0.045	2.44	0.31	5.44
2.102^a		0.047	2.46	0.31	5.46
2.103^a		0.022	3.67	-	6.67
2.104^a		0.005	3.49	0.37	6.49
2.105		0.11	3.67	0.26	6.67
2.106		0.57	2.98	0.29	5.96

The amide series furnished highly potent and novel ATX inhibitors containing both the benzyl carbamate and 3,5-dichlorobenzyl carbamate **2.100–2.103**. The regiochemistry of the heteroatoms on the benzo[*d*]oxazol-2(3*H*)-one ZBG was reversed with compound **2.105**, and as a result this compound was less potent than **2.103** and **2.104**. This could be attributed to the binding mode changing so the carbamate moiety interacts with the zinc atom, or rotation around the piperidin-4-ylmethanamine core to enable *N*-zinc interactions, which causes the carbonyl moiety to clash with the enzyme surface (**Figure 40 c**). Additional modifications included an ethylenediamine core **2.106**, with reduced ATX inhibition, which reinforces the need for rigid cores such as the piperazine, methylamino piperidine and

(aminomethyl)piperidin-4-ol. The removal of the basic nitrogen on the piperazine due to the extended methylaminopiperdine core, and additionally an alcohol moiety to give the (aminomethyl)piperidin-4-ol core had no observed detrimental effect on ATX inhibition. Compound **2.100** has an improved physicochemical profile with reduced cLogD, PFI and increased LLE_{AT} coupled with moderate potency despite the presence of the benzyl carbamate tail. The addition of this alcohol moiety into the core resolved the issue of lipophilicity when in combination with the problematic benzo[*d*]oxazol-2(3*H*)-one ZBG, and 3,5-dichlorobenzyl carbamate tail, resulting in a potent and lead-like profile **2.101**.

In silico modelling suggests that the binding mode of compounds **2.102**, **2.100**, and **2.106** are identical to **2.97** (**Figure 39**, **Table 19**), with the nitrogen of the benzo[*d*]oxazol-2(3*H*)-one electrostatically interacting with the zinc atoms (**Figure 40 a**). Also, analogous to compound **2.97**, the proton on the amide bond can potentially hydrogen bond to the Tyr306 residue. (**Figure 40 a-b**, and **c**) Tyr306 is an important residue for ATX inhibition, hydrogen bonding to the ester moiety in the core region of the native species LPA.^{122,1} Compound **2.101**, which has the core region flipped, based on *in silico* results might not interact with Tyr306, instead with the alcohol projecting out towards the tunnel of ATX. This could explain the slight drop in potency observed with these compounds.

Compound **2.100** is proposed to form an intramolecular hydrogen bond between the alcohol of the 4-(aminomethyl)piperidin-4-ol and the carbonyl adjacent to the benzo[*d*]oxazol-2(3*H*)-one, which could, increase the lipophilicity of the compound due to the removal of a hydrogen bond donor and acceptor from the molecule.

Compound **2.106** could form a 3.028 Å hydrogen bond with Tyr306 through the carbonyl of the amide group (**Figure 40 c**). The longer distance could explain the drop in ATX inhibition through a weaker electrostatic interaction. Additionally, the alkyl chain on **2.101** does not have the beneficial hydrophobic interactions with the π electrons on Tyr306, and additionally *in silico* docking suggests the amide moiety may be too far from the residue to form anything more than a very weak hydrogen bond, which perhaps explains why this compound is a less efficient ATX inhibitor (**Figure 40 d**).

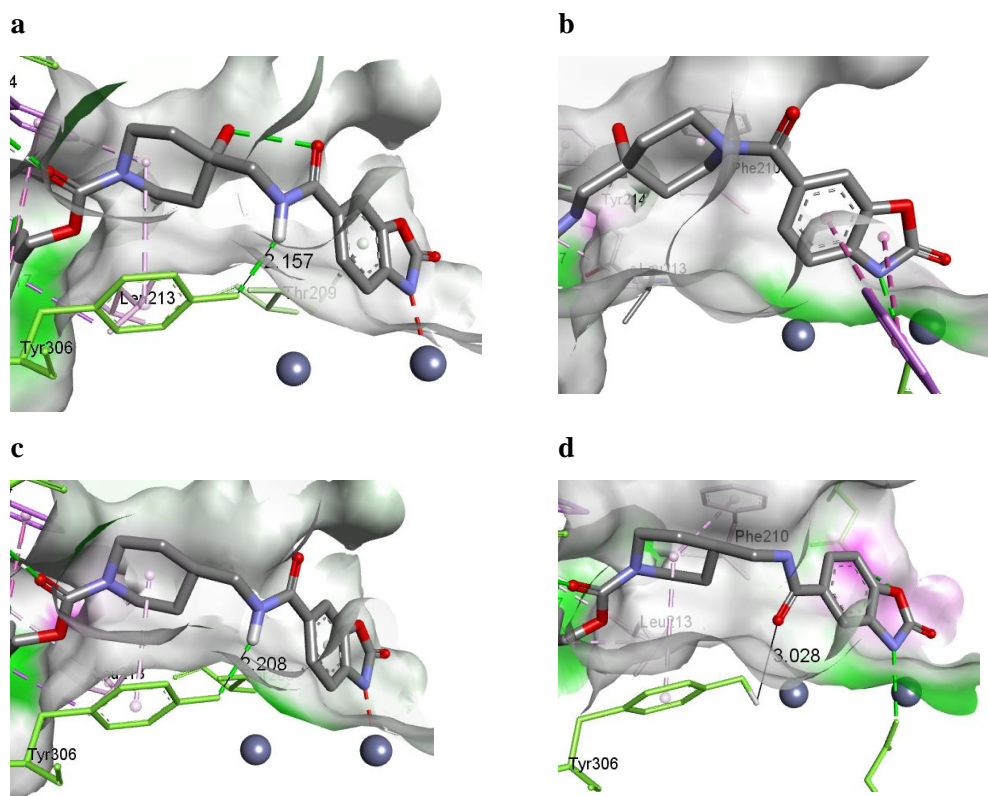


Figure 40 *In silico* modelling of compounds in GOLD¹³⁰ and viewed in DSvisualizer.⁴⁸ **a)** **2.100** in the active site, with intramolecular hydrogen bonding between the alcohol and carbonyl adjacent the benzo[*d*]oxazol-2(3*H*)-one showing the distance of hydrogen bonding between NH and Tyr306 R-OH. **b)** **2.101** in the active site without hydrogen bonding to Tyr306, and the piperidin-4-ol alcohol projecting towards the tunnel. **c)** **2.103** in the active site, the N-H hydrogen bonds with Tyr306 at a distance of 2.208 Å. **d)** **2.105** in the active site, the C=O hydrogen bonds with Tyr306 at a greater distance of 3.028 Å.

2.4.12. Substituted Piperazine Cores

The location of the piperazine core of PF-8380 when bound to ATX is nearby the tunnel, and as discussed in Section 2.2., this region is able to accommodate ligands. Accordingly, substitution from the piperazine ring with lipophilic groups was targeted to project either towards the tunnel region, or towards the large hydrophobic pocket in an effort to increase potency (**Table 21**).

Table 21 Substituted and bicyclic diamine cores.

	Structure	K _i (μ M)	cLogD	LLE _{AT}	PFI
2.107		0.006	2.82	0.37	5.82
2.108		0.009	2.82	0.34	5.82
2.109		0.002	4.02	0.30	7.02
2.110		0.073	4.76	0.29	5.76
2.111		0.96	3.77	0.22	6.77
2.112		0.82	3.77	0.20	6.77
2.113		1.7	1.93	-	2.31
2.114		> 30	3.33	0.20	5.33

Compounds **2.107–2.108** containing a methyl moiety are potent ATX inhibitors without the 3,5-dichloro substitution, suggesting that favourable interactions between the additional methyl group in the tunnel or entrance to the pocket could be compensating for the removal of the 3,5-dichloro groups. The physicochemical properties are improved without the presence of the 3,5-dichloro group. Compounds **2.109–2.110** are again potent ATX inhibitors with the addition of the 3,5-dichlorobenzyl carbamate tail, however a sub-optimal physicochemical

profile coupled with poor solubility made these compounds a poor choice for further optimisation. Piperazine substitution with an isopropyl group **2.113** and the (1*S*,4*S*)-2,5-diazabicyclo[2.2.1]heptane diamine **2.114** were bulky and inflexible, probably clashing with the enzyme surface. Further to this, the benzo[*d*]oxazol-2(3*H*)-one analogue of **2.114** could not be tested in the biochemical assay due to insolubility in DMSO, which was a recurring problem with these cores. We hypothesised that a larger lipophilic group projecting towards the pocket might allow for removal of the lipophilic tail, in principle reducing the cLogD within this series. Compounds **2.111–2.112** contain a benzyl substituted piperazine, however are unfortunately less potent compounds than the methylpiperazine compounds, suggesting that either the full tri-substituted compound occupying each region of the enzyme is needed for potency, or the compound is not residing in the proposed region of the enzyme. *In silico* modelling suggests that the benzyl group may be within the hydrophobic pocket with the *N*-Boc projecting towards the tunnel, explaining the micromolar activity (**Figure 41**).

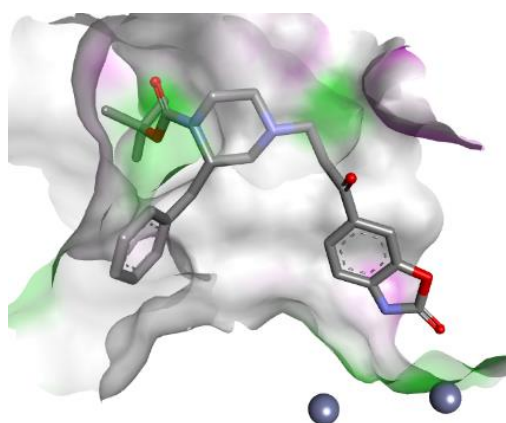


Figure 41 *In silico* modelling of compound **2.111** with a benzyl substituted piperazine in the active site of ATX in GOLD¹³⁰ and DS visualizer.⁴⁸

2.5. The Development of Novel Series of ATX Inhibitors with a Spirocyclic Core

The 2,6-diazaspiro[3.3]heptane core is a known piperazine isostere that is reported to increase the solubility, conformational rigidity, increase the sp^3 nature,¹⁴⁹ and modify the pKa of the basic nitrogen (PF-8380 $pK_{aBH} = 5.95$, **2.116** $pK_{aBH} = 6.50$ calculated using JChem for Excel).¹⁵⁰ Additionally the 2,6-diazaspiro[3.3]heptane core is a full angstrom longer than the piperazine, which is proposed to allow the compound to extend further from the active site, and as a result reside deeper inside the large hydrophobic pocket (**Figure 42**). Despite the

potential for drastically improved physicochemical properties and a growing number of reported spirodiamines by Hoffman-La Roche (**Table 8**), this core has not been reported as a motif within either the literature or patented ATX inhibitors.^{151,152} As a result of this, the subsequent series of compounds developed contained this 2,6-diazaspiro[3.3]heptane core in order to probe the effect of the novel core on both physicochemical properties and potency.

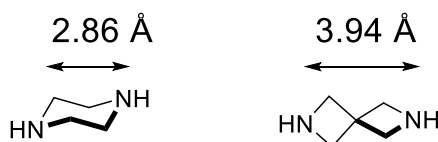


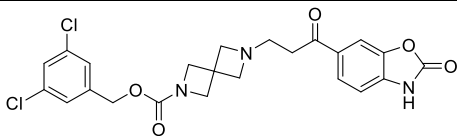
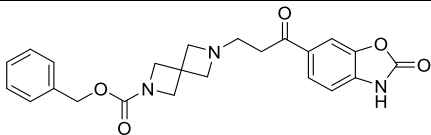
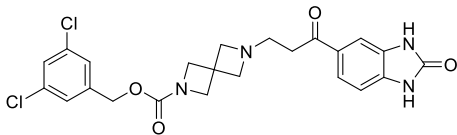
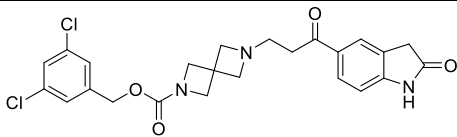
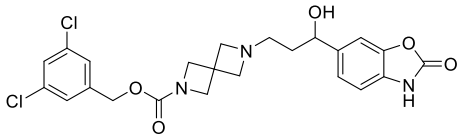
Figure 42 Comparison of the length of the piperazine and 2,6-diazaspiro[3.3]heptane core.¹⁵⁰

After establishing a robust structure-activity relationship in the PF-8380 series, and identifying potent ATX inhibitors, we initially proposed the synthesis of direct analogues of PF-8380 and **2.42** (**Table 12**) containing the 2,6-diazaspiro[3.3]heptane core, and small modifications to the ZBG similar to compounds **2.56** and **2.58** (**Table 14**), which we had previously established resulted in potent ATX inhibitors (**Table 22**). The initial compound proposed revealed that there was an improvement in the predicted physicochemical properties and the potency of compound **2.115**, which is the direct analogue of PF-8380 (**2.115** cLogD = 3.27, LLE_{AT} = 0.34, PFI = 6.27, **Table 22**). This led to the development of a novel spirocyclic series, which could be further developed with the aim of generating a lead-like compound.

2.5.1. Hit Identification of a 2,6-diazaspiro[3.3]heptane Core as a Bioisostere of Piperazine

Using the knowledge gained from the SAR study of PF-8380, small modifications were made to the ZBG of **2.115**, with the 3,5-dichlorobenzyl carbamate, and benzylcarbamate tail (**Table 22**). In order to further improve the physicochemical parameters, the alcohol analogue of **2.115** was also synthesised.

Table 22 Investigation of a novel 2,6-diazaspiro[3.3]heptane core.

	Structure	K _i (μ M)	cLogD	LLE _{AT}	PFI
2.115		0.001	3.27	0.34	6.27
2.116		0.005	2.06	0.40	5.06
2.117		0.051	3.08	0.27	6.08
2.118		0.19	3.00	0.26	5.00
2.119		0.002	2.76	0.40	5.76

2.115 was a highly potent compound, which confirmed that the additional length, rigidity, sp^3 nature of the core, and potentially the increased pK_{aBH} were beneficial to ATX inhibition. With these promising initial results the benzyl carbamate analogue **2.116** was synthesised and found to be equipotent with the initial hit **2.115**, despite removal of the integral chloro groups. The cLogD and PFI were reduced, solubility increased, and LLE_{AT} improved, as suggested by the design hypothesis. The increased potency of **2.116** is believed to be a direct result of the added compound length and rigidity of the core region, forcing the benzyl carbamate tail further into the hydrophobic pocket, which is not observed in the parent series where the removal of the di-chloro atoms results in a 7-fold loss in potency (**Table 12**). Altering the benzo[*d*]oxazol-2(3*H*)-one to a indolin-2-one **2.118**, and 1,3-dihydro-2*H*-benzo[*d*]imidazol-2-one **2.117** decreased the potency compared to the piperazine analogues, although the core beneficially impacts the physicochemical properties. Compound **2.117** was reduced to the alcohol **2.119**, resulting in excellent physicochemical properties, with nanomolar potency.

2.5.2. Identification of Alternative Zinc Binding Groups in the Spirocyclic Series

As discussed above, the spirocyclic series identified 2,6-diazaspiro[3.3]heptane as a competent piperazine isostere. Initial compounds **2.115**, **2.116**, and **2.119** with structural similarities to PF-8380 and one to two SAR changes from the parent compound resulted in potent ATX inhibitors with improved physicochemical properties (**Table 22**). As a result of this, compounds that contained the 2,6-diazaspiro[3.3]heptane core and 3,5-dichlorobenzyl carbamate tail were synthesised with alternative ZBG to the benzo[*d*]oxazol-2(3*H*)-one of the PF series. By altering the ZBG, which was identified during the PF SAR as contributing to low aqueous solubility, it was postulated that the physicochemical properties could be improved further. The second iteration of ZBGs screened contained HBD and HBA to target hydrogen bonding interactions with the Thr209 residue in the active site, and additionally nitrogen containing ZBGs were explored based upon the binding mode of PF-8380 which was known through co-crystallography within ATX.¹²² This led to the inclusion of the 1,3-dihydro-2*H*-benzo[*d*]imidazol-2-one, and indolin-2-one ZBG linked to the 2,6-diazaspiro[3.3]heptane core as both the sulfonamide and amide with compounds **2.121–2.121**, and **2.126–2.128** (**Table 23**), which were active compounds within the PF series. Although these compounds are shorter in length than the previous sub-series of compounds they were targeted initially based upon synthetic expediency.

ZBGs that were not explored within the PF series included a sulfonamide motif **2.122** (**Table 23**) similar to Hoffman-La Roche compounds (**Table 8**), which should be able to interact with the zinc atoms and hydrogen bond to Thr209.^{123,151} Additionally, benzimidazole, and benzotriazole groups **2.123–2.124** (**Table 23**) are established ZBGs that have been used as scaffolds in potent ATX inhibitors within Hoffman-La Roche and Merck patents (**Table 8**).^{151,125} Finally, a novel 1-hydroxy-1,3-dihydrobenzoxaborole ZBG (**Table 23**), which should interact with the zinc similarly to HA155 (**Figure 29**), and is identified as potentially having improved aqueous solubility and reduced likelihood of C-B bond cleavage.^{153–155} Further to this, the Lewis Acidity of boron which allows formation of the boronate, could enable the formation of a covalent bond between nearby catalytic Thr209 residue and the 1-hydroxy-1,3-dihydrobenzoxaborole, providing an attractive scaffold for a lead-like ATX inhibitor.

Table 23 Zinc binding groups with the 2,6-diazaspiro[3.3]heptane core. ^aSynthesised by another member of our laboratory.¹⁴⁷

	Structure	K_i (μM)	cLogD	LLE _{AT}	PFI
2.120		0.029	2.68	0.32	5.68
2.121		0.27	2.43	0.29	4.43
2.122		0.056	2.18	0.33	4.18
2.123		0.054	2.86	0.31	5.86
2.124		0.095	2.84	0.30	5.84
2.125		0.091	3.63	0.26	5.63
2.126		0.17	0.30	0.29	5.75
2.127^a		0.094	2.93	0.29	5.93
2.128		3.4	2.93	0.22	5.93

In silico modelling of some of the most potent compounds **2.122**, **2.124**, **2.125**, and **2.127** (Figure 43) show the different possible binding poses of these compounds at the catalytic site.

The benzo[*d*]oxazol-2(3*H*)-one ZBG of compound **2.127** is believed to interact with the Thr209, and the distal zinc atom with the carbonyl moiety, however the predicted distances based on *in silico* modeling are large (Predicted distance to Thr209 = 3.99 Å, predicted distance to distal zinc atom 4.59 Å, **Figure 43 a**). These distances suggest that a longer linker length could be optimal for interactions within the active site. The regiochemistry of the benzo[*d*]oxazol-2(3*H*)-one was investigated, and compound **2.128** with the 5-substituted benzo[*d*]oxazol-2(3*H*)-one resulted in a significantly less potent ATX inhibitor. This signifies that the 6-substituted benzo[*d*]oxazol-2(3*H*)-one compound **2.127** is optimum for interacting with the zinc atom within this ZBG motif. Compound **2.122** interacts the with distal zinc atom through the sulfonamide (Predicted distance = 3.97 Å and 3.27 Å), and appears not to interact with the Thr209 residue (**Figure 43 b**). The 1-hydroxy-1,3-dihydrobenzoxaborole ZBG of compound **2.125** is predicted to have a slightly higher pKa value, and is unlikely to be ionised in the assay conditions (**2.125** pKa = 11.75), however the borocycle can hydrogen bond through the alcohol moiety to the Thr209 residue (Predicted distance = 3.77 Å) (**Figure 43 c**). Equally the benzotriazole containing compound **2.124** is capable of hydrogen bonding to Thr209 (Predicted distance = 3.05 Å), despite *in silico* docking predicting no zinc interactions (**Figure 43 d**).

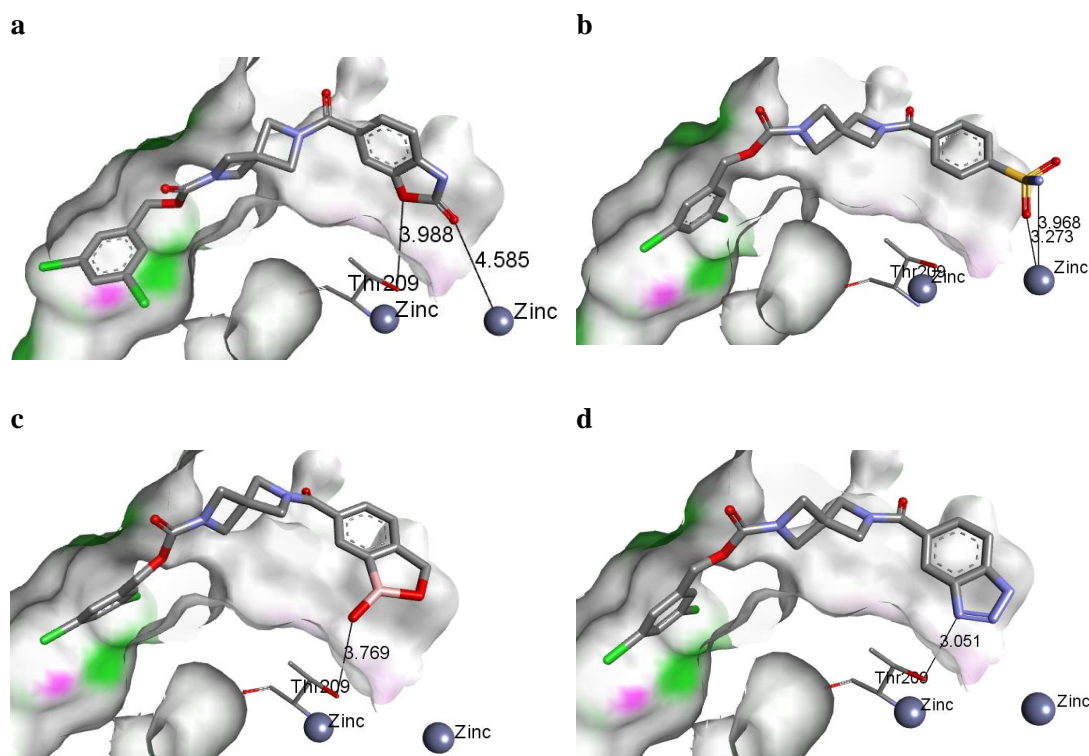


Figure 43 *In silico* modelling in GOLD¹³⁰ and DS visualizer⁴⁸ of **a**) benzo[*d*]oxazol-2(3*H*)-one ZBG compound **2.127**. **b**) Sulfonamide ZBG **2.122**. **c**) Borocycle ZBG **2.125**. **d**) Benzimidazole ZBG **2.124**.

Although compounds have been identified which are novel, potent, and have lead-like physicochemical properties, based on *in silico* results, the length of the compounds could be extended to increase the potency further. The 3,5-dichlorobenzyl carbamate tail resides at the edge of the hydrophobic pocket and the ZBG, albeit interacting with Thr209, is predicted not to be close enough to the distal zinc atom in the active site, as observed with the co-crystal structure of PF-8380 and **2.1** (**Figure 33**).

2.5.3. Identification of a Homologated (2-azaspiro[3.3]heptan-6-yl)methanamine

Core

As discussed above, the amide linked 2,6-diazaspiro[3.3]heptane cores resulted in compounds **2.127**, **2.122**, **2.125** and **2.126** having promising levels of activity (**Table 23**). However, the difference in length between the initial hit compound **2.115** (**Table 22**) is evident, and *in silico* analysis suggesting homologation of the core could be beneficial.

As a direct result of the decreased length there is a drop in potency, which could either be attributed to the pKa difference due the loss of the basic nitrogen centre, or the length of the compound. To investigate the effect of length of the compounds on activity, compounds were synthesised using a (2-azaspiro[3.3]heptan-6-yl)methanamine core (Green, **Figure 44**) that was envisioned to have the requisite length to bind in the active site analogously to the direct PF-8380 analogue containing the 2,6-diazaspiro[3.3]heptane core **2.115** (Yellow, **Figure 44**). Again the 3,5-dichlorobenzyl carbamate tail is reasoned to act as a conformational lock, with the compounds potency determined by increased proximity to the active site zinc atoms.

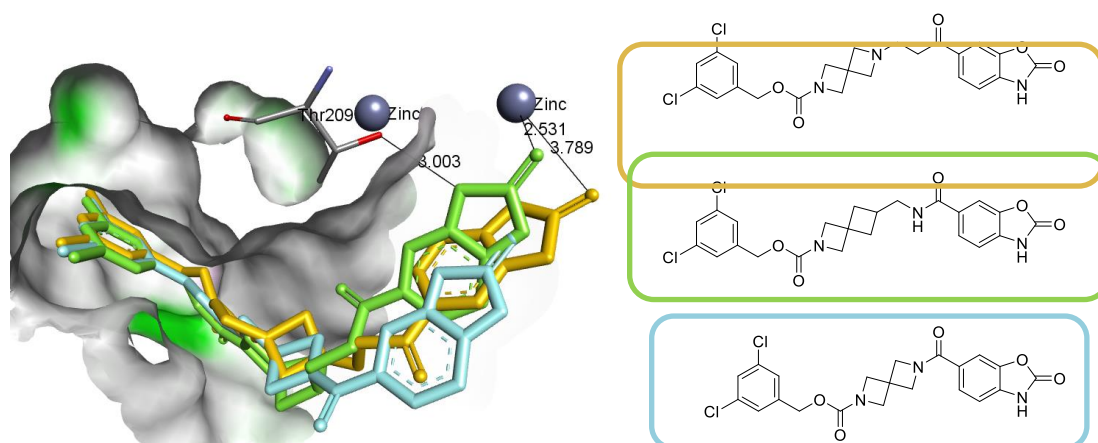
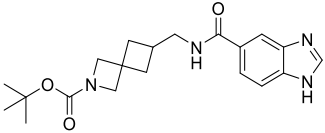
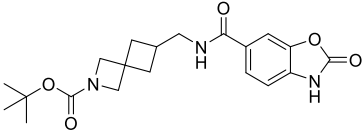
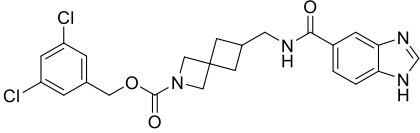


Figure 44 Compounds docked in GOLD and viewed in DS visualizer.^{48,130} Overlay of compound **2.115** (orange, $K_i = 0.001 \mu\text{M}$), **2.127** (blue, $K_i = 0.094 \mu\text{M}$), and proposed PF analogue with the (2-azaspiro[3.3]heptan-6-yl)methanamine core core (green) showing the vector change in the zinc binding region.

Table 24 Homologated (2-azaspiro[3.3]heptan-6-yl)methanamine core.

	Structure	K _i (μ M)	cLogD	LLE _{AT}	PFI
2.129		> 30	1.71	-	3.71
2.130		> 30	2.26	-	3.78
2.131		0.010	3.59	0.30	6.59

Akin to the original series of PF-8380 analogues (**Table 12**), the *N*-Boc protected compounds **2.129–2.130** (**Table 24**) are not potent inhibitors, however these are tested in the assay as valuable intermediates. By contrast, **2.131** (**Table 24**) is a potent ATX inhibitor, which confirms that the added length is essential for optimum compound potency in comparison to the truncated progenitor compound **2.123**. Although the physicochemical properties are slightly worse than a few key compounds in the hit to lead development, further optimisation of this lead could deliver a suitable *in vivo* candidate.

In silico docking of **2.123** and **2.131** shows the increased length of **2.131**, with the 3,5-dichlorobenzyl carbamate tail projecting further into the hydrophobic pocket. Hydrophobic interactions are also potentially attained with residue Met512, which so far have only been observed with the co-crystal structure of LPA (**Figure 8**). The *in silico* docking suggests that the ZBG remains in the same position as the truncated progenitor compound **2.123**. However, it is not clear whether the 3,5-dichlorobenzyl carbamate tail would move further into the hydrophobic pocket as indicated here (**Figure 45**), or if the ZBG would position itself closer to the distal zinc atom as observed in the PF-8380 crystal structure (**Figure 30**).¹²²

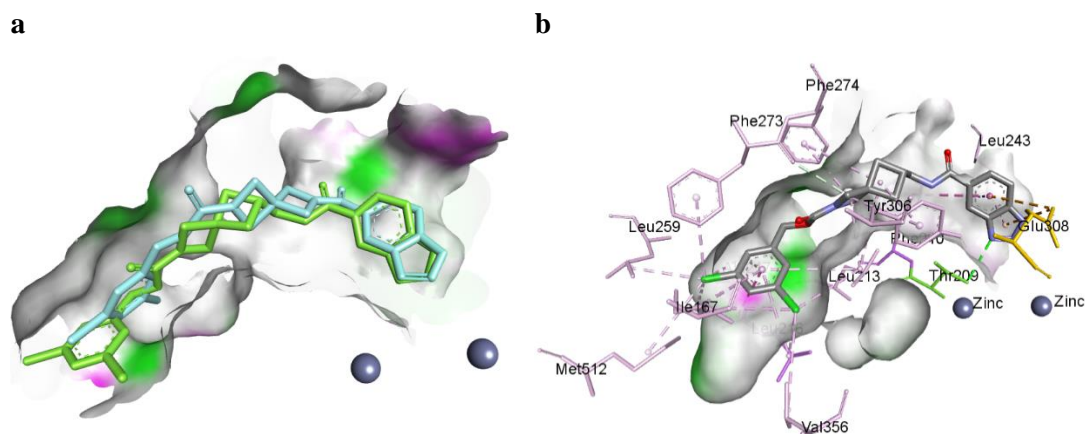


Figure 45 a) Overlay of *in silico* modelling in GOLD and DS visualizer of **2.123** and **2.131**.^{48,130} b) Key residues for potency with **2.131**.

This novel series of compounds containing the 2,6-diazaspiro[3.3]heptane core resulted in both potent and novel ATX inhibitors, with improved physicochemical properties compared to PF-8380, and the direct analogue containing the 2,6-diazaspiro[3.3]heptane core **2.115** (Table 22). Due to the slight decrease in potency observed in truncated compounds **2.120**–**2.128** (Table 23) it was envisioned that the replacement of the 2,6-diazaspiro[3.3]heptane core with an extended (2-azaspiro[3.3]heptan-6-yl)methanamine core could regain potency. This modification resulted in a novel and potent ATX inhibitor compound **2.131** (Table 24). Additional *in silico* docking suggests that **2.131** could potentially interact with Met512 deep inside the hydrophobic pocket of ATX, similarly to LPA, which is to date unknown by co-crystallised and docked ATX inhibitors. Overall this series provides two novel spirocyclic cores capable of improving the physicochemical properties of ATX inhibitors whilst retaining potency.

2.6. BJEH Cell Based aAssay

Due to the involvement of ATX in cancer and proliferative diseases (Section 1.2.6.), a selection of compounds from the emerging lead series were tested in a cell based BJEH assay.² This is a cell based assay with fibroblast cell lines, which can then be stained with antibodies in order to observe the effect of ATX inhibition on downstream signalling pathways. The downstream signalling pathway considered in this assay is the phosphorylation of AKT, which prompts a complex signalling response that enhances migration, proliferation and apoptosis of cells (Section 1.2.6., Figure 21).^{156,157} Activity is observed in this assay when the phosphorylation of AKT is ablated due to inhibition of ATX. Compounds were tested in an

Alamar Blue cytotoxicity assay alongside the bis-*p*NPP biochemical assay screen, with compounds showing no signs of cytotoxicity progressed for testing thus eliminating the possibility of a false positive result due to cell death. Following the co-crystal structure with ATX, compound **2.1** (**Figure 47**) was tested in the cell-based assay at different concentrations to generate a dose-response curve. The dose response curve generated for ATX inhibition with regards to the phosphorylation of AKT indicates **2.1** is a potent ATX inhibitor in the cell based assay. Potency gained from this assay is reinforced by the knowledge that compound **2.1** has a defined binding mode. This *in vitro* assay shows **2.1** can significantly inhibit ATX which results in decreased phosphorylation of AKT, and is consistent with the biochemical assay results, providing promising results for further *in vivo* analysis.

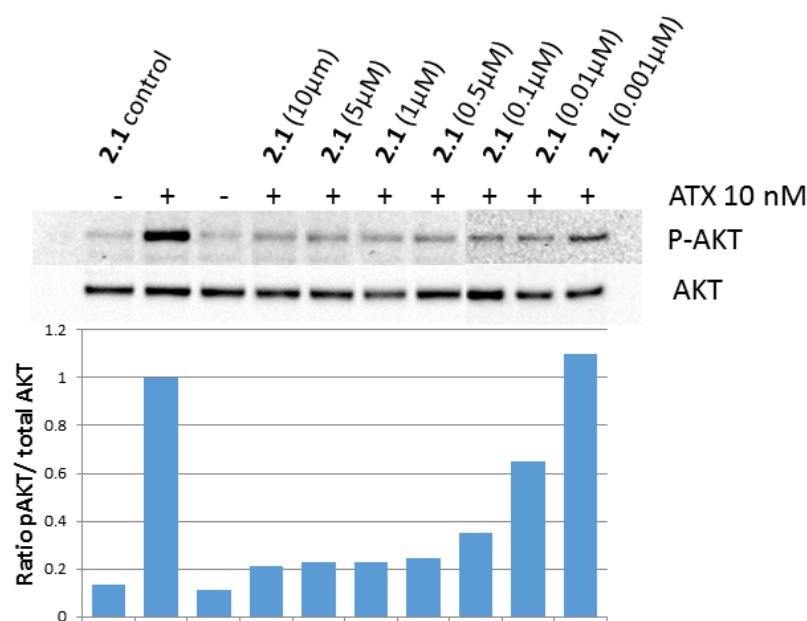


Figure 46 Dose response curve of **2.1** in the cell by NK1. The control blot contains the inhibitor **2.1** in the cell media, then the next blot contains ATX and LPA showing phosphorylation of AKT as a negative control, and thirdly the cell media alone.

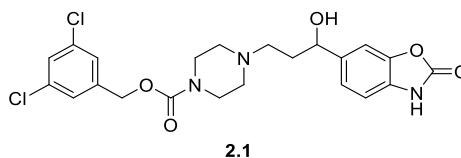


Figure 47 Structure of compound **2.1**.

Additionally, compounds **2.58**, **2.99**, **2.103**, and **2.104** (**Figure 49**) which all exhibited excellent potency in the biochemical assay, were tested in the BJEH cell based assay at a 5

μM concentration (**Figure 48**). Additionally, PF-8380 and compound **2.1** were tested as comparator compounds in this cell based assay. The next series of compounds tested in the BJEH cell based assay were **2.99**, **2.110**, **2.115**, and **2.119** (**Figure 49**), which also significantly reduced the phosphorylation of AKT (**Figure 48**). All compounds showed good levels of inhibition of ATX, and hence inhibition of the phosphorylation of AKT further strengthening the connection between the bis-*p*NPP assay and activity in a cellular context.

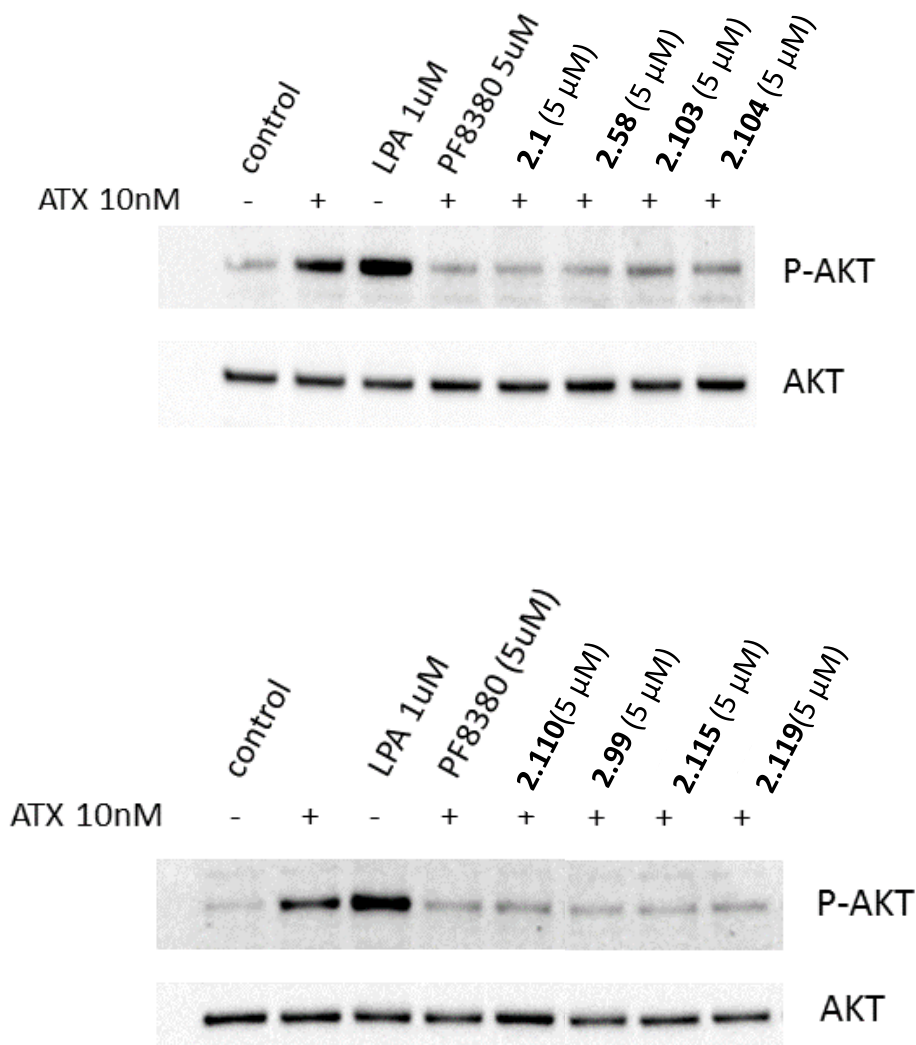


Figure 48 Compounds tested in BJEH fibroblast cell based assay by NKI for the phosphorylation of AKT. The controls are the cell based media alone, ATX alone, and then LPA alone which is expected to have significant downstream signalling effects by phosphorylating AKT.

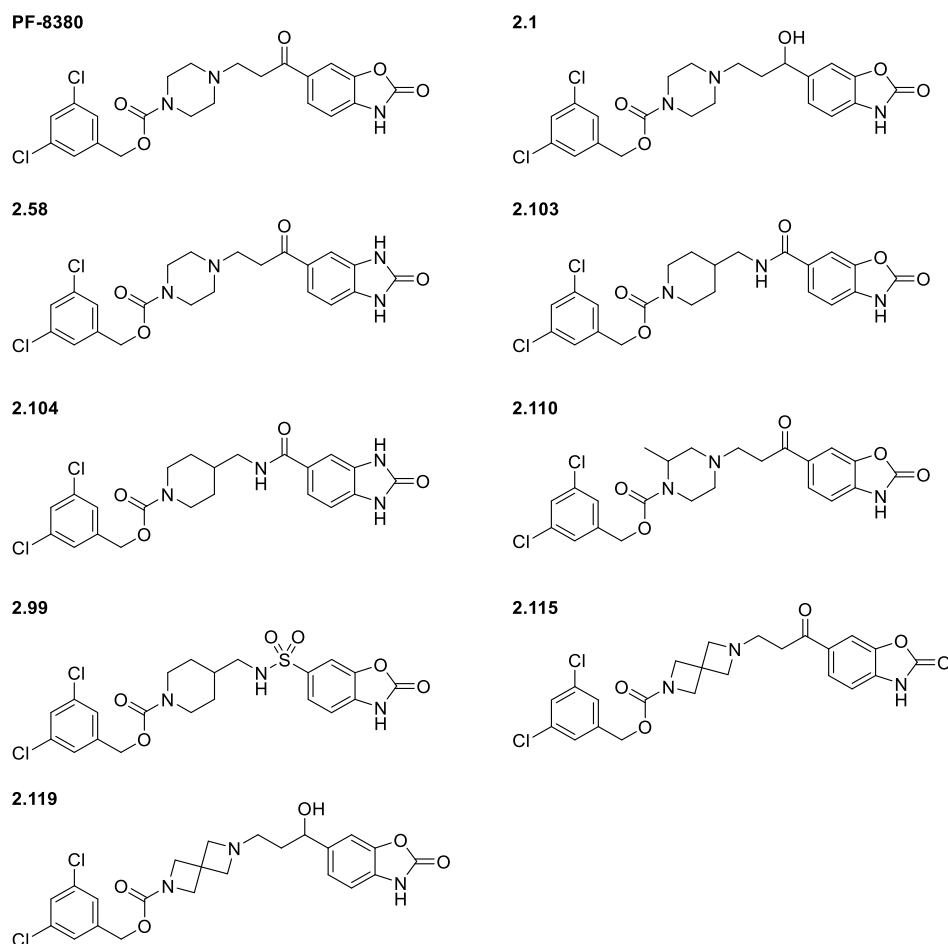


Figure 49 Compounds tested in the BJEH cell-based assay.

This is an important observation as frequently there is a decrease in activity between a biochemical assay and a cell based assay. As biochemical assays measure potency of the compound directly with the enzyme, and the cell based assay can be compromised by poor cell permeability or competition with alternative cellular substrates. Accordingly, it is important to identify a good correlation within a lead series between both assays before a compound is progressed further.¹⁵⁸

2.7. Analysis of the physicochemical profile

While establishing the SAR around the PF series the key physicochemical parameters were monitored. Key compounds were taken from several sub-series in the SAR study and the aqueous solubility and cLogD were plotted (**Figure 50**). This graphically represents progression from PF-8380 ($K_i = 0.008 \mu\text{M}$, $\text{cLogD} = 3.62$, $\text{Sol} = 24 \mu\text{M}$, **Table 12**) to three lead-like compounds with physicochemical properties (**2.100** $K_i = 0.17 \mu\text{M}$, $\text{cLogD} = 1.23$,

Sol = 459 μ M, **2.116** K_i = 0.005 μ M, cLogD = 2.06, Sol = 353 μ M, and **2.122** (K_i = 0.056 μ M, cLogD = 2.18, Sol = 167 μ M, **Table 23, Figure 50**). Compounds **2.116** and **2.122** maintain the potency already achieved by PF-8380, with **2.116** being a two-point structural change and **2.122** a 3-point change, which makes this compound structurally unique from the parent compound. Compound **2.100** (K_i = 0.17 μ M, cLogD = 1.23, **Table 20**) is a novel compound developed in the amide series, and overall has the best physicochemical profile, however is less potent, so could also be a valid candidate for further profiling.

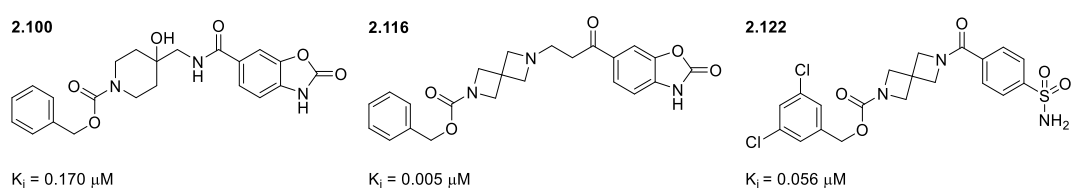
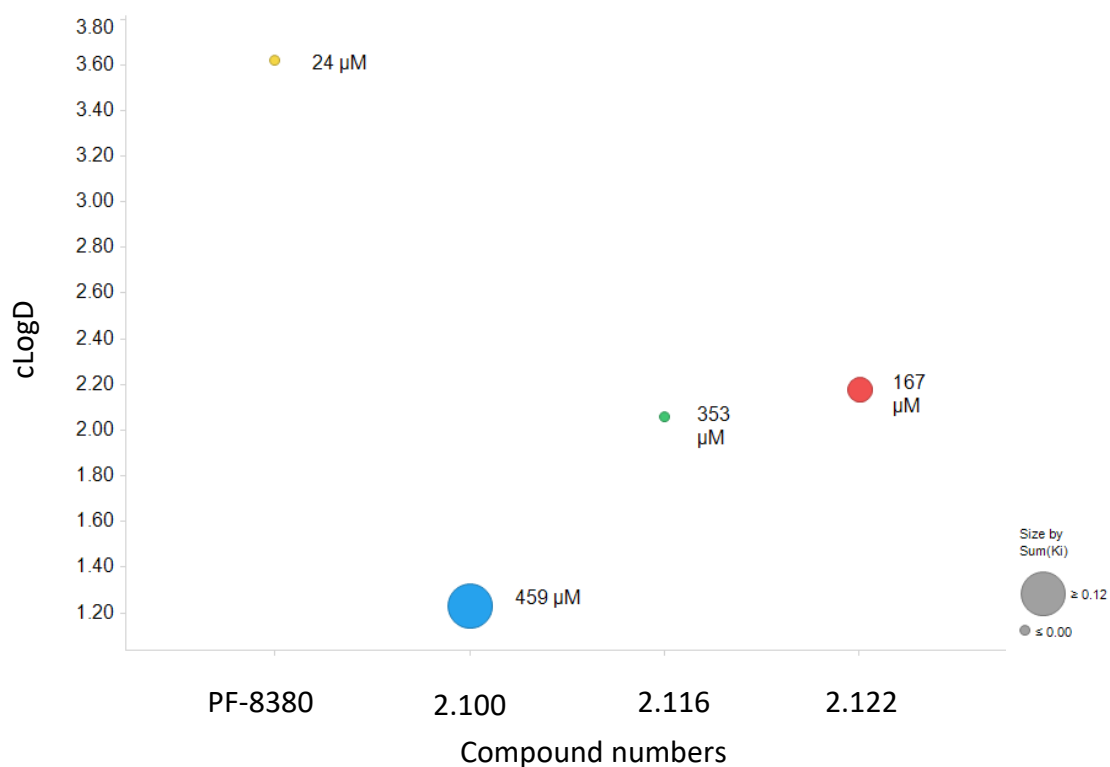


Figure 50 The development of cLogD from PF-8380 to compound **2.100**, **2.116**, and **2.122**. Size of circle indicates the K_i (large K_i = large circle) and the solubility in μ M indicated.¹⁵⁹

Lead-like compounds **2.100**, **2.116**, and **2.122** emerged with encouraging physicochemical properties combined with good potency compared to each series (**Figure 50**). Analysis of the physicochemical properties of these compounds with Spotfire¹⁵⁹ (MWT < 500, cLogD < 3

and $PFI < 7$) shows these compounds lie within favourable parameters, and outperform other key compounds from each series developed (**Figure 51, Figure 52**).

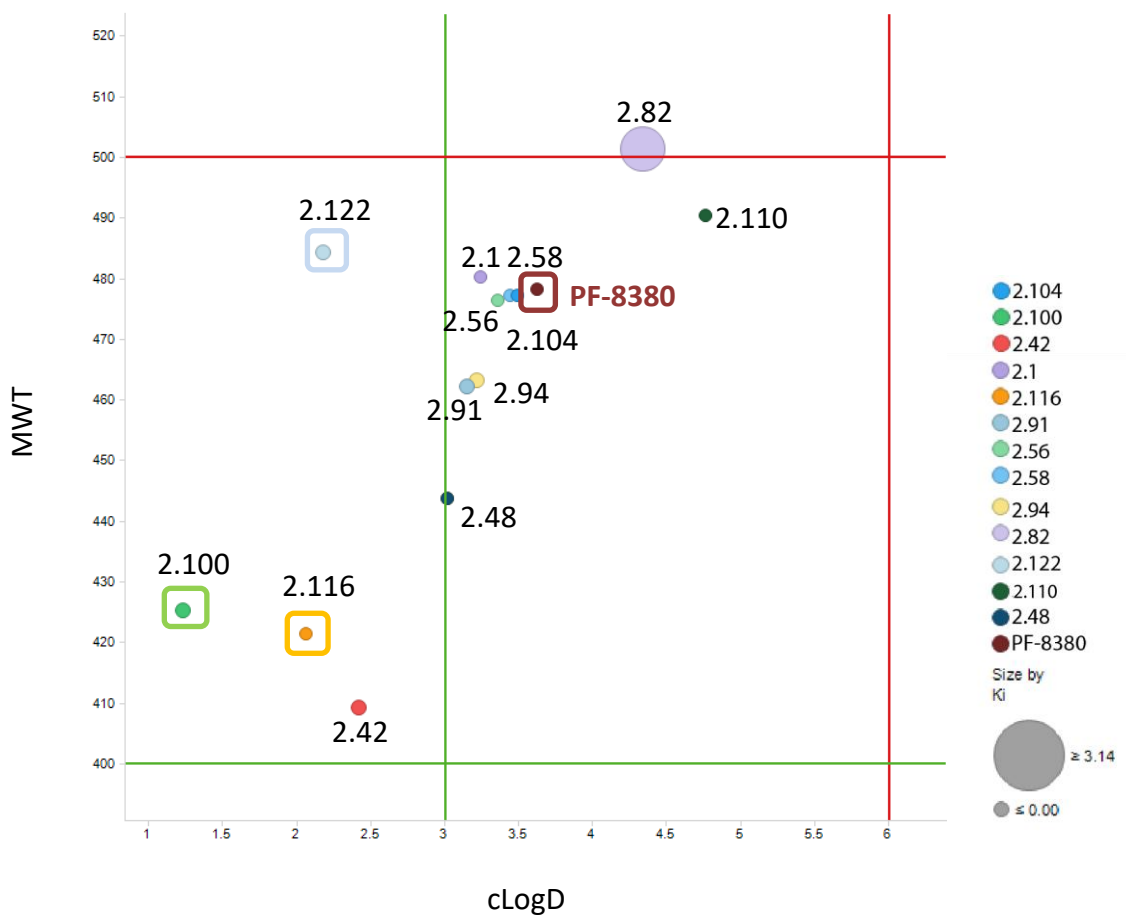


Figure 51 cLogD vs MWT 2.100 green, 2.116 orange, and 2.122 blue. Trends analysed using Spotfire.¹⁵⁹ Size of circle indicates the K_i (large K_i = large circle) and the colours represent a compound from each sub-series. The key for these compounds are present in **Figure 52**.

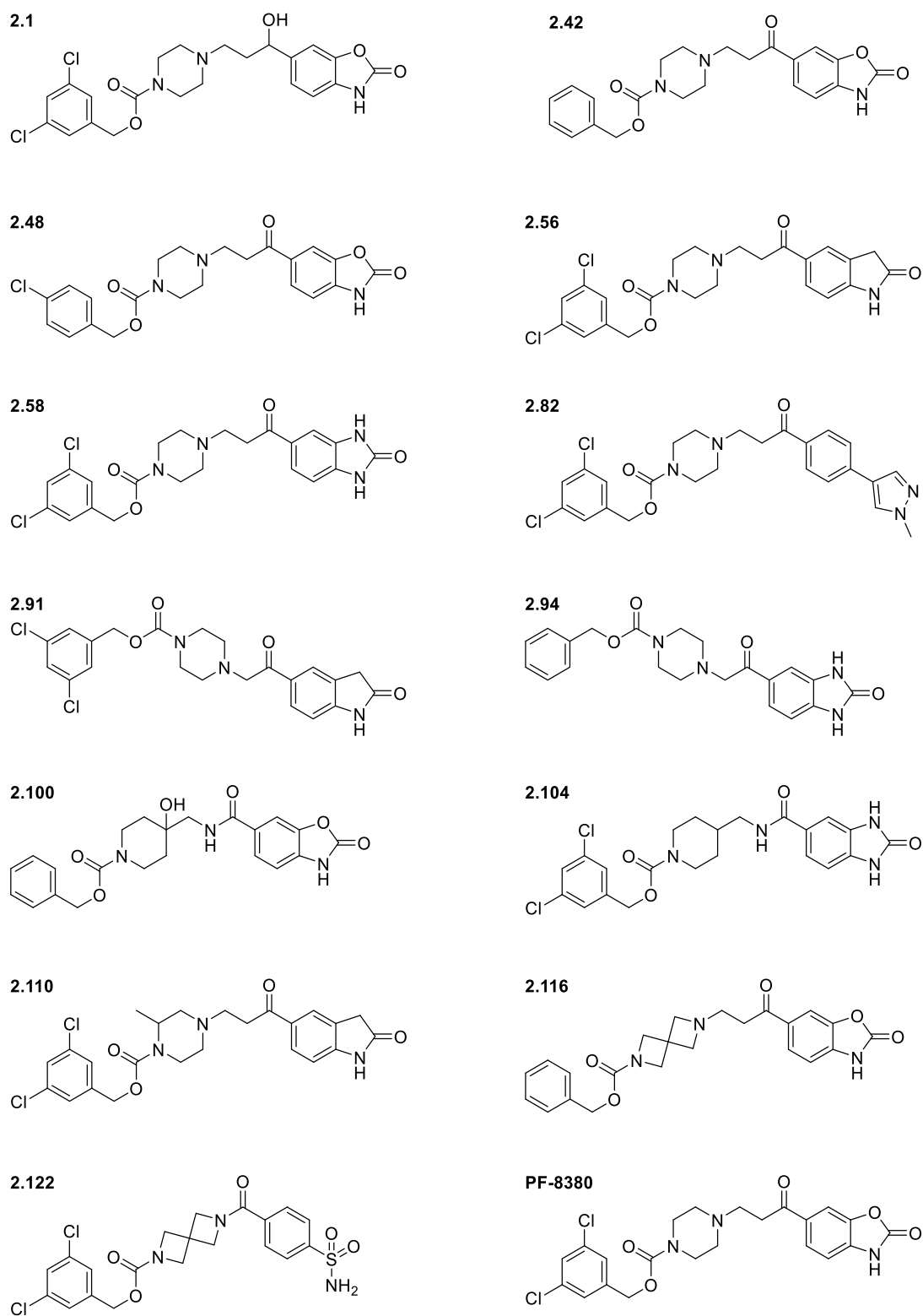


Figure 52 Compounds from each sub-series of compounds present in **Figure 51**.

The improvement of solubility, cLogD, and PFI were important aspects considered throughout this project. The graph below highlights the development of the compounds through the PF-8380 SAR study, with an ideal compound possessing a $c\text{LogD} < 3$, $\text{PFI} < 7$, $\text{LLE}_{\text{AT}} > 0.3$ (**Figure 53**).

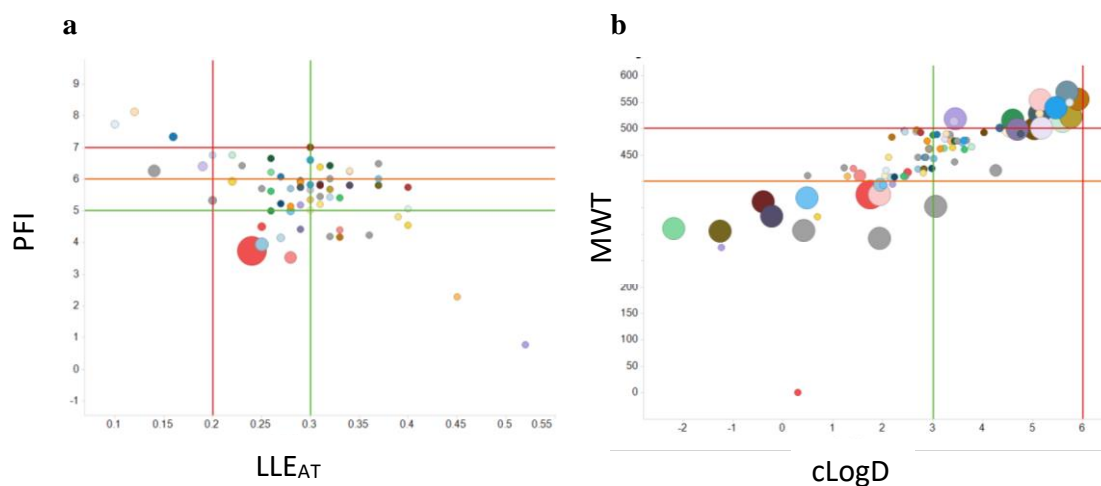


Figure 53 a) Compound library of LLE_{AT} vs PFI. b) cLogD vs MWT. (Larger K_i with a bigger circle) using Spotfire.¹⁵⁹

Within this compound library there is an optimum range for lipophilicity of $c\text{LogD} = \sim 2\text{-}4$ (**Figure 54**). Although a decreased cLogD is physicochemically preferable, the presence of a lipophilic region on these compounds is essential for occupancy of the hydrophobic pocket of ATX to achieve potency. In this instance LLE_{AT} is an important parameter to consider the balance between potency and lipophilicity. A number of the compounds in this library contain both $\text{LLE}_{\text{AT}} > 0.3$, and $c\text{LogD} < 3$, with good potency. Compound **2.116** (**Table 22**, $K_i = 0.005 \mu\text{M}$, $c\text{LogD} = 2.06$), **2.119** (**Table 22**, $K_i = 0.002 \mu\text{M}$, $c\text{LogD} = 2.76$), **2.122** (**Table 23**, ($K_i = 0.056 \mu\text{M}$, $c\text{LogD} = 2.18$) and **2.131** (**Table 24**, ($K_i = 0.010 \mu\text{M}$, $c\text{LogD} = 2.84$) all are within the desired parameters-delivering lead-like compounds for ATX inhibition (**Figure 54**).

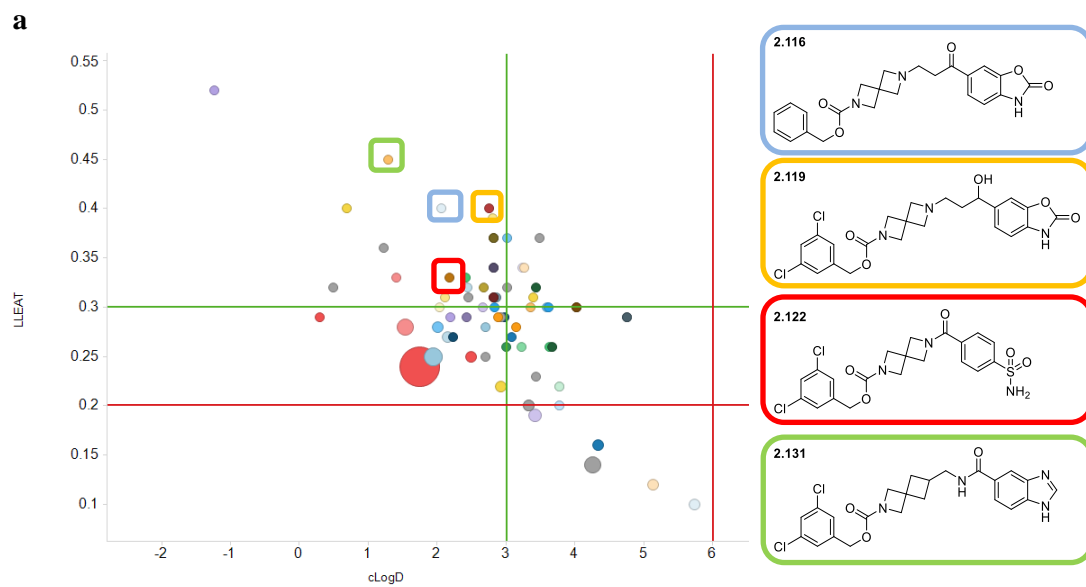


Figure 54 LLE vs chromLogD of the compound library with the size of the circle corresponding to the K_i of the compounds.¹⁵⁹

2.8. Conclusion

Tool compound PF-8380 ($K_i = 0.008 \mu\text{M}$, **Table 12**) was first disclosed in the patent literature as a potent ATX inhibitor.⁹⁵ At the outset of the project we proposed the benzo[*d*]oxazol-2(3*H*)-one ZBG of PF-8380 interacts electrostatically with the zinc atoms in the active site, and the lipophilic tail is located within the hydrophobic pocket, much like the bioactive product of ATX, LPA (**Figure 8**). The binding mode of PF-8380 within ATX was confirmed by *in silico* analysis and co-crystallography of PF-8380 by Jones *et al*, and of a closely related alcohol analogue of PF-8380, **2.1**, bound with ATX (**Figure 33**).¹²¹ After confirmation of this hypothesis, we developed a comprehensive structure–activity relationship of PF-8380, as this information is not possible to definitively extract from the current patent literature.

Exploration of this SAR in the lipophilic tail region showed that aromaticity is important for ATX inhibition (**Table 12**), however bulky lipophilic groups such as the cyclohexyl tail (**Table 13**) can compensate for the removal of the aromaticity with improved physicochemical properties. In particular, aromatic moieties containing aromatic 3,5-dichloro substitution generate the most potent ATX inhibitors. The 3-chloro and 4-chloro (**Table 13**) mono substituted benzyl carbamates are equipotent to the 3,5-dichloro counterparts, although they unfortunately provided no beneficial improvement in solubility. Attempts were made to tune the cLogD through making changes in this region (**Table 13**), however this resulted in diminished levels of potency. Based on the results of this study, the lipophilic moiety chosen for the remaining series of compounds consisted of the 3,5-dichlorobenzyl carbamate for optimal potency and the benzylcarbamate for more favourable physicochemical properties.

Zinc binding group modifications verified the complete removal of benzo[*d*]oxazol-2(3*H*)-one was detrimental to activity. The initial SAR screen utilised only small modifications to the benzo[*d*]oxazol-2(3*H*)-one to an indolin-2-one and 1,3-dihydro-2*H*-benzo[*d*]imidazol-2-one, resulting in potent compounds due to the nitrogen of the ZBG electrostatically interacting with the distal zinc atom. A further ZBG screen was investigated (**Table 23**), and with this knowledge more structurally diverse groups appeared. The most potent ZBGs are shown below (**Figure 55**) with the corresponding pKa. Jones *et al* reported that the optimum acidic pKa of these compounds to beneficially interact with the zinc atoms is in the range of ~8–11.¹²² This pKa range is suggested to allow the anion to be formed at physiological pH, so the compound can interact with the zinc as observed in the crystal structure (**Figure 33**). Outliers include the hydroxamic acid compound **2.68** (**Table 15**), which although is suggested to be in the correct pKa range, has the incorrect linker length to reach both the active site and hydrophobic pocket of the enzyme. The benzimidazole, indolin-2-one and 1,3-dihydro-2*H*-

benzo[*d*]imidazol-2-one ZBGs all have a pKa in the range of 11-13 suggesting that the anion is unlikely to be formed at physiological and assay pH, however, potent compounds have emerged with these ZBGs. This suggests that consideration of pKa alone is not truly indicative of good co-ordination to zinc, and additionally the presence of the Thr209 and crystallographic H₂O in the enzyme active site, suggests there are also HBD/HBA hydrogen bonding factors which contribute to potency, as all three of these ZBGs often result in potent ATX inhibitors (**Table 14**, **Table 23**).

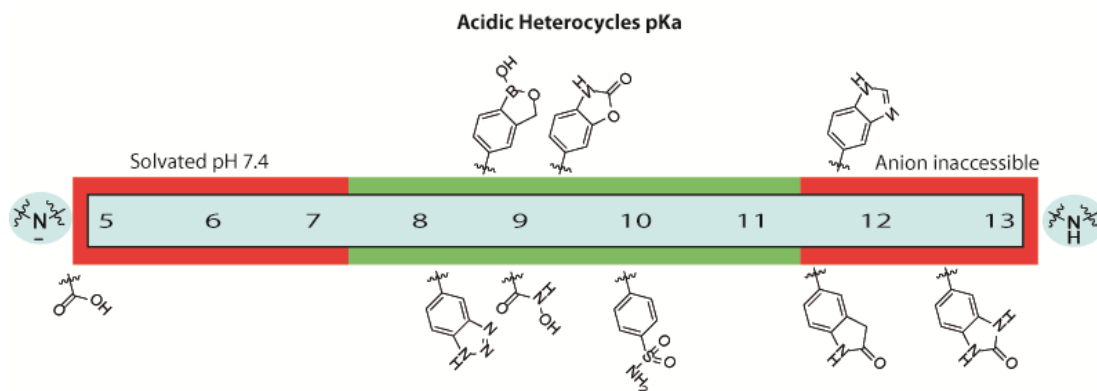


Figure 55 pKa analysis of ZBGs with the optimum range as 8-11.¹²²

The core region can be significantly altered and retain potency if a potent ZBG and the 3,5-dichlorobenzyl carbamate tail are both present. This is observed in the truncated series (**Table 17**) where all ATX activity is lost without these two key pharmacophoric features, likely as these compounds were potentially too short to reach both key regions for good levels of potency. After reasoning that the length of the compound was important for potency, the core region was altered to a series of sulfonamide (**Table 19**), and amide (**Table 20**) linked compounds with a methylaminopiperidine core. Both of these series led to novel and potent leads compared to PF-8380, with improved physicochemical properties. Further progression of these compounds with a 4-(aminomethyl)piperidin-4-ol core considerably advanced the physicochemical profile whilst maintaining potency, and led to compound **2.100** (**Table 20**) which had the best physicochemical profile in this sub-series compounds. Due to such a large improvement in physicochemical properties, the 3,5-dichlorobenzyl carbamate could be used in this series to yield a more potent ATX inhibitor **2.101** (**Table 20**), again with improved physicochemical properties compared to PF-8380. **Figure 56** summarised the structure-activity relationship devised around PF-8380 in this study.

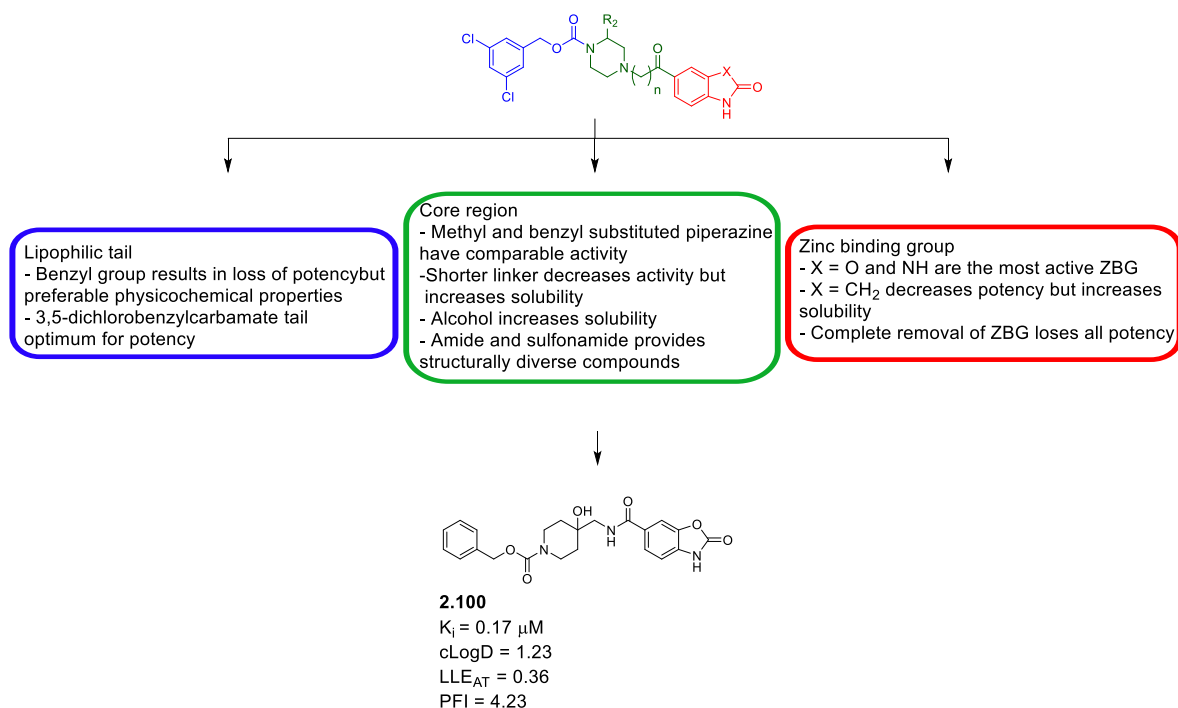


Figure 56 PF-8380 SAR summary highlighting the key pharmacophoric features required for activity.

During the course of the SAR study a novel 2,6-diazaspiro[3.3]heptane core was identified to improve the physicochemical properties, with an additional 1 Å added to the compound length compared to PF-8380. Based on *in silico* modelling the 3,5-dichlorobenzyl carbamate tail resides in the hydrophobic pocket with the same positioning as the parent compound, moving the ZBG in closer proximity to the zinc atoms and Thr209, resulting in a highly potent hit compound from this novel series (**Table 22**). Further optimisation of this sub-series with two-point SAR changes from PF-8380 included reduction to the alcohol **2.119** (**Table 22**), and use of the benzyl carbamate tail **2.116** (**Table 22**), which both had low nanomolar potency and encouraging physicochemical profiles. To generate novel structures away from the PF-8380 motif, a further sub-series was developed containing amide, and sulfonamide linked compounds, with the most potent ATX inhibitors consisting of benzo[*d*]oxazol-2(3*H*)-one, benzimidazole, benzotriazole, 1-hydroxy-1,3-dihydrobenzoxaborole and sulfonamide ZBG (**Table 22**). Most of these compounds exhibited good physicochemical properties and were highly potent ATX inhibitors. However, this class of amide and sulfonamide compounds are notably shorter in length, potentially resulting in sub-optimal interactions in the active site and the hydrophobic pocket. As a result another further sub-series was designed with an extended (2-azaspiro[3.3]heptan-6-yl)methanamine core, similar to the length of PF-8380, again with a

3-point SAR change, resulting in novel and potent ATX inhibitors. The optimisation trajectory discussed above is shown in **Figure 57**.

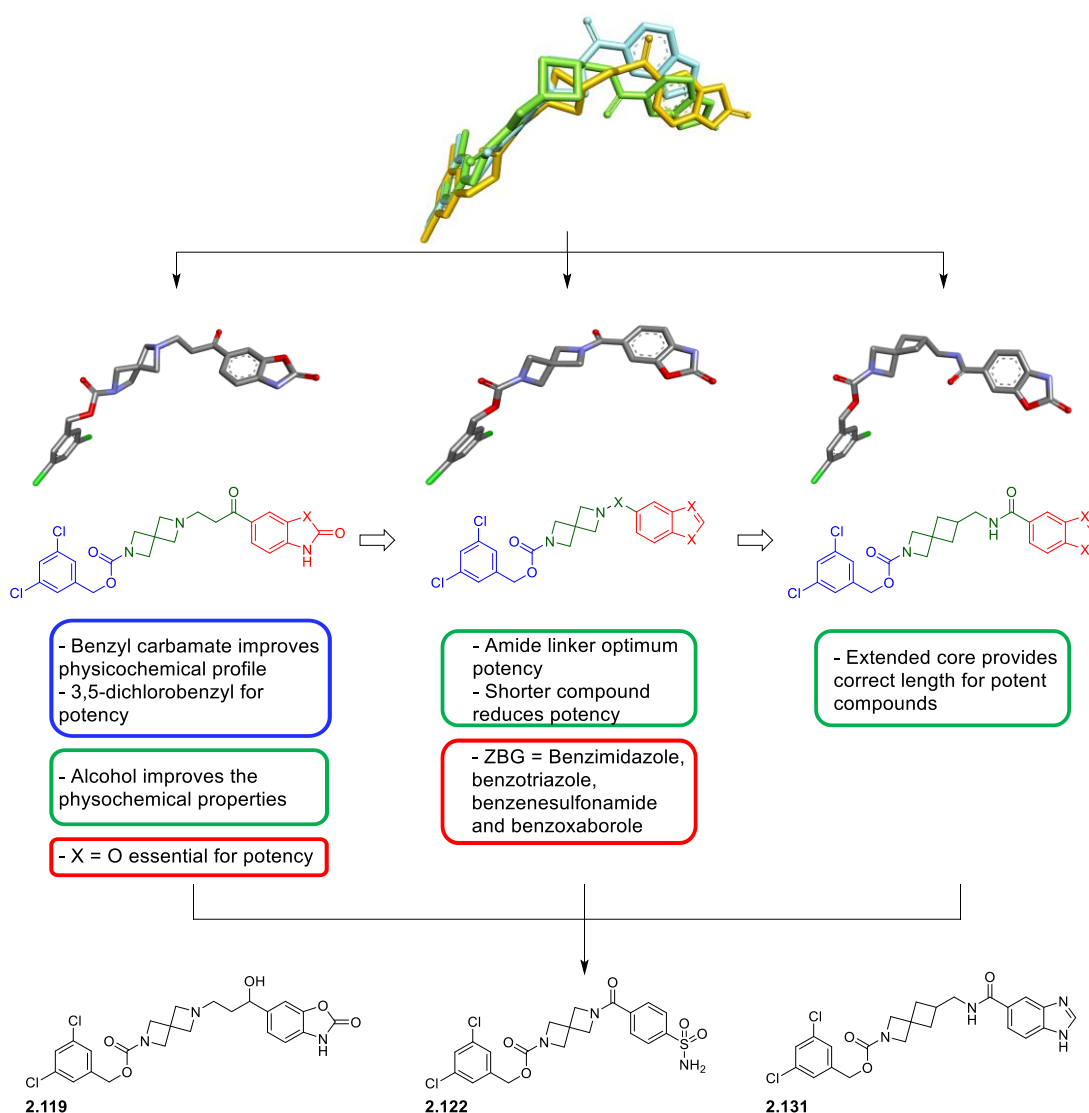


Figure 57 Development of compound with spirocyclic cores.

Due to encouraging levels of potency against ATX in the biochemical assay compounds **2.1**, **2.58**, **2.99**, **2.103**, **2.104**, **2.109**, **2.115**, and **2.119** were tested in a cell based BJEH assay, and were shown to reduce the phosphorylation of AKT, a downstream signalling pathway implicated in IPF, cancer and proliferative diseases (**Figure 46**, **Figure 48**).

Overall, during this study we have developed a more robust understanding of the PF-8380 SAR, and established the binding mode through co-crystallisation with ATX in conjunction

with docking studies. The physicochemical properties were optimised and led to a hit compound, which was then further optimised to furnish several lead-like compounds. These compounds had improved physicochemical properties and were shown to have a significant effect on downstream signalling pathways in a cell based assay. The identification of these lead-like compounds positions the project well for further DMPK analysis and potential *in vivo* study to determine the effects of compounds on LPA synthesis in mice (**Figure 58**).

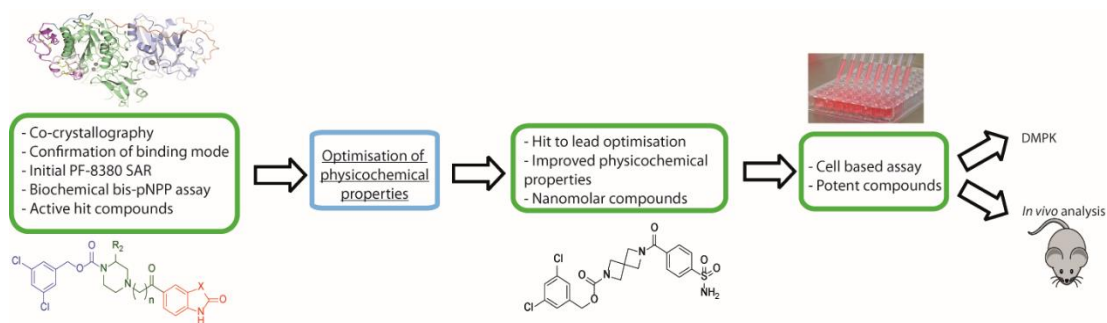


Figure 58 Project development and future work.

2.9. Future work

Identifying that compound **2.131** (Table 24) is a highly potent competitive inhibitor, further compounds including the alternative zinc binding group developed in this study (Table 23) could be synthesised to improve the physicochemical properties of this compound.

Throughout the SAR and hit to lead optimisation several lead-like compounds emerged with good physicochemical profiles. In particular, these included compounds **2.100**, **2.116**, **2.119**, **2.122**, **2.125**, and **2.131** (Figure 59).

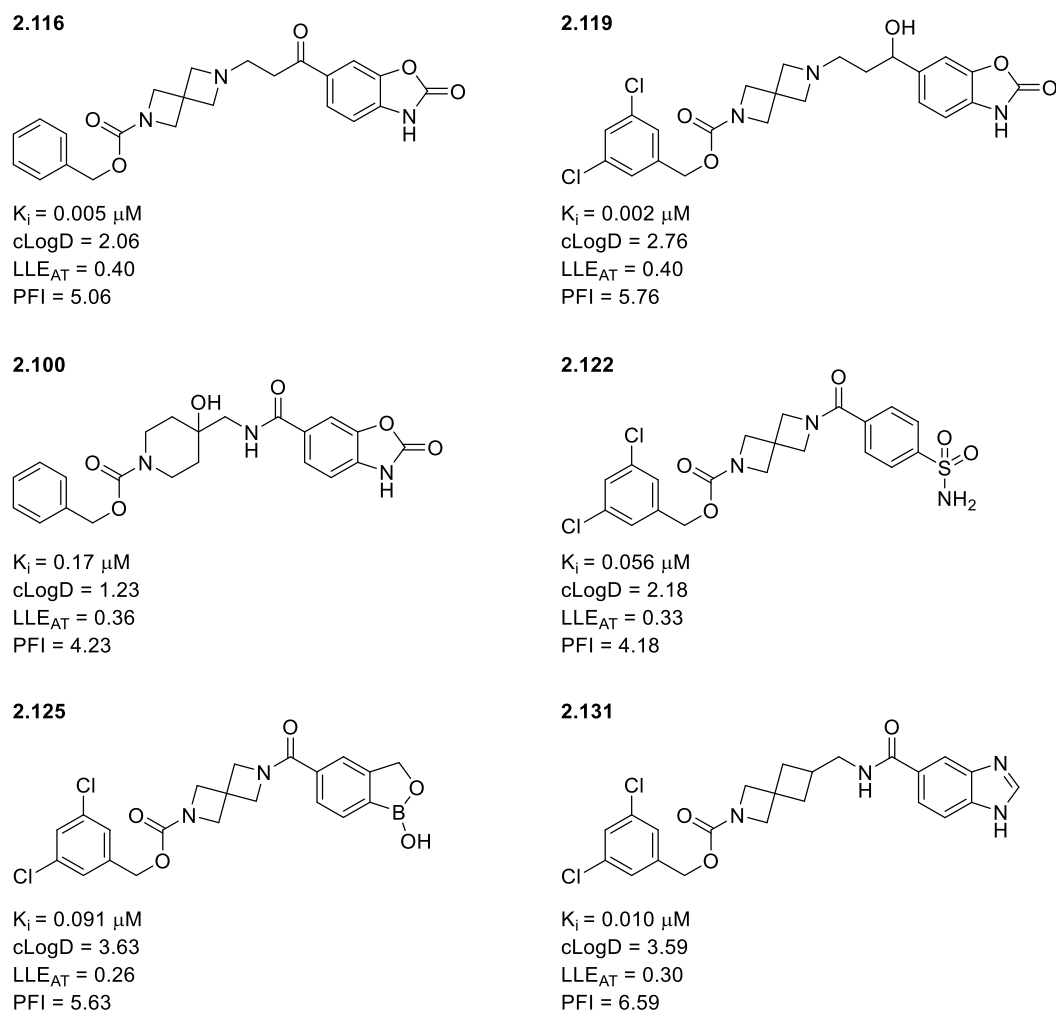


Figure 59 Lead-like compounds developed in this project.

Possibly the most interesting of these cores is the 4-(aminomethyl)piperidin-4-ol, which displays significant levels of potency without the 3,5-dichlorobenzyl carbamate tail, much like the 2,6-diazaspiro[3.3]heptane core. Using the amide linked ZBG identified in the current

study (**Table 23**) combined with either the benzyl carbamate, 3,5-dichlorobenzyl carbamate, or the *para*-chlorobenzyl carbamate tail, novel ATX inhibitors would be developed that potentially have a superior physicochemical profile. Compounds containing the secondary amide **2.134–2.136** and the tertiary amide **2.140–2.142** can be synthesised in an array format, with both analogues likely to result in potent ATX inhibitors (**Figure 60**).

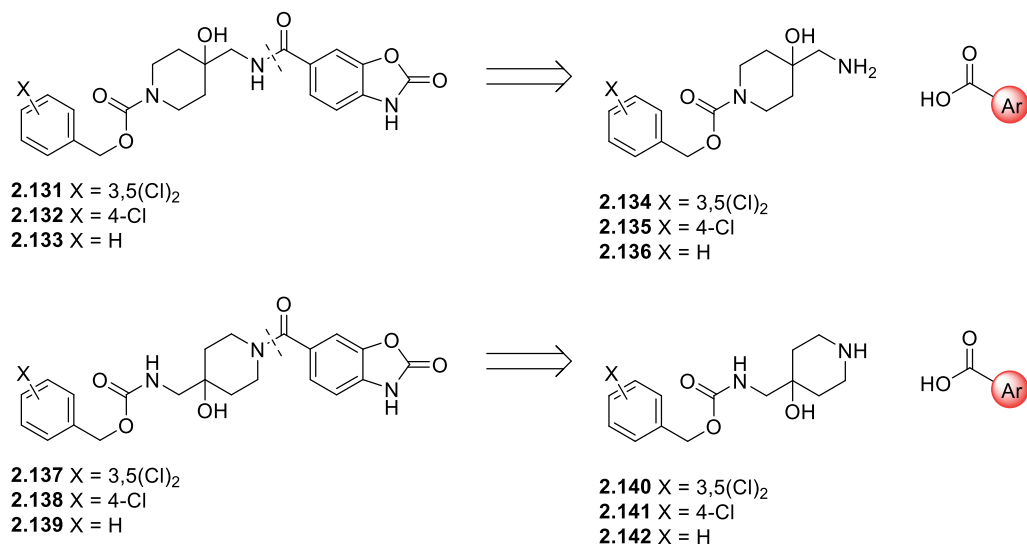


Figure 60 Series 2 ZBG screen containing the 4-(aminomethyl)piperidin-4-ol core.

Additionally, exploiting the knowledge that changes in this core region do not negate ATX inhibition, a 6-(aminomethyl)-2-azaspiro[3.3]heptan-6-ol core (**Figure 61**) would be interesting to investigate further to improve the physicochemical properties.

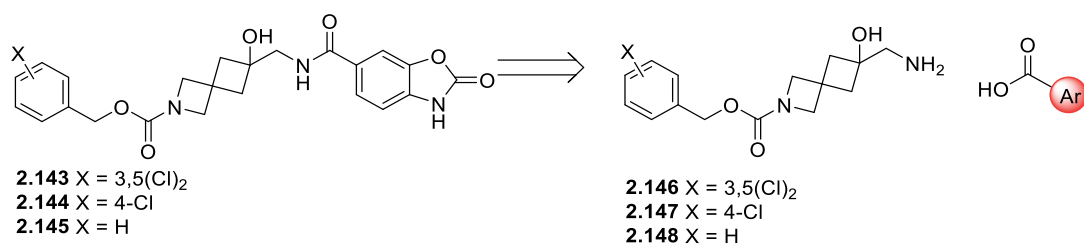


Figure 61 Development of a 6-(aminomethyl)-2-azaspiro[3.3]heptan-6-ol core.

Focussing on the ZBG, it is apparent that at present this class of competitive ATX inhibitors mainly target the distal zinc atom in a monodentate binding mode, with a few compounds

potentially hydrogen bonding with Thr209 based on *in silico* modelling. Building blocks can be synthesised which interact with the zinc atoms in a bidentate binding mode, or additionally interact with both zinc atoms in order to increase affinity at the active site (**Figure 62**). Additionally, a phenyloxazoline ligand can co-ordinate in a bi-dentate fashion.¹⁶⁰

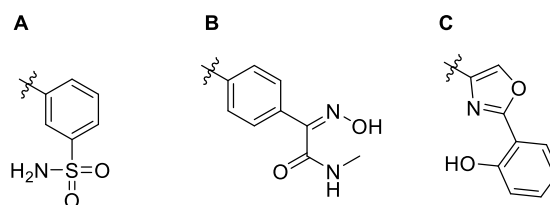


Figure 62 Alternative zinc binding groups.

The compounds have been developed based on improving the physicochemical parameters. Ideally DMPK profiling of the key lead-like compounds would give guidance on which key series is worth developing for *in vivo* analysis. Ultimately, these studies will demonstrate the utility of our emerging lead series in the treatment of diseases of societal need that implicate ATX.

2.10. Experimental

2.10.1. GOLD Docking Procedure

In silico molecular modelling was performed using Chem3D and GOLD software.^{130,161}

Preparation of the compound-Compound structures were prepared in Chem3D with an MM2 energy minimisation of each compound, which is saved as a mol. file for GOLD docking.^{130,161}

Preparation of the protein-A co-crystal structure of Autotaxin with compound **2.1** was obtained from NKI with the enzyme co-ordinates as a PDB file (unpublished work). The enzyme was prepared by adding all hydrogen atoms, and retaining all waters present. All ligands were deleted from the enzyme, and compound **2.1** saved as a reference ligand. The binding site was defined by selecting the reference ligand, selecting all atoms within 10 Å. The cavity was detected to restrict atom selection to the solvent-accessible surface and to force all H bond donors and acceptors to be treated as solvent accessible. The Gold_phosphodiesterase_VS template was selected and the mol. file of the compound to be docked prepared in Chem3D was selected, with **2.1** as a reference ligand. The scoring function was CHEMPLP with a slow genetic algorithm configuration.^{130,161}

Analysis of docked poses-The different poses were analysed within the prepared enzyme, using **2.1** as a comparison in DS Visualizer. The poses were assessed for the resemblance to the docked pose of **2.1**, avoiding clashes with the enzyme and unfavourable interactions, with the most likely compound pose used for SAR rationale.⁴⁸

2.10.2. Biology.

2.10.3. Bis-*p*NPP Assay Procedure

In a 96 well plate 20 ng/mL autotaxin was incubated with 3 mM bis-*p*NPP at 30 °C for 30 min in 50mM Tris-HCl buffer (pH 8.5) containing 10 mM CaCl₂ and 0.02% Triton X. Liberated bis-*p*nitrophenol was measured using a Wallac Victor2 1420 multilabel counter (Perkin Elmer, Beaconsfield, UK) in absorbance mode at 405 nm. The background was determined by incubating bis-*p*NPP in the absence of the enzyme. Activity of the compounds was determined by subtracting the average background from all results and expressing the compound activity as a percentage of the enzyme-substrate reaction in the absence of compound. PF-8380 or compound **2.44** in the concentration range of 0.1–300 nM, or 1 nM–3µM, respectively in half log units was included as a standard compound in every assay plate. The potential inhibitors

were initially tested against ATX at a concentration of 30 μM ; samples which showed less than 40% hydrolysis of the substrate were considered to be active. Dose response curves, in the concentration ranges of 10 nM–30 μM , 3 nM–10 μM , 1 nM–3 μM , 0.1 nM–300 nM in half log units, to calculate K_i values were performed on compounds reaching the designated activity threshold. The concentration ranges were chosen in accordance with the activity at 10 nM–30 μM in half log units. Data was expressed as a mean \pm SEM was plotted using GraphPad Prism 7.0 for Windows software.¹⁶²

2.10.4. Chemistry

2.10.5. General

All reagents and solvents were obtained from commercial suppliers and were used without further purification unless otherwise stated. Purification was carried out according to standard laboratory methods.

2.10.6. Experimental Details

Reactions were carried out using conventional glassware. Room temperature was generally 18 $^{\circ}\text{C}$. Reactions were carried out at elevated temperatures using a temperature-regulated hotplate/stirrer.

2.10.7. Purification of Products

Thin layer chromatography was carried out using Merck silica plates coated with fluorescent indicator UV254. These were analysed under 254 nm UV light or developed using potassium permanganate solution. Normal phase flash chromatography was carried out using ZEOprep 60 HYD 40-63 μm silica gel. Strong cation exchange was carried out using Silicycle SilicaPrepTM or ISOLUTE[®] Propylsulfonic acid functionalised silica (SCX-2) cartridges. Weak anion exchange was carried out using ISOLUTE[®] Aminopropyl functionalised silica (NH_2) cartridges.

2.10.8. Analysis of Products

Fourier Transformed Infra-Red (FTIR) spectra were obtained on a Shimadzu IRAffinity-1 machine. ^1H , ^{13}C , and ^{11}B NMR spectra were obtained on a Bruker AV 400 at 400 MHz, 101 MHz, and 128 MHz, or a Bruker AV500 at 500 MHz and 125 MHz, respectively. Chemical shifts are reported in ppm and coupling constants are reported in Hz with CDCl_3 referenced at 7.26 (^1H) and 77.1 ppm (^{13}C), $\text{DMSO-}d_6$ referenced at 2.50 (^1H) and 39.5 ppm (^{13}C), and $\text{MeOD-}d_4$ referenced at 3.31 (^1H) and 49.0 ppm (^{13}C). High-resolution mass spectra were

obtained through analysis at the EPSRC UK National Mass Spectrometry Facility at Swansea University and The University of Glasgow.

2.10.9. HPLC Procedures

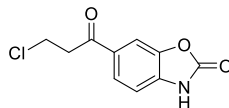
Reverse phase HPLC was carried out on a Gilson 151 Preparative HPLC, using a gradient of 5–95% MeCN in H₂O.

Mass-directed automatic purification (MDAP) was carried out using a ZQ MS using alternate-scan positive and negative electrospray and a summed UV wavelength of 210–350 nm and an Xselect CSH C18 column (150 mm x 30 mm, 5 μm packing diameter, 40 mL/min flow rate). The gradient used was either 15–100% MeCN in H₂O with 0.1% formic acid buffer, or 15–55% MeCN in H₂O with 0.1% formic acid buffer.

2.10.10. General Procedures

General Procedure A: Friedel Crafts Acylation Reaction for the Formation of Alkyl Chlorides

For example, for the preparation of **6-(3-chloropropanoyl)benzo[*d*]oxazol-2(3*H*)-one, 2.6**.



To a round-bottomed flask was added AlCl₃ (74.16 g, 0.75 mmol, 6.8 equiv), and DMF (24 mL) was added dropwise at 0 °C. After 15 min 3-chloropropanoyl chloride (10.60 mL, 0.11 mol, 1.2 equiv) was added followed by benzo[*d*]oxazol-2(3*H*)-one (10.0 g, 0.07 mol, 1.0 equiv) portion wise at 0° C and then the reaction was heated to 70 °C and stirred for 2 h. The reaction mixture was quenched slowly onto ice (300 g) and the precipitate filtered under vacuum. The crude material was filtered with H₂O (500 mL), dried under vacuum and recrystallized from EtOH (10 mL) to afford the desired product as a beige crystalline solid (5.95 g, 36%). Consistent with previously reported spectral analysis.¹⁴⁰

MPt: 162–161 °C

ν_{\max} (neat): 3233, 1765, 1660, 1611, 1445 cm⁻¹.

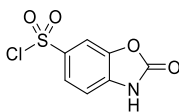
¹H NMR (DMSO-*d*₆, 400 MHz): 12.07 (s, 1H), 7.85–7.79 (m, 2H), 7.16 (d, *J* = 6.1, 2.2 Hz, 1H), 3.91 (t, *J* = 6.3 Hz, 2H), 3.51 (t, *J* = 6.3 Hz, 2H), NH observed.

¹³C NMR (DMSO-*d*₆, 101 MHz) δ 195.2, 154.3, 143.3, 135.1, 130.5, 125.1, 109.3, 108.8, 40.5, 1 × C not observed (under DMSO peak).

HRMS: exact mass calculated for [M+H]⁺ (C₁₀H₉ClN₁O₃) [M+H]⁺ requires 226.0265 *m/z*, found 226.0265 *m/z*.

General Procedure B: Reaction for the Formation of Sulfonyl Chlorides

For example, for the preparation of **2-oxo-2,3-dihydrobenzo[d]oxazole-6-sulfonyl chloride**, **2.11**.



To a round bottom flask equipped with a reflux condenser was added 2-benzoxazolinone (2.00 g, 14.80 mmol, 1.0 equiv) and sulfonyl chloride (4.93 mL, 60.80 mmol, 4.1 equiv) was added dropwise at 0 °C. The reaction mixture was heated to 50 °C and left to stir for 2 h. The reaction mixture was then quenched onto ice (400 g) and the resulting precipitate was filtered under vacuum. The crude material was filtered with H₂O, dried in a dessicator to afford the desired product as a pink solid (2.22 g, 64%). No previously reported data.¹⁴³

ν_{\max} (neat): 3223, 1727, 1478, 918, 812 cm⁻¹.

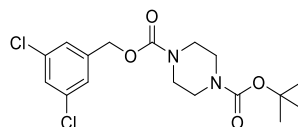
¹H NMR (DMSO-*d*₆, 400 MHz): δ 11.79 (s, 1H), 7.48 (d, *J* = 2.0 Hz, 1H), 7.20 (dd, *J* = 2.0, 8.3 Hz, 1H), 7.10 (d, *J* = 8.3 Hz, 1H).

¹³C NMR (DMSO-*d*₆, 101 MHz): δ 154.1, 143.8, 129.4, 125.7, 123.6, 110.7, 110.2.

HRMS: exact mass calculated for [M+H]⁺ (C₇H₅ClNO₄S) requires 233.9809 *m/z*, found 233.9806 *m/z*.

General Procedure C: Carbamate Formation

For example, for the preparation of, **1-(tert-butyl) 4-(3,5-dichlorobenzyl) piperazine-1,4-dicarboxylate, 2.18 a.**



To a round bottom flask was added (3,5-dichlorophenyl)methanol (1.04 g, 5.91 mmol, 1.1 equiv), CDI (0.96 g, 5.91 mmol, 1.1 equiv), DMF (5 mL) and stirred for 30 min at 0 °C. *Tert*-butyl piperazine-1-carboxylate (1.00 g, 5.37 mmol, 1.0 equiv) was added to the reaction mixture and stirred for 30 min at room temperature. H₂O (10 mL) was added and the precipitate was filtered with H₂O, and dried in a dessicator to afford the desired product as a white solid (1.87 g, 90 %). Consistent with previously reported spectral analysis.¹⁴⁰

ν_{\max} (neat): 2847, 1698, 1678, 1418 cm⁻¹.

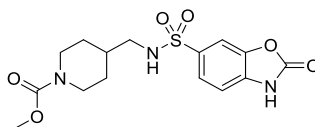
¹H NMR (CDCl₃, 400 MHz): δ 7.34 (t, J = 1.9 Hz, 1H), 7.25 (d, J = 1.9 Hz, 2H), 5.10 (s, 2H), 3.55-3.48 (m, 4H), 3.48-3.42 (m, 4H), 1.49 (s, 9H).

¹³C NMR (CDCl₃, 101 MHz): δ 154.8, 154.7, 140.0, 153.3, 128.4, 126.3, 80.4, 65.8, 43.9, 28.5. 1 × C not observed (coincident).

HRMS: exact mass calculated for [M+NH₄]⁺ (C₁₇H₂₆Cl₂N₃O₄) requires 406.1295 m/z , found 406.1293 m/z .

General Procedure D: Methyl Carbamate Formation

For example, for the preparation of, **methyl 4-(((2-oxo-2,3-dihydrobenzo[*d*]oxazole)-6-sulfonamido)methyl)piperidine-1-carboxylate, 2.97**.



To a round bottom flask was added 2-oxo-*N*-(piperidin-4-ylmethyl)-2,3-dihydrobenzo[*d*]oxazole-6-sulfonamide 2,2,2-trifluoroacetate **2.93** (250 mg, 0.59 mmol, 1.0 equiv) and NEt₃ (174 μL, 1.24 mmol, 2.1 equiv), followed by methyl chloroformate (50 μL, 0.65 mmol, 1.1 equiv), in THF (2 mL). The reaction was stirred at room temperature for 16 h, concentrated *in vacuo*, and purified by column chromatography on silica (80% petroleum ether in EtOAc), then triturated in MeCN to afford the desired product as a white solid (62 mg, 22%).

ν_{max} (neat): 3260, 2955, 2864, 1674, 1601, 1530, 1418 cm⁻¹.

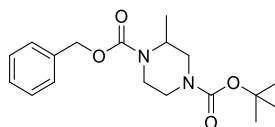
¹H NMR (DMSO-*d*₆, 400 MHz): 7.73–7.64 (m, 2H), 7.22 (d, *J* = 8.10 Hz, 1H), 4.07 (d, *J* = 8.1 Hz, 2H), 3.66 (s, 3H), 2.79–2.69 (m, 4H), 1.73–1.57 (m, 3H), 1.21–1.04 (m, 2H). 2 × H not observed (exchangeable).

¹³C NMR (DMSO-*d*₆, 101 MHz): δ 155.0, 154.3, 143.0, 134.1, 133.9, 123.0, 109.7, 107.7, 52.1, 47.7, 43.2, 35.5, 29.1.

HRMS exact mass calculated for [M+H]⁺ (C₁₅H₂₀N₃O₆S) requires 370.1067 *m/z*, found 370.1071 *m/z*.

General Procedure E: N-Benzyl Carbamate Formation

For example, for the preparation of, **1-benzyl 4-(*tert*-butyl) 2-methylpiperazine-1,4-dicarboxylate, 2.34**.



To a round bottom flask was added *tert*-butyl 3-methylpiperazine-1-carboxylate (100.05 mg, 0.50 mmol, 1.0 equiv), *N*-(benzyloxycarbonyloxy)succinimide (136.90 mg, 0.55 mmol, 1.1 equiv), NaHCO₃ (66.4 mg, 0.75 mmol, 1.5 equiv), THF (1 mL), H₂O (1 mL) and stirred for 16 h at room temperature. The reaction mixture was diluted with H₂O (20 mL) and the organics were extracted with EtOAc (2 × 20 mL), dried with a hydrophobic frit and concentrated *in vacuo* to afford the desired product as a clear oil (154 mg, 89%). Consistent with previously reported spectral analysis.¹⁶³

ν_{\max} (neat): 2972, 2928, 1692, 1416 cm⁻¹.

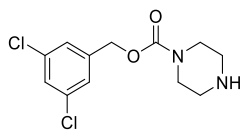
¹H NMR (CDCl₃, 400 MHz): δ 7.36–7.27 (m, 5H), 5.14 (s, 2H), 4.31–4.25 (m, 1H), 4.04–3.93 (m, 1H), 3.91–3.85 (m, 1H), 3.85–3.78 (m, 1H), 3.15–3.07 (m, 1H), 3.04–2.97 (m, 1H), 2.87–2.78 (m, 1H), 1.45 (s, 9H), 1.16 (d, $J = 6.7$ Hz, 3H).

¹³C NMR (CDCl₃, 101 MHz, 323.15 K): δ 155.1, 155.0, 136.7, 128.4, 128.0, 127.8, 79.9, 67.2, 47.3, 38.7, 28.3, 15.2. 2 × C not observed (coincident).

HRMS: exact mass calculated for [M+NH₄]⁺ (C₁₈H₃₀N₃O₄) requires 352.2231 m/z , found 352.2230 m/z .

General Procedure F: N-Boc Deprotection

For example, for the preparation of, **3,5-dichlorobenzyl piperazine-1-carboxylate, 2.22 a**.



To a round bottom flask was added 1-(*tert*-butyl) 4-(3,5-dichlorobenzyl) piperazine-1,4-dicarboxylate **2.18 a** (1.87g, 4.80 mmol) and a mixture of trifluoroacetic acid (1 mL) and CH₂Cl₂ (1 mL). The reaction was then stirred at room temperature for 2 h. The reaction mixture was concentrated *in vacuo* and purified with strong cation exchange (propylsulfonic acid functionalised silica, 2 N NH₃ in MeOH) to afford the desired product as a white solid (0.53 g, 60%). Consistent with previously reported spectral analysis.¹⁴⁰

ν_{\max} (neat): 1670, 1425 cm⁻¹.

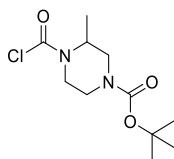
¹H NMR (CDCl₃, 400 MHz): δ 7.26 (t, $J = 1.7$ Hz, 1H), 7.20 (d, $J = 1.8$ Hz, 2H), 5.04 (s, 2H), 3.51–3.45 (m, 4H), 2.88–2.81 (m, 4H), 2.02 (s, 1H).

¹³C NMR (CDCl₃, 101 MHz): δ 154.7, 140.1, 135.1, 128.2, 126.1, 65.6, 45.5, 44.4.

HRMS: exact mass calculated for [M+H]⁺ (C₁₂H₁₅Cl₂N₂O₂) requires 290.0539 m/z , found 290.0534 m/z .

General Procedure G: *N*-carbamoyl Chloride Synthesis

For example, for the preparation of, *tert*-butyl 4-(chlorocarbonyl)-3-methylpiperazine-1-carboxylate, **2.28**.

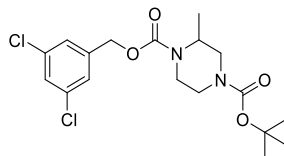


To a two neck flask equipped with a condenser was added *tert*-butyl 3-methylpiperazine-1-carboxylate (100 mg, 0.50 mmol, 1.0 equiv), dry CH₂Cl₂ (1 mL), pyridine (60 μL, 0.75 mmol, 1.5 equiv) under N₂ at 0 °C. A solution of triphosgene (84 mg, 0.28 mmol, 0.6 equiv) in dry CH₂Cl₂ (1 mL) was added and the yellow mixture was then stirred at room temperature for 1 h. The reaction mixture was quenched using 1N HCl (20 mL), stirred for 1 h at room temperature. The organics were extracted with CH₂Cl₂ (1 × 20 mL), combined, dried with a hydrophobic frit, and concentrated *in vacuo* to afford the desired product as a yellow solid which was telescoped into the next step for the synthesis of **2.30**. Consistent with reported appearance, no reported data.¹⁴⁵

¹H NMR (CDCl₃, 400 MHz): δ 4.48 (s, 1H), 4.07 (d, *J* = 13.6 Hz, 2H), 3.90 (s, 1H), 3.29 (s, 1H), 3.09 (d, *J* = 12.4 Hz, 1H), 2.92 (s, 1H), 1.47 (s, 9H), 3.09 (d, *J* = 12.4 Hz, 3H)

General Procedure H: *N*-benzyl Carbamate Synthesis from the Carbamoyl Chloride Intermediate

For example, for the preparation of, **4-(*tert*-butyl) 1-(3,5-dichlorobenzyl) 2-methylpiperazine-1,4-dicarboxylate, 2.30**.



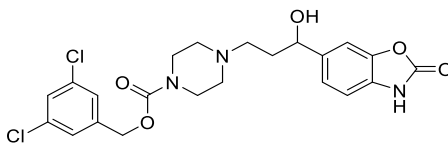
To a round bottom flask was added *tert*-butyl 4-(chlorocarbonyl)-3-methylpiperazine-1-carboxylate **2.28** (103 mg, 0.39 mmol, 1.0 equiv), NaH (14 mg, 0.59 mmol, 1.5 equiv), (3,5-dichlorophenyl)methanol (69 mg, 0.39 mmol, 1.0 equiv), and DMF (1 mL) at 0 °C, and then stirred at room temperature for 16 h. The reaction mixture was quenched using H₂O (20 mL) and the organics were extracted with EtOAc (2 × 20 mL), dried with a hydrophobic frit, and concentrated *in vacuo* to a residue that was purified by column chromatography on silica (70–80% petroleum ether in EtOAc) to afford the desired product as a yellow oil which was telescoped to the next step for the synthesis of **2.32** (100 mg, 50% over 2 steps).

¹H NMR (DMSO-*d*₆, 400 MHz): δ 7.45–7.47 (m, 1H), 7.40–7.37 (m, 2H), 5.11 (s, 2H), 4.27–4.17 (m, 1H), 3.90–3.69 (m, 3H), 3.15–3.04 (m, 1H), 3.03–2.94 (m, 1H), 2.93–2.84 (m, 1H), 1.42 (s, 9H), 1.10 (d, *J* = 6.7 Hz, 3H).

¹³C NMR (DMSO-*d*₆, 101 MHz, 353.15 K): δ 153.9, 153.7, 140.8, 126.9, 125.6, 124.5, 78.6, 64.4, 61.3, 46.8 (46.7), 42.6, 38.0, 27.6, 14.7. Rotameric mixture observed (minor rotamer in brackets.)

General Procedure I: NaBH₄ Reduction.

For example, for the preparation of **3,5-dichlorobenzyl 4-(3-oxo-3-(2-oxo-2,3-dihydrobenzo[d]oxazol-6-yl)propyl)piperazine-1-carboxylate, 2.1.**



To a round bottom flask was added 3,5-dichlorobenzyl 4-(3-oxo-3-(2-oxo-2,3-dihydrobenzo[d]oxazol-6-yl)propyl)piperazine-1-carboxylate **PF-8380** (60 mg, 0.24 mmol, 1.0 equiv), NaBH₄ (18 mg, 0.92 mmol, 3.8 equiv) and EtOH (2 mL) at 0 °C. The reaction was then stirred at room temperature for 16 h. The crude mixture was concentrated *in vacuo* to a residue that was purified using preparative high performance liquid chromatography on silica (5–20–95% MeCN in H₂O) to afford the desired product as a white solid (11 mg, 18%). No previous reported spectral analysis.⁹⁵

ν_{max} (neat): 3421, 1750, 1694, 1667, 1198, 1134, 799, 722 cm⁻¹

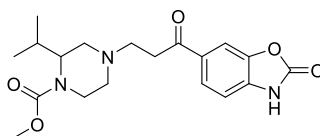
¹H NMR (CDCl₃, 400 MHz): δ 7.33 (t, *J* = 1.9 Hz, 1H), 7.30–7.27 (m, 1H), 7.25 (d, *J* = 1.9, 2H), 7.16 (dd, *J* = 1.2, 8.1 Hz, 1H), 7.01 (d, *J* = 8.0 Hz, 1H), 5.10 (s, 2H), 4.98 (dd, *J* = 4.2, 7.4 Hz, 1H), 3.62 (t, *J* = 4.8, 4H), 2.82–2.72 (m, 1H), 2.72–2.58 (m, 3H), 2.58–2.46 (m, 2H), 1.94–1.85 (m, 2H). 2 × H not observed (exchangeable).

¹³C NMR (DMSO-*d*₆, 101 MHz): δ 154.9, 154.1, 143.6, 139.6, 139.5, 134.7, 127.74, 127.71, 125.6, 120.7, 108.9, 107.2, 74.7, 65.2, 56.6, 52.4, 43.3, 33.5

HRMS: exact mass calculated for [M+H]⁺ (C₂₂H₂₄N₃O₅) requires 480.1091 *m/z*, found 480.1088 *m/z*.

General Procedure J: Alkylation Reaction.

For example, for the preparation of **methyl 2-isopropyl-4-(3-oxo-3-(2-oxo-2,3-dihydrobenzo[d]oxazol-6-yl)propyl)piperazine-1-carboxylate, 2.113**.



To a round bottom flask equipped with a reflux condenser was added 6-(3-chloropropanoyl)benzo[d]oxazol-2(3H)-one **2.6** (171 mg, 0.76 mmol, 1.0 equiv), methyl 2-isopropylpiperazine-1-carboxylate **2.41** (155 mg, 0.83 mmol, 1.1 equiv), NEt_3 (127 μL , 0.91 mmol, 1.2 equiv), MeCN (5 mL), and the reaction was stirred at 80 °C for 5 h. The reaction mixture was allowed to cool to room temperature, diluted with Et_2O (10 mL) and the precipitate collected and filtered under vacuum with H_2O (10 mL). The crude material was purified using preparative high performance liquid chromatography (5–95% MeCN in H_2O) to afford the desired product as a white solid (35 mg, 12%).

ν_{max} (neat): 3030, 2959, 1771, 1691, 1670, 1447, 1178, 1121 cm^{-1}

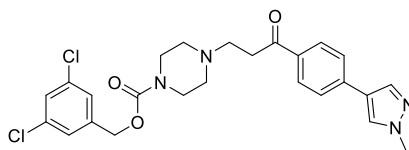
^1H NMR (CDCl_3 , 400 MHz): δ 8.03–7.97 (dd, $J = 1.5, 8.2$ Hz, 1H), 7.92 (d, $J = 1.4$, 1H), 7.25 (d, $J = 8.2$ Hz, 1H), 4.42–4.18 (m, 1H), 4.16–3.91 (m, 1H), 3.91–3.82 (m, 1H), 3.79 (s, 3H), 3.74–3.58 (m, 5H), 3.30–3.22 (m, 2H), 3.22–3.11 (m, 1H), 2.46–2.30 (m, 1H), 1.35 (t, $J = 7.2$ Hz, 1H), (d, $J = 5.6$ Hz, 3H), 0.90 (d, $J = 6.0$ Hz, 3H).

^{13}C NMR ($\text{DMSO}-d_6$, 101 MHz): δ 197.6, 155.2, 154.4, 143.3, 134.7, 131.1, 125.0, 109.3, 108.9, 53.4, 53.1, 52.6, 52.2, 45.6, 35.4, 25.6, 19.9, 18.7, 8.5

HRMS: exact mass calculated for $[\text{M}+\text{H}]^+$ ($\text{C}_{19}\text{H}_{26}\text{N}_3\text{O}_5$) requires 376.1867 m/z , found 376.1872 m/z .

General Procedure K: Suzuki-Miyaura Cross Coupling.

For example, for the preparation of **3,5-dichlorobenzyl 4-(3-oxo-3-(2-oxo-2,3-dihydrobenzo[d]oxazol-6-yl)propyl)piperazine-1-carboxylate, 2.82.**



To an oven dried microwave vial was added 3,5-dichlorobenzyl 4-(3-(4-bromophenyl)-3-oxopropyl)piperazine-1-carboxylate **2.72** (49 mg, 0.10 mmol, 1.0 equiv), 1-methyl-4-(4,4,5,5-tetramethyl-1,3,2-dioxaborolan-2-yl)-1*H*-pyrazole (36 mg, 0.17 mmol, 1.7 equiv), Pd(dppf)Cl₂·CH₂Cl₂ (4 mg, 4 mol%), K₃PO₄ (65 mg, 0.30 mmol, 3.0 equiv). The vial was capped and purged with N₂ before addition of THF (0.4 mL) and H₂O (9 μL). The reaction was then stirred at 90 °C for 16 h. The reaction was cooled to room temperature and the crude mixture was filtered through celite with EtOAc and concentrated *in vacuo* to a residue that was purified using column chromatography on silica (2–10% MeOH in EtOAc) to afford the desired product as a yellow solid (50 mg, 79%).

ν_{max} (neat): 2926, 1679, 1705 cm⁻¹.

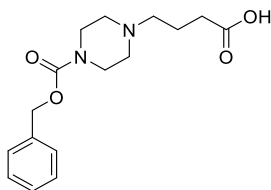
¹H NMR (CDCl₃, 400 MHz): δ 7.94 (d, *J* = 8.6 Hz, 2H), 7.82 (s, 1H), 7.70 (s, 1H), 7.54 (d, *J* = 8.6 Hz, 2H), 7.28 (t, *J* = 1.9 Hz, 1H), 7.21 (d, *J* = 1.9 Hz, 2H), 5.05 (s, 2H), 3.96 (s, 3H), 3.56–3.51 (m, 4H), 3.17 (t, *J* = 7.2 Hz, 2H), 2.88 (t, *J* = 7.2 Hz, 2H), 2.54–2.46 (m, 4H).

¹³C NMR (CDCl₃, 101 MHz): δ 197.5, 154.1, 139.7, 137.1, 136.6, 134.6, 134.1, 128.4, 127.6, 127.1, 125.6, 124.7, 121.6, 65.0, 52.7, 52.3, 43.4, 38.7, 35.5.

HRMS: exact mass calculated for [M+H]⁺ (C₂₅H₂₇Cl₂N₄O₃) requires 501.1455 *m/z*, found 501.1445 *m/z*.

General Procedure L: *Tert*-butyl Ester Hydrolysis

For example, for the preparation of **4-(4-((benzyloxy)carbonyl)piperazin-1-yl)butanoic acid, 2.65**.



To a round bottom flask was added benzyl 4-(4-(*tert*-butoxy)-4-oxobutyl)piperazine-1-carboxylate **2.132** (51 mg, 0.14 mmol), trifluoroacetic acid (1 mL) and CH₂Cl₂ (1 mL). The reaction was then stirred at room temperature for 4 h, and concentrated *in vacuo* to a residue that was purified by column chromatography on silica (2–10% MeOH in EtOAc) to afford the desired product as a white solid (43 mg, 19% over 2 steps).

ν_{\max} (neat): 2951, 1698, 1425, 1248 cm⁻¹

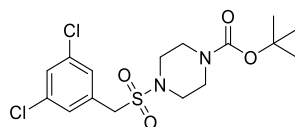
¹H NMR (CDCl₃, 400 MHz): δ 7.41–7.30 (m, 5H), 5.19 (s, 2H), 4.05–3.83 (m, 4H), 3.24–3.06 (m, 6H), 2.52 (t, *J* = 6.4 Hz, 2H), 2.18–2.06 (m, 2H). 1 × H not observed (exchangeable).

¹³C NMR (CDCl₃, 101 MHz): δ 154.3, 135.5, 128.1, 127.9, 127.6, 67.3, 56.9, 51.3, 41.0, 19.4, 2 × C not observed (coincident).

HRMS: exact mass calculated for [M+H]⁺ (C₁₆H₂₃N₂O₄) requires 307.1652 *m/z*, found 307.1649 *m/z*.

General Procedure M: Sulfonylation

For example, for the preparation of *tert*-butyl 4-((3,5-dichlorobenzyl)sulfonyl)piperazine-1-carboxylate, **2.26**.



To a round bottom flask was added (3,5-dichlorophenyl)methanesulfonyl chloride (110 mg, 0.42 mmol, 1.0 equiv), *tert*-butyl piperazine-1-carboxylate (78 mg, 0.42 mmol, 1.0 equiv), NEt₃ (64 μ L, 0.46 mmol, 1.1 equiv) and CH₂Cl₂ (2 mL). The reaction was diluted with H₂O (20 mL) and the organics were extracted with CH₂Cl₂ (2 \times 50 mL), dried with a hydrophobic frit and concentrated *in vacuo* to yield a white solid (152 mg, 88%).

ν_{\max} (neat): 2075, 2605, 1689, 1576, 1429, 1136 cm⁻¹.

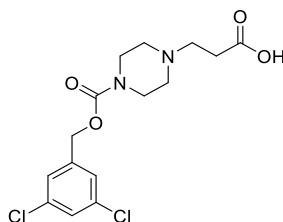
¹H NMR (CDCl₃, 500 MHz): δ 7.40–7.36 (m, 1H), 7.31–7.26 (m, 2H), 4.11 (s, 2H), 3.49–3.37 (m, 4H), 3.22–3.07 (m, 4H), 1.46 (s, 9H).

¹³C NMR (CDCl₃, 126 MHz): δ 153.8, 134.8, 131.3, 128.6, 128.5, 80.1, 55.1, 45.4, 43.1, 27.8.

HRMS: exact mass calculated for [M+NH₄]⁺ (C₁₆H₂₆Cl₂N₃O₄S) requires 426.1016 *m/z*, found 426.1014 *m/z*.

General Procedure N: Ester Hydrolysis with LiOH

For example, for the preparation of **3-(4-(((3,5-dichlorobenzyl)oxy)carbonyl)piperazin-1-yl)propanoic acid, 2.64**.



To a round bottom flask was added 3,5-dichlorobenzyl 4-(3-ethoxy-3-oxopropyl)piperazine-1-carboxylate **2.130** (852 mg, 1.5 mmol, 1.0 equiv), LiOH (107 mg, 4.48 mmol, 3.0 equiv) in THF (10 mL), and stirred at 40 °C for 16 h. The reaction was cooled, and quenched with 1M HCl (100 mL), and the organics were extracted with EtOAc (40 mL) and washed with brine (40 mL). The organics were dried with a hydrophobic frit and concentrated *in vacuo* to yield a white solid (116 mg, 14% over 2 steps)

ν_{\max} (neat): 2924, 1699, 1415 cm^{-1} .

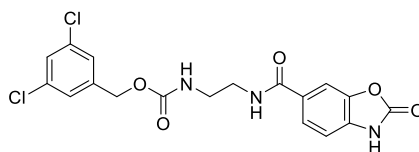
^1H NMR (MeOD- d_4 , 500 MHz) δ 7.43–7.40 (m, 1H), 7.40–7.37 (m, 2H), 5.14 (s, 2H), 3.95–3.72 (m, 4H), 3.47 (t, $J = 7.1$ Hz, 2H), 3.41–3.33 (m, 4H), 2.90 (t, $J = 7.2$ Hz, 2H). 1 \times H not observed (exchangeable).

^{13}C NMR (MeOD- d_4 , 101 MHz): δ 171.2, 153.9, 139.8, 134.3, 127.3, 125.8, 65.4, 51.9, 50.9, 40.0, 27.5.

HRMS: exact mass calculated for $[\text{M}-\text{H}]^-$ ($\text{C}_{15}\text{H}_{17}\text{Cl}_2\text{N}_2\text{O}_4$) requires 359.0571 m/z , found 359.0566 m/z .

General Procedure O: Amidation Reaction with HATU

For example, for the preparation of **3,5-dichlorobenzyl (2-(2-oxo-2,3-dihydrobenzo[*d*]oxazole-6-carboxamido)ethyl)carbamate, 2.106**.



To a round bottom flask was added 2-oxo-2,3-dihydrobenzo[*d*]oxazole-6-carboxylic acid **2.13** (34 mg, 0.21 mmol, 1.1 equiv), DIPEA (36 μ L, 0.57 mmol, 2.7 equiv), and HATU (79 mg, 0.21 mmol, 1.1 equiv) in DMF (2 mL) and stirred at room temperature for 15 min. 3,5-dichlorobenzyl (2-aminoethyl)carbamate **2.25 a** (50 mg, 0.19 mmol, 1.0 equiv) was added and the reaction stirred at room temperature for 16 h. The reaction was diluted with H₂O and filtered under vacuum to yield the desired product as a white solid (23 mg, 29%).

ν_{\max} (neat): 3301, 1780, 1747, 1699, 1645 cm^{-1} .

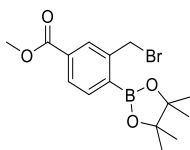
¹H NMR (DMSO-*d*₆, 500 MHz): δ 8.45 (s, 1H), 7.74–7.68 (m, 2H), 7.53 (s, 1H), 7.47 (t, *J* = 5.4 Hz, 1H), 7.42–7.37 (m, 2H), 7.14 (d, *J* = 8.1 Hz, 1H), 5.03 (s, 2H), 3.40–3.26 (m, 2H, multiplet under H₂O peak), 3.24–3.14 (m, 2H).

¹³C NMR (DMSO-*d*₆, 101 MHz): δ 165.5, 155.9, 154.5, 143.0, 141.6, 134.0, 132.9, 128.4, 127.2, 126.0, 123.7, 109.1, 108.3, 63.7. 2 X aliphatic C not observed (coincident).

HRMS: exact mass calculated for [M+H]⁺ (C₁₈H₁₆Cl₂N₃O₅) requires 424.0462 *m/z*, found 424.0462 *m/z*.

General Procedure P: Alkyl Bromination.

For example, for the preparation of methyl 3-(bromomethyl)-4-(4,4,5,5-tetramethyl-1,3,2-dioxaborolan-2-yl)benzoate, **2.16**.



To a microwave vial was added methyl 3-methyl-4-(4,4,5,5-tetramethyl-1,3,2-dioxaborolan-2-yl)benzoate (200 mg, 0.72 mmol, 1.0 equiv), AIBN (24 mg, 0.14 mmol, 0.2 equiv) and NBS (135 mg, 0.76 mmol, 1.1 equiv) and the vial sealed and purged under N₂. To the vial was added CCl₄ and the reaction was heated at 80 °C for 16 h. Further NBS (26 mg, 0.14 mmol, 0.2 equiv) was added and the reaction heated at 80 °C for 5 h with a UV lamp. The reaction was cooled, filtered under vacuum and concentrated *in vacuo* and purified by column chromatography on silica (0–10% EtOAc in petroleum ether) to afford the desired product as a white solid which was telescoped in to the next step for the synthesis of **2.17**. No previously reported spectral analysis.¹⁶⁴

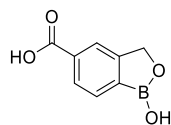
¹H NMR (DMSO-*d*₆, 400 MHz): δ 8.03 (s, 1H), 7.93–7.81 (m, 3H), 4.91 (s, 2H), 3.91 (s, 3H); 1.37 (s, 12H).

¹³C NMR (DMSO-*d*₆, 101 MHz): δ 166.9, 145.0, 136.9, 132.9, 131.1, 128.7, 84.7, 52.6, 33.4, 25.2. Carbon bearing boron not observed.

¹¹B NMR (CDCl₃, 128 MHz): δ 30.56.

General Procedure Q: Hydrolysis and Borocycle Cyclisation.

For example, for the preparation of **1-hydroxy-1,3-dihydrobenzo[*c*][1,2]oxaborole-5-carboxylic acid, 2.17.**



To a separating funnel was added methyl 3-(bromomethyl)-4-(4,4,5,5-tetramethyl-1,3,2-dioxaborolan-2-yl)benzoate **2.16** (110 mg, 0.72 mmol, 1.0 equiv) in diethyl ether (30 mL). The organics were washed with 15% w/v KOH (3 x 30 mL) and the aqueous layer stirred for 1 h at room temperature. 6N HCl was added dropwise whilst stirring until a white precipitate appeared (~10 mL), which was filtered under vacuum to afford the desired product as a white solid (19 mg, 15 % over 2 steps). Commercially available, CAS: 1801711-87-4.

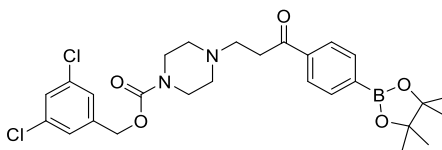
^1H NMR (DMSO- d_6 , 400 MHz): δ 13.04 (s, 1H), 9.37 (s, 1H), 7.97 (s, 1H), 7.92 (d, $J = 7.6$ Hz, 1H), 7.83 (d, $J = 7.6$ Hz, 1H), 5.05 (s, 2H).

^{13}C NMR (DMSO- d_6 , 101 MHz): δ 167.9, 154.6, 133.2, 131.0, 128.2, 122.7, 70.4. C-B C not observed.

^{11}B NMR (DMSO- d_6 , 128 MHz): δ 30.70.

General Procedure R: Miyaura Borylation

For example, for the preparation of **3,5-dichlorobenzyl 4-(3-oxo-3-(4-(4,4,5,5-tetramethyl-1,3,2-dioxaborolan-2-yl)phenyl)propyl)piperazine-1-carboxylate, 2.80**.



To a flask was added 3,5-dichlorobenzyl 4-(3-(4-bromophenyl)-3-oxopropyl)piperazine-1-carboxylate **2.72** (100 mg, 0.20 mmol, 1.0 equiv), B_2Pin_2 (56 mg, 0.22 mmol, 1.1 equiv), $Pd(dppf)Cl_2 \cdot CH_2Cl_2$ (7 mg, 4 mol%), KOAc (59 mg, 0.60 mmol, 3.0 equiv), 1,4-dioxane (0.8 mL). The vial was capped and purged with N_2 and heated at 90 °C for 24 h. The crude mixture was filtered through celite with EtOAc, concentrated under vacuum to a residue that was purified using column chromatography on silica (80% EtOAc in petroleum ether to 2–10% MeOH in EtOAc) to afford the desired product as a yellow solid (68 mg, 62%).

ν_{max} (neat): 2921, 1659, 1679, 1669 cm^{-1} .

1H NMR ($CDCl_3$, 400 MHz): δ 7.93–7.84 (m, 4H), 7.30–7.28 (m, 1H), 7.23–7.19 (m, 2H), 5.06 (s, 2H), 3.52–3.47 (m, 4H), 3.18 (t, $J = 7.2$ Hz, 2H), 2.85 (t, $J = 7.2$ Hz, 2H), 2.52–2.43 (m, 4H), 1.36 (s, 12H).

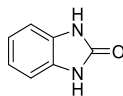
^{13}C NMR ($CDCl_3$, 101 MHz): δ 199.3, 154.8, 140.3, 138.9, 135.2, 135.1, 128.3, 127.1, 126.2, 84.4, 65.6, 53.2, 53.0, 44.0, 36.5, 25.0. C-B C not observed.

^{11}B NMR ($CDCl_3$, 128 MHz): δ 30.92.

HRMS: exact mass calculated for $[M-H]^+$ ($C_{27}H_{32}BCl_2N_2O_5$) requires 545.1776 m/z , found 545.1770 m/z .

2.10.11. Experimental Procedures

1,3-dihydro-2H-benzo[d]imidazol-2-one, 2.2.



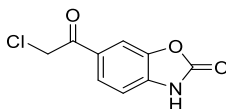
Prepared according to General Procedure C, using benzene-1,2-diamine (1.00 g, 9.20 mmol, 1.0 equiv), DMF (15 mL), and CDI (1.50 g, 9.20 mmol, 1.0 equiv) to afford the desired product as a purple solid (752 mg, 61%). Consistent with previously reported spectral analysis.¹⁶⁵ Commercially available, CAS: 615-16-7.

ν_{\max} (neat): 3014, 2899, 2808, 2730, 1683, 1715, 1198 cm^{-1} .

^1H NMR (DMSO- d_6 , 400 MHz): δ 10.55 (s, 2H), 6.91 (s, 4H).

^{13}C NMR (DMSO- d_6 , 101 MHz): δ 155.2, 129.6, 120.3, 108.4.

6-(2-chloroacetyl)benzo[d]oxazol-2(3H)-one, 2.5.



Prepared according to General Procedure A, using AlCl_3 (18.54 g, 139.04 mmol, 7.5 equiv), DMF (6 mL), 2-chloroacetylchloride (1.75 mL, 22.0 mmol, 1.2 equiv) and 2-benzoxazolinone (2.5 g, 18.50 mmol, 1 equiv) to afford the desired product as a beige solid (3.02 g, 78%). Consistent with previously reported spectral analysis.¹⁶⁶

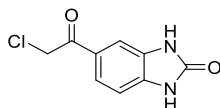
ν_{\max} (neat): 3192, 1935, 1770, 1679, 1613 cm^{-1}

^1H NMR (DMSO- d_6 , 400 MHz): δ 12.12 (s, 1H), 7.88 (d, $J = 1.2$ Hz, 1H), 7.86 (dd, $J = 1.6$, 8.2, 1H), 7.23 (d, $J = 8.0$ Hz, 1H), 5.16 (s, 2H).

^{13}C NMR (DMSO- d_6 , 101 MHz): δ 190.1, 154.3, 143.2, 135.4, 128.4, 125.6, 109.6, 109.3, 47.3.

HRMS: exact mass calculated for $[\text{M}+\text{H}]^+$ ($\text{C}_9\text{H}_7\text{ClNO}_3$) requires 212.0109 m/z , found 212.0106 m/z .

5-(2-chloroacetyl)indolin-2-one, 2.7.



Prepared according to General Procedure A, using AlCl₃ (2.49 g, 18.60 mmol, 2.5 equiv), DCE (4 mL), 2-chloroacetyl chloride (1.19 mL, 15.00 mmol, 2 equiv), 1,3-dihydro-2*H*-benzo[*d*]imidazol-2-one (1.00 g, 7.50 mmol, 1 equiv) to afford the desired product as a brown solid (1.58 g, 43%). Consistent with previously reported ¹H spectral analysis.¹⁶⁶

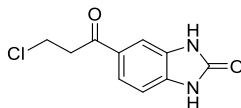
ν_{max} (neat): 3235, 1715, 1680, 1233, 1123, 817 cm⁻¹.

¹H NMR (DMSO-*d*₆, 400 MHz): δ 11.11 (s, 1H), 10.95 (s, 1H), 7.68 (dd, *J* = 1.7, 8.2 Hz, 1H), 7.50 (d, *J* = 1.6 Hz, 1H), 7.05 (d, *J* = 8.2 Hz, 1H), 5.13 (s, 2H).

¹³C NMR (DMSO-*d*₆, 101 MHz): δ 190.3, 155.4, 134.6, 129.8, 127.1, 122.8, 108.1, 108.07, 47.3.

HRMS: exact mass calculated for [M+H]⁺ (C₉H₈ClN₂O₂) requires 211.0269 *m/z*, found 211.0268 *m/z*.

5-(3-chloropropanoyl)indolin-2-one, 2.8.



Prepared according to General Procedure A, using AlCl₃ (2.49 g, 18.60 mmol, 2.5 equiv), DCE (4 mL), 3-chloropropanoyl chloride (1.43 mL, 15.00 mmol, 2 equiv), 1,3-dihydro-2*H*-benzo[*d*]imidazol-2-one (1.00 g, 7.50 mmol, 1 equiv) to afford the desired product as a pink solid (1.69 g, 84%). No previously reported spectral data.¹⁶⁷

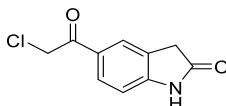
ν_{max} (neat): 2943, 1671 cm⁻¹

¹H NMR (DMSO-*d*₆, 400 MHz): δ 11.06 (s, 1H), 11.06 (s, 1H), 7.69 (dd, *J* = 1.7, 8.2 Hz, 1H), 7.49 (d, *J* = 1.5 Hz, 1H), 7.03 (d, *J* = 8.2 Hz, 1H), 3.92 (t, *J* = 6.3 Hz, 2H), 3.50 (t, *J* = 6.3 Hz, 2H).

^{13}C NMR (DMSO- d_6 , 101 MHz): δ 195.5, 155.4, 134.3, 129.8, 129.4, 122.4, 108.0, 107.7, 40.25, 39.8.

HRMS: exact mass calculated for $[\text{M}+\text{H}]^+$ ($\text{C}_{10}\text{H}_{10}\text{ClN}_2\text{O}_2$) requires 225.0425 m/z , found 225.0425 m/z .

5-(2-chloroacetyl)indolin-2-one, 2.9.



Prepared according to General Procedure A, using AlCl_3 (7.60 g, 57.00 mmol, 7.6 equiv), DMF (3 mL), 2-chloroacetyl chloride (0.716 mL, 8.99 mmol, 1.2 equiv), indolin-2-one (1.00 g, 7.50 mmol, 1 equiv), to afford the desired product as a beige solid (1.00 g, 66%). No previously reported spectral data.¹⁴²

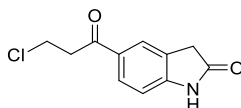
ν_{max} (neat): 3235, 1715, 1680, 1233, 1123, 817 cm^{-1} .

^1H NMR (DMSO- d_6 , 400 MHz): δ 10.83 (s, 1H), 7.91–7.87 (m, 2H), 7.83 (s, 1H), 5.08 (s, 2H), 3.57 (s, 2H).

^{13}C NMR (DMSO- d_6 , 101 MHz): δ 190.2, 176.7, 149.0, 129.7, 127.8, 126.3, 124.5, 108.9, 47.0, 35.4.

HRMS: exact mass calculated for $[\text{M}+\text{H}]^+$ ($\text{C}_{10}\text{H}_9\text{ClNO}_2$) requires 210.0316 m/z , found 210.0312 m/z .

5-(3-chloropropanoyl)indolin-2-one, 2.10.



Prepared according to General Procedure A, using AlCl_3 (7.60 g, 57.00 mmol, 7.6 equiv), DMF (3 mL), 3-chloropropanoyl chloride (0.87 mL, 9.02 mmol, 1.2 equiv), indolin-2-one (1.00 g, 7.50 mmol, 1 equiv) to afford the desired product as a beige solid (1.04 g, 62%). No previously reported spectral data.¹⁴¹

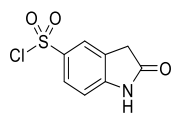
ν_{\max} (neat): 3051, 2874, 1705, 1661, 1610, 1123, 773, 704 cm^{-1} .

^1H NMR (DMSO- d_6 , 400 MHz): δ 10.79 (s, 1H), 7.89 (dd, $J = 8.2, 1.6$ Hz, 1H), 7.83 (s, 1H), 6.94 (t, $J = 7.9$ Hz, 1H), 3.92 (t, $J = 6.3$ Hz, 2H), 3.56 (s, 2H), 3.46 (t, $J = 6.3$ Hz, 2H).

^{13}C NMR (DMSO- d_6 , 101 MHz): δ 195.4, 176.7, 148.6, 130.0, 129.2, 126.2, 124.2, 108.8, 40.2, 35.5. $1 \times \text{C}$ not observed (under solvent peak).

HRMS: exact mass calculated for $[\text{M}+\text{H}]^+$ ($\text{C}_{11}\text{H}_{11}\text{ClNO}_2$) requires 224.0473 m/z , found 224.0468 m/z .

2-oxoindoline-5-sulfonyl chloride, 2.12.



Prepared according to General Procedure **B**, using chlorosulfonic acid (2.50 mL, 37.61 mmol, 5 equiv), indolin-2-one (1.00 g, 7.50 mmol, 1 equiv), to afford the desired product as a pink solid (0.82 g, 47%).

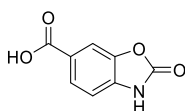
ν_{\max} (neat): 3092, 2880, 1714, 1616, 1492, 1362 cm^{-1} .

^1H NMR (DMSO- d_6 , 400 MHz): δ 10.44 (s, 1H), 7.47–7.42 (m, 2H), 6.74 (d, $J = 7.9$ Hz, 1H), 3.47 (s, 2H).

^{13}C NMR (DMSO- d_6 , 101 MHz): δ 176.6, 143.8, 141.6, 125.1, 125.0, 122.0, 107.8, 35.7.

HRMS: exact mass calculated for $[\text{M}+\text{H}]^+$ ($\text{C}_8\text{H}_6\text{ClNO}_3\text{S}$) requires 231.9835 m/z , found 231.9839 m/z .

2-oxo-2,3-dihydrobenzo[d]oxazole-6-carboxylic acid, 2.13.



Prepared according to General Procedure **C**, with 4-amino-3-hydroxybenzoic acid (500 mg, 3.26 mmol, 1 equiv), 1,1'-carbonyldiimidazole (582 mg, 3.59 mmol, 1.1 equiv) and DMF (2

mL). The reaction was diluted with H₂O (50 mL), and the precipitate filtered under vacuum filtration to yield a white solid which was used without further purification (270 mg, 46%). Consistent with previously reported spectral analysis.¹⁶⁸

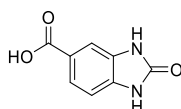
ν_{\max} (neat): 3178, 1683, 1286 cm⁻¹

¹H NMR (DMSO-*d*₆, 400 MHz) δ 12.02 (s, 1H), 7.80 (dd, *J* = 8.2, 1.3 Hz, 1H), 7.74 (s, 1H), 7.17 (d, *J* = 8.1 Hz, 1H).

¹³C NMR (DMSO-*d*₆, 101 MHz): δ 166.7, 154.3, 143.0, 134.5, 126.0, 124.4, 110.0, 109.4.

HRMS: exact mass calculated for [M-H]⁻ (C₈H₄NO₄) requires *m/z* 178.0146, found *m/z* 178.0146.

2-oxo-2,3-dihydrobenzo[d]oxazole-5-carboxylic acid, 2.14.



Prepared according to General Procedure C, 3,4-diaminobenzoic acid (1.00 g, 6.57 mmol, 1.0 equiv), 1,1'-carbonyldiimidazole (1.17 mg, 7.22 mmol, 1.1 equiv) and DMF (5 mL). The reaction was diluted with H₂O (50 mL), and the precipitate filtered under vacuum filtration to yield a brown solid (116 mg, 10%). Commercially available, CAS: 23814-14-4.

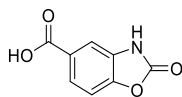
ν_{\max} (neat): 3093, 1676, 1699, 1685, 1306 cm⁻¹.

¹H NMR (500 MHz, DMSO-*d*₆) δ 10.97 (s, 1H), 10.82 (s, 1H), 7.61 (dd, *J* = 1.5, 8.2 Hz, 1H), 7.46 (app. s, 1H), 6.99 (d, *J* = 8.2 Hz, 1H).

¹³C NMR (101 MHz, DMSO-*d*₆): δ 167.4, 155.3, 133.5, 129.4, 122.82, 122.77, 109.1, 107.9.

HRMS: exact mass calculated for [M-H]⁻ (C₈H₅N₂O₃) requires *m/z* 177.0306, found *m/z* 177.0307.

2-oxo-2,3-dihydrobenzo[d]oxazole-5-carboxylic acid, 2.15.



Prepared according to General Procedure C, 3-amino-4-hydroxybenzoic acid (1.00 g, 6.53 mmol, 1.0 equiv), 1,1'-carbonyldiimidazole (1.17 mg, 7.19 mmol, 1.1 equiv) and DMF (5 mL). The reaction was diluted with H₂O (50 mL), and the precipitate filtered under vacuum filtration to yield a brown solid (95 mg, 8%). No previously reported data.¹⁶⁹

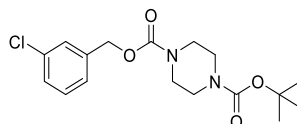
ν_{\max} (neat): 3159, 2600, 1761, 1560, 1399 cm⁻¹.

¹H NMR (DMSO-*d*₆, 500 MHz): δ 12.98 (s, 1H), 11.86 (s, 1H), 7.74 (dd, *J* = 8.4, 1.6 Hz, 1H), 7.56 (d, *J* = 1.5 Hz, 1H), 7.39 (t, *J* = 8.0 Hz, 1H).

¹³C NMR (DMSO-*d*₆, 101 MHz): δ 166.7, 154.2, 146.5, 130.6, 126.4, 124.0, 110.3, 109.4.

HRMS: exact mass calculated for [M-H]⁻ (C₈H₄NO₄) requires *m/z* 178.0146, found *m/z* 178.0146.

1-(*tert*-butyl) 4-(3-chlorobenzyl) piperazine-1,4-dicarboxylate, 2.18 c.



Prepared according to General Procedure C, using (3-chlorophenyl)methanol (842 μ L, 5.91 mmol, 1.1 equiv), CDI (0.96 g, 5.91 mmol, 1.1 equiv) *tert*-butyl piperazine-1-carboxylate (1.00 g, 5.36 mmol, 1.0 equiv) and DMF (5 mL). The reaction was diluted with H₂O (50 mL), the organics extracted with EtOAc (2 x 50 mL), washed with brine (2 x 50 mL), dried with a hydrophobic frit and concentrated *in vacuo* to yield a clear oil (904 mg, 47%). No previously reported spectral analysis.¹²⁸

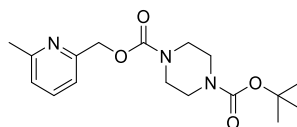
ν_{\max} (neat): 2977, 1691, 1413, 1225 cm⁻¹.

¹H NMR (CDCl₃, 400 MHz): δ 7.40–7.20 (m, 4H), 5.12 (s, 2H), 3.55–3.34 (m, 8H), 1.48 (s, 9H).

^{13}C NMR (CDCl_3 , 101 MHz) δ 154.4, 154.1, 138.0, 133.9, 129.3, 127.8, 127.4, 125.4, 79.7, 65.9, 43.2, 27.9, $1 \times \text{C}$ not observed (coincident).

HRMS: exact mass calculated for $[\text{M}+\text{NH}_4]^+$ ($\text{C}_{17}\text{H}_{27}\text{ClN}_3\text{O}_4$) requires 372.1685 m/z , found 372.1682 m/z .

1-(*tert*-butyl) 4-((6-methylpyridin-2-yl)methyl) piperazine-1,4-dicarboxylate, 2.18 e.



Prepared according to General Procedure C, using (6-methylpyridin-2-yl)methanol (1.00 g, 8.12 mmol, 1.1 equiv), CDI (1.32 g, 8.12 mmol, 1.1 equiv), DMF (5 mL), *tert*-butyl piperazine-1-carboxylate (1.37 g, 7.38 mmol, 1.0 equiv) to afford the desired product by vacuum filtration with H_2O (200 mL) as a white solid (1.74 g, 63%).

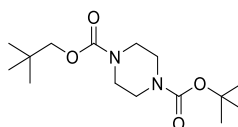
ν_{max} (neat) 2981, 2935, 1685, 1416 cm^{-1} .

^1H NMR (CDCl_3 , 400 MHz): δ 7.58 (d, $J = 7.7$ Hz, 1H), 7.13 (d, $J = 7.6$ Hz, 1H), 7.08 (d, $J = 7.6$ Hz, 1H), 5.22 (s, 2H), 3.60–3.36 (m, 8H), 2.55 (s, 3H), 1.46 (s, 9H).

^{13}C NMR (CDCl_3 , 101 MHz): δ 157.6, 155.2, 154.5, 154.1, 136.6, 122.0, 118.0, 79.7, 67.4, 43.3, 27.9, 23.8. $1 \times \text{C}$ not observed (coincident).

HRMS: exact mass calculated for $[\text{M}+\text{H}]^+$ ($\text{C}_{17}\text{H}_{25}\text{N}_3\text{O}_4$) requires 336.1918 m/z , found 336.1915 m/z .

1-(*tert*-butyl) 4-neopentyl piperazine-1,4-dicarboxylate, 2.18 f.



Prepared according to General Procedure C, using 2,2-dimethylpropan-1-ol (0.24 g, 2.68 mmol, 1.1 equiv), CDI (0.52 g, 2.68 mmol, 1.1 equiv), DMF (2 mL), *tert*-butyl piperazine-1-carboxylate (0.5 g, 2.68 mmol, 1.0 equiv) to afford the desired product as a white solid (0.44 g, 54%).

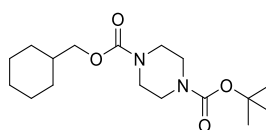
ν_{\max} (neat): 1685, 1423, 1234 cm^{-1} .

^1H NMR (CDCl_3 , 500 MHz): δ 3.79 (s, 2H), 3.53–3.33 (m, 8H), 1.46 (s, 9H), 0.94 (s, 9H).

^{13}C NMR (CDCl_3 , 101 MHz): δ 155.8, 154.8, 80.3, 75.1, 43.7, 31.7, 28.5, 26.6, 1 \times C not observed (coincident).

HRMS: exact mass calculated for $[\text{M}+\text{NH}_4]^+$ ($\text{C}_{15}\text{H}_{32}\text{N}_3\text{O}_4$) requires 318.2387 m/z , found 318.2386 m/z .

1-(*tert*-butyl) 4-(cyclohexylmethyl) piperazine-1,4-dicarboxylate, 2.18 g.



Prepared according to General Procedure C, using cyclohexylmethanol (2.14 mL, 17.50 mmol, 1.1 equiv), CDI (2.84 g, 17.50 mmol, 1.1 equiv), DMF (5 mL), *tert*-butyl piperazine-1-carboxylate (2.96 g, 15.90 mmol, 1.0 equiv) to afford the desired product as a white solid (4.79 g, 92%).

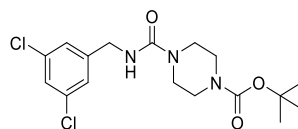
ν_{\max} (neat): 2922, 2852, 1684, 1424 cm^{-1} .

^1H NMR (CDCl_3 , 400 MHz): δ 3.92 (d, $J = 6.6$ Hz, 2H), 3.49–3.38 (m, 8H), 1.75 (d, $J = 10.6$ Hz, 4H), 1.72–1.59 (m, 2H), 1.48 (s, 9H), 1.33–1.13 (m, 3H), 0.99 (q, $J = 11.6, 11.9$ Hz, 2H).

^{13}C NMR (CDCl_3 , 101 MHz): δ 155.1, 154.2, 79.6, 70.3, 43.1, 36.9, 29.2, 27.9, 25.9, 25.2. 1 \times C not observed (coincident).

HRMS: exact mass calculated for $[\text{M}+\text{NH}_4]^+$ ($\text{C}_{17}\text{H}_{30}\text{N}_2\text{O}_4\text{NH}_4$) requires 344.2544 m/z , found 344.2544 m/z .

***Tert*-butyl 4-((3,5-dichlorobenzyl)carbamoyl)piperazine-1-carboxylate, 2.18 h.**



Prepared according to General Procedure C, using (3,5-dichlorophenyl)methanamine (0.24 g, 1.34 mmol, 1.1 equiv), CDI (0.18 g, 1.48 mmol, 1.1 equiv), DMF (2 mL), *tert*-butyl piperazine-1-carboxylate (0.25 mg, 1.34 mmol, 1.0 equiv) to afford the desired product as a white solid (0.17 g, 32%).

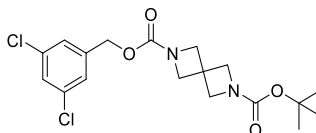
ν_{\max} (neat): 3334, 1698, 1629, 1534, 1234 cm^{-1} .

^1H NMR (DMSO- d_6 , 400 MHz): δ 7.45 (t, J = 1.8 Hz, 1H), 7.29 (d, J = 1.8 Hz, 2H), 7.23 (t, J = 5.8 Hz, 1H), 4.22 (d, J = 5.6 Hz, 2H), 3.36–3.20 (m, 8H), 1.40 (s, 9H), NH observed.

^{13}C NMR (DMSO- d_6 , 101 MHz): δ 157.2, 153.8, 145.4, 133.7, 126.1, 125.9, 79.0, 43.1, 42.7, 28.0, 1 \times C not observed (coincident).

HRMS: exact mass calculated for $[\text{M}+\text{NH}_4]^+$ ($\text{C}_{17}\text{H}_{23}\text{Cl}_2\text{N}_3\text{O}_3\text{NH}_4$) requires 405.1455 m/z , found 405.1455 m/z .

2-(*tert*-butyl) 6-(3,5-dichlorobenzyl) 2,6-diazaspiro[3.3]heptane-2,6-dicarboxylate, 2.19 a.



Prepared according to General Procedure C, using (3,5-dichlorophenyl)methanol (800 mg, 4.52 mmol, 1.1 equiv), CDI (735 mg, 4.52 mmol, 1.1 equiv), *tert*-butyl 2,6-diazaspiro[3.3]heptane-2-carboxylate hemioxalate (1.0 g, 4.11 mmol, 1.0 equiv) and DMF(6 mL) to afford the desired product as a white solid (1.60 g, 97%).

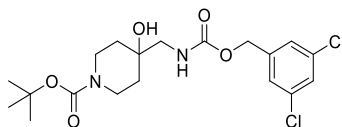
ν_{\max} (neat): 2959, 2975, 2875, 1704 cm^{-1} .

^1H NMR (CDCl_3 , 400 MHz): δ 7.28 (t, J = 1.9 Hz, 1H), 7.19 (d, J = 1.9 Hz, 2H), 5.00 (s, 2H), 4.12 (s, 4H), 4.03 (s, 4H), 1.41 (s, 9H).

^{13}C NMR (CDCl_3 , 101 MHz): δ 156.0, 155.4, 139.9, 135.2, 128.3, 126.3, 80.0, 35.2, 59.5, 32.8, 28.4. 1 \times C not observed (coincident).

HRMS: exact mass calculated for $[M+Na]^+$ ($C_{18}H_{22}Cl_2N_2NaO_4$) requires 423.0849 m/z , found 423.0847 m/z .

3,5-dichlorobenzyl 4-(((*tert*-butoxycarbonyl)amino)methyl)-4-hydroxypiperidine-1-carboxylate, 2.20.



Prepared according to General Procedure C, using (3,5-dichlorophenyl)methanol (422 mg, 2.38 mmol, 1.1 equiv), CDI (386 mg, 2.38 mmol, 1.1 equiv), DMF (2 mL), *tert*-butyl ((4-hydroxypiperidin-4-yl)methyl)carbamate (500 mg, 2.17 mmol, 1.0 equiv) and purified by column chromatography with silica (60-80% EtOAc in petroleum ether) to afford the desired product as a clear oil (704 mg, 75%).

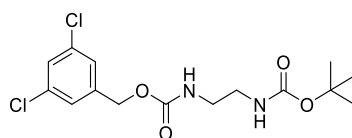
ν_{\max} (neat): 3296, 2922, 2975, 1728, 1658, 1436 cm^{-1} .

1H NMR ($CDCl_3$, 500 MHz): δ 7.32–7.26 (m, 1H), 7.24–7.18 (m, 2H), 5.50 (s, 1H), 5.04 (s, 2H), 3.84–3.73 (m, 2H), 3.49–3.43 (t, $J = 3.8$ Hz, 1H), 3.27–3.13 (m, 4H), 1.58–1.48 (m, 4H), 1.45 (s, 9H).

^{13}C NMR ($CDCl_3$, 101 MHz): δ 156.5, 154.3, 139.3, 134.6, 127.7, 125.5, 79.2, 69.5, 64.8, 50.6, 39.1, 34.1, 27.9.

HRMS: exact mass calculated for $[M+H]^+$ ($C_{19}H_{27}Cl_2N_2O_5$) requires 433.1292 m/z , found 433.1293 m/z .

***Tert*-butyl (3,5-dichlorobenzyl) ethane-1,2-diyl dicarbamate, 2.21.**



Prepared according to General Procedure **C**, using (3,5-dichlorophenyl)methanol (250 mg, 1.41 mmol, 1.1 equiv), CDI (229 mg, 1.41 mmol, 1.1 equiv), DMF (2 mL), *tert*-butyl (2-aminoethyl)carbamate (203 μ L, 1.28 mmol, 1.0 equiv) to afford the desired product as a white solid (403 mg, 62%).

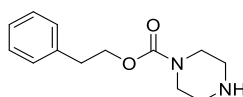
ν_{\max} (neat): 3357, 3322, 2944, 2985, 1664, 1535 cm^{-1} .

^1H NMR (CDCl_3 , 500 MHz): δ 7.30–7.27 (m, 1H), 7.23–7.20 (m, 2H), 5.36 (s, 1H), 5.02 (s, 2H), 4.87 (s, 1H), 3.35–3.19 (m, 4H), 1.43 (s, 9H).

^{13}C NMR (CDCl_3 , 101 MHz): δ 155.7, 139.5, 134.6, 127.6, 125.6, 124.5, 79.3, 64.5, 41.3, 39.9, 27.8.

HRMS: exact mass calculated for $[\text{M}+\text{Na}]^+$ ($\text{C}_{15}\text{H}_{20}\text{Cl}_2\text{N}_2\text{O}_4\text{Na}$) requires 399.0849 m/z , found 399.0839 m/z .

Phenethyl piperazine-1-carboxylate, **2.22 b**.



Prepared according to General Procedure **F**, with 1-(*tert*-butyl) 4-phenethyl piperazine-1,4-dicarboxylate **2.18 b** (393 mg, 1.17 mmol) using trifluoroacetic acid (2 mL), CH_2Cl_2 (2 mL) and concentrated *in vacuo* to afford the desired product as a clear oil (283 mg, 100%).

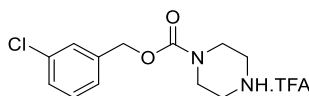
ν_{\max} (neat): 2968, 2745, 2659, 2533, 1692, 1428 cm^{-1} .

^1H NMR (CDCl_3 , 500 MHz): δ 7.30–7.25 (m, 2H), 7.22–7.18 (m, 3H), 4.28 (t, $J = 7.0$ Hz, 2H), 3.45–3.30 (m, 4H), 2.92 (t, $J = 7.0$ Hz, 2H), 2.81–2.67 (m, 4H), 2.50 (s, 1H).

^{13}C NMR (CDCl_3 , 101 MHz): δ 155.0, 137.8, 128.6, 128.1, 126.1, 65.6, 45.3, 44.3, 35.2.

HRMS: exact mass calculated for $[\text{M}+\text{H}]^+$ ($\text{C}_{13}\text{H}_{19}\text{N}_2\text{O}_2$) requires 235.1441 m/z , found 235.1440 m/z .

3-chlorobenzyl piperazine-1-carboxylate, **2.22 c**.



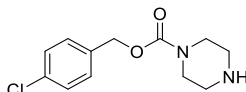
Prepared according to General Procedure **F**, with 1-(*tert*-butyl) 4-(3-chlorobenzyl) piperazine-1,4-dicarboxylate **2.18 c** (180 mg, 0.51 mmol) using trifluoroacetic acid (2 mL), CH₂Cl₂ (2 mL) and concentrated *in vacuo* to afford the desired product as a clear oil and the trifluoroacetic acid salt which was telescoped into the next step for the synthesis of **2.49**.

ν_{\max} (neat) 2740, 2501, 1691, 1429 cm⁻¹.

¹H NMR (CDCl₃, 400 MHz): δ 13.08 (s, 2H), 8.51 (s, 2H), 7.43–7.18 (m, 4H), 5.15 (s, 2H), 3.93–3.76 (m, 4H), 3.39–3.21 (m, 4H).

HRMS: exact mass calculated for [M+H]⁺ (C₁₂H₁₅ClN₂O₂) requires 255.0895 *m/z*, found 255.0895 *m/z*.

4-chlorobenzyl piperazine-1-carboxylate, **2.22 d**.



Prepared according to General Procedure **F**, with 1-(*tert*-butyl) 4-(4-chlorobenzyl) piperazine-1,4-dicarboxylate **2.18 d** (150 mg, 0.42 mmol) using trifluoroacetic acid (1 mL), CH₂Cl₂ (2 mL), quenched with NaOH (50 mL), the organics were extracted with CH₂Cl₂ (2 × 50 mL) and concentrated *in vacuo* to afford the desired product as a white solid (90 mg, 84%).

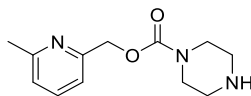
ν_{\max} (neat): 2624, 2469, 1719, 1668, 1430 cm⁻¹.

¹H NMR (CDCl₃, 400 MHz): δ 7.35–7.27 (m, 4H), 5.09 (s, 2H), 3.51–3.43 (m, 4H), 2.91–2.73 (m, 4H). 1 × H not observed (exchangeable).

¹³C NMR (CDCl₃, 101 MHz): δ 154.6, 134.8, 133.4, 128.8, 128.2, 65.8, 45.3, 44.4.

HRMS: exact mass calculated for [M+H]⁺ (C₁₂H₁₆ClN₂O₂) requires 255.0895 *m/z*, found 255.0897 *m/z*.

(6-methylpyridin-2-yl)methyl piperazine-1-carboxylate, 2.22 e.



Prepared according to General Procedure **F**, with 1-(*tert*-butyl) 4-((6-methylpyridin-2-yl)methyl) piperazine-1,4-dicarboxylate **2.18 e** (1.5 g, 4.4 mmol) using trifluoroacetic acid (3 mL), CH₂Cl₂ (3 mL), quenched with NaOH (50 mL), the organics were extracted with CH₂Cl₂ (2 × 50 mL) and concentrated *in vacuo* to afford the desired product as a white solid (257 mg, 26%).

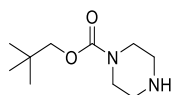
ν_{\max} (neat): 3406, 2922, 2870, 1694, 1435 cm⁻¹.

¹H NMR (CDCl₃, 400 MHz): δ 7.60–7.47 (m, 1H), 7.15–7.06 (m, 1H), 7.06–6.97 (m, 1H), 5.17 (s, 2H), 3.56–3.36 (m, 4H), 2.86–2.69 (m, 4H), 2.47 (s, 3H), 2.41 (s, 1H).

¹³C NMR (CDCl₃, 101 MHz): δ 158.1, 156.0, 155.1, 137.0, 122.3, 118.4, 67.8, 45.8, 45.0, 24.4.

HRMS: exact mass calculated for [M+H]⁺ (C₁₂H₁₈N₃O₂) requires 236.1394 *m/z*, found 236.1393 *m/z*.

Neopentyl piperazine-1-carboxylate, 2.22 f.



Prepared according to General Procedure **F**, with 1-(*tert*-butyl) 4-neopentyl piperazine-1,4-dicarboxylate **2.18 f** (398 mg, 1.33 mmol) using trifluoroacetic acid (3 mL), CH₂Cl₂ (3 mL), quenched with NaOH (50 mL), the organics were extracted with CH₂Cl₂ (2 × 50 mL) and concentrated *in vacuo* to afford the desired product as a white solid (256 mg, 95 %).

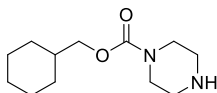
ν_{\max} (neat): 2963, 2907, 2873, 1684, 1423 cm⁻¹.

¹H NMR (CDCl₃, 500 MHz): δ 3.67 (s, 2H), 3.38–3.31 (m, 4H), 2.74–2.68 (m, 4H), 2.40 (s, 1H), 0.84 (s, 9H).

^{13}C NMR (CDCl_3 , 101 MHz): δ 155.5, 74.6, 45.6, 44.5, 31.4, 26.4.

HRMS: exact mass calculated for $[\text{M}+\text{H}]^+$ ($\text{C}_{10}\text{H}_{21}\text{N}_2\text{O}_2$) requires 201.1598 m/z , found 201.1594 m/z .

Cyclohexylmethyl piperazine-1-carboxylate, 2.22 g.



Prepared according to General Procedure **F**, with 1-(*tert*-butyl) 4-(cyclohexylmethyl) piperazine-1,4-dicarboxylate **2.18 g** (4.78 g, 14.6 mmol) using trifluoroacetic acid (5 mL), CH_2Cl_2 (5 mL) and quenched with NaOH (50 mL), the organics extracted with CH_2Cl_2 (2 \times 50 mL) and concentrated *in vacuo* to afford the desired product as a white solid (3.45 g, 100 %). No previously reported spectra.¹⁷⁰

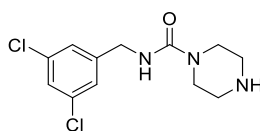
ν_{max} (neat): 2926, 2854, 1696, 1426, 1240.

^1H NMR (CDCl_3 , 400 MHz): δ 3.88 (d, $J = 6.4$ Hz, 2H), 3.52–3.41 (m, 4H), 3.52–3.41 (m, 4H), 2.77 (s, 1H), 1.80–1.55 (m, 6H), 1.34–1.08 (m, 3H), 0.96 (q, $J = 11.9$ Hz, 2H).

^{13}C NMR (CDCl_3 , 101 MHz): δ (155.8) 155.5, 80.9, 71.1 (70.7), 51.3, 44.7, 43.8, 42.9, (37.5) 37.4, (29.80) 29.77, (26.52) 26.47, (25.81) 25.75. Rotameric mixture observed (minor rotamer in brackets, where observed).

HRMS: exact mass calculated for $[\text{M}+\text{H}]^+$ ($\text{C}_{12}\text{H}_{23}\text{N}_2\text{O}_2$) requires m/z 227.1754, found m/z 227.1753.

***N*-(3,5-dichlorobenzyl)piperazine-1-carboxamide, 2.22 h.**



Prepared according to General Procedure **F**, with *tert*-butyl 4-((3,5-dichlorobenzyl)carbamoyl)piperazine-1-carboxylate **2.18 h** (150 mg, 0.40 mmol) using trifluoroacetic acid (1 mL), CH₂Cl₂ (2 mL) and quenched with NaOH (50 mL), the organics extracted with CH₂Cl₂ (2 × 50 mL) and concentrated *in vacuo* to afford the desired product as a white solid (103 mg, 93%).

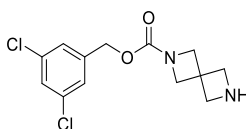
ν_{\max} (neat): 3007, 2825, 2501, 1633, 1676, 1574, 1546, 1202 cm⁻¹.

¹H NMR (CDCl₃, 400 MHz): δ 7.23–7.20 (m, 1H), 7.15 (d, *J* = 1.4 Hz, 2H), 5.08 (s, 1H), 4.34 (d, *J* = 5.8 Hz, 2H), 3.39–3.31 (m, 4H), 2.87–2.79 (m, 4H), 1.78 (s, 1H).

¹³C NMR (CDCl₃, 101 MHz): δ 157.0, 142.7, 134.5, 126.8, 125.4, 45.3, 44.4, 43.4.

HRMS: exact mass calculated for [M+H]⁺ (C₁₂H₁₆Cl₂N₃O) requires 288.0665 *m/z*, found 288.0668 *m/z*.

3,5-dichlorobenzyl 2,6-diazaspiro[3.3]heptane-2-carboxylate, **2.23 a**.



Prepared according to General Procedure **C**, using 2-(*tert*-butyl) 6-(3,5-dichlorobenzyl) 2,6-diazaspiro[3.3]heptane-2,6-dicarboxylate **2.19 a** (1.60 g, 4.00 mmol) and a mixture of trifluoroacetic acid (3 mL) and CH₂Cl₂ (3 mL). The reaction was concentrated *in vacuo* to afford the desired product as a white solid (1.59 g, 96%).

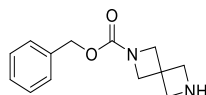
ν_{\max} (neat): 2946, 2875, 1706 cm⁻¹.

¹H NMR (400 MHz, CDCl₃): δ 7.28 (t, *J* = 1.9 Hz, 1H), 7.20 (d, *J* = 1.9 Hz, 2H), 5.00 (s, 2H), 4.11 (s, 4H), 3.76 (s, 4H), 2.31 (s, 1H).

¹³C NMR (101 MHz, CDCl₃): δ 155.6, 140.1, 135.1, 128.3, 126.3, 65.1, 57.5, 38.0, 1 × C not observed (coincident).

HRMS: exact mass calculated for $[M+H]^+$ ($C_{13}H_{15}Cl_2N_2O_2$) requires 301.0505 m/z , found 301.0509 m/z .

Benzyl 2,6-diazaspiro[3.3]heptane-2-carboxylate, **2.23 b**.



Prepared according to General Procedure **C**, using 2-benzyl 6-(*tert*-butyl) 2,6-diazaspiro[3.3]heptane-2,6-dicarboxylate **2.19 b** (100 mg, 0.30 mmol) and a mixture of trifluoroacetic acid (1 mL) and CH_2Cl_2 (1 mL). The reaction was then stirred at room temperature, concentrated *in vacuo* and purified by strong cation exchange (propylsulfonic acid functionalised silica, 2 N NH_3 in MeOH) to afford the desired product as a white solid (62 mg, 89%).

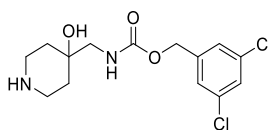
ν_{max} (neat): 3195, 3152, 2968, 2847, 1658, 1594, 1431 cm^{-1} .

1H NMR (400 MHz, $CDCl_3$): δ 7.36–7.27 (m, 5H), 5.05 (s, 2H), 4.06 (s, 4H), 3.71 (s, 4H), 2.24 (s, 1H).

^{13}C NMR (101 MHz, $CDCl_3$): δ 156.2, 136.7, 128.5, 128.1, 128.0, 66.7, 60.1, 57.5, 38.0.

HRMS: exact mass calculated for $[M+H]^+$ ($C_{13}H_{17}N_2O_2$) requires 301.0505 m/z , found 301.0509 m/z .

3,5-dichlorobenzyl 4-(aminomethyl)-4-hydroxypiperidine-1-carboxylate, **2.24**.



Prepared according to General Procedure **C**, using *tert*-butyl(3,5-dichlorobenzyl)propane-1,3-diyl dicarbamate **2.20** (492 mg, 1.64 mmol), trifluoroacetic acid (2 mL) and CH_2Cl_2 (2 mL) at room temperature for 2 h. The reaction was diluted with 1 M NaOH (40 mL) and the organics were extracted with EtOAc (40 mL), washed with brine (40 mL), dried with a hydrophobic frit and concentrated *in vacuo* to afford the desired product as a clear oil (473 mg, 86 %).

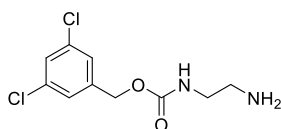
ν_{\max} (neat): 3305, 2940, 2845, 1700, 1574 cm^{-1} .

^1H NMR (CDCl_3 , 500 MHz): δ 7.31–7.28 (m, 1H), 7.22–7.16 (m, 2H), 5.34 (br. s, 1H), 5.03 (s, 2H), 3.26–3.15 (m, 2H), 2.98–2.79 (m, 4H), 2.25–1.99 (m, 2H), 1.61–1.43 (m, 4H).

^{13}C NMR (CDCl_3 , 101 MHz): δ 127.0, 140.0, 135.2, 28.3, 126.2, 70.3, 65.3, 51.1, 42.3, 36.0.

HRMS: exact mass calculated for $[\text{M}+\text{H}]^+$ ($\text{C}_{14}\text{H}_{19}\text{Cl}_2\text{N}_2\text{O}_3$) requires 333.0767 m/z , found 333.0770 m/z .

3,5-dichlorobenzyl (2-aminoethyl)carbamate, 2.25.



Prepared according to General Procedure F, using *tert*-butyl (3,5-dichlorobenzyl)propane-1,3-diylidicarbamate **2.21** (725 mg, 1.92 mmol), trifluoroacetic acid (3 mL) and CH_2Cl_2 (3 mL) at room temperature for 2 h. The reaction was diluted with 1 M NaOH (40 mL) and the organics were extracted with EtOAc (40 mL), washed with brine (40 mL), dried with a hydrophobic frit and concentrated *in vacuo* to afford the desired product as a white solid (224 mg, 82 %).

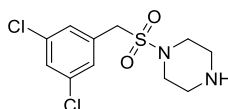
ν_{\max} (neat): 3301, 2935, 2871, 1700, 1573 cm^{-1} .

^1H NMR (CDCl_3 , 400 MHz): δ 7.34–7.28 (m, 1H), 7.26–7.21 (m, 2H), 5.68 (s, 1H), 5.04 (s, 2H), 3.32 (dd, $J = 6.2, 12.4$ Hz, 2H), 2.81 (t, $J = 6.5$ Hz, 2H), 1.66 (d, $J = 6.5$ Hz, 2H), 1.47 (s, 2H).

^{13}C NMR (CDCl_3 , 101 MHz): δ 156.3, 140.1, 135.0, 128.0, 126.0, 64.9, 43.7, 41.5.

HRMS: exact mass calculated for $[\text{M}+\text{H}]^+$ ($\text{C}_{11}\text{H}_{15}\text{Cl}_2\text{N}_2\text{O}_2$) requires 277.0505 m/z , found 277.0503 m/z .

1-((3,5-dichlorobenzyl)sulfonyl)piperazine, 2.27.



Prepared according to General Procedure **F**, with *tert*-butyl 4-((3,5-dichlorobenzyl)sulfonyl)piperazine-1-carboxylate **2.26** (140 mg, 0.34 mmol) using trifluoroacetic acid (400 μ L), CH_2Cl_2 (2 mL), quenched with NaOH (20 mL), the organics were extracted with CH_2Cl_2 (2×20 mL) and concentrated *in vacuo* to afford the desired product as a white solid (102 mg, 96%).

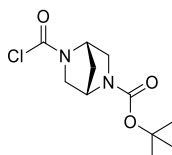
ν_{max} (neat): 3248, 3081, 1926, 1954, 1571, 1440, 1321.

^1H NMR (CDCl_3 , 400 MHz): δ 7.40–7.35 (m, 1H), 7.35–7.27 (m, 2H), 4.08 (s, 2H), 3.22–3.14 (m, 4H), 2.89–2.83 (m, 4H), 1.94 (s, 1H).

^{13}C NMR (CDCl_3 , 101 MHz): δ 134.8, 131.5, 128.6, 128.5, 54.7, 46.4, 45.4.

HRMS: exact mass calculated for $[\text{M}+\text{H}]^+$ ($\text{C}_{11}\text{H}_{14}\text{Cl}_2\text{N}_2\text{O}_2\text{S}$) requires m/z 309.0226, found m/z 309.0230.

***Tert*-butyl (1*S*,4*S*)-5-(chlorocarbonyl)-2,5-diazabicyclo[2.2.1]heptane-2-carboxylate, 2.29.**

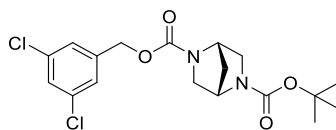


Prepared according to General Procedure **G**, using *tert*-butyl (1*S*,4*S*)-2,5-diazabicyclo[2.2.1]heptane-2-carboxylate (100 mg, 0.50 mmol, 1.0 equiv), triphosgene (74 mg, 0.25 mmol, 0.5 equiv), pyridine (60 μ L, 0.75 mmol, 1.5 equiv) in CH_2Cl_2 (1 mL) to afford the desired product as a yellow solid. Telescoped into the next step for the synthesis of **2.31**.

^1H NMR (CDCl_3 , 400 MHz): δ 4.71 (d, $J = 11.3$ Hz, 1H), 4.65–4.42 (m, 1H), 3.67–3.31 (m, 4H), 1.97–1.86 (m, 2H), 1.45 (s, 9H).

^{13}C NMR (CDCl_3 , 101 MHz): δ 153.9, 80.4, 62.2, 61.6, 59.4, 58.9, 57.8, 57.1, 56.5, 56.2, 55.6, 53.8, 53.4, 53.1, 52.7, 37.3, 37.2, 36.8, 36.7, 28.4. Rotameric mixture observed.

2-(*tert*-butyl) 5-(3,5-dichlorobenzyl) (1*S*,4*S*)-2,5-diazabicyclo[2.2.1]heptane-2,5-dicarboxylate, 2.31.

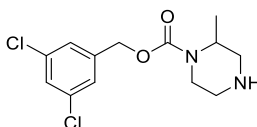


Prepared according to General Procedure **F**, using *tert*-butyl (1*S*,4*S*)-5-(chlorocarbonyl)-2,5-diazabicyclo[2.2.1]heptane-2-carboxylate **2.29** (105 mg, 0.40 mmol, 1.0 equiv), (3,5-dichlorophenyl)methanol (71.4 mg, 0.40 mmol, 1.0 equiv), NaH (24 mg, 0.60 mmol, 1.5 equiv) in DMF (1 mL) to afford the desired product as a white solid which was telescoped into the next step for the synthesis of **2.33**.

¹H NMR (CDCl₃, 400 MHz): δ 7.48 (t, *J* = 1.9 Hz, 1H), 7.40–7.36 (m, 2H), 5.10 (s, 2H), 4.50–4.45 (m, 1H), 3.41–4.36 (m, 1H), 3.43–3.36 (m, 1H), 3.34–3.18 (m, 3H), 1.85–1.80 (m, 2H), 1.41 (s, 9H).

¹³C NMR (CDCl₃, 101 MHz, 323K): δ 153.2, 153.1, 140.9, 133.7, 126.9, 125.6, 124.5, 78.5, 64.1, 56.5, 53.5, 53.3, 36.0, 27.7. Rotameric mixture observed.

3,5-dichlorobenzyl 2-methylpiperazine-1-carboxylate, 2.32.



Prepared according to General Procedure **F**, with 4-(*tert*-butyl) 1-(3,5-dichlorobenzyl) 2-methylpiperazine-1,4-dicarboxylate **2.30** (100 mg, 0.25 mmol) using trifluoroacetic acid (1 mL), CH₂Cl₂ (1 mL) and purified by strong cation exchange (propylsulfonic acid functionalised silica, 2 N NH₃ in MeOH) to afford the desired product as a clear oil (75 mg, 80%).

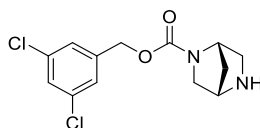
ν_{max} (neat): 2942, 2868, 1693, 1572, 1415 cm⁻¹.

¹H NMR (CDCl₃, 400 MHz): δ 7.31 (t, *J* = 1.9 Hz, 1H), 7.24 (d, *J* = 1.9 Hz, 2H), 5.09 (s, 2H), 4.32–4.21 (m, 1H), 3.87 (d, *J* = 12.3, 1H), 3.11 (t, *J* = 12.7 Hz, 1H), 3.04–2.87 (m, 2H), 2.82 (d, *J* = 12.1 Hz, 1H), 2.72 (td, *J* = 3.5, 12.2, 12.3 Hz, 1H), 1.89 (s, 1H), 1.29 (d, *J* = 6.9 Hz, 3H).

^{13}C NMR (CDCl_3 , 101 MHz): δ 154.2, 139.8, 134.6, 127.6, 125.5, 64.9, 49.7, 46.5, 45.4, 39.3, 14.6.

HRMS: exact mass calculated for $[\text{M}+\text{H}]^+$ ($\text{C}_{13}\text{H}_{17}\text{Cl}_2\text{N}_2\text{O}_2$) requires 303.0662 m/z , found 303.0668 m/z .

3,5-dichlorobenzyl (1*S*,4*S*)-2,5-diazabicyclo[2.2.1]heptane-2-carboxylate, 2.33.



Prepared according to General Procedure **F**, with 2-(*tert*-butyl) 5-(3,5-dichlorobenzyl) (1*S*,4*S*)-2,5-diazabicyclo[2.2.1]heptane-2,5-dicarboxylate **2.31** (160 mg, 0.40 mmol) using trifluoroacetic acid (1 mL), CH_2Cl_2 (3 mL) and purified by strong cation exchange (propylsulfonic acid functionalised silica, 2 N NH_3 in MeOH) to afford the desired product as an orange oil (130 mg, 87% over 3 steps).

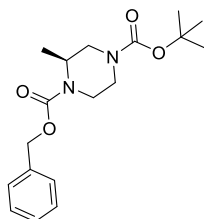
ν_{max} (neat): 2943, 1680, 1416 cm^{-1} .

^1H NMR (CDCl_3 , 400 MHz): δ 7.32 (dd, $J = 1.9, 4.0$ Hz, 1H), 7.23 (dd, $J = 1.7, 6.0$ Hz, 2H), 5.08 (m, 2H), 4.58–4.44 (m, 1H), 3.85–3.76 (m, 1H), 3.52–3.42 (m, 1H), 3.35–3.26 (m, 1H), 3.20–2.99 (m, 2H), 1.89–1.72 (m, 2H).

^{13}C NMR (CDCl_3 , 101 MHz): δ 153.3 (153.5), 139.6, 139.5, 134.59, 134.57, 127.70, 127.65, 125.7, 125.6, 64.8, 64.7, 56.4, 56.2, 56.0, 55.6, 55.0, 54.0, 52.0, 51.7, 36.6, 36.1. Rotameric mixture observed (minor rotamer in brackets, where observed).

HRMS: exact mass calculated for $[\text{M}+\text{H}]^+$ ($\text{C}_{13}\text{H}_{14}\text{Cl}_2\text{N}_2\text{O}_2$) requires 301.0505 m/z , found 301.0508 m/z .

1-benzyl 4-(*tert*-butyl) (*S*)-2-methylpiperazine-1,4-dicarboxylate, 2.35.



Prepared according to General Procedure **E**, using (*S*)-*tert*-butyl-3-methylpiperazine-1-carboxylate (200 mg, 0.99 mmol, 1.1 equiv), NaHCO₃ (84 mg, 0.99 mmol, 1.0 equiv), *N*-(benzyloxycarbonyloxy)succinimide (249 mg, 0.99 mmol, 1.0 equiv), THF (0.5 mL), H₂O (0.5 mL) to afford the desired product as a clear oil (325 mg, 97%).

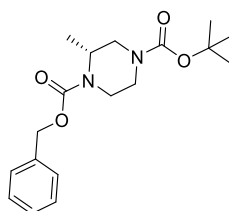
ν_{\max} (neat): 2977, 1693, 1418 cm⁻¹.

¹H NMR (CDCl₃, 400 MHz): 7.40–7.29 (m, 5H), 5.16 (app. d, *J* = 2.1 Hz, 2H), 4.37–4.27 (m, 1H), 3.89 (d, *J* = 13.4 Hz, 1H), 3.86–3.77 (m, 1H), 3.16–3.07 (m, 1H), 3.07–2.96 (m, 1H), 2.91–2.74 (m, 1H), 2.83 (s, 1H), 1.48 (s, 9H), 1.18 (d, *J* = 6.8 Hz, 3H).

¹³C NMR (CDCl₃, 101 MHz): δ 155.3, 155.2, 136.7, 128.6, 128.2, 128.0, 80.1, 67.3, 47.4, 38.8, 28.5, 15.3. 2 \times C not observed (coincident).

HRMS exact mass calculated for [M+H]⁺ (C₁₈H₂₇N₂O₄) [M+H]⁺ requires 235.1441 *m/z*, found 235.1440 *m/z*.

1-benzyl 4-(*tert*-butyl) (*R*)-2-methylpiperazine-1,4-dicarboxylate, 2.36.



Prepared according to General Procedure **E**, (*R*)-*tert*-butyl-3-methylpiperazine-1-carboxylate (1.0 g, 4.99 mmol, 1.0 equiv), NaHCO₃ (419 mg, 4.99 mmol, 1.0 equiv), *N*-(benzyloxycarbonyloxy)succinimide (1.24 g, 4.99 mmol, 1.0 equiv), THF (2.5 mL), H₂O (2.5 mL) to afford the desired product as a clear oil (1.66 g, 99%).

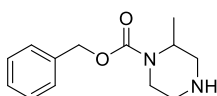
ν_{\max} (neat): 2977, 2935, 1690, 1428 cm⁻¹.

^1H NMR (CDCl_3 , 400 MHz): 7.41–7.29 (m, 5H), 5.14 (d, $J = 2.0$ Hz, 2H), 4.38–4.27 (m, 1H), 4.18–3.96 (m, 1H), 3.89 (d, $J = 13.4$ Hz, 1H), 3.86–3.75 (m, 1H), 3.26–3.07 (m, 1H), 3.01 (d, $J = 11.3$ Hz, 1H), 2.95–2.70 (m, 1H), 1.46 (s, 9H), 1.16 (d, $J = 6.8$ Hz, 3H).

^{13}C NMR (CDCl_3 , 101 MHz): δ 155.3, 155.2, 136.8, 128.6, 128.2, 128.0, 80.1, 67.4, 47.4, 38.8, 28.5, 15.4. $2 \times \text{C}$ not observed (coincident).

HRMS exact mass calculated for $[\text{M}+\text{H}]^+$ ($\text{C}_{18}\text{H}_{27}\text{N}_2\text{O}_4$) $[\text{M}+\text{H}^+]$ requires 235.1441 m/z , found 235.1438 m/z .

Benzyl 2-methylpiperazine-1-carboxylate, **2.37**.



Prepared according to General Procedure **F**, with 1-benzyl 4-(*tert*-butyl) 2-methylpiperazine-1,4-dicarboxylate **2.34** (154 mg, 0.46 mmol) using trifluoroacetic acid (1 mL), CH_2Cl_2 (1 mL) and purified by strong cation exchange (propylsulfonic acid functionalised silica, 2 N NH_3 in MeOH) to afford the desired product as a clear oil (108 mg, 61%).

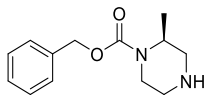
ν_{max} (neat): 1670, 1425 cm^{-1} .

^1H NMR (CDCl_3 , 400 MHz): δ 7.40–7.27 (m, 5H), 5.14 (d, $J = 2.6$ Hz, 2H), 4.33–4.24 (m, 1H), 3.90 (d, $J = 13.4$ Hz, 1H), 3.22 (s, 1H), 3.09 (td, $J = 3.3, 13.0$ Hz, 1H), 2.99 (d, $J = 13.5$ Hz, 1H), 2.92 (dd, $J = 4.1, 12.5$ Hz, 1H), 2.81 (d, $J = 12.4$ Hz, 1H), 2.70 (d, $J = 6.9$ Hz, 3H). $1 \times \text{H}$ not observed (exchangeable).

^{13}C NMR (CDCl_3 , 101 MHz): δ 155.2, 136.8, 128.4, 127.9, 127.8, 67.1, 49.8, 46.6, 45.5, 39.3, 14.9.

HRMS: exact mass calculated for $[\text{M}+\text{H}]^+$ ($\text{C}_{13}\text{H}_{19}\text{N}_2\text{O}_2$) requires 235.1441 m/z , found 235.1441 m/z .

Benzyl (*S*)-2-methylpiperazine-1-carboxylate, **2.38**.



Prepared according to General Procedure **F**, using (*S*)-1-benzyl 4-*tert*-butyl 2-methylpiperazine-1,4-dicarboxylate **2.35** (323 mg, 0.97 mmol), trifluoroacetic acid (1 mL), CH₂Cl₂ (2 mL) and purified by strong cation exchange (propylsulfonic acid functionalised silica, 4% NEt₃ in MeOH) to afford the desired product as a clear oil (167 mg, 74%).

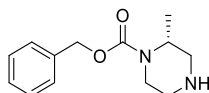
ν_{\max} (neat): 2966, 1676, 1425 cm⁻¹.

¹H NMR (CDCl₃, 400 MHz): δ 7.42–7.26 (m, 5H), 5.16 (app. d, $J = 2.4$ Hz, 2H), 4.37–4.26 (m, 1H), 3.91 (dd, $J = 2.1, 13.4$ Hz, 1H), 3.11 (td, $J = 3.4, 12.9, 13.2$ Hz, 1H), 3.04–2.98 (m, 1H), 2.94 (dd, $J = 4.1, 12.4$ Hz, 1H), 2.82 (d, $J = 12.4$ Hz, 1H), 2.77–2.68 (m, 3H), 1.28 (d, $J = 6.9$ Hz, 3H).

¹³C NMR (CDCl₃, 101 MHz): δ 155.3, 136.9, 128.6, 128.1, 127.9, 67.2, 50.0, 46.7, 45.8, 39.5, 15.1.

HRMS: exact mass calculated for [M+H]⁺ (C₁₃H₁₈N₂O₂) requires 235.1441 m/z , found 235.1440 m/z .

Benzyl (*R*)-2-methylpiperazine-1-carboxylate, **2.39**.



Prepared according to General Procedure **F**, using (*R*)-1-benzyl 4-*tert*-butyl 2-methylpiperazine-1,4-dicarboxylate **2.36** (1.66 g, 4.97 mmol), trifluoroacetic acid (3 mL), CH₂Cl₂ (4 mL) and purified by strong cation exchange (propylsulfonic acid functionalised silica, 4% NEt₃ in MeOH) to afford the desired product as a clear oil (660 mg, 57%).

ν_{\max} (neat): 2977, 1675, 1418 cm⁻¹.

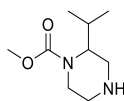
¹H NMR (CDCl₃, 400 MHz): δ 7.43–7.29 (m, 5H), 5.16 (d, $J = 2.4$ Hz, 2H), 4.37–4.26 (m, 1H), 3.93 (dd, $J = 1.9, 13.4$ Hz, 1H), 3.11 (td, $J = 3.3, 13.0, 13.2$ Hz, 1H), 3.01 (d, $J = 12.3$

Hz, 1H), 2.95 (dd, $J = 4.1, 12.4$ Hz, 1H), 2.83 (d, $J = 12.4$ Hz, 1H), 2.78-2.67 (m, 3H), 1.28 (d, $J = 6.9$ Hz, 3H).

^{13}C NMR (CDCl_3 , 101 MHz): δ 155.0, 136.5, 128.7, 128.3, 128.1, 67.6, 48.7, 45.8, 44.6, 37.9, 15.1.

HRMS: exact mass calculated for $[\text{M}+\text{H}]^+$ ($\text{C}_{13}\text{H}_{19}\text{N}_2\text{O}_2$) requires 235.1441 m/z , found 235.1438 m/z .

4-(*tert*-butyl) 1-methyl 2-isopropylpiperazine-1,4-dicarboxylate, 2.41.



To a round bottom flask was added *tert*-butyl 3-isopropylpiperazine-1-carboxylate (99.7 mg, 0.44 mmol, 1.1 equiv), NEt_3 (68 μL , 0.48 mmol, 1.0 equiv) in THF (5 mL). Methyl chloroformate (37 μL , 0.48 mmol, 1.0 equiv) was added drop wise at 0 $^\circ\text{C}$ and stirred for 16 h at room temperature. The crude mixture was quenched with saturated sodium bicarbonate solution (5 mL) and concentrated *in vacuo* to a residue that was purified by column chromatography on silica (2–10% MeOH in EtOAc). The compound *N*-Boc deprotected by degradation on silica chromatography to afford the desired product as a clear oil (64 mg, 51 % 2 steps).

ν_{max} (neat): 2961, 1688, 1445 cm^{-1}

^1H NMR (CDCl_3 , 400 MHz): δ 4.14 (d, $J = 13.5$ Hz, 1H), 3.95–3.84 (m, 1H), 3.67 (s, 3H), 3.46 (d, $J = 13.2$ Hz, 1H), 3.34 (d, $J = 12.7$ Hz, 1H), 3.25 (t, $J = 13.8$ Hz, 1H), 2.94 (dd, $J = 4.5, 13.3$, 1H), 2.86 (td, $J = 4.0, 12.6$ Hz, 1H), 2.48 (app. s, 1H), 0.99 (d, $J = 6.5$ Hz, 3H), 0.83 (d, $J = 6.6$ Hz, 3H). $1 \times \text{H}$ not observed (exchangeable).

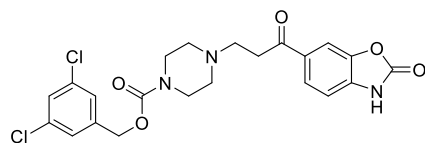
^{13}C NMR (CDCl_3 , 400 MHz): δ 155.5, 55.1, 53.2, 43.2, 42.8, 36.0, 25.9, 20.0, 18.7.

HRMS: exact mass calculated for $[\text{M}+\text{H}]^+$ ($\text{C}_9\text{H}_{19}\text{N}_2\text{O}_2$) requires 187.1439 m/z , found 187.1441 m/z .

3,5-dichlorobenzyl

4-(3-oxo-3-(2-oxo-2,3-dihydrobenzo[*d*]oxazol-6-yl)propyl)piperazine-1-carboxylate, PF-8380.

4-(3-oxo-3-(2-oxo-2,3-dihydrobenzo[*d*]oxazol-6-yl)propyl)piperazine-1-carboxylate, PF-8380.



Prepared according to General Procedure **J**, using 3,5-dichlorobenzyl piperazine-1-carboxylate **2.22 a** (153 mg, 0.53 mmol, 1.1 equiv), 6-(3-chloropropanoyl)benzo[*d*]oxazol-2(3*H*)-one **2.6** (100 mg, 0.44 mmol, 1.0 equiv), MeCN (3 mL), NEt₃ (80 μL, 0.57 mmol, 1.2 equiv) to afford the desired product as a white solid (104 mg, 49%). Consistent with previously reported data.⁹⁵

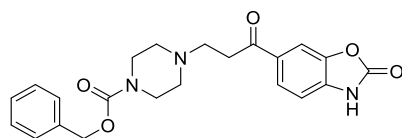
ν_{max} (neat): 1766, 1674, 1443, 797, 754 cm⁻¹.

¹H NMR (DMSO-*d*₆, 400 MHz): δ 7.87–7.83 (m, 2H), 7.58–7.53 (m, 1H), 7.41 (d, *J* = 1.6 Hz, 2H), 7.17 (t, *J* = 6.1 Hz, 1H), 5.11 (s, 2H), 3.44–3.33 (s, 4H), 3.18 (t, *J* = 7.1 Hz, 2H), 2.70 (t, *J* = 7.1 Hz, 2H), 2.43–2.37 (m 4H). 1 × C not observed (exchangeable).

¹³C NMR (DMSO-*d*₆, 101 MHz): δ 195.0, 154.4, 153.8, 143.3, 140.8, 135.4, 134.1, 130.1, 127.6, 126.3, 125.2, 109.6, 109.0, 65.2, 51.1, 50.8, 40.7, 32.6.

HRMS: exact mass calculated for [M+H]⁺ (C₂₂H₂₂Cl₂N₃O₅) requires 478.0931 *m/z*, found 478.0926 *m/z*.

Benzyl 4-(3-oxo-3-(2-oxo-2,3-dihydrobenzo[*d*]oxazol-6-yl)propyl)piperazine-1-carboxylate, 2.42.



Prepared according to General Procedure **J**, using 6-(3-chloropropanoyl) benzo[*d*]oxazol-2(3*H*)-one **2.6** (201.1 mg, 0.89 mmol, 1.0 equiv), MeCN (5 mL), PS-DIPEA (295.7 mg, 0.64 mmol, 1.2 equiv), benzyl piperazine-1-carboxylate (190 μL, 0.97 mmol, 1.1 equiv) to afford the desired product as a white solid (190.5 mg, 52%). Consistent with previously reported data.⁹⁵

ν_{\max} (neat): 1764, 1705, 1666, 1246 cm^{-1} .

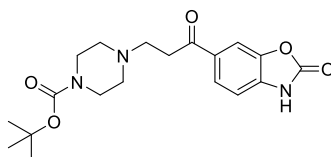
^1H NMR (DMSO- d_6 , 400 MHz): δ 11.99 (s, 1H), 7.87–7.84 (m, 2H), 7.40–7.29 (m, 5H), 7.18 (d, $J = 8.7$ Hz, 1H), 5.07 (s, 2H), 3.40–3.35 (m, 4H), 3.18 (t, $J = 7.5$, 2H), 2.69 (t, $J = 7.2$, 2H), 2.42–2.39 (m, 4H).

^{13}C NMR (DMSO- d_6 , 101 MHz): δ 197.5, 154.7, 154.3, 143.4, 136.9, 135.2, 130.9, 128.4, 127.8, 127.5, 125.0, 109.4, 108.8, 66.1, 52.8, 52.3, 43.4, 35.4.

HRMS: exact mass calculated for $[\text{M}+\text{H}]^+$ ($\text{C}_{22}\text{H}_{24}\text{N}_3\text{O}_5$) requires 410.1710 m/z , found 410.1710 m/z .

HRMS ($\text{C}_{22}\text{H}_{23}\text{N}_3\text{O}_5$) $[\text{M}+\text{H}^+]$ requires 410.1710, found $[\text{M}+\text{H}^+]$ 410.1710.

***Tert*-Butyl 4-(3-oxo-3-(2-oxo-2,3-dihydrobenzo[*d*]oxazol-6-yl)propyl)piperazine-1-carboxylate, 2.43.**



Prepared according to General Procedure **J**, using 6-(3-chloropropanoyl)benzo[*d*]oxazol-2(3*H*)-one **2.6** (200 mg, 0.89 mmol, 1.0 equiv), MeCN (5 mL), Et_3N (90 μL , 0.64 mmol, 1.2 equiv), *tert*-butyl piperazine-1-carboxylate (181.5 mg, 0.97 mmol, 1.1 equiv) to afford the desired product as a white solid (297 mg, 89%). Consistent with previously reported data.^{95,140}

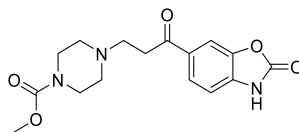
ν_{\max} (neat): 1772, 1764, 1168 cm^{-1} .

^1H NMR (DMSO- d_6 , 400 MHz): δ 7.86–7.82 (m, 2H), 7.17 (d, $J = 8.6$ Hz, 1H), 3.31–3.25 (m, 4H), 3.17 (t, $J = 7.2$ Hz, 2H), 2.68 (t, $J = 7.2$ Hz, 2H), 2.40–2.33 (m, 4H), 1.39 (s, 9H).

^{13}C NMR (DMSO- d_6 , 101 MHz): δ 197.5, 154.6, 153.8, 143.4, 135.2, 130.9, 125.0, 109.3, 108.8, 78.7, 52.9, 52.4, 35.4, 28.0. $1 \times \text{C}$ not observed (coincident).

HRMS: exact mass calculated for $[\text{M}+\text{H}]^+$ ($\text{C}_{19}\text{H}_{25}\text{N}_3\text{O}_5$) requires m/z 376.1867, found m/z 376.1866.

Methyl 4-(3-oxo-3-(2-oxo-2,3-dihydrobenzo[*d*]oxazol-6-yl)propyl)piperazine-1-carboxylate, 2.44.



Prepared according to General Procedure **J**, using using 6-(3-chloropropanoyl)benzo[*d*]oxazol-2(3*H*)-one **2.6** (201.1 mg, 0.89 mmol, 1.0 equiv), MeCN (5 mL), PS-DIPEA (0.48 g, 0.64 mmol, 1.2 equiv), methyl piperazine-1-carboxylate (144 μ L, 0.98 mmol, 1.1 equiv) to afford the desired product as a white solid (219.6 mg, 74%).

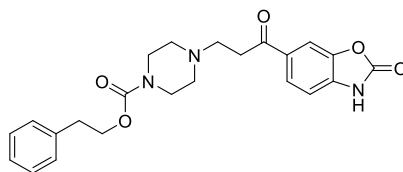
ν_{\max} (neat): 1774, 1687, 1168 cm^{-1} .

^1H NMR (DMSO-*d*₆, 400 MHz): δ 7.87–.83 (m, 2H), 7.18 (d, $J = 8.6$ Hz, 1H), 3.58 (s, 3H), 3.39 – 3.29 (m, 4H), 3.18 (t, $J = 7.2$ Hz, 2H), 2.70 (t, $J = 7.1$ Hz, 2H), 2.45–2.32 (m, 4H).

^{13}C NMR (DMSO-*d*₆, 101 MHz): δ 197.5, 154.6, 153.8, 143.4, 135.2, 130.9, 125.0, 109.3, 108.8, 78.7, 52.9, 52.4, 35.4, 28.0.

HRMS: exact mass calculated for $[\text{M}+\text{H}]^+$ ($\text{C}_{16}\text{H}_{20}\text{N}_3\text{O}_5$) requires 334.1397 m/z , found 334.1395 m/z .

Phenethyl 4-(3-oxo-3-(2-oxo-2,3-dihydrobenzo[*d*]oxazol-6-yl)propyl)piperazine-1-carboxylate, 2.46.



Prepared according to General Procedure **J**, using 6-(3-chloropropanoyl)benzo[*d*]oxazol-2(3*H*)-one **2.18 b** (172 mg, 0.76 mmol, 1.0 equiv), phenethyl piperazine-1-carboxylate **2.6** (280 mg, 0.84 mmol, 1.1 equiv), NEt_3 (128 μ L, 0.91 mmol, 1.2 equiv), MeCN (2 mL) to afford the desired product as a white solid (52 mg, 16%). Consistent with previously reported data.⁹⁵

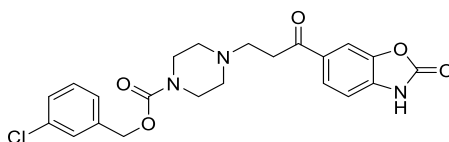
ν_{\max} (neat): 3441, 2825, 1775, 1699, 1438 cm^{-1} .

^1H NMR (DMSO- d_6 , 500 MHz): δ 7.85–7.83 (m, 2H), 7.32–7.20 (m, 5H), 7.18 (d, J = 8.4 Hz, 1H), 4.18 (t, J = 6.8 Hz, 2H), 3.34–3.26 (m, 4H), 3.17 (t, J = 7.1 Hz, 2H), 2.88 (t, J = 6.7 Hz, 2H), 2.36 (t, J = 7.1 Hz, 2H), 2.41–2.28 (m, 4H).

^{13}C NMR (DMSO- d_6 , 101 MHz): δ 197.4, 154.6, 154.3, 143.3, 138.2, 135.0, 130.9, 128.9, 128.3, 126.3, 125.0, 109.3, 108.9, 65.3, 52.8, 52.2, 43.3, 35.4, 34.8.

HRMS: exact mass calculated for $[\text{M}+\text{H}]^+$ ($\text{C}_{23}\text{H}_{26}\text{N}_3\text{O}_5$) $[\text{M}+\text{H}]^+$ requires 424.1867 m/z , found 424.1863 m/z .

3-chlorobenzyl 4-(3-oxo-3-(2-oxo-2,3-dihydrobenzo[*d*]oxazol-6-yl)propyl)piperazine-1-carboxylate, 2.47.



Prepared according to General Procedure **J**, using 6-(3-chloropropanoyl)benzo[*d*]oxazol-2(3*H*)-one **2.6** (91 mg, 0.40 mmol, 1.0 equiv), 3-chlorobenzyl piperazine-1-carboxylate **2.22 c** (100 mg, 0.44 mmol, 1.1 equiv), NEt_3 (67 μL , 0.48 mmol, 1.2 equiv), MeCN (2 mL) to afford the desired product as white solid (43 mg, 19% over 2 steps). Consistent with previously reported data.⁹⁵

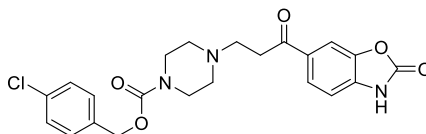
ν_{max} (neat): 1763, 1676, 1448, 1196 cm^{-1} .

^1H NMR (DMSO- d_6 , 500 MHz): 7.87–7.83 (m, 2H), 7.44–7.30 (m, 5H), 7.17 (d, J = 8.6 Hz, 1H), 5.07 (s, 2H), 3.46–3.29 (m, 4H, under H_2O peak), 3.18 (t, J = 7.1 Hz, 2H), 2.69 (t, J = 7.1 Hz, 2H), 2.45–2.36 (m, 4H).

^{13}C NMR (DMSO- d_6 , 101 MHz): δ 197.4, 154.8, 154.2, 143.4, 139.5, 135.4, 133.0, 130.8, 130.3, 127.7, 127.3, 126.1, 125.0, 109.3, 108.8, 65.3, 52.9, 52.3, 43.5, 35.4.

HRMS: exact mass calculated for $[\text{M}-\text{H}]^-$ ($\text{C}_{22}\text{H}_{21}\text{ClN}_3\text{O}_5$) $[\text{M}-\text{H}]^-$ requires 442.1167 m/z , found 442.1175 m/z .

4-chlorobenzyl 4-(3-oxo-3-(2-oxo-2,3-dihydrobenzo[*d*]oxazol-6-yl)propyl)piperazine-1-carboxylate, 2.48.



Prepared according to General Procedure **J**, using 6-(3-chloropropanoyl)benzo[*d*]oxazol-2(3*H*)-one **2.6** (86 mg, 0.38 mmol, 1.0 equiv), 4-chlorobenzyl piperazine-1-carboxylate **2.22 d** (107 mg, 0.42 mmol, 1.1 equiv), NEt₃ (64 μL, 0.46 mmol, 1.2 equiv), MeCN (2 mL) and purified by trituration in MeOH and vacuum filtration to afford the desired product as a white solid (57 mg, 36%). Consistent with previously reported data.⁹⁵

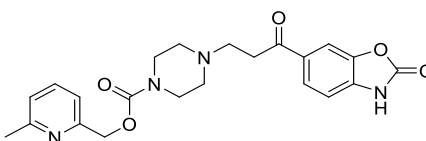
ν_{max} (neat): 3443, 2825, 1770, 1691, 1438 cm⁻¹.

¹H NMR (DMSO-*d*₆, 500 MHz): δ 7.88–7.85 (m, 2H), 7.46–7.35 (m, 4H), 7.19 (d, *J* = 8.5 Hz, 1H), 5.07 (s, 2H), 3.43–3.34 (m, 4H), 3.19 (t, *J* = 7.1 Hz, 2H), 2.70 (t, *J* = 7.1 Hz, 2H), 2.45–2.38 (m, 4H). 1 × H not observed (exchangeable).

¹³C NMR (DMSO-*d*₆, 101 MHz): δ 197.4, 154.6, 154.2, 143.3, 135.9, 135.1, 132.4, 130.9, 129.4, 128.4, 125.0, 109.3, 108.9, 65.3, 52.8, 52.3, 43.4, 35.4.

HRMS: exact mass calculated for [M+H]⁺ (C₂₂H₂₃ClN₃O₅) requires 444.1321 *m/z*, found 444.1319 *m/z*.

(6-methylpyridin-2-yl)methyl 4-(3-oxo-3-(2-oxo-2,3-dihydrobenzo[*d*]oxazol-6-yl)propyl)piperazine-1-carboxylate, 2.51.



Prepared according to General Procedure **J**, using 6-(3-chloropropanoyl)benzo[*d*]oxazol-2(3*H*)-one **2.6** (87 mg, 0.39 mmol, 1.0 equiv), (6-methylpyridin-2-yl)methyl piperazine-1-carboxylate **2.22 e** (100 mg, 0.43 mmol, 1.1 equiv), NEt₃ (66 μL, 0.47 mmol, 1.2 equiv), MeCN (2 mL) to afford the desired product as a white solid (41 mg, 24%).

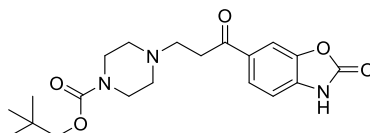
ν_{max} (neat): 3383, 2912, 1782, 1684, 1630, 1444 cm⁻¹.

^1H NMR (DMSO- d_6 , 500 MHz): δ 7.87 (d, $J = 7.5$ Hz, 2H), 7.70 (t, $J = 7.7$ Hz, 1H), 7.22–7.16 (m, 2H), 7.15 (d, $J = 7.7$ Hz, 1H), 5.09 (s, 2H), 3.52–3.34 (m, 4H) (partially under H₂O peak), 3.20 (t, $J = 7.0$ Hz, 2H), 2.72 (t, $J = 7.0$ Hz, 2H), 2.45 (m, 7H).

^{13}C NMR (DMSO- d_6 , 101 MHz): δ 197.5, 157.4, 155.8, 154.6, 154.2, 143.4, 137.2, 134.1, 130.9, 125.0, 122.1, 117.8, 109.4, 108.9, 66.8, 52.9, 52.3, 43.5, 35.4, 23.9.

HRMS: exact mass calculated for $[\text{M}+\text{H}]^+$ (C₂₂H₂₄N₄O₅) $[\text{M}+\text{H}]^+$ requires 425.1819 m/z , found 425.1817 m/z .

Neopentyl 4-(3-oxo-3-(2-oxo-2,3-dihydrobenzo[*d*]oxazol-6-yl)propyl)piperazine-1-carboxylate, 2.52.



Prepared according to General Procedure **J**, using 6-(3-chloropropanoyl)benzo[*d*]oxazol-2(3*H*)-one **2.6** (255 mg, 1.13 mmol, 1.0 equiv), neopentyl piperazine-1-carboxylate **2.22 f** (250 mg, 1.25 mmol, 1.1 equiv), NEt₃ (190 μL , 1.36 mmol, 1.2 equiv), MeCN (2 mL) to afford the desired product as a white solid (113 mg, 23%).

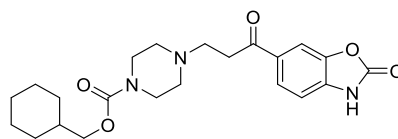
ν_{max} (neat): 3275, 2961, 1780, 1699 cm^{-1} .

^1H NMR (DMSO- d_6 , 500 MHz): δ 7.88–7.83 (m, 2H), 7.17 (d, $J = 8.5$ Hz, 1H), 3.69 (s, 2H), 3.44–3.29 (m, 4H), 3.18 (t, $J = 7.1$ Hz, 2H), 2.69 (t, $J = 7.1$ Hz, 2H), 2.43–2.36 (m, 4H), 0.89 (s, 9H).

^{13}C NMR (DMSO- d_6 , 101 MHz): δ 197.4, 154.6, 154.6, 143.4, 135.0, 130.9, 125.0, 109.3, 108.9, 73.8, 52.9, 52.3, 43.3, 35.4, 31.3, 26.2.

HRMS: exact mass calculated for $[\text{M}+\text{H}]^+$ (C₂₀H₂₇N₃O₅) requires 390.2023 m/z , found 390.2025 m/z .

Cyclohexylmethyl 4-(3-oxo-3-(2-oxo-2,3-dihydrobenzo[*d*]oxazol-6-yl)propyl)piperazine-1-carboxylate, 2.53.



Prepared according to General Procedure **J**, using 6-(3-chloropropanoyl)benzo[*d*]oxazol-2(3*H*)-one **2.6** (91 mg, 0.40 mmol), cyclohexylmethyl piperazine-1-carboxylate **2.22 g** (100 mg, 0.44 mmol), NEt₃ (67 μL, 0.48 mmol), MeCN (2 mL) at 80 °C for 2 h to afford the desired product as a white solid (43 mg, 26%).

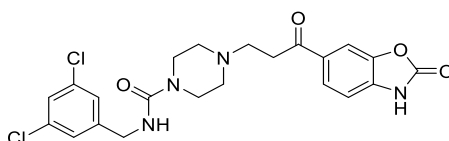
ν_{max} (neat): 3454, 2927, 2855, 1769, 1671, 1622, 1425 cm⁻¹.

¹H NMR (DMSO-*d*₆, 500 MHz): δ 7.89–7.81 (m, 2H), 7.18 (d, *J* = 8.6 Hz, 1H), 3.81 (t, *J* = 8.3 Hz, 2H), 3.40–3.25 (m, 4H), 3.19 (dd, *J* = 9.6, 16.6 Hz, 2H), 2.70 (t, *J* = 7.1 Hz, 2H), 2.45–2.34 (m, 4H), 1.74–1.53 (m, 6H), 1.28–1.04 (m, 4H), 0.94 (dd, *J* = 11.0, 22.2 Hz, 2H).

¹³C NMR (DMSO-*d*₆, 101 MHz): δ 197.5, 154.6, 143.4, 135.2, 130.9, 125.0, 109.3, 108.8, 69.6, 52.9, 52.3, 43.3, 36.9, 35.4, 29.1, 25.9, 25.2.1 × C not observed (coincident).

HRMS: exact mass calculated for [M+H]⁺ (C₂₂H₃₀N₃O₅) requires 424.1867 *m/z*, found 424.1863 *m/z*.

***N*-(3,5-dichlorobenzyl)-4-(3-oxo-3-(2-oxo-2,3-dihydrobenzo[*d*]oxazol-6-yl)propyl)piperazine-1-carboxamide, 2.54.**



Prepared according to General Procedure **J**, using 6-(3-chloropropanoyl)benzo[*d*]oxazol-2(3*H*)-one **2.6** (75 mg, 0.33 mmol), *N*-(3,5-dichlorobenzyl)piperazine-1-carboxamide **2.22 h** (105 mg, 0.36 mmol), NEt₃ (56 μL, 0.40 mmol), MeCN (2 mL) at 80 °C for 2 h to afford the desired product as a beige solid (12 mg, 11%). Consistent with previously reported data.⁹⁵

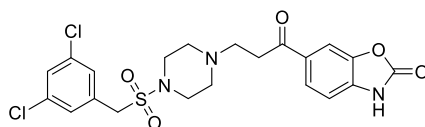
ν_{max} (neat): 3365, 3024, 2935, 2864, 1764, 1664.

^1H NMR (DMSO- d_6 , 500 MHz) δ 7.88–7.84 (m, 2H), 7.46–7.42 (app. s, 1H), 7.31–7.26 (m, 2H), 7.19–7.12 (m, 2H), 4.23–4.19 (app. d, 2H), 3.34–3.27 (m, 4H under H₂O peak), 3.19 (t, $J = 7.1$ Hz, 2H), 2.68 (t, $J = 7.1$ Hz, 2H), 2.41–2.34 (m, 4H).

^{13}C NMR (DMSO- d_6 , 101 MHz): δ 157.0, 154.5, 145.3, 143.4, 135.2, 133.8, 130.4, 126.2, 126.0, 125.2, 109.5, 109.0, 51.4, 42.8, 42.5, 41.5, 40.5. 1 \times C not observed (coincident).

HRMS: exact mass calculated for $[\text{M}+\text{H}]^+$ (C₂₂H₂₃Cl₂N₄O₄) requires 477.0191 m/z , found 477.1084 m/z .

6-(3-(4-((3,5-dichlorobenzyl)sulfonyl)piperazin-1-yl)propanoyl)benzo[*d*]oxazol-2(3*H*)-one, 2.55.



Prepared according to General Procedure **J**, using 6-(3-chloropropanoyl)benzo[*d*]oxazol-2(3*H*)-one **2.6** (60 mg, 0.26 mmol, 1.0 equiv), 1-((3,5-dichlorobenzyl)sulfonyl)piperazine **2.27** (90 mg, 0.29 mmol, 1.1 equiv), NEt₃ (43 μL , 0.31 mmol, 1.2 equiv), MeCN (2 mL) to afford the desired product as white solid (41 mg, 24%).

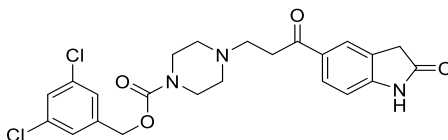
ν_{max} (neat): 2929, 2823, 1775, 1678, 1440, 1267 cm^{-1} .

^1H NMR (DMSO- d_6 , 400 MHz): 7.88–7.84 (m, 2H), 7.65–7.62 (m, 1H), 7.50–7.46 (m, 2H), 7.19 (d, $J = 8.0$ Hz, 1H), 4.50 (s, 2H), 3.20 (t, $J = 7.0$ Hz, 2H), 3.16–3.08 (m, 4H), 2.72 (t, $J = 7.0$ Hz, 2H), 2.49–2.43 (m, 4H). 1 \times H not observed (exchangeable).

^{13}C NMR (DMSO- d_6 , 101 MHz): δ 197.4, 154.6, 143.4, 135.1, 133.8, 133.8, 130.9, 129.6, 127.8, 125.0, 109.3, 108.9, 52.9, 52.6, 52.1, 45.4, 35.4.

HRMS: exact mass calculated for $[\text{M}-\text{H}]^+$ (C₂₁H₂₁Cl₂N₃O₅S) requires 498.0652 m/z , found 498.0645 m/z .

3,5-dichlorobenzyl 4-(3-oxo-3-(2-oxoindolin-5-yl)propyl)piperazine-1-carboxylate, 2.56.



Prepared according to General Procedure **J**, using 5-(3-chloropropanoyl)indolin-2-one **2.10** (70 mg, 0.31 mmol, 1.0 equiv), 3,5-dichlorobenzyl piperazine-1-carboxylate **2.22 a** (104 mg, 0.49 mmol, 1.1 equiv), NEt₃ (72 μL, 0.54 mmol, 1.2 equiv), MeCN (3 mL) at 50 °C for 48 h. The reaction was diluted with H₂O (20 mL), the organics were extracted using EtOAc (2 × 20 mL), dried with a hydrophobic frit, and concentrated *in vacuo* to give a residue that was purified by column chromatography with silica (2–10% MeOH in EtOAc) to afford the desired product as an orange solid (19 mg, 11%).

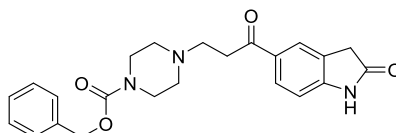
ν_{max} (neat): 2921, 2852, 1673, 1615, 1234, 734 cm⁻¹.

¹H NMR (DMSO-*d*₆, 400 MHz): 10.77 (s, 1H), 7.89 (dd, *J* = 1.6, 8.2, 2H), 7.86–7.81 (m, 1H), 7.58 (t, *J* = 1.9 Hz, 1H), 7.43 (d, *J* = 1.9 Hz, 1H), 6.90 (d, *J* = 8.2 Hz, 1H), 5.08 (s, 2H), 3.56 (s, 2H), 3.48–3.37 (m, 4H), 3.13 (t, *J* = 7.2 Hz, 2H), 2.69 (t, *J* = 7.2 Hz, 2H), 2.45–2.36 (m, 4H).

¹³C NMR (DMSO-*d*₆, 101 MHz): δ 197.6, 176.7, 154.0, 148.3, 141.2, 134.0, 129.1, 127.4, 126.1, 125.0, 124.2, 108.7, 64.7, 53.0, 52.3, 43.5, 35.5, 35.2.

HRMS: exact mass calculated for (C₂₃H₂₄Cl₂N₃O₄) [M+H⁺] requires 476.1138 *m/z*, found, 476.1133 *m/z*.

Benzyl 4-(3-oxo-3-(2-oxoindolin-5-yl)propyl)piperazine-1-carboxylate, 2.57.



Prepared according to General Procedure **J**, using 5-(3-chloropropanoyl)indolin-2-one **2.10** (70 mg, 0.31 mmol, 1.0 equiv), benzyl piperazine-1-carboxylate **2.22 b** (95 μL, 0.36 mmol, 1.1 equiv), NEt₃ (53 μL, 0.38 mmol, 1.2 equiv), MeCN (2 mL) at 50 °C for 16 h. The reaction was diluted with H₂O (20 mL) and the organics were extracted using EtOAc (2 × 20 mL), dried with a hydrophobic frit and concentrated *in vacuo* to afford a residue that was purified

by column chromatography with silica (2–10% MeOH in EtOAc) to afford the desired product as an orange solid (40 mg, 22%).

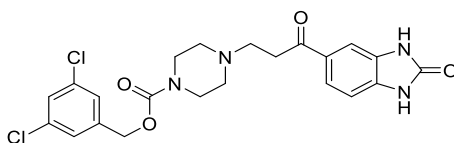
ν_{\max} (neat): 2922, 1691, 1614, 1236, 1118 cm^{-1} .

^1H NMR (DMSO- d_6 , 400 MHz): δ 7.94–7.84 (m, 2H), 7.42–7.30 (m, 5H), 6.95 (d, $J = 8.2$ Hz, 1H), 5.15 (s, 2H), 3.59 (s, 2H), 3.57–3.49 (m, 4H), 3.15 (t, $J = 7.3$ Hz, 2H), 2.87 (t, $J = 7.3$ Hz, 2H), 2.56–2.43 (m, 4H). $1 \times \text{H}$ not observed (exchangeable).

^{13}C NMR (DMSO- d_6 , 101 MHz): δ 197.0, 177.2, 154.7, 146.6, 136.2, 131.2, 129.0, 128.0, 127.5, 127.4, 125.1, 124.1, 108.8, 66.7, 52.7, 52.4, 43.2, 35.4, 35.3.

HRMS: exact mass calculated for ($\text{C}_{23}\text{H}_{26}\text{N}_3\text{O}_4$) [$\text{M}+\text{H}^+$] requires 408.1918 m/z , found 408.1916 m/z .

3,5-dichlorobenzyl 4-(3-oxo-3-(2-oxo-2,3-dihydro-1H-benzo[d]imidazol-5-yl)propyl)piperazine-1-carboxylate, 2.58.



Prepared according to General Procedure **J**, using 5-(3-chloropropanoyl)-1,3-dihydro-2H-benzo[d]imidazol-2-one **2.8** (71 mg, 0.31 mmol, 1.0 equiv), 3,5-dichlorobenzyl piperazine-1-carboxylate **2.22 a** (103 mg, 0.35 mmol, 1.1 equiv), NEt_3 (52 μL , 0.37 mmol, 1.2 equiv), MeCN (2 mL) at 80 $^\circ\text{C}$ for 0.5 h. The reaction was cooled and Et_2O (10 mL) added and the white precipitate was collected and filtered under vacuum with H_2O (50 mL), washed with 1N HCl (10 mL), H_2O (20 mL) and dried in a vacuum dessicator to afford the desired product as white solid (47.8 mg, 29%).

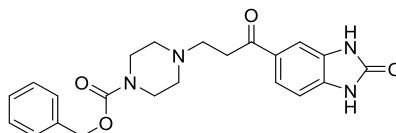
ν_{\max} (neat): 2952, 2424, 1714, 1671 cm^{-1} .

^1H NMR (DMSO- d_6 , 400 MHz): 11.02 (s, 1H), 10.86 (s, 1H), 7.71 (d, $J = 8.3$, 1H), 7.61–7.55 (m, 1H), 7.55–7.50 (m, 1H), 7.50–7.42 (m, 2H), 7.06 (d, $J = 8.2$ Hz, 1H), 5.08 (s, 2H), 4.20–4.04 (m, 2H), 3.70–3.36 (m, 8H), 3.20–3.01 (m, 2H).

^{13}C NMR (DMSO- d_6 , 101 MHz): δ 156.0, 154.4, 141.3, 134.9, 134.6, 130.3, 129.5, 128.0, 126.8, 122.9, 108.5, 108.3, 65.6, 51.3, 45.9, 42.7, 8.9. $1 \times \text{C}$ not observed (coincident).

HRMS: exact mass calculated for (C₂₂H₂₃Cl₂N₄O₄) [M+H⁺] requires 477.1086 *m/z*, found 477.1085 *m/z*.

Benzyl 4-(3-oxo-3-(2-oxo-2,3-dihydro-1*H*-benzo[*d*]imidazol-5-yl)propyl)piperazine-1-carboxylate, 2.59.



Prepared according to General Procedure **J**, using 5-(3-chloropropanoyl)-1,3-dihydro-2*H*-benzo[*d*]imidazol-2-one **2.8** (100 mg, 0.45 mmol, 1.0 equiv), benzyl piperazine-1-carboxylate **2.22 b** (94 μ L, 0.49 mmol, 1.1 equiv), NEt₃ (76 μ L, 0.54 mmol, 1.2 equiv), MeCN (2 mL) at 80 °C for 0.5 h. The reaction was cooled and Et₂O (10 mL) added and the white precipitate was collected and filtered under vacuum with H₂O (50 mL), washed with 1N HCl (10 mL), H₂O (20 mL) and dried in a vacuum dessicator to afford the desired product as white solid (83.5 mg, 45%).

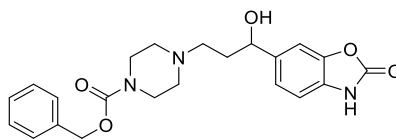
ν_{max} (neat): 3084, 2822, 2770, 1749, 1690, 1666 cm⁻¹.

¹H NMR (DMSO-*d*₆, 400 MHz): 11.02 (s, 1H), 10.85 (s, 1H), 7.69 (dd, *J* = 1.6, 8.2, 1H), 7.49 (d, *J* = 1.5, 1H), 7.43–7.27 (m, 5H), 7.01 (d, *J* = 8.2 Hz, 1H), 5.08 (s, 2H), 3.42–3.35 (m, 4H), 3.14 (t, *J* = 7.2, 2H), 2.69 (t, *J* = 7.1, 2H), 2.45–2.37 (m, 4H).

¹³C NMR (DMSO-*d*₆, 101 MHz): δ 197.7, 155.4, 154.3, 136.9, 134.0, 129.8, 129.7, 128.4, 127.8, 127.5, 122.3, 107.9, 107.7, 66.1, 53.0, 52.3, 43.4, 35.3.

HRMS: exact mass calculated for (C₂₂H₂₅N₄O₄) [M+H⁺] requires 409.1870 *m/z*, found [M+H⁺] 409.1870 *m/z*.

Benzyl 4-(3-hydroxy-3-(2-oxo-2,3-dihydrobenzo[*d*]oxazol-6-yl)propyl)piperazine-1-carboxylate, 2.61.



Prepared according to General Procedure **I**, using benzyl 4-(3-oxo-3-(2-oxo-2,3-dihydrobenzo[*d*]oxazol-6-yl)propyl)piperazine-1-carboxylate **2.42** (100 mg, 0.24 mmol, 1.0 equiv), NaBH₄ (35 mg, 0.92 mmol, 3.8 equiv) and EtOH (5 mL) and purified by trituration in CH₂Cl₂ to afford the desired product as a white solid (96 mg, 96%).

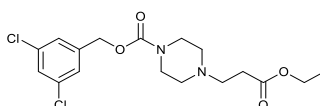
ν_{\max} (neat): 3345, 1705, 999, 815 cm⁻¹.

¹H NMR (DMSO-*d*₆, 400 MHz): δ 7.42–7.27 (m, 5H), 7.15 (d, *J* = 1.1 Hz, 1H), 7.03 (dd, *J* = 1.3, 8.1 Hz, 1H), 6.95 (d, *J* = 7.9 Hz, 1H), 5.06 (s, 2H), 4.58 (dd, *J* = 5.1, 7.6, 1H), 3.42–3.28 (m, 4H), 2.38–2.23 (m, 6H), 1.80–1.65 (m, 2H). 2 × H not observed (exchangeable).

¹³C NMR (DMSO-*d*₆, 101 MHz): δ 156.4, 154.9, 144.3, 140.2, 137.4, 131.6, 128.9, 128.3, 128.0, 121.2, 109.7, 106.9, 71.4, 66.6, 55.2, 53.0, 44.0, 36.8.

HRMS: exact mass calculated for [M+H]⁺ (C₂₂H₂₆N₃O₅) requires *m/z* 429.1802, found *m/z* 429.1800.

3,5-dichlorobenzyl 4-(3-ethoxy-3-oxopropyl)piperazine-1-carboxylate, 2.62.



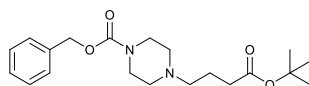
Prepared according to General Procedure **J**, using ethyl 3-chloropropanoate (428 mg, 3.13 mmol, 1.0 equiv), 3,5-dichlorobenzyl piperazine-1-carboxylate (1.0 g, 3.45 mmol, 1.1 equiv), NEt₃ (526 μ L, 3.76 mmol, 1.2 equiv), MeCN (10 mL) at 50 °C for 16 h. The reaction was diluted with H₂O (20 mL), the organics were extracted using CH₂Cl₂ (2 × 20 mL), dried with a hydrophobic frit, and concentrated *in vacuo* to give a residue that was purified by column chromatography with silica (60–80% EtOAc in petroleum ether) to afford the desired product as a white solid, which was telescoped into the next step for the synthesis of **2.64**.

ν_{\max} (neat): 2981, 2942, 2905, 2815, 1699, 1574, 1232 cm⁻¹

^1H NMR (CDCl_3 , 500 MHz): 7.27 (t, $J = 3.1$ Hz, 1H), 7.22–7.17 (m, 2H), 5.04 (s, 2H), 4.12 (q, $J = 7.1$ Hz, 2H), 3.53–3.44 (m, 4H), 2.70 (t, $J = 7.2$ Hz, 2H), 2.51–2.38 (m, 6H), 1.27–1.19 (m, 3H).

^{13}C NMR (CDCl_3 , 101 MHz): δ 171.7, 154.1, 139.6, 134.6, 127.6, 125.6, 65.0, 60.0, 53.0, 52.0, 43.3, 31.8, 13.7.

3,5-dichlorobenzyl 4-(4-(*tert*-butoxy)-4-oxobutyl)piperazine-1-carboxylate, 2.63.

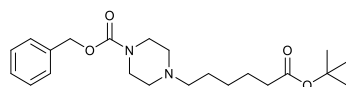


Prepared according to General Procedure **J**, using *tert*-butyl 4-bromobutanoate (164 mg, 0.76 mmol, 1.0 equiv), benzyl piperazine-1-carboxylate (161 mg, 0.83 mmol, 1.1 equiv), NEt_3 (109 μL , 0.83 mmol, 1.2 equiv), MeCN (20 mL) at 80 $^\circ\text{C}$ for 5 h. The reaction was concentrated *in vacuo* to give a residue that was purified by column chromatography with silica (2–10% MeOH in CH_2Cl_2) to afford the desired product as a white solid which was telescoped into the next step for the synthesis of **2.65**.

^1H NMR (CDCl_3 , 400 MHz): 7.37–7.26 (m, 5H), 5.12 (s, 2H), 3.54–3.45 (m, 4H), 2.44–2.31 (m, 6H), 2.24 (t, $J = 7.4$ Hz, 2H), 1.82–1.71 (m, 2H), 1.43 (s, 9H).

^{13}C NMR (CDCl_3 , 101 MHz): δ 172.3, 154.7, 136.2, 128.0, 127.5, 127.4, 79.7, 66.6, 57.1, 52.3, 43.2, 32.8, 27.6, 21.5.

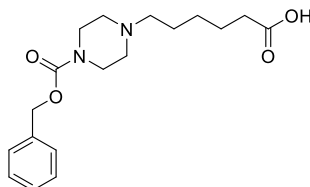
Benzyl 4-(6-(*tert*-butoxy)-6-oxohexyl)piperazine-1-carboxylate, 2.64.



Prepared according to General Procedure **J**, using *tert*-butyl 6-bromohexanoate (132 mg, 0.53 mmol, 1.0 equiv), benzyl piperazine-1-carboxylate (120 μL , 0.58 mmol, 1.1 equiv), NEt_3 (761 μL , 0.58 mmol, 1.2 equiv), MeCN (2 mL) at 80 $^\circ\text{C}$ for 2 h. The reaction was concentrated *in vacuo* to give a residue that was purified by column chromatography with silica (2–10% MeOH in CH_2Cl_2) to afford the desired product as a white solid which was telescoped into the next step for the synthesis of **2.66**.

^1H NMR (CDCl_3 , 400 MHz): 7.37–7.28 (m, 5H), 5.11 (s, 2H), 3.69–3.61 (m, 4H), 2.63–2.47 (m, 5H), 2.20 (t, $J = 7.4$ Hz, 2H), 1.69–1.55 (m, 5H), 1.42 (s, 9H), 1.37–1.28 (m, 2H).

6-(4-((benzyloxy)carbonyl)piperazin-1-yl)hexanoic acid, 2.66.



Prepared according to General Procedure **L**, using benzyl 4-(6-(*tert*-butoxy)-6-oxohexyl)piperazine-1-carboxylate **2.64** (85 mg, 0.22 mmol), trifluoroacetic acid (1 mL) and CH_2Cl_2 (1 mL). The reaction was concentrated *in vacuo* to a residue that was purified using silica chromatography (2–10% MeOH in EtOAc) to afford the desired product as a white solid (23 mg, 13% over 2 steps).

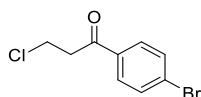
ν_{max} (neat): 3221, 3020, 1670, 1617 cm^{-1} .

^1H NMR (CDCl_3 , 400 MHz): δ 8.98 (s, 1H), 7.41–7.29 (m, 5H), 5.14 (s, 2H), 3.88–3.77 (m, 4H), 3.02–2.86 (m, 4H), 2.85–2.76 (m, 2H), 2.31 (t, $J = 7.2$ Hz, 2H), 1.76 (dt, $J = 7.8, 15.5$ Hz, 2H), 1.70–1.59 (m, 2H), 1.45–1.35 (m, 2H).

^{13}C NMR (CDCl_3 , 101 MHz): δ 176.4, 154.3, 135.6, 128.1, 127.8, 127.6, 67.2, 56.9, 51.3, 41.0, 33.6, 25.8, 23.9, 23.4.

HRMS: exact mass calculated for $[\text{M}+\text{H}]^+$ ($\text{C}_{18}\text{H}_{27}\text{N}_2\text{O}_4$) requires 335.1965 m/z , found 335.1961 m/z .

1-(4-bromophenyl)-3-chloropropan-1-one, 2.71.



Prepared according to General Procedure **A**, using 1-bromobenzene (1.34 mL, 1.3 mmol, 1.0 equiv), AlCl_3 (13.17 g, 9.8 mmol, 7.6 equiv), 3-chloropropanoyl chloride (1.52 mL, 1.6 mmol, 1.2 equiv), DMF (6 mL) at 70 $^\circ\text{C}$ for 2 h. The reaction was cooled and quenched onto ice

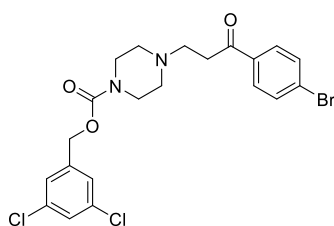
(500g) and the resulting precipitate filtered under vacuum to afford the desired product as a yellow solid (3.2 g, 100%). Commercially available, CAS: 31736-73-9.

ν_{\max} (neat): 2975, 2933, 1682, 1587, 1399 cm^{-1} .

^1H NMR (CDCl_3 , 400 MHz): 7.83 (d, $J = 8.6$ Hz, 2H), 7.64 (d, $J = 8.6$ Hz, 2H), 3.92 (t, $J = 6.8$ Hz, 12H), 3.43 (t, $J = 6.8$ Hz, 2H).

^{13}C NMR (CDCl_3 , 101 MHz): δ 195.9, 135.2, 132.2, 129.7, 129.0, 41.4, 38.6.

3,5-dichlorobenzyl 4-(3-(4-bromophenyl)-3-oxopropyl)piperazine-1-carboxylate, 2.72.



Prepared according to General Procedure J, using 1-(4-bromophenyl)-3-chloropropan-1-one **2.71** (78 mg, 0.31 mmol, 1.0 equiv), 3,5-dichlorobenzyl piperazine-1-carboxylate 2,2,2-trifluoroacetate **2.22 a** (100 mg, 0.35 mmol, 1.1 equiv), NEt_3 (52 μL , 0.37 mmol, 1.2 equiv), MeCN (4 mL) at 80 $^\circ\text{C}$ for 16 h. The reaction was diluted with Et_2O and H_2O (20 mL) added. The suspension was extracted using Et_2O (2×20 mL). The organics were then collected, dried (hydrophobic frit), and concentrated under vacuum to give a residue that was purified by silica chromatography (80–90% EtOAc in petroleum ether) to afford the desired product as a yellow solid (143 mg, 92%).

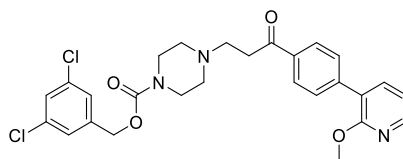
ν_{\max} (neat): 2158, 1699, 1678 cm^{-1} .

^1H NMR (CDCl_3 , 400 MHz): 7.83 (d, $J = 8.7$ Hz, 2H), 7.62 (d, $J = 8.6$ Hz, 2H), 7.31 (t, $J = 1.9$ Hz, 1H), 7.23 (d, $J = 1.9$ Hz, 2H), 5.08 (s, 2H), 3.58–3.50 (m, 4H), 3.15 (t, $J = 7.2$ Hz, 2H), 2.86 (t, $J = 7.2$ Hz, 2H), 2.55–2.45 (m, 4H).

^{13}C NMR (CDCl_3 , 101 MHz): δ 197.3, 154.1, 139.6, 135.1, 134.6, 131.5, 129.0, 127.9, 127.6, 125.6, 65.0, 52.5, 52.4, 43.4, 35.7.

HRMS: exact mass calculated for $(\text{C}_{21}\text{H}_{22}\text{BrCl}_2\text{N}_2\text{O}_3)$ $[\text{M}+\text{H}^+]$ requires 501.0162 m/z , found 501.0150 m/z .

3,5-dichlorobenzyl 4-(3-(4-(2-methoxypyridin-3-yl)phenyl)-3-oxopropyl)piperazine-1-carboxylate, 2.73.



Prepared according to General Procedure **K**, using 3,5-dichlorobenzyl 4-(3-(4-bromophenyl)-3-oxopropyl)piperazine-1-carboxylate **2.72** (50 mg, 0.10 mmol, 1.0 equiv), (2-methoxypyridin-3-yl)boronic acid (31.2 mg, 0.20 mmol, 2 equiv), Pd(dppf)Cl₂·CH₂Cl₂ (4 mg, 4 mol%), K₃PO₄ (65 mg, 0.31 mmol, 3.1 equiv), THF (0.4 mL) and H₂O (9 μL). The crude mixture was filtered through celite with EtOAc, concentrated under vacuum to a residue that was purified using column chromatography on silica (0–10% MeOH in EtOAc) to afford the desired product as a yellow solid (18 mg, 53%).

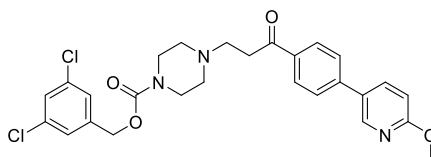
ν_{\max} (neat): 2927, 2857, 1705, 1574, 1456, 1395 cm⁻¹.

¹H NMR (CDCl₃, 400 MHz): δ 8.20 (dd, J = 1.9, 5.0 Hz, 1H), 8.01 (m, 2H), 7.68–7.62 (m, 3H), 7.30 (t, J = 1.9 Hz, 1H), 7.22 (d, J = 1.9 Hz, 2H), 7.02–6.98 (m, 1H), 5.07, (s, 2H), 3.98 (s, 3H), 3.55–3.50 (m, 4H), 3.21 (t, J = 7.2 Hz, 2H), 2.89 (t, J = 7.2 Hz, 2H), 2.54–2.48 (m, 4H).

¹³C NMR (CDCl₃, 101 MHz): δ 198.5, 160.9, 154.8, 146.8, 142.0, 140.3, 138.7, 135.8, 135.2, 129.6, 128.3, 128.1, 126.2, 123.5, 117.3, 65.7, 53.8, 53.2, 53.0, 44.0, 36.3.

HRMS: exact mass calculated for [M+H]⁺ (C₂₇H₂₈Cl₂N₃O₄) requires 528.1451 m/z , found 528.1445 m/z 513.1335.

3,5-dichlorobenzyl 4-(3-(4-(6-methoxypyridin-3-yl)phenyl)-3-oxopropyl)piperazine-1-carboxylate, 2.74.



Prepared according to General Procedure **K**, using 3,5-dichlorobenzyl 4-(3-(4-bromophenyl)-3-oxopropyl)piperazine-1-carboxylate **2.72** (53 mg, 0.11 mmol, 1.0 equiv), 2-methoxy-5-(4,4,5,5-tetramethyl-1,3,2-dioxaborolan-2-yl)pyridine (48 mg, 0.22 mmol, 2.0 equiv),

Pd(dppf)Cl₂·CH₂Cl₂ (6 mg, 7 mol%), K₃PO₄ (67 mg, 0.32 mmol, 2.90 equiv), THF (0.4 mL) and H₂O (9 μL). The crude mixture was filtered through celite with EtOAc, concentrated under vacuum to a residue that was purified using column chromatography on silica (0–10% MeOH in EtOAc) to afford the desired product as a yellow solid (38 mg, 70%).

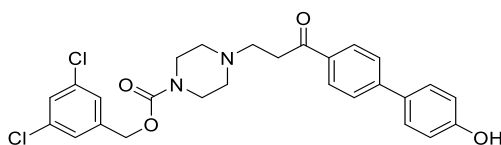
ν_{max} (neat): 2943, 1700, 1683, 1290 cm⁻¹.

¹H NMR (CDCl₃, 400 MHz): δ 8.46 (d, *J* = 2.5 Hz, 1H), 8.05 (d, *J* = 8.4 Hz, 2H), 7.85 (dd, *J* = 2.65, 8.6 Hz, 1H), 7.65 (d, *J* = 8.4 Hz, 2H), 7.34–7.31 (m, 1H), 7.24 (d, *J* = 1.8 Hz, 2H), 6.87 (d, *J* = 8.6 Hz, 1H), 5.09, (s, 2H), 4.02 (s, 3H), 3.59–3.51 (m, 4H), 3.22 (t, *J* = 7.2 Hz, 2H), 2.91 (t, *J* = 7.2 Hz, 2H), 2.56–2.48 (m, 4H).

¹³C NMR (CDCl₃, 101 MHz): δ 197.8, 163.8, 154.2, 144.9, 142.1, 139.7, 136.8, 135.1, 134.6, 128.3, 128.2, 127.7, 126.2, 125.6, 110.6, 65.0, 53.2, 52.6, 43.4, 35.7. 1 × C not observed (coincident).

HRMS: exact mass calculated for [M+H]⁺ (C₂₇H₂₈Cl₂N₃O₄) requires 513.1342 *m/z*, found 513.1335 *m/z*.

3,5-dichlorobenzyl 4-(3-(4'-hydroxy-[1,1'-biphenyl]-4-yl)-3-oxopropyl)piperazine-1-carboxylate, 2.75.



Prepared according to General Procedure **K**, using 3,5-dichlorobenzyl 4-(3-(4-bromophenyl)-3-oxopropyl)piperazine-1-carboxylate **2.72** (50 mg, 0.10 mmol, 1.0 equiv), 4-(4,4,5,5-tetramethyl-1,3,2-dioxaborolan-2-yl)phenol (45 mg, 0.20 mmol, 2.0 equiv), Pd(dppf)Cl₂·CH₂Cl₂ (6 mg, 7 mol%), K₃PO₄ (64 mg, 0.30 mmol, 3.0 equiv), THF (0.4 mL) and H₂O (9 μL). The crude mixture was filtered through celite with EtOAc, concentrated under vacuum to a residue that was purified using column chromatography on silica (80–100% EtOAc in petroleum ether) to afford the desired product as a white solid (26 mg, 50%).

ν_{max} (neat): 2921, 2865, 1571, 1699 cm⁻¹.

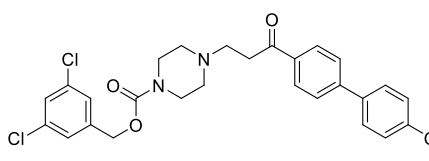
¹H NMR (CDCl₃, 400 MHz): δ 7.98 (d, *J* = 8.5 Hz, 2H), 7.62 (d, *J* = 8.6 Hz, 2H), 7.52 (d, *J* = 8.7 Hz, 2H), 7.31 (t, *J* = 1.9 Hz, 1H), 7.23 (d, *J* = 1.9 Hz, 2H), 6.93 (d, *J* = 8.7 Hz, 2H), 5.08

(s, 2H), 3.61–3.52 (m, 4H), 3.21 (t, $J = 7.2$ Hz, 2H), 2.91 (t, $J = 7.2$ Hz, 2H), 2.59–2.49 (m, 4H). 1 × H not observed (exchangeable).

^{13}C NMR (CDCl_3 , 101 MHz): δ 198.4, 156.7, 154.8, 145.6, 140.0, 135.1, 134.7, 131.8, 128.7, 128.6, 128.2, 126.6, 126.1, 116.2, 66.7, 53.2, 52.9, 43.7, 35.9.

HRMS: exact mass calculated for $[\text{M}+\text{H}]^+$ ($\text{C}_{27}\text{H}_{27}\text{Cl}_2\text{N}_2\text{O}_4$) requires 513.1342 m/z , found 513.1335 m/z .

3,5-dichlorobenzyl 4-(3-(4'-methoxy-[1,1'-biphenyl]-4-yl)-3-oxopropyl)piperazine-1-carboxylate, 2.76.



Prepared according to General **K**, using 3,5-dichlorobenzyl 4-(3-(4-bromophenyl)-3-oxopropyl)piperazine-1-carboxylate **2.72** (49 mg, 0.10 mmol, 1.0 equiv), (4-methoxyphenyl)boronic acid (33 mg, 0.22 mmol, 2.2 equiv), $\text{Pd}(\text{dppf})\text{Cl}_2 \cdot \text{CH}_2\text{Cl}_2$ (4 mg, 5 mol%), K_3PO_4 (72 mg, 0.34 mmol, 3.4 equiv), THF (0.4 mL) and H_2O (9 μL). The crude mixture was filtered through celite with EtOAc, concentrated under vacuum to a residue that was purified using column chromatography on silica (80–100% EtOAc in petroleum ether) to afford the desired product as a brown gum (29 mg, 55%).

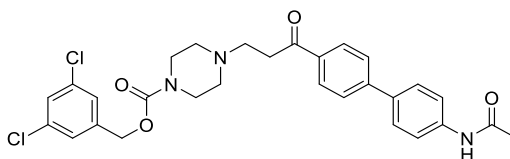
ν_{max} (neat): 3075, 2934, 1671, 1696, 1601 cm^{-1} .

^1H NMR (CDCl_3 , 400 MHz): δ 8.03 (d, $J = 8.6$ Hz, 2H), 7.67 (d, $J = 8.6$ Hz, 2H), 7.60 (d, $J = 8.9$ Hz, 2H), 7.32 (t, $J = 1.9$ Hz, 1H), 7.25 (d, $J = 1.9$ Hz, 2H), 7.02 (d, $J = 8.9$ Hz, 2H), 5.09 (s, 2H), 3.88 (s, 3H), 3.59–3.52 (m, 4H), 3.22 (t, $J = 7.2$ Hz, 2H), 2.91 (t, $J = 7.2$ Hz, 2H), 2.57–2.50 (m, 4H).

^{13}C NMR (CDCl_3 , 101 MHz): δ 197.9, 159.5, 154.2, 145.0, 139.6, 134.6, 134.4, 131.6, 128.2, 127.9, 127.7, 126.2, 125.6, 113.9, 65.0, 54.9, 52.7, 52.4, 43.4, 35.6.

HRMS: exact mass calculated for $[\text{M}+\text{H}]^+$ ($\text{C}_{28}\text{H}_{29}\text{Cl}_2\text{N}_2\text{O}_4$) requires 527.1499 m/z , found 527.1490 m/z .

3,5-dichlorobenzyl 4-(3-(4-acetamidophenyl)-3-oxopropyl)piperazine-1-carboxylate, 2.77.



Prepared according to General Procedure **K**, using 3,5-dichlorobenzyl 4-(3-(4-bromophenyl)-3-oxopropyl)piperazine-1-carboxylate **2.72** (52 mg, 0.10 mmol, 1.0 equiv), *N*-(4-(4,4,5,5-tetramethyl-1,3,2-dioxaborolan-2-yl)phenyl)acetamide (53 mg, 0.20 mmol, 2.0 equiv), Pd(dppf)Cl₂·CH₂Cl₂ (6 mg, 7 mol%), K₃PO₄ (63 mg, 0.30 mmol, 3.0 equiv), THF (0.4 mL) and H₂O (9 μL). The crude mixture was filtered through celite with EtOAc, concentrated under vacuum to a residue that was purified using column chromatography on silica (80% EtOAc in petroleum ether) to afford the desired product as a yellow solid (46 mg, 82%).

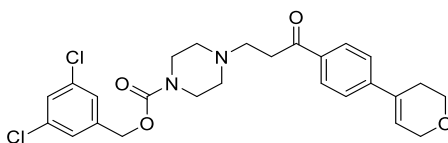
ν_{\max} (neat): 3344, 2925, 1664, 1598, 1241 cm⁻¹.

¹H NMR (CDCl₃, 400 MHz): δ 8.03–7.99 (m, 2H), 7.68–7.65 (m, 2H), 7.64–7.57 (m, 4H), 7.36 (s, 1H), 7.30 (t, *J* = 1.9 Hz, 1H), 7.22 (d, *J* = 1.9 Hz, 2H), 5.06 (s, 2H), 3.56–3.48 (m, 4H), 3.20 (t, *J* = 7.2 Hz, 2H), 2.88 (t, *J* = 7.2 Hz, 2H), 2.55–2.47 (m, 4H), 2.21 (s, 3H).

¹³C NMR (CDCl₃, 101 MHz): δ 198.5, 168.5, 154.8, 145.3, 140.2, 138.3, 135.6, 135.5, 135.2, 128.8, 128.3, 128.0, 127.0, 126.2, 120.3, 65.7, 53.3, 53.0, 44.0, 36.3, 24.8,

HRMS: exact mass calculated for [M+H]⁺ (C₂₃H₂₆Cl₂N₃O₄) requires 554.1608 *m/z*, found 554.1601 *m/z*.

3,5-dichlorobenzyl 4-(3-(4-(3,6-dihydro-2H-pyran-4-yl)phenyl)-3-oxopropyl)piperazine-1-carboxylate, 2.78.



Prepared according to General Procedure **K**, using 3,5-dichlorobenzyl 4-(3-(4-bromophenyl)-3-oxopropyl)piperazine-1-carboxylate **2.72** (50 mg, 0.10 mmol, 1.0 equiv), 2-(3,6-dihydro-2H-pyran-4-yl)-4,4,5,5-tetramethyl-1,3,2-dioxaborolane (50 mg, 0.24 mmol, 2.4 equiv),

Pd(dppf)Cl₂·CH₂Cl₂ (5 mg, 6 mol%), K₃PO₄ (86 mg, 0.41 mmol, 4.0 equiv), THF (0.4 mL) and H₂O (9 μL). The crude mixture was filtered through celite with EtOAc, concentrated under vacuum to a residue that was purified using column chromatography on silica (80% EtOAc in petroleum ether) to afford the desired product as a yellow solid (40 mg, 79%).

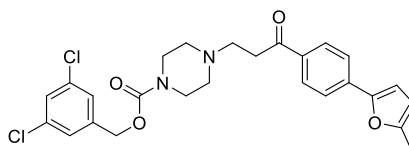
ν_{max} (neat): 2807, 1703, 1677 cm⁻¹.

¹H NMR (CDCl₃, 400 MHz): δ 7.95 (d, *J* = 8.4 Hz, 2H), 7.50 (d, *J* = 8.4 Hz, 2H), 7.34–7.31 (m, 1H), 7.24 (d, *J* = 1.6 Hz, 2H), 6.33–6.28 (m, 1H), 5.08 (s, 2H), 4.37 (q, *J* = 2.7 Hz, 2H), 3.97 (t, *J* = 5.4 Hz, 2H), 3.57–3.50 (m, 4H), 3.19 (t, *J* = 7.3 Hz, 2H), 2.88 (t, *J* = 7.2 Hz, 2H), 2.61–2.47 (m, 6H).

¹³C NMR (CDCl₃, 101 MHz): δ 197.8, 154.2, 144.3, 139.6, 135.0, 134.6, 132.9, 127.9, 127.7, 125.6, 124.6, 124.3, 65.4, 65.0, 63.8, 52.7, 52.4, 43.4, 35.6, 26.5.

HRMS: exact mass calculated for [M+H]⁺ (C₂₆H₂₉Cl₂N₂O₄) requires 503.1499 *m/z*, found 503.1486 *m/z*.

3,5-dichlorobenzyl 4-(3-(4-(5-methylfuran-2-yl)phenyl)-3-oxopropyl)piperazine-1-carboxylate, 2.79.



Prepared according to General Procedure **K**, using 3,5-dichlorobenzyl 4-(3-(4-bromophenyl)-3-oxopropyl)piperazine-1-carboxylate **2.72** (47 mg, 0.10 mmol, 1.0 equiv), 4,4,5,5-tetramethyl-2-(5-methylfuran-2-yl)-1,3,2-dioxaborolane (42 mg, 0.20 mmol, 2.0 equiv), Pd(dppf)Cl₂·CH₂Cl₂ (10 mg, 12 mol%), K₃PO₄ (70 mg, 0.33 mmol, 3.0 equiv), THF (0.4 mL) and H₂O (9 μL). The crude mixture was filtered through celite with EtOAc, concentrated under vacuum to a residue that was purified using column chromatography on silica (2–10% MeOH in EtOAc) to afford the desired product as a yellow solid (40 mg, 79%).

ν_{max} (neat): 2921, 1679, 1669, 1659 cm⁻¹.

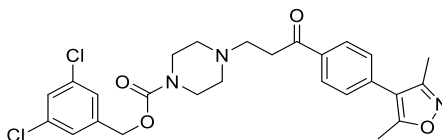
¹H NMR (CDCl₃, 400 MHz): δ 7.97 (d, *J* = 8.7 Hz, 2H), 7.71 (d, *J* = 8.6 Hz, 2H), 7.33 (t, *J* = 1.9 Hz, 1H), 7.25 (d, *J* = 1.9 Hz, 2H), 6.72 (d, *J* = 3.3 Hz, 1H), 6.15–6.12 (m, 1H), 5.09 (s,

2H), 3.59–3.51 (m, 4H), 3.20 (t, $J = 7.3$ Hz, 2H), 2.89 (t, $J = 7.3$ Hz, 2H), 2.59–2.479 (m, 4H), 2.42 (s, 3H).

^{13}C NMR (CDCl_3 , 101 MHz): δ 197.5, 154.2, 253.1, 150.6, 139.6, 134.8, 134.6, 134.1, 128.2, 127.7, 125.6, 122.5, 108.3, 107.9, 65.0, 52.7, 52.4, 43.4, 35.5, 13.3. $1 \times \text{C}$ not observed (coincident).

HRMS: exact mass calculated for $[\text{M}+\text{H}]^+$ ($\text{C}_{26}\text{H}_{27}\text{Cl}_2\text{N}_2\text{O}_4$) requires 501.1342 m/z , found 501.1329 m/z .

3,5-dichlorobenzyl 4-(3-(4'-methoxy-[1,1'-biphenyl]-4-yl)-3-oxopropyl)piperazine-1-carboxylate, 2.81.



Prepared according to General Procedure **K**, using 3,5-dichlorobenzyl 4-(3-(4-bromophenyl)-3-oxopropyl)piperazine-1-carboxylate **2.72** (50 mg, 0.10 mmol, 1.0 equiv), 3,5-dimethyl-4-(4,4,5,5-tetramethyl-1,3,2-dioxaborolan-2-yl)isoxazole (45 mg, 0.22 mmol, 2.2 equiv), $\text{Pd}(\text{dppf})\text{Cl}_2 \cdot \text{CH}_2\text{Cl}_2$ (6 mg, 7 mol%), K_3PO_4 (64 mg, 0.30 mmol, 3.0 equiv), THF (0.4 mL) and H_2O (9 μL). The crude mixture was filtered through celite with EtOAc, concentrated under vacuum to a residue that was purified using column chromatography on silica (80–100% EtOAc in petroleum ether) to afford the desired product as a brown gum (27 mg, 52%).

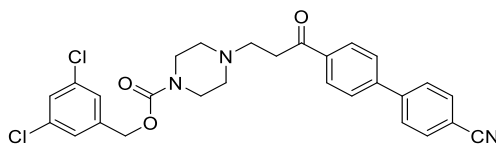
ν_{max} (neat): 2925, 2856, 1705, 1424 cm^{-1} .

^1H NMR (CDCl_3 , 400 MHz): δ 8.03 (d, $J = 8.5$ Hz, 2H), 7.39 (d, $J = 8.5$ Hz, 2H), 7.32 (t, $J = 1.9$ Hz, 1H), 7.24 (d, $J = 1.9$ Hz, 2H), 5.06 (s, 2H), 3.55–3.50 (m, 4H), 3.21 (t, $J = 17.2$ Hz, 2H), 2.89 (t, $J = 17.2$ Hz, 2H), 2.55–2.47 (m, 4H), 2.44 (s, 3H), 2.29 (s, 3H).

^{13}C NMR (CDCl_3 , 101 MHz): δ 197.7, 165.4, 157.8, 154.2, 139.6, 135.3, 135.1, 134.6, 131.7, 128.7, 128.1, 125.6, 115.4, 65.0, 52.5, 43.4, 36.7, 11.3, 10.4.

HRMS: exact mass calculated for $[\text{M}+\text{H}]^+$ ($\text{C}_{26}\text{H}_{27}\text{Cl}_2\text{N}_3\text{O}_4$) requires 516.1443 m/z , found 516.1443 m/z .

3,5-dichlorobenzyl 4-(3-(4'-cyano-[1,1'-biphenyl]-4-yl)-3-oxopropyl)piperazine-1-carboxylate, 2.83.



Prepared according to General Procedure **K**, using 3,5-dichlorobenzyl 4-(3-(4-bromophenyl)-3-oxopropyl)piperazine-1-carboxylate **2.72** (50 mg, 0.10 mmol, 1.0 equiv), 4-(4,4,5,5-tetramethyl-1,3,2-dioxaborolan-2-yl)benzotrile (47 mg, 0.21 mmol, 2.1 equiv), Pd(dppf)Cl₂·CH₂Cl₂ (7 mg, 9 mol%), K₃PO₄ (65 mg, 0.30 mmol, 3.0 equiv), THF (0.4 mL) and H₂O (9 μL). The crude mixture was filtered through celite with EtOAc, concentrated under vacuum to a residue that was purified using column chromatography on silica (80–100% EtOAc in petroleum ether) to afford the desired product as a brown gum (25 mg, 48%).

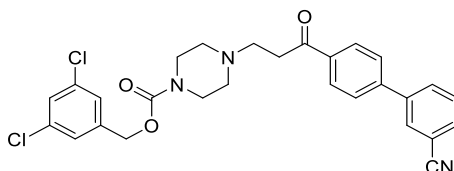
ν_{\max} (neat): 2927, 2200, 1706, 1696, 1605, 1572 cm⁻¹.

¹H NMR (CDCl₃, 400 MHz): δ 8.06 (d, *J* = 8.5 Hz, 2H), 7.79–7.67 (m, 6H), 7.30 (t, *J* = 1.9 Hz, 1H), 7.22 (d, *J* = 1.9 Hz, 2H), 5.06 (s, 2H), 3.55–3.49 (m, 4H), 3.22 (t, *J* = 7.2 Hz, 2H), 2.89 (t, *J* = 7.2 Hz, 2H), 2.54–2.46 (m, 4H).

¹³C NMR (CDCl₃, 101 MHz): δ 198.2, 144.2, 143.6, 140.1, 136.6, 135.1, 132.79, 132.76, 132.7, 128.9, 127.9, 127.5, 126.1, 118.6, 112.0, 65.5, 53.0, 52.9, 43.9, 36.3.

HRMS: exact mass calculated for [M+H]⁺ (C₂₈H₂₆Cl₂N₃O₃) requires 522.1346 *m/z*, found 522.1340 *m/z*.

3,5-dichlorobenzyl 4-(3-(3'-cyano-[1,1'-biphenyl]-4-yl)-3-oxopropyl)piperazine-1-carboxylate, 2.84.



Prepared according to General Procedure **K**, using 3,5-dichlorobenzyl 4-(3-(4-bromophenyl)-3-oxopropyl)piperazine-1-carboxylate **2.72** (50 mg, 0.10 mmol, 1.0 equiv), 3-(4,4,5,5-tetramethyl-1,3,2-dioxaborolan-2-yl)benzotrile (46 mg, 0.21 mmol, 2.1 equiv),

Pd(dppf)Cl₂·CH₂Cl₂ (7 mg, 9 mol%), K₃PO₄ (64 mg, 0.30 mmol, 3.0 equiv), THF (0.4 mL) and H₂O (9 μL). The crude mixture was filtered through celite with EtOAc, concentrated under vacuum to a residue that was purified using column chromatography on silica (80–100% EtOAc in petroleum ether) to afford the desired product as a brown gum (39 mg, 75%).

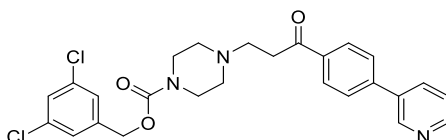
ν_{max} (neat): 2923, 2855, 2200, 1697, 1684, 1424 cm⁻¹.

¹H NMR (CDCl₃, 400 MHz): δ 8.08 (d, *J* = 8.6 Hz, 2H), 7.92 (t, *J* = 1.5 Hz, 1H), 7.88–7.85 (m, 1H), 7.72–7.66 (m, 3H), 7.61 (t, *J* = 7.6 Hz, 1H), 7.31 (t, *J* = 1.9 Hz, 1H), 7.24 (d, *J* = 1.9 Hz, 2H), 5.09 (s, 2H), 3.59–3.52 (m, 4H), 3.24 (t, *J* = 7.2 Hz, 2H), 2.92 (t, *J* = 7.2 Hz, 2H), 2.58–2.49 (m, 4H).

¹³C NMR (CDCl₃, 101 MHz): δ 154.8, 143.6, 141.2, 140.2, 136.5, 135.3, 131.8, 131.7, 131.0, 130.0, 129.1, 128.3, 127.5, 126.3, 118.7, 113.4, 65.7, 53.1, 53.0, 43.8, 36.2, 30.4.

HRMS: exact mass calculated for [M+H]⁺ (C₂₈H₂₆Cl₂N₃O₃) requires 522.1346 *m/z*, found 522.1340 *m/z*.

3,5-dichlorobenzyl 4-(3-oxo-3-(4-(pyridin-3-yl)phenyl)propyl)piperazine-1-carboxylate, 2.85.



Prepared according to General Procedure **K**, using 3,5-dichlorobenzyl 4-(3-(4-bromophenyl)-3-oxopropyl)piperazine-1-carboxylate **2.72** (50 mg, 0.10 mmol, 1.0 equiv), 3-(4,4,5,5-tetramethyl-1,3,2-dioxaborolan-2-yl)pyridine (41 mg, 0.20 mmol, 2.0 equiv), Pd(dppf)Cl₂·CH₂Cl₂ (5 mg, 6 mol%), K₃PO₄ (64 mg, 0.30 mmol, 3.0 equiv), THF (0.4 mL) and H₂O (9 μL). The crude mixture was filtered through celite with EtOAc, concentrated under vacuum to a residue that was purified using column chromatography on silica (80–100% EtOAc in petroleum ether) to afford the desired product as a brown gum (6 mg, 11%).

ν_{max} (CDCl₃): 2951, 2925, 2860 cm⁻¹.

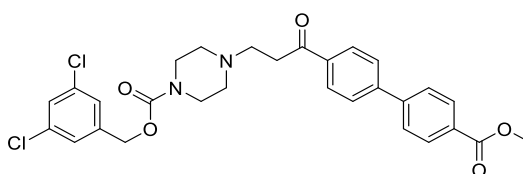
¹H NMR (CDCl₃, 400 MHz): δ 8.89 (d, *J* = 1.8 Hz, 2H), 8.65 (dd, *J* = 1.4, 4.8 Hz, 1H), 8.07 (d, *J* = 8.5 Hz, 2H), 7.92 (ddd, *J* = 1.7, 2.3, 8.0 Hz, 1H), 7.69 (d, *J* = 8.5 Hz, 2H), 7.41 (ddd, *J*

= 0.7, 4.9, 7.9 Hz, 1H), 7.31 (t, $J = 1.9$ Hz, 1H), 7.22 (d, $J = 1.9$ Hz, 2H), 5.07 (s, 2H), 3.57–3.50 (m, 4H), 3.22 (t, $J = 7.2$ Hz, 2H), 2.90 (t, $J = 7.2$ Hz, 2H), 2.59–2.48 (m, 4H).

^{13}C NMR (CDCl_3 , 101 MHz): δ 155.0, 149.8, 148.8, 140.5, 135.8, 135.5, 134.9, 129.3, 128.6, 127.8, 126.5, 124.1, 66.0, 53.4. $6 \times \text{C}$ not observed (coincident).

HRMS: exact mass calculated for $[\text{M}+\text{H}]^+$ ($\text{C}_{26}\text{H}_{26}\text{Cl}_2\text{N}_3\text{O}_3$) requires 498.1346 m/z , found 498.1339 m/z .

3,5-dichlorobenzyl 4-(3-(4'-(methoxycarbonyl)-[1,1'-biphenyl]-4-yl)-3-oxopropyl)piperazine-1-carboxylate, 2.86.



Prepared according to General Procedure **K**, using 3,5-dichlorobenzyl 4-(3-(4-bromophenyl)-3-oxopropyl)piperazine-1-carboxylate **2.72** (55 mg, 0.11 mmol, 1.0 equiv), (4-(methoxycarbonyl)phenyl)boronic acid (54 mg, 0.30 mmol, 3.0 equiv), $\text{Pd}(\text{dppf})\text{Cl}_2 \cdot \text{CH}_2\text{Cl}_2$ (4 mg, 5 mol%), K_3PO_4 (64 mg, 0.30 mmol, 3.0 equiv), THF (0.4 mL) and H_2O (9 μL). The crude mixture was filtered through celite with EtOAc, concentrated under vacuum to a residue that was purified using column chromatography on silica (80–100% EtOAc in petroleum ether) to afford the desired product as a brown gum (10 mg, 18%).

ν_{max} (neat): 2927, 2856, 1718, 1692, 1681, 1574 cm^{-1} .

^1H NMR (CDCl_3 , 400 MHz): δ 8.13 (d, $J = 8.5$ Hz, 2H), 8.05 (d, $J = 8.5$ Hz, 2H), 7.74–7.67 (m, 4H), 7.30 (t, $J = 1.9$ Hz, 1H), 7.22 (d, $J = 1.9$ Hz, 2H), 5.06 (s, 2H), 3.96 (s, 3H), 3.56–3.50 (m, 4H), 3.22 (t, $J = 7.2$ Hz, 2H), 2.90 (t, $J = 7.2$ Hz, 2H), 2.53–2.48 (m, 4H).

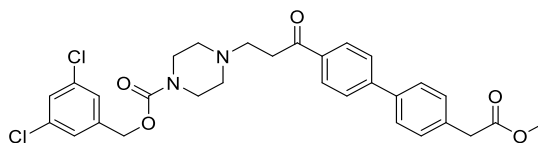
^{13}C NMR (CDCl_3 , 101 MHz): δ 198.5, 154.8, 144.7, 144.3, 140.3, 136.4, 135.2, 130.4, 130.0, 128.8, 128.3, 127.7, 127.4, 126.2, 65.7, 53.2, 53.0, 52.4, 44.0, 36.4. $1 \times \text{C}$ not observed (coincident).

HRMS: exact mass calculated for $[\text{M}+\text{H}]^+$ ($\text{C}_{29}\text{H}_{29}\text{Cl}_2\text{N}_2\text{O}_5$) requires 555.1448 m/z , found 555.1441 m/z .

3,5-dichlorobenzyl

4-(3-(4'-(2-methoxy-2-oxoethyl)-[1,1'-biphenyl]-4-yl)-3-

oxopropyl)piperazine-1-carboxylate, **2.87**.



Prepared according to General Procedure **K**, using 3,5-dichlorobenzyl 4-(3-(4-bromophenyl)-3-oxopropyl)piperazine-1-carboxylate **2.72** (55 mg, 0.11 mmol, 1.0 equiv), methyl 2-(4-(4,4,5,5-tetramethyl-1,3,2-dioxaborolan-2-yl)phenyl)acetate (57 mg, 0.21 mmol, 2.1 equiv), Pd(dppf)Cl₂·CH₂Cl₂ (6 mg, 7 mol%), K₃PO₄ (64 mg, 0.30 mmol, 3.0 equiv), THF (0.4 mL) and H₂O (9 μL). The crude mixture was filtered through celite with EtOAc, concentrated under vacuum to a residue that was purified using column chromatography on silica (80–100% EtOAc in petroleum ether) to afford the desired product as a brown gum (44 mg, 79%).

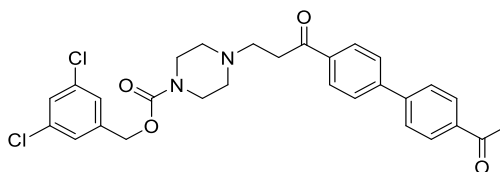
ν_{\max} (neat): 2927, 1739, 1684, 1425 cm⁻¹.

¹H NMR (CDCl₃, 400 MHz): δ 8.02 (d, J = 8.5 Hz, 2H), 7.68 (d, J = 8.5 Hz, 2H), 7.59 (d, J = 8.3 Hz, 2H), 7.39 (d, J = 8.3 Hz, 2H), 7.30 (t, J = 1.9 Hz, 1H), 7.22 (d, J = 1.9 Hz, 2H), 5.07 (s, 2H), 3.72 (s, 3H), 3.65 (app. s, 2H), 3.67–3.60 (m, 4H), 3.40–3.31 (m, 2H), 3.15–3.07 (m, 2H), 2.81–2.69 (m, 4H).

¹³C NMR (CDCl₃, 101 MHz): δ 171.9, 154.6, 145.9, 139.9, 138.7, 135.3, 135.2, 134.4, 130.1, 128.9, 128.5, 127.6, 127.4, 126.4, 66.0, 52.9, 52.7, 52.3, 43.1, 40.9. 2 × C not observed (coincident).

HRMS: exact mass calculated for [M+H]⁺ (C₃₀H₃₁Cl₂N₂O₅) requires 569.1605 m/z , found 569.1599 m/z .

3,5-dichlorobenzyl 4-(3-(4'-acetyl-[1,1'-biphenyl]-4-yl)-3-oxopropyl)piperazine-1-carboxylate, 2.88.



Prepared according to General Procedure **K**, using 3,5-dichlorobenzyl 4-(3-(4-bromophenyl)-3-oxopropyl)piperazine-1-carboxylate **2.72** (55 mg, 0.11 mmol, 1.0 equiv), 1-(4-(4,4,5,5-tetramethyl-1,3,2-dioxaborolan-2-yl)phenyl)ethan-1-one (57 mg, 0.23 mmol, 2.3 equiv), Pd(dppf)Cl₂.CH₂Cl₂ (8 mg, 10 mol%), K₃PO₄ (64 mg, 0.30 mmol, 3.0 equiv), THF (0.4 mL) and H₂O (9 μL). The crude mixture was filtered through celite with EtOAc, concentrated under vacuum to a residue that was purified using column chromatography on silica (80-100% EtOAc in petroleum ether) to afford the desired product as a brown gum (48 mg, 88%).

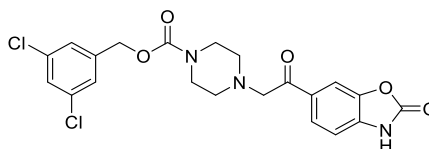
ν_{\max} (neat): 2923, 2855, 1702, 1678, 1232 cm⁻¹.

¹H NMR (CDCl₃, 400 MHz): δ 8.05 (d, *J* = 8.1 Hz, 4H), 7.75–7.69 (m, 4H), 7.30 (t, *J* = 1.9 Hz, 1H), 7.22 (d, *J* = 1.9 Hz, 2H), 5.06 (s, 2H), 3.56–3.50 (m, 4H), 3.21 (t, *J* = 7.2 Hz, 2H), 2.89 (t, *J* = 7.2 Hz, 2H), 2.64 (s, 3H), 2.53–2.48 (m, 4H).

¹³C NMR (CDCl₃, 101 MHz): δ 198.4, 197.7, 154.8, 144.6, 144.4, 140.3, 136.8, 136.4, 135.2, 129.2, 128.9, 128.3, 127.7, 127.6, 126.2, 65.6, 53.2, 53.0, 44.0, 36.4, 26.8.

HRMS: exact mass calculated for [M+H]⁺ (C₂₉H₂₉Cl₂N₂O₄) requires 539.1499 *m/z*, found 539.1492 *m/z*.

3,5-dichlorobenzyl 4-(2-oxo-2-(2-oxo-2,3-dihydrobenzo[*d*]oxazol-6-yl)ethyl)piperazine-1-carboxylate, 2.89.



Prepared according to General Procedure **J**, using 6-(2-chloroacetyl)benzo[*d*]oxazol-2(3*H*)-one **2.5** (100 mg, 0.47 mmol, 1.0 equiv), 3,5-dichlorobenzyl piperazine-1-carboxylate **2.22 a** (150 mg, 0.52 mmol, 1.2 equiv), NEt₃ (80 μL, 0.56 mmol, 1.2 equiv), MeCN (5 mL) at 50 °C

for 16 h. The reaction was concentrated *in vacuo* and H₂O (20 mL) added. The organics were extracted using CH₂Cl₂ (2 × 20 mL), dried with a hydrophobic frit and concentrated *in vacuo* to afford a residue that was purified by preparative high performance liquid chromatography (20–95% MeCN in H₂O) to afford the desired product as a white solid (10 mg, 5%). Consisted with reported data.⁹⁵

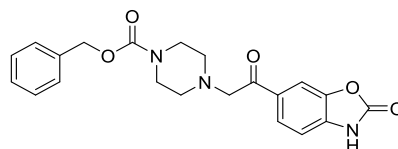
ν_{\max} (neat): 2924, 1771, 1687, 1422, 1195, 1136, 797 cm⁻¹.

¹H NMR (CDCl₃, 400 MHz): δ 7.88 (dd, *J* = 1.3, 8.0 Hz, 1H), 7.83 (d, *J* = 1.1 Hz, 1H), 7.32 (t, *J* = 1.8 Hz, 1H), 7.24 (d, *J* = 1.8 Hz, 2H), 7.18 (d, *J* = 8.2 Hz, 1H), 5.10 (s, 2H), 3.86 (s, 2H), 3.67–3.59 (m, 4H), 2.64 (s, 4H). 1 × H not observed (exchangeable).

¹³C NMR (CDCl₃, 101 MHz): δ 154.7, 154.4, 143.8, 141.3, 136.8, 134.6, 128.3, 128.1, 126.8, 126.1, 110.3, 109.8, 109.4, 65.7, 60.4, 52.1. 1 × C not observed.

HRMS: exact mass calculated for (C₂₁H₂₀N₃O₅) [M+H⁺] requires 464.0771 *m/z*, found [M+H⁺] 464.0775 *m/z*.

Benzyl 4-(2-oxo-2-(2-oxo-2,3-dihydrobenzo[*d*]oxazol-6-yl)ethyl)piperazine-1-carboxylate, 2.90.



Prepared according to General Procedure **J**, using 6-(2-chloroacetyl)benzo[*d*]oxazol-2(3*H*)-one **2.5** (100 mg, 0.44 mmol, 1.0 equiv), benzyl piperazine-1-carboxylate **2.22 b** (94 μ L, 0.48 mmol, 1.1 equiv), PS-DIPEA (85 mg, 0.66 mmol, 1.2 equiv), MeCN (5 mL) at 80 °C for 16 h. The precipitate was collected and filtered under vacuum with MeOH (20 mL) and purified using column chromatography with silica (2–10% MeOH in CH₂Cl₂) to afford the desired product as a yellow solid (64 mg, 37%).

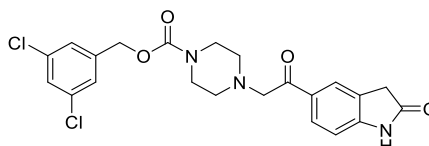
ν_{\max} (CH₂Cl₂): 2930, 1780, 1706, 1674 cm⁻¹.

¹H NMR (CDCl₃, 101 MHz): δ 7.91–7.85 (m, 1H), 7.85–7.80 (m, 1H), 7.45–7.29 (m, 5H), 7.17 (d, *J* = 8.0 Hz, 1H), 5.16 (s, 2H), 3.94–3.79 (m, 2H), 3.71–3.54 (m, 4H), 2.76–2.54 (m, 4H).

^{13}C NMR (DMSO- d_6 , 101 MHz): δ 193.9, 154.84, 154.77, 143.3, 136.0, 133.9, 130.2, 128.0, 127.6, 127.4, 124.3, 109.3, 109.1, 66.8, 63.6, 52.6, 43.02.

HRMS: exact mass calculated for (C₂₁H₂₂N₃O₅) [M+H⁺] requires 396.1554 m/z , found 396.1552 m/z .

3,5-dichlorobenzyl 4-(2-oxo-2-(2-oxoindolin-5-yl)ethyl)piperazine-1-carboxylate, 2.91.



Prepared according to General Procedure **J**, using 5-(2-chloroacetyl)indolin-2-one **2.9** (34 mg, 0.16 mmol, 1.0 equiv), 3,5-dichlorobenzyl piperazine-1-carboxylate **2.22 a** (51 mg, 0.18 mmol, 1.1 equiv), NEt₃ (27 μL , 0.19 mmol, 1.2 equiv), MeCN (2 mL) at 50 °C for 48 h. The reaction was diluted with H₂O (20 mL), the organics were extracted using CH₂Cl₂ (2 \times 20 mL), dried with a hydrophobic frit, and concentrated *in vacuo* to give a residue that was purified by column chromatography with silica (2–10% MeOH in EtOAc) to afford the desired product as an orange solid (19 mg, 26%).

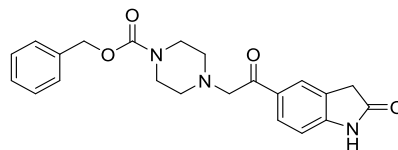
ν_{max} (neat): 2922, 1682, 1614, 1233, 798 cm^{-1}

^1H NMR (DMSO- d_6 , 400 MHz): 8.82 (s, 1H), 7.99–7.94 (m, 1H), 7.94–7.90 (m, 1H), 7.32 (t, $J = 1.9$ Hz, 1H), 7.25 (d, $J = 1.9$ Hz, 2H), 6.96 (d, $J = 8.2$ Hz, 1H), 5.09 (s, 1H), 3.82 (s, 3H), 3.69–3.57 (m, 6H), 2.67–2.57 (m, 4H).

^{13}C NMR (CDCl₃, 101 MHz): δ 194.2, 176.8, 154.2, 146.7, 139.6, 134.6, 130.2, 129.1, 127.7, 125.6, 125.0, 124.3, 108.8, 65.1, 63.6, 52.6, 43.3, 35.3.

HRMS: exact mass calculated for (C₂₂H₂₂Cl₂N₃O₄) [M+H⁺] requires 462.0982 m/z , found 462.0975 m/z .

Benzyl 4-(2-oxo-2-(2-oxoindolin-5-yl)ethyl)piperazine-1-carboxylate, 2.92.



Prepared according to General Procedure **J**, using 5-(2-chloroacetyl)indolin-2-one **2.9** (100 mg, 0.48 mmol, 1.0 equiv), benzyl piperazine-1-carboxylate **2.22 b** (101 μ L, 0.53 mmol, 1.1 equiv), NEt₃ (80 μ L, 0.57 mmol, 1.2 equiv), MeCN (2 mL) at 50 °C for 48 h. The reaction was diluted with H₂O (20 mL), the organics were extracted using CH₂Cl₂ (2 \times 20 mL), dried with a hydrophobic frit, and concentrated *in vacuo* to give a residue that was purified by column chromatography with silica (2–10% MeOH in EtOAc) to afford the desired product as an orange solid (52 mg, 28%).

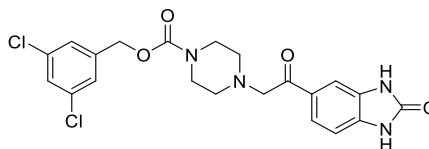
ν_{\max} (neat): 2922, 1682, 1614, 1230, 1114 cm⁻¹.

¹H NMR (CDCl₃, 400 MHz): δ 10.74 (s, 1H), 7.99–7.93 (m, 1H), 7.93–7.88 (m, 1H), 7.41 – 7.30 (m, 5H), 6.89 (d, *J* = 8.2 Hz, 1H), 5.08 (s, 2H), 3.80 (s, 2H), 3.55 (s, 2H), 3.47–3.34 (m, 4H). 4 \times H under DMSO-*d*₆ peak.

¹³C NMR (DMSO-*d*₆, 101 MHz): δ 195.2, 176.7, 154.4, 148.4, 136.9, 129.4, 129.2, 128.4, 127.8, 127.5, 125.9, 124.3, 108.6, 66.1, 63.2, 52.3, 43.4, 35.5.

HRMS: exact mass calculated for (C₂₂H₂₄N₃O₄) [M+H⁺] requires 394.1761 *m/z*, found [M+H⁺] 394.1766 *m/z*.

3,5-dichlorobenzyl 4-(2-oxo-2-(2-oxo-2,3-dihydro-1H-benzo[d]imidazol-5-yl)ethyl)piperazine-1-carboxylate, 2.93.



Prepared according to General Procedure **J**, using 5-(2-chloroacetyl)-1,3-dihydro-2H-benzo[d]imidazol-2-one **2.7** (99 mg, 0.47 mmol, 1.0 equiv), 3,5-dichlorobenzyl piperazine-1-carboxylate **2.22 a** (151 mg, 0.52 mmol, 1.1 equiv), NEt₃ (80 μ L, 0.56 mmol, 1.2 equiv), MeCN (2 mL) at 50 °C for 16 h. The reaction was diluted with H₂O (20 mL), the organics

were extracted using CH₂Cl₂ (2 × 20 mL), dried with a hydrophobic frit, and concentrated *in vacuo* to give a residue that was purified by column chromatography with silica (2–10% MeOH in EtOAc) to afford the desired product as a brown solid (120 mg, 55 %).

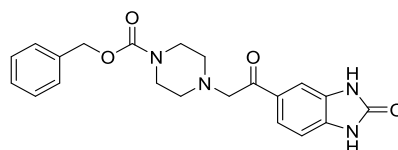
ν_{max} (neat): 3193, 3078, 1739, 1712, 1665 cm⁻¹.

¹H (DMSO-*d*₆, 400 MHz): 11.02 (s, 1H), 10.90 (s, 1H), 7.71 (dd, *J* = 1.6, 8.3, 1H), 7.57 (t, *J* = 1.9, 1H), 7.52 (d, *J* = 1.4, 1H), 7.43 (d, *J* = 8.2, 2H), 7.01 (d, *J* = 8.2 Hz, 1H), 5.09 (s, 2H), 3.85 (s, 2H), 3.51–3.37 (m, 4H), 4 × H under DMSO.

¹³C NMR (DMSO-*d*₆, 150 MHz): δ 195.8, 155.9, 154.5, 141.8, 134.6, 134.5, 130.1, 129.3, 127.9, 126.7, 122.9, 108.41, 108.37, 65.2, 63.8, 52.8, 44.0.

HRMS: exact mass calculated for (C₂₁H₂₁Cl₂N₄O₄) [M+H⁺] requires 463.0934 *m/z*, found 463.0925 *m/z*.

3,5-dichlorobenzyl 4-(2-oxo-2-(2-oxo-2,3-dihydro-1*H*-benzo[*d*]imidazol-5-yl)ethyl)piperazine-1-carboxylate, 2.94.



Prepared according to General Procedure **J**, using 5-(2-chloroacetyl)-1,3-dihydro-2*H*-benzo[*d*]imidazol-2-one **2.7** (200 mg, 0.95 mmol, 1.0 equiv), 3,5-dichlorobenzyl piperazine-1-carboxylate **2.22 b** (200 μL, 1.04 mmol, 1.1 equiv), NEt₃ (160 μL, 1.14 mmol, 1.2 equiv), MeCN (2 mL) at 50 °C for 16 h. The reaction was diluted with H₂O (20 mL), the organics were extracted using CH₂Cl₂ (2 × 20 mL), dried with a hydrophobic frit, and concentrated *in vacuo* to give a residue that was purified by column chromatography with silica (2–10% MeOH in EtOAc) to afford the desired product as a brown solid (38 mg, 10 %).

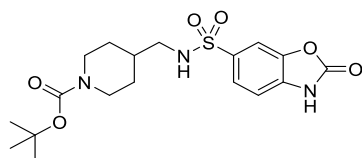
ν_{max} (neat): 3169, 2927, 1696, 1675, 1239 cm⁻¹.

¹H (DMSO-*d*₆, 400 MHz): 11.02 (s, 1H), 10.85 (s, 1H), 7.69 (dd, *J* = 1.6, 8.2, 1H), 7.51 (d, *J* = 1.4, 1H), 7.42–7.29 (m, 5H), 7.00 (d, *J* = 8.2, 1H), 5.08 (s, 2H), 3.82 (s, 2H), 3.46–3.35 (m, 4H), 4 × under DMSO.

^{13}C NMR (DMSO- d_6 , 101 MHz): δ 195.3, 155.4, 154.4, 136.9, 134.1, 129.6, 128.8, 128.4, 127.8, 127.5, 122.4, 107.92, 107.87, 66.2, 63.3, 52.3, 43.5.

HRMS: exact mass calculated for (C₂₁H₂₃N₄O₄) [M+H⁺] requires 395.1714 m/z , found 395.1712 m/z .

***Tert*-butyl 4-(((2-oxo-2,3-dihydrobenzo[*d*]oxazole)-6-sulfonamido)methyl)piperidine-1-carboxylate, 2.95.**



Prepared according to General Procedure **J**, using 2-oxo-2,3-dihydrobenzo[*d*]oxazole-6-sulfonyl chloride **2.11** (200 mg, 0.93 mmol, 1.0 equiv), *tert*-butyl 4-(aminomethyl)piperidine-1-carboxylate (200 μL , 0.95 mmol, 1.1 equiv), NEt₃ (132 μL , 0.95 mmol, 1.2 equiv), MeCN (2 mL) at 80 °C for 4 h. The reaction was concentrated *in vacuo* and purified by column chromatography on silica (80% EtOAc in petroleum ether) to afford the desired product as a yellow solid (117 mg, 33%).

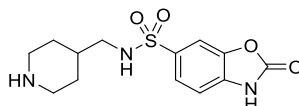
ν_{max} (neat): 3258, 1796, 1651, 1157, 912 cm^{-1} .

^1H NMR (DMSO- d_6 , 400 MHz): 12.09 (s, 1H), 7.64 (d, $J = 1.4$ Hz, 1H), 7.60 (m, 2H), 7.26 (d, $J = 8.2$ Hz, 1H), 3.88 (d, $J = 12.4$ Hz, 2H), 2.61 (t, $J = 6.4$ Hz, 4H), 1.59 (d, $J = 13.2$ Hz, 2H), 1.55–1.47 (m, 1H), 1.38 (s, 9H), 1.04–0.87 (m, 2H).

^{13}C NMR (DMSO- d_6 , 150 MHz): δ 154.2, 153.8, 142.9, 134.0, 133.9, 123.1, 109.7, 107.7, 78.4, 47.8, 39.64 (under DMSO), 35.6, 29.1, 28.0.

HRMS: exact mass calculated for [M+H⁺] (C₁₈H₂₆N₃O₆S) requires 429.1802 m/z , found 429.1800 m/z .

2-oxo-*N*-(piperidin-4-ylmethyl)-2,3-dihydrobenzo[*d*]oxazole-6-sulfonamide, 2.96.



Prepared according to General Procedure **F**, using *tert*-butyl 4-(((2-oxo-2,3-dihydrobenzo[*d*]oxazole)-6-sulfonamido)methyl)piperidine-1-carboxylate **2.92** (99 mg, 0.24 mmol), trifluoroacetic acid (0.2 mL), CH₂Cl₂ (1.8 mL) and purified by strong cation exchange (propylsulfonic acid functionalised silica, 2N NH₃ in MeOH) to afford the desired product as a white solid (71 mg, 94%).

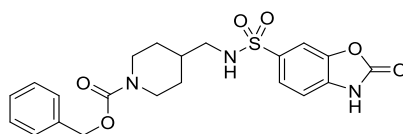
ν_{\max} (neat): 3159, 1672, 1470, 1273, 1134, 821, 711 cm⁻¹.

¹H NMR (DMSO-*d*₆, 400 MHz): 7.28 (dd, *J* = 1.9, 8.1 Hz, 2H), 7.20 (d, *J* = 1.8 Hz, 1H), 6.86 (d, *J* = 8.1 Hz, 1H), 3.20–3.12 (m, 3H), 2.71 (td, *J* = 2.3, 12.2, 11.8, 2H), 2.56 (d, *J* = 5.6 Hz, 1H), 1.72 (d, *J* = 13.4 Hz, 2H), 1.57 (dd, *J* = 5.5, 9.1 Hz, 1H), 1.20–1.08 (m, 2H).

¹³C NMR (DMSO-*d*₆, 101 MHz): δ 146.2, 127.3, 121.2, 109.6, 104.0, 47.5, 43.4, 33.9, 27.0. 2 \times C not observed (coincident).

HRMS: exact mass calculated for (C₁₃H₁₈N₃O₄S) [M+H]⁺ requires 312.1013 *m/z*, found 312.1010 *m/z*.

Benzyl 4-(((2-oxo-2,3-dihydrobenzo[*d*]oxazole)-6-sulfonamido)methyl)piperidine-1-carboxylate, 2.98.



Prepared according to General Procedure **E**, using 2-oxo-*N*-(piperidin-4-ylmethyl)-2,3-dihydrobenzo[*d*]oxazole-6-sulfonamide **2.98** (58 mg, 0.19 mmol, 1.0 equiv), NaHCO₃ (25 mg, 0.29 mmol, 1.5 equiv), *N*-(benzyloxycarbonyloxy)succinimide (53 mg, 0.21 mmol, 1.1 equiv), THF (2 mL), H₂O (2 mL). The residue was purified by column chromatography on silica (0–10% MeOH in CH₂Cl₂) to afford the desired product as a white solid (7 mg, 8%).

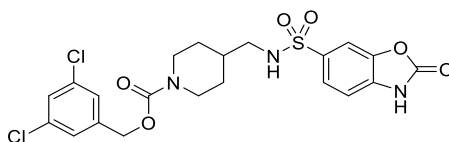
ν_{\max} (neat): 3277, 1796, 1761, 1687, 1163, 1060 cm⁻¹.

^1H NMR (DMSO- d_6 , 400 MHz): 7.66–7.57 (m, 2H), 7.41–7.29 (m, 5H), 7.26 (d, $J = 8.1$ Hz, 1H), 5.05 (s, 2H), 3.96 (d, $J = 13.2$ Hz, 2H), 2.87–2.68 (m, 2H), 2.60 (t, $J = 6.8$ Hz, 2H), 1.62 (d, $J = 13.2$ Hz, 2H), 1.71–1.48 (m, 3H), 1.21–1.04 (m, 2H). $2 \times \text{H}$ not observed (exchangeable).

^{13}C NMR (DMSO- d_6 , 101 MHz): δ 154.3, 143.0, 137.0, 134.1, 133.9, 128.4, 127.8, 127.5, 123.0, 109.7, 107.7 66.0, 47.7, 43.2, 35.5, 29.0. $1 \times \text{C}$ not observed (coincident).

HRMS: exact mass calculated for $[\text{M}+\text{H}]^+$ ($\text{C}_{21}\text{H}_{24}\text{N}_3\text{O}_6\text{S}$) requires 446.1380 m/z , found 446.1379 m/z .

3,5-dichlorobenzyl **4-(((2-oxo-2,3-dihydrobenzo[*d*]oxazole)-6-sulfonamido)methyl)piperidine-1-carboxylate, 2.99.**



Prepared according to General Procedure C, using 2-oxo-*N*-(piperidin-4-ylmethyl)-2,3-dihydrobenzo[*d*]oxazole-6-sulfonamide 2,2,2-trifluoroacetate **2.98** (251 mg, 0.59 mmol, 1.0 equiv), (3,5-dichlorophenyl)methanol (115 mg, 0.65 mmol, 1.1 equiv), CDI (105 mg, 0.65 mmol, 1.1 equiv), DMF (2 mL). The precipitate was triturated with petroleum ether to afford the desired product as a white solid (121 mg, 36%).

ν_{max} (neat): 3263, 2859, 1748, 1698, 1426 cm^{-1} .

^1H NMR (400 MHz, CDCl_3): 7.72 (dd, $J = 1.7, 8.2$, 1H), 7.69 (d, $J = 1.5$, 1H), 7.30 (t, $J = 1.9$ Hz, 1H), 7.22 (d, $J = 1.9$, 2H), 7.19 (d, $J = 8.2$, 1H), 5.12–5.04 (m, 2H), 4.17 (d, $J = 11.8$ Hz, 2H), 3.00 (s, 1H), 2.93 (s, 1H), 2.90–2.72 (m, 4H), 1.79–1.65 (m, 3H), 1.22–1.04 (m, 2H).

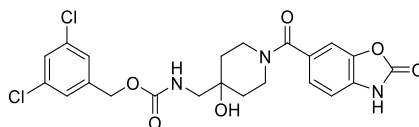
^{13}C NMR (400 MHz, DMSO): δ 154.3, 143.0, 137.0, 134.1, 133.9, 128.4, 127.8, 127.5, 123.0, 109.7, 107.7 66.0, 47.7, 43.2, 35.5, 29.0. $1 \times \text{aromatic C}$ not observed (coincident).

HRMS: exact mass calculated for $[\text{M} + \text{NH}_4]^+$ ($\text{C}_{21}\text{H}_{25}\text{N}_4\text{O}_6\text{S}$) requires 531.0866 m/z , found 531.0859 m/z .

3,5-dichlorobenzyl

4-hydroxy-4-((2-oxo-2,3-dihydrobenzo[*d*]oxazole-6-

carboxamido)methyl)piperidine-1-carboxylate, 2.101.



Prepared according to General Procedure **O**, using 2-oxo-2,3-dihydrobenzo[*d*]oxazole-6-carboxylic acid **2.13** (60 mg, 0.17 mmol, 1.1 equiv), DMF (2 mL), DIPEA (156 μ L, 0.45 mmol, 3.0 equiv, HATU (0.16 g, 0.38 mmol, 2.5 equiv), 3,5-dichlorobenzyl 4-(aminomethyl)-4-hydroxypiperidine-1-carboxylate **2.24** (100 mg, 0.15 mmol) to afford the desired product as a white gum (32 mg, 22%).

ν_{\max} (neat): 2925, 1771, 1699, 1596, 1438 cm^{-1} .

^1H NMR (MeOD-*d*₄, 500 MHz): δ 7.38–7.24 (m, 4H), 7.25 (dd, $J = 1.4, 8.0$ Hz, 1H), 7.15 (d, $J = 8.1$ Hz, 1H), 5.05 (s, 2H), 4.71 (s, 1H), 3.75 (d, $J = 12.9$ Hz, 2H), 3.29 (s, 2H), 3.21–3.05 (m, 2H), 1.45 (s, 4H). 1 \times H not observed (exchangeable).

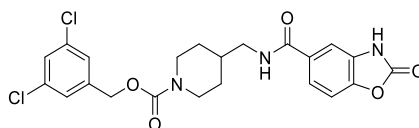
^{13}C NMR (MeOD-*d*₄, 101 MHz): δ 166.1, 166.0, 154.4, 154.4, 143.0, 137.1, 132.9, 128.4, 127.7, 127.4, 123.8, 109.1, 108.4, 69.1, 66.0, 49.4, 39.6, 34.1.

HRMS: exact mass calculated for $[\text{M}-\text{H}]^+$ ($\text{C}_{22}\text{H}_{20}\text{Cl}_2\text{N}_3\text{O}_6$) $[\text{M}-\text{H}]^+$ requires m/z 494.0880, found m/z 494.0873.

3,5-dichlorobenzyl

4-((2-oxo-2,3-dihydrobenzo[*d*]oxazole-5-

carboxamido)methyl)piperidine-1-carboxylate, 2.105.



Prepared according to General Procedure **C**, using *tert*-butyl 4-((2-oxo-2,3-dihydrobenzo[*d*]oxazole-5-carboxamido)methyl)piperidine-1-carboxylate (51 mg, 0.19 mmol, 1.0 equiv), (3,5-dichlorophenyl)methanol (36 mg, 0.20 mmol, 1.1 equiv), CDI (32 mg, 0.20 mmol, 1.1 equiv), DMF (2 mL) and purified with silica chromatography (60% EtOAc in petroleum ether to 10% MeOH in EtOAc) to afford the desired product as a white solid (12 mg, 2% over 3 steps).

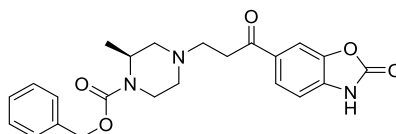
ν_{\max} (neat): 2929, 2858, 1775, 1685, 1645, 1471 cm^{-1} .

^1H NMR (CDCl_3 , 500 MHz): δ 9.49 (s, 1H), 7.62 (d, $J = 1.3$ Hz, 1H), 7.28 (t, $J = 1.9$ Hz, 1H), 7.23–7.18 (m, 3H), 6.43 (t, $J = 6.0$ Hz, 1H), 5.06 (s, 2H), 4.26–4.13 (m, 2H), 3.47–3.32 (m, 2H), 2.90–2.73 (m, 2H), 1.89–1.65 (m, 6H), 0.93–0.75 (m, 2H).

^{13}C NMR (CDCl_3 , 101 MHz): δ 167.3, 154.9, 154.8, 146.3, 140.4, 135.2, 130.9, 130.4, 128.3, 126.2, 121.1, 109.8, 109.7, 65.7, 45.7, 44.1, 36.4, 29.8.

HRMS: exact mass calculated for $[\text{M}-\text{H}]^+$ ($\text{C}_{22}\text{H}_{20}\text{Cl}_2\text{N}_3\text{O}_5$) requires 478.0931 m/z , found 478.0924 m/z .

Benzyl (S)-2-methyl-4-(3-oxo-3-(2-oxo-2,3-dihydrobenzo[d]oxazol-6-yl)propyl)piperazine-1-carboxylate, 2.107.



Prepared according to General Procedure **J**, using 6-(3-chloropropanoyl)benzo[d]oxazol-2(3H)-one **2.6** (500 mg, 2.22 mmol, 1.0 equiv), (S)-benzyl 2-methylpiperazine-1-carboxylate **2.38** (571 mg, 2.44 mmol, 1.1 equiv), NEt_3 (371 μL , 2.66 mmol, 1.2 equiv), MeCN (4.4 mL) to afford the desired product as a white solid (771 mg, 82%).

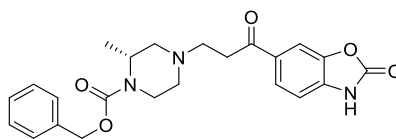
ν_{\max} (neat): 2972, 2836, 1697, 1680, 1425 cm^{-1} .

^1H NMR ($\text{MeOD}-d_4$, 400 MHz): δ 8.34 (s, 1H), 7.91 (dd, $J = 1.6, 8.2$ Hz, 2H), 7.84 (d, $J = 1.3$ Hz, 1H), 7.39–7.27 (m, 5H), 7.17 (d, $J = 8.2$ Hz, 1H), 5.11 (app. d, $J = 5.9$ Hz, 2H), 4.31–4.21 (m, 1H), 3.87 (d, $J = 13.2$ Hz, 1H), 3.21–3.06 (m, 2H), 2.89 (d, $J = 11.2$ Hz, 1H), 2.85–2.72 (m, 3H), 2.24 (dd, $J = 3.9, 11.3$ Hz, 1H), 2.07 (td, $J = 3.4, 11.8$ Hz, 1H), 1.19 (d, $J = 6.8$ Hz, 3H).

^{13}C NMR ($\text{DMSO}-d_6$, 101 MHz): δ 197.6, 154.5, 154.2, 143.3, 136.9, 135.0, 131.0, 128.4, 127.7, 127.4, 125.0, 109.3, 108.8, 66.0, 56.9, 53.1, 52.6, 46.8, 39.0, 35.4, 15.8.

HRMS: exact mass calculated for $[\text{M}+\text{H}]^+$ ($\text{C}_{23}\text{H}_{26}\text{N}_3\text{O}_5$) requires 424.1867 m/z , found 424.1872 m/z .

Benzyl **(R)-2-methyl-4-(3-oxo-3-(2-oxo-2,3-dihydrobenzo[*d*]oxazol-6-yl)propyl)piperazine-1-carboxylate, 2.108.**



Prepared according to General Procedure **J**, using 6-(3-chloropropanoyl)benzo[*d*]oxazol-2(3*H*)-one **2.6** (100 mg, 0.43 mmol, 1.0 equiv), (*R*)-benzyl 2-methylpiperazine-1-carboxylate **2.39** (114 mg, 0.49 mmol, 1.1 equiv), NEt₃ (74 μL, 0.53 mmol, 1.2 equiv), MeCN (0.4 mL) and purified by mass directed automated purification with silica (15–55% MeCN in H₂O with formic acid) to afford the desired product as a white solid (27 mg, 14%).

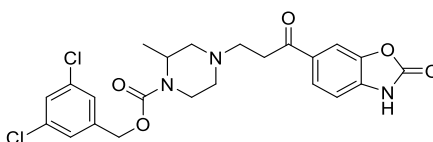
ν_{max} (neat): 2976, 2817, 1782, 1684, 1624, 1427 cm⁻¹.

¹H NMR (MeOD-*d*₄, 400 MHz): δ 8.20 (br. s, 1H), 7.91 (dd, *J* = 1.5, 8.2 Hz, 1H), 7.83 (d, *J* = 1.4 Hz, 1H), 7.38–7.26 (m, 5H), 7.17 (d, *J* = 8.2 Hz, 1H), 5.12 (app. d, *J* = 3.5 Hz, 2H), 4.38–4.28 (m, 1H), 3.95 (d, *J* = 13.7 Hz, 1H), 3.19 (td, *J* = 3.2, 13.7 Hz, 1H), 3.05 (d, *J* = 11.7 Hz, 1H), 3.02–2.86 (m, 3H), 2.47 (dd, *J* = 4.1, 11.7 Hz, 1H), 2.29 (td, *J* = 3.5, 11.9 Hz, 1H), 1.23 (d, *J* = 6.9 Hz, 3H).

¹³C NMR (MeOD-*d*₄, 101 MHz): δ 199.0, 156.7, 156.6, 145.4, 138.0, 136.4, 132.9, 129.5, 129.2, 128.9, 126.6, 110.4, 110.3, 68.4, 58.1, 54.5, 54.0, 48.4, 39.7, 16.1. 1 × C not observed (coincident).

HRMS: exact mass calculated for [M+H]⁺ (C₂₃H₂₆N₃O₅) requires 424.1867 *m/z*, found 424.1872 *m/z*.

3,5-dichlorobenzyl **2-methyl-4-(3-oxo-3-(2-oxo-2,3-dihydrobenzo[*d*]oxazol-6-yl)propyl)piperazine-1-carboxylate, 2.09.**



Prepared according to General Procedure **J**, using 6-(3-chloropropanoyl)benzo[*d*]oxazol-2(3*H*)-one **2.6** (68 mg, 0.30 mmol, 1.0 equiv), 3,5-dichlorobenzyl 2-methylpiperazine-1-carboxylate **2.32** (98 mg, 0.32 mmol, 1.1 equiv), NEt₃ (50 μL, 0.36 mmol, 1.2 equiv), MeCN

(2 mL) and purified using column chromatography with silica (80–95% EtOAc in petroleum ether) to afford the desired product as a yellow solid (57 mg, 36%).

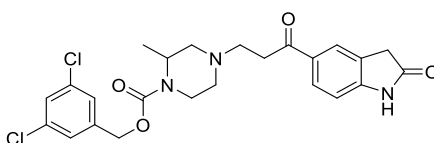
ν_{\max} (neat): 2969, 2816, 1779, 1679 cm^{-1} .

^1H NMR (CDCl_3 , 400 MHz): δ 7.90–7.85 (m, 1H), 7.85–7.82 (m, 1H), 7.33–7.29 (m, 1H), 7.25–7.21 (m, 2H), 7.16 (d, $J = 8.2$, 1H), 5.09, (s, 2H), 4.37–4.26 (m, 1H), 3.91 (d, $J = 13.1$ Hz, 1H), 3.16 (t, $J = 7.0$ Hz, 3H), 2.93–2.77 (m, 3H), 2.72 (d, $J = 11.2$ Hz, 1H), 2.29 (dd, $J = 3.9, 11.2$ Hz, 1H), 2.12 (td, $J = 3.4, 11.8$ Hz, 1H), 1.25 (d, $J = 6.8$ Hz, 3H). $1 \times \text{H}$ not observed (exchangeable).

^{13}C NMR (CDCl_3 , 101 MHz): δ 197.3, 155.3, 154.7, 144.0, 140.2, 135.1, 133.8, 132.3, 128.1, 126.0, 125.3, 109.7, 109.4, 65.5, 57.6, 53.3, 53.1, 47.4, 39.5, 36.1, 16.2.

HRMS: exact mass calculated for $[\text{M}+\text{H}]^+$ ($\text{C}_{23}\text{H}_{24}\text{Cl}_2\text{N}_3\text{O}_5$) requires 493.1119 m/z , found 493.1113 m/z .

3,5-dichlorobenzyl 2-methyl-4-(3-oxo-3-(2-oxoindolin-5-yl)propyl)piperazine-1-carboxylate, 2.110.



Prepared according to General Procedure **J**, using 5-(3-chloropropanoyl)indolin-2-one **2.10** (67 mg, 0.30 mmol, 1.0 equiv), 3,5-dichlorobenzyl 2-methylpiperazine-1-carboxylate **2.32** (94 mg, 0.31 mmol, 1.1 equiv), NEt_3 (50 μL , 0.36 mmol, 1.2 equiv), MeCN (2 mL) and purified using column chromatography with silica (80% EtOAc in petroleum ether) to afford the desired product as a pink solid (59 mg, 40%).

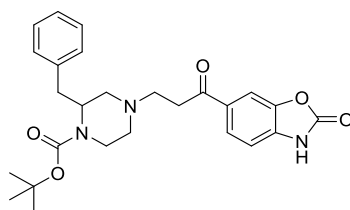
ν_{\max} (neat): 2811, 1673, 1615, 1416 cm^{-1} .

^1H NMR (CDCl_3 , 400 MHz): δ 9.17 (s, 1H), 7.94–7.82 (m, 2H), 7.29 (t, $J = 1.9$ Hz, 1H), 7.21 (d, $J = 1.8$ Hz, 2H), 6.95 (d, $J = 8.2$ Hz, 1H), 5.07 (s, 1H), 4.34–4.23 (m, 1H), 3.89 (d, $J = 13.0$ Hz, 1H), 3.59 (s, 2H), 3.23–3.07 (m, 3H), 2.91–2.65 (m, 4H), 2.28 (d, $J = 8.4$ Hz, 1H), 2.11 (t, $J = 10.3$ Hz, 1H), 1.24 (d, $J = 6.9$ Hz, 3H).

^{13}C NMR (CDCl_3 , 101 MHz): δ 197.7, 177.7, 154.6, 147.1, 140.2, 135.1, 131.9, 129.5, 128.1, 126.0, 125.5, 124.6, 109.3, 65.4, 57.6, 53.4, 53.2, 47.4, 39.4, 35.9, 16.2. $1 \times \text{C}$ not observed (coincident).

HRMS: exact mass calculated for $[\text{M}+\text{H}]^+$ ($\text{C}_{24}\text{H}_{26}\text{Cl}_2\text{N}_3\text{O}_4$) requires 491.1326 m/z , found 491.1316 m/z .

(\pm)-*tert*-butyl 2-benzyl-4-(3-oxo-3-(2-oxo-2,3-dihydrobenzo[*d*]oxazol-6-yl)propyl)piperazine-1-carboxylate, **2.111**.



Prepared according to General Procedure **J**, using 6-(3-chloropropanoyl)benzo[*d*]oxazol-2(3*H*)-one **2.6** (100 mg, 0.44 mmol, 1.0 equiv), *tert*-butyl 2-benzylpiperazine-1-carboxylate (136 mg, 0.36 mmol, 1.1 equiv) and NEt_3 (65 μL , 0.43 mmol, 1.2 equiv) in MeCN (5 mL), and heated to 80 $^\circ\text{C}$ for 5 h. The reaction was cooled with ice and product precipitated with addition of Et_2O , which was further washed with H_2O to yield white solid. Purification by preparative HPLC (5–95% MeCN in H_2O) yielded a white solid (51.4 mg, 25%).

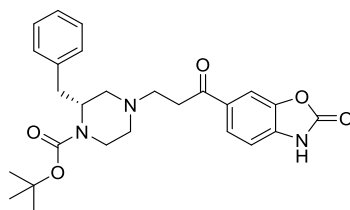
ν_{max} (neat): 1782, 1668, 1618 cm^{-1} .

^1H NMR ($\text{MeOD-}d_4$, 400 MHz): δ 8.22 (app. s, 1H), 7.92 (dd, $J = 8.2, 1.5$ Hz, 1H), 7.83 (d, $J = 1.3$ Hz, 1H), 7.26–7.10 (m, 6H), 4.35–4.25 (m, 1H), 3.95 (d, $J = 13.0$ Hz, 1H), 3.21–3.15 (m, 1H), 3.12–3.04 (m, 1H), 2.98–2.84 (m, 4H), 2.32–2.18 (m, 2H), 1.30 (s, 9H).

^{13}C NMR ($\text{MeOD-}d_4$, 101 MHz): δ 194.6, 154.8, 153.1, 143.5, 135.1, 130.0, 128.6, 127.9, 126.1, 124.9, 108.7, 108.4, 87.2, 87.1, 80.4, 52.6, 51.7, 31.5, 26.3. $3 \times \text{C}$ not observed (coincident).

HRMS: exact mass calculated for $[\text{M}+\text{H}]^+$ ($\text{C}_{26}\text{H}_{32}\text{N}_3\text{O}_5$) requires 466.2341 m/z , found 466.2336 m/z .

***Tert*-butyl (R)-2-benzyl-4-(3-oxo-3-(2-oxo-2,3-dihydrobenzo[d]oxazol-6-yl)propyl)piperazine-1-carboxylate, 2.112.**



Prepared according to General Procedure **J**, using 6-(3-chloropropanoyl)benzo[d]oxazol-2(3H)-one **2.6** (100 mg, 0.44 mmol, 1.0 equiv), *tert*-butyl 2-benzylpiperazine-1-carboxylate (135 mg, 0.36 mmol, 1.1 equiv) and NEt₃ (65 μL, 0.43 mmol, 1.2 equiv) in MeCN (5 mL), and heated to 80 °C for 5 h. The reaction was cooled with ice and product precipitated with addition of Et₂O, which was further washed with H₂O to yield white solid. Purification by preparative HPLC (5–95% MeCN in H₂O) yielded a white solid (35 mg, 17%).

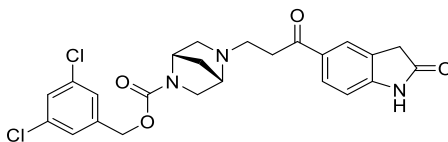
ν_{\max} (neat): 1782, 1668, 1618, 1416 cm⁻¹.

¹H NMR (MeOD-*d*₄, 400 MHz): δ 7.99 (dd, *J* = 8.2, 1.5 Hz, 1H), 7.91–7.86 (m, 1H), 7.39–7.14 (m, 7H), 4.89 (s, 2H), 4.77–4.67 (m, 1H), 4.39–4.17 (m, 1H), 3.73–3.58 (m, 6H), 3.58–3.44 (m, 2H), 3.21–2.85 (m, 2H), 1.41–1.09 (m, 9H).

¹³C NMR (MeOD-*d*₄, 101 Hz): δ 194.5, 154.8, 153.1, 143.5, 135.1, 130.0, 128.6, 128.5, 128.3, 127.9, 126.1, 124.9, 108.7, 108.4, 31.5, 26.3. 6 × C not observed (coincident).

HRMS: exact mass calculated for [M+H⁺] (C₂₆H₃₂N₃O₅) requires 466.2336 *m/z*, found 466.2341 *m/z*.

3,5-dichlorobenzyl (1*S*,4*S*)-5-(3-oxo-3-(2-oxoindolin-5-yl)propyl)-2,5-diazabicyclo[2.2.1]heptane-2-carboxylate, 2.114.



Prepared according to General Procedure **J**, using 5-(3-chloropropanoyl)indolin-2-one **2.10** (46 mg, 0.20 mmol, 1.0 equiv), 3,5-dichlorobenzyl (1*S*,4*S*)-2,5-diazabicyclo[2.2.1]heptane-2-carboxylate **2.33** (68 mg, 0.22 mmol, 1.1 equiv), NEt₃ (34 μL, 0.38 mmol, 1.2 equiv), MeCN

(1 mL) at 50 °C for 4 h. The reaction was diluted with H₂O (20 mL), the organics were extracted using CH₂Cl₂ (2 × 20 mL), dried with a hydrophobic frit, and concentrated *in vacuo* to give a residue that was purified by column chromatography with silica (2–10% MeOH in CH₂Cl₂) to afford the desired product as a clear oil (82 mg, 77%).

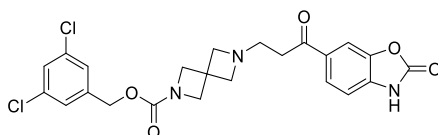
ν_{\max} (CH₂Cl₂): 1699, 1674, 1411 cm⁻¹.

¹H NMR (CDCl₃, 400 MHz): δ 9.12 (s, 1H), 7.94–7.85 (m, 2H), 7.33–7.29 (m, 1H), 7.26–7.21 (m, 1H), 6.95 (d, *J* = 8.1, 1H), 5.15–4.09 (m, 2H), 4.47–4.37 (m, 1H), 3.68–3.54 (m, 4H), 3.28 (dd, *J* = 1.8, 10.2 Hz, 1H), 3.16–2.93 (m, 5H), 2.76–2.61 (m, 1H), 2.19 (s, 1H), 1.93–1.86 (m, 1H), 1.76 (t, *J* = 8.9 Hz, 1H).

¹³C NMR (CDCl₃, 101 MHz): δ 197.1, 177.1, 153.5, 153.4, 146.64, 146.61, 139.7, 134.6, 131.2, 131.1, 129.0, 127.6, 127.6, 123.6, 125.5, 125.1, 124.1, 108.8, 64.8, 64.6, 61.3, 60.7, 59.8, 59.4, 57.3, 57.1, 49.4, 49.3, 49.2, 49.0, 37.7, 37.6, 35.7, 35.4, 35.1, 30.5. Rotameric mixture present.

HRMS: exact mass calculated for [M+H]⁺ (C₂₄H₂₄Cl₂N₃O₄) requires 488.1138 *m/z*, found 488.1130 *m/z*.

3,5-dichlorobenzyl 6-(3-oxo-3-(2-oxo-2,3-dihydrobenzo[*d*]oxazol-6-yl)propyl)-2,6-diazaspiro[3.3]heptane-2-carboxylate, 2.115.



Prepared according to General Procedure **J**, using 6-(3-chloropropanoyl)benzo[*d*]oxazol-2(3*H*)-one **2.6** (36.5 mg, 0.16 mmol, 1.0 equiv), 3,5-dichlorobenzyl 2,6-diazaspiro[3.3]heptane-2-carboxylate **2.23 a** (53.6 mg, 0.18 mmol, 1.1 equiv), NEt₃ (27 μ L, 0.19 mmol, 1.2 equiv) in MeCN (2 mL) and stirred at 80°C for 1 h. The reaction was cooled and H₂O (20 mL) was added resulting in a white precipitate, which was filtered under vacuum to afford the desired product as a white solid (37 mg, 42 %).

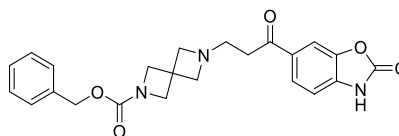
ν_{\max} (neat): 3067, 2948, 2877, 1771, 1706, 1416 cm⁻¹.

¹H NMR (DMSO-*d*₆, 400 MHz): δ 7.82 (dq, *J* = 1.6, 3.3 Hz, 2H), 7.55 (t, *J* = 1.9 Hz, 1H), 7.39 (d, *J* = 1.9 Hz, 2H), 7.20 (d, *J* = 8.6 Hz, 1H), 5.02 (s, 2H), 4.05 (s, 4H), 3.67 (s, 4H), 3.14 (t, *J* = 6.8 Hz, 2H), 3.00 (t, *J* = 6.7 Hz, 2H). 1 × H not observed (exchangeable).

¹³C NMR (DMSO-*d*₆, 101 MHz): δ 196.4, 155.1, 154.6, 143.4, 141.2, 135.4, 134.0, 127.4, 126.1, 125.1, 109.4, 108.8, 64.1, 63.0, 51.9, 34.9, 33.1. 2 × C not observed (coincident).

HRMS: exact mass calculated for [M+H]⁺ (C₂₃H₂₂Cl₂N₃O₅) requires 490.0931 *m/z*, found 490.0924 *m/z*.

Benzyl 6-(3-oxo-3-(2-oxo-2,3-dihydrobenzo[*d*]oxazol-6-yl)propyl)-2,6-diazaspiro[3.3]heptane-2-carboxylate, 2.116.



Prepared according to General Procedure J, using 6-(3-chloropropanoyl)benzo[*d*]oxazol-2(3*H*)-one **2.6** (55 mg, 0.24 mmol, 1.0 equiv), benzyl 2,6-diazaspiro[3.3]heptane-2-carboxylate **2.23 b** (62 mg, 0.27 mmol, 1.1 equiv) and NEt₃ (41 μL, 0.29 mmol, 1.2 equiv) in MeCN (2 mL) to afford the desired product as a white solid (31 mg, 30 %).

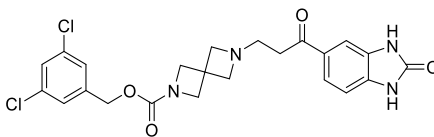
ν_{max} (neat): 2946, 2873, 1771, 1698, 1661 cm⁻¹.

¹H NMR (CDCl₃, 400 MHz): δ 7.82–7.75 (m, 2H), 7.37–7.28 (m, 5H), 7.07 (d, *J* = 8.1 Hz, 1H), 5.08 (s, 2H), 4.07 (s, 4H), 3.37 (s, 4H), 2.98 (t, *J* = 6.9 Hz, 2H), 2.85 (t, *J* = 7.0 Hz, 2H). 1 × H not observed (exchangeable).

¹³C NMR (CDCl₃, 101 MHz): δ 196.8, 156.4, 155.1, 144.2, 136.7, 134.2, 132.1, 128.6, 128.2, 128.1, 125.4, 109.8, 109.4, 66.9, 64.5, 54.2, 36.7, 34.0. 1 × C not observed (coincident).

HRMS: exact mass calculated for [M+H]⁺ (C₂₃H₂₄N₃O₅) requires 422.1710 *m/z*, found 422.1717 *m/z*.

3,5-dichlorobenzyl 6-(3-oxo-3-(2-oxo-2,3-dihydro-1H-benzo[d]imidazol-5-yl)propyl)-2,6-diazaspiro[3.3]heptane-2-carboxylate, 2.117.



To a round bottom flask was added 5-(3-chloropropanoyl)-1,3-dihydro-2*H*-benzo[*d*]imidazol-2-one **2.8** (67 mg, 0.30 mmol, 1.0 equiv), 3,5-dichlorobenzyl 2,6-diazaspiro[3.3]heptane-2-carboxylate trifluoroacetate **2.23 a** (137 mg, 0.33 mmol, 1.1 equiv) and NEt₃ (93 μL, 0.66 mmol, 2.2 equiv) in MeCN (2 mL) and stirred at 80°C for 1 h. The reaction was cooled and H₂O (20 mL) was added resulting in a white precipitate, which was filtered under vacuum to afford the desired product as a white solid (65 mg, 44 %).

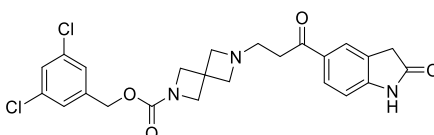
ν_{max} (neat): 2949, 2817, 2877, 2832, 1733, 1696 1680 cm⁻¹

¹H NMR (DMSO-*d*₆, 400 MHz): δ 11.03 (s, 1H), 10.85 (s, 1H), 7.64 (dd, *J* = 1.6, 8.2 Hz, 1 H), 7.55 (t, *J* = 1.9 Hz, 1H), 7.45 (d, *J* = 1.3 Hz, 1H), 7.39 (d, *J* = 1.9 Hz, 2H), 7.01 (d, *J* = 8.2 Hz, 1H), 5.01 (s, 2H), 4.08–3.93 (s, 4H), 3.35–3.26 (s, 4H), 2.95 (t, *J* = 6.9 Hz, 2H), 2.71 (t, *J* = 6.6 Hz, 2H).

¹³C NMR (DMSO-*d*₆, 101 MHz): δ 197.4, 155.5, 155.2, 141.3, 134.1, 134.0, 129.8, 129.7, 127.4, 126.2, 122.3, 107.9, 107.7, 64.1, 63.4, 53.9, 35.9, 33.3, 1 × C not observed (coincident).

HRMS: exact mass calculated for [M+H]⁺ (C₂₃H₂₃Cl₂N₄O₄) requires 489.1091 *m/z*, found 489.1085 *m/z*.

3,5-dichlorobenzyl 6-(3-oxo-3-(2-oxoindolin-5-yl)propyl)-2,6-diazaspiro[3.3]heptane-2-carboxylate, 2.118.



Prepared according to General Procedure **J**, using 5-(3-chloropropanoyl)indolin-2-one **2.10** (36.5 mg, 0.16 mmol, 1.0 equiv), 3,5-dichlorobenzyl 2,6-diazaspiro[3.3]heptane-2-carboxylate **2.23 a** (53.6 mg, 0.18 mmol, 1.1 equiv) and NEt₃ (27 μL, 0.19 mmol, 1.2 equiv) in MeCN (2 mL) to yield the desired product as a white solid (37 mg, 42 %).

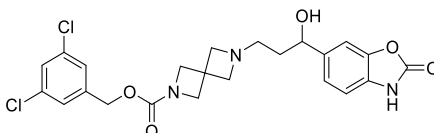
ν_{\max} (CDCl₃): 3236, 3076, 2950, 2877, 1712, 1618, 1417 cm⁻¹.

¹H NMR (CDCl₃, 400 MHz): δ 7.89–7.82 (m, 2H), 7.29 (t, J = 1.9 Hz, 1H), 7.20 (d, J = 1.9 Hz, 2H), 6.91 (d, J = 8.2 Hz, 1H), 5.00 (s, 2H), 4.10–4.04 (m, 4H), 3.96 (s, 2H), 3.47–3.41 (m, 4H), 3.02–2.95 (m, 2H), 2.94–2.84 (m, 2H). 1 \times H not observed (exchangeable).

¹³C NMR (101 MHz, CDCl₃): δ 176.4, 155.6, 140.1, 135.2, 129.7, 128.4, 126.31, 126.26, 125.7, 124.9, 109.2, 65.2, 64.4, 36.8, 34.0. 5 \times C not observed (coincident).

HRMS: exact mass calculated for [M+H]⁺ (C₂₄H₂₄Cl₂N₃O₄) requires 488.1138 m/z , found 488.1131 m/z .

3,5-dichlorobenzyl 6-(3-hydroxy-3-(2-oxo-2,3-dihydrobenzo[*d*]oxazol-6-yl)propyl)-2,6-diazaspiro[3.3]heptane-2-carboxylate, 2.119.



Prepared according to General Procedure I, using 3,5-dichlorobenzyl 3,5-dichlorobenzyl 6-(3-oxo-3-(2-oxo-2,3-dihydrobenzo[*d*]oxazol-6-yl)propyl)-2,6-diazaspiro[3.3]heptane-2-carboxylate **2.119** (179 mg, 0.37 mmol, 1.0 equiv), NaBH₄ (41 mg, 1.09 mmol, 3.0 equiv) and EtOH (1.8 mL) and purified using preparative mass directed automated purification with (15–100% MeCN in H₂O with formic acid buffer) to afford the desired product as a white solid (37 mg, 21 %).

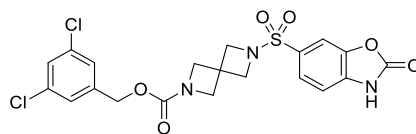
ν_{\max} (CDCl₃): 3333, 2950, 2856, 2877, 1773, 1706, 1419 cm⁻¹.

¹H NMR (DMSO-*d*₆, 400 MHz): δ 8.21 (s, 1H), 7.55 (t, J = 1.9 Hz, 1H), 7.39 (d, J = 1.9 Hz, 2H), 7.19 (d, J = 1.3 Hz, 1H), 7.07 (dd, J = 1.3, 8.1 Hz, 1H), 7.00 (d, J = 8.0 Hz, 1H), 5.01 (s, 2H), 4.57 (dd, J = 5.4, 7.3 Hz, 1H), 4.11–3.93 (s, 4H), 3.31 (s, 4H), 2.43 (t, J = 7.2 Hz, 1H), 1.64–1.51 (m, 2H). 2 \times H not observed (exchangeable).

¹³C NMR (DMSO-*d*₆, 101 MHz): δ 164.1, 155.6, 155.0, 143.7, 141.7, 140.9, 134.5, 129.3, 127.9, 126.6, 121.5, 109.5, 107.3, 70.8, 64.6, 63.6, 55.6, 37.1, 33.8.

HRMS: exact mass calculated for [M+H]⁺ (C₂₃H₂₄Cl₂N₃O₅) requires m/z 492.1088, found m/z 492.1078.

3,5-dichlorobenzyl **6-((2-oxo-2,3-dihydrobenzo[*d*]oxazol-6-yl)sulfonyl)-2,6-diazaspiro[3.3]heptane-2-carboxylate, 2.120.**



Prepared according to General Procedure **M**, using 2-oxo-2,3-dihydrobenzo[*d*]oxazole-6-sulfonyl chloride **2.11** (70 mg, 0.30 mmol, 1.0 equiv), 2,6-diazaspiro[3.3]heptane-2-carboxylate trifluoroacetate salt **2.23 a** (137 mg, 0.33 mmol, 1.1 equiv), NEt₃ (93 μL, 2.2 mmol, 0.66 equiv) in MeCN (2 mL) and H₂O (20 mL) was added to the reaction and a white precipitate filtered under vacuum to afford the desired product as a white solid (7 mg, 5 %).

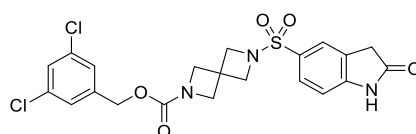
ν_{max} (neat): 2944, 2875, 1769, 1706 cm⁻¹.

¹H NMR (DMSO-*d*₆, 400 MHz): δ 7.69 (d, *J* = 1.6 Hz, 1H), 7.60 (dd, *J* = 1.7, 8.2 Hz, 1H), 7.54 (t, *J* = 1.9 Hz, 1H), 7.36 (d, *J* = 1.9 Hz, 2H), 7.33 (d, *J* = 8.2 Hz, 1H), 4.98 (s, 2H), 3.90 (s, 4H), 3.84 (s, 4H). 1 × H not observed (exchangeable).

¹³C NMR (DMSO-*d*₆, 101 MHz): δ 155.0, 154.1, 143.2, 141.1, 135.2, 134.0, 127.4, 126.7, 126.1, 124.9, 109.9, 109.3, 64.1, 59.8, 58.3, 32.0.

HRMS: exact mass calculated for [M+NH₄]⁺ (C₂₀H₂₁Cl₂N₄O₆S) requires 515.0553 *m/z*, found 515.0546 *m/z*.

3,5-dichlorobenzyl **6-((2-oxoindolin-5-yl)sulfonyl)-2,6-diazaspiro[3.3]heptane-2-carboxylate, 2.121.**



To a round bottom flask was added 2-oxoindoline-5-sulfonyl chloride **2.12** (35 mg, 0.15 mmol, 1.0 equiv), 2,6-diazaspiro[3.3]heptane-2-carboxylate trifluoroacetate salt **2.23 a** (69 mg, 0.17 mmol, 1.1 equiv), NEt₃ (46 μL, 0.33 mmol, 2.2 equiv) in MeCN (1 mL) and stirred at 50 °C for 16 h. H₂O (20 mL) was added to the reaction and the precipitate filtered under vacuum to afford the desired product as a red solid (5 mg, 3%).

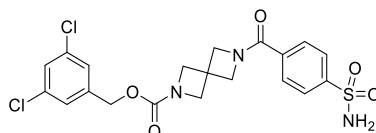
ν_{\max} (neat): 2944, 2877, 1709, 1620 cm^{-1}

^1H NMR (DMSO- d_6 , 400 MHz): δ 10.85 (s, 1H), 7.63 (dd, $J = 1.8, 8.2$ Hz, 1H), 7.61–7.58 (m, 1H), 7.54 (t, $J = 1.9$ Hz, 1H), 7.36 (d, $J = 1.9$ Hz, 2H), 7.03 (d, $J = 8.2$ Hz, 1H), 4.98 (s, 2H), 3.90 (s, 4H), 3.81 (s, 4H), 3.61 (s, 2H). 1 \times H not observed (exchangeable).

^{13}C NMR (DMSO- d_6 , 101 MHz): δ 176.4, 155.0, 148.5, 141.1, 134.0, 128.9, 127.4, 127.0, 126.1, 125.8, 124.2, 109.1, 64.1, 59.6, 35.6, 32.0, 1 \times C not observed (coincident).

HRMS: exact mass calculated for $[\text{M}+\text{H}]^+$ ($\text{C}_{21}\text{H}_{20}\text{Cl}_2\text{N}_3\text{O}_5\text{S}$) requires 496.0495 m/z , found 496.0490 m/z .

3,5-dichlorobenzyl 6-(4-sulfamoylbenzoyl)-2,6-diazaspiro[3.3]heptane-2-carboxylate, 2.122.



To a round bottom flask was added 4-sulfamoylbenzoic acid (50 mg, 0.24 mmol, 1.0 equiv), 4-methylmorpholine (132 μL , 1.2 mmol, 5.0 equiv) and then HATU (91 mg, 0.24 mmol, 1.0 equiv) in DMF (1 mL) and stirred at room temperature for 15 mins. To the flask was added 3,5-dichlorobenzyl 2,6-diazaspiro[3.3]heptane-2-carboxylate trifluoroacetate salt **2.23 a** (105 mg, 0.25 mmol, 1.0 equiv) and stirred at room temperature for 16 h, H_2O (20 mL) was added to the reaction and a white precipitate filtered under vacuum to afford the desired product as a white solid (53 mg, 46 %).

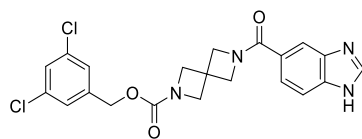
ν_{\max} (neat): 3077.9, 2951, 2881, 1708, 1572, 1419 cm^{-1} .

^1H NMR (DMSO- d_6 , 400 MHz): δ 7.88 (d, $J = 8.6$ Hz, 2H), 7.78 (d, $J = 8.6$ Hz, 2H), 7.57 (t, $J = 1.9$ Hz, 1H), 7.49 (s, 1H), 7.42–7.39 (m, 2H), 5.02 (s, 2H), 4.47–4.38 (m, 2H), 4.21 (s, 2H), 4.18–4.02 (m, 4H).

^{13}C NMR (DMSO- d_6 , 101 MHz): δ 167.5, 155.1, 146.0, 141.2, 136.0, 134.0, 128.3, 127.4, 126.2, 126.1, 125.7, 64.1, 62.7, 62.3, 58.4, 33.2, 32.7.

HRMS: exact mass calculated for $[\text{M}+\text{H}]^+$ ($\text{C}_{20}\text{H}_{20}\text{Cl}_2\text{N}_3\text{O}_5\text{S}$) requires 484.0495 m/z , found 484.0487 m/z .

3,5-dichlorobenzyl 6-(1*H*-benzo[*d*]imidazole-5-carbonyl)-2,6-diazaspiro[3.3]heptane-2-carboxylate, 2.123.



To a round bottom flask was added 1*H*-benzo[*d*]imidazole-5-carboxylic acid (27 mg, 0.17 mmol, 1.0 equiv), DIPEA (84 μ L, 0.48 mmol, 3.0 equiv) and then COMU (69 mg, 0.16 mmol, 1.0 equiv) in DMF (1 mL) and stirred at room temperature for 15 mins. To the flask was added 3,5-dichlorobenzyl 2,6-diazaspiro[3.3]heptane-2-carboxylate trifluoroacetate salt **2.23 a** (68 mg, 0.16 mmol, 1.0 equiv) and stirred at room temperature for 16 h, aqueous HCl (1M, 20 mL) was added to the reaction and the organics were extracted with EtOAc (20 mL), washed with brine (20 mL), dried with a hydrophobic frit and concentrated *in vacuo*. The crude material was triturated with petroleum ether to afford the desired product as a beige solid (60 mg, 81%).

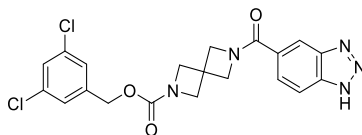
ν_{\max} (neat): 2724, 1670, 1593, 1445 cm^{-1} .

^1H NMR (CDCl_3 , 500 MHz): δ 8.12 (s, 1H), 8.04–7.83 (m, 1H), 7.70–7.40 (m, 1H), 7.31–7.28 (m, 1H), 7.2–7.19 (m, 2H), 5.02 (s, 2H), 4.60–4.28 (m, 4H), 4.25–4.14 (m, 4H), 2.95 (s, 1H).

^{13}C NMR (CDCl_3 , 101 MHz): δ 171.1, 158.1, 155.5, 139.9, 135.3, 128.4, 127.6, 126.44, 126.36, 125.2, 66.3, 65.42, 65.37, 63.8, 50.9, 48.6, 40.3, 33.5. Rotameric mixture observed.

HRMS: exact mass calculated for $[\text{M}+\text{H}]^+$ ($\text{C}_{21}\text{H}_{19}\text{Cl}_2\text{N}_4\text{O}_3$) requires 445.0829 m/z , found 445.0824 m/z .

3,5-dichlorobenzyl 6-(1*H*-benzo[*d*][1,2,3]triazole-5-carbonyl)-2,6-diazaspiro[3.3]heptane-2-carboxylate, 2.124.



To a round bottom flask was added 1*H*-benzo[*d*][1,2,3]triazole-5-carboxylic acid (26 mg, 0.16 mmol, 1.0 equiv), DIPEA (84 μ L, 0.48 mmol, 3.0 equiv) and then COMU (69 mg, 0.16 mmol, 1.0 equiv) in DMF (1 mL) and stirred at room temperature for 15 mins. To the flask was added 3,5-dichlorobenzyl 2,6-diazaspiro[3.3]heptane-2-carboxylate trifluoroacetate salt **2.23 a** (68

mg, 0.16 mmol, 1.0 equiv) and stirred at room temperature for 16 h, aqueous HCl (1M, 20 mL) was added to the reaction and the organics were extracted with EtOAc (20 mL), washed with brine (20 mL), dried with a hydrophobic frit and concentrated *in vacuo*. The crude material was purified with column chromatography with silica (60% EtOAc in petroleum ether – 100% MeOH) to afford the desired product as a beige solid (28 mg, 40%).

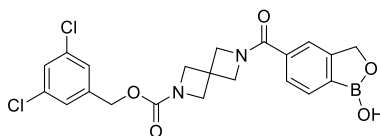
ν_{\max} (neat): 2359, 2330, 1673, 1595, 1447 cm^{-1} .

$^1\text{H NMR}$ (CDCl_3 , 500 MHz): δ 8.27-8.14 (m, 1H), 7.93-7.68 (m, 2H), 7.31-7.28 (m, 1H), 7.23-7.18 (m, 2H), 5.08 (s, 2H), 4.58–4.37 (m, 4H), 4.32–4.14 (m, 4H), 2.50 (s, 1H).

$^{13}\text{C NMR}$ (CDCl_3 , 101 MHz): δ 169.9, 155.5, 139.6, 135.1, 128.3, 126.2, 65.4, 63.6, 59.2, 33.4. $6 \times \text{C}$ not observed (coincident).

HRMS: exact mass calculated for $[\text{M}+\text{H}]^+$ ($\text{C}_{20}\text{H}_{18}\text{Cl}_2\text{N}_5\text{O}_3$) requires 446.0781 m/z , found 446.0784 m/z .

3,5-dichlorobenzyl 6-(1-hydroxy-1,3-dihydrobenzo[*c*][1,2]oxaborole-5-carbonyl)-2,6-diazaspiro[3.3]heptane-2-carboxylate, 2.125.



To a round bottom flask was added 1-hydroxy-1,3-dihydrobenzo[*c*][1,2]oxaborole-5-carboxylic acid **2.17** (233 mg, 0.13 mmol, 1.0 equiv), PyBOP (67 mg, 0.13 mmol, 1.0 equiv), HOBt (20 mg, 0.13 mmol, 1.0 equiv) and DIPEA (45 μL , 0.26 mmol, 2.0 equiv) in DMF (0.26 mL) and stirred at room temperature for 15 mins. To the flask was added 3,5-dichlorobenzyl 2,6-diazaspiro[3.3]heptane-2-carboxylate trifluoroacetate salt **2.23 a** (54 mg, 0.13 mmol, 1.0 equiv) and stirred at room temperature for 16 h, the reaction was diluted with H_2O (20 mL), the organics were extracted with EtOAc (20 mL), washed with H_2O (20 mL), dried with a hydrophobic frit and concentrated *in vacuo*. The crude material was purified by silica chromatography with 0–5% MeOH in CH_2Cl_2 to yield the desired product as a white solid (10 mg, 17 %).

ν_{\max} (neat): 2981, 2845, 1684 cm^{-1} .

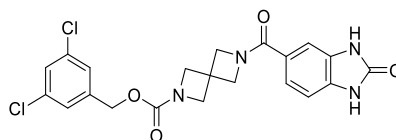
^1H NMR (CDCl_3 , 400 MHz): δ 7.78 (d, $J = 7.6$ Hz, 1H), 7.62 (s, 1H), 7.55 (d, $J = 7.5$ Hz, 1H), 7.31 (t, $J = 1.9$ Hz, 1H), 7.21 (d, $J = 1.8$ Hz, 2H), 5.12 (s, 2H), 5.02 (s, 2H), 4.45–4.31 (m, 4H), 4.28–4.13 (m, 4H).

^{13}C NMR (101 MHz, CDCl_3): δ 170.7, 155.7, 154.6, 140.1, 135.50, 135.47, 131.0, 128.7, 126.8, 126.6, 121.0, 71.5, 65.6, 30.1. $3 \times \text{C}$ not observed, including carbon bearing boron.

^{11}B NMR (CDCl_3 , 128 MHz): δ 30.63.

HRMS: exact mass calculated for $[\text{M}-\text{H}]^-$ ($\text{C}_{21}\text{H}_{18}\text{BCl}_2\text{N}_2\text{O}_5$) requires 459.0692 m/z , found 459.0681 m/z .

3,5-dichlorobenzyl 6-(2-oxo-2,3-dihydro-1H-benzo[d]imidazole-5-carbonyl)-2,6-diazaspiro[3.3]heptane-2-carboxylate, 2.126.



Prepared according to General Procedure **O**, using 2-oxo-2,3-dihydro-1H-benzo[d]imidazole-5-carboxylic acid **2.14** (50 mg, 0.28 mmol, 1.1 equiv), DIPEA (174 μL , 1.0 mmol, 4.0 equiv), HATU (107 mg, 0.28 mmol, 1.1 equiv), 3,5-dichlorobenzyl 2,6-diazaspiro[3.3]heptane-2-carboxylate trifluoroacetate salt **2.23 a** (106 mg, 0.25 mmol, 1.0 equiv) and DMF (2 mL) and a white precipitate filtered under vacuum to afford the desired product as a white solid (19 mg, 24 %).

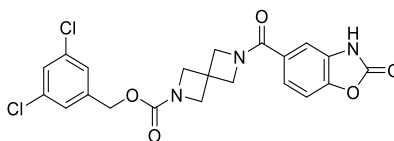
ν_{max} (neat): 1697, 1427, 1328 cm^{-1} .

^1H NMR ($\text{DMSO}-d_6$, 400 MHz): δ 11.02 (s, 1H), 10.85 (s, 1H), 7.65 (dd, $J = 1.6, 8.2$ Hz, 1H), 7.56 (t, $J = 1.9$ Hz, 2H), 7.45 (d, $J = 1.4$ Hz, 1H), 7.40 (d, $J = 1.9$ Hz, 1H), 7.01 (d, $J = 8.2$ Hz, 1H), 5.01 (s, 2H), 4.48–4.40 (app. s, 2H), 4.23–4.02 (app. s, 6H).

^{13}C NMR ($\text{DMSO}-d_6$, 101 MHz): δ 169.0, 155.3, 155.1, 141.2, 134.0, 132.1, 129.5, 127.4, 126.2, 125.2, 120.9, 108.0, 107.8, 64.1, 32.7. $2 \times \text{C}$ not observed (coincident).

HRMS: exact mass calculated for $[\text{M}-\text{H}]^-$ ($\text{C}_{21}\text{H}_{17}\text{Cl}_2\text{N}_4\text{O}_4$) requires 459.0632 m/z , found 459.0628 m/z .

3,5-dichlorobenzyl 6-(2-oxo-2,3-dihydrobenzo[*d*]oxazole-5-carbonyl)-2,6-diazaspiro[3.3]heptane-2-carboxylate, 2.127.



To a round bottom flask was added 2-oxo-2,3-dihydrobenzo[*d*]oxazole-5-carboxylic acid **2.15** (50 mg, 0.24 mmol, 1.0 equiv), 4-methylmorpholine (132 μ L, 1.2 mmol, 5.0 equiv) and then HATU (91 mg, 0.24 mmol, 1.0 equiv) in DMF (1 mL) and stirred at room temperature for 15 mins. To the flask was added 3,5-dichlorobenzyl 2,6-diazaspiro[3.3]heptane-2-carboxylate trifluoroacetate salt **2.23 a** (105 mg, 0.25 mmol, 1.0 equiv) and stirred at room temperature for 16 h. Purified by silica chromatography with 80–100% EtOAc in petroleum ether (44mg, 60 %).

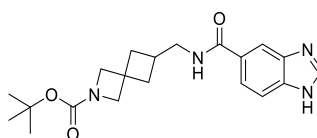
ν_{\max} (neat): 3076, 2948, 2875, 1766, 1706, 1600, 1417 cm^{-1} .

^1H NMR (DMSO-*d*₆, 400 MHz): δ 7.43 (d, J = 1.4 Hz, 1H), 7.30–7.28 (m, 2H), 7.21 (d, J = 1.8 Hz, 2H), 7.15 (d, J = 8.3 Hz, 1H), 5.02 (s, 2H), 4.49–4.32 (m, 4H), 4.29–4.14 (m, 4H). 1 \times H not observed (exchangeable).

^{13}C NMR (CDCl₃, 101 MHz): δ 169.7, 155.6, 154.9, 146.1, 139.5, 135.3, 130.6, 128.6, 128.4, 126.4, 122.4, 110.3, 109.6, 65.4, 33.5. 2 \times C not observed (coincident).

HRMS: exact mass calculated for $[\text{M}+\text{H}]^+$ (C₂₁H₁₈Cl₂N₃O₅) requires 462.0618 m/z , found 462.0615 m/z .

***Tert*-butyl 6-((1*H*-benzo[*d*]imidazole-5-carboxamido)methyl)-2-azaspiro[3.3]heptane-2-carboxylate, 2.129.**



Prepared according to General Procedure **D**, with 1*H*-benzo[*d*]imidazole-5-carboxylic acid (110 mg, 0.68 mmol, 1.1 equiv), HATU (259 mg, 0.68 mmol, 1.1 equiv), *tert*-butyl 6-

(aminomethyl)-2-azaspiro[3.3]heptane-2-carboxylate (140 mg, 0.62 mmol, 1.0 equiv) and DIPEA (324 μ L, 1.85 mmol, 3.0 equiv) in DMF (2.0 mL). The organics were extracted with EtOAc (2 \times 40 mL), washed with brine (40 mL), dried with a hydrophobic frit and concentrated *in vacuo*. The crude material was purified by column chromatography with silica (10% MeOH in CH₂Cl₂) to afford the desired product as a white solid (209 mg, 91 %).

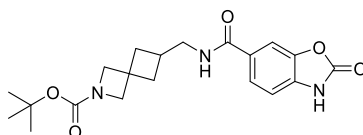
ν_{\max} (neat): 3365, 2974, 2929, 2871, 1682, 1643, 1419 cm⁻¹.

¹H NMR (CDCl₃, 400 MHz): δ 8.13–8.05 (m, 2H), 7.62 (d, *J* = 8.3 Hz, 1H), 7.54–7.48 (m, 1H), 7.13 (s, 1H), 3.88–3.73 (m, 2H), 3.47 (s, 2H), 3.44–3.39 (m, 2H), 2.47–2.37 (m, 1H), 2.26–2.16 (m, 2H), 1.93–1.84 (m, 2H), 1.41 (s, 9H).

¹³C NMR (101 MHz, CDCl₃): δ 169.0, 156.4, 143.2, 129.3, 121.7, 115.5, 79.6, 61.3, 45.1, 36.7, 34.3, 29.5, 28.5. 3 \times C not observed (coincident).

HRMS: exact mass calculated for [M+H]⁺ (C₂₀H₂₈N₄O₃) requires 3711.2078 *m/z*, found 371.2081 *m/z*.

***Tert*-butyl 6-((2-oxo-2,3-dihydrobenzo[*d*]oxazole-6-carboxamido)methyl)-2-azaspiro[3.3]heptane-2-carboxylate, 2.130.**



Prepared according to General Procedure D, with 2-oxo-2,3-dihydrobenzo[*d*]oxazole-6-carboxylic acid **2.13** (122 mg, 0.68 mmol, 1.1 equiv), HATU (259 mg, 0.68 mmol, 1.1 equiv), *tert*-butyl 6-(aminomethyl)-2-azaspiro[3.3]heptane-2-carboxylate (140 mg, 0.62 mmol, 1.0 equiv) and DIPEA (324 μ L, 1.85 mmol, 3.0 equiv) in DMF (2.0 mL). The organics were extracted with EtOAc (2 \times 40 mL), washed with brine (40 mL), dried with a hydrophobic frit and concentrated *in vacuo*. The crude material was purified by column chromatography with silica (50–80% EtOAc in petroleum ether) to afford the desired product as a white solid (85 mg, 35 %).

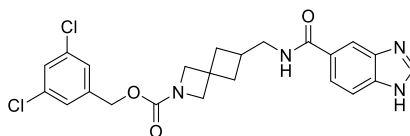
ν_{\max} (neat): 3359, 3084, 2974, 2927, 2871, 1769, 1496, 1414 cm⁻¹.

¹H NMR (CDCl₃, 400 MHz): δ 10.36 (s, 1H), 7.61–7.52 (m, 2H), 7.18–7.08 (m, 1H), 6.99 (d, *J* = 7.8 Hz, 1H), 3.91–1.76 (m, 4H), 3.45–3.34 (m, 2H), 2.50–2.36 (m, 1H), 2.29–2.19 (m, 2H), 1.40 (s, 9H). 1 × H not observed (exchangeable).

¹³C NMR (CDCl₃, 101 MHz): δ 167.6, 156.6, 155.5, 143.7, 132.9, 129.1, 123.8, 109.8, 109.0, 79.9, 45.3, 38.8, 36.7, 34.4, 29.4, 28.5.

HRMS: exact mass calculated for [M+Na]⁺ (C₂₀H₂₅N₃NaO₅) requires 410.1686 *m/z*, found 410.1683 *m/z*.

3,5-dichlorobenzyl **6-((1H-benzo[*d*]imidazole-5-carboxamido)methyl)-2-azaspiro[3.3]heptane-2-carboxylate, 2.131.**



Prepared according to General Procedure C, with *N*-((2-azaspiro[3.3]heptan-6-yl)methyl)-1H-benzo[*d*]imidazole-5-carboxamide (160 mg, 0.61 mmol, 1.0 equiv), (3,5-dichlorophenyl)methanol (120 mg, 0.68 mmol, 1.1 equiv), CDI (110 mg, 0.68 mmol, 1.1 equiv) in DMF (1.0 mL). The reaction was diluted with H₂O (20 mL) organics were extracted with EtOAc (2 × 20 mL), washed with brine (40 mL), dried with a hydrophobic frit and concentrated *in vacuo*. The crude material was purified by column chromatography with silica (50–80% EtOAc in petroleum ether) to afford the desired product as a white solid (37 mg, 13%).

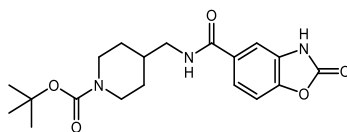
ν_{\max} (neat): 3268, 2966, 2871, 1690, 1574, 1415 cm⁻¹.

¹H NMR (400 MHz, CDCl₃): δ 8.28 (s, 1H), 8.13 (s, 1H), 7.76 (d, *J* = 8.4 Hz, 1H), 7.65 (d, *J* = 8.3 Hz, 2H), 7.37–7.34 (m, 1H), 7.30–7.26 (m, 2H), 5.02 (s, 2H), 4.08–3.88 (m, 4H), 3.40 (d, *J* = 7.1 Hz, 2H), 3.35 (s, 1H), 2.50 (dt, *J* = 7.6, 15.2 Hz, 1H), 2.35–2.30 (m, 2H), 2.05–1.98 (m, 2H).

¹³C NMR (CDCl₃, 101 MHz): δ 170.8, 157.5, 144.7, 142.2, 136.21, 136.17, 130.5, 128.9, 127.2, 123.1, 66.1, 45.9, 37.3, 36.0, 30.5. 4 × C not observed.

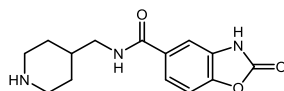
HRMS: exact mass calculated for [M+H]⁺ (C₂₃H₂₃Cl₂N₄O₃) requires 473.1142 *m/z*, found 473.1138 *m/z*.

***Tert*-butyl 4-((2-oxo-2,3-dihydrobenzo[*d*]oxazole-5-carboxamido)methyl)piperidine-1-carboxylate, 2.149.**



Prepared according to General Procedure **O**, using 2-oxo-2,3-dihydrobenzo[*d*]oxazole-5-carboxylic acid **2.15** (200 mg, 1.12 mmol, 1.1 equiv), DMF (2 mL), DIPEA (395 μ L, 3.06 mmol, 3.0 equiv), HATU (426 mg, 1.02 mmol, 1.0 equiv), *tert*-butyl 4-(aminomethyl)piperidine-1-carboxylate (218 mg, 0.15 mmol) and purified by strong cation exchange (propylsulfonic acid functionalised silica, 2N NH₃) to yield the desired product as a clear oil, which was telescoped into the next step for the synthesis of **2.150**.

2-oxo-*N*-(piperidin-4-ylmethyl)-2,3-dihydrobenzo[*d*]oxazole-5-carboxamide, 2.150.



Prepared according to General Procedure **F**, using *tert*-butyl 4-((2-oxo-2,3-dihydrobenzo[*d*]oxazole-5-carboxamido)methyl)piperidine-1-carboxylate, trifluoroacetic acid (1 mL) and CH₂Cl₂ (2 mL) and purified by strong cation exchange (propylsulfonic acid functionalised silica, 2N NH₃ in MeOH) to yield the desired product as a white solid, which was telescoped into the next step for the synthesis of **2.102**.

**Chapter 3 – Structure Based Design of Selective Autotaxin Inhibitors
with a Novel Binding Mode**

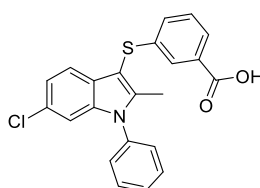
3.1. Introduction to Bile Salts as ATX Inhibitors and Allosteric Inhibitors

The development of allosteric inhibitors of ATX constitutes a relatively new field of research for ATX inhibition. Inhibitors that bind in the allosteric site of ATX reside in the tunnel region (Pink, **Figure 63**).



Figure 63 2D diagram showing the allosteric site in the tunnel of ATX (pink), and the orthosteric site in the active site and hydrophobic pocket of ATX (purple).

Allosteric compounds PAT-347 and TUDCA designed by PharmAkea and NKI respectively, were previously discussed in Section 1.8.2. as the most recent examples of allosteric non-competitive inhibitors which reside in the tunnel of ATX (**Table 9**).^{45,129,171} Additionally to compound 1.10 discussed in Section 1.8.2., compound 3.1 developed by Amira is reported in the patent literature with an $IC_{50} < 0.3 \mu M$ for ATX inhibition in the choline release assay, which is discussed further in Section 1.9.. The compound was also synthesised within our laboratories as a part of a related SAR study around these compounds (**Figure 64**).^{171,172}



3.1

Figure 64 The structure of Amira compound 3.1.¹⁷¹

Through kinetic analysis and co-crystallisation of **3.1** bound to ATX by collaborators NKI (**Figure 65 a and b**), compound **3.1** was shown to be a non-competitive ATX inhibitor which resides in the allosteric site of ATX similarly to PAT-347. The benzoic acid moiety resides at the entrance to the tunnel nearby the solvent interface, with the indole moiety residing between the tunnel and core region of the enzyme. The aromatic moieties, chlorine atom and the methyl on the indole are stabilised in the enzyme by hydrophobic interactions with Phe249, Phe210, His251, and Trp254 (**Figure 65 a**).

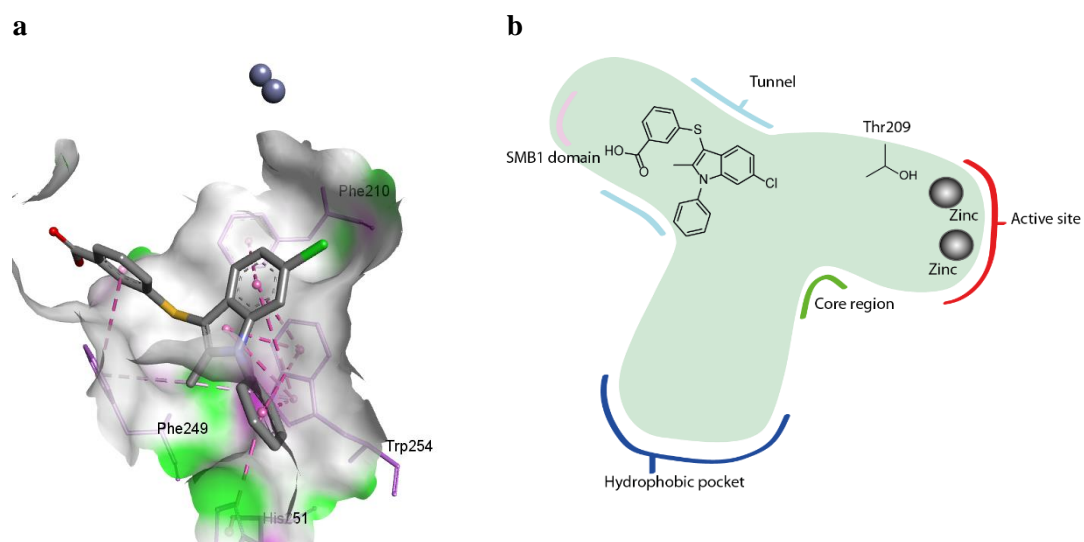


Figure 65 a) Co-crystallography of **3.1** bound to ATX, viewed in DSVisualizer. **b)** 2D diagram of **3.1** in the tunnel of ATX.⁴⁸

Similarly to the co-crystal structure of **3.1**, PharmAkea co-crystallised several indole-based compounds within both the allosteric and orthosteric site of ATX (**Figure 66**).⁴⁵ Of the compounds identified, one of these compounds, PAT-347, was identified as a non-competitive allosteric inhibitor which resides in the tunnel of ATX, whilst PAT-078 was reported as a competitive inhibitor which occupies both the hydrophobic pocket and the tunnel of ATX.

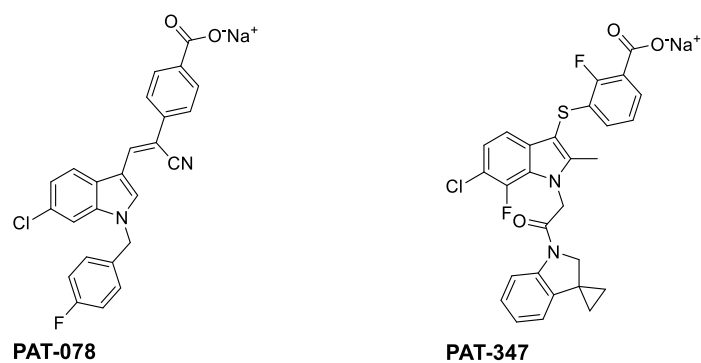


Figure 66 Compound developed by PharmAkea with novel binding modes.

The co-crystal structure of PAT-347 shows that the compound resides in the tunnel of ATX with LPA 14:0 co-crystallised nearby in the orthosteric site, aiding the kinetic analysis by confirming that the compound acts as a non-competitive inhibitor (**Figure 67 a**). The carboxylic acid of PAT-347 resides near the entrance to the tunnel and hydrogen bonds with nearby residues Val278, Ser277, and Ser82, with the chlorine atom on the indole interacting with hydrophobic residues Leu214, Ala218, Trp255, and Phe275. The spiro[cyclopropane-1,3'-indoline] interacts hydrophobically with Trp261, and Pro259, with additional edge to face π -stacking of Trp255 and His252. In comparison, PAT-078 is reported as a competitive ATX inhibitor which is located in the hydrophobic pocket and partially in the tunnel of ATX (**Figure 67 b**). The pendant fluorobenzene resides in the hydrophobic pocket, similarly to PF-8380 and HA155, which were previously discussed in Section 1.8.2. and Section 2.2., with edge to face π -stacking with Phe274 and hydrophobic interactions with Ile168, Leu217, and Ala305 stabilising this lipophilic group in the pocket. The chlorine atom that resides at the entrance to the hydrophobic pocket interacts with hydrophobic residue Ile168, and the indole and benzoic acid groups both edge to face π -stack with Tyr307, which as discussed in Chapter 2 was observed to be important for achieving potency in the core region of the orthosteric inhibitors. The nitrile of PAT-078 hydrogen bonds to Trp260 in the tunnel region.

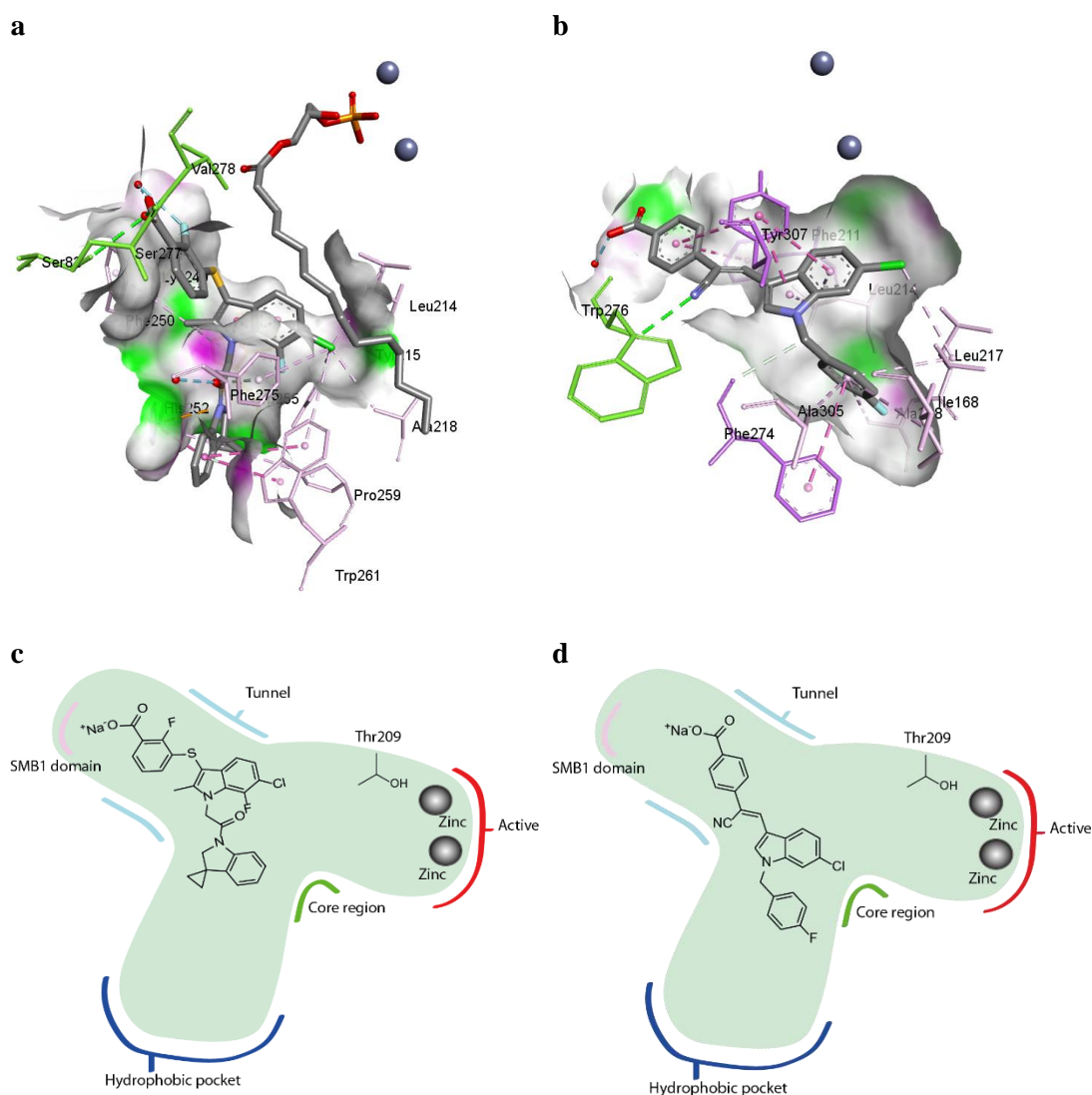


Figure 67 Crystal structures of PAT-347 and PAT-078 **a)** Non-competitive inhibitor PAT-347 bound to ATX in the tunnel region, co-crystallised with LPA at the orthosteric site. **b)** Competitive inhibitor PAT-078 bound to ATX in the hydrophobic pocket and partially in the tunnel region. **c)** 2D diagram of PAT-347 in the orthosteric site of ATX. **d)** 2D diagram of PAT-078 in the orthosteric site of ATX.

Compound PAT-347 and PAT-078 exemplify how the mode of inhibition can be altered from non-competitive to competitive inhibitor when a compound has additional affinity in a region of the orthosteric site, which includes either the hydrophobic pocket or the zinc binding region. In the case of PAT-078 the fluorobenzyl group is able to act as a hydrophobic anchor, outcompeting LPA at the orthosteric site.⁴⁵ There are similarities in the binding mode of PAT-078 with GLPG1690, which was previously discussed in Section 1.8.2. as both compounds are potent ATX inhibitors which bind in the tunnel and the hydrophobic pocket of ATX.

Another allosteric ATX inhibitor was recently reported by Keune *et al.* during studies into the phosphodiesterase activity of ATX residual electron density was observed within the tunnel region of the apo form of the enzyme. Upon further elucidation of the structure it appeared that the electron density belonged to a steroid molecule (**Table 9, Figure 68**).³ The particular steroid observed was tauroursodeoxycholic acid (TUDCA), which is an endogenous bile salt ($IC_{50} = 10.4 \mu\text{M}$) present in the cellular media (**Figure 68**). Further analysis of the ability of other related bile salts to inhibit ATX identified that structurally similar fragments of TUDCA were also able ATX inhibitors, and a modest SAR scope within the tunnel region was established.³ The bile salts identified include ursodeoxycholic acid (UDCA, $IC_{50} = 8.8 \mu\text{M}$, X = OH, **Figure 68 b**), taurochenodeoxycholic acid (TCDCA, $IC_{50} = 6.8 \mu\text{M}$, X = Taurine, **Figure 68 b**), and glycochenodeoxycholic acid (GCDCA, $IC_{50} = 8.1 \mu\text{M}$, X = Glycine, **Figure 68 b**), which are reported as micromolar non-competitive ATX inhibitors.³ The bile salts identified as ATX inhibitors contained a terminal carboxylic acid, taurine, and glycine, respectively. The SAR scope revealed that the (*R, S*)- stereochemistry of the alcohols on the A and B ring (green, **Figure 68 b**) are important for ATX inhibition, with each projecting with the correct vector to hydrogen bond with Trp260 and Tyr82 residues within the tunnel of ATX, respectively (**Figure 69**). In addition to this, Keune *et al* reported functionalisation from the C ring with substituents (blue, **Figure 68 b**) resulted in inactive compounds.³ The right hand side of the bile salts could contain moieties such as taurine and glycine, which resided nearby the tunnel in the core region of the enzyme without a negative effect on ATX inhibition.

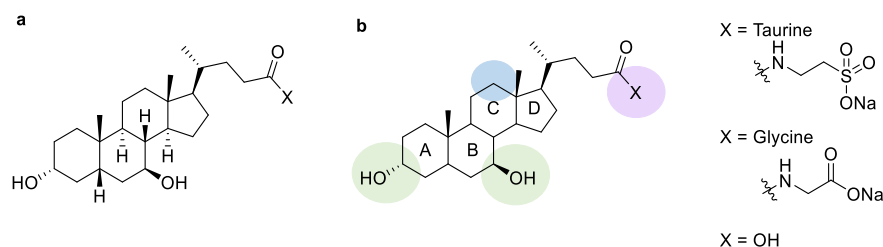


Figure 68 a) Stereochemistry of the UDCA fragment, which shall be simplified to the structure in **b)** throughout. For UDCA X = OH **b)** Functionality important for activity on bile salts.

The TUDCA crystal structure was solved with LPA residing in the hydrophobic pocket by Keune *et al* confirming their kinetic analysis determining the compound acts as a non-competitive inhibitor of ATX. The sulfonic acid fragment on the steroid is believed to interact with a nearby Arg246 residue, however based on the SAR established by Keune *et al* does not appear essential for ATX inhibition.³

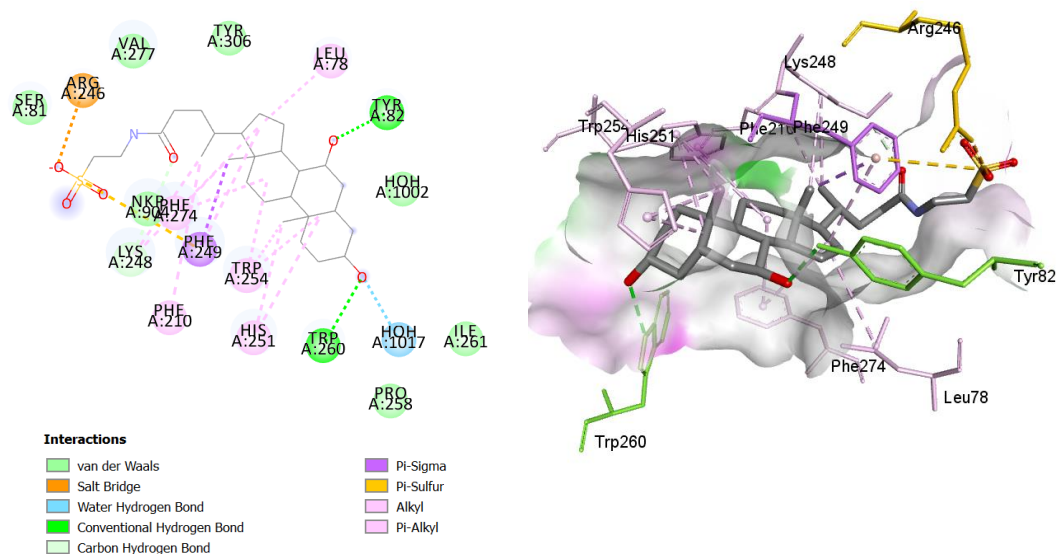


Figure 69 Co-crystal structure of TUDCA bound to ATX (PDB ID: 5DLW), viewed in DS visualizer.^{3,48}

Although the significance of the sulfonic acid moiety that interacts with Arg246 is uncertain, it is believed that this region could be tethered to an additional lipophilic fragment which potentially resides in the hydrophobic pocket of ATX. The design of a hybrid that spans both the orthosteric and allosteric site would likely switch the binding mode to competitive inhibition as observed with compounds PAT-078 and GLPG1690. Due to the potential for hybrid inhibitors to reside in both the tunnel and the hydrophobic pocket, the hybrids could outcompete LPA in either the orthosteric or the allosteric site of the enzyme. Although it has not been confirmed, it is believed that the tunnel could be an entrance for LPC into the active site, and an exit route for LPA.^{3,90,173} The design of a competitive inhibitor which resides in the tunnel could hinder the entrance of LPC into the active site of the enzyme, or conversely impede the exit of LPA.

Both TUDCA and PF-8380 analogue **2.1** have been co-crystallised bound to ATX by NKI.³ The crystal structure of TUDCA shows the taurine tether in the core region of ATX, nearby the piperazine core of **2.1** (**Figure 70**). It was postulated that linking the terminal acid moiety of TUDCA to the nearby piperazine of **2.1** could create an ATX inhibitor which binds in the tunnel and hydrophobic pocket of ATX, and could therefore modulate the mode of inhibition of the resulting hybrids to competitive inhibition (**Figure 70**).³

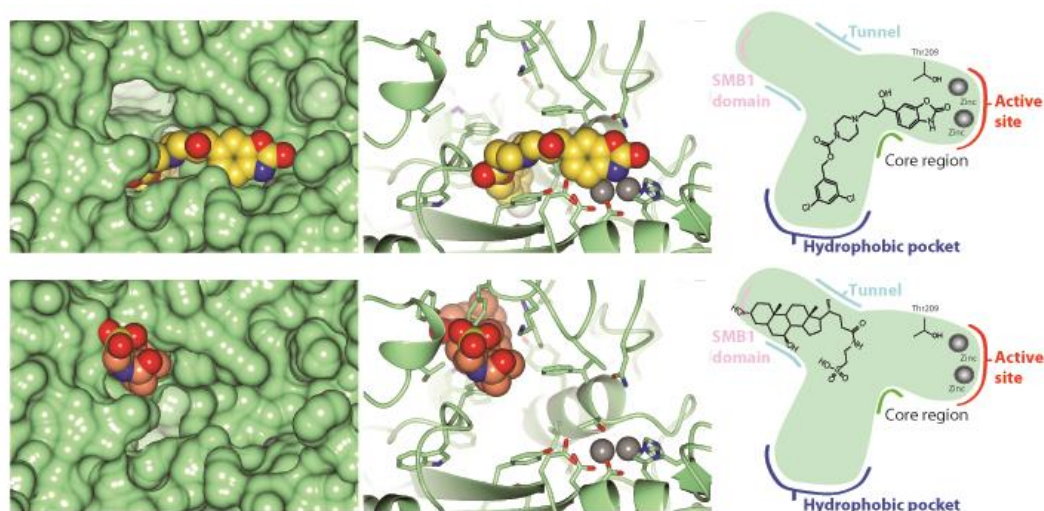


Figure 70 Design of steroid-PF hybrids that reside in the tunnel-active site. Co-crystallisation of **2.1** and TUDCA in the orthosteric and allosteric sites of ATX, respectively.³

3.2. Aims

Based on all of the above, the purpose of this study was to use a structure-guided approach to rationally design novel ATX inhibitors which target the hydrophobic pocket and tunnel of ATX with a novel binding mode. Through investigation of the co-crystal structures of TUDCA and **2.1** (**Figure 70**), we envisioned a hybrid inhibitor that could span from the tunnel to the hydrophobic pocket, constructed from a steroid moiety, and a lipophilic motif, respectively. Using an analogue of TUDCA, UDCA, an allosteric ATX inhibitor with similar potency to TUDCA ($K_i = 8.8 \mu\text{M}$), a hydrophobic pocket moiety identified from the SAR previously established in Chapter 2 can be installed, furnishing a hybrid compound (**Figure 71**). Within the PF series discussed in Chapter 2 we identified the 3,5-dichlorobenzyl carbamate tail as a potent lipophilic moiety, which could be combined with either a piperazine or a spirocyclic core to yield potent ATX inhibitors. Utilising the key fragments from the steroid and the knowledge developed within the PF series, we aimed to use structure-based design to generate a targeted compound library, using crystallographic data during our optimisation trajectory to confirm the proposed hypothesis. Through this approach, we expected to modify the micromolar steroidal allosteric inhibitors into more potent competitive ATX inhibitors, thus developing a valuable series of tool compounds with a novel binding mode. We aimed to demonstrate the effect of these compounds in a cell based assay for the phosphorylation of AKT, to determine the effect of the inhibitor on modulating downstream signalling in a pathway implicated in both fibrosis and cancer.^{58,174,175} Additionally, we sought to profile the

most promising compounds in an *in vivo* assay of ATX activity to fully validate the utility of the tool compounds developed during this study.

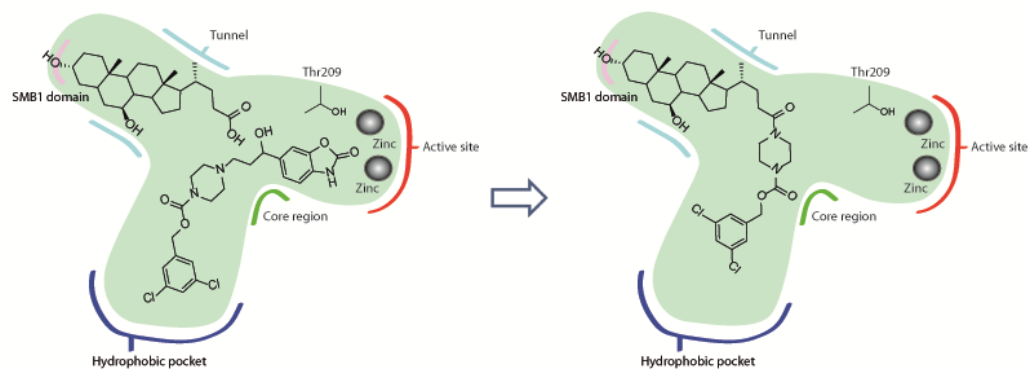
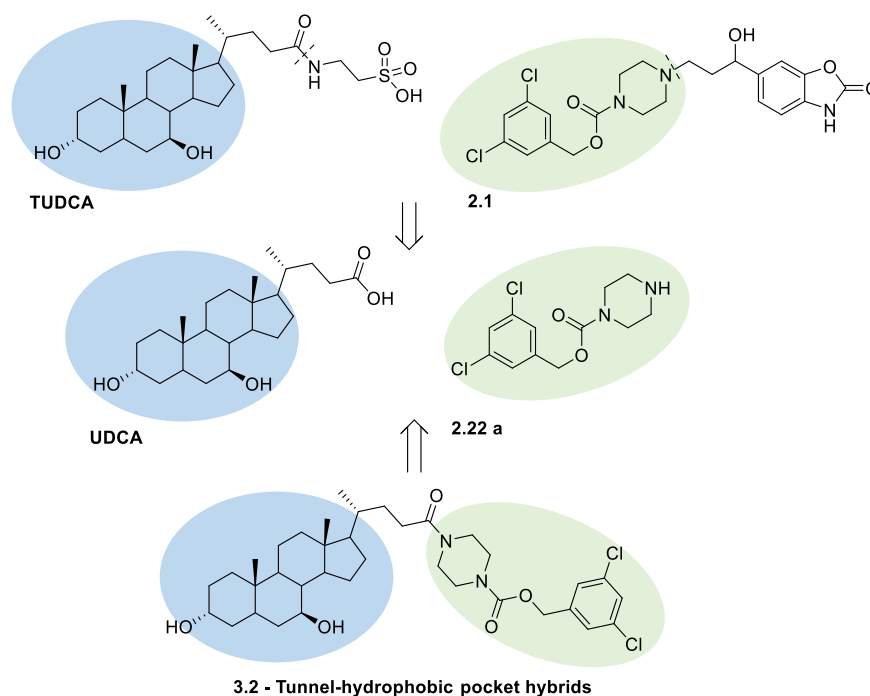


Figure 71 Design of the steroid-PF hybrids that reside in the tunnel-hydrophobic pocket.

3.2.1. Retrosynthesis

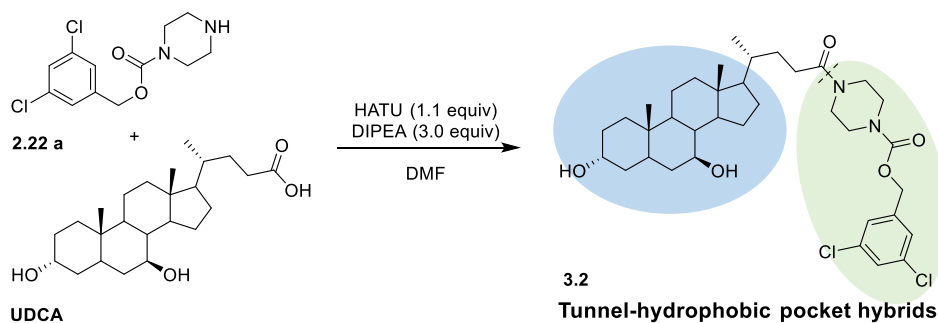
The proposed hybrid PF-UDCA compounds could be expediently synthesised from UDCA and the corresponding diamine building block **2.22 a** (**Scheme 26**). This creates compounds with a diamine core region that could potentially link the tunnel to the hydrophobic pocket.



Scheme 26 Retrosynthesis of the hybrid compounds from TUDCA and **2.1**.

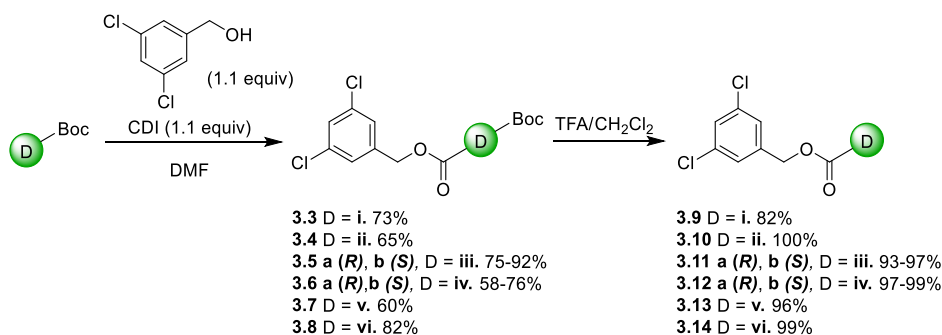
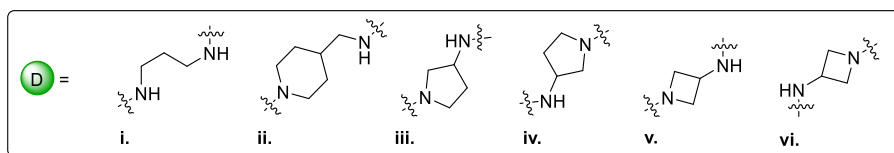
3.2.2. Synthetic Strategy

The forward synthesis for these hybrid ATX inhibitors consists of an amidation reaction with diamine intermediate **2.22 a** (**Scheme 10**) and steroid UDCA (**Scheme 27**) to yield the corresponding hybrid compounds.

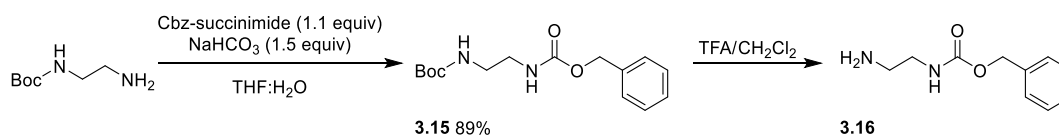


Scheme 27 Forward synthesis of tunnel-hydrophobic pocket hybrids and tunnel-active site hybrids.

In order to expand the scope to develop a compound library, the diamine building blocks synthesised in Chapter 2 (Section 2.3.2) were used for the synthesis of hydrophobic pocket hybrids. The diamines either contained a benzyl or 3,5-dichlorobenzyl carbamate tail, as previously described in Chapter 2 (**Scheme 10**), and leverages the SAR previously established for this part of the protein where a 3,5-dichlorobenzyl carbamate was shown to impart potency. The diamine cores that were initially used in this synthesis include piperazine, 2,6-diazaspiro[3.3]heptane, ethane-1,2-diamine, propane-1,3-diamine, aminoazetidine, and aminopyrrolidine **i–vi**. (**Scheme 28**) which were synthesised with either a 3,5-dichlorobenzyl carbamate or benzyl carbamate tail, akin to intermediates in Section 2.3.2. (**Scheme 29**).

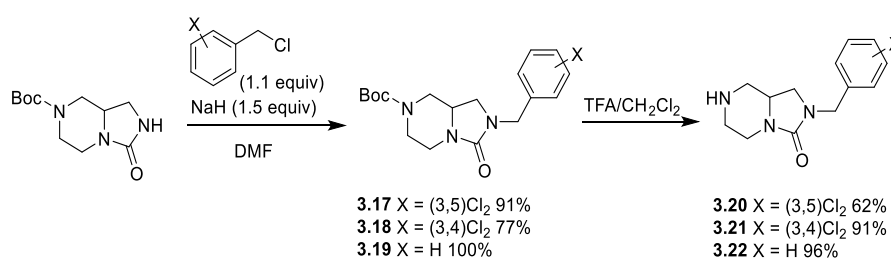


Scheme 28 The synthesis of diamine core building blocks **3.9–3.14**.



Scheme 29 The synthesis of intermediate **3.16**.

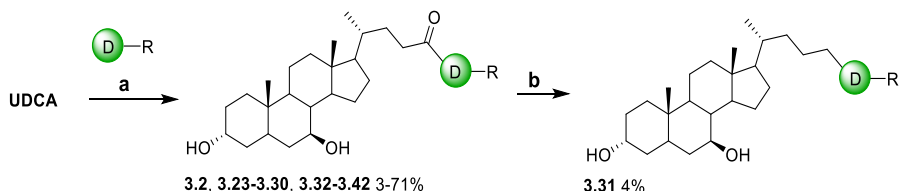
An additional diamine core within this study was the *tert*-butyl 3-oxohexahydroimidazo[1,5-*a*]pyrazine-7(1*H*)-carboxylate, which was synthesised *via* an alkylation reaction, and subsequent *N*-Boc deprotection under acidic conditions to reveal the free amine **3.20–3.22** (**Scheme 30**).



Scheme 30 Synthesis of intermediates with the hexahydroimidazo[1,5-*a*]pyrazin-3(2*H*)-one core.

The final compounds **3.2**, **3.23–3.30**, and **3.32–3.42** can be synthesised *via* an amidation reaction with the relevant diamine intermediate and UDCA. The final compounds can be

further modified by amide bond reduction to yield the tertiary amine using borane-THF (**Scheme 31**). Compound **3.31** containing a basic centre on the piperazine could increase the solubility of the compound and determine the significance of the amide moiety for ATX inhibition.



Scheme 31 Synthesis of final compounds *via a*) amidation reaction with HATU (1.1 equiv), DIPEA (5.0 equiv) and DMF *b*) Borane reduction with BH₃-THF.

3.3. Biochemical Assays to Aid Confirmation of the Binding Mode Hypothesis

As previously discussed in Section 1.9, there are four commonly used ATX inhibition assays, which include the *bis**p*-NPP, *p*NP-TMP, LPC and FS-3. Within this study, the *bis**p*-NPP, *p*NP-TMP, and LPC biochemical assays were used to aid determination of the proposed binding mode of the hybrid inhibitors, alongside co-crystallography with ATX. At the outset of this project, we proposed to design compounds that bind in the tunnel and the hydrophobic pocket of ATX (pink, **Figure 72**). The binding mode of the active substrates within the catalytic region of ATX are highlighted in **Figure 72** and emphasise the reasoning for the use of these three assays. The LPC assay is related to affinity of LPA in the active site and hydrophobic pocket (orthosteric site), and potentially the tunnel of ATX, and therefore if the hybrids bind to ATX in the manner proposed they would be active in this biochemical assay. The *p*NP-TMP biochemical assay indicates ATX inhibition of a nucleotide substrate, with the active substrate residing in a smaller nucleotide binding pocket at the entrance to the hydrophobic pocket. Again, compounds should be active in this assay if they bind in the proposed binding mode. The *bis**p*-NPP biochemical assay, which was the assay employed in Chapter 2, is specific for the affinity at the zinc atoms, and in relation to this study without a ZBG, it is expected that inhibitors would be inactive in this assay.

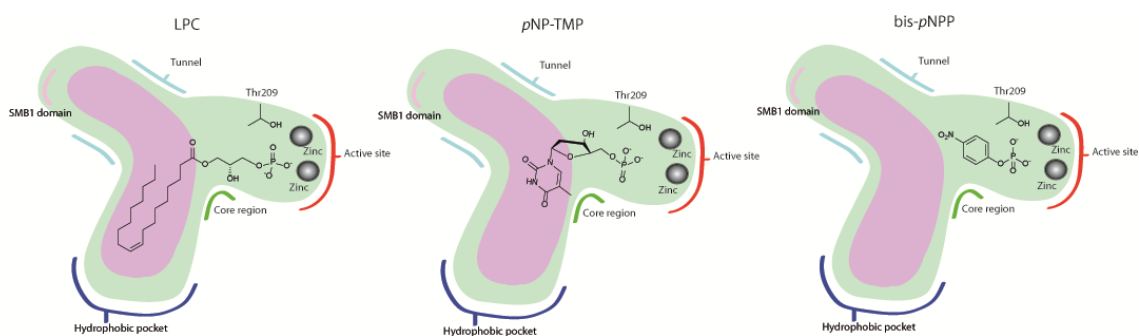


Figure 72 The LPC, *p*NP-TMP, and bis-*p*NPP biochemical assays with the proposed inhibitor binding mode (pink).

3.4. Results and Discussion - Tunnel-hydrophobic Pocket Hybrids

3.4.1. Initial Compound Screen of Tunnel-hydrophobic Pocket Hybrids

From the consideration of the allosteric ATX inhibitor TUDCA, the initial compound synthesised contained an extended ethylenediamine moiety **3.23**, which had the potential to be equipotent to TUDCA (**Table 25 a**). The benzyl carbamate, and 3,5-dichlorobenzyl carbamate lipophilic tail analogues with the same ethylenediamine spacer were also synthesised, to provide a flexible linker between the steroid and the lipophilic tail regions. To assess the length of this flexible spacer it was both contracted **3.26** and homologated **3.27** to assess the distance necessary to interact with both the tunnel and the hydrophobic pocket of the enzyme for optimal ATX inhibition. Constrained analogues containing a piperazine or 2,6-diazaspiro[3.3]heptane core, with either benzyl, 3,5-dichlorobenzyl or cyclohexyl lipophilic regions **3.2, 3.28–3.31** were also prepared (**Table 25**), again leveraging the previously developed SAR in the PF-8380 series.

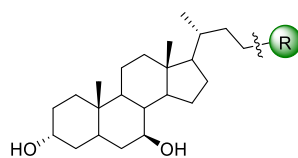
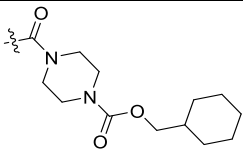
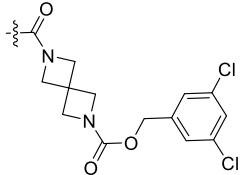
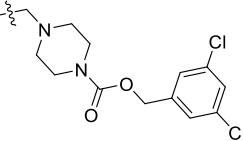


Table 25 Initial ATX inhibition of compounds. ^aTUDCA ^bUDCA.

	R	LPC IC₅₀ (μM)	<i>p</i>NP-TMP IC₅₀ (μM)	bis-<i>p</i>NPP IC₅₀ (μM)
a		10.4	-	-
b		8.8	-	-
3.23		> 30	-	-
3.24		> 30	-	-
3.25		0.20	0.24	> 30
3.26		> 30	-	-
3.27		0.56	-	-
3.28		> 30	-	-
3.2		0.13	0.096	> 30

3.29		> 30	-	-
3.30		1.5	0.78	0.48
3.31		0.81	1.5	> 30

The ethylene diamine compound **3.7** with no lipophilic anchor was inactive compared to parent compounds TUDCA and UDCA, however, unexpectedly when an unsubstituted benzyl carbamate was present in compound **3.24** no increase in activity was achieved (**Table 25**). This result differs somewhat from the pattern established in the SAR study of PF-8380 (**Table 12**) discussed in Chapter 2, where the benzyl carbamate often resulted in potent ATX inhibitors. However, as discussed in Section 1.9. and Section 3.3. assay selection is contingent on the binding mode of the inhibitor and might not account for affinity within the hydrophobic pocket. Within the PF-8380 series the bis-*p*NPP assay was employed, and as discussed previously this assay is biased towards activity in the active site. This explains how compounds within the PF-8380 series with a benzyl carbamate tail are potent inhibitors because they contain a ZBG, however, the hybrid inhibitors **3.23–3.31** do not, which explains the lack of potency in the bis-*p*NPP assay. As discussed previously, the LPC and *p*NP-TMP assay are more relevant biochemical assays for the detection of inhibitors which bind in the tunnel and the hydrophobic pocket of the enzyme.¹³² The lack of potency observed with benzyl carbamate tails in the LPC assay concludes that the benzyl carbamate tail is not a useful motif within this series of hybrid compounds, and as a result compounds were synthesised with a 3,5-dichlorobenzyl carbamate tail which we have shown to act as a hydrophobic anchor. This modification resulted in a potent compound **3.25**, reinforcing the importance of the 3,5-dichlorobenzyl carbamate tail.

The length of the diamine linker was modified, using 3,5-dichlorobenzylamine **3.38**, and the propylenediamine core **3.27**, revealing that a reduced length resulted in inactive compounds, which are unable to extend towards the hydrophobic pocket. The homologated linker slightly decreased activity, which could be due to the increase in rotatable bonds causing an entropic

penalty to adopt the lowest energy binding pose, and as a result reducing potency. Alternatively, the length of the compound could move either the steroid or the 3,5-dichlorobenzyl carbamate tail from their optimum positions in the tunnel, and hydrophobic pocket, respectively. The diamine cores which restricted flexibility and reduced the number of rotatable bonds resulted in a potent ATX inhibitor as noted with the piperazine analogue **3.2** (**Table 25**). Although the piperazine is conformationally flexible there are fewer poses that can be adopted by the compounds in the active site compared to **3.25**, and using this core it was found that compounds **3.28** and **3.29** were inactive ATX inhibitors, reinforcing the need for the 3,5-dichlorobenzyl carbamate tail as an essential component in conferring potency in the hybrid series.

The most potent compounds **3.25** and **3.2** were also profiled in the *p*NP-TMP and bis-*p*NPP biochemical assays. As discussed previously, the *p*NP-TMP assay contains a nucleotide thymidine monophosphate, as ATX is also capable of hydrolysing nucleotides. These assays provide alternative substrates for determining ATX inhibition. Compounds **3.25** and **3.2** displayed good ATX inhibition in the *p*NP-TMP assay, and were inactive in the bis-*p*NPP assay, which provides biochemical confirmation of our hypothesised binding mode.

Compound **3.30** containing the more constrained 2,6-diazaspiro[3.3]heptane core previously identified as part of the PF study in Chapter 2 was found to be a weak inhibitor in the LPC and *p*NP-TMP biochemical assays, however exhibited moderate potency in the bis-*p*NPP assay, which is an unusual result for these tunnel-hydrophobic pocket binding compounds as previously discussed in Section **3.3**. It is believed that the lack of potency in the LPC and *p*NP-TMP assays are due to the inability of the compound to fill both the tunnel and the hydrophobic pocket because of the inflexibility of the core region. As a result of this the 3,5-dichlorobenzyl 2,6-diazaspiro[3.3]heptane-2-carboxylate moiety could reside unfavourably in the active site of the enzyme or block access to the active site, outcompeting the bis-*p*NPP substrate at the active site resulting in potency within this assay (**Figure 73**). However, there were no biochemical assays available which would confirm this hypothesis.

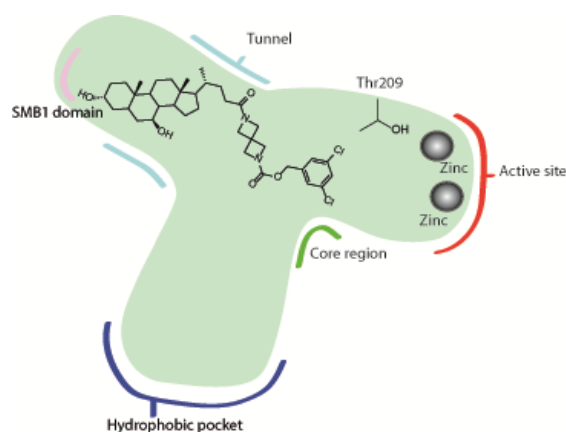


Figure 73 Hybrid compound **3.30** containing UDCA in the tunnel region and a 3,5-dichlorobenzyl carbamate moiety in the core region blocking entrance to the active site.

Active compound **3.2** was further elaborated by a borane reduction of the amide bond to yield the tertiary amine **3.31**. This compound could increase the solubility of the compound and probe the necessity for the carbonyl moiety for ATX inhibition. Evaluation of the tertiary amine **3.31** (**Table 25**) showed decreased ATX inhibition in both the LPC and *p*NP-TMP assay. As a result of the drop in potency, no further analogues of this type were synthesised.

3.4.2. Crystallography of Compounds Bound in ATX

To verify our initially proposed binding mode hypothesis which is inferred from the biochemical assay data, compounds **3.25** and **3.31** were co-crystallised bound to ATX by collaborators at NKI. Pleasingly, data at good resolution was obtained and showed the 3,5-dichlorobenzyl carbamate tail of compound **3.30** resides in the hydrophobic pocket, interacting with hydrophobic residues Ile167, Ala30, Leu216, Leu213, Ala217, and edge to face π -stacking with Phe273 (**Figure 74**). Additionally, the aromatic ring of Trp260 can hydrophobically interact with the chlorine on the lipophilic region, potentially increasing the affinity of the ligand. The core region of the compound interacts minimally with surrounding residues, simply forming hydrophobic interactions with the Tyr306 residue, analogously to the core region in the PF-8380 series discussed in Chapter 2 (**Figure 33**). Within the tunnel region of the enzyme, as indicated in Section 3.1., the alcohol moieties present on the A and B ring of the steroid hydrogen bond with Trp260 and Tyr82, respectively. Beneficial hydrophobic interactions arise from the methyl groups between the A-B rings, and the C-D rings with His251, and Phe249, respectively. Phe274 and Trp260 are important residues for activity

within this series as they both interact with the inhibitor in the tunnel region and the hydrophobic pocket.

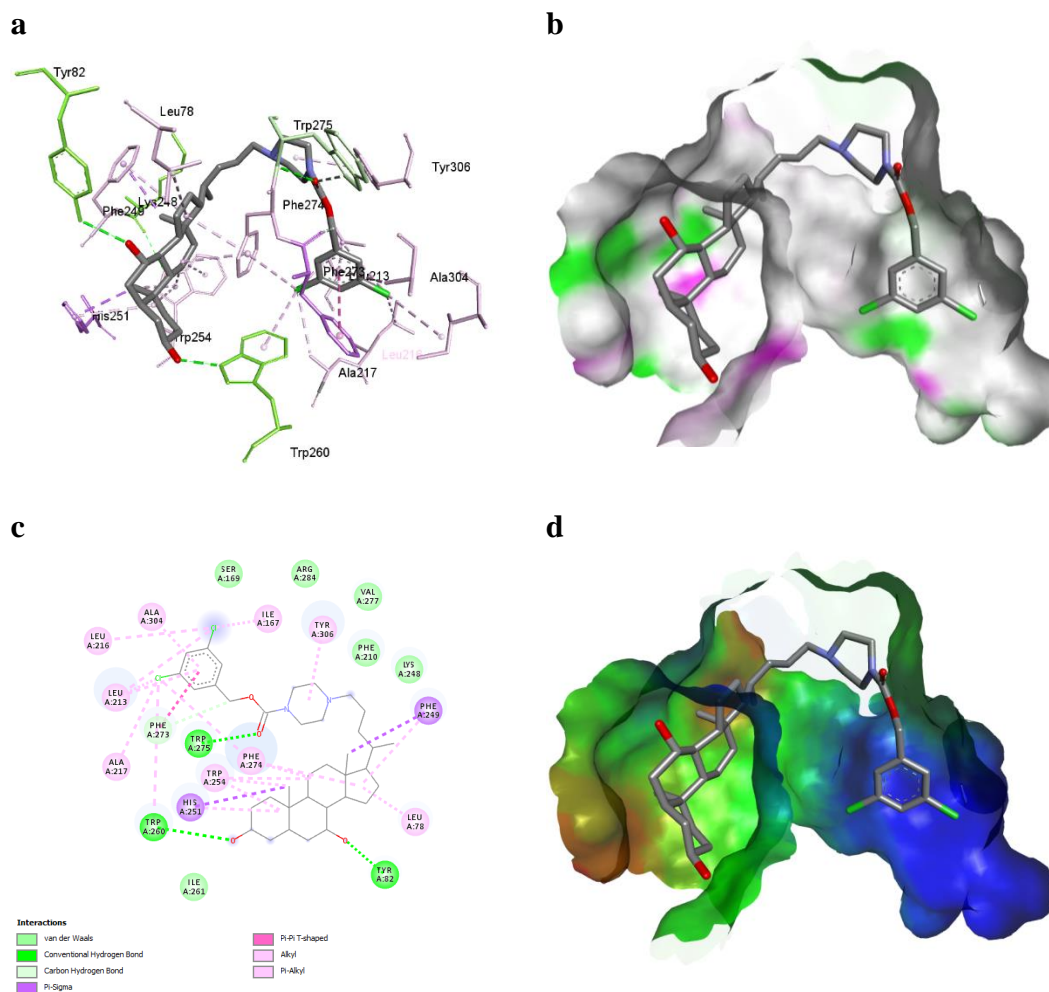


Figure 74 The crystal structure of compound **3.31** by NKL, viewed in DS visualiser⁴⁸ **a)** **3.31** and the nearby residues for interactions on ATX. **b)** **3.31** bound to ATX with HBD (pink) /HBA(green) surface. **c)** The 2D interaction map of nearby residues. **d)** Hydrophobicity surface of the enzyme with **3.31** bound (lipophilic–blue, neutral–green, polar–red.).

An overlay of the crystal structure of **3.31** and TMP both bound to ATX explains the drop in potency of the compound in the *p*NP-TMP assay as TMP resides in the active site of ATX where the amide carbonyl on **3.2** would be located (**Figure 75**). As a result, it is believed that the amide of **3.2** can outcompete TMP, which increases the potency in the *p*NP-TMP assay, whereas TMP can fit into the active site with compound **3.31**.

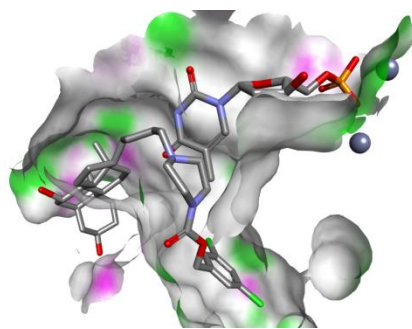


Figure 75 The crystal structure overlay of **3.31** and TMP (PDB ID: 4GTX) viewed in DS visualizer^{48, 176}

Compound **3.25** interacts identically with the enzyme as compound **3.31** does, proving that the correct linker length, and a degree of flexibility to create a U-shaped pose in the active site allows interactions in both the tunnel and hydrophobic pocket, which in turn produces potent ATX inhibitors (**Figure 76**).

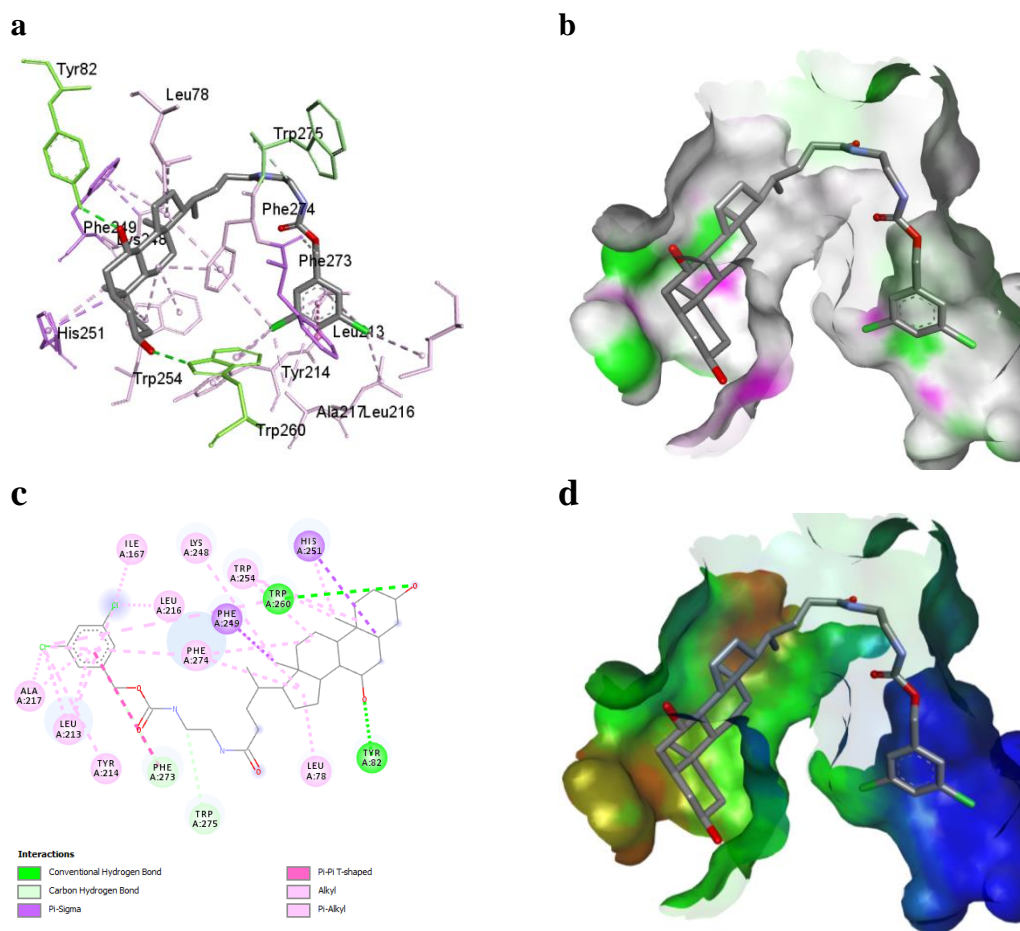


Figure 76 The crystal structure of compound **3.25** by NKI, viewed in DS visualiser⁴⁸ **a)** **3.25** and the nearby residues for interactions on ATX. **b)** **3.25** bound to ATX with HBD (pink)/HBA (green) surface. **c)** The 2D interaction map of nearby residues. **d)** Hydrophobicity surface of the enzyme with **3.25** bound (lipophilic–blue, neutral–green, polar–red.).

Based on these co-crystal structures (**Figure 74**, **Figure 76**) it is evident that the U-shape of the molecule is integral to activity. Both the piperazine core which adopts a boat conformation, and the ethylenediamine are clearly flexible enough to create the necessary vector. An overlay of these two crystal structures show how the steroid moiety and the 3,5-dichlorobenzyl carbamate tail are both acting as hydrophobic anchors, with both portions showing minimal movement from the optimum pose based on the initial crystal structures of TUDCA and **2.1** (**Figure 77**). These two crystal structures confirm our binding mode hypothesis, and allow for the design of further ATX inhibitors in the following series, with the aim of improving potency and the degree of competitive inhibition.

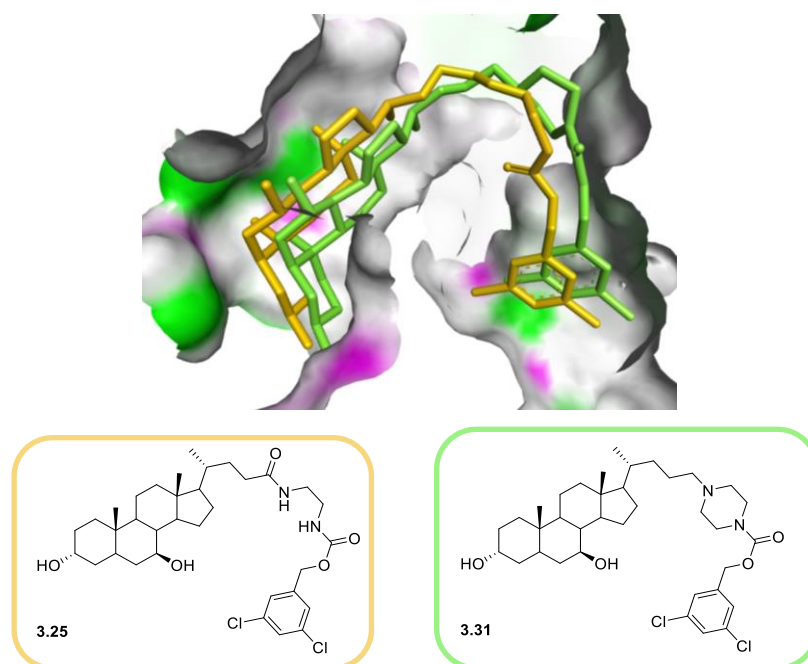


Figure 77 Overlay of the crystal structures of compound **3.25** and **3.31** in the active site of ATX views in DS visualizer.⁴⁸

In an attempt to minimally restrict the flexibility of these diamine cores to decrease the entropic penalty, whilst maintaining a similar motif to the piperazine with enough flexibility to mimic the U-shape of compounds **3.25** and **3.31**, a hexahydroimidazo[1,5-*a*]pyrazin-3(2*H*)-one core was used as a spacer unit (**Table 26**).

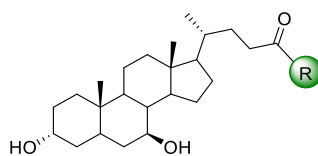


Table 26 Inhibitors containing a hexahydroimidazo[1,5-*a*]pyrazin-3(2*H*)-one core.

	R	LPC IC ₅₀ (μM)
3.32		> 30
3.33		2.1
3.34		> 30

Compounds **3.32–3.34** were tested in the LPC assay, which revealed that only compound **3.33** was a micromolar ATX inhibitor (**Table 26**). Although the hexahydroimidazo[1,5-*a*]pyrazin-3(2*H*)-one core could reduce the entropy penalty when adopting the minimum energy binding pose within the enzyme, it is clear that the linker region is too constrained to form the correct shape needed for ATX inhibition, or the compound could clash with the enzyme surface.

3.4.3. Structure-based Design of ATX Inhibitors

Based on the structural data of ATX inhibitors **3.25**, and **3.31**, and the U-shaped conformation adopted, diamine linkers that could increase the flexibility and facilitate access to this conformation were proposed. These cores included the aminomethylpiperidine, 3-aminopyrrolidine, aminoazetidone, and 4-(aminomethyl)piperidin-4-ol (**Figure 78**), which change the vector of the compounds. The electron density of the ethylenediamine linker region within the co-crystal structure of **3.25** was less defined than the piperazine in compound **3.31**, suggesting a more rigid structure would decrease the entropic penalty accrued with flexibility and rotatable bonds. Diamine cores that allow the compound to be close to the adopted binding mode conformation both bound and unbound to the enzyme were postulated to result in potent compounds.

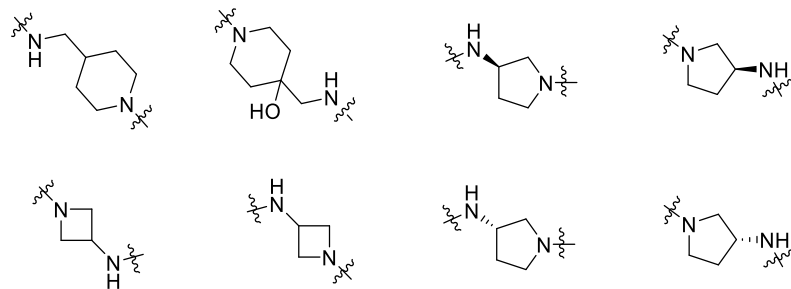


Figure 78 Diamine cores for the synthesis of hybrid compounds.

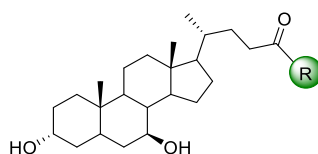
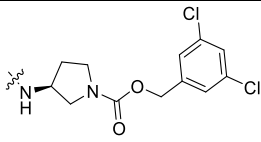
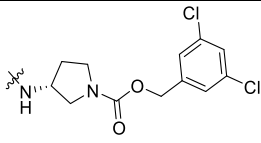
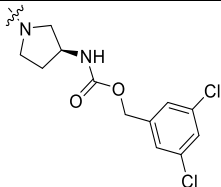
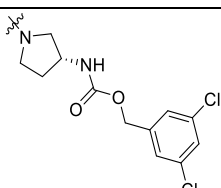


Table 27 ATX inhibitors containing novel diamine cores. Inh = Inhibition (C) Competitive Inhibition (NC) Non-competitive inhibition (UC) Uncompetitive Inhibition.

	R	LPC IC₅₀ (μM)
3.35		2.5
3.36		0.100
3.37		1.000
3.38		0.208

3.39		0.717
3.40		0.020
3.41		0.500
3.42		0.313

Compound **3.35**, using the aminomethylpiperidine core resulted in a micromolar ATX inhibitor, which is 3.5 times more potent than the progenitor steroid UDCA. Replacement with the 4-(aminomethyl)piperidin-4-ol core led to inhibitor **3.35** which was found to be 88 times more potent than UDCA. The alcohol moiety on the piperidine ring could be acting as a lock, reducing the flexibility of the piperidine ring, and allowing the compound to easily adopt the active binding pose. Alternatively, there could be hydrogen bond interactions with the tertiary alcohol as it projects in the same vector as the tunnel of ATX, which is solvent exposed. Further to this, the regiochemistry of the 4-(aminomethyl)piperidin-4-ol core is different to the aminomethylpiperidine core, and as a result the potency could be based on the tertiary amide **3.36** having increased potency over the secondary amide **3.35**.

The aminoazetidine core on compounds **3.37** and **3.38** resulted in potent inhibitors. The core region does not have any beneficial hydrophobic interactions within the enzyme based on *in silico* analysis (**Figure 79**), however the core enables access to a U-shaped conformation which allows the compound to interact in both the tunnel and the hydrophobic pocket of the enzyme, potentially accounting for the potency observed. With the aminomethylpiperidine (**3.35** and **3.36**) and aminoazetidine cores (**3.37** and **3.38**) the exocyclic carbamate results in the most potent ATX inhibitors, however, the aminopyrrolidine cores do not follow this general trend.

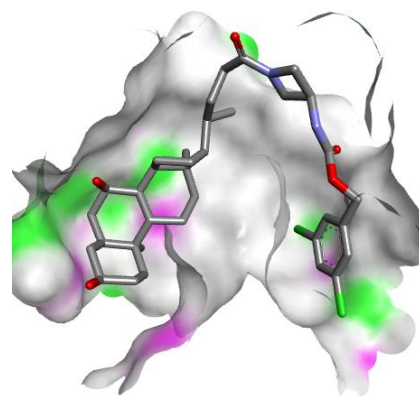


Figure 79 *In silico* docking of **3.38** in ATX in GOLD¹³⁰ and viewed in DS visualizer⁴⁸.

The series of compounds **3.39–3.42** containing the 3-aminopyrrolidine core were all potent ATX inhibitors, and each compound was proposed to bind in a similar mode to the precursor compounds **3.39** and **3.31**, based upon *in silico* docking in GOLD.¹³⁰ The aminopyrrolidine core on compound **3.40** resulted in the most potent ATX inhibitor (**Table 27**), with a 500-fold increase in activity compared to the parent compound UDCA. A co-crystal structure was obtained of **3.40** bound to ATX (**Figure 80**), which showed the binding mode of the steroid moiety in a similar position as the crystal structure of TUDCA (**Figure 70**). The alcohol moieties of the A and B ring of the steroid interact with Trp260 and Tyr82 residues within the tunnel region, respectively (**Figure 80 a** and **c**). The hydrophobic interactions observed with the 3,5-dichlorobenzyl carbamate tail are also almost identical to the co-crystal structure of the PF-8380 analogue **2.1** discussed in Chapter 2 (**Figure 70**, **Figure 33**). Interestingly, two residues, Trp260 and Phe274, which are discussed as being important residues for ATX inhibition, hydrogen bond and form hydrophobic interactions with both the tunnel steroid moiety and the 3,5-dichlorobenzyl carbamate moiety, respectively (**Figure 80 b**)³

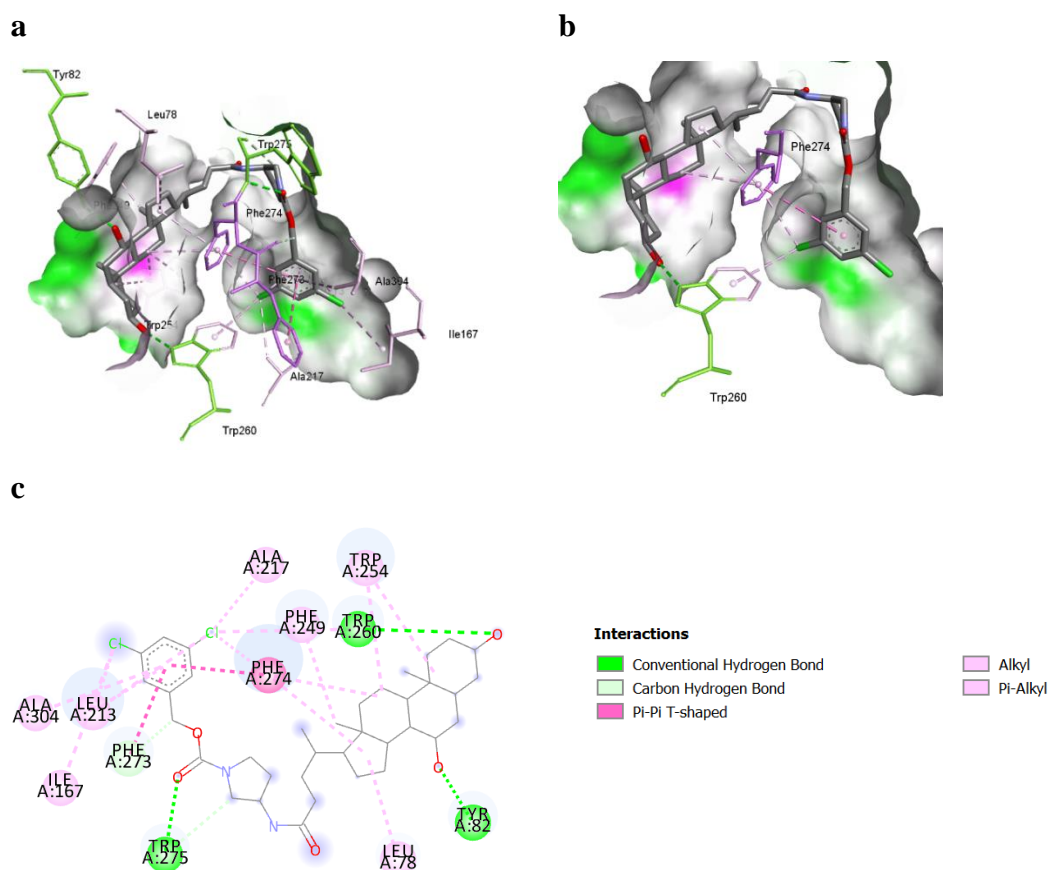


Figure 80 Co-crystal structure of **3.40** bound to ATX by NKI, viewed in DS visualizer. **a)** Co-crystal structure and nearby residues. **b)** Co-crystal structure and two important residues for potency which interact with both the tunnel and hydrophobic pocket region. **c)** 2D interaction map generated from DS visualizer of nearby residue interactions.⁴⁸

3.4.4. Enzyme Kinetics

An enzyme inhibitor can be either competitive, non-competitive, or un-competitive. Competitive inhibitors bind to the orthosteric site of the enzyme and outcompete the natural substrate, whereas non-competitive inhibitors bind to the enzyme at a site distinct to that of the natural substrate (**Figure 81**). Alternatively, un-competitive inhibitors bind to a site on the enzyme once the enzyme-substrate complex has formed. The compounds discussed within this study consist of both competitive and non-competitive inhibitors.^{178,179} The kinetics of each of these types of inhibitors can be determined using the relationships described below.



Figure 81 Binding sites of non-competitive and competitive inhibitors with the enzyme.

In the case of Autotaxin, the natural substrate LPC ($S = \text{LPC}$) binds to the enzyme ($E = \text{ATX}$) to form the enzyme-substrate complex ($\text{ES} = \text{ATX-LPC}$) with a rate of formation equal to k_{on} (rate of formation of $\text{ES} = k_{\text{on}}$). After formation of the ES complex either product ($P = \text{LPA}$) can be released from the enzyme at a rate of formation equal to k_2 (rate of formation of $P = k_2$), or the substrate can dissociate from the enzyme at a rate equal to k_{off} (rate of dissociation of $\text{ES} = k_{\text{off}}$) (**Figure 82 a**).¹⁷⁸ The equilibrium between E , S , and the ES complex is referred to as K_D , which equals $k_{\text{off}}/k_{\text{on}}$. The rate at which P is formed releasing the enzyme from the ES complex equals k_2/k_{-2} , however considering the process close to time = 0 we can assume that there is limited P generated and **a** can be simplified to **b** and the rate of formation of P equals k_{cat} (**Figure 82 b**).¹⁷⁸

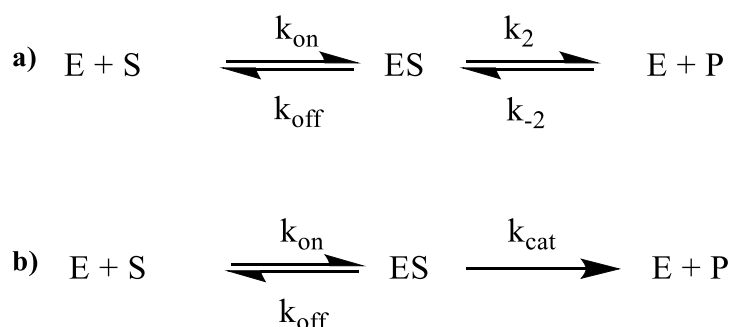


Figure 82 a) Rate of formation of the enzyme-substrate complex (ES), and the release of product P . **b)** Michaelis-Menten equation.

From this relationship the Michaelis-Menten equation, which describes the kinetics of an enzyme substrate interaction, is derived. Firstly, the initial rate of the reaction (v) is defined at time = 0, as the rate of formation of P multiplied by the concentration of the ES complex (**Figure 83 a**). During the derivation of this equation a few assumptions are made, these include the steady state assumption, which is to say that $[\text{ES}]$ remains constant regardless of the concentration of $[\text{S}]$ and $[\text{P}]$, i.e. the rate of formation of ES (**Figure 83 b**) equals the dissociation of P from ES (**Figure 83 c and d**). This assumption determines the quantity of $[\text{ES}]$ as a ratio of $[\text{E}][\text{S}]/[\text{ES}]$, which defines the Michaelis-Menten constant K_M ($K_M = (k_{\text{off}}+k_{\text{cat}})/k_{\text{on}}$) (**Figure 83 f**).¹⁷⁸ K_M equals the substrate concentration when the reaction rate is half the maximal value (V_{max}), and a high value of K_M indicates weak binding of the substrate and *vice versa*.¹⁷⁸

- a) $v = k_{\text{cat}}[\text{ES}]$
- b) $\frac{d[\text{ES}]}{dt} = k_{\text{on}}[\text{E}][\text{S}]$
- c) $\frac{-d[\text{ES}]}{dt} = (k_{\text{off}}+k_{\text{cat}})[\text{ES}]$
- d) $k_{\text{on}}[\text{E}][\text{S}] = (k_{\text{off}}+k_{\text{cat}})[\text{ES}]$
- e) $[\text{E}][\text{S}]/[\text{ES}] = (k_{\text{off}}+k_{\text{cat}})/k_{\text{on}}$
- f) $K_{\text{M}} = (k_{\text{off}}+k_{\text{cat}})/k_{\text{on}}$

Figure 83 a) The initial rate of reaction b) The rate of formation of ES c) The rate of breakdown of ES d) The steady state assumption of ES e) Rearrangement of equation f) Definition of the Michaelis-Menten constant.

The Michaelis-Menten constant (**Figure 83 f**) can be inserted back into equation **e** to yield an equation for the concentration of the ES complex (**Figure 84 g**), however $[\text{E}]$ must now be defined. Due to the substrate concentration being much greater than the enzyme concentration ($[\text{S}] > [\text{E}]$), the concentration of enzyme without substrate bound is defined as the total amount of available enzyme $[\text{E}]_{\text{T}}$ minus the ES complex formed (**Figure 84 h**). Equation **h** can be substituted back into equation **g**, and rearranged for the concentration of ES to yield **j**, which can be displayed in two formats (**Figure 84 j**).¹⁷⁸

$$\text{g) } [\text{ES}] = \frac{[\text{E}][\text{S}]}{K_{\text{M}}}$$

$$\text{h) } [\text{E}] = [\text{E}]_{\text{T}} - [\text{ES}]$$

$$\text{i) } [\text{ES}] = \frac{([\text{E}]_{\text{T}} - [\text{ES}])[\text{S}]}{K_{\text{M}}}$$

$$\text{j) } [\text{ES}] = \frac{[\text{E}]_{\text{T}} [\text{S}]/K_{\text{M}}}{1 + [\text{S}]/K_{\text{M}}} \quad \text{or} \quad [\text{ES}] = [\text{E}]_{\text{T}} \frac{[\text{S}]}{[\text{S}] + K_{\text{M}}}$$

Figure 84 g) The concentration of the ES complex. h) The total concentration of E present. i) The concentration of the ES complex taking into account the concentration of E available. j) The concentration of the ES complex present with defined constants.

Equation **j** defines the concentration of the ES complex, and when it is substituted back into equation **a** for the initial rate of the reaction (**Figure 83**) equation **k** is derived. This equation corresponds to the initial rate of the formation of P, with the concentration of the ES complex now defined (**Figure 85 k**). This can be further modified by addition of the maximal rate of reaction V_{\max} , which equals the rate of formation of P when the S occupies the total amount of enzyme available $[E]_T$ ($V_{\max} = k_{\text{cat}}[E]_T$, **Figure 85 l**). V_{\max} is also known as the turnover rate of the enzyme when it is fully saturated. Equation **l** corresponds to the Michaelis-Menten equation, and plotting this results in a non-linear regression for an enzyme catalysed reaction described in **Figure 87**, which reveals V_{\max} and K_M .

$$\mathbf{k) } v = k_{\text{cat}}[E]_T \frac{[S]}{[S]+K_M}$$

$$\mathbf{l) } v = V_{\max} \frac{[S]}{[S]+K_M} \quad \mathbf{Michaelis-Menten}$$

Figure 85 a) The initial rate of the reaction **b)** The Michaelis-Menten equation.

The Michaelis-Menten curve (**Figure 85** equation **l**) can also be plotted as a non-linear regression (**Figure 87 A** and **C**), and can also be displayed as a Lineweaver-Burk plot (**Figure 87 B** and **D**). The non-linear regression is a plot of the percentage ATX activity versus the substrate concentration (**Figure 87 A**), and the Lineweaver-Burk plot is the reciprocal of the maximal velocity versus the reciprocal of substrate concentration (**Figure 87 B**).

Lineweaver-Burk

$$\frac{1}{v} = \frac{K_M}{V_{\max}} \times \frac{1}{S} + \frac{1}{V_{\max}}$$

Figure 86 Lineweaver-Burk equation.

In the case of a competitive inhibitor both the inhibitor and substrate compete at the active site of the enzyme, therefore when the concentration of the substrate is increased, more enzyme is bound to the substrate, and less enzyme is available for the inhibitor to bind to. This is observed with a linear regression as when the inhibitor concentration is increased the overall ATX activity decreases and less P is formed (**Figure 87 A**). However, the V_{\max} remains the same,

and apparent K_M increases due to less ES complex formation (**Figure 87 A**). A Lineweaver-Burk plot of a competitive inhibitor shows this much more clearly, and as observed with increasing substrate concentration there is no effect on V_{max} , and apparent K_M increases along with the slope equating to K_M/V_{max} (**Figure 87 B**). The initial rate of reaction v is when substrate concentration is almost equal to K_M , and equates to the initial rate of reaction as $v = V_{max}/2$.

Alternatively, with non-competitive inhibition the inhibitor is able to bind to the enzyme to form an EI complex, and additionally also bind to the ES complex to form ESI, which leads to no formation of product. As a result of this the V_{max} is decreased because there is less enzyme available for the substrate to bind to in order to generate product. The K_M remains unchanged, which is also observed with the Lineweaver-Burk plot (**Figure 87 C and D**), and the slope of the curve, K_M/V_{max} , increases by the same amount as the decrease in V_{max} (**Figure 87 D**).

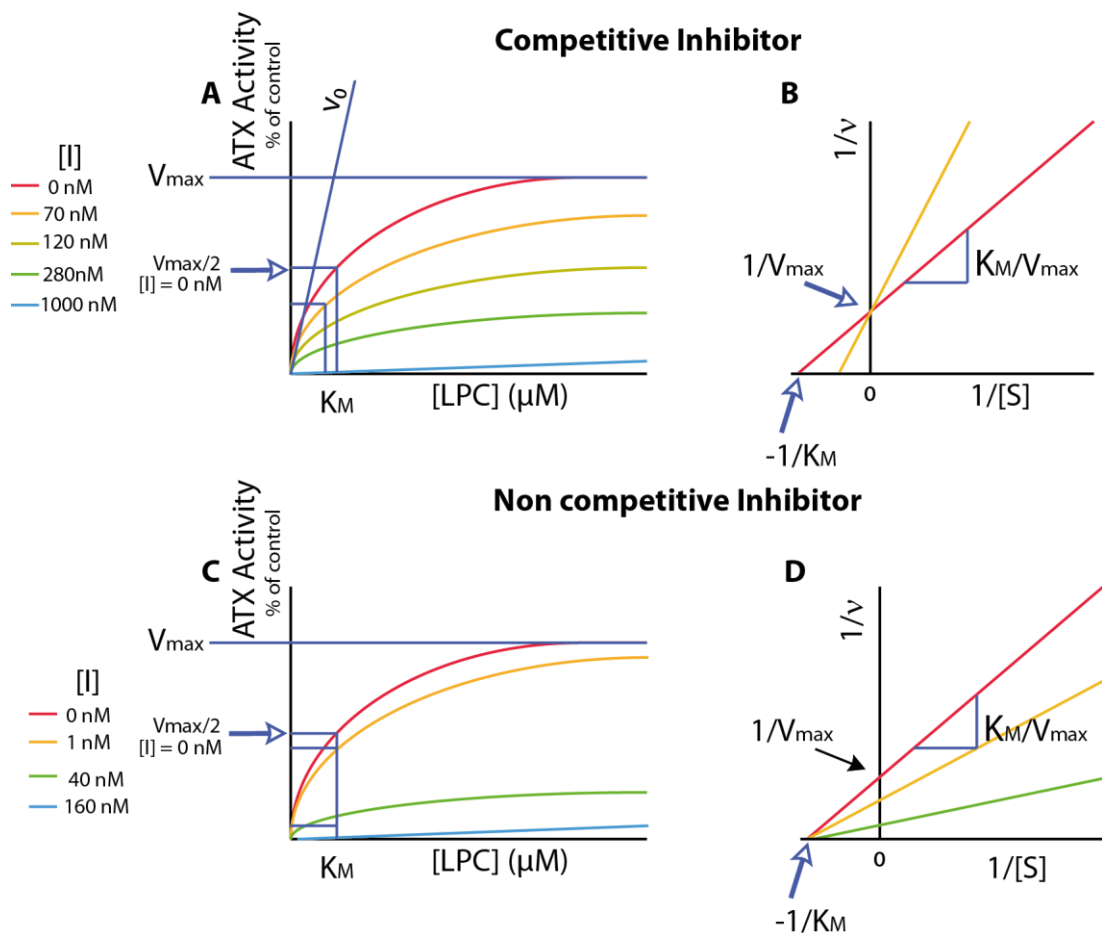


Figure 87 Comparison of a competitive and non-competitive ATX inhibitor through a linear regression (**A, C**) and a Lineweaver-Burk plot (**B, D**).

The active site of ATX is slightly more complex than the basic model of competitive and non-competitive inhibitors (**Figure 88 a**), and the site for non-competitive inhibitors is the tunnel adjacent to the active site where the natural substrate binds. TUDCA is reported as a non-competitive inhibitor of ATX, which means that both the inhibitor and substrate can bind to the enzyme simultaneously (**Figure 88 b**).³ PF-8380 is an example of a competitive inhibitor which binds at the orthosteric site of ATX (active site and hydrophobic pocket) (**Figure 88 c**). The hybrid compounds designed in this project bind in the tunnel region and hydrophobic pocket, outcompeting LPA for the orthosteric site, thus making them competitive ATX inhibitors (**Figure 88 d**).

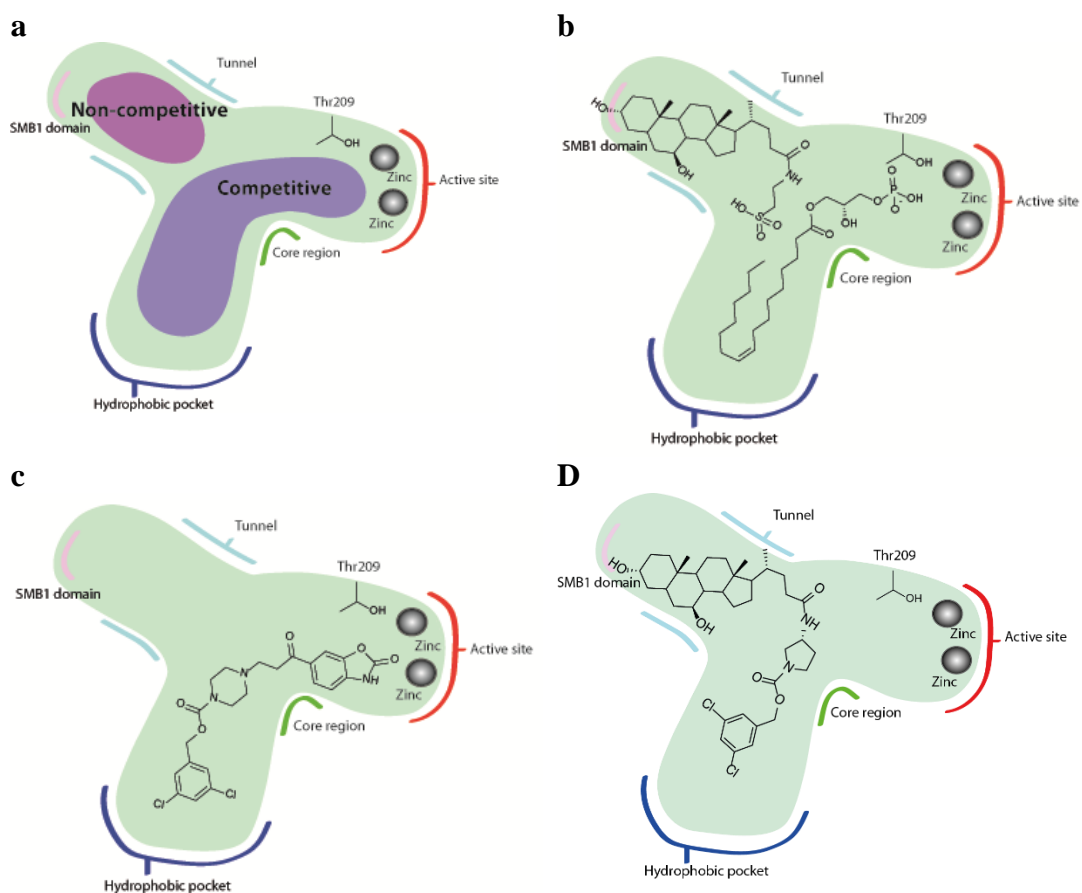


Figure 88 a) Regions of non-competitive ATX inhibitors and competitive inhibitors **b**) TUDCA in the non-competitive site and LPA in the competitive site (bioactive product of ATX after hydrolysis of LPC) **c**) PF-8380 residing in the competitive site of ATX **d**) **3.40** in both the tunnel and hydrophobic pocket acting as a competitive inhibitor.

As the steroid TUDCA was identified from residual electron density in the apo form of ATX, it is plausible that TUDCA is bound to ATX in the assay media.³ Therefore, before an inhibitor can bind to ATX, TUDCA must dissociate from the tunnel region of the enzyme (K_D).¹⁸⁰ At this stage either the natural substrate LPC can bind and be hydrolysed by ATX to produce bioactive LPA and choline, or the competitive inhibitor can bind at the orthosteric site (**Figure 89**), inhibiting hydrolysis of LPC.

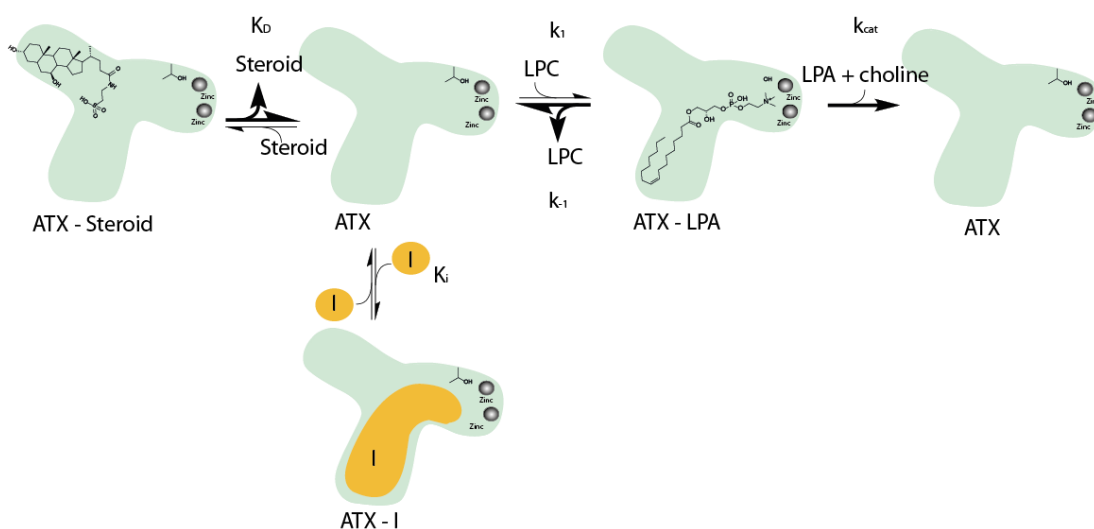


Figure 89 Mechanism for competitive inhibition of ATX.¹⁸⁰

With a non-competitive inhibitor, again TUDCA must first dissociate from this allosteric position, then either the usual process of LPC hydrolysis can occur at the orthosteric site, or non-competitive inhibition can occur to form ATX with the bound inhibitor (ATX-I) (**Figure 90**). With the non-competitive inhibitor LPC can still bind to the enzyme in the orthosteric site, which can lead to dissociation of the allosteric inhibitor (k_i') and hydrolysis of LPC to LPA (k_{cat} **Figure 90**). Alternatively, hydrolysis can occur in the presence of the inhibitor leading to dissociation of both LPA, choline, and the allosteric inhibitor (k_{cat}' **Figure 90**).

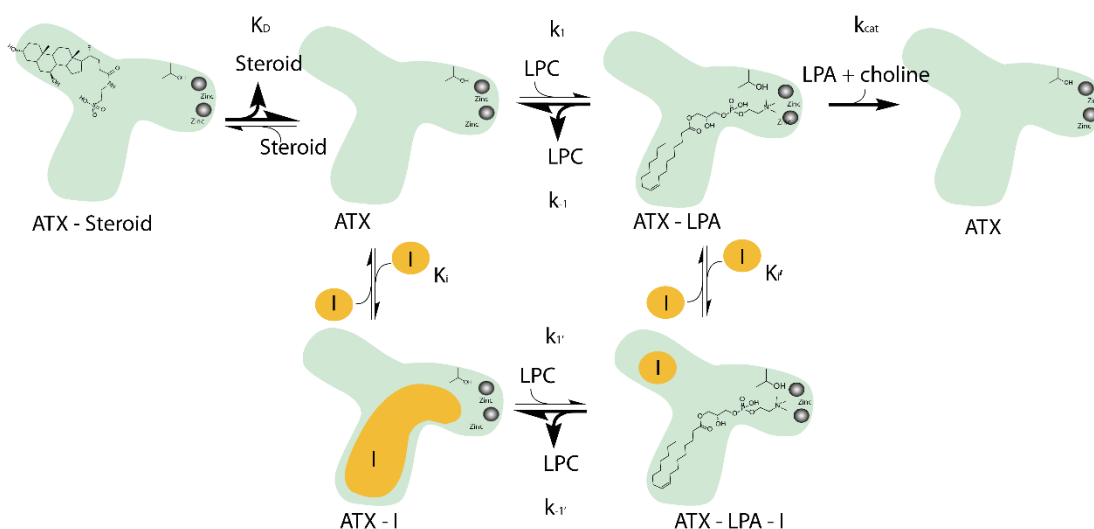


Figure 90 Mechanism for non-competitive inhibition of ATX.¹⁸⁰

3.4.5. Mode of Inhibition of ATX Inhibitors

As stated in a previous study, Keune *et al* confirmed that TUDCA, and UDCA are partial non-competitive inhibitors of ATX.³ Compounds **3.25**, **3.2**, **3.30**, **3.31**, and **3.40** (**Figure 91**) were analysed with a non-linear regression through Michaelis-Menten kinetics and viewed with a Lineweaver-Burk plot at increasing concentrations of inhibitors. To determine whether the mode of inhibition is competitive or non-competitive the reaction kinetics can be plotted with a non-linear regression which takes into account for the concentration of the inhibitor to determine the global fit (**Table 26**) based upon equations in **Figure 92**.¹⁸⁰

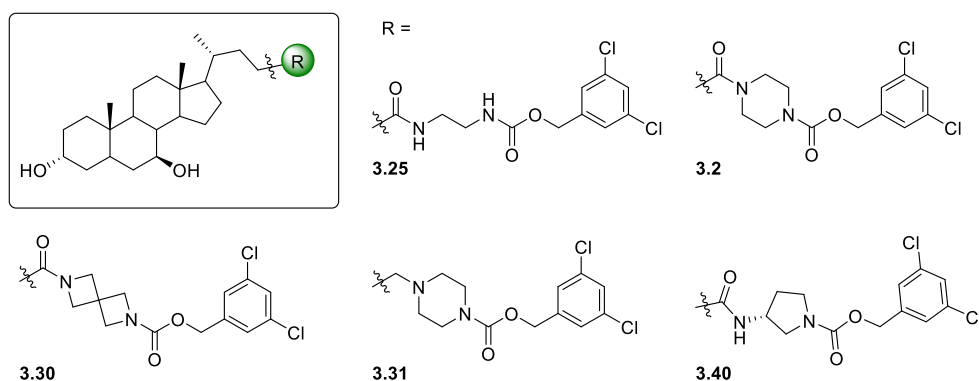


Figure 91 Compounds **3.25**, **3.2**, **3.30**, **3.31**, and **3.40**.

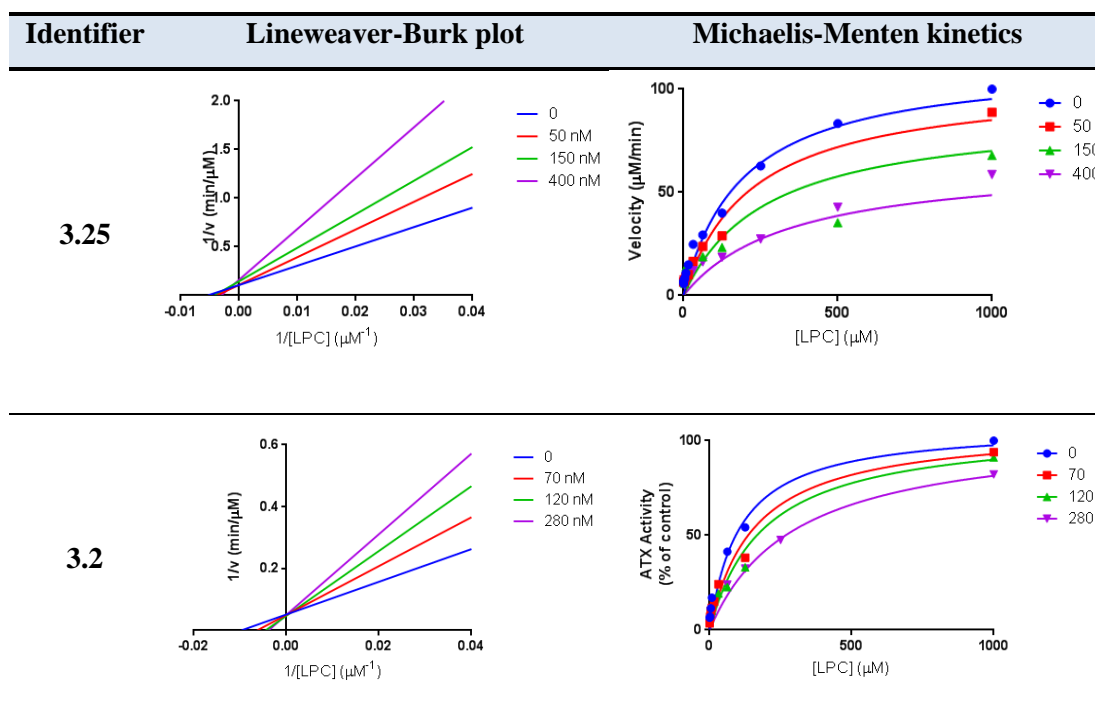
$$\text{Competitive Inhibitor } v = \frac{V_{\max} [S]}{K_M(1 + [I]/K_i) + [S]}$$

$$\text{Non-competitive Inhibitor } v = \frac{(V_{\max} [S])}{(K_M + [S])(1 + [I]/K_i)}$$

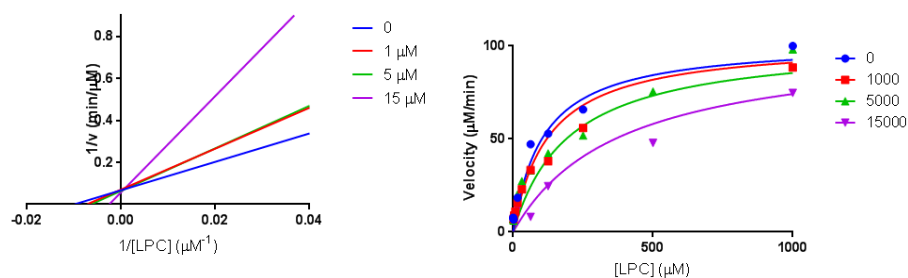
Figure 92 Equations for competitive and non-competitive inhibitors.¹⁸⁰

Analysis of the compounds showed that certain compounds were capable of switching the mode of inhibition from non-competitive, such as TUDCA, to competitive inhibition (**Table 26, Table 28**).¹⁸⁰ This data correlates with the observed binding mode from co-crystal structure data, which reveals the hybrid compounds reside in ATX within the tunnel, and hydrophobic region where the natural substrate resides.

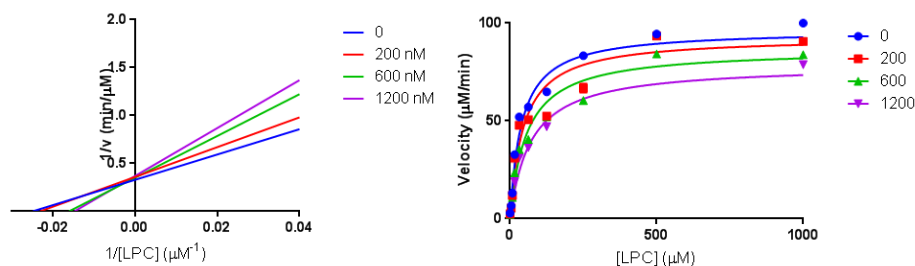
Table 28 Lineweaver-Burk and Michaelis-Menten plots of compounds **3.25**, **3.2**, **3.29**, **3.30**, and **3.25** reported by Keune *et al.*¹⁸⁰



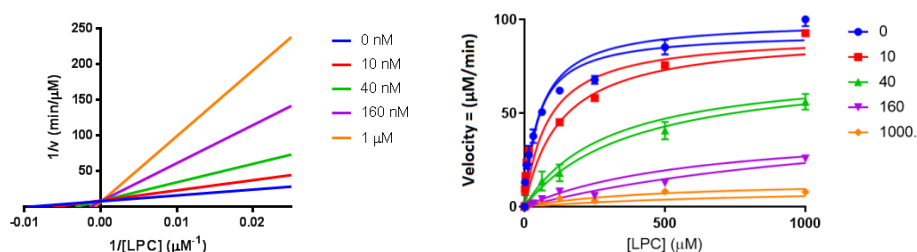
3.30



3.31



3.40



Despite the inhibition mode switching to a competitive nature, the overall percentage inhibition of the compound (I_{\max}) is an important parameter. If the hybrid compounds, which reside in the tunnel and pocket of the enzyme, can outcompete both LPC and LPA for the orthosteric site of the enzyme then overall percentage inhibition of the enzyme will increase. In this case K_M becomes αK_M , and K_i will become αK_i (**Figure 93**).^{178,181} For a non-competitive inhibitor, or when no inhibitor is present, $\alpha = 1$ and the Michaelis-Menten equation defined in **Figure 85** applies. For a competitive inhibitor, $\alpha > 1$, and in the case of an efficacious competitive inhibitor there is a small concentration of inhibitor present due to more EI complex formation, and as a result a smaller K_i value, which overall results in a larger value for α . As the concentration of a competitive inhibitor is increased, so does the value of α , and as a result we observe the Lineweaver-Burk plot previously discussed (**Figure 87, Table 28**).^{179,181}

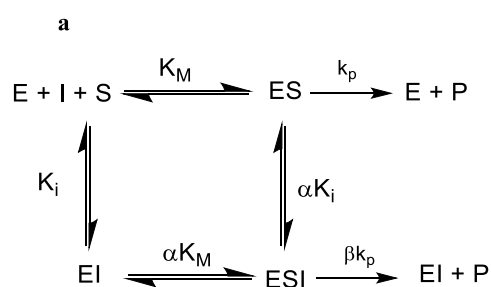


Figure 93 a) The enzyme-inhibitor binding equilibria b) The Michaelis-Menten equation taking into account for αK_M and the definition of α .^{179,181}

The overall percentage inhibition of ATX (I_{max}) was calculated, and interestingly the most potent compound **3.40** which contains the aminopyrrolidine core exhibited 100% competitive inhibition of ATX (**Table 29**). This shows the development from the non-competitive progenitor compound TUDCA, to compound **3.40**, which exhibited competitive inhibition with an I_{max} of 100% and a K_i of 0.006 μ M. The mode of inhibition for **3.2**, **3.30**, and **3.40** is indicative of competitive inhibitor.

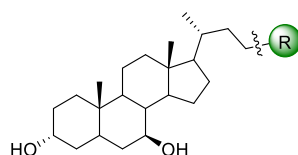
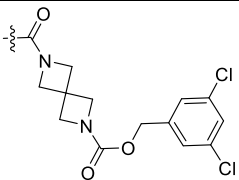
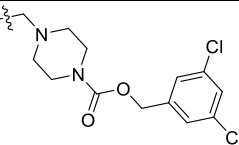
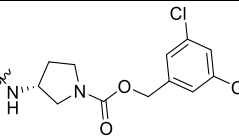


Table 29 ^aTUDCA ^bUDCA. The mode of inhibition of compounds (C) Competitive Inhibition (NC) Non-competitive inhibition (UC) Uncompetitive Inhibition.¹⁸⁰

	R	Mode of Inh	I_{max}	K_i
a		NC	57	6.65
3.25		NC	41	0.25
3.2		C	18	0.132

3.30		C	25	10
3.31		NC	22	0.60
3.40		C	100	0.006

3.4.6. BJEH Cell Based Assay and *in vivo* Activity

After the discovery of compound **3.40** as a potent ATX inhibitor, and co-crystal structure data which confirms the proposed binding mode, the potency was then determined in a cell based assay to determine if the inhibitor engages with the target in a physiological environment. Compound **3.40** containing the aminopyrrolidine core was tested in a fibroblast BJEH assay for the phosphorylation of AKT, as previously discussed in Chapter 1 by NKI. The first blot shows a control reaction with the cell media alone, and the second a control with ATX and no inhibitor which shows phosphorylation of AKT. **3.40** was tested as a dose response curve at decreasing concentrations, with significant inhibitory effects of the AKT signalling pathway at dilute concentrations of 0.5 μM (**Figure 95**). This shows that **3.40** can reduce the phosphorylation of AKT and hence reduce the effects of downstream signalling through the inhibition of ATX.

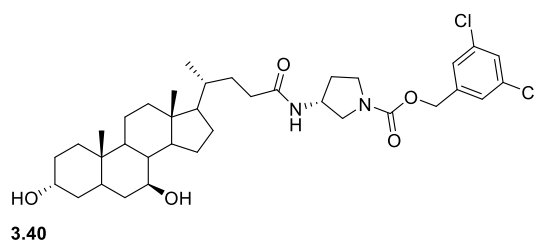


Figure 94 The structure of **3.40**.

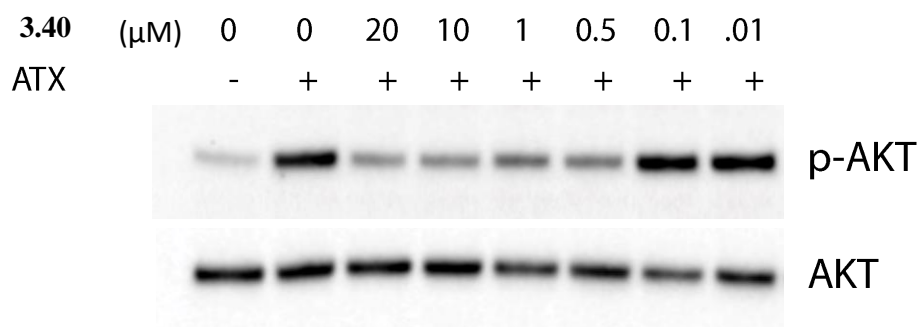


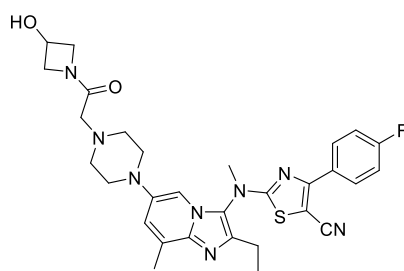
Figure 95 BJEH cell based assay for a dose response curve of **3.40** by NKI.

The correlation between the biochemical assay and the cell based assay indicates significant effects on the downstream signalling in cells based upon ATX inhibition.

The biochemical assays discussed within these projects are valuable for identifying direct inhibition of the identified target, in this case ATX. However, *in vivo* there are likely other factors which could interfere with the inhibitor reaching the desired target.¹⁸² This can include poor physicochemical and pharmacokinetics properties, and interactions with competing proteins and receptors. Therefore, pharmacodynamic results in a cellular or mammalian environment can differ to the biochemical assay, which is related directly to the inhibition of a target. Therefore, when a correlation between a biochemical assay and *in vivo* assay is observed it often concludes that the correct target has been inhibited in a cellular or *in vivo* environment to result in the desired pharmacodynamic response. In the case of the cell based BJEH assay the effect observed is the inhibition of phosphorylation of AKT, through inhibition of ATX which stops hydrolysis of LPC to LPA reaching LPAR in the cell based assay. Based upon the promising cellular data, compound **3.40** containing the aminopyrrolidine core was dosed in mice to determine the effect of the compound on the extracellular LPA at the site of injury *in vivo*.^{68,183} This should help to further validate the effect of ATX inhibition observed with the target in the biochemical assay with the pharmacodynamic effect observed in the cellular assay.

As previously discussed, the extracellular LPA levels in mice after Bleomycin induced injury are elevated, and as a result of this, an *in vivo* model can be used to determine if ATX inhibitors can reduce circulating LPA levels at the site of injury.^{68,183} Recent compounds GLPG1690 and PF-8380 have been tested *in vivo* within mice by Galapagos and Jones *et al*, both showing a significant effect on the reduction of extracellular LPA at the site of injury.^{85,184} Galapagos

studied the *in vivo* effect on the reduction of LPA 18:2 over 24 h, showing a substantial decrease even at 3 mg/kg over the extended period (green, **Figure 97**).



GLPG1690

Figure 96 The structure of GLPG1690.

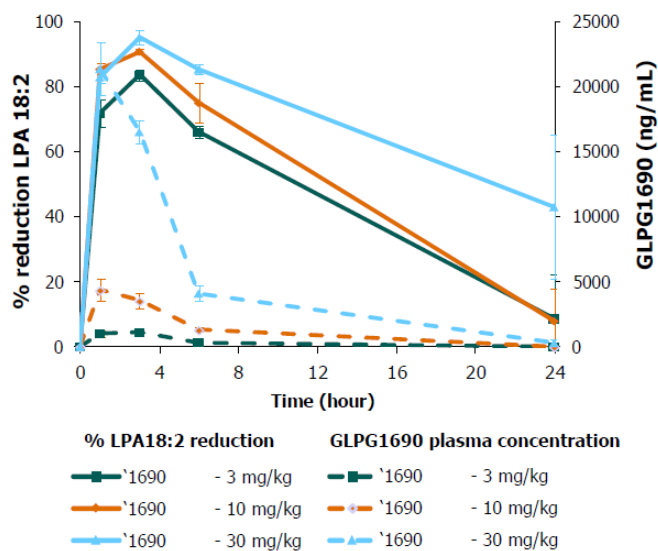
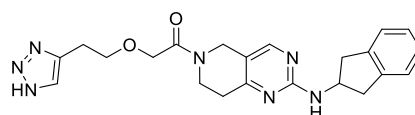


Figure 97 *In vivo* LPA reduction of 18:2 of GLPG1690 at 3, 10, and 30 mg/kg in mice.

Comparatively, compound **3.43** (**Figure 98**) developed by Eli Lilly is an orthosteric ATX inhibitor developed by Eli Lilly, which is potent in the LPC biochemical assay ($IC_{50} = 1.7$ nM).¹²² This inhibitor was reported to reduce the LPA levels in mice at 10 mg/kg to a significant extent after 8 h (Red, **Figure 99**). Due to the short half life of LPA, the LPA levels increase rapidly again after the concentration of the drug in the plasma is diminished (black, **Figure 99**).¹⁸³



3.43

Figure 98 The structure of orthosteric ATX inhibitor **3.43** developed by Jones *et al.*

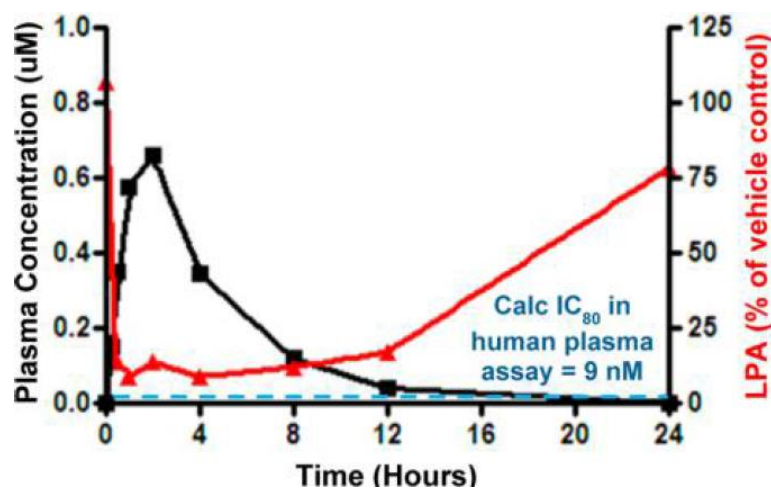


Figure 99 *In vivo* results of dosing compound **3.43** in mice by Jones *et al.* Red = concentration of LPA, black = concentration of **3.43**.

It can be noted that the orthosteric inhibitor GLPG1690 has a substantial effect on the reduction of LPA for a longer period of time compared to **3.43**, however this result only analyses LPA 18:2, whereas Jones *et al* includes all the isoforms of LPA giving a more realistic gauge of LPA reduction at the site of injury. In this study carried out in collaboration with Morris *et al* PF-8380 was tested as a positive control alongside the most potent compound **3.40** in an *in vivo* mouse model.¹⁷⁷ If a pharmacodynamic effect is observed, which in this case correlates to a reduction in LPA in the plasma of mice, it indicates that the inhibitor interacts with the target in a physiological environment. The compounds were initially dissolved at 50 mg mL⁻¹ in hydroxypropyl cellulose/tween and administered to the mice intraperitoneally at 10 mg kg⁻¹. After 8 h the plasma was isolated from the blood and analysed by mass spectrometry for the presence of extracellular LPA.¹⁸³ Overall there is a substantial decrease in extracellular LPA with both PF-8380 and **3.40** compared to the control vehicles (**Figure 100**). This shows that **3.40** reduces the circulating LPA at the site of injury in mice to the same extent as PF-8380.

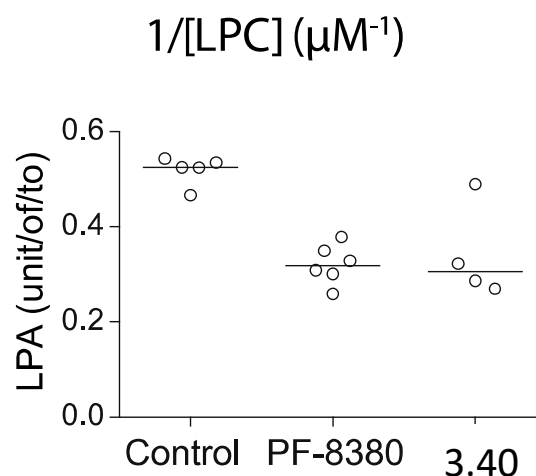


Figure 100 The effect of PF-8380 and **3.40** on extracellular LPA levels in mice (circles), with a median value indicated by a line. Students unpaired two tailed T-test suggests the difference of PF-8380 and **3.39** to the control is significant ($p < 0.05$). Results by Morris *et al.*¹⁸³

This pharmacodynamic result is concluded to be significant ($p < 0.05$), confirming *in vivo* effects which are comparable to **3.43** and GLPG1690 which is currently in clinical trials for the treatment of IPF. This suggests that this competitive ATX inhibitor with an alternative binding mode could be a valuable tool compound for ATX inhibition towards the treatment of diseases such as IPF and cancer.

3.5. Conclusions

The overall optimisation campaign is summarised in **Figure 101**. After identification of TUDCA and UDCA, bile salts which act as partial non-competitive inhibitors of ATX ($K_i = 10$ and $8.8 \mu\text{M}$ respectively), a structure-based design approach was taken to propose a novel hybrid series of compounds, which could occupy both the allosteric tunnel region and the hydrophobic pocket of ATX. Analysis of the first series of compounds provided active hybrid ATX inhibitors, which both contained the 3,5-dichlorobenzyl carbamate lipophilic tail with either an ethylenediamine linker **3.39** or a piperazine linker **3.2**. Further to this, we obtained co-crystal structures of these compounds bound to ATX, which validated our original design hypothesis. The co-crystal structures highlighted the need for a U-shaped conformation, and subsequent compounds were designed with linkers including aminomethyl piperidine, azetidin-3-amine, and 3-aminopyrrolidine cores to achieve this conformation, whilst limiting the flexibility of the compounds. Using this approach, we identified several highly potent ATX inhibitors, including the most potent ATX inhibitor **3.40** with an aminopyrrolidine core ($K_i = 0.020 \mu\text{M}$). Kinetic analysis of the compounds revealed that the hybrid ATX inhibitors were competitive inhibitors of ATX, which can outcompete LPA in the tunnel and the active site of ATX. This provides a novel chemotype for inhibition of ATX which may allow for selectivity over other members of the ENPP family due to the unique existence of the large hydrophobic pocket within ATX. Compound **3.40** reduced downstream signalling in the AKT pathway by inhibiting ATX and thus limiting the phosphorylation of AKT, which activates that pathway. In addition to this, we demonstrated that the most potent compound **3.40** reduced extracellular LPA levels *in vivo* in a mouse model with comparable efficacy to the orthosteric inhibitor PF-8380. These data confirm that the correlation observed between the target inhibition in the biochemical assay correlates well with cell based ATX inhibition, and *in vivo* reduction of plasma LPA, which are pathway relevant models for inhibition of ATX. The substantial pharmacodynamic effect observed *in vivo* is a promising step towards further profiling of this nascent lead series in phenotypic models for IPF or cancer, which can help to further validate ATX as a disease modifying target for these diseases.

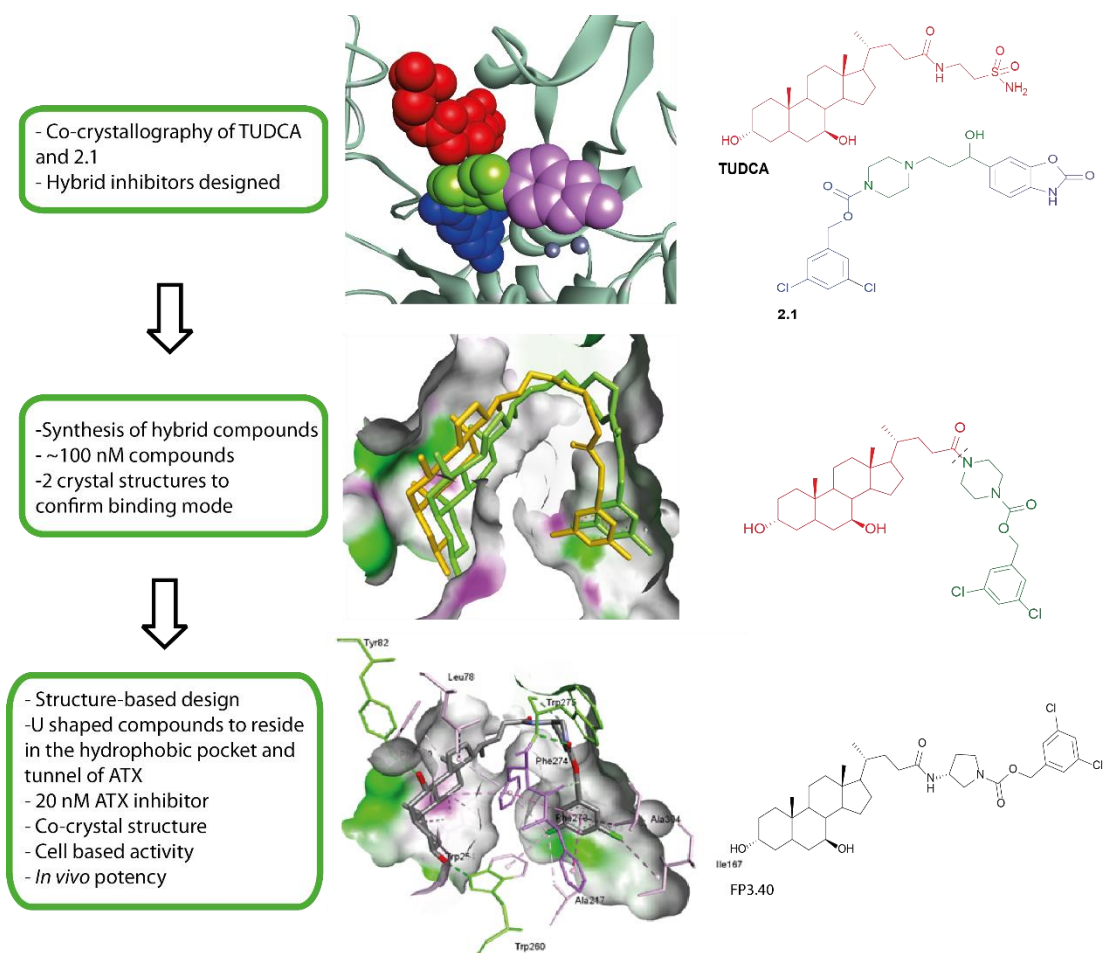


Figure 101 Optimisation trajectory using biostructural data.

3.6. Future Work

Based upon the hybrid compounds developed within this study, it was clear that a U-shaped conformation is necessary for the steroid to optimally reside in the tunnel, and the 3,5-dichlorobenzyl carbamate tail in the hydrophobic pocket of ATX. Crystallographic data confirmed the initially proposed binding mode hypothesis with ethylenediamine **3.25**, piperazine **3.2**, and the most potent compound with an aminopyrrolidine core **3.40**. As a result of the observed compound vector, additional cores can be investigated in order to promote this shape in the active site of the enzyme. These included a (1*S*,4*S*)-2,5-diazabicyclo[2.2.1]heptane core (**Figure 102 A**), which will help to lock the piperazine in a boat shaped confirmation similar to the crystal structure of **3.2**. The piperidin-3-amine and piperidin-3-ylmethanamine cores (**Figure 102 B and C**) are variants of compound **3.35**, and these templates should probe whether this vector increases the potency of the compounds. Additionally pyrrolidin-3-ylmethanamine and 3-(aminomethyl)pyrrolidin-3-ol cores (**Figure 102 D and E**) could promote an inhibitor shape that aids ATX inhibition, with core **E** containing an alcohol moiety to improve the solubility.

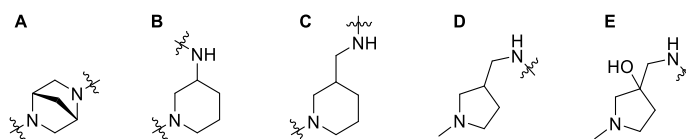


Figure 102 Novel cores to probe the SAR of the tunnel-hydrophobic pocket inhibitors.

Another potential avenue to investigate is to switch the binding mode from a tunnel-hydrophobic pocket inhibitor to a tunnel-active site inhibitor. From consideration of the crystal structure of **2.1** and HA155 in the active site of ATX, it can also be envisaged that tunnel-active site inhibitors could be synthesised by attaching the ZBG to the steroid moiety (**Figure 103**). An amine fragment of **2.1** and HA155 consisting of either the 6-glycylbenzo[d]oxazol-2(3H)-one or a (4-glycylphenyl)boronic acid moiety (**Figure 103**).

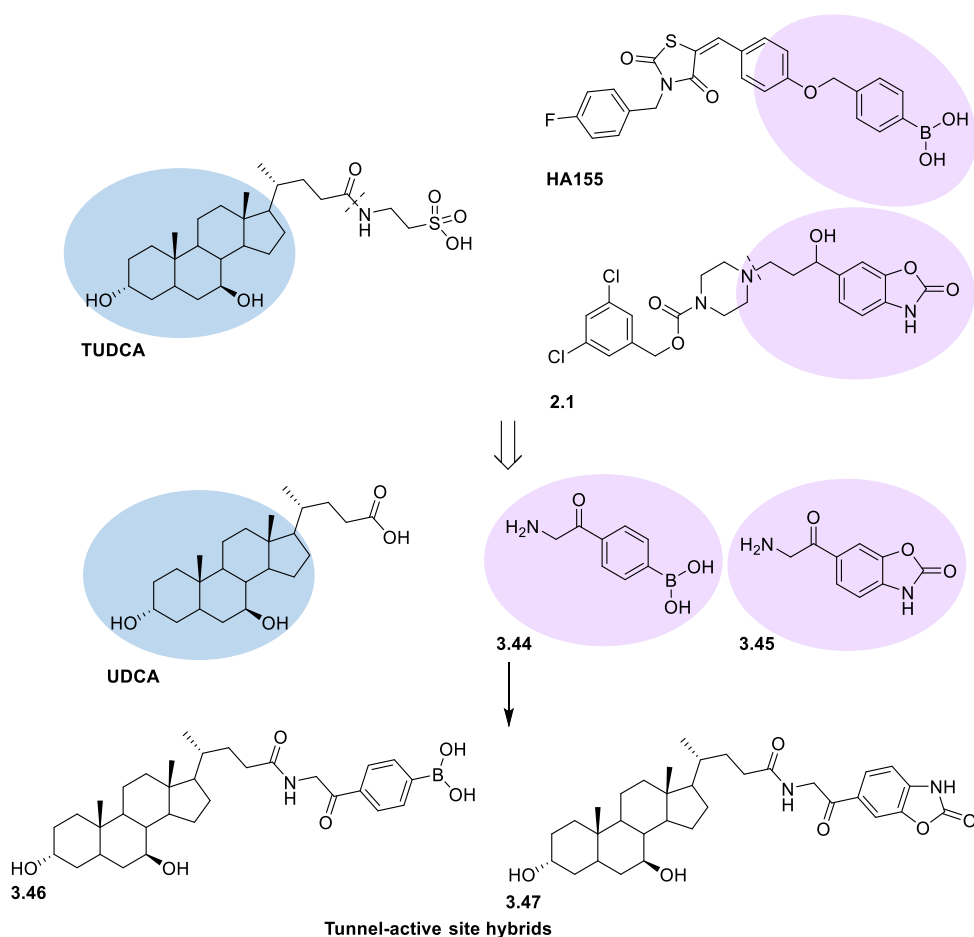


Figure 103 Tunnel and active site hybrids based around compound 2.1 and HA155.

These compounds can be synthesised similarly to the tunnel-hydrophobic pocket hybrids that contain either the boronic acid moiety or the benzo[*d*]oxazol-2(3*H*)-one, with an amine tether to increase the length of the compounds. Preliminary synthesis of compounds containing the benzo[*d*]oxazol-2(3*H*)-one ZBG suggested that insolubility would be problematic within this series. Therefore, a series of analogues containing the boronic acid and sulfonamide moiety from compound 2.120 (Chapter 2) should help to improve the solubility whilst maintaining compound potency (**Figure 104**). Compound 3.48 contains the sulfonamide ZBG identified in Chapter 2 with an ethylenediamine linker, and a direct analogue containing the boronic acid 3.49 is also postulated to result in a potent ATX inhibitor (**Figure 104**). Compound 3.49 can be further modified to an ether linkage with 3.50 to probe the necessary SAR landscape around these inhibitors, as no co-crystal structure or SAR exists around these highly novel tunnel-active site inhibitors (**Figure 104**). Additionally, an amide linked phenyl boronic acid compound 3.51 introduces linker changes that help to probe the SAR in this region (**Figure 104**). Compounds 3.48–3.51 were docked in ATX using GOLD and all exhibited the desired

binding mode, with the sulfonamide or the boronic acid interacting with the distal zinc atoms in the active site (**Figure 105**).

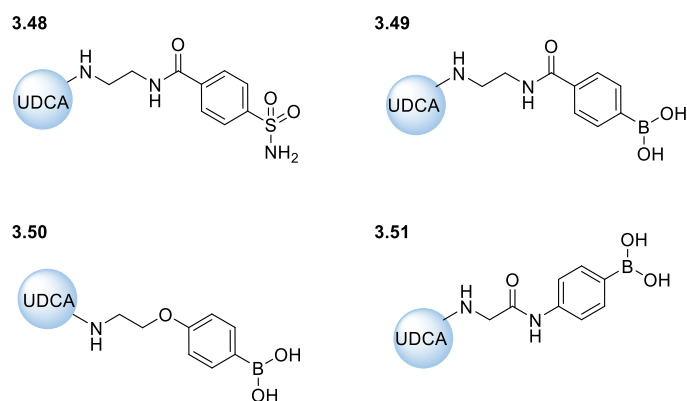


Figure 104 Proposed tunnel-active site compounds.

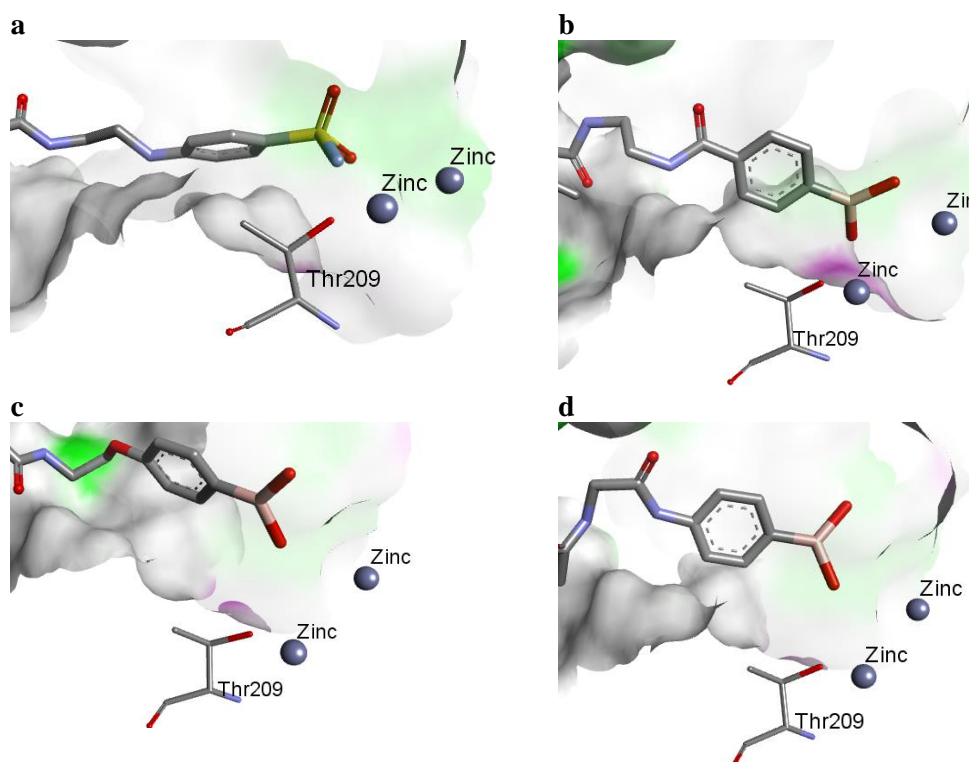


Figure 105 *In silico* modelling of compounds **3.48–3.51** **Figure 104** using GOLD and DS Visualizer.^{48,130}

Additionally, using an aminopyrrolidine motif used in the potent tunnel-hydrophobic pocket binding hybrid **3.40**, removal of the 3,5-dichloro hydrophobic anchor to a boronic acid could switch the binding mode into a tunnel-active site hybrid with the boronic acid at the active site

of the enzyme (**Figure 106**). This one-point change from compound **3.40** containing the 3,5-dichlorobenzyl carbamate tail to the bionic acid moiety is highlighted in **Figure 107**.

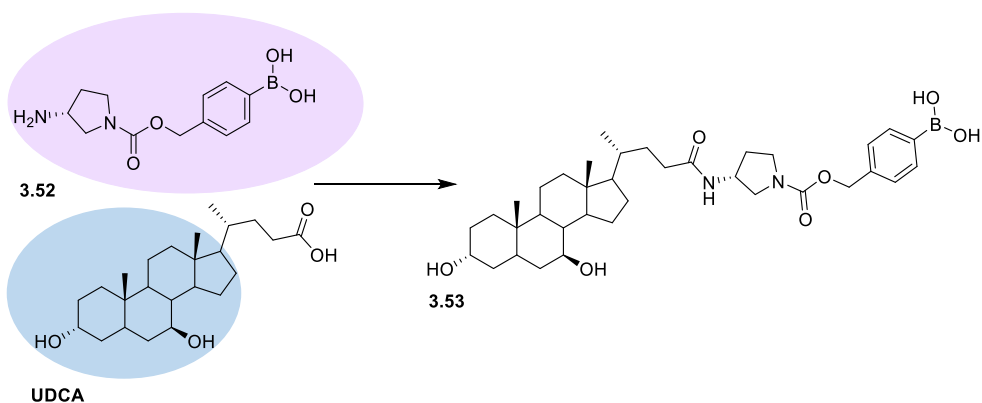


Figure 106 Proposed synthesis of a tunnel-active site inhibitor.

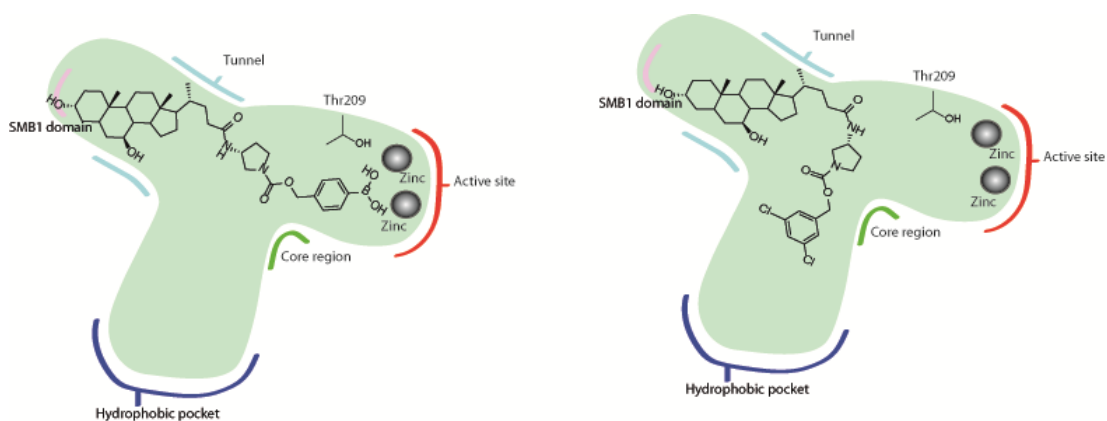


Figure 107 2D diagrams showing the proposed compound in the tunnel-active site and **3.40** in the tunnel-hydrophobic pocket.

Overall, significant further opportunities exist to optimise the emerging series to profile a robust series of assets, which will be of value in probing the association of ATX in a variety of disease states.

3.7. Experimental

3.7.1. General

All reagents and solvents were obtained from commercial suppliers and were used without further purification unless otherwise stated. Purification was carried out according to standard laboratory methods.

3.7.2. Experimental Details

Reactions were carried out using conventional glassware. Room temperature was generally 18 °C. Reactions were carried out at elevated temperatures using a temperature-regulated hotplate/stirrer.

3.7.3. Purification of Products

Thin layer chromatography was carried out using Merck silica plates coated with fluorescent indicator UV254. These were analysed under 254 nm UV light or developed using potassium permanganate solution. Normal phase flash chromatography was carried out using ZEOprep 60 HYD 40-63 µm silica gel. Strong cation exchange was carried out using Silicycle SilicaPrep™ or ISOLUTE® Propylsulfonic acid functionalised silica (SCX-2) cartridges. Weak anion exchange was carried out using ISOLUTE® Aminopropyl functionalised silica (NH₂) cartridges.

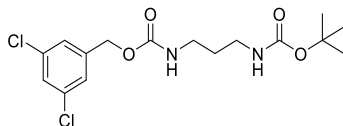
3.7.4. Analysis of Products

Fourier Transformed Infra-Red (FTIR) spectra were obtained on a Shimadzu IRAffinity-1 machine. ¹H and ¹³C, NMR spectra were obtained on a Bruker AV 400 at 400 MHz and 101 MHz, respectively and a Bruker AVIIIHD500 at 500 MHz and 126 MHz, respectively. Chemical shifts are reported in ppm and coupling constants are reported in Hz with CDCl₃ referenced at 7.26 (¹H) and 77.1 ppm (¹³C) and DMSO-*d*₆ referenced at 2.50 (¹H) and 39.52 ppm (¹³C). High-resolution mass spectra were obtained through analysis at the EPSRC UK National Mass Spectrometry Facility at Swansea University or in the School of Chemistry at the University of Glasgow.

3.7.5. General Procedures

General Procedure A: Carbamate Formation

For example, for the preparation of *tert*-butyl (3,5-dichlorobenzyl) propane-1,3-diylidicarbamate, **3.3**.



Prepared according to General Procedure A, using (3,5-dichlorophenyl)methanol (559 mg, 3.16 mmol, 1.1 equiv), CDI (512 mg, 3.16 mmol, 1.1 equiv), *tert*-butyl (2-aminopropyl)carbamate (500 mg, 2.87 mmol, 1.0 equiv) and DMF (5 mL). The reaction was diluted with H₂O and the organics extracted with EtOAc (2 × 40 mL), washed with brine (3 × 20 mL), dried with a hydrophobic frit and concentrated *in vacuo*. The crude material was purified by column chromatography on silica (80% EtOAc in petroleum ether) to afford the desired product as a white solid (790 mg, 73 %).

ν_{max} (neat): 3340, 2970, 2933, 2888, 1686, 1524 cm⁻¹.

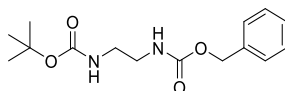
¹H NMR (CDCl₃, 500 MHz): δ 7.28–7.26 (m, 1H), 7.21–7.19 m, 2H), 5.54 (s, 1H), 5.01 (s, 2H), 4.85 (s, 1H), 3.26–3.12 (m, 4H), 1.69–1.54 (m, 2H), 1.42 (s, 9H).

¹³C NMR (CDCl₃, 101 MHz): δ 156.7, 156.3, 140.3, 135.1, 128.1, 126.1, 79.5, 65.0, 37.9, 37.2, 30.6, 28.5.

HRMS: exact mass calculated for [M+Na]⁺ (C₁₆H₂₂Cl₂N₂NaO₄) requires 399.0849 *m/z*, found 399.0839 *m/z*.

General Procedure B: *N*-Benzyl Carbamate Formation

For example, for the preparation of **benzyl *tert*-butyl ethane-1,2-diyl dicarbamate, 3.15**.



To a round bottom flask was added *tert*-butyl 3-methylpiperazine-1-carboxylate (100 mg, 0.50 mmol, 1.00 equiv), *N*-(benzyloxycarbonyloxy)succinimide (137 mg, 0.55 mmol, 1.10 equiv) and NaHCO₃ (66.4 mg, 0.75 mmol, 1.40 equiv), in THF:H₂O (1 mL:1 mL) and stirred for 16 h at room temperature. The reaction mixture was diluted with H₂O (20 mL) and the organics were extracted with EtOAc (2 × 20 mL), dried with a hydrophobic frit and concentrated *in vacuo* to afford the desired product as a clear oil (154 mg, 89%). Consistent with previously reported spectral analysis.¹⁸⁵

ν_{max} (neat): 3314, 2977, 2931, 1689, 1546 cm⁻¹.

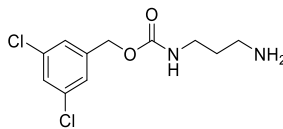
¹H NMR (CDCl₃, 400 MHz): δ 7.39–7.28 (m, 5H), 5.29 (s, 1H), 5.09 (s, 2H), 4.94 (s, 1H), 3.32–3.15 (m, 4H), 1.42 (s, 9H).

¹³C NMR (CDCl₃, 101 MHz): δ 156.3, 155.9, 136.0, 128.0, 127.63, 127.60, 79.1, 66.2, 41.0, 40.1, 27.9.

HRMS: exact mass calculated for [M+H]⁺ (C₁₅H₂₃N₂O₄) requires 295.1652 *m/z*, found 295.1654 *m/z*.

General Procedure C: N-Boc Deprotection

For example, for the preparation of **3,5-dichlorobenzyl(3-aminopropyl)carbamate, 3.9**.



Prepared according to General Procedure C, using *tert*-butyl (3,5-dichlorobenzyl)propane-1,3-diylidicarbamate **3.3** (725 mg, 1.92 mmol), trifluoroacetic acid (3 mL) and CH₂Cl₂ (3 mL) at room temperature for 2 h. The reaction was diluted with 1 M NaOH (40 mL) and the organics were extracted with EtOAc (40 mL), washed with brine (40 mL), dried with a hydrophobic frit and concentrated *in vacuo* to afford the desired product as a white solid (224 mg, 82 %).

ν_{\max} (neat): 3301, 2935, 2871, 1700, 1573 cm⁻¹.

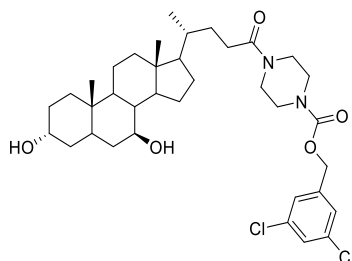
¹H NMR (CDCl₃, 400 MHz): δ 7.34–7.28 (m, 1H), 7.26–7.21 (m, 2H), 5.68 (s, 1H), 5.04 (s, 2H), 3.32 (dd, *J* = 6.2, 12.4 Hz, 2H), 2.81 (t, *J* = 6.5 Hz, 2H), 1.66 (d, *J* = 6.5 Hz, 2H), 1.47 (s, 2H).

¹³C NMR (CDCl₃, 101 MHz): δ 155.5, 139.7, 134.5, 127.5, 125.5, 64.3, 39.4, 38.9, 32.2.

HRMS: exact mass calculated for [M+H]⁺ (C₁₁H₁₅Cl₂N₂O₂) requires 277.0505 *m/z*, found 277.0503 *m/z*.

General Procedure D: HATU Amidation

For example, for the preparation of, **3,5-dichlorobenzyl-4-((4R)-4-((3R,7S,10S,13R)-3,7-dihydroxy-10,13-dimethylhexadecahydro-1H-cyclopenta[*a*]phenanthren-17-yl)pentanoyl)piperazine-1-carboxylate, 3.2.**



To a round bottom flask was added ursodeoxycholic acid (100 mg, 0.26 mmol, 1.1 equiv) in DMF (1 mL), DIPEA (180 μ L, 1.02 mmol, 4.0 equiv) and then 1-[bis(dimethylamino)methylene]-1*H*-1,2,3-triazolo[4,5-*b*]pyridinium 3-oxide hexafluorophosphate (HATU, 97 mg, 0.26 mmol, 1.1 equiv). After stirring at room temperature for 15 min 3,5-dichlorobenzyl piperazine-1-carboxylate (67 mg, 0.23 mmol, 1.0 equiv) was added and stirred for 16 h at room temperature. The reaction mixture was diluted with H₂O (20 mL) and the resulting precipitate filtered under vacuum. The crude material was purified by column chromatography on silica (0–10% MeOH in EtOAc) to afford the desired product as a clear solid (87 mg, 51%).

ν_{\max} (neat): 3496, 2931, 2866, 1708, 1637, 1421, 1231 cm^{-1} .

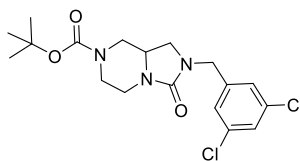
¹H NMR (CDCl₃, 500 MHz): δ 7.32–7.30 (m, 1H), 7.24–7.21 (m, 2H), 5.08 (s, 2H), 3.65–3.44 (m, 9H), 2.42–2.32 (m, 1H), 2.28–2.18 (m, 1H), 2.02–1.96 (m, 1H), 1.96–1.85 (m, 1H), 1.85–1.74 (m, 4H), 1.74–1.63 (m, 3H), 1.63–1.55 (m, 2H), 1.53–1.39 (m, 6H), 1.38–1.22 (m, 5H), 1.17–0.98 (m, 3H), 0.96–0.91 (m, 6H), 0.67 (s, 3H).

¹³C NMR (CDCl₃, 101 MHz): δ 172.4, 154.8, 139.9, 135.3, 128.5, 126.4, 71.54, 71.47, 66.0, 55.9, 55.1, 45.4, 43.9, 42.6, 40.3, 39.3, 37.4, 37.0, 35.6, 35.1, 34.2, 31.5, 30.5, 28.8, 27.0, 23.5, 21.3, 18.8, 12.3. 2 \times C not observed.

HRMS: exact mass calculated for [M+Na]⁺ (C₃₆H₅₂Cl₂N₂NaO₅) requires 685.3145 m/z , found 685.3119 m/z .

General Procedure E: Amine Alkylation

For example, for the preparation of *tert*-butyl 2-(3,5-dichlorobenzyl)-3-oxohexahydroimidazo[1,5-*a*]pyrazine-7(1*H*)-carboxylate, **3.17**.



To a round bottom flask was added *tert*-butyl 3-oxohexahydroimidazo[1,5-*a*]pyrazine-7(1*H*)-carboxylate (200 mg, 0.83 mmol, 1.0 equiv) in DMF (2 mL), followed by NaH (60% mineral oil, 55 mg, 0.91 mmol, 1.1 equiv) and stirred for 30 min at 0 °C. 1,3-dichloro-5-(chloromethyl)benzene (162 mg, 0.83 mmol, 1.0 equiv) was added and stirred for 16 h at room temperature. The reaction mixture was diluted with H₂O (20 mL) and the resulting precipitate filtered under vacuum to afford the desired product as a yellow solid which was used in the next step without further purification (302 mg, 91%).

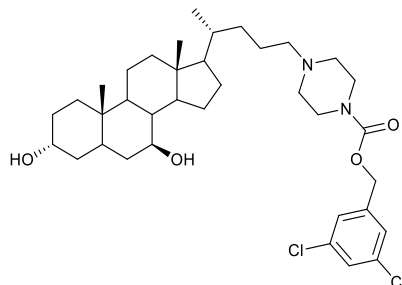
ν_{\max} (neat): 2927, 2858, 1693, 1681 cm⁻¹.

¹H NMR (CDCl₃, 500 MHz): δ 7.28 (t, J = 1.9 Hz, 1H), 7.14 (d, J = 1.5 Hz, 2H), 4.41–4.24 (m, 2H), 4.20–3.94 (m, 2H), 3.86 (dd, J = 2.8, 13.2 Hz, 1H), 3.63–3.54 (m, 1H), 3.33 (t, J = 8.7 Hz, 1H), 2.92 (td, J = 3.2, 12.7 Hz, 1H), 2.86–2.73 (m, 2H), 2.59 (s, 1H), 1.46 (s, 9H).

¹³C NMR (CDCl₃, 101 MHz): δ 158.4, 154.0, 140.1, 134.8, 127.4, 125.9, 80.0, 50.2, 46.8, 45.4, 40.1, 29.2, 27.9. 1 × C not observed.

General Procedure F: Amide Reduction

For example, for the preparation of, **3,5-dichlorobenzyl-4-((4R)-4-((3R,7S,10S,13R)-3,7-dihydroxy-10,13-dimethylhexadecahydro-1H-cyclopenta[*a*]phenanthren-17-yl)pentanoyl)piperazine-1-carboxylate, 3.31.**



To a round bottom flask at 0 °C was added 3,5-dichlorobenzyl 4-((4R)-4-((3R,7S,10S,13R)-3,7-dihydroxy-10,13-dimethylhexadecahydro-1H-cyclopenta[*a*]phenanthren-17-yl)pentanoyl)piperazine-1-carboxylate (92 mg, 0.14 mmol, 1.0 equiv), THF (5 mL), BH₃.THF (1 M, 700 μL, 0.70 mmol, 5.0 equiv) and the reaction stirred at 70 °C for 16 h. The reaction mixture was cooled to room temperature, quenched with 1 M HCl (20 mL) and stirred for 1 h. The organics were extracted with EtOAc (20 mL), washed with brine (20 mL), dried with a hydrophobic frit and concentrated *in vacuo*. The crude material was purified by column chromatography on silica (0–100% MeOH in CH₂Cl₂) to afford the desired product as a white solid (4 mg, 4%).

ν_{max} (neat): 3381, 2929, 2866, 1708, 1635 cm⁻¹.

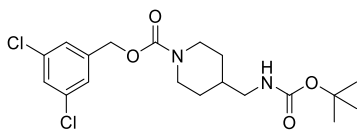
¹H NMR (CDCl₃, 500 MHz): δ 7.33–7.31 (m, 1H), 7.23 (d, *J* = 1.7 Hz, 2H), 5.08 (s, 2H), 3.66–3.43 (m, 12H), 2.43–2.34 (m, 1H), 2.29–2.18 (m, 1H), 2.03–1.97 (m, 1H), 1.96–1.86 (m, 1H), 1.85–1.74 (m, 4H), 1.71–1.62 (m, 2H), 1.62–1.53 (m, 4H), 1.52–1.41 (m, 6H), 1.39–1.32 (m, 2H), 1.29–1.21 (m, 2H), 1.19–1.11 (m, 2H), 1.11–1.01 (m, 2H), 0.99–0.92 (m, 6H), 0.68 (s, 3H).

¹³C NMR (CDCl₃, 126 MHz): δ 172.4, 139.9, 135.3, 128.5, 126.4, 71.6, 71.5, 66.0, 55.9, 55.1, 51.0, 45.5, 43.9, 42.6, 40.3, 39.3, 37.5, 37.0, 35.7, 35.1, 34.2, 31.5, 30.5, 28.9, 27.1, 23.5, 21.3, 18.8, 12.3. 3 × C not observed.

HRMS: exact mass calculated for [M+H]⁺ (C₃₆H₅₅Cl₂N₂O₄) requires 649.3533 *m/z*, found 649.3506 *m/z*.

3.7.6. Experimental Details

3,5-dichlorobenzyl 4-(((*tert*-butoxycarbonyl)amino)methyl)piperidine-1-carboxylate, 3.4.



Prepared according to General Procedure **A**, using (3,5-dichlorophenyl)methanol (454 mg, 2.57 mmol, 1.1 equiv), CDI (417 mg, 2.57 mmol, 1.1 equiv), *tert*-butyl (piperidin-4-ylmethyl)carbamate (500 mg, 2.33 mmol, 1.0 equiv) and DMF (5 mL) to afford the desired product as a white solid (630 mg, 65 %).

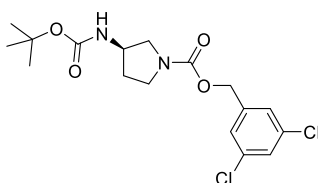
ν_{\max} (neat): 3368, 2923, 2851, 1707, 1681 cm^{-1} .

^1H NMR (CDCl_3 , 500 MHz): δ 7.29 (t, $J = 1.9$ Hz, 1H), 7.22 (d, $J = 1.9$ Hz, 2H), 5.08 (s, 2H), 4.62 (s, 1H), 4.26–4.10 (m, 2H), 3.09–2.94 (m, 2H), 2.89–2.63 (m, 2H), 1.83 (s, 1H), 1.71 (d, $J = 14.4$ Hz, 2H), 1.44 (s, 9H), 1.21–1.07 (m, 2H).

^{13}C NMR (CDCl_3 , 101 MHz): δ 155.5, 154.2, 139.8, 134.6, 127.6, 125.5, 78.9, 64.9, 45.4, 43.4, 36.1, 29.0, 27.9.

HRMS: exact mass calculated for $[\text{M}+\text{H}]^+$ ($\text{C}_{19}\text{H}_{27}\text{Cl}_2\text{N}_2\text{O}_4$) requires 417.1342 m/z , found 417.1344 m/z .

3,5-dichlorobenzyl (*R*)-3-(((*tert*-butoxycarbonyl)amino)pyrrolidine-1-carboxylate, 3.5 a.



Prepared according to General Procedure **A**, using (3,5-dichlorophenyl)methanol (422 mg, 2.38 mmol, 1.1 equiv), CDI (386 mg, 2.38 mmol, 1.1 equiv), *tert*-butyl ((4-hydroxypiperidin-4-yl)methyl)carbamate (500 mg, 2.17 mmol, 1.0 equiv) and DMF (5 mL). The crude material was purified by column chromatography on silica (60–80% EtOAc in petroleum ether) to afford the desired product as a white solid (704 mg, 75 %).

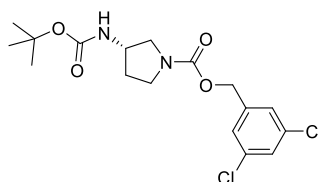
ν_{\max} (neat): 3301, 2981, 1706, 1681 cm^{-1} .

^1H NMR (CDCl_3 , 400 MHz): δ 7.28 (t, $J = 1.8$ Hz, 1H), 7.23–7.20 (m, 2H), 5.04 (s, 2H), 4.73 (d, $J = 6.5$ Hz, 1H), 4.20 (s, 1H), 3.65 (td, $J = 6.4, 10.2$ Hz, 1H), 3.54–3.42 (m, 2H), 3.31–3.20 (m, 1H), 2.20–2.07 (m, 1H), 1.92–1.76 (m, 1H), 1.43 (s, 9H).

^{13}C NMR (CDCl_3 , 101 MHz): δ 154.7, 153.8 (153.7), 139.7, 134.6, 127.6, 125.6, 79.4, 64.7, 51.5 (51.3), 50.0 (49.3), 42.9 (43.5), 31.5 (30.5), 27.9. Rotameric mixture observed, (minor rotamer observed in brackets).

HRMS: exact mass calculated for $[\text{M}+\text{Na}]^+$ ($\text{C}_{17}\text{H}_{22}\text{Cl}_2\text{N}_2\text{NaO}_4$) requires 411.0849 m/z , found 411.0843 m/z .

3,5-dichlorobenzyl (*S*)-3-((*tert*-butoxycarbonyl)amino)pyrrolidine-1-carboxylate, 3.5 b.



Prepared according to General Procedure A, using (3,5-dichlorophenyl)methanol (515 mg, 2.95 mmol, 1.1 equiv), CDI (478 mg, 2.95 mmol, 1.1 equiv), *tert*-butyl (*S*)-pyrrolidin-3-ylcarbamate (500 mg, 2.17 mmol, 1.0 equiv) and DMF (5 mL). The reaction was diluted with H_2O (40 mL) and the organics extracted with EtOAc (40 mL), washed with brine (3 x 40 mL), dried with a hydrophobic frit and concentrated *in vacuo*. The crude material was purified by column chromatography on silica (60–80% EtOAc in petroleum ether) to afford the desired product as a white solid (959 mg, 92 %).

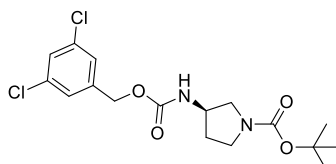
ν_{\max} (neat): 3329, 2979, 2883, 1684 cm^{-1} .

^1H NMR (CDCl_3 , 500 MHz): δ 7.29 (t, $J = 1.8$ Hz, 1H), 7.24–7.20 (m, 2H), 5.05 (s, 2H), 4.67 (s, 1H), 4.21 (s, 1H), 3.71–3.61 (m, 1H), 3.55–3.43 (m, 2H), 3.32–3.20 (m, 1H), 2.21–2.07 (m, 1H), 1.93–1.77 (m, 1H), 1.43 (s, 9H).

^{13}C NMR (CDCl_3 , 101 MHz): δ 155.3, 154.43 (154.36), 140.3, 135.2, 128.2, 126.2, 80.0, 65.4, 52.2 (51.9), 50.7 (49.9), 44.5 (44.1), 32.1 (31.2), 28.5. Rotameric mixture observed, (minor rotamer observed in brackets).

HRMS: exact mass calculated for $[M+Na]^+$ ($C_{17}H_{22}Cl_2N_2NaO_4$) requires 411.0849 m/z , found 411.0837 m/z .

***Tert*-butyl (*R*)-3-(((3,5-dichlorobenzyl)oxy)carbonyl)amino)pyrrolidine-1-carboxylate, 3.6 a.**



Prepared according to General Procedure A, using (3,5-dichlorophenyl)methanol (552 mg, 3.18 mmol, 1.2 equiv), CDI (479 mg, 3.18 mmol, 1.2 equiv), *tert*-butyl (*R*)-3-aminopyrrolidine-1-carboxylate (500 mg, 2.68 mmol, 1.0 equiv) and DMF (5 mL). The crude material was purified by column chromatography on silica (60–80% EtOAc in petroleum ether) to afford the desired product as a white solid (605 mg, 58 %).

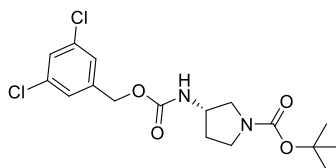
ν_{\max} (neat): 3335, 1702, 1687, 1524 cm^{-1} .

1H NMR ($CDCl_3$, 500 MHz): δ 7.31-7.27 (m, 1H), 7.23-7.15 (m, 2H), 5.02 (s, 2H), 4.23 (s, 1H), 3.64-3.57 (m, 1H), 3.50-3.35 (m, 2H), 3.31-3.14 (m, 1H), 2.12 (s, 1H), 1.99-1.70 (m, 2H), 1.44 (s, 9H).

^{13}C NMR ($CDCl_3$, 101 MHz): δ 154.7, 154.0, 139.2, 134.6, 127.7, 125.7, 79.2, 64.6, 51.3, 50.6 (49.9), 43.4 (43.1), 31.5 (30.6), 28.0. Rotameric mixture observed, (minor rotamer observed in brackets).

HRMS: exact mass calculated for $[M+Na]^+$ ($C_{17}H_{22}Cl_2N_2NaO_4$) requires 411.0849 m/z , found 411.0843 m/z .

***Tert*-butyl (S)-3-(((3,5-dichlorobenzyl)oxy)carbonyl)amino)pyrrolidine-1-carboxylate, 3.6 b.**



Prepared according to General Procedure A, using (3,5-dichlorophenyl)methanol (515 mg, 2.95 mmol, 1.1 equiv), CDI (478 mg, 2.95 mmol, 1.1 equiv), *tert*-butyl (S)-3-aminopyrrolidine-1-carboxylate (500 mg, 2.68 mmol, 1.0 equiv) and DMF (5 mL). The crude material was purified by column chromatography on silica (60–80% EtOAc in petroleum ether) to afford the desired product as a white solid (787 mg, 76 %).

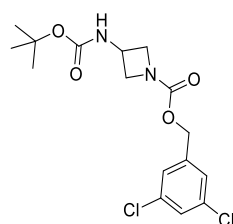
ν_{\max} (neat): 3298, 2979, 2886, 1675, 1408 cm^{-1} .

^1H NMR (CDCl_3 , 500 MHz): δ 7.30–7.26 (m, 1H), 7.20 (d, $J = 1.9$ Hz, 2H), 5.22 (s, 1H), 5.01 (s, 2H), 4.22 (s, 1H), 3.63–3.55 (m, 1H), 3.46–3.34 (m, 2H), 3.30–3.13 (m, 1H), 2.17–2.07 (m, 1H), 1.95–1.76 (m, 1H), 1.43 (s, 9H).

^{13}C NMR (CDCl_3 , 101 MHz): δ 154.8, 154.0, 139.3, 134.6, 127.7, 125.6, 79.1, 64.5, 51.3, 50.6 (49.9), 43.4 (43.1), 31.5 (30.6), 28.0. Rotameric mixture observed, (minor rotamer observed in brackets).

HRMS: exact mass calculated for $[\text{M}+\text{Na}]^+$ ($\text{C}_{17}\text{H}_{22}\text{Cl}_2\text{N}_2\text{NaO}_4$) requires 411.0849 m/z , found 411.0835 m/z .

3,5-dichlorobenzyl 3-((*tert*-butoxycarbonyl)amino)azetidine-1-carboxylate, 3.7.



Prepared according to General Procedure A, using (3,5-dichlorophenyl)methanol (544 mg, 3.19 mmol, 1.1 equiv), CDI (518 mg, 3.19 mmol, 1.1 equiv), *tert*-butyl azetidin-3-ylcarbamate (500 mg, 2.83 mmol, 1.0 equiv) and DMF (5 mL). The reaction was diluted with H_2O (40 mL)

and the organics were extracted with EtOAc (40 mL), washed with brine (3 x 40 mL), dried with a hydrophobic frit and concentrated *in vacuo*. The crude material was purified by column chromatography on silica (60–80% EtOAc in petroleum ether) to afford the desired product as a white solid (654 mg, 60 %).

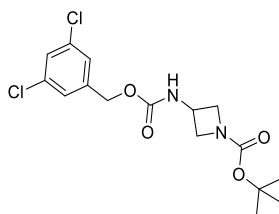
ν_{\max} (neat): 3346, 2979, 3071, 2884, 1706, 1689 cm^{-1} .

^1H NMR (CDCl_3 , 400 MHz): δ 7.31–7.27 (m, 1H), 7.23–7.15 (m, 2H), 5.07–4.94 (m, 3H), 4.52–4.38 (m, 1H), 4.30 (app. t, $J = 7.8$ Hz, 2H), 3.84 (dd, $J = 5.2, 9.3$ Hz, 2H), 1.43 (s, 9H).

^{13}C NMR (CDCl_3 , 101 MHz): δ 155.1, 154.3, 139.4, 134.6, 127.7, 125.6, 79.8, 64.6, 56.7, 40.3, 27.8.

HRMS: exact mass calculated for $[\text{M}+\text{Na}]^+$ ($\text{C}_{16}\text{H}_{20}\text{Cl}_2\text{N}_2\text{NaO}_4$) requires 397.0692 m/z , found 397.0686 m/z .

***Tert*-butyl 3-(((3,5-dichlorobenzyl)oxy)carbonyl)amino)azetidine-1-carboxylate, 3.8.**



Prepared according to General Procedure A, using (3,5-dichlorophenyl)methanol (544 mg, 3.19 mmol, 1.1 equiv), CDI (518 mg, 3.19 mmol, 1.1 equiv), *tert*-butyl azetidin-3-ylcarbamate (500 mg, 2.83 mmol, 1.0 equiv) and DMF (5 mL). The reaction was diluted with H_2O (40 mL) and the organics were extracted with EtOAc (40 mL), washed with brine (3 x 40 mL), dried with a hydrophobic frit and concentrated *in vacuo*. The crude material was purified by column chromatography on silica (60–80% EtOAc in petroleum ether) to afford the desired product as a white solid (898 mg, 82 %).

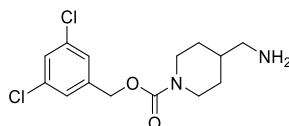
ν_{\max} (neat): 3296, 2968, 2933, 2984, 1730, 1669 cm^{-1} .

^1H NMR (CDCl_3 , 500 MHz): δ 7.32–7.28 (m, 1H), 7.23–7.19 (m, 2H), 5.38 (s, 1H), 5.03 (s, 2H), 4.49–4.39 (m, 1H), 4.22 (app. t, $J = 8.4$ Hz, 2H), 3.76 (dd, $J = 5.3, 9.4$ Hz, 2H), 1.43 (s, 9H).

^{13}C NMR (CDCl_3 , 101 MHz): δ 155.6, 154.5, 139.1, 134.7, 127.8, 125.7, 79.4, 64.7, 56.3, 40.5, 27.8.

HRMS: exact mass calculated for $[\text{M}+\text{Na}]^+$ ($\text{C}_{16}\text{H}_{20}\text{Cl}_2\text{N}_2\text{NaO}_4$) requires 397.0692 m/z , found 397.0685 m/z .

3,5-dichlorobenzyl 4-(aminomethyl)piperidine-1-carboxylate, 3.10.



Prepared according to General Procedure C, using 3,5-dichlorobenzyl 4-(((*tert*-butoxycarbonyl)amino)methyl)piperidine-1-carboxylate **3.4** (630 mg, 1.51 mmol), trifluoroacetic acid (2 mL) and CH_2Cl_2 (2 mL) at room temperature for 2 h. The reaction was diluted with 1 M NaOH (40 mL) and the organics were extracted with EtOAc (40 mL), washed with brine (40 mL), dried with a hydrophobic frit and concentrated *in vacuo* to afford the desired product as a clear oil (478 mg, 100 %).

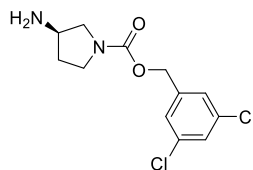
ν_{max} (neat): 2922, 2953, 1696 cm^{-1} .

^1H NMR (CDCl_3 , 500 MHz): δ 7.29–7.25 (m, 1H), 7.22–7.18 (m, 2H), 5.04 (s, 2H), 4.26–4.06 (m, 2H), 2.89–2.68 (m, 2H), 2.58 (d, $J = 6.4$ Hz, 2H), 1.73 (d, $J = 12.3$ Hz, 2H), 1.55–1.28 (m, 3H), 1.20–1.03 (m, 2H).

^{13}C NMR (CDCl_3 , 101 MHz): δ 154.8, 140.5, 135.1, 128.1, 126.1, 65.4, 47.9, 44.2, 39.4, 29.7.

HRMS: exact mass calculated for $[\text{M}+\text{H}]^+$ ($\text{C}_{14}\text{H}_{19}\text{Cl}_2\text{N}_2\text{O}_2$) requires 317.0818 m/z , found 317.0822 m/z .

3,5-dichlorobenzyl(*R*)-3-aminopyrrolidine-1-carboxylate, **3.11 a**.



Prepared according to General Procedure **C**, using 3,5-dichlorobenzyl(*R*)-3-((*tert*-butoxycarbonyl)amino)pyrrolidine-1-carboxylate **3.5 a** (307 mg, 0.81 mmol), trifluoroacetic acid (1 mL) and CH₂Cl₂ (2 mL) at room temperature for 2 h. The reaction was diluted with 1 M NaOH (10 mL) and the organics were extracted with EtOAc (10 mL), washed with brine (10 mL), dried with a hydrophobic frit and concentrated *in vacuo* to afford the desired product as a white solid (230 mg, 97 %).

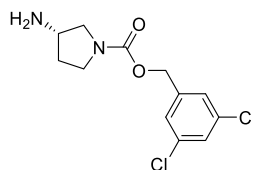
ν_{\max} (neat): 3335, 1702, 1697, 1524 cm⁻¹.

¹H NMR (CDCl₃, 400 MHz): δ 7.27–7.26 (m, 1H), 7.24–7.20 (m, 2H), 5.05 (s, 2H), 3.64–3.53 (m, 3H), 3.52–3.41 (m, 1H), 3.17–3.05 (m, 1H), 2.14–2.01 (m, 1H), 1.76–1.60 (m, 1H), 1.47 (s, 2H).

¹³C NMR (CDCl₃, 101 MHz): δ 154.5, 140.5, 135.1, 128.1, 126.1, 65.2, 54.8, 54.4, 51.5, 50.6, 44.8, 44.4, 34.8, 34.2. Rotameric mixture observed.

HRMS: exact mass calculated for [M+H]⁺ (C₁₂H₁₅Cl₂N₂O₂) requires 289.0505 *m/z*, found 289.0510 *m/z*.

3,5-dichlorobenzyl(*S*)-3-aminopyrrolidine-1-carboxylate, **3.11 b**.



Prepared according to General Procedure **C**, using 3,5-dichlorobenzyl 3,5-dichlorobenzyl (*S*)-3-aminopyrrolidine-1-carboxylate **3.5 b** (611 mg, 2.11 mmol), trifluoroacetic acid (1 mL) and CH₂Cl₂ (2 mL) at room temperature for 2 h. The reaction was diluted with 1 M NaOH (10 mL) and the organics were extracted with EtOAc (10 mL), washed with brine (10 mL), dried with

a hydrophobic frit and concentrated *in vacuo* to afford the desired product as a white solid (568 mg, 93 %).

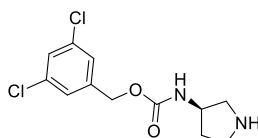
ν_{\max} (neat): 3288, 3076, 2977, 2886, 1719, 1662, 1418 cm^{-1} .

^1H NMR (CDCl_3 , 400 MHz): δ 7.30–7.24 (m, 1H), 7.22–7.16 (m, 2H), 5.00 (s, 2H), 3.58–3.57 (m, 3H), 3.45–3.34 (m, 1H), 3.11–3.00 (m, 1H), 2.05–1.95 (m, 1H), 1.70–1.53 (m, 1H), 1.38 (s, 2H).

^{13}C NMR (CDCl_3 , 101 MHz): δ 153.8, 139.9, 134.4, 127.4, 125.5, 64.5, 54.1 (53.7), 50.8 (49.9), 44.2 (43.8), 34.1 (33.5). Rotameric mixture observed, (minor rotamer observed in brackets).

HRMS: exact mass calculated for $[\text{M}+\text{Na}]^+$ ($\text{C}_{12}\text{H}_{14}\text{Cl}_2\text{N}_2\text{NaO}_2$) requires 311.0325 m/z , found 311.0318 m/z .

3,5-dichlorobenzyl (*R*)-pyrrolidin-3-ylcarbamate, **3.12 a**.



Prepared according to General Procedure C, using *tert*-butyl (*R*)-3-((((3,5-dichlorobenzyl)oxy)carbonyl)amino)pyrrolidine-1-carboxylate **3.6 a** (579 mg, 1.48 mmol), trifluoroacetic acid (1 mL) and CH_2Cl_2 (2 mL) at room temperature for 2 h. The reaction was diluted with 1 M NaOH (10 mL) and the organics were extracted with EtOAc (10 mL), washed with brine (10 mL), dried with a hydrophobic frit and concentrated *in vacuo* to afford the desired product as a white solid (418 mg, 97 %).

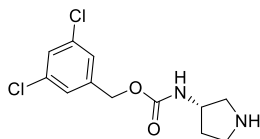
ν_{\max} (neat): 3290, 3076, 2976, 1719, 1663 cm^{-1} .

^1H NMR (CDCl_3 , 500 MHz): δ 7.30–7.21 (m, 1H), 7.21–7.13 (m, 2H), 5.52 (br. s, 1H), 4.99 (s, 2H), 4.13 (s, 1H), 3.12–2.93 (m, 2H), 2.93–2.82 (m, 1H), 2.82–2.71 (m, 1H), 2.39–2.13 (m, 1H), 2.09 (d, $J = 5.9$ Hz, 1H), 1.67–1.53 (m, 1H).

^{13}C NMR (CDCl_3 , 101 MHz): δ 155.0, 139.5, 134.5, 127.6, 125.5, 64.3, 52.9, 51.4, 44.8, 32.6.

HRMS: exact mass calculated for $[M+Na]^+$ ($C_{12}H_{14}Cl_2N_2NaO_2$) requires 289.0505 m/z , found 289.0504 m/z .

3,5-dichlorobenzyl (*S*)-pyrrolidin-3-ylcarbamate, 3.12 b.



Prepared according to General Procedure C, using *tert*-butyl (*S*)-3-(((3,5-dichlorobenzyl)oxy)carbonyl)amino)pyrrolidine-1-carboxylate **3.6 b** (753 mg, 1.48 mmol), trifluoroacetic acid (1 mL) and CH_2Cl_2 (2 mL) at room temperature for 2 h. The reaction was diluted with 1 M NaOH (10 mL) and the organics were extracted with EtOAc (10 mL), washed with brine (10 mL), dried with a hydrophobic frit and concentrated *in vacuo* to afford the desired product as a white solid (555 mg, 99 %).

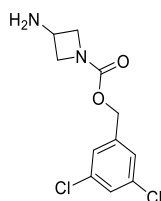
ν_{max} (neat): 3316, 2963, 2873, 1696, 1574 cm^{-1} .

1H NMR ($CDCl_3$, 400 MHz): δ 7.29–7.26 (m, 1H), 7.22–7.13 (m, 2H), 5.36 (br. s, 1H), 5.00 (s, 2H), 4.13 (s, 1H), 3.15–2.97 (m, 2H), 2.90–2.82 (m, 1H), 2.82–2.73 (m, 1H), 2.16–1.97 (m, 2H), 1.66–1.51 (m, 1H).

^{13}C NMR ($CDCl_3$, 101 MHz): δ 155.5, 140.2, 135.2, 128.2, 126.2, 65.0, 53.8, 52.1, 45.6, 33.3.

HRMS: exact mass calculated for $[M+H]^+$ ($C_{12}H_{15}Cl_2N_2O_2$) requires 289.0505 m/z , found 289.0502 m/z .

3,5-dichlorobenzyl 3-aminoazetidine-1-carboxylate, 3.13.



Prepared according to General Procedure C, using 3,5-dichlorobenzyl 3-((*tert*-butoxycarbonyl)amino)azetidine-1-carboxylate **3.7** (619 mg, 1.65 mmol), trifluoroacetic acid

(2 mL) and CH₂Cl₂ (2 mL) at room temperature for 2 h. The reaction was diluted with 1 M NaOH (10 mL) and the organics were extracted with EtOAc (10 mL), washed with brine (10 mL), dried with a hydrophobic frit and concentrated *in vacuo* to afford the desired product as a white solid (435 mg, 96 %).

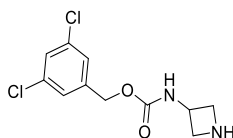
ν_{\max} (neat): 3378, 3071, 2951, 2877, 1706 cm⁻¹.

¹H NMR (CDCl₃, 500 MHz): δ 7.29–7.24 (m, 1H), 7.21–7.16 (m, 2H), 5.00 (s, 2H), 4.23 (dd, $J = 5.2, 11.0$ Hz, 2H), 3.86–3.76 (m, 1H), 3.66 (d, $J = 3.2$ Hz, 2H), 1.59 (s, 2H).

¹³C NMR (CDCl₃, 101 MHz): δ 155.8, 140.2, 135.1, 128.2, 126.2, 65.0, 59.7, 43.1.

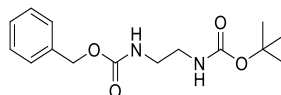
HRMS: exact mass calculated for [M+Na]⁺ (C₁₁H₁₂Cl₂N₂NaO₂) requires 297.0168 *m/z*, found 297.0166 *m/z*.

3,5-dichlorobenzyl azetidín-3-ylcarbamate, 3.14.



Prepared according to General Procedure C, using 3,5-dichlorobenzyl 3-((*tert*-butoxycarbonyl)amino)azetidín-1-carboxylate **3.8** (814 mg, 2.17 mmol), trifluoroacetic acid (2 mL) and CH₂Cl₂ (2 mL) at room temperature for 2 h. The reaction was diluted with 1 M NaOH (10 mL) and the organics were extracted with EtOAc (10 mL), washed with brine (10 mL), dried with a hydrophobic frit and concentrated *in vacuo* to afford the desired product as a white solid used in the next step without further purification for the synthesis of **3.38** (589 mg, 99 %).

Benzyl *tert*-butyl ethane-1,2-diylldicarbamate, 3.15.



Prepared according to General Procedure A, using benzyl alcohol (500 μ L, 4.8 mmol, 1.1 equiv), CDI (780 mg, 4.8 mmol, 1.1 equiv), *tert*-butyl (2-aminoethyl)carbamate (691 μ L, 4.4 mmol, 1.0 equiv) and DMF (4 mL). The reaction was diluted with H₂O (100 mL) and the organics extracted with CH₂Cl₂ (2 \times 100 mL), washed with brine (2 \times 100 mL), dried with a

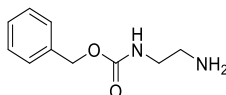
hydrophobic frit and concentrated *in vacuo*. The crude material was purified by column chromatography on silica (80% EtOAc in petroleum ether) to afford the desired product as a white solid (1.16 g, 92%). Consistent with previously reported spectral analysis.¹⁸⁶

¹H NMR (CDCl₃, 500 MHz): δ 7.38–7.28 (m, 5H), 5.29 (s, 1H), 5.09 (s, 2H), 4.94 (s, 1H), 3.33–3.16 (m, 4H), 1.42 (s, 9H).

¹³C NMR (CDCl₃, 101 MHz): δ 156.3, 155.9, 136.0, 128.0, 127.63, 127.60, 79.1, 66.2, 41.0, 40.1, 27.9.

HRMS: exact mass calculated for [M+H]⁺ (C₁₅H₂₄N₂O₄) requires 295.1652 *m/z*, found 295.1654 *m/z*.

Benzyl (2-aminoethyl)carbamate, **3.16**.



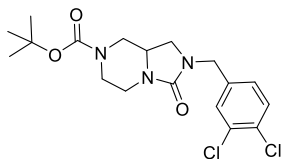
Prepared according to General Procedure C, using benzyl tert-butyl ethane-1,2-diyldicarbamate **3.15** (1.18 g, 4.00 mmol), trifluoroacetic acid (2 mL) and CH₂Cl₂ (5 mL) at room temperature for 2 h. The reaction was diluted with 1 M NaOH (40 mL) and the organics were extracted with EtOAc (40 mL), washed with brine (40 mL), dried with a hydrophobic frit and concentrated *in vacuo* to afford the desired product as a white solid (520 mg, 67 %). Commercially available, CAS: 72080-83-2.

¹H NMR (CDCl₃, 400 MHz): δ 7.36–7.22 (m, 5H), 5.47 (br. s, 1H), 5.08 (s, 2H), 3.22–3.11 (m, 2H), 2.81–2.69 (m, 2H), 1.70 (s, 2H).

¹³C NMR (CDCl₃, 101 MHz): δ 156.8, 136.6, 128.5, 128.1, 66.7, 43.7, 41.6. 1 × C not observed (coincident).

HRMS: exact mass calculated for [M+H]⁺ (C₁₀H₁₅N₂O₂) requires 195.1128 *m/z*, found 195.1127 *m/z*.

***Tert*-butyl 2-(3,4-dichlorobenzyl)-3-oxohexahydroimidazo[1,5-*a*]pyrazine-7(1*H*)-carboxylate, 3.18.**



Prepared according to general procedure **D**, using *tert*-butyl 3-oxohexahydroimidazo[1,5-*a*]pyrazine-7(1*H*)-carboxylate (200 mg, 0.83 mmol, 1.0 equiv), NaH 60% mineral oil (36 mg, 0.91 mmol, 1.1 equiv), 1,2-dichloro-4-(chloromethyl)benzene (114 μ L, 0.83 mmol, 1.0 equiv) and DMF (1.0 mL) for 16 h. The reaction was diluted with H₂O (20 mL) and filtered under vacuum, the resulting precipitate was purified by column chromatography on silica (80% EtOAc in petroleum ether) to afford the desired product as a white solid (256 mg, 77 %).

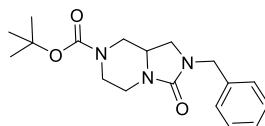
ν_{\max} (neat): 2981, 2936, 2886, 2860, 1683 cm^{-1} .

¹H NMR (CDCl₃, 400 MHz): δ 7.55–7.30 (m, 2H), 7.09 (d, $J = 7.6$ Hz, 1H), 4.32 (q, $J = 15.2$ Hz, 2H), 4.03 (s, 1H), 4.03 (s, 1H), 3.84 (d, $J = 11.6$, 1H), 3.57 (s, 1H), 3.30 (t, $J = 8.6$, 1H), 2.90 (t, $J = 11.9$, 1H), 2.81 (dd, $J = 4.7, 8.5$, 2H), 2.57 (s, 1H), 1.45 (s, 1H).

¹³C NMR (CDCl₃, 101 MHz): δ 158.4, 153.9, 137.0, 136.9, 132.2, 131.1, 130.2, 130.0, 129.4, 127.3, 126.9, 80.0, 50.2, 46.5, 45.2, 44.0, 40.0, 29.2, 27.8.

HRMS: exact mass calculated for [M+Na]⁺ (C₁₈H₂₃Cl₂N₃NaO₃) requires 422.1009 m/z , found 422.0990 m/z .

***Tert*-butyl 2-(benzyl)-3-oxohexahydroimidazo[1,5-*a*]pyrazine-7(1*H*)-carboxylate, 3.19.**



Prepared according to general procedure **D**, using *tert*-butyl 3-oxohexahydroimidazo[1,5-*a*]pyrazine-7(1*H*)-carboxylate (100 mg, 0.41 mmol, 1.0 equiv), NaH 60% mineral oil (18 mg, 0.46 mmol, 1.1 equiv), benzylbromide (50 μ L, 0.42 mmol, 1.0 equiv) and DMF (1.0 mL) for 16 h. The reaction was diluted with H₂O (20 mL) and filtered under vacuum. The resulting

precipitate was purified by column chromatography on silica (60–80% EtOAc in petroleum ether) to afford the desired product as a white solid (139 mg, 100 %).

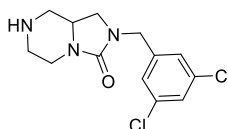
ν_{\max} (neat): 2976, 2923, 1680 cm^{-1} .

^1H NMR (CDCl_3 , 400 MHz): δ 7.32–7.26 (m, 2H), 7.26–7.10 (m, 3H), 4.35 (s, 2H), 3.99 (s, 1H), 3.83 (d, $J = 10.6$ Hz, 1H), 3.56–3.48 (m, 1H), 3.26 (t, $J = 8.7$ Hz, 1H), 2.87 (td, $J = 2.7, 12.6, 12.6$ Hz, 1H), 2.87 (td, $J = 2.7, 12.6$ Hz, 1H), 2.77 (dd, $J = 4.7, 9.1$ Hz, 1H), 1.42 (s, 1H).

^{13}C NMR (CDCl_3 , 101 MHz): δ 157.8, 154.0, 136.4, 128.2, 127.6, 127.0, 79.8, 50.2, 47.4, 45.1, 40.0, 27.8.

HRMS: exact mass calculated for $[\text{M}+\text{H}]^+$ ($\text{C}_{18}\text{H}_{26}\text{N}_3\text{O}_3$) requires 332.1974 m/z , found 332.1967 m/z

2-(3,5-dichlorobenzyl)hexahydroimidazo[1,5-*a*]pyrazin-3(2*H*)-one, 3.20.



Prepared according to General Procedure C, using *tert*-butyl 2-(3,5-dichlorobenzyl)-3-oxohexahydroimidazo[1,5-*a*]pyrazine-7(1*H*)-carboxylate **3.17** (300 mg, 0.75 mmol), trifluoroacetic acid (0.5 mL) and CH_2Cl_2 (2 mL) at room temperature for 2 h. The reaction was diluted with 1 M NaOH (10 mL) and the organics were extracted with EtOAc (10 mL), washed with brine (10 mL), dried with a hydrophobic frit and concentrated *in vacuo* to afford the desired product as a white solid (140 mg, 62 %).

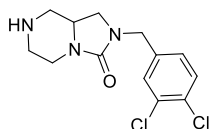
ν_{\max} (neat): 3301, 2920, 2853, 1675 cm^{-1} .

^1H NMR (CDCl_3 , 400 MHz): δ 7.24 (t, $J = 1.9$ Hz, 1H), 7.12 (d, $J = 1.8$ Hz, 2H), 4.35 (d, $J = 15.4$ Hz, 1H), 4.24 (d, $J = 15.4$ Hz, 1H), 3.86–3.78 (m, 1H), 3.64–3.53 (m, 1H), 3.28 (t, $J = 8.6$ Hz, 1H), 2.99–2.87 (m, 3H), 2.77 (dd, $J = 5.2, 8.8$ Hz, 1H), 2.73–2.63 (m, 1H), 2.57–2.48 (m, 1H), 1.74 (s, 1H).

^{13}C NMR (CDCl_3 , 101 MHz): δ 158.6, 140.5, 134.7, 127.2, 125.9, 125.84, 125.80, 51.4, 49.8, 46.8, 45.8, 44.8, 41.3.

HRMS: exact mass calculated for $[M+H]^+$ ($C_{13}H_{16}Cl_2N_3O$) requires 300.0665 m/z , found 300.0654 m/z .

2-(3,4-dichlorobenzyl)hexahydroimidazo[1,5-*a*]pyrazin-3(2*H*)-one, 3.21.



Prepared according to general procedure **C**, using *tert*-butyl 2-(3,5-dichlorobenzyl)-3-oxohexahydroimidazo[1,5-*a*]pyrazine-7(1*H*)-carboxylate **3.18** (167 mg, 0.42 mmol, 1.0 equiv), trifluoroacetic acid (0.5 mL) and CH_2Cl_2 (2 mL) until the reaction had gone to completion by tlc. The reaction was diluted with 1M NaOH (10 mL) and extracted with EtOAc (10 mL). The organics were washed with brine (10 mL), dried with a hydrophobic frit and concentrated *in vacuo* to afford the desired product as a clear gum (114 mg, 91 %).

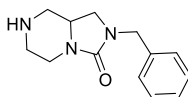
ν_{max} (neat): 3286, 2925, 2855, 1665 cm^{-1} .

1H NMR ($CDCl_3$, 400 MHz): δ 7.42–7.25 (m, 2H), 7.14–6.97 (m, 1H), 4.38–4.14 (m, 2H), 3.80 (t, $J = 9.8$ Hz, 1H), 3.69–3.54 (s, 1H), 3.25 (dd, $J = 8.3, 16.8$ Hz, 1H), 3.06 (d, $J = 18.7$ Hz, 1H), 3.01–2.87 (m, 3H), 2.71 (ddd, $J = 9.2, 15.7, 26.2$ Hz, 2H), 2.50 (dd, $J = 10.4, 20.2$ Hz, 1H), 1.21 (d, $J = 9.4$ Hz, 1H).

^{13}C NMR ($CDCl_3$, 101 MHz): δ 159.2, 137.6, 130.7, 129.9, 127.4, 51.5, 49.8, 47.1, 46.3, 45.0, 41.4.

HRMS: exact mass calculated for $[M+H]^+$ ($C_{13}H_{16}Cl_2N_3O$) requires 300.0657 m/z , found 300.0657 m/z .

2-benzylhexahydroimidazo[1,5-*a*]pyrazin-3(2*H*)-one, 3.22.



Prepared according to general procedure **C**, using *tert*-butyl 2-(3,5-dichlorobenzyl)-3-oxohexahydroimidazo[1,5-*a*]pyrazine-7(1*H*)-carboxylate **3.19** (109 mg, 0.32 mmol, 1.0 equiv), trifluoroacetic acid (0.5 mL) and CH_2Cl_2 (2 mL) until the reaction had gone to

completion by tlc. The reaction was diluted with 1M NaOH (10 mL) and extracted with EtOAc (10 mL). The organics were washed with brine (10 mL), dried with a hydrophobic frit and concentrated *in vacuo* to afford the desired product as a white solid (73 mg, 96 %).

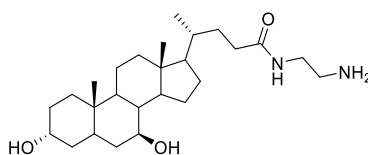
ν_{\max} (neat): 3301, 2020, 2853, 1675 cm^{-1} .

^1H NMR (CDCl_3 , 400 MHz): δ 7.30 (t, $J = 7.2$ Hz, 2H), 7.24 (dd, $J = 7.5, 8.7$ Hz, 3H), 4.35 (q, $J = 15.0$ Hz, 2H), 3.89–3.79 (m, 1H), 3.53 (tdd, $J = 4.4, 6.7, 8.7$ Hz, 1H), 3.24 (t, $J = 8.7$ Hz, 1H), 2.90 (qd, $J = 3.5, 11.4, 11.0$ Hz, 3H), 2.75 (dd, $J = 5.0, 8.9$ Hz, 1H), 2.67 (td, $J = 3.6, 12.3, 11.9$ Hz, 1H), 2.50 (t, $J = 11.2$ Hz, 1H), 1.82 (s, 1H).

^{13}C NMR (CDCl_3 , 101 MHz): δ 158.9, 136.7, 128.1, 127.5, 126.9, 51.4, 49.7, 47.4, 45.6, 44.8, 41.3.

HRMS: exact mass calculated for $[\text{M}+\text{H}]^+$ ($\text{C}_{13}\text{H}_{18}\text{N}_3\text{O}$) requires 232.1444 m/z , found 232.1444 m/z .

(4R)-N-(2-aminoethyl)-4-((3R,7S,10S,13R)-3,7-dihydroxy-10,13-dimethylhexadecahydro-1H-cyclopenta[*a*]phenanthren-17-yl)pentanamide, 3.23.



Prepared according to General Procedure C, using *tert*-butyl (2-((4R)-4-((3R,7S,10S,13R)-3,7-dihydroxy-10,13-dimethylhexadecahydro-1H-cyclopenta[*a*]phenanthren-17-yl)pentanamido)ethyl)carbamate **2.53** (936 mg, 1.75 mmol, 1.0 equiv), trifluoroacetic acid (2 mL), CH_2Cl_2 (4 mL), diluted with 1 M NaOH (100 mL), the organics were extracted with EtOAc (100 mL), washed with brine (100 mL), dried with a hydrophobic frit and concentrated *in vacuo* to afford the desired product as a white solid (605 mg, 63 %).

ν_{\max} (neat): 3283, 2935, 2669, 1715, 1654, 1157 cm^{-1} .

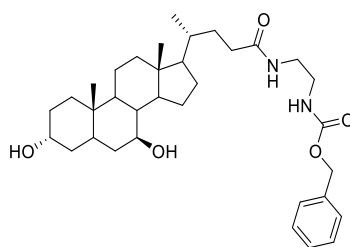
^1H NMR (CDCl_3 , 500 MHz): δ 9.36 (s, 1H), 7.89 (s, 1H), 4.42 (d, $J = 4.6$ Hz, 1H), 3.85 (d, $J = 6.8$ Hz, 1H), 3.21 (t, $J = 5.4$ Hz, 2H), 3.17 (t, $J = 5.5$ Hz, 2H), 2.13–2.03 (m, 1H), 1.99–1.90 (m, 2H), 1.86–1.80 (m, 1H), 1.86–1.80 (m, 1H), 1.80–1.71 (m, 1H), 1.70–1.60 (m, 3H), 1.51–

1.43 (m, 3H), 1.42–1.26 (m, 7H), 1.23–1.06 (m, 3H), 1.03–0.92 (m, 2H), 0.89–0.85 (m, 6H), 0.61 (s, 3H).

^{13}C NMR (CDCl_3 , 101 MHz): δ 173.0, 69.7, 69.4, 55.9, 54.7, 43.1, 43.0, 42.2, 39.8, 39.2, 38.7, 37.7, 37.30, 37.26, 34.9, 34.8, 33.7, 32.4, 31.5, 30.2, 28.1, 26.7, 23.3, 20.8, 18.4, 12.0.

HRMS: exact mass calculated for $[\text{M}+\text{H}]^+$ ($\text{C}_{26}\text{H}_{47}\text{N}_2\text{O}_3$) requires 435.3581 m/z , found 435.3576 m/z .

Benzyl (2-((4R)-4-((3R,7S,10S,13R)-3,7-dihydroxy-10,13-dimethylhexadecahydro-1H-cyclopenta[*a*]phenanthren-17-yl)pentanamido)ethyl)carbamate, 3.24.



Prepared according to General Procedure **E** with ursodeoxycholic acid (445 mg, 1.13 mmol, 1.1 equiv), DIPEA (720 μL , 4.12 mmol, 4.0 equiv), HATU (430 mg, 0.13 mmol, 1.1 equiv), benzyl (2-aminoethyl)carbamate (200 mg, 1.03 mmol, 1.0 equiv) and DMF (5 mL). The crude material was subjected to the purification outlined in the General Procedure (silica gel, 0–10% MeOH in CH_2Cl_2) to afford the desired product as a clear solid (399 mg, 68 %).

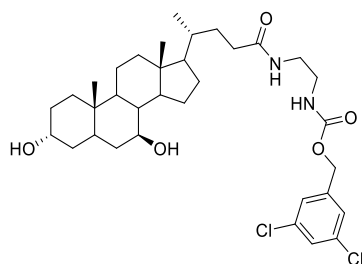
ν_{max} (neat): 3298, 2933, 2866, 1706, 1652, 1527 cm^{-1} .

^1H NMR (CDCl_3 , 500 MHz): δ 7.39–7.28 (m, 5H), 6.10 (s, 1H), 5.29 (s, 1H), 5.09 (s, 2H), 3.63–3.52 (m, 2H), 3.41–3.28 (m, 4H), 2.21–2.16 (m, 1H), 2.08–2.01 (m, 1H), 2.01–1.96 (m, 1H), 1.91–1.84 (m, 1H), 1.82–1.75 (m, 3H), 1.73–1.64 (m, 4H), 1.61–1.54 (m, 3H), 1.52–1.39 (m, 5H), 1.34–1.20 (m, 6H), 1.16–1.09 (m, 1H), 1.06–0.99 (m, 2H), 0.95–0.88 (m, 6H), 0.67 (s, 3H).

^{13}C NMR (CDCl_3 , 101 MHz): δ 174.6, 157.4, 136.5, 128.7, 128.3, 128.2, 71.6, 71.5, 67.0, 55.9, 55.1, 43.9, 42.6, 41.2, 40.3, 39.4, 37.5, 37.0, 35.6, 35.1, 34.2, 33.7, 31.9, 30.5, 28.8, 27.0, 23.5, 21.3, 18.6, 12.3. $2 \times \text{C}$ not observed.

HRMS: exact mass calculated for $[\text{M}+\text{Na}]^+$ ($\text{C}_{34}\text{H}_{52}\text{N}_2\text{NaO}_5$) requires 591.3768 m/z , found 591.3746 m/z .

3,5-dichlorobenzyl (2-((4*R*)-4-((3*R*,7*S*,10*S*,13*R*)-3,7-dihydroxy-10,13-dimethylhexadecahydro-1*H*-cyclopenta[*a*]phenanthren-17-yl)pentanamido)ethyl)carbamate, **3.25**.



Prepared according to General Procedure **E** with ursodeoxycholic acid (176 mg, 0.45 mmol, 1.1 equiv), DIPEA (286 μ L, 1.64 mmol, 4.0 equiv), HATU (171 mg, 0.45 mmol, 1.1 equiv), 3,5-dichlorobenzyl (2-aminoethyl)carbamate (107 mg, 0.41 mmol, 1.0 equiv) and DMF (2 mL). The crude material was subjected to the purification outlined in the General Procedure (silica gel, 0–10% MeOH in CH_2Cl_2) to afford the desired product as a clear solid (134 mg, 51 %).

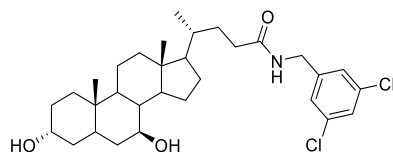
ν_{max} (neat): 3329, 2933, 2864, 1706, 1652, 1574 cm^{-1} .

^1H NMR (CDCl_3 , 400 MHz): δ 7.30–7.27 (m, 1H), 7.23–7.19 (m, 2H), 6.34 (br. s, 1H), 5.73 (br. s, 1H), 5.01 (s, 2H), 3.65–3.50 (m, 2H), 3.42–3.25 (m, 4H), 2.27–2.12 (m, 1H), 2.11–2.00 (m, 1H), 2.00–1.93 (m, 1H), 1.88–1.71 (m, 5H), 1.70–1.61 (m, 2H), 1.60–1.53 (m, 2H), 1.50–1.35 (m, 5H), 1.35–1.16 (m, 6H), 1.14–0.98 (m, 3H), 0.97–0.87 (m, 6H), 0.64 (s, 3H).

^{13}C NMR (CDCl_3 , 101 MHz): δ 175.0, 156.9, 140.1, 135.2, 128.2, 126.1, 71.4, 65.1, 56.01, 55.95, 55.1, 43.8, 42.6, 41.2, 40.3, 39.9, 39.4, 37.5, 37.2, 35.6, 35.1, 34.2, 33.6, 32.0, 30.4, 28.8, 27.0, 23.5, 21.3, 18.6, 12.2. $1 \times \text{C}$ not observed.

HRMS: exact mass calculated for $[\text{M}+\text{Na}]^+$ ($\text{C}_{34}\text{H}_{50}\text{Cl}_2\text{N}_2\text{NaO}_5$) requires 659.2989 m/z , found 659.2965 m/z .

(4R)-N-(3,5-dichlorobenzyl)-4-((3R,7S,10S,13R)-3,7-dihydroxy-10,13-dimethylhexadecahydro-1H-cyclopenta[*a*]phenanthren-17-yl)pentanamide, 3.26.



Prepared according to General Procedure **E** with ursodeoxycholic acid (100 mg, 0.26 mmol, 1.0 equiv), DIPEA (180 μ L, 1.02 mmol, 4.0 equiv), HATU (97 mg, 0.26 mmol, 1.0 equiv), 3,5-dichlorobenzylamine (35 μ L, 0.26 mmol, 1.0 equiv) and DMF (1 mL). The crude material was subjected to the purification outlined in the General Procedure (silica gel, 0–10% MeOH in CH_2Cl_2) to afford the desired product as a white solid (14 mg, 10%).

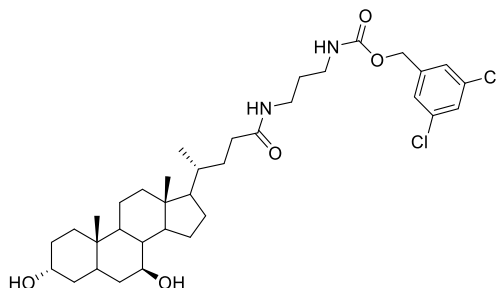
ν_{max} (neat): 3296, 2931, 2866, 1654, 1574, 1434 cm^{-1} .

^1H NMR (CDCl_3 , 400 MHz): δ 7.28–7.25 (m, 1H), 7.15 (d, $J = 1.9$ Hz, 2H), 5.80 (s, 1H), 4.39 (d, $J = 6.1$ Hz, 2H), 3.64–3.54 (m, 2H), 2.35–2.25 (m, 1H), 2.18–2.09 (m, 1H), 1.99 (dt, $J = 3.0, 12.4$ Hz, 1H), 1.94–1.85 (m, 1H), 1.85–1.74 (m, 3H), 1.70–1.63 (m, 2H), 1.62–1.55 (m, 3H), 1.53–1.39 (m, 6H), 1.38–1.20 (m, 6H), 1.17–0.97 (m, 3H), 0.96–0.91 (m, 6H), 0.67 (s, 3H).

^{13}C NMR (CDCl_3 , 101 MHz): δ 173.6, 142.1, 135.4, 127.8, 126.2, 71.6, 71.5, 55.9, 55.1, 43.9, 42.7, 42.6, 40.3, 39.3, 37.5, 37.0, 35.5, 35.1, 34.2, 33.7, 31.9, 30.5, 28.8, 27.0, 23.5, 21.3, 18.6, 12.3. 1 \times C not observed.

HRMS: exact mass calculated for $[\text{M}+\text{Na}]^+$ ($\text{C}_{31}\text{H}_{45}\text{Cl}_2\text{NNaO}_3$) requires 572.2669 m/z , found 572.2650 m/z .

3,5-dichlorobenzyl (3-((4*R*)-4-((3*R*,7*S*,10*S*,13*R*)-3,7-dihydroxy-10,13-dimethylhexadecahydro-1*H*-cyclopenta[*a*]phenanthren-17-yl)pentanamido)propyl)carbamate, **3.27**.



Prepared according to General Procedure **E** with ursodeoxycholic acid (156 mg, 0.39 mmol, 1.1 equiv), DIPEA (314 μ L, 1.8 mmol, 4.0 equiv), HATU (151 mg, 0.39 mmol, 1.1 equiv), 3,5-dichlorobenzyl (3-aminopropyl)carbamate (100 mg, 0.36 mmol, 1.0 equiv) and DMF (1 mL). The crude material was subjected to the purification outlined in the General Procedure (silica gel, 0–10% MeOH in CH_2Cl_2) to afford the desired product as a clear solid (39 mg, 16 %).

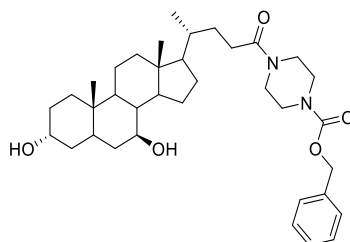
ν_{max} (neat): 3813, 2933, 2866, 1708, 1654, 1574, 1542 cm^{-1} .

^1H NMR (CDCl_3 , 400 MHz): δ 7.31–7.28 (m, 1H), 7.25–7.21 (m, 2H), 5.92 (s, 1H), 5.33 (s, 1H), 5.03 (s, 2H), 3.62–3.55 (m, 2H), 3.51–3.46 (m, 2H), 3.35–3.31 (m, 2H), 3.26–3.18 (m, 2H), 2.29–2.20 (m, 1H), 2.16–2.04 (m, 1H), 2.03–1.96 (m, 1H), 1.95–1.86 (m, 1H), 1.84–1.74 (m, 4H), 1.71–1.55 (m, 7H), 1.53–1.39 (m, 6H), 1.37–1.21 (m, 4H), 1.14 (td, $J = 3.1, 12.6$ Hz, 1H), 1.10–0.98 (m, 2H), 0.97–0.90 (m, 6H), 0.67 (s, 3H).

^{13}C NMR (CDCl_3 , 101 MHz): δ 174.4, 156.6, 140.3, 135.2, 128.2, 126.1, 71.6, 71.5, 65.1, 55.9, 55.1, 43.9, 42.6, 40.3, 39.3, 37.7, 37.5, 37.0, 36.0, 35.6, 35.1, 34.2, 33.8, 32.0, 30.5, 30.2, 28.8, 27.0, 23.5, 21.3, 18.6, 12.3. $1 \times \text{C}$ not observed.

HRMS: exact mass calculated for $[\text{M}+\text{Na}]^+$ ($\text{C}_{35}\text{H}_{52}\text{Cl}_2\text{N}_2\text{NaO}_5$) requires 673.3145 m/z , found 673.3113 m/z .

Benzyl-4-((4R)-4-((3R,7S,10S,13R)-3,7-dihydroxy-10,13-dimethylhexadecahydro-1H-cyclopenta[*a*]phenanthren-17-yl)pentanoyl)piperazine-1-carboxylate, 3.28.



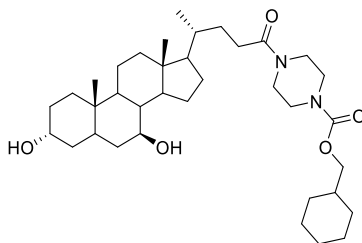
Prepared according to General Procedure **E** with ursodeoxycholic acid (500 mg, 1.27 mmol, 1.1 equiv), DIPEA (450 μ L, 2.57 mmol, 2.0 equiv), HATU (243 mg, 1.27 mmol, 1.1 equiv), benzylpiperazine-1-carboxylate (223 μ L, 1.16 mmol, 1.0 equiv) and DMF (5 mL). The crude material was subjected to the purification outlined in the General Procedure (silica gel, 0–10% MeOH in CH_2Cl_2) to afford the desired product as a clear solid (258 mg, 37%).

ν_{max} (neat): 3374, 2929, 2866, 1702, 1630 cm^{-1} .

^1H NMR (CDCl_3 , 500 MHz): δ 7.39–7.30 (m, 5H), 5.15 (s, 2H), 3.63–3.54 (m, 4H), 3.56–3.40 (m, 7H), 2.41–2.33 (m, 1H), 2.26–2.17 (m, 1H), 1.99 (d, $J = 12.5$ Hz, 1H), 1.95–1.85 (m, 1H), 1.84–1.73 (m, 4H), 1.71–1.63 (m, 3H), 1.62–1.55 (m, 2H), 1.52–1.39 (m, 6H), 1.39–1.21 (m, 5H), 1.19–0.97 (m, 3H), 0.97–0.91 (m, 6H), 0.67 (s, 3H).

^{13}C NMR (CDCl_3 , 101 MHz): δ 172.4, 155.3, 136.5, 128.7, 128.4, 128.2, 71.6, 71.5, 67.6, 55.9, 55.1, 45.5, 43.9, 42.6, 41.4, 40.3, 39.3, 37.4, 37.0, 35.6, 35.1, 34.2, 31.5, 30.5, 28.8, 27.0, 23.5, 21.3, 18.8, 12.3. $2 \times$ aliphatic C not observed.

HRMS: exact mass calculated for $[\text{M}+\text{Na}]^+$ ($\text{C}_{36}\text{H}_{54}\text{N}_2\text{NaO}_5$) requires 617.3925 m/z , found 617.3915 m/z .

Cyclohexylmethyl**4-((4*R*)-4-((3*R*,7*S*,10*S*,13*R*)-3,7-dihydroxy-10,13-dimethylhexadecahydro-1*H*-cyclopenta[*a*]phenanthren-17-yl)pentanoyl)piperazine-1-carboxylate, 3.29.**

Prepared according to procedure **E** with UDCA (380 mg, 0.97 mmol, 1.1 equiv), DMF (5 mL), DIPEA (766 μ L, 4.4 mmol, 5.0 equiv) and then HATU (369 mg, 0.97 mmol, 1.1 equiv). After stirring at room temperature for 15 mins cyclohexylmethyl piperazine-1-carboxylate (200 mg, 0.88 mmol, 1.0 equiv) was added and stirred for 16 hr at room temperature. The reaction mixture was diluted with H₂O (50 mL) and the resulting white precipitate filtered under vacuum. The crude material was purified by weak anion exchange (aminopropyl functionalised silica, MeOH) followed by strong cation exchange (propylsulfonic acid functionalised silica, MeOH) to yield the desired product as a white solid (126 mg, 71%).

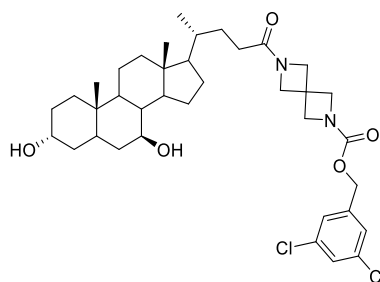
ν_{\max} (neat): 3448, 2929, 2856, 1697, 1635, 1429 cm^{-1} .

¹H NMR (CDCl₃, 400 MHz): δ 3.91 (d, J = 6.5 Hz, 2H), 3.63–3.54 (m, 4H), 3.52–3.41 (m, 7H), 2.43–2.33 (m, 1H), 2.28–2.18 (m, 1H), 2.04–1.96 (m, 1H), 1.95–1.85 (m, 1H), 1.85–1.76 (m, 3H), 1.75–1.71 (m, 3H), 1.68–1.63 (m, 3H), 1.61–1.54 (m, 4H), 1.50–1.40 (m, 6H), 1.37–1.21 (m, 7H), 1.17–1.00 (m, 5H), 0.97–0.91 (m, 7H), 0.67 (s, 3H).

¹³C NMR (CDCl₃, 101 MHz): δ 171.8, 155.1, 70.9, 70.8, 70.4, 55.2, 54.5, 44.9, 43.3, 43.1, 41.9, 40.8, 39.6, 38.7, 36.9, 36.8, 36.4, 35.0, 34.4, 33.6, 30.9, 29.8, 29.2, 28.2, 27.9, 26.4, 25.9, 25.2, 22.9, 20.7, 18.1, 11.7.

HRMS: exact mass calculated for [M+Na]⁺ (C₃₆H₆₀N₂NaO₅) requires 623.4394 m/z , found 623.4372 m/z .

3,5-dichlorobenzyl **6-((4R)-4-((3R,7S,10S,13R)-3,7-dihydroxy-10,13-dimethylhexadecahydro-1H-cyclopenta[*a*]phenanthren-17-yl)pentanoyl)-2,6-diazaspiro[3.3]heptane-2-carboxylate, 3.30.**



Prepared according to procedure **E** with UDCA (100 mg, 0.26 mmol, 1.0 equiv), DMF (1 mL), DIPEA (223 μ L, 1.28 mmol, 5.0 equiv) and then HATU (107 mg, 0.28 mmol, 1.1 equiv). After stirring at room temperature for 15 mins 3,5-dichlorobenzyl 2,6-diazaspiro[3.3]heptane-2-carboxylate trifluoroacetic acid salt (106 mg, 0.26 mmol, 1.0 equiv) was added and stirred for 16 h at room temperature. The reaction mixture was diluted with H₂O (20 mL) and the resulting white precipitate filtered under vacuum. The crude material was subjected to the purification outlined in the General Procedure (silica gel, 0–10% MeOH in CH₂Cl₂) to afford the desired product as a clear solid (107 mg, 62%).

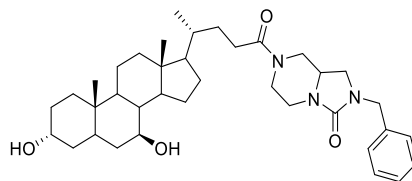
ν_{max} (neat): 3407, 2933, 2869, 1712, 1633 cm^{-1} .

¹H NMR (CDCl₃, 400 MHz): δ 7.31–7.29 (m, 1H), 7.22–7.19 (m, 2H), 5.02 (s, 2H), 4.24 (s, 2H), 4.16 (s, 4H), 4.11 (s, 2H), 3.64–3.52 (m, 2H), 2.15–2.04 (m, 1H), 2.03–1.94 (m, 1H), 1.86–1.72 (m, 4H), 1.72–1.64 (m, 4H), 1.62–1.55 (m, 3H), 1.51–1.40 (m, 6H), 1.36–1.20 (m, 5H), 1.17–1.09 (m, 1H), 1.07–0.98 (m, 2H), 0.96–0.88 (m, 6H), 0.67 (s, 3H).

¹³C NMR (CDCl₃, 101 MHz): δ 173.2, 154.9, 139.2, 134.6, 127.8, 125.7, 70.9, 70.8, 64.7, 59.8, 59.2, 27.4, 55.2, 54.4, 43.3, 41.9, 39.7, 38.7, 36.8, 36.4, 34.9, 34.4, 33.6, 32.1, 30.3, 29.8, 28.1, 27.9, 26.4, 22.9, 20.7, 18.0, 11.7.

HRMS: exact mass calculated for [M+H]⁺ (C₃₇H₅₃Cl₂N₂O₅) requires 675.3326 m/z , found 675.3323 m/z .

2-benzyl-7-((4*R*)-4-((3*R*,7*S*,10*S*,13*R*)-3,7-dihydroxy-10,13-dimethylhexadecahydro-1*H*-cyclopenta[*a*]phenanthren-17-yl)pentanoyl)hexahydroimidazo[1,5-*a*]pyrazin-3(2*H*)-one, 3.32.



Prepared according to procedure **E** with UDCA (136 mg, 0.35 mmol, 1.1 equiv), DMF (1 mL), DIPEA (224 μ L, 1.02 mmol, 4.0 equiv) and then HATU (97 mg, 0.26 mmol, 1.1 equiv). After stirring at room temperature for 15 mins 3,5-2-benzylhexahydroimidazo[1,5-*a*]pyrazin-3(2*H*)-one (73 mg, 0.32 mmol, 1.0 equiv) was added and stirred for 16 h at room temperature. The reaction mixture was diluted with H₂O (20 mL) and the resulting white precipitate filtered under vacuum. The crude material was subjected to the purification outlined in the General Procedure (silica gel, 0–10% MeOH in CH₂Cl₂) to afford the desired product as a clear solid as a mixture of rotamers at room temperature (84 mg, 43%).

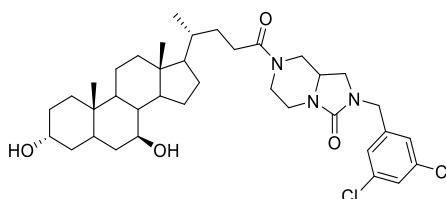
ν_{\max} (neat): 3407, 2929, 2964, 1685, 1637, 1465, 1430 cm⁻¹.

¹H NMR (CDCl₃, 400 MHz, 323K): δ 7.34–7.19 (m, 5H), 4.59 (s, 1H), 4.39 (s, 2H), 3.95 (d, J = 11.9 Hz, 1H), 3.85–3.65 (m, 1H), 3.65–3.50 (m, 3H), 3.31 (t, J = 8.7 Hz, 1H), 3.21–3.01 (m, 1H), 3.00–2.88 (m, 1H), 2.88–2.81 (m, 1H), 2.45–2.32 (m, 1H), 2.30–2.18 (m, 1H), 2.03–1.96 (m, 1H), 1.91–1.76 (m, 5H), 1.70–1.56 (m, 5H), 1.52–1.39 (m, 6H), 1.38–1.23 (m, 5H), 1.16–1.03 (m, 3H), 0.95 (m, 6H), 0.68 (s, 3H).

¹³C NMR (CDCl₃, 101 MHz): δ 172.6, 172.2, 159.3, 159.1, 136.8, 128.8, 128.2, 127.7, 71.4, 55.8, 55.0, 53.6, 51.4, 50.8, 49.5, 48.0, 45.7, 45.5, 45.2, 43.9, 42.5, 41.4, 41.2, 40.7, 40.2, 39.3, 37.4, 37.0, 35.6, 35.0, 34.2, 31.5, 30.5, 30.4, 28.8, 27.0, 23.5, 21.3, 18.7, 12.3.

HRMS: exact mass calculated for [M+Na]⁺ (C₃₇H₅₅N₃NaO₄) requires 628.4085 m/z , found 628.4063 m/z .

2-(3,5-dichlorobenzyl)-7-((4R)-4-((3R,7S,10S,13R)-3,7-dihydroxy-10,13-dimethylhexadecahydro-1H-cyclopenta[*a*]phenanthren-17-yl)pentanoyl)hexahydroimidazo[1,5-*a*]pyrazin-3(2H)-one, 3.33.



Prepared according to General Procedure **E** with ursodeoxycholic acid (120 mg, 0.31 mmol, 1.1 equiv), DIPEA (244 μ L, 1.50 mmol, 5.0 equiv), HATU (117 mg, 0.31 mmol, 1.1 equiv), 2-(3,5-dichlorobenzyl)hexahydroimidazo[1,5-*a*]pyrazin-3(2H)-one (73 mg, 0.32 mmol, 1.0 equiv) and DMF (2 mL). The crude material was subjected to the purification outlined in the General Procedure (silica gel, 0–10% MeOH in CH_2Cl_2) to afford the desired product as a clear solid (80 mg, 36%).

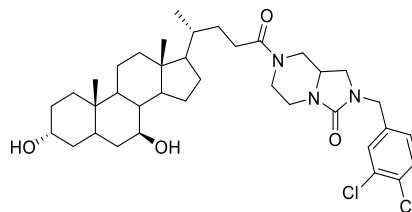
ν_{max} (neat): 3404, 2931, 2864, 1691, 1635, 1429 cm^{-1} .

^1H NMR (CDCl_3 , 400 MHz, 323 K): δ 7.30–7.27 (m, 1H), 7.16–7.12 (m, 2H), 4.72–4.57 (m, 1H), 4.38 (d, $J = 15.4$ Hz, 1H), 4.29 (d, $J = 15.5$ Hz, 1H), 3.95 (d, $J = 12.1$ Hz, 1H), 3.84–3.71 (m, 1H), 3.64–.53 (m, 3H), 3.35 (t, $J = 8.6$ Hz, 1H), 3.20–3.04 (m, 1H), 3.01–2.84 (m, 2H), 2.43–2.32 (m, 1H), 2.32–2.19 (m, 1H), 2.00 (d, $J = 12.5$ Hz, 1H), 1.95–1.75 (m, 5H), 1.71–1.65 (m, 2H), 1.63–1.56 (m, 2H), 1.56–1.40 (m, 8H), 1.38–1.02 (m, 8H), 1.00–0.92 (m, 6H), 0.67 (s, 3H).

^{13}C NMR (CDCl_3 , 101 MHz): δ 172.6, 159.0, 140.5, 135.5, 128.0, 126.5, 71.51, 71.46, 60.5, 55.8, 55.1, 50.8, 47.3, 46.0, 45.5, 45.3, 43.9, 42.5, 41.2, 40.3, 39.3, 37.4, 37.0, 35.6, 35.0, 34.2, 31.5, 30.5, 30.4, 28.8, 27.0, 23.5, 21.3, 18.8, 12.3.

HRMS: exact mass calculated for $[\text{M}+\text{Na}]^+$ ($\text{C}_{37}\text{H}_{53}\text{Cl}_2\text{N}_3\text{NaO}_4$) requires 696.3305 m/z , found 696.3289 m/z .

2-(3,4-dichlorobenzyl)-7-((4*R*)-4-((3*R*,7*S*,10*S*,13*R*)-3,7-dihydroxy-10,13-dimethylhexadecahydro-1*H*-cyclopenta[*a*]phenanthren-17-yl)pentanoyl)hexahydroimidazo[1,5-*a*]pyrazin-3(2*H*)-one, 3.34.



Prepared according to procedure **E** with UDCA (115 mg, 0.29 mmol, 1.1 equiv), DMF (2 mL), DIPEA (236 μ L, 1.35 mmol, 5.0 equiv) and then HATU (110 mg, 0.29 mmol, 1.1 equiv). After stirring at room temperature for 15 mins 2-(3,4-dichlorobenzyl)hexahydroimidazo[1,5-*a*]pyrazin-3(2*H*)-one (80 mg, 0.27 mmol, 1.0 equiv) was added and stirred for 16 h at room temperature. The reaction mixture was diluted with H₂O (20 mL) and the resulting white precipitate filtered under vacuum. The crude material was subjected to the purification outlined in the General Procedure (silica gel, 0–10% MeOH in CH₂Cl₂) to afford the desired product as a clear solid (53mg, 29%).

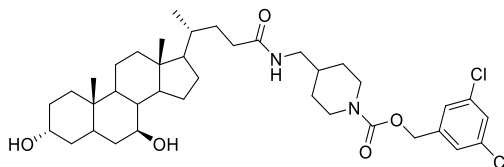
ν_{\max} (neat): 3406, 2929, 2864, 1691, 1635 cm^{-1} .

¹H NMR (CDCl₃, 400 MHz, 323 K): δ 7.41 (d, J = 8.2 Hz, 1H), 7.35 (d, J = 2.0 Hz, 1H), 7.10(dd, J = 1.8, 8.2 Hz, 1H), 4.64–4.62 (m, 1H), 4.42–4.27 (m, 2H), 3.99–3.89 (m, 1H), 3.85–3.66 (m, 1H), 3.65–3.51 (m, 3H), 3.34 (t, J = 8.7 Hz, 1H), 2.96–2.82 (m, 2H), 2.47–2.31 (m, 1H), 2.32–2.17 (m, 1H), 2.06–1.97 (m, 1H), 1.94–1.74 (m, 5H), 1.70–1.57 (m, 4H), 1.49–1.41 (m, 6H), 1.37–1.21 (m, 7H), 1.19–1.03 (m, 3H), 0.99–0.92 (m, 6H), 0.69 (s, 3H).

¹³C NMR (CDCl₃, 101 MHz): δ 172.0, 171.6, 157.4, 158.3, 136.7, 132.2, 131.2, 130.2, 129.4, 126.9, 70.82, 70.78, 59.9, 55.3, 54.5, 52.9, 50.8, 50.2, 48.9, 46.5, 45.3, 45.1, 44.8, 44.7, 43.3, 41.9, 40.8, 40.6, 40.1, 39.6, 36.8, 36.5, 35.0, 34.4, 33.6, 30.93, 30.87, 29.9, 29.8, 28.2, 26.4, 22.9, 20.7, 18.1, 13.7, 11.7.

HRMS: exact mass calculated for [M+Na]⁺ (C₃₇H₅₃Cl₂N₃NaO₄) requires 696.3305 m/z , found 696.3296 m/z .

3,5-dichlorobenzyl-4-(((4*R*)-4-((3*R*,7*S*,10*S*,13*R*)-3,7-dihydroxy-10,13-dimethylhexadecahydro-1*H*-cyclopenta[*a*]phenanthren-17-yl)pentanamido)methyl)piperidine-1-carboxylate, 3.35.



Prepared according to General Procedure **E** with ursodeoxycholic acid (136 mg, 0.35 mmol, 1.1 equiv), DIPEA (223 μ L, 1.28 mmol, 4.0 equiv), HATU (133 mg, 0.35 mmol, 1.1 equiv), 3,5-dichlorobenzyl 4-(aminomethyl)piperidine-1-carboxylate (100 mg, 0.32 mmol, 1.0 equiv) and DMF (2 mL). The crude material was subjected to the purification outlined in the General Procedure (silica gel, 0–10% MeOH in CH_2Cl_2) to afford the desired product as a clear solid (80 mg, 36 %).

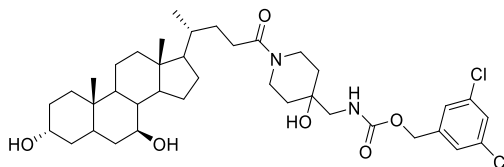
ν_{max} (neat): 3323, 2931, 2866, 1691, 1654 cm^{-1} .

^1H NMR (CDCl_3 , 400 MHz): δ 7.31–7.29 (m, 1H), 7.23–7.20 (m, 2H), 5.52 (s, 1H), 5.05 (s, 2H), 4.27–4.09 (m, 2H), 3.65–3.53 (m, 2H), 3.26–3.08 (m, 2H), 2.89–2.79 (m, 2H), 2.30–2.21 (m, 1H), 2.14–2.03 (m, 1H), 2.02–1.96 (m, 1H), 1.95–1.86 (m, 1H), 1.85–1.75 (m, 3H), 1.74–1.63 (m, 4H), 1.63–1.55 (m, 4H), 1.55–1.39 (m, 6H), 1.38–1.12 (m, 7H), 1.10–0.98 (m, 2H), 0.97–0.90 (m, 6H), 0.67 (s, 3H).

^{13}C NMR (CDCl_3 , 101 MHz): δ 173.8, 154.8, 140.4, 135.2, 128.2, 126.2, 71.6, 71.5, 65.6, 55.9, 55.1, 44.9, 44.0, 43.9, 42.6, 40.3, 39.3, 37.5, 37.0, 36.3, 35.5, 35.1, 34.2, 33.8, 32.0, 30.5, 29.8, 28.8, 27.0, 23.5, 21.3, 28.6, 12.3. $1 \times \text{C}$ not observed.

HRMS: exact mass calculated for $[\text{M}+\text{Na}]^+$ ($\text{C}_{38}\text{H}_{56}\text{Cl}_2\text{N}_2\text{NaO}_5$) requires 713.3458 m/z , found 713.3425 m/z .

3,5-dichlorobenzyl-4-(((4R)-4-((3R,7S,10S,13R)-3,7-dihydroxy-10,13-dimethylhexadecahydro-1H-cyclopenta[*a*]phenanthren-17-yl)pentanamido)methyl)-4-hydroxypiperidine-1-carboxylate, 3.36.



Prepared according to General Procedure **E** with ursodeoxycholic acid (67 mg, 0.17 mmol, 1.1 equiv), DIPEA (131 μ L, 0.75 mmol, 5.0 equiv), HATU (65 mg, 0.17 mmol, 1.1 equiv), 3,5-dichlorobenzyl 4-(aminomethyl)-4-hydroxypiperidine-1-carboxylate (50 mg, 0.15 mmol, 1.0 equiv) and DMF (1 mL). The crude material was subjected to the purification outlined in the General Procedure (silica gel, 0–10% MeOH in CH_2Cl_2) to afford the desired product as a clear solid (5.1 mg, 3 %).

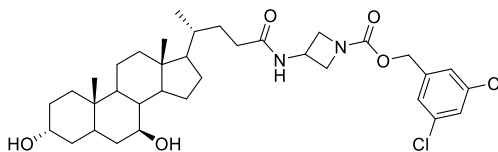
ν_{max} (neat): 3357, 2929, 2866, 1702, 1618, 1574 cm^{-1} .

^1H NMR (CDCl_3 , 400 MHz): δ 7.34–7.28 (m, 1H), 7.25 (d, $J = 1.7$ Hz, 2H), 5.28 (s, 1H), 5.05 (s, 2H), 4.26 (d, $J = 12.9$ Hz, 1H), 3.64–3.54 (m, 3H), 3.43 (t, $J = 11.4$ Hz, 1H), 3.34–3.25 (m, 1H), 3.22–3.15 (m, 1H), 3.11 (t, $J = 11.4$ Hz, 1H), 2.45–2.34 (m, 1H), 2.32–2.19 (m, 1H), 2.04–1.97 (m, 1H), 1.96–1.86 (m, 1H), 1.85–1.73 (m, 4H), 1.69–1.64 (m, 2H), 1.62–1.54 (m, 6H), 1.53–1.47 (m, 3H), 1.46–1.40 (m, 4H), 1.38–1.28 (m, 5H), 1.19–0.98 (m, 3H), 0.97–0.90 (m, 6H), 0.70 (s, 3H).

^{13}C NMR (CDCl_3 , 101 MHz): δ 172.2, 157.3, 139.8, 135.3, 128.4, 126.2, 71.6, 71.5, 70.4, 65.6, 55.9, 55.1, 51.4, 43.9, 42.6, 41.7, 40.3, 39.3, 37.5, 37.4, 37.0, 35.7, 35.5, 35.1, 34.8, 34.2, 31.7, 30.52, 30.48, 28.8, 27.1, 23.5, 21.3, 18.8, 12.3. Rotameric mixture observed.

HRMS: exact mass calculated for $[\text{M}+\text{Na}]^+$ ($\text{C}_{38}\text{H}_{56}\text{Cl}_2\text{N}_2\text{NaO}_6$) requires 729.3408 m/z , found 729.3372 m/z .

3,5-dichlorobenzyl-3-((4R)-4-((3R,7S,10S,13R)-3,7-dihydroxy-10,13-dimethylhexadecahydro-1H-cyclopenta[*a*]phenanthren-17-yl)pentanamido)azetidine-1-carboxylate, 3.37.



Prepared according to General Procedure **E** with ursodeoxycholic acid (157 mg, 0.40 mmol, 1.1 equiv), DIPEA (314 μ L, 1.8 mmol, 4.0 equiv), HATU (152 mg, 0.40 mmol, 1.1 equiv), 3,5-dichlorobenzyl 3-aminoazetidine-1-carboxylate (100 mg, 0.36 mmol, 1.0 equiv) and DMF (1 mL). The crude material was subjected to the purification outlined in the General Procedure (silica gel, 0–10% MeOH in CH_2Cl_2) to afford the desired product as a clear solid (108 mg, 46 %).

ν_{max} (neat): 3400, 2933, 2865, 1699, 1654, 1574, 1419 cm^{-1} .

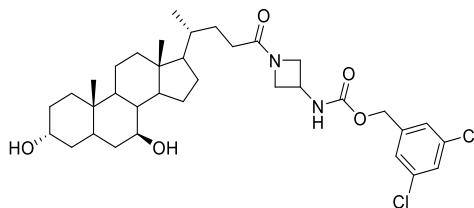
^1H NMR (CDCl_3 , 500 MHz): δ 7.30–7.27 (m, 1H), 7.21–7.17 (m, 2H), 6.51 (br. s, 1H), 5.00 (s, 2H), 4.69–4.62 (m, 1H), 4.35–4.28 (m, 2H), 3.83 (dd, $J = 5.2, 9.3$ Hz, 2H), 3.60–3.51 (m, 2H), 2.31–2.19 (m, 1H), 2.12–2.02 (m, 1H), 2.02–1.94 (m, 1H), 1.93–1.84 (m, 3H), 1.82–1.72 (m, 4H), 1.69–1.62 (m, 2H), 1.61–1.54 (m, 2H), 1.50–1.45 (m, 2H), 1.44–1.39 (m, 4H), 1.35–1.18 (m, 5H), 1.16–0.98 (m, 3H), 0.95–0.88 (m, 6H), 0.65 (s, 3H).

^{13}C NMR (CDCl_3 , 101 MHz): δ 173.8, 155.7, 140.0, 135.2, 128.3, 126.2, 71.43, 71.38, 65.2, 56.0, 55.1, 50.8, 43.9, 43.8, 42.6, 40.3, 39.9, 39.4, 37.5, 37.1, 35.6, 35.0, 34.2, 33.4, 31.8, 30.4, 28.8, 27.0, 23.5, 21.3, 18.6, 12.3.

HRMS: exact mass calculated for $[\text{M}+\text{Na}]^+$ ($\text{C}_{35}\text{H}_{50}\text{Cl}_2\text{N}_2\text{NaO}_5$) requires 671.2989 m/z , found 671.2957 m/z .

3,5-dichlorobenzyl

(1-((4*R*)-4-((3*R*,7*S*,10*S*,13*R*)-3,7-dihydroxy-10,13-dimethylhexadecahydro-1*H*-cyclopenta[*a*]phenanthren-17-yl)pentanoyl)azetidin-3-yl)carbamate, 3.38.



Prepared according to General Procedure **E** with ursodeoxycholic acid (157 mg, 0.40 mmol, 1.1 equiv), DIPEA (314 μ L, 1.8 mmol, 4.0 equiv), HATU (152 mg, 0.40 mmol, 1.1 equiv), 3,5-dichlorobenzyl azetidin-3-ylcarbamate (100 mg, 0.36 mmol, 1.0 equiv) and DMF (1 mL). The crude material was subjected to the purification outlined in the General Procedure (silica gel, 0–10% MeOH in CH_2Cl_2) to afford the desired product as a clear solid (140 mg, 60 %).

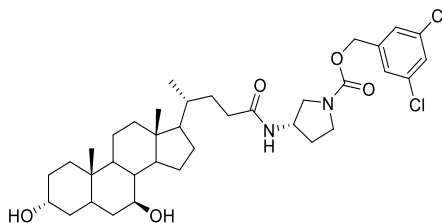
ν_{max} (neat): 3400, 2933, 2865, 1708, 1637, 1438, 1449 cm^{-1} .

^1H NMR (CDCl_3 , 400 MHz): δ 7.33–7.29 (m, 1H), 7.23–7.19 (m, 2H), 5.63 (br. s, 1H), 5.04 (s, 2H), 4.55–4.46 (m, 1H), 4.41 (t, $J = 8.0$ Hz, 1H), 4.29 (t, $J = 9.1$ Hz, 1H), 3.97 (dd, $J = 5.1, 8.5$ Hz, 1H), 3.83 (dd, $J = 5.2, 10.3$ Hz, 1H), 3.64–3.52 (m, 2H), 2.16–2.04 (m, 1H), 2.03–1.95 (m, 2H), 1.92–1.84 (m, 1H), 1.83–1.74 (m, 4H), 1.73–1.70 (m, 2H), 1.69–1.63 (m, 2H), 1.62–1.54 (m, 2H), 1.53–1.38 (m, 5H), 1.34–1.20 (m, 5H), 1.16–0.99 (m, 3H), 0.96–0.88 (m, 6H), 0.66 (s, 3H).

^{13}C NMR (CDCl_3 , 101 MHz): δ 174.1, 169.1, 139.7, 135.3, 128.5, 126.3, 71.6, 71.5, 65.4, 58.1, 55.9, 55.1, 54.9, 51.0, 43.9, 42.6, 40.9, 40.3, 39.3, 37.5, 37.0, 35.6, 35.1, 34.2, 31.0, 30.5, 28.8, 28.7, 27.0, 23.5, 21.3, 18.7, 12.3.

HRMS: exact mass calculated for $[\text{M}-\text{H}]^-$ ($\text{C}_{35}\text{H}_{49}\text{Cl}_2\text{N}_2\text{O}_5$) requires 647.3024 m/z , found 647.3021 m/z .

3,5-dichlorobenzyl ((3*S*)-3-((4*R*)-4-((3*R*,7*S*,10*S*,13*R*)-3,7-dihydroxy-10,13-dimethylhexadecahydro-1*H*-cyclopenta[*a*]phenanthren-17-yl)pentanamido)cyclopentyl)carbamate, 3.39.



Prepared according to General Procedure **E** with ursodeoxycholic acid (200 mg, 0.51 mmol, 1.1 equiv), DIPEA (330 μ L, 0.19 mmol, 4.0 equiv), HATU (194 mg, 0.51 mmol, 1.1 equiv), 3,5-dichlorobenzyl 3,5-dichlorobenzyl (*S*)-3-aminopyrrolidine-1-carboxylate (136 mg, 0.47 mmol, 1.0 equiv) and DMF (10 mL). The crude material was subjected to the purification outlined in the General Procedure (silica gel, 0–10% MeOH in CH_2Cl_2) to afford the desired product as a clear solid (54 mg, 17%).

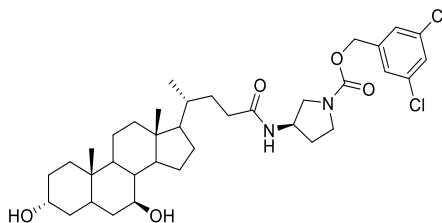
ν_{max} (neat): 3450, 3415, 3030, 3963, 2940, 2862, 1725, 1637 cm^{-1} .

^1H NMR (CDCl_3 , 400 MHz): δ 7.32–7.29 (m, 1H), 7.25–7.21 (m, 2H), 5.91 (s, 1H), 5.04 (s, 2H), 4.46 (m, 1H), 3.72–3.61 (m, 3H), 3.62–3.54 (m, 2H), 3.54–3.46 (m, 2H), 3.25 (t, $J = 12.1$ Hz, 1H), 2.25–2.12 (m, 2H), 2.10–2.01 (m, 1H), 2.02–1.96 (m, 1H), 1.83–1.73 (m, 5H), 1.69–1.62 (m, 2H), 1.60–1.53 (m, 2H), 1.50–1.37 (m, 5H), 1.25–1.18 (m, 8H), 1.14–0.97 (m, 3H), 0.96–0.86 (m, 6H), 0.65 (s, 3H).

^{13}C NMR (CDCl_3 , 101 MHz): δ 173.7, 154.5, 140.2, 135.2, 128.3, 126.2, 71.4, 65.4, 58.5, 55.9, 55.1, 51.7, 49.5, 48.7, 44.6, 44.2, 43.9, 42.6, 40.3, 39.4, 38.7, 37.4, 37.1, 35.5, 35.0, 34.2, 33.5, 32.0, 31.8, 30.9, 30.4, 28.8, 27.0, 23.5, 21.3, 18.6, 18.5, 12.2. Rotameric mixture observed.

HRMS: exact mass calculated for $[\text{M}+\text{Na}]^+$ ($\text{C}_{36}\text{H}_{52}\text{Cl}_2\text{N}_2\text{NaO}_5$) requires 685.3145 m/z , found 685.3129 m/z .

3,5-dichlorobenzyl ((3*R*)-3-((4*R*)-4-((3*R*,7*S*,10*S*,13*R*)-3,7-dihydroxy-10,13-dimethylhexadecahydro-1*H*-cyclopenta[*a*]phenanthren-17-yl)pentanamido)cyclopentyl)carbamate, 3.40.



Prepared according to General Procedure **E** with ursodeoxycholic acid (149 mg, 0.38 mmol, 1.1 equiv), DIPEA (306 μ L, 1.75 mmol, 5.0 equiv), HATU (145 mg, 0.38 mmol, 1.1 equiv), 3,5-dichlorobenzyl ((3*R*)-3-aminocyclopentyl)carbamate (100 mg, 0.35 mmol, 1.0 equiv) and DMF (10 mL). The crude material was subjected to the purification outlined in the General Procedure (silica gel, 0–10% MeOH in CH₂Cl₂) to afford the desired product as a clear solid (82 mg, 35%).

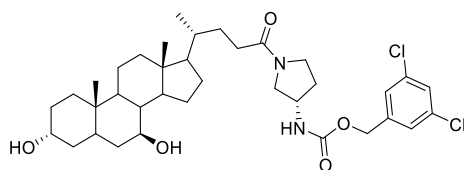
ν_{max} (neat): 3301, 2931, 2968, 1697, 1654, 1420 cm⁻¹.

¹H NMR (CDCl₃, 400 MHz): δ 7.29–7.26 (m, 1H), 7.22–7.18 (m, 2H), 5.03 (s, 2H), 4.50–4.41 (m, 1H), 3.72–3.60 (m, 1H), 3.60–3.42 (m, 4H), 3.30–3.20 (m, 1H), 2.25–2.12 (m, 2H), 2.08–2.01 (m, 1H), 1.99–1.93 (m, 1H), 1.89–1.71 (m, 6H), 1.68–1.61 (m, 2H), 1.58–1.53 (m, 2H), 1.49–1.38 (m, 6H), 1.31–1.19 (m, 5H), 1.14–0.97 (m, 3H), 0.96–0.87 (m, 6H), 0.63 (s, 3H). NH not observed.

¹³C NMR (CDCl₃, 101 MHz): δ 173.8, 154.4, 140.2, 135.1, 128.2, 126.2, 71.31, 71.26, 65.4, 56.0, 55.1, 51.6, 49.4, 48.6, 44.6, 44.2, 43.8, 43.7, 42.6, 40.3, 39.4, 37.4, 37.2, 35.5, 35.0, 34.1, 33.5, 31.9, 30.9, 30.4, 28.8, 27.0, 23.5, 21.3, 18.6, 12.2. Rotameric mixture observed.

HRMS: exact mass calculated for [M+NH₄]⁺ (C₃₆H₅₆Cl₂N₃O₅) requires 680.3592 *m/z*, found 380.3588 *m/z*.

3,5-dichlorobenzyl ((3*S*)-1-((4*R*)-4-((3*R*,7*S*,10*S*,13*R*)-3,7-dihydroxy-10,13-dimethylhexadecahydro-1*H*-cyclopenta[*a*]phenanthren-17-yl)pentanoyl)pyrrolidin-3-yl)carbamate, 3.41.



Prepared according to General Procedure **E** with ursodeoxycholic acid (200 mg, 0.51 mmol, 1.1 equiv), DIPEA (330 μ L, 0.19 mmol, 4.0 equiv), HATU (194 mg, 0.51 mmol, 1.1 equiv), 3,5-dichlorobenzyl 3,5-dichlorobenzyl (*S*)-pyrrolidin-3-ylcarbamate (136 mg, 0.47 mmol, 1.0 equiv) and DMF (10 mL). The crude material was subjected to the purification outlined in the General Procedure (silica gel, 0–10% MeOH in CH_2Cl_2) to afford the desired product as a clear solid (56 mg, 18%).

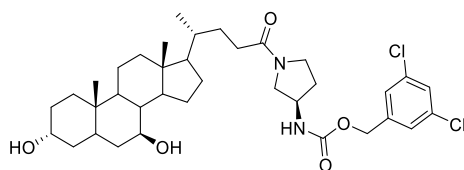
ν_{max} (neat): 3294, 2931, 2866, 1708, 1626, 1436 cm^{-1} .

^1H NMR (CDCl_3 , 500 MHz): δ 7.32–7.29 (m, 1H), 7.26–7.21 (m, 2H), 5.08–5.02 (m, 2H), 4.34–4.20 (m, 1H), 3.77–3.65 (m, 1H), 3.65–3.48 (m, 4H), 3.45–3.29 (m, 1H), 2.33–2.23 (m, 1H), 2.20–2.11 (m, 1H), 2.06–1.97 (m, 1H), 1.95–1.87 (m, 1H), 1.84–1.74 (m, 4H), 1.71–1.64 (m, 2H), 1.62–1.53 (m, 5H), 1.52–1.41 (m, 6H), 1.37–1.30 (m, 2H), 1.30–1.21 (m, 4H), 1.17–1.11 (m, 1H), 1.09–0.98 (m, 2H), 0.97–0.91 (m, 6H), 0.67 (d, $J = 2.0$ Hz, 3H).

^{13}C NMR (CDCl_3 , 101 MHz): δ 172.8, 172.7, 155.4, 139.8, 139.7, 135.3, 128.5, 126.3, 71.6, 71.5, 65.3, 55.9, 55.1, 52.6, 51.5, 51.1, 50.0, 44.6, 43.9, 43.8, 42.6, 40.3, 39.3, 37.5, 37.0, 35.6, 35.1, 34.2, 32.5, 31.8, 31.4, 31.0, 30.5, 29.8, 28.8, 27.1, 23.5, 21.3, 18.8, 12.3. Rotameric mixture observed.

HRMS: exact mass calculated for $[\text{M}+\text{Na}]^+$ ($\text{C}_{36}\text{H}_{52}\text{Cl}_2\text{N}_2\text{NaO}_5$) requires 685.3145 m/z , found 685.3113 m/z .

3,5-dichlorobenzyl ((3R)-1-((4R)-4-((3R,7S,10S,13R)-3,7-dihydroxy-10,13-dimethylhexadecahydro-1H-cyclopenta[*a*]phenanthren-17-yl)pentanoyl)pyrrolidin-3-yl)carbamate, 3.42.



Prepared according to General Procedure **E** with ursodeoxycholic acid (149 mg, 0.38 mmol, 1.1 equiv), DIPEA (306 μ L, 1.75 mmol, 5.0 equiv), HATU (145 mg, 0.38 mmol, 1.1 equiv), 3,5-dichlorobenzyl (*R*)-pyrrolidin-3-ylcarbamate (100 mg, 0.35 mmol, 1.0 equiv) and DMF (10 mL). The crude material was subjected to the purification outlined in the General Procedure (silica gel, 0–10% MeOH in CH₂Cl₂) to afford the desired product as a clear solid (36 mg, 15%).

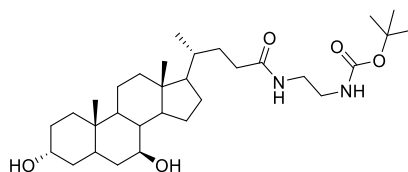
ν_{max} (neat): 3298, 2933, 2868, 1706, 1624, 1436 cm⁻¹.

¹H NMR (CDCl₃, 500 MHz): δ 7.33–7.30 (m, 1H), 7.24–7.21 (m, 2H), 5.07–5.02 (m, 2H), 5.02–4.97 (m, 1H), 4.36–4.21 (m, 1H), 3.78–3.65 (m, 1H), 3.62–3.50 (m, 4H), 3.45–3.31 (m, 1H), 2.33–2.22 (m, 1H), 2.22–2.09 (m, 1H), 2.04–1.97 (m, 1H), 1.93–1.86 (m, 1H), 1.85–1.75 (m, 4H), 1.71–1.63 (m, 2H), 1.63–1.55 (m, 4H), 1.53–1.47 (m, 2H), 1.47–1.41 (m, 4H), 1.39–1.18 (m, 6H), 1.17–0.98 (m, 3H), 0.97–0.90 (m, 6H), 0.67 (s, 3H). NH not observed.

¹³C NMR (CDCl₃, 101 MHz): δ 172.8, 172.7, 155.6, 155.5, 139.9, 139.8, 135.24, 135.20, 128.4, 128.3, 126.23, 126.20, 71.5, 71.4, 65.22, 65.15, 55.9, 55.1, 52.5, 51.5, 51.0, 50.8, 50.0, 44.7, 43.85, 43.82, 43.78, 42.6, 40.3, 39.3, 37.4, 37.1, 35.6, 35.5, 35.1, 34.2, 32.4, 31.8, 31.4, 31.0, 30.4, 28.82, 28.78, 27.0, 23.5, 21.3, 18.7, 12.3. Rotameric mixture observed.

HRMS: exact mass calculated for [M+H]⁺ (C₃₆H₅₃Cl₂N₂O₅) requires 663.3326 *m/z*, found 663.3323 *m/z*.

***Tert*-butyl (2-((4*R*)-4-((3*R*,7*S*,10*S*,13*R*)-3,7-dihydroxy-10,13-dimethylhexadecahydro-1*H*-cyclopenta[*a*]phenanthren-17-yl)pentanamido)ethyl)carbamate, 3.53.**



Prepared according to procedure **E** with ursodeoxycholic acid (1.00 g, 2.55 mmol, 1.1 equiv), DIPEA (1.62 mL, 9.24 mmol, 4.0 equiv), HATU (970 mg, 2.55 mmol, 1.1 equiv), *tert*-butyl (2-aminoethyl)carbamate (372 mg, 2.31 mmol, 1.0 equiv) and DMF (10 mL). The crude material was subjected to the purification outlined in the General Procedure (silica gel, 0–10% MeOH in CH₂Cl₂) to afford the desired product as a clear solid (108 mg, 46 %).

ν_{max} (neat): 3329, 2933, 2864, 1706, 1652, 1574 cm⁻¹.

¹H NMR (CDCl₃, 400 MHz): δ 6.25 (s, 1H), 4.96 (s, 1H), 3.65–3.53 (m, 2H), 3.40–3.28 (m, 2H), 3.40–3.28 (m, 2H), 3.29–3.22 (m, 2H), 2.31–2.15 (m, 1H), 2.12–2.03 (m, 1H), 2.03–1.96 (m, 1H), 1.94–1.84 (m, 1H), 1.84–1.74 (m, 4H), 1.74–1.63 (m, 5H), 1.62–1.54 (m, 2H), 1.46–1.40 (m, 11H), 1.38–1.21 (m, 5H), 1.17–0.99 (m, 3H), 0.94–0.90 (m, 6H), 0.67 (s, 3H).

¹³C NMR (CDCl₃, 101 MHz): δ 174.5, 157.2, 79.9, 71.6, 71.5, 55.9, 55.1, 43.9, 42.6, 41.0, 40.4, 40.3, 39.3, 37.5, 37.0, 35.6, 35.1, 34.2, 33.7, 31.9, 30.5, 28.8, 28.5, 27.0, 23.5, 21.3, 18.6, 12.3. 1 \times C not observed.

HRMS: exact mass calculated for [M+Na]⁺ (C₃₁H₅₄N₂NaO₅) requires 557.3925 *m/z*, found 557.3906 *m/z*.

References

- 1 H. Nishimasu, S. Okudaira, K. Hama, E. Mihara, N. Dohmae, A. Inoue, R. Ishitani, J. Takagi, J. Aoki and O. Nureki, *Nat. Struct. Mol. Biol.*, 2011, **18**, 205–12.
- 2 M. G. K. Benesch, Y. M. Ko, T. P. W. McMullen and D. N. Brindley, *FEBS Lett.*, 2014, **588**, 2712–2727.
- 3 Keune W-J, H. Jens, B. Ruth, T. Dagmar, K. Andreas, H. Tatjana, R. P. Joosten, S. Manjula, A. J. Morris, M.-R. Elisa, W. H. Moolenaar, R. P. Oude Elferink and A. Perrakis, *Nat. Commun.*, 2016, **7**, 1–7.
- 4 C. B. Nanthakumar, R. J. D. Hatley, S. Lemma, J. Gauldie, R. P. Marshall and S. J. F. Macdonald, *Nat. Rev. Drug Discov.*, 2015, **14**, 693–720.
- 5 T. E. King, A. Pardo and M. Selman, *Lancet*, 2011, **378**, 1949–61.
- 6 S. Moll, L. Chaykovska, M. Meier, D. C. Budd, I. Formentini, S. Pomposiello and M. Prunotto, *Drug Discov. Today*, 2013, **18**, 582–91.
- 7 A. Pardo and M. Selman, *Int. J. Biochem. Cell Biol.*, 2002, **34**, 1534–8.
- 8 M. Selman and A. Pardo, *Proc. Am. Thorac. Soc.*, 2006, **3**, 364–72.
- 9 A. Scriabine and D. U. Rabin, *Adv. Pharmacol.*, 2009, **57**, 419–64.
- 10 S. Moll, L. Chaykovska, M. Meier, D. C. Budd, I. Formentini, S. Pomposiello and M. Prunotto, *Drug Discov. Today*, 2013, **18**, 582–91.
- 11 M. Selman and A. Pardo, *Respir. Res.*, 2002, **3**, 3.
- 12 B. D. Uhal, *Eur. Respir. Rev.*, 2008, **17**, 138–144.
- 13 S. Fichtner-Feigl, W. Strober, K. Kawakami, R. K. Puri and A. Kitani, *Nat. Med.*, 2006, **12**, 99–106.
- 14 D. L. Clarke, A. M. Carruthers, T. Mustelin and L. A. Murray, *Fibrogenes. Tissue Repair*, 2013, **6**, 20.
- 15 N. Ahluwalia, B. S. Shea and A. M. Tager, *Am. J. Respir. Crit. Care Med.*, 2014, **190**, 867–878.
- 16 H. V Woodcock and T. M. Maher, *F1000 Prime Reports*, 2014, **6**, 16.
- 17 M. Mylla and R. Kaarteenaho, *Eur. Clin. Respir. J.*, 2015, **2**, 1–10.
- 18 T. R. Ramalingam, R. L. Gieseck, T. H. Acciani, K. M Hart, A. W. Cheever, M. M. Mentink-Kane, K. M. Vannella and T. A. Wynn, *J. Pathol.*, 2016, **239**, 344–354.
- 19 N. W. Todd, I. G. Luzina and S. P. Atamas, *Fibrogenesis Tissue Repair*, 2012, **5**, 11.
- 20 H. Loomis-King, K. R. Flaherty and B. B. Moore, *Curr. Opin. Pharmacol.*, 2013, **13**, 377–85.
- 21 C. P. Atkins, Y. K. Loke and A. M. Wilson, *Respir. Med.*, 2014, **108**, 376–87.
- 22 W. D. Hardie, T. R. Korfhagen, M. A. Sartor, A. Prestridge, M. Medvedovic, T. D. Le

- Cras, M. Ikegami, S. C. Wesselkamper, C. Davidson, M. Dietsch, W. Nichols, J. A. Whitsett and G. D. Leikauf, *Am. J. Respir. Cell Mol. Biol.*, 2007, **37**, 309–321.
- 23 T. Cheng, Q. Liu, R. Zhang, Y. Zhang, J. Chen, R. Yu and G. Ge, *J. Mol. Cell Biol.*, 2014, **6**, 506–515.
- 24 <http://www.gilead.com/news/press-releases/2016/1/g>, 17-09-16.
- 25 L. Fala, *Am. Heal. Drugs Benefits*, 2015, **8**, 101–104.
- 26 T. Lear and B. B. Chen, *Cytokine*, 2016, **88**, 193–195.
- 27 P. W. Noble, C. Albera, W. Z. Bradford, U. Costabel, M. K. Glassberg, D. Kardatzke, T. E. King, L. Lancaster, S. A. Sahn, J. Szwarcberg, D. Valeyre and R. M. du Bois, *Lancet*, 2011, **377**, 1760–9.
- 28 T. E. King, W. Z. Bradford, S. Castro-Bernardini, E. A. Fagan, I. Glaspole, M. K. Glassberg, E. Gorina, P. M. Hopkins, D. Kardatzke, L. Lancaster, D. J. Lederer, S. D. Nathan, C. A. Pereira, S. A. Sahn, R. Sussman, J. J. Swigris and P. W. Noble, *N. Engl. J. Med.*, 2014, **370**, 2083–92.
- 29 V. Cottin and T. Maher, *Eur. Respir. Rev.*, 2015, **24**, 58–64.
- 30 C. Pasquinelli, in *PPF Summit*, 2013.
- 31 S. Tabuchi, *Lipids Health Dis.*, 2015, **14**, 56.
- 32 E. M. van der Aar, L. Fagard, J. Desrivot, S. Dupont, B. Heckmann, R. Blaque, L. Gheylr, J. Ralic and F. Vanhoutte, in *ATS International conference*, 2016, p. A2701.
- 33 B. Heckmann, R. Blanqué, N. Desroy, S. Dupont, C. Cottereaux, A. Monjardet, E. Wakselman, N. T. D. Dirven, T. Christophe, B. Hrvacic, J. Ralic, F. Marsais, E. Van Der Aar and R. Brys, in *American Thoracic Society International Conference*, Galapagos, San Francisco, 2016, p. A4532.
- 34 M. Ongenaert, S. D. R. Blanqué, R. Brys, E. van der Aar and B. Heckmann, in *ERS*, Galapagos, London, 2016.
- 35 <https://clinicaltrials.gov/ct2/show/NCT0261205>. GlaxoSmithKline, *Clin. Trials.gov*, 8-10-2016.
- 36 L. A. van Meeteren and W. H. Moolenaar, *Prog. Lipid Res.*, 2007, **46**, 145–60.
- 37 K. Nakanaga, K. Hama and J. Aoki, *J. Biochem.*, 2010, **148**, 13–24.
- 38 X. Chu, X. Wei, S. Lu and P. He, *Int. J. Clin. Exp. Med.*, 2015, **8**, 17117–17122.
- 39 Z. Fulkerson, T. Wu, M. Sunkara, C. Vander Kooi, A. J. Morris and S. S. Smyth, *J. Biol. Chem.*, 2011, **286**, 34654–34663.
- 40 D. Sheppard, *Eur. Respir. Rev.*, 2008, **17**, 157–162.
- 41 J. Hausmann, S. Kamtekar, E. Christodoulou, J. E. Day, T. Wu, Z. Fulkerson, H. M. H. G. Albers, L. A. van Meeteren, A. J. S. Houben, L. van Zeijl, S. Jansen, M. Andries, T. Hall, L. E. Pegg, T. E. Benson, M. Kasiem, K. Harlos, C. W. Vander Kooi, S. S. Smyth, H. Ovaa, M. Bollen, A. J. Morris, W. H. Moolenaar and A. Perrakis, *Nat. Struct. Mol. Biol.*, 2011, **18**, 198–204.

- 42 K. M. Antoniou, G. a Margaritopoulos and N. M. Sifakas, *Eur. Respir. Rev.*, 2013, **22**, 281–91.
- 43 A. Moeller, K. Ask, D. Warburton, J. Gauldie and M. Kolb, *Int. J. Biochem. Cell Biol.*, 2008, **40**, 362–382.
- 44 M. Umezu-goto, Y. Kishi, A. Taira, K. Hama, N. Dohmae, K. Takio, T. Yamori, G. B. Mills, K. Inoue, J. Aoki and H. Arai, *J. Cell Biol.*, 1999, **158**, 227–233.
- 45 A. J. Stein, G. Bain, P. Prodanovich, A. M. Santini, J. Darlington, N. M. P. Stelzer, R. S. Sidhu, J. Schaub, L. Goulet, D. Lonergan, I. Calderon, J. F. Evans, J. H. Hutchinson, G. Bain and E. C. Real, *Mol. Pharmacol.*, 2015, **88**, 982–992.
- 46 J. Hausmann, W.-J. Keune, A. L. H. Ederveen, L. Van Zeijl, R. P. Joosten and A. Perrakis, *J. Struct. Biol.*, 2016, **195**, 199–206.
- 47 T. Clair, H. Y. Lee, L. a. Liotta and M. L. Stracke, *J. Biol. Chem.*, 1997, **272**, 996–1001.
- 48 Dassault Systèmes BIOVIA, 2016, Discovery Studio Modeling Environment.
- 49 J. Morita, K. Kano, K. Kato, H. Takita, H. Sakagami, Y. Yamamoto, E. Mihara, H. Ueda, T. Sato, H. Tokuyama, H. Arai, H. Asou, J. Takagi, R. Ishitani, H. Nishimasu, O. Nureki and J. Aoki, *Sci. Rep.*, 2016, **6**, 20995.
- 50 M. L. Stracke, H. C. Krutzsch, E. J. Unsworth, A. Arestad, V. Cioce, E. Schiffmann and L. A. Liotta, *J. Biol. Chem.*, 1992, **267**, 2524–9.
- 51 J. Fox, S. Peel, B. Liu, I. Sayers and I. Hall, in *British Pharmacological Society*, 2002, vol. 10, pp. 2002–2002.
- 52 L. Federico, K. J. Jeong, C. P. Vellano and G. B. Mills, *J. Lipid Res.*, 2015, **57**, 25–35.
- 53 R. Zent and A. Pozzi, in *Cell-Extracellular Matrix Interactions in Cancer*, Springer Science, 2010, pp. 1–314.
- 54 S. Johansson, G. Svineng, K. Wennerberg, A. Armulik and L. Lohikangas, *Front. Biosci.*, 1997, **11**, 126–146.
- 55 A. Tabchy, *Nat. Struct. Mol. Biol.*, 2013, **18**, 117–118.
- 56 K. Hama, J. Aoki, M. Fukaya, Y. Kishi, T. Sakai, R. Suzuki, H. Ohta, T. Yamori, M. Watanabe, J. Chun and H. Arai, *J. Biol. Chem.*, 2004, **279**, 17634–17639.
- 57 R. Leblanc and O. Peyruchaud, *Exp. Cell Res.*, 2015, **333**, 183–189.
- 58 X. Yang, B. Chen, T. Liu and X. Chen, *Eur. J. Pharmacol.*, 2014, **734**, 83–90.
- 59 Y. Sun, W. Zhang, J. F. Evans, A. Floreani, Z. Zou, Y. Nishio, R. Qi, P. S. C. Leung, C. L. Bowlus and M. E. Gershwin, *Autoimmun. Rev.*, 2016, **15**, 795–800.
- 60 A. J. S. Houben and W. H. Moolenaar, *Cancer Metastasis Rev.*, 2011, **30**, 557–65.
- 61 M. Umezu-Goto, J. Tanyi, J. Lahad, S. Liu, S. Yu, R. Lapushin, Y. Hasegawa, Y. Lu, R. Trost, T. Bevers, E. Jonasch, K. Aldape, J. Liu, R. D. James, C. G. Ferguson, Y. Xu, G. D. Prestwich and G. B. Mills, *J. Cell. Biochem.*, 2004, **92**, 1115–1140.

- 62 L. Nalysnyk, J. Cid-Ruzafa, P. Rotella and D. Esser, *Eur. Respir. Rev.*, 2012, **21**, 355–61.
- 63 B. Ley, H. R. Collard and T. E. King, *Am. J. Respir. Crit. Care Med.*, 2011, **183**, 431–40.
- 64 J. A. Bjoraker, J. H. Ryu, M. K. Edwin, J. L. Myers, H. D. Tazelaar, D. R. Schroeder and K. P. Offord, *Am. J. Respir. Crit. Care Med.*, 1998, **157**, 199–203.
- 65 National Institute for Health and Care Excellence, Ed., in *NICE technology appraisal guidance*, 2013, pp. 1–64.
- 66 J. Spond, N. Case, R. W. Chapman, Y. Crawley, R. W. Egan, J. Fine, J. A. Hey, W. Kreutner, T. Kung, P. Wang and M. Minnicozzi, *Pulmonary*, 2015, **16**, 207–214.
- 67 I. Sevastou, E. Kaffe, M.-A. Mouratis and V. Aidinis, *Biochim. Biophys. Acta*, 2013, **1831**, 42–60.
- 68 A. M. Tager, P. LaCamera, B. S. Shea, G. S. Campanella, M. Selman, Z. Zhao, V. Polosukhin, J. Wain, B. a Karimi-Shah, N. D. Kim, W. K. Hart, A. Pardo, T. S. Blackwell, Y. Xu, J. Chun and A. D. Luster, *Nat. Med.*, 2008, **14**, 45–54.
- 69 Y. Qian, M. Hamilton, A. Sidduri, S. Gabriel, Y. Ren, R. Peng, R. Kondru, A. Narayanan, T. Truitt, R. Hamid, Y. Chen, L. Zhang, A. J. Fretland, R. A. Sanchez, K.-C. Chang, M. Lucas, R. C. Schoenfeld, D. Laine, M. E. Fuentes, C. S. Stevenson and D. C. Budd, *J. Med. Chem.*, 2012, **55**, 7920–39.
- 70 K. E. Black, E. Berdyshev, G. Bain, F. V Castelino, B. S. Shea, C. K. Probst, B. A. Fontaine, I. Bronova, L. Goulet, D. Lagares, N. Ahluwalia, R. S. Knipe, V. Natarajan and A. M. Tager, *FASEB J.*, 2016, **30**, 2435–2450.
- 71 A. M. Tager, *Am. J. Respir. Cell Mol. Biol.*, 2012, **47**, 563–565.
- 72 R. Blanqué, N. Desroy, S. Dupont, C. Cottreaux, F. Marsais, L. Lepescheux, A. Monjardet, W. Laenen, V. Russell, E. Van Der Aar, R. Brys and B. Heckmann, in *European Respiratory Society Proceedings*, Galapagos, 2015.
- 73 P. L. McCormack, *Drugs*, 2015, **75**, 817–822.
- 74 N. Desroy, in *ERS International Congress*, Galapagos, Amsterdam, 2015.
- 75 H. Taniguchi, M. Ebina, Y. Kondoh, T. Ogura, a Azuma, M. Suga, Y. Taguchi, H. Takahashi, K. Nakata, a Sato, M. Takeuchi, G. Raghu, S. Kudoh and T. Nukiwa, *Eur. Respir. J.*, 2010, **35**, 821–9.
- 76 O. Hilberg, U. Simonsen, R. du Bois and E. Bendstrup, *Clin. Respir. J.*, 2012, **6**, 131–43.
- 77 K. J. Grattendick, J. M. Nakashima, L. Feng, S. N. Giri and S. B. Margolin, *Int. Immunopharmacol.*, 2008, **8**, 679–87.
- 78 H. V Woodcock, P. L. Molyneaux and T. M. Maher, *Drug Des. Devel. Ther.*, 2013, **7**, 503–10.
- 79 D. Bouros, *Lancet*, 2011, **377**, 1727–9.

- 80 S. Nakayama, H. Mukae, N. Sakamoto and T. Kakugawa, *Life Sci.*, 2008, **82**, 210–217.
- 81 V. Cottin, *Eur. Respir. Rev.*, 2013, **22**, 26–32.
- 82 F. Hilberg, G. J. Roth, M. Krssak, S. Kautschitsch, W. Sommergruber, U. Tontschgrunt, P. Garin-chesa, G. Bader, A. Zoephel, J. Quant, A. Heckel and W. J. Rettig, *Cancer Res.*, 2008, **12**, 4774–4782.
- 83 L. Richeldi, R. M. du Bois, G. Raghu, A. Azuma, K. K. Brown, U. Costabel, V. Cottin, K. R. Flaherty, D. M. Hansell, Y. Inoue, D. S. Kim, M. Kolb, A. G. Nicholson, P. W. Noble, M. Selman, H. Taniguchi, M. Brun, F. Le Maulf, M. Girard, S. Stowasser, R. Schlenker-Herceg, B. Disse and H. R. Collard, *N. Engl. J. Med.*, 2014, **370**, 2071–2082.
- 84 T. Corte, F. Bonella, B. Crestani, M. G. Demedts, L. Richeldi, C. Coeck, K. Pelling, M. Quaresma and J. A. Lasky, *Respir. Res.*, 2015, **16**, 116.
- 85 E. M. Van Der Aar, L. Fagard, J. Desrivot, S. Dupont, B. Heckmann, R. Blanqué, L. Gheyle, J. Ralic and F. Vanhoutte, in *ERS International Congress, Amsterdam, Galapagos, Amsterdam*, 2015.
- 86 A. Andersson-Sjöland, C. G. de Alba, K. Nihlberg, C. Becerril, R. Ramírez, A. Pardo, G. Westergren-Thorsson and M. Selman, *Int. J. Biochem. Cell Biol.*, 2008, **40**, 2129–2140.
- 87 S. Estany, V. Vicens-Zygmunt, R. Llatjós, A. Montes, R. Penín, I. Escobar, A. Xaubet, S. Santos, F. Manresa, J. Dorca and M. Molina-Molina, *BMC Pulm. Med.*, 2014, **14**, 120.
- 88 X. Zhang, H. Liu, T. Hock, V. J. Thannickal and Y. Y. Sanders, *Int. J. Mol. Sci.*, 2013, **14**, 19605–19617.
- 89 J. Blackburn and J. P. Mansell, *Nat. Rev. Cancer*, 2012, **50**, 756–762.
- 90 M. Gotoh, Y. Fujiwara, J. Yue, J. Liu, S. Lee, J. Fells, A. Uchiyama, K. Murakami-Murofushi, S. Kennel, J. Wall, R. Patil and R. G. L. B. D. D. M. G. J. Tigyi, *Biochem. Soc. Trans.*, 2013, **16**, 387–393.
- 91 M. G. K. Benesch, X. Tang, T. Maeda, A. Ohhata, Y. Y. Zhao, B. P. C. Kok, J. Dewald, M. Hitt, J. M. Curtis, T. P. W. McMullen and D. N. Brindley, *FASEB J.*, 2014, **28**, 2655–2666.
- 92 M. B. Colovic, D. Z. Krstic, T. D. Lazarevic-Pasti, A. M. Bondzic and V. M. Vasic, *Curr. Neuropharmacol.*, 2013, **11**, 315–335.
- 93 Z. Sobol, M. E. Engel, E. Rubitski, W. W. Ku, J. Aubrecht and R. H. Schiestl, *Mutat. Res. - Genet. Toxicol. Environ. Mutagen.*, 2007, **633**, 80–94.
- 94 S. R. Bhave, D. Y. a Dadey, R. M. Karvas, D. J. Ferraro, R. P. Kotipatruni, J. J. Jaboin, A. N. Hallahan, T. a Dewees, A. G. Linkous, D. E. Hallahan and D. Thotala, *Front. Oncol.*, 2013, **3**, 236.
- 95 K. Schiemann, M. Schultz, A. Blaukat, I. Kober, 2010/0222341 A1, *Merck KGA, 2010/0222341 A1*, 2010.
- 96 J. S. Munger, X. Huang, H. Kawakatsu, M. J. D. Griffiths, S. L. Dalton, J. Wu, J.-F.

- Pittet, N. Kaminski, C. Garat, M. A. Matthay, D. B. Rifkin and D. Sheppard, *Cell*, 2016, **96**, 319–328.
- 97 N. A. Anderson, I. B. Campbell, B. J. Fallon, S. M. Lynn, S. J. F. Macdonald, J. M. Pritchard, P. A. Procopiou, S. L. Sollis and L. R. Thorp, *Org. Biomol. Chem.*, 2016, **14**, 5992–6009.
- 98 T. Sato, K. Sugimoto, A. Inoue, S. Okudaira, J. Aoki and H. Tokuyama, *Bioorg. Med. Chem. Lett.*, 2012, **22**, 4323–6.
- 99 H. Ohta, K. Sato, N. Murata, A. Damirin, E. Malchinkhuu, J. Kon, T. Kimura, M. Tobo, Y. Yamazaki, T. Watanabe, M. Yagi, M. Sato, R. Suzuki, H. Murooka, T. Sakai, T. Nishitoba, D.-S. Im, H. Nochi, K. Tamoto, H. Tomura and F. Okajima, *Mol. Pharmacol.*, 2003, **64**, 994–1005.
- 100 J. S. Swaney, C. Chapman, L. D. Correa, K. J. Stebbins, a R. Broadhead, G. Bain, a M. Santini, J. Darlington, C. D. King, C. S. Baccei, C. Lee, T. a Parr, J. R. Roppe, T. J. Seiders, J. Ziff, P. Prasit, J. H. Hutchinson, J. F. Evans and D. S. Lorrain, *J. Pharmacol. Exp. Ther.*, 2011, **336**, 693–700.
- 101 H. M. H. G. Albers and H. Ovaa, *Chem. Rev.*, 2012, **112**, 2593–603.
- 102 M. Kawaguchi, T. Okabe, S. Okudaira, H. Nishimasu, R. Ishitani, H. Kojima, O. Nureki, J. Aoki and T. Nagano, *ACS Chem. Biol.*, 2013, **8**, 1713–1721.
- 103 A. B. Hoeglund, H. E. Bostic, A. L. Howard, I. W. Wanjala, M. D. Best, D. L. Baker and A. L. Parrill, *J. Med. Chem.*, 2010, **53**, 1056–66.
- 104 M. P. Gleeson, *J. Med. Chem.*, 2008, **51**, 817–34.
- 105 P. D. Leeson and B. Springthorpe, *Nat. Rev. Drug Discov.*, 2007, **6**, 881–90.
- 106 ChemAxon, 2013, JChem Excel.
- 107 M. C. Wenlock, R. P. Austin, P. Barton, A. M. Davis and P. D. Leeson, *J. Med. Chem.*, 2003, **46**, 1250–1256.
- 108 P. D. Leeson and R. J. Young, *ACS Med. Chem. Lett.*, 2015, **6**, 722–725.
- 109 G. F. Smith, in *Progress in Medicinal Chemistry*, 2011, vol. 50, pp. 1–47.
- 110 C. A. Lipinski, F. Lombardo, B. W. Dominy and P. J. Feeney, *Adv. Drug Deliv. Rev.*, 2001, **46**, 3–26.
- 111 A. L. Hopkins, G. M. Keserü, P. D. Leeson, D. C. Rees and C. H. Reynolds, *Nat. Rev. Drug Discov.*, 2014, **13**, 105–21.
- 112 P. N. Mortenson and C. W. Murray, *J. Comput. Aided. Mol. Des.*, 2011, **25**, 663–667.
- 113 H. van de Waterbeemd, D. A. Smith, K. Beaumont and D. K. Walker, *J. Med. Chem.*, 2001, **44**, 1313–1333.
- 114 R. J. Young, D. V. S. Green, C. N. Luscombe and A. P. Hill, *Drug Discov. Today*, 2011, **16**, 822–30.
- 115 D. F. Veber, S. R. Johnson, H. Cheng, B. R. Smith, K. W. Ward and K. D. Kopple, *J. Med. Chem.*, 2002, **45**, 2615–2623.

- 116 A. M. Tager, *Am. J. Respir. Cell Mol. Biol.*, 2012, **47**, 563–5.
- 117 L. A. van Meeteren, P. Ruurs, E. Christodoulou, J. W. Goding, H. Takakusa, K. Kikuchi, A. Perrakis, T. Nagano and W. H. Moolenaar, *J. Biol. Chem.*, 2005, **280**, 21155–61.
- 118 G. Jiang, D. Madan and G. D. Prestwich, *Bioorg. Med. Chem. Lett.*, 2015, **21**, 5098–5101.
- 119 D. D. Norman, A. Ibezim, W. E. Scott, S. White, A. L. Parrill and D. L. Baker, *Bioorg. Med. Chem.*, 2013, **21**, 5548–60.
- 120 H. M. H. G. Albers, L. A. van Meeteren, D. a Egan, E. W. van Tilburg, W. H. Moolenaar and H. Ovaa, *J. Med. Chem.*, 2010, **53**, 4958–67.
- 121 H. M. H. G. Albers, L. J. D. Hendrickx, R. J. P. van Tol, J. Hausmann, A. Perrakis and H. Ovaa, *J. Med. Chem.*, 2011, **54**, 4619–26.
- 122 S. B. Jones, L. A. Pfeifer, T. J. Bleisch, T. J. Beauchamp, J. D. Durbin, V. J. Klimkowski, N. E. Hughes, C. J. Rito, Y. Dao, J. M. Gruber, H. Bui, M. G. Chambers, S. Chandrasekhar, C. Lin, D. J. Mccann, D. R. Mudra, J. L. Oskins, C. A. Swearingen, K. Thirunavukkarasu and B. H. Norman, *ACS Med. Chem. Lett.*, 2016, **7**, 857–861.
- 123 J. Hert, D. Hunziker, P. Mattel, H. Mauser, G. Tang and L. Wang, *Hoffman-La Roche, WO2014139978A1*, 2014.
- 124 Y. D. Thomas James Beauchamp, S. B. Jones, B. H. Norman and L. A. Pfeifer, *Eli Lilly, US2014200231A1*, 2014.
- 125 W. Staehle, K. Schiemann, M. Schultz, US 2012/0015959 A1, *Merck*, 2012.
- 126 U. Baettig, D. Beattie, D. M. Legrand, A. S. Lister, J. McKenna, D. W. Pearce, A. D. Sandham, E. Stanley, O. R. Steward and C. Thomson, *Novartis, WO2015008229A1*, 2014.
- 127 U. B. David Beattie, D. M. Legrand, A. S. Lister, J. McKenna, D. W. Pearce, D. A. Sandham, O. R. Steward and C. Thomson, *Novartis, WO2015008230A1*, 2014.
- 128 K. Schiemann, M. Schultz, A. Blaukat and I. Kober, *Merck, US 8,791,111 B2*, 2014.
- 129 R. J. Roppe, A. T. Parr and H. J. Hutchinson, *Amira Pharm. WO 2012/166415*, 2012.
- 130 G. Jones, P. Willett, R. C. Glen, A. R. Leach and R. Taylor, *J. Mol. Biol.*, 1997, **26**, 727–748.
- 131 H. M. H. G. Albers, A. Dong, L. A. van Meeteren, D. a Egan, M. Sunkara, E. W. van Tilburg, K. Schuurman, O. van Tellingen, A. J. Morris, S. S. Smyth, W. H. Moolenaar and H. Ovaa, *Proc. Natl. Acad. Sci. U. S. A.*, 2010, **107**, 7257–7262.
- 132 H. Albers, *Development of ATX and DUSP inhibitors : inhibiting phosphate ester hydrolysis in biology*, 2012.
- 133 C. G. Ferguson, C. S. Bigman, R. D. Richardson, L. A. Van Meeteren, W. H. Moolenaar and G. D. Prestwich, *Org. Lett.*, 2006, **8**, 2023–2026.
- 134 Cayman Chemical, 2015, 10010706, Product Information PF–8380 Item No. 120.

- 135 J. Gierse, A. Thorarensen, K. Beltey, E. Bradshaw-pierce, L. Cortes-burgos, T. Hall, A. Johnston, M. Murphy, O. Nemirovskiy, S. Ogawa, L. Pegg, M. Pelc, M. Prinsen, M. Schnute, J. Wendling, S. Wene, R. Weinberg, A. Wittwer, B. Zweifel and J. Masferrer, 2010, **2**, 310–317.
- 136 P. Rezácová, D. Borek, S. F. Moy, A. Joachimiak and Z. Otwinowski, *Proteins*, 2008, **70**, 311–319.
- 137 M. M. Harding, *Acta Crystallogr. Sect. D Biol. Crystallogr.*, 2000, **56**, 857–867.
- 138 A. Krężel and W. Maret, *Arch. Biochem. Biophys.*, 2016, **16**, 30130–8.
- 139 S. Nakao, M. Mabuchi, T. Shimizu, Y. Itoh, Y. Takeuchi, M. Ueda, H. Mizuno, N. Shigi, I. Ohshio, K. Jinguji, Y. Ueda, M. Yamamoto, T. Furukawa, S. Aoki, K. Tsujikawa and A. Tanaka, *Bioorganic Med. Chem. Lett.*, 2014, **24**, 1071–1074.
- 140 P.-D. St-Cœur, D. Ferguson, P. Morin and M. Touaibia, *Arch. Pharm. (Weinheim)*, 2013, **346**, 91–7.
- 141 G. W. Forrest and H. W. Hamilton, *Warn. Company, US2004142933A1*, 2004.
- 142 L. Sun, N. Tran, C. Liang, F. Tang, A. Rice, R. Schreck, K. Waltz, L. K. Shawver, G. McMahon and C. Tang, *J. Med. Chem.*, 1999, **42**, 5120–5130.
- 143 M. E. Karimova, D. A. Dushamov, N. S. Mukhamedov, K. M. Academy, K. Region and K. Alimjan, *Chem. Heterocycl. Compd.*, 2011, **47**, 90–95.
- 144 S. K. Chellappan, R. E. Hormann and I. Shulman, *Intrexon Corp. US2014274954A1*, 2014.
- 145 Q. Zeng, J. Wang, Z. Cheng, K. Chen, P. Johnström, K. Varnäs, D. Y. Li, Z. F. Yang and X. Zhang, *J. Med. Chem.*, 2015, **58**, 8200–8215.
- 146 J. W. B. Fyfe, C. P. Seath and A. J. B. Watson, *Angew. Chemie Int. Ed.*, 2014, **53**, 12077–12080.
- 147 E. L. Duffy, *Approaches to Lead Generation for Idiopathic Pulmonary Fibrosis Targets*, PhD Thesis, The University of Strathclyde, 2016.
- 148 J. A. Jacobsen, J. L. Major Jourden, M. T. Miller and S. M. Cohen, *Biochim. Biophys. Acta - Mol. Cell Res.*, 2010, **1803**, 72–94.
- 149 J. M. Oldham and I. Noth, *Respir. Med.*, 2014.
- 150 J. Burkhard and E. M. Carreira, *Org. Lett.*, 2008, **10**, 3525–3526.
- 151 P. Di Giorgio, J. Hert, D. Hunziker, H. Kuehne, P. Mattei, M. Rudolph and G. Bernard, *Hoffman-La Roche, WO2015144605A1*, 2015.
- 152 J. Hert, D. M. Hunziker, P. Mattei, H. Mauser, G. Tang, L. Wang, *WO2014139978A1*, 2014.
- 153 J. Zhang, M. Zhu, Y. Lin and H. Zhou, *Sci. China Chem.*, 2013, **56**, 1372–1381.
- 154 C. T. Liu, J. W. Tomsho and S. J. Benkovic, *Bioorganic Med. Chem.*, 2014, **22**, 4462–4473.

- 155 Y. K. Zhang, J. J. Plattner, E. E. Easom, R. T. Jacobs, D. Guo, V. Sanders, Y. R. Freund, B. Campo, P. J. Rosenthal, W. Bu, F. J. Gamo, L. M. Sanz, M. Ge, L. Li, J. Ding and Y. Yang, *J. Med. Chem.*, 2015, **58**, 5344–5354.
- 156 F. Hilberg, G. J. Roth, M. Krssak, S. Kautschitsch, W. Sommergruber, U. Tontsch-Grunt, P. Garin-Chesa, G. Bader, A. Zoepfel, J. Quant, A. Heckel and W. J. Rettig, *Cancer Res.*, 2008, **68**, 4774–4782.
- 157 B. D. Bringardner, C. P. Baran, T. D. Eubank and B. Marsh, *Antioxid. Redox Signal.*, 2009, **10**, 287–301.
- 158 J. Strelow and J. Weidner, *Mechanism of Action Assays for Enzymes Assay Guidance Manual*, Eli Lilly & Company and the National Center for Advancing Translational Sciences, 2012.
- 159 TIBCO, 2016, TIBCO Spotfire v 7.6.0.
- 160 Y. Li and P. M. Woster, *Medchemcomm*, 2015, **6**, 613–618.
- 161 Cambridgesoft, 2016, Chem3D v15.1.
- 162 Graphpad Software, 2016, GraphPad Prism v 7.0.
- 163 J.-C. Andrez, P. R. Bichler, C.-A. Chen, S. Chowdhury, S. M. Decker, C. M. Dehnhardt, T. Focken, M. E. Grimwood, I. W. Hemeon, Q. Jia, J. Li, Z. Liu, D. F. Ortwine, B. Safina, D. Sutherlin, T. Sheng, S. Sun, A. D. White, M. S. Wilson, A. Y. Zenova and J. Zhu, *Genentech, inc. Xenon Pharm. inc.*, WO2015078374 A1, 2015.
- 164 H. Guo, D. Kato, J. O. Link, M. L. Mitchell, J. P. Parrish, N. Squires, J. Sun, J. Taylor, E. M. Bacon, E. Canales, A. Cho, J. J. Cottell, M. C. Desai, R. L. Halcolm, E. S. Krygowski, S. E. Lazerwith, Q. Liu, R. Mackman, J.-H. Pyun, J. H. Saugier, J. D. Trenkle, W. C. Tse, R. W. Vivian, S. D. Schroeder, W. J. Watkins, L. Xu, Z.-Y. Yang, T. Kellar, X. Sheng, M. O. H. Clarke, C. Chou, M. Graupe, H. Jin, R. McFadden, M. R. Mish, S. E. Metobo, B. W. Phillips and C. Venkataramani, *Gilead Sci. Inc.*, WO 2010132601 A1, 2010.
- 165 K. E. Schwiebert, D. N. Chin, J. C. MacDonald and G. M. Whitesides, *J. Am. Chem. Soc.*, 1996, **118**, 4018–4029.
- 166 E. B. Kornberg, A. R. Lewthwaite, D. D. Manning, S. S. Nikam and L. I. Scott, *Warn. Company*, WO0250070A3, 2000.
- 167 H. Prucher, R. Gottschlich, J. Leibrock and H. Schwartz, *Merck*, US5698553A, 1995.
- 168 O. Moradei, I. Paquin, S. Frecherre, T. Mallais, S. Roy, R. Machaalani, A. Vaisburh, J. M. Besterman, P. Tessier, J. Mancuso, D. Smil, S. Leit and R. Deziel, *Methylgen Inc.*, WO2007118137A1, 2007.
- 169 J. Li, R. Yang, R. Song, H. Zhu, N. Wu, L. Yun, R. Su and R. Zhao, *Inst. Pharmacol. Toxicol. Acad. Mil. Med. Sci. P.L.A. Beijing*, US2011319423A1.
- 170 M. J. B. Reginald David Adams, P. E. J. Davidson, E. C. Dawson, R. A. George, L. H. Mansell, P. Mattei, J. Mizrahi, H. M. Nettekoven, M. R. Pratt, R. J. R. Anthony, S. Roever, J.-L. Specklin, H. Stalder and K. Wilkinson, *F. Hoffman-La Roche, Vernalis Res. Limited*, WO0248124A2, 2002.

- 171 Amira Pharmaceuticals, WO2012024620A2, *Amira Pharm. WO2012024620A2*, 2012.
- 172 L. M. Miller, W.-J. Keune, D. Castagna, L. Young, E. Duffy, F. Potjewyd, F. Salgado, P. E. Garcia, D. Seeman, J. M. Pritchard, A. Perakis, S. J. F. Macdonald, C. Jamieson and A. J. B. Watson, 2016, Manuscript in Submission.
- 173 D. Castagna, D. C. Budd, S. J. F. Macdonald, C. Jamieson and A. J. B. Watson, *J. Med. Chem.*, 2016.
- 174 A. Riaz, Y. Huang and S. Johansson, *Int. J. Mol. Sci.*, 2016, **17**, 1–13.
- 175 E. Makarev, E. Izumchenko, F. Aihara, P. T. Wysocki, Q. Zhu, A. Buzdin, D. Sidransky, A. Zhavoronkov and A. Atala, *Cell Cycle*, 2016, **15**, 1667–1673.
- 176 K. Kato, H. Nishimasu, S. Okudaira, E. Mihara, R. Ishitani, J. Takagi, J. Aoki and O. Nureki, *Proc. Natl. Acad. Sci. U. S. A.*, 2012, **109**, 16876–81.
- 177 W.-J. Keune, F. Potjewyd, A. Perrakis, C. Jamieson, A. J. B. Watson, F. Salgado, T. Heidebrecht, L. Chelvarajan, A. A. Latif, S. Soman, S. J. F. Macdonald, A. J. Morris and A. J. B. Watson, 2016, Unpublished work.
- 178 J. M. Berg, J. L. Tymoczko, G. J. G. Jr. and L. Stryer, *Biochemistry*, Kate Ahr Parker, 8th edn., 2015.
- 179 R. A. Copeland, *Evaluation of Enzyme Inhibitors in Drug Discovery: A Guide for Medicinal Chemists and Pharmacologists: Second Edition*, 2013.
- 180 F. S. Polo, *Kinetic Study of the LysoPLD Activity of ATX*, Masters Thesis, VU University Amsterdam and The Netherlands Cancer Institute, 2016.
- 181 H. György, K. József, K. Mihály and E. Al., in *Introduction to Practical Biochemistry*, 2013, pp. 42–59.
- 182 J. P. Hughes, S. S. Rees, S. B. Kalindjian and K. L. Philpott, *Br. J. Pharmacol.*, 2011, **162**, 1239–1249.
- 183 A. K. Salous, M. Panchatcharam, M. Sunkara, P. Mueller, A. Dong, Y. Wang, G. a Graf, S. S. Smyth and A. J. Morris, *J. Lipid Res.*, 2013, **54**, 2775–84.
- 184 K. Thirunavukkarasu, B. Tan, C. Swearingen, G. Rocha, H. Bui, D. McCann, S. Jones, B. Norman, L. Pfeifer and J. Saha, *J. Pharmacol. Exp. Ther.*, 2016.
- 185 M. Cal, M. Jaremko, Ł. Jaremko and P. Stefanowicz, *J. Pept. Sci.*, 2013, **19**, 9–15.
- 186 Z. Xu, J. C. DiCesare and P. W. Baures, *J. Comb. Chem.*, 2010, **12**, 248–54.